Thermodynamic and Kinetic Modelling of Iron(III) Reduction with Sulfur Dioxide Gas

by

Chris Biley

Dissertation presented for the Degree

of

DOCTOR OF PHILOSOPHY

(Extractive Metallurgical Engineering)

in the Faculty of Engineering
at Stellenbosch University

Supervisor:
Dr. J.D.T. Steyl

Co-supervisor:
Prof. S.M. Bradshaw

March 2015

Declaration

By submitting this dissertation electronically, I declare that the entirety of the work contained therein is my own, original work, that I am the sole author thereof (save to the extent explicitly otherwise stated), that reproduction and publication thereof by Stellenbosch University will not infringe any third party rights and that I have not previously in its entirety or in part submitted it for obtaining any qualification.

Date: 23 February 2015 .....

Abstract

Thermodynamic and Kinetic Modelling of Iron(III) Reduction with Sulfur Dioxide Gas

C.A. Biley

Dissertation: PhD (Extractive Metallurgical Engineering)

March 2015

Recent developments in the atmospheric treatment of low-grade nickel laterite ores at Anglo American plc has culminated in the conceptual iron-focused laterite (ARFe) process. In addition to the recovery of nickel and cobalt from laterite ore, this process uniquely aims to recover iron as a saleable by-product. The reduction of soluble iron(III) (Fe(III)) by sulfur dioxide gas (SO_2) is central to the ARFe concept and represents a complex, multiphase system involving simultaneous gas-liquid mass transfer, thermodynamic speciation and chemical reaction. The chemistry of iron-containing systems is generally poorly understood and accurately predicting their behaviour is challenging, especially under aggressive hydrometallurgical conditions.

The primary objective of this work is the development of an engineering model capable of describing the rate and extent of ferric reduction with SO_2 under conditions typical of the ARFe process. Thermodynamic considerations provide a rigorous framework for the interpretation of chemical reactions, however little experimental data are openly available for the associated solution species in acidic iron sulfate systems.

A key contribution of this work, and critical for the development of the overall model, is the direct measurement of speciation in iron sulfate solutions. Raman and UV-vis spectroscopy were utilised to make direct speciation measurements in the various subsystems of the $Fe_2(SO_4)_3$-$FeSO_4$-H_2SO_4-H_2O system that were previously unavailable in the open literature. The $FeSO_4^+$ and $Fe(SO_4)_2^-$ species were explicitly identified and measurements were supported and rationalised by static computational quantum mechanical calculations and ultimately permit the calibration of a robust, ion-interaction solution

model with the explicit recognition of the important solution species up to 1.6 mol/kg $Fe_2(SO_4)_3$, 0.8 mol/kg H_2SO_4 over 25 – 90 °C.

Batch and continuous Fe(III) reduction kinetics were measured and the effects of initial $Fe_2(SO_4)_3$ and H_2SO_4 concentrations, temperature and in-situ neutralisation quantified. The retardation effect of sulfuric acid was observed to be the most significant factor influencing the initial reaction rate and the achievable extent of reduction at fixed residence time, which varied between about 20 and 80 % after 180 minutes of reaction.

A reaction mechanism that is limited by the slow ligand-to-metal electron transfer in the $Fe^{III}SO_3^+$ solution species' decomposition is proposed and spectroscopic measurements and computational quantum mechanical calculations are used to support this mechanism. A kinetic model, comprising a system of differential mass-balance equations, is incorporated into the thermodynamic framework. This reaction model permits the prediction of kinetic profiles over the full range of experimental conditions and can be incorporated into more elaborate simulation models of the ARFe circuit.

The specific original contributions of this work are

- The direct measurement of aqueous speciation in the $Fe_2(SO_4)_3$-H_2SO_4-H_2O system by Raman and UV-vis spectroscopy
- The development of a modelling framework to characterise speciation, activity coefficients and solubility in the mixed $Fe_2(SO_4)_3$-$FeSO_4$-H_2SO_4-H_2O system.
- The measurement of Fe(III) reduction kinetics using SO_2 in concentrated sulfate solutions as a function of initial composition and temperature.
- The development of a solution reaction model of Fe(III) reduction with SO_2 that accurately predicts the solution speciation and reaction rate with time as a function of composition and temperature.

Lastly, the vast complexity of industrial systems will nearly always result in a lack of specific experimental data that are required for the development of phenomenological models. This work emphasises the crucial role that engineering studies hold in the generation of such data to derive maximum practical value for industrial process development and optimisation.

Uittreksel

Termodinamiese en Kinetiese Modellering van Yster(III) Vermindering met Swaweldioksiedgas

("Thermodynamic and Kinetic Modelling of Iron(III) Reduction with Sulfur Dioxide Gas")

C.A. Biley

Proefskrif: PhD (Extractive Metallurgical Engineering)

Maart 2015

Onlangse ontwikkelinge in die atmosferiese behandeling van lae-graad nikkel lateriet erts by Anglo American plc het gelei tot die konseptuele yster gefokus lateriet (ARFe) proses. Bykommend tot die herwinning van nikkel en kobalt uit laterite erts is hierdie proses uniek en daarop gemik om yster te herwin as 'n verkoopbare by-produk. Die vermindering van oplosbare yster(III) (Fe(III)) met swaeldioksied (SO_2) is sentraal tot die ARFe konsep en verteenwoordig 'n komplekse, multifase stelsel wat gelyktydige gas-vloeistof massa-oordrag, termodinamiese spesiasie en chemiese reaksie behels. Die oplossingschemie van ysterstelsels word, oor die algemeen, swak verstaan en om hul gedrag akuraat te voorspel is 'n uitdaging, veral onder aggressiewe hidrometallurgiese kondisies.

Die primêre doel van hierdie werk is die ontwikkeling van 'n ingenieursmodel wat die tempo en omvang van yster(III) vermindering met SO_2 onder tipiese ARFe proses toestande beskryf. Termodinamiese oorwegings stel 'n streng raamwerk voor vir die interpretasie van chemiese reaksies, alhoewel daar egter min eksperimentele data openlik beskikbaar is vir die gepaardgaande oplossing spesies in suur yster(III) sulfaat stelsels. 'n Belangrike bydrae van hierdie werk, en van kritieke belang vir die ontwikkeling van die algehele model, is die direkte meting van spesiasie in yster(III) sulfaat oplossings. Raman en UV-vis spektroskopie is gebruik om direkte spesiasie metings te maak in die verskillende subsisteme van die $Fe_2(SO_4)_3$-$FeSO_4$-H_2SO_4-H_2O stelsel wat voorheen nie in die oop literatuur beskikbaar was nie. Die $FeSO_4^+$ en $Fe(SO_4)_2^-$ spesies uis ekplisiet

geidentifiseer, terwyl die metings ondersteun en gerasionaliseer is deur statiese kwantummeganiese berekeninge wat uiteindelik die kalibrasie van ’n robuuste, ioon-interaksie model tot gevolg hê wat ook die belangrike oplossingspesies duidelik beklemtoon tot en met 1.6 mol/kg $Fe_2(SO_4)_3$, 0.8 mol/kg H_2SO_4 en tussen 25 – 90 °C.

Enkellading en kontinue yster(III) verminderingskinetika is gemeet en die gevolge van die aanvanklike $Fe_2(SO_4)_3$ en H_2SO_4 konsentrasies, temperatuur en in-situ neutralisasie is gekwantifiseer. Die waargeneemde vertragingseffek van swaelsuur is die mees beduidende faktor wat die aanvanklike reaksietempo en die haalbare reaksie omvangsvermindering na ’n vaste residensietyd van 180 minute bepaal, wat wissel tussen ongeveer 20 en 80%.

’n Reaksiemeganisme word voorgestel wat beperk word deur die stadige ligand-tot-metaal elektronoordrag in ontbinding van die $Fe(III)SO_3^+$ oplossing-spesies en wat verder deur spektroskopiese metings en kwantummeganiese berekenings ondersteun word. A kinetiese model, wat bestaan uit ’n stelsel van gedifferensieerde massa-balans vergelykings, is in die termodinamiese raamwerk geinkorporeer. Hierdie reaksie-model laat die voorspelling van kinetiese profiele toe oor die volle omvang van die eksperimentele toestande en kan in meer uitgebreide simulasie modelle van die ARFe proces geinkorporeer word.

Die spesifieke en oorspronklike bydraes van hierdie werk is

- Die direkte meting van die spesiasie in die $Fe_2(SO_4)_3-H_2SO_4-H_2O$ stelsel deur Raman en UV-vis spektroskopie
- Die ontwikkeling van ’n modelraamwerk om spesiasie, aktiwiteitskoëffisiënte en oplosbaarheid in die gemengde $Fe_2(SO_4)_3-FeSO_4-H_2SO_4-H_2O$ stelsel te karakteriseer.
- Die meting van yster(III) vermideringskinetieka deur SO_2 in gekonsentreerde sulfate oplossings te gebruik as ’n funksie van die aanvanklike samestelling en temperatuur.
- Die ontwikkeling van ’n oplossingsreaksie-model van yster(III) vermindering met SO_2 wat die oplossing-spesiasie en reaksietempo met die tyd as ’n funksie van samestelling en temperatuur akkuraat voorspel.

Laastens, die oorgrote kompleksiteit van industriële stelsels sal byna altyd lei tot ’n gebrek van spesifieke eksperimentele data wat nodig is vir die ontwikkeling van fenomenologiese modelle. Hierdie werk beklemtoon die belangrike rol wat ingenieursstudies speel in die generasie van data wat sodanig tot maksimum praktiese waarde vir industriële prosesontwikkeling en optimalisering lei.

It can scarcely be denied that the supreme goal of all theory is to make the irreducible basic elements as simple and as few as possible without having to surrender the adequate representation of a single datum of experience.

Einstein, A., 1934, On the method of theoretical physics,
Philosophy of Science, Vol. 1, No. 2, pp. 163-169.

Acknowledgements

I would like to express my sincere gratitude to the following people for their support, assistance and interesting and fruitful discussions throughout this work:

Dr. Johann Steyl - Stellenbosch University

Prof. Steven Bradshaw - Stellenbosch University

Dr. Rudolph Erasmus - University of the Witwatersrand

Mr. Max Pelser - Anglo American plc

Dr. Leslie Bryson - Anglo American plc

Mr. Jeremy Mann - Anglo American plc

Mr. Paul Dempsey - (formerly) Anglo American plc

Dr. Maggie Burger - University of Pretoria

Dr. John Marsh - Sherritt Gordon

Mr. Jan Smit - Ecometales Limited

Contents

Nomenclature

Constants

b	Pitzer Constant - 1.2	$[\,(\mathrm{mol.kg^{-1}})^{1/2}\,]$
e	Electron charge - $1.602\,176\,487 \cdot 10^{-19}$	$[\,\mathrm{C}\,]$
k	Boltzmann coefficient - $1.380\,650\,4 \cdot 10^{-23}$	$[\,\mathrm{J.K^{-1}}\,]$
N_A	Avogadro's Number - $6.022\,141\,79 \cdot 10^{23}$	$[\,\mathrm{mol^{-1}}\,]$
R_g	Molar gas constant - $8.314\,472$	$[\,\mathrm{J.mol.K^{-1}}\,]$
ϵ_0	Vacuum permittivity - $8.854\,187\,817 \cdot 10^{-12}$	$[\,\mathrm{F.m^{-1}}\,]$
π	Pi - $3.141\,592\,654$	$[\,-\,]$

Variables

a	Debye-Hückel parameter	$[\,\mathrm{m}\,]$
A	Debye-Hückel parameter	$[\,(\mathrm{mol.kg^{-1}})^{1/2}\,]$
A_i	Integrated band area	$[\,\mathrm{a.u.}\,]$
A_i	Absorbance	$[\,\mathrm{a.u.}\,]$
a_i	Activity	$[\,\mathrm{mol.kg^{-1}}\,]$
B	Debye-Hückel parameter	$[\,(\mathrm{mol.kg^{-1}})^{1/2}.\mathrm{m^{-1}}\,]$
B_{ij}	Pitzer binary parameter (unlike)	$[\,(\mathrm{mol.kg^{-1}})^{-1}\,]$
C_{ij}	Pitzer binary parameter	$[\,(\mathrm{mol.kg^{-1}})^{-2}\,]$
c_i	Molar concentration	$[\,\mathrm{mol.dm^{-3}}\,]$
d	Density	$[\,\mathrm{mol.m^{-3}}\,]$
D	Ioninc diffusivity	$[\,\mathrm{m^2.s^{-1}}\,]$
Δx	Change in property x	$[\,-\,]$
e	Electron charge	$[\,\mathrm{C}\,]$
E_a	Activation Energy	$[\,\mathrm{J/mol}\,]$

F	Pitzer electrostatic function	$[\,\mathrm{C}^{-2}\,]$
G	Gibbs free energy	$[\,\mathrm{J}\,]$
g_{ij}	Radial distribution function	$[\,-\,]$
H	Enthalpy	$[\,\mathrm{J}\,]$
I	Ionic strength	$[\,\mathrm{mol.kg}^{-1}\,]$
J_i	Relative Molal Scattering Coefficient	$[\,-\,]$
K	Step-wise equilibrium constant	$[\,-\,]$
k	Rate constant	$[\,\mathrm{N/A}\,]$
k_c	Liquid mass transfer coefficient	$[\,\mathrm{m}^{-2}.\mathrm{s}^{-1}.\mathrm{dm}^3\,]$
k_La	Overall mass transfer coefficient	$[\,\mathrm{s}^{-1}\,]$
k_p	Vapour mass transfer coefficient	$[\,\mathrm{mol.m}^{-2}.\mathrm{s}^{-1}.\mathrm{Pa}^{-1}\,]$
m	Molal concentration	$[\,\mathrm{mol.kg}^{-1}\,]$
M	Mass	$[\,\mathrm{g}\,]$
MW_i	Molecular weight	$[\,\mathrm{g.mol}^{-1}\,]$
n_i	Amount	$[\,\mathrm{mol}\,]$
P	Pressure	$[\,\mathrm{Pa}\,]$
p	Partial pressure	$[\,\mathrm{Pa}\,]$
p_i	Pitzer Temperature Dependence Parameter	$[\,-\,]$
q	HSO_4^- stability constant parameter	$[\,-\,]$
r	Radius	$[\,\mathrm{m}\,]$
S	Entropy	$[\,\mathrm{J}\,]$
T	Temperature	$[\,\mathrm{K}\,]$
u_{ij}	Intermolecular mean force potential	$[\,\mathrm{k_B.T.m}^{-1}\,]$
w_i	Solubility product temperature dependence parameter	$[\,-\,]$
z	Relative charge	$[\,-\,]$
α_i	Pitzer constant	$[\,(\mathrm{mol.kg}^{-1})^{-1/2}\,]$
α_i	Dissociation fraction	$[\,\%\,]$
β	Cumulative equilibrium constant	$[\,-\,]$
$\beta_{ij}^{(0,1,2)}$	Pitzer binary parameter	$[\,(\mathrm{mol.kg}^{-1})^{-1}\,]$
d_{ion}	Ionic diameter	$[\,]$
ϵ_0	Vacuum permittivity	$[\,\mathrm{m}^{-3}.\mathrm{kg}^{-1}.\mathrm{s}^4.\mathrm{A}^2\,]$

ϵ_r	Relative permittivity	$[-]$
ϵ_i	Molar extinction coefficient	$[\,\mathrm{mol.dm^{-3}.cm^{-1}}\,]$
F	Objective function value	$[-]$
$\gamma_\pm$	Mean activity coefficient	$[-]$
γ_i	Individual ion activity coefficient	$[-]$
λ	Pitzer neutral species parameter	$[\,(\mathrm{mol.kg^{-1}})^{-2}\,]$
λ	Wavelength	$[\,\mathrm{nm}\,]$
λ_{ij}	Second virial coefficient	$[\,(\mathrm{mol.kg^{-1}})^{-2}\,]$
μ_{ijk}	Third virial coefficient	$[\,(\mathrm{mol.kg^{-1}})^{-3}\,]$
μ_i	Chemical potential	$[\,\mathrm{J.mol^{-1}}\,]$
ν_i	Stoichiometric coefficient	$[-]$
ν	Wavenumber or Raman shift	$[\,\mathrm{cm^{-1}}\,]$
Ω	Water molality	$[\,\mathrm{mol.kg^{-1}}\,]$
ϕ	Osmotic coefficient	$[-]$
Φ	Mass transfer enhancement factor	$[-]$
Φ_{ij}	Pitzer binary mixing parameter	$[\,(\mathrm{mol.kg^{-1}})^{-1}\,]$
Ψ_{ijk}	Pitzer ternary mixing parameter	$[\,(\mathrm{mol.kg^{-1}})^{-2}\,]$
ρ	Density	$[\,\mathrm{kg.m^3}\,]$
σ_i	Raman cross section	$[\,\mathrm{cm^2.molecules^{-1}}\,]$
θ_{ij}	Pitzer composite binary mixing parameter	$[\,(\mathrm{mol.kg^{-1}})^{-1}\,]$
$\tilde{\nu}$	Raman shift	$[\,\mathrm{cm^{-1}}\,]$
${}^E\theta_{ij}$	Higher order electrostatic effects	$[\,(\mathrm{mol.kg^{-1}})^{-1}\,]$
$\dot{X}$	Time derivative of X	$[\,\mathrm{s^{-1}}\,]$
X	Conversion	$[\,\%\,]$
x_i	Chemical analysis	$[\,\mathrm{mg/L}\,]$

Naming Conventions

Fe^{3+}	Hydrated ferric ion
Fe(III)	Total amount of ferric ion, i.e., all species. Used interchangeably with ferric
S(IV)	Total sulfur in the +4 oxidation state

S(VI)	Total sulfur in the +6 oxidation state
Par_{Pitzer}	Generic Pitzer parameters ($\beta^{(i)}_{MX}$, C_{MX}, etc.)
T_d	Tetrahedral symmetry
Λ	Symmetry representation

Subscripts/Superscripts

w	Water
0	Standard state
ex	Excess
id	Ideal
a	Anion
c	Cation
ref	Reference
b	Bulk
sat	Saturations
sp	Solubility Product

Acronyms

AARD	Average Absolute Relative Deviation
AAD	Average Absolute Deviation
ADF	Amsterdam Density Functional
CIP	Contact Ion Pair
COSMO	Conductor-Like Screening Model
DFT	Density Functional Theory
DO	Dissolved Oxygen
FWHH	Full-Width at Half-Height
HOMO	Highest Occupied Molecular Orbital
LUMO	Lowest Unoccupied Molecular Orbital
ORP	Oxidation/Reduction Potential
RSD	Relative Standard Deviation
RTD	Residence Time Distribution

PCA	Principal Component Analysis
SIP	Solvent Separated Ion Pair
2SIP	Doubly Solvent Separated Ion Pair
SVD	Singular value decomposition
SSA	Steady-State Approximation
SSE	Sum-of-Squared Error
STP	Standard Temperature and Pressure
TZ2P	Triple Zeta with Two Polarisation Functions basis set
XC	Exchange-Correlation Energy

Chapter 1

Introduction

1.1 Background and context

1.1.1 Laterite treatment technologies

The rapidly growing demand for base metals worldwide and the continued degeneration of base metal ore grades has made it increasingly important to develop processes for economical recovery of metals from low grade ores and secondary sources that cannot be treated efficiently by current processes. A recent estimate of the world's land-based nickel reserves reports that approximately 70% is present in the form of laterites, i.e. low grade oxide ores such as limonite (iron rich) and saprolite (magnesium rich) (Norgate and Jahanshahi, 2010). However, it has been estimated that only approximately 42% of current nickel production originates from the processing of laterite ores (McDonald and Whittington, 2008). Trends in historical nickel production, presented in Figure 1.1, highlight that the future of this commodity is undoubtedly going to involve the treatment of laterite ores that typically have lower grades and contain more impurities than the sulfide reserves.

Limonitic and saprolitic laterite ores are formed by a weathering of parent rock consisting of Fe-Mg-Si-O minerals and prolonged leaching of metals including valuable base metals into lower zones through the process of laterization, which can concentrate nickel and cobalt by a factor of 3 to 30 times that of the parent rock (Smit and Steyl, 2006). Typically, these ores contain approximately 1-3% nickel and a large fraction of iron and/or magnesium; with magnesium generally leaching to the lower saprolitic layers. Current processes for the treatment of nickel laterites include: pyrometallurgical treatment (FeNi smelting); the Caron process; the High Pressure Acid Leach (HPAL) process; as well as other sulphate and chloride based atmospheric processes (see McDonald and Whitting-

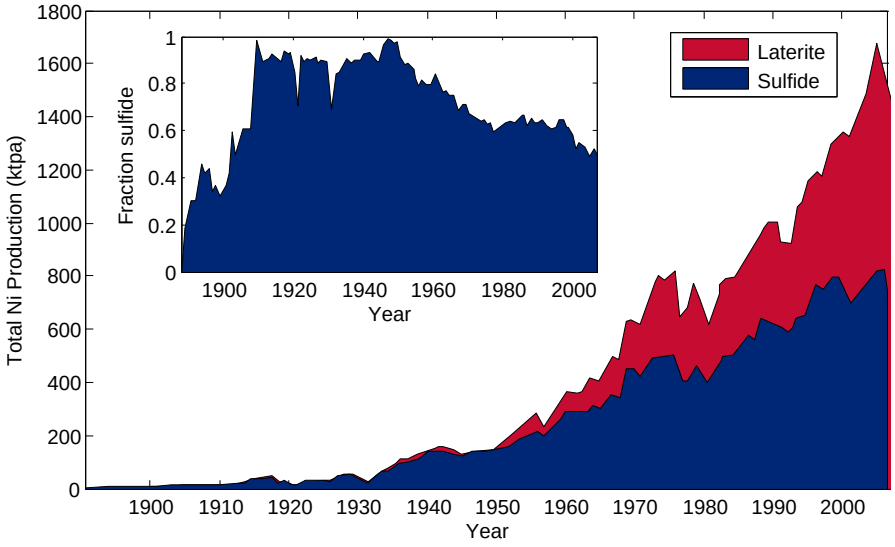

Figure 1.1: Historical nickel production from laterite and sulfide ores. Data from Mudd (2010).

ton (2008) and references within for a comprehensive review of current practices). However, the large fraction of acid consuming gangue minerals in these ores increases reagent costs, generates large waste streams and presents a key difficulty for the hydrometallurgical processing of laterites. Also, these processes are typically sensitive to the relative concentrations of contained impurities and thus the natural variability of the ore mineralogy due to variations in the geology presents additional difficulties (McDonald and Whittington, 2008).

Current trends in laterite treatment technology are moving towards atmospheric hydrometallurgical leaching to avoid the intensive capital requirements of large-scale autoclaves. Recent research themes at Anglo American PLC, have been focused on the development of processing circuits aimed at directly treating low grade laterite ores in an economic and sustainable manner (Smit and Steyl, 2006; Smit et al., 2011, 2012). The key aspect of these technologies is the regeneration of reagents within a closed-loop circuit, which shifts the cost drivers of the process from reagent-based to energy-based. This shift has the potential to unlock economic value as well as significantly decrease the waste generation of the process.

The ARFe process (Smit et al., 2011) was designed to treat iron-rich, nickel laterite ores and, along with high recoveries of the contained base metals, recover a high-purity, saleable iron by-product and regenerate leaching reagents within the process. The details of this process are discussed in Section 2.1, but briefly, the key steps in the hydrometal-

lurgical process involve the atmospheric leaching of laterite ore in sulfate media with SO_2, the removal of key impurity metals (excluding iron), the recovery of value metals contained in the ore (primarily nickel and cobalt) and the recovery of a pure iron sulfate salt. This salt is then treated pyrometallurgically to release sulfur as SO_2 to be recycled to the leaching section and generate an iron oxide product that is saleable in the context of blending with other iron ore concentrates.

Central to the ARFe concept is the generation of acid by absorption and reaction of SO_2 into the leaching liquor to reduce Fe(III) that is leached from the oxide ore. In this context, the solution phase reduction of Fe(III) by SO_2 in order to generate acid for leaching is proposed to occur according to the overall reaction stoichiometry shown in Equation 1.1.1.

$$\mathrm{Fe_2(SO_4)_{3(aq)} + SO_{2(g)} + 2\,H_2O_{(l)} \longrightarrow 2\,FeSO_{4(aq)} + 2\,H_2SO_{4(aq)}} \tag{1.1.1}$$

Ultimately, since SO_2 is the primary lixiviant source in the ARFe process, an improved understanding of the key drivers (and hindrances) to this reaction will determine the technical and economic feasibility of the ARFe leaching circuit and can, in conjunction with appropriate laterite leaching models, be incorporated into steady-state simulations of the circuit.

1.1.2 Additional applications

Iron is one of the earth's most abundant elements and, as noted above, sulfide ores represent a large fraction of the earth's naturally occurring minerals. As such, the ferric-ferrous sulfate and SO_2 systems, while central to the ARFe circuit chemistry, are widespread throughout various industrial and natural processes.

Iron is present as an unwanted impurity in nearly all hydrometallurgical refining circuits and typically needs to be removed and disposed in a safe and efficient manner. Typically this is done by precipitation to form a range of solids such as hematite, goethite or jarosite (Dutrizac and Monhemius, 1986). Numerous studies have been dedicated to the removal of iron from refractory gold sulfide ore (Berezowsky and Weir, 1989; Berezowsky et al., 1991) and zinc pressure leaching (Buban et al., 1999; Ismael and Carvalho, 2003), and PGM matte sulfide circuits (Dutrizac and Monhemius, 1986). Additionally, and undoubtedly more important in the future, heap or pressure leaching of chalcopyrite ($CuFeS_2$) ores and concentrates has been thoroughly investigated in the open literature (Dutrizac, 1981; Hackl et al., 1995; Wang, 2005; Kinnunen et al., 2006). With declining ore grades, many of these processes' economics are sensitive to residue disposal costs and thus effective iron management is critical. Extensive work has been carried out on

the operation and optimisation of these precipitation reactions on laboratory and industrial scale, but there still remains large gaps in our knowledge of the solution speciation leading to the formation (and rate of formation) of these precipitates.

Moreover, with tightening environmental constraints being imposed on industry, it is becoming increasingly important to produce stable waste residues. Significant work has been carried out on the stability of iron-rich residues from metallurgical plants, particularly since these precipitates often contain significant amounts of heavy metals such as As and Cd and can release these into the environment if not disposed of correctly (Welham et al., 2000). It is now well-understood that waste dumps containing plant tailings and waste residues readily oxidise and dissolve to form Acid Mine Drainage (AMD) that is typically characterised by extremely low pH (in natural systems) and a significant fraction of iron. Knowledge of the solublities of the various components of these solutions and the chemical species that are formed during the chemical processes is central to understanding the long-term effects of AMD and potential remediation strategies thereof (Johnson and Hallberg, 2005).

Besides the iron systems, sulfite is also routinely used as a cheap reducing agent in many hydrometallurgical circuits, for instance the reductive precipitation of Se and Te from copper advance solutions prior to electrowinning, typically carried out with Na_2SO_3 or SO_2 (Weir et al., 1982; Baldwin et al., 1983). Another application of sulfite is the leaching of Mn-rich deep sea nodules (Pahlman and Khalafalla, 1988; Das et al., 2000). Recently too, mixtures of SO_2/O_2 have been shown be a powerful oxidant and have potential application in rapid Fe(II) oxidation at low temperature as well as Mn(II) oxidation to form the sparingly soluble Mn(III) ion.

Sulfur dioxide is also released into the atmosphere by numerous natural and industrial activities and is most important as the precursor for acid rain production. As such, much work has been carried out on the atmospheric autooxiation of sulfite, which is catalysed by even trace amounts of transition metals (Brandt and van Eldik, 1995). A large body of work in these dilute systems has been performed, although large discrepancies regarding the exceedingly complex reaction mechanisms still exist.

Thus, while the ferric-ferrous and sulfite systems are important for the development of the ARFe process, these systems have a large number of applications outside these confines and, as briefly outlined here, significant gaps in our knowledge of these systems remain a key difficulty in the design and operation of efficient and sustainable industrial processes.

1.2 Scope of this study

Mass-and-energy-balance models provide an extremely useful tool in the development of conceptual circuits as well as understanding the operation of existing processes. Specifically, such models provide an enhanced means of interpreting impacts of laboratory test findings on full-scale operations and facilitate analysis of the complex interactions typically associated with industrial flowsheets. However, the development of such models is often hindered by the level of understanding of the fundamental chemistry of these processes and ultimately limits the predictive ability of these models. Despite the wide number of industrial and natural processes containing soluble iron species, comparatively little is known of their inherent chemistry, i.e., the thermodynamic and kinetic behaviour of species in these systems, particularly under aggressive and concentrated conditions typically encountered in hydrometallurgy. This is attributed, at least in part, to the complex nature of these systems and the inherent difficulties associated with their study.

The ARFe leaching circuit represents a complex hydrometallurgical system with a number of integrated unit operations and recycle streams. In order to develop an understanding of this system, the various processes need to be examined independently, while remaining cognisant of the inherent interrelationships associated with the process. The specific scope of this study is thus to investigate the chemical aspects controlling the rate and achievable extent of ferric reduction with SO_2 under conditions expected in the ARFe leaching circuit. However, as stressed above, the widespread prevalence of iron-containing systems and the general lack of knowledge of the chemistry of these systems under aggressive hydrometallurgical conditions makes the insights into the chemical behaviour of iron in concentrated solutions developed in this work much more widely applicable.

Moreover, while the scope of this work is to investigate the fundamental aspects of the system of interest, distinct focus on the practical use of these findings will be made, and the implications for the optimal operation of the ARFe leaching circuit highlighted.

1.3 Study objectives

The ultimate engineering objective of this work is the development of a kinetic model of ferric reduction with SO_2 in concentrated sulfate solutions at elevated temperature. Such a model will facilitate enhanced process simulation of the larger ARFe flowsheet to highlight key process economics and technical feasibility. The predictive ability of such models is largely influenced by the assumptions on which they are constructed and, in

the case of this specific system, the quantification of solution phase speciation and the associated kinetic data have not been developed in the literature. Instead of relying on complex assumptions regarding the chemistry of this system, the measurement and characterisation of solution speciation, particularly in acidic ferric sulfate solutions form a central part of the study. This newly measured data facilitates the development of an advanced, engineering modelling framework for predicting kinetics in the case-study system.

The specific objectives of this work are:

1. To quantify the rate and extent of Fe(III) reduction using SO_2 in concentrated, acidic sulfate solutions relevant to the conditions expected in the ARFe conceptual circuit.

2. To systematically investigate solution speciation in the various binary and ternary systems in the Fe^{3+}-Fe^{2+}-H^+-SO_4^{2-}-SO_2-H_2O system and to define the main species present in concentrated sulfate solutions.

3. To develop a self-consistent thermodynamic modelling framework to consolidate the measured solution speciation trends and provide a platform for interpreting kinetic processes in the reactive system.

4. To develop an engineering modelling framework that is capable of quantifying the kinetics of ferric reduction with SO_2 under aggressive hydrometallurgical conditions.

1.4 Summaries of work

The primary areas of work presented in this thesis are summarised as follows:

Chapter 2 reviews the current state of knowledge of the thermodynamics of various binary and ternary systems pertinent to the overall reactive system as well as addresses previous studies that involve the use of SO_2 as a reagent in ferric-containing systems. An outline of solution modelling techniques and theory is also briefly discussed.

Chapter 3 presents the experimental apparatus, procedures and analyses used throughout this study.

Chapter 4 presents an investigation into the thermodynamics of the various sub-systems applicable to this study. Static computational DFT calculations are used to rationalise the trends observed in Raman and UV-vis spectral measurements of solutions and ultimately quantify previously unavailable speciation data in the Fe^{3+}-Fe^{2+}-H^{+}-SO_4^{2-}-H_2O system over 25 - 90 °C.

Chapter 5 presents the systematic development of a multi-component solution model that characterises solution speciation data using a practical, minimum-parameter approach.

Chapter 6 details the investigation into the reaction kinetics of ferric reduction with SO_2, including mass transfer, as a function of acid and ferric concentrations, temperature and batch vs. continuous operation. On the basis of the experimental findings, a reaction mechanism is proposed and validated using spectroscopic measurements and static DFT calculations.

Chapter 7 extends the proposed reaction mechanism to develop a modelling framework for the kinetic process of ferric reduction with SO_2 that is based on the thermodynamic basis developed in Chapter 5. The resulting solution model provides an excellent characterisation of observed kinetic trends and facilitates the calculation of the achievable reaction extents and rates in laboratory and commercial reactors.

Chapter 8 presents the conclusions of the study and highlights the most important aspects of this study for the development of the ARFe concept.

Chapter 2

Literature Review

The primary objective of this study involves the development of a solution modelling framework to describe of the kinetics of ferric reduction with sulfur dioxide in concentrated sulfate solutions, applicable to conditions expected in the ARFe process concept. Knowledge of the pertinent chemistry, existing modelling frameworks, and key aspects of the various Fe^{3+}-Fe^{2+}-H^{+}-SO_4^{2-}-SO_2-H_2O subsystems is thus required. This chapter presents a review the current state of knowledge regarding these systems as well as the concepts of mass transfer and solution modelling. The hypothesized importance of the characterisation of thermodynamic speciation in understanding the reaction kinetics in the system above thus requires particular focus in the various subsystems as well as previous investigations into kinetics in systems containing dissolved sulfite in the presence transition metals.

2.1 The ARFe process[1]

Nickel laterites are difficult to exploit economically due to variable mineralogical composition, stable oxide compounds, low nickel grade and limited up-grading potential. Nickel occurs as a minor metal hosted in almost all of the other minerals by substitution or inclusions, making it difficult to upgrade using conventional physical methods. The processing of laterites requires energy and/or aggressive chemical attack to recover nickel as well as near complete treatment of the bulk ore, which results in large operational costs. As such, processes developed for nickel laterites need to be robust to accommodate variability in mineral composition, efficient in the utilisation of energy and reagents and highly

[1]This section was published in its entirety in Biley et al. (2013)

effective in recovering nickel. The economics will also benefit from producing saleable by-product from the bulk elements in the deposit.

2.1.1 Regenerative atmospheric leaching

Current trends in the development of processes for nickel laterites are moving towards atmospheric hydrometallurgical flowsheets aimed at reducing capital cost. The processes are operated under aggressive conditions resulting in almost complete digestion of the ore. The high reagent additions are compensated by regenerating the primary reagents from intermediate by-products. A number of these regenerative atmospheric leach (RAL) processes have been proposed including systems using the sulfate, chloride and nitrate systems (McDonald and Whittington, 2008; McCarthy and Brock, 2011). Anglo American has also developed and piloted a RAL process known as the Anglo Research Nickel (ARNi) process (Smit and Steyl, 2006; Steyl and Smit, 2008). This process utilises a mixed sulfate-chloride system and is capable of treating the full spectrum of minerals present in laterites. An additional challenge subsequently set to the development team was to recover other saleable by-products, in particular iron from limonitic type ore deposits, leading to the development of the iron focussed laterite (ARFe) process (Smit et al., 2011).

ARFe is a sulfate based atmospheric leaching process where the primary reagents are regenerated from an intermediate by-product by thermal decomposition. The concept of the ARFe process is illustrated in Figure 2.1 where limonite ore is simplified as FeOOH. In the lixiviant cycle, ore is digested using acid to produce a base metal sulfate solution. The acid is generated in solution by absorbing and oxidising SO_2 to sulfate, while reducing Fe(III) to Fe(II). Ferrous sulfate is recovered as an intermediate crystal product and the solution is returned to the leach to close the cycle and the crystal product is further processed in the sulfur cycle. Ferrous sulfate is thermally decomposed to produce iron oxide and SO_2, which is returned to the lixiviant cycle to close the circuit. SO_2 is the primary reagent in this process concept and is fully regenerated.

2.1.2 ARFe base-case block flow diagram

The ARFe processing concept is translated into a base-case block flow diagram in Figure 2.2 (adapted from Smit et al. (2011)). The chemistry of the key unit processes are discussed in Section 3 of this paper. Limonite ore is digested in the leaching step by direct addition of SO_2, which is known to accelerate the leaching of limonitic ores (McDonald and Whittington, 2008). The direct addition of SO_2 produces more protons per mole

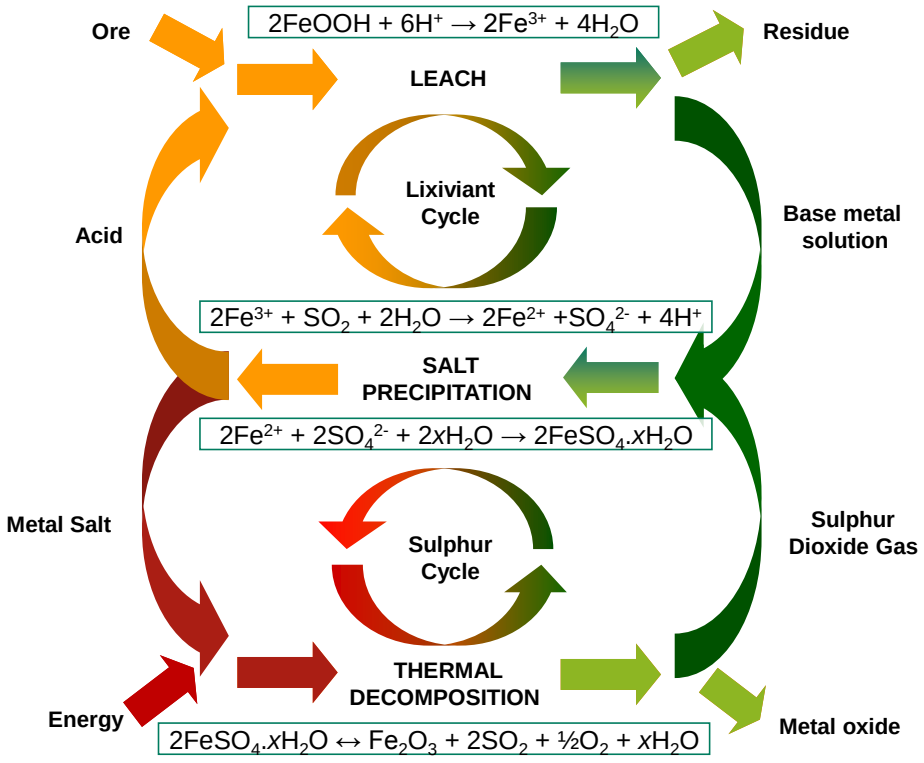

Figure 2.1: Schematic figure of the ARFe concept showing the interactions between the hydrometallurgical and pyrometallurgical circuits, clearly showing the regenerative sulfur cycle. Taken from Biley et al. (2013).

sulfur ($4H^+/SO_4^{2-}$) as compared to H_2SO_4 ($2H^+/SO_4^{2-}$). The amount of acid produced at complete reduction of Fe(III) from the ore is insufficient for the leaching requirement. Additional acid can be generated by re-oxidation of Fe(II) in solution or by the addition of H_2SO_4 to the process, further described in Section 3. The leaching step operates close to the solubility limit of ferrous sulfate. A dissolution step is included after the leaching to dissolve any crystals that may have formed by adjusting the temperature. After solid-liquid separation, the solution it is sent to the crude crystallisation step to produce $FeSO_4 \cdot 7\,H_2O$ by cooling crystallisation. The hepta-hydrate form of ferrous sulfate has a large capacity to incorporate other divalent base metals in its structure. This facilitates the recovery of the minor base metals from solution into a bulk crystal for further processing. This eliminates the neutralisation requirements usually associated conventional circuits and decouples the leaching and value recovery circuits. The solution

from crystallisation is returned to the leach step to complete the leaching section.

The $FeSO_4 \cdot 7\,H_2O$ crystals are further processed to separate the metals in a second circuit called the value-recovery section. The function of this section is not only to recover the value metals (nickel and cobalt), but also to recover a sufficiently pure ferrous sulfate product from which a saleable by-product can be produced. The crystals are dissolved and then neutralised to remove aluminium, chromium and iron(III). Next, nickel and cobalt are recovered in the mixed sulfide precipitation step using hydrogen sulfide. The mixed sulfide precipitate is the final nickel product in the base-case circuit. Mixed sulfide precipitation produces a ferrous sulfate solution which is then subjected to the evaporation step to remove excess water and simultaneously form ferrous sulphate monohydrate ($FeSO_4 \cdot H_2O$) crystals.

Both the neutralisation and mixed sulfide precipitation steps require neutralising agents and it would be undesirable to introduce any foreign cations into the closed circuit. For this reason ferrous hydroxide is used as the primary neutralising agent, which is generated from neutralisation of a bleed stream with a commonly available neutralising agent. The bleed stream also aids the removal of excess water and other group (I) and (II) metals (sodium, potassium and magnesium) from the circuit.

The $FeSO_4 \cdot H_2O$ produced from the value-recovery section is transferred to the decomposition section. In this circuit the ferrous sulfate is decomposed thermally to iron oxide (a by-product) and SO_2. Decomposition of ferrous sulfate is an endothermic reaction occurring at temperatures approaching 1000 °C. The SO_2 stream is split between a direct addition to the leaching step and production of H_2SO_4 in an acid plant. The split is dictated by the total acid demand of the ore and the amount of iron(III) ions extracted from the ore; with direct addition sufficient for the complete reduction of these ions.

2.1.3 Iron deportment control

Iron is the predominant metallic species in limonitic ores and it is crucial to manage the solubility of ferrous sulfate in the circuit to control the deportment of iron. In the leach section, ferrous sulfate needs to be retained in solution during solid-liquid separation step to minimise losses to the residue and then allowed to crystallise in the crude crystallisation step to recover the intermediate product. Illustrated in Figure 2.3 is the solubility behaviour of pure ferrous sulfate as a function of temperature between 25 and 100 °C. The leach is operated close to the boiling point of the solution to achieve high leaching kinetics. The operating conditions and the amount of iron extracted would result in supersaturation at point 1. It exceeds the solubility of $FeSO_4 \cdot H_2O$ causing ferrous sulfate to crystallise, lowering the solution concentration to point 2. To avoid ferrous sulfate

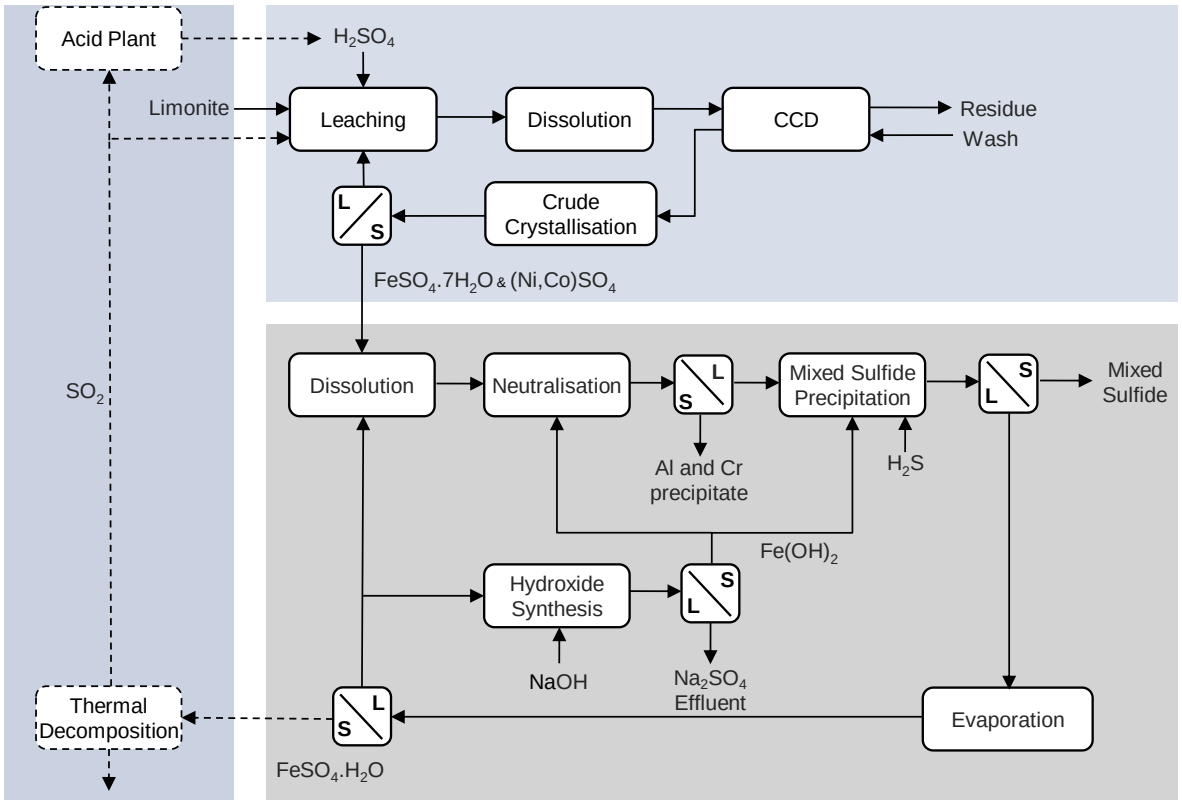

Figure 2.2: Block-flow diagram: The ARFe base-case (adapted from Smit et al. (2011)). The leaching, value-recovery and pyrometallurgical circuits are highlighted in the blocks as well as the major products in each stream.

losses during solid-liquid separation, the temperature is lowered causing the $FeSO_4 \cdot H_2O$ to dissolve (point 3). The solution is then further cooled in the crude crystallisation step causing the formation of $FeSO_4 \cdot 7\,H_2O$ and reducing the solution concentration to point 4 which is returned to the leaching step.

The circuit is a closed loop and the solution can only accommodate as much iron from the leaching step as can be removed during the cooling crystallisation step. The concentration of point 1 is determined by the amount of iron extracted and is related to the leach pulp density. Point 4 lies on the solubility curve and the extent of crystallisation is therefore determined by the operating temperature of the crystalliser. As a result, the leach pulp density is limited to approximately 10% (solids/(solids+water)) for a typical limonite ore and a crystalliser temperature of 20 °C. The value recovery section is similarly constrained between the solubility in the dissolution step and the evaporation step.

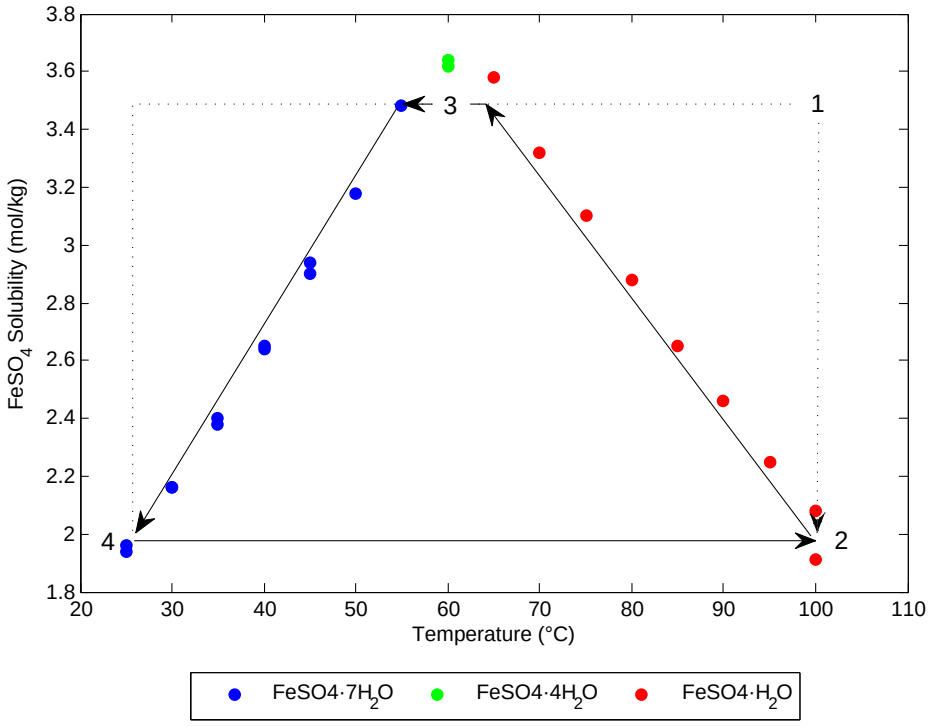

Figure 2.3: Solubility behaviour of ferrous sulfate at selected points in the ARFe leach section. Point 1 & 2: Atmospheric leaching operation (maximum temperature); Point 3: Dissolution (maximum solubility); Point 4: Crude crystallisation (minimum temperature). Data points from Linke and Seidell (1965).

2.1.4 Atmospheric leaching

The dissolution of FeOOH, i.e., the main component of the ore, in acidic sulfate media produces Fe(III) ion in solution and consumes 3 mol H^+/mol Fe, presented in Reaction 2.1.1. Central to the ARFe process concept is the exploitation of the oxidized form of leached iron to oxidise SO_2 in solution and thereby partially regenerating the acid consumed during leaching, shown in Reaction 2.1.2.

$$2\,\mathrm{FeOOH}_{(s)} + 3\,\mathrm{H_2SO_4} \longrightarrow \mathrm{Fe_2(SO_4)}_{3(aq)} + 4\,\mathrm{H_2O}_{(l)} \tag{2.1.1}$$

$$\mathrm{Fe_2(SO_4)}_{3(aq)} + \mathrm{SO}_{2(g)} + 2\,\mathrm{H_2O}_{(l)} \longrightarrow 2\,\mathrm{FeSO}_{4(aq)} + 2\,\mathrm{H_2SO}_{4(aq)} \tag{2.1.2}$$

If sufficient Fe(III) is available in solution to facilitate the high conversion, the reduction to Fe(II) using SO_2 is capable of producing two thirds of the acid demand of the idealised FeOOH phase. In order to maintain the acid balance of the circuit, additional

Fe(III) ion can be generated by oxidizing process solution with oxygen or air, according to Reaction 2.1.3.

$$2\,FeSO_{4(aq)} + 0.5\,O_{2(g)} + H_2SO_{4(aq)} \longrightarrow Fe_2(SO_4)_{3(aq)} + H_2O_{(l)} \tag{2.1.3}$$

A complete reduction-oxidation cycle of Reactions 2.1.2 and 2.1.3 will produce the balance of the acid demand of the FeOOH phase and additional cycling will be required to meet the complete acid demand of the ore. Alternatively, H_2SO_4 can be added directly to the leaching circuit to fulfil acid requirements.

While the ARFe concept is still in a developmental stage, the ranges of typical conditions expected in the leaching operation can be summarised as follows (Smit et al., 2011; Biley et al., 2013):

- Total soluble iron concentrations are governed by the solubility limits of $FeSO_4$ in the leaching liquor, that is, between 1 - 3.6 mol/kg from Figure 2.3, allowing for the depression of solubility by other solution components.
- Total H_2SO_4 concentrations of 0.5 - 2 mol/kg.
- Base and other impurity metals at concentrations of similar ratio to iron as in the laterite ore, i.e., typically less than 5% of the total ionic concentration.
- Temperatures at or close to the boiling point of the solution.
- SO_2 and/or O_2 gas sparged into the solution at atmospheric pressure.

These conditions represent the boundaries on concentrations and temperature for the ARFe leaching section, that form the basis for the focus of the experimental work in this study.

2.2 Gas-liquid mass transfer

In the study of reactions kinetics in systems where a gaseous reagent is used, it is imperative that the effects of mass transfer are quantified to ensure these can be separated from the underlying chemical reaction kinetics. The principles of mass transfer of a gas into solution have been well documented and are typically expressed in the form:

$$\frac{dC_A}{dt} = \Phi k_L a (C_A^{sat} - C_A) \tag{2.2.1}$$

Where C_A is the concentration of the gaseous reagent in solution, C_A^{sat} is the solubility concentration of the gas in the solution and k_La is the overall mass transfer coefficient. The enhancement factor, Φ, accounts for the enhancement of mass transfer by chemical reaction in the gas-liquid film (Charpentier, 1981). Ideally, mass transfer coefficients should be measured under conditions either where reaction of the gas is negligible (i.e., a direct method) or where the enhancement factor of the specific reaction can be reliably estimated. By examining the ratio of maximum possible conversion in the gas-liquid film and the maximum diffusion transport through the gas-liquid film, one may ascertain the potential for reaction in the film and subsequent enhancement of mass transfer. This chemical-rate-to-physical-rate ratio is captured in the dimensionless Hatta number, written for a $(mn)^{th}$ order reaction (Charpentier, 1981):

$$Ha = \frac{1}{k_L}\sqrt{\frac{2}{m+1}k_{mn}D_A(C_A^{sat})^{m-1}(C_B^b)^n} \tag{2.2.2}$$

Where k_L is the liquid mass transfer resistance, k_{mn} is the $(mn)^{th}$ order rate constant, D_A and C_A^{sat} the diffusivity and solubility of the gaseous species in the solution and C_B^b is the bulk concentration of the solution phase reagent. By examining the size of the Hatta number, the relative importance of mass transfer enhancement by reaction in the film can be inferred; with $Ha >> 1$ suggesting the reaction occurs entirely in the liquid film ($\Phi >> 1$) and with $Ha << 1$ with essentially no reaction occurring within the film ($\Phi \approx 1$). For intermediate values of Ha, various regimes are important and an approximate enhancement factor can be estimated from the solution to a general form of mass transport equations for gas A into solution B (see Charpentier (1981)). Difficulties in estimating the enhancement factor are induced via the scarcity of reliable diffusivity coefficients and, in certain cases, the underlying mechanism of reaction such that Equation 2.2.2 becomes difficult to quantify.

Alternative means of characterising mass transfer rates involve experimental methods in the reaction vessel of interest. The oxidation of sulfite by oxygen in aqueous media is a common method for determination of the mass transfer coefficients. Although the rate of sulfite oxidation is quite slow, the reaction is catalysed by transition metals and typically sufficient cobalt is added to ensure that the Ha number is approximately unity. Under these conditions, provided the heat generation of the oxidation can be managed, the oxidation reaction does not occur in the gas-liquid boundary, but is sufficiently fast to ensure that the concentration of oxygen in the bulk is zero. With reference to Equation 2.2.1, knowledge of the oxygen saturation and measurement of the sulfite concentration with time (stoichiometrically related to the oxygen concentration) facilitate the determination

of the mass transfer coefficient.

Of course, while the mass transfer coefficient can be measured in this way, for typical hydrometallurgical reactions or conditions, no knowledge of the enhancement factors (or even the Ha number) is available and other means of determining if mass transfer limitations are present are typically used. For instance, since agitation speed and gas flow rate are both known to affect mass transfer, these can be used to determine if mass transfer limitations exist. Further details of specific methods of mass transfer measurement will be discussed in Chapter 3.

2.3 Solution thermodynamics

2.3.1 Basic thermodynamic principles

The Gibbs free energy is a key concept in dealing with chemical thermodynamics and is related to the enthalpy and entropy of a specific system via the well known thermodynamic relationship:

$$G = H - TS \tag{2.3.1}$$

Of greater use is a partial derivative of the total Gibbs free energy with respect to the amount of component i in the system, which yields the partial molar Gibbs free energy or the chemical potential of this component in the system:

$$\mu_i = \bar{G}_i = \left(\frac{\partial G}{\partial n_i}\right)_{T,P,n_i \neq n_j} \tag{2.3.2}$$

Generally speaking, all the chemical potentials of the components which comprise a system determine the equilibrium state of that system, since matter always transitions spontaneously from a region of high chemical potential to a region of low chemical potential. The point of equilibrium thus lies where all the chemical potentials of a system are equivalent. As with all thermodynamic properties, a standard state reference is required and for an ideal system, the ideal chemical potential can be shown to be equal to:

$$\mu_i^{id} = \mu_i^0 + RT \ln x_i \tag{2.3.3}$$

where x_i is the mole fraction of species i in the system. However, in order to quantify real systems, one needs to account for the non-idealities involved due to interactions among the various components. This is incorporated into the chemical potential by an excess function:

$$\mu_i = \mu_i^{id} + \mu_i^{ex} \tag{2.3.4}$$

To determine the equilibrium point of a specific system, knowledge of the standard state and the excess contributions to the chemical potential are required. This concept is developed further, specifically for the case of aqueous chemical thermodynamics through the definition of the equilibrium constant.

2.3.2 Definition of the equilibrium constant

To account for chemical equilibria between dissociated ions and complexes (or species in another phase), mathematical mass-action expressions are employed. Each mass-action equation is defined by an equilibrium constant, typically defined as the ratio of concentrations of the associated species to the product of concentration of their constituent free ions, written in simplest form:

$$\mathrm{M}^{\mathrm{m+}}_{(\mathrm{aq})} + \mathrm{X}^{\mathrm{x-}}_{(\mathrm{aq})} \rightleftharpoons \mathrm{MX}^{(\mathrm{m-x})+}_{(\mathrm{aq})} \tag{2.3.5}$$

$$K_{i,T,P} = \frac{[\mathrm{MX}^{(\mathrm{m-x})+}_{(\mathrm{aq})}]}{[\mathrm{M}^{\mathrm{m+}}_{(\mathrm{aq})}][\mathrm{X}^{\mathrm{x-}}_{(\mathrm{aq})}]} = \frac{m_{MX}}{m_M \cdot m_X} \tag{2.3.6}$$

where square brackets represent the molal concentrations of each component. These equilibrium constants are readily measured by traditional thermodynamic means (i.e., potentiometry, calorimetry, colligative properties, etc.) and typically extrapolated, by suitable treatment, to zero ionic strength to give the standard state thermodynamic equilibrium constant, K^0_i, for the specific species. However, measured equilibrium constants such as those in Equation 2.3.6 are only valid at the conditions they were measured at and will vary with solution concentrations, temperature and pressure. Thus, activities (written as curly brackets in Equation 2.3.7) are used to capture the variation in the *apparent* species concentrations and facilitate the calculation of the thermodynamic equilibrium constant at infinite dilution, which is only a function of temperature:

$$K^{\circ}_{i,T,P} = \frac{\{\mathrm{MX}^{(\mathrm{m-x})+}_{(\mathrm{aq})}\}}{\{\mathrm{M}^{\mathrm{m+}}_{(\mathrm{aq})}\}\{\mathrm{X}^{\mathrm{x-}}_{(\mathrm{aq})}\}} = \frac{m_{MX}}{m_M \cdot m_X} \cdot \frac{\gamma_{MX}}{\gamma_M \cdot \gamma_X} = K_{i,T,P} \cdot \Gamma_{i,T,P} \tag{2.3.7}$$

Similarly, step-wise (K_n) and cumulative (β_n) forms of the equilibrium constants are often published in the literature and they are related as follow:

$$K^0_n = \frac{a_{MX_n}}{a_{MX_{n-1}} a_X} = \frac{m_{MX_n}}{m_{MX_{n-1}} m_X} \cdot \frac{\gamma_{MX_n}}{\gamma_{MX_{n-1}} \gamma_X} = K_n \cdot \frac{\gamma_{MX_n}}{\gamma_{MX_{n-1}} \gamma_X} \tag{2.3.8}$$

$$\beta^0_n = \frac{a_{MX_n}}{a_M a^n_X} = \frac{m_{MX_n}}{m_M m^n_X} \cdot \frac{\gamma_{MX_n}}{\gamma_M \gamma^n_X} = \beta_n \cdot \frac{\gamma_{MX_n}}{\gamma_M \gamma^n_X} \tag{2.3.9}$$

The thermodynamic equilibrium constant is directly related to the partial molar Gibbs free energy of reaction according to Equation 2.3.10, of which the activity coefficients describe the excess Gibbs free energy contribution:

$$K^0_{i,T,P} = \exp\left(\frac{-\Delta\bar{G}^0_{i,T,P}}{RT}\right) \tag{2.3.10}$$

Thus, knowledge of the thermodynamic equilibrium constant *and* the variation in species activity coefficients for a range of conditions, facilitates the calculation of the concentrations of the free and associated ions of a particular system which can be performed with the appropriate mass-action equations and an overall mass balance.

2.3.3 Excess Gibbs free energy

Activity coefficients, introduced above, attempt to describe the *apparent* solution concentration and account for non-idealities in the an electrolyte system. Activity coefficients are directly related to the excess partial molar free energy of species i in a solution in the following way:

$$\mu_i^{ex} = RT \ln \gamma_i \tag{2.3.11}$$

Combining with Equations 2.3.3 and 2.3.4 yields:

$$\mu_i = \mu^0 + RT \ln m_i\gamma_i = \mu^0 + RT \ln a_i \tag{2.3.12}$$

where a_i is the activity of species i in the solution. These equations have been presented in a molal basis, which is often useful in thermodynamic studies, with unsymmetrical, rational activity coefficients. That is, the pure component reference state for the solvent, $\gamma_{solvent} \to 1$ as $x_{solvent} \to 1$, and the infinitely dilute reference state for the solute ions, $\gamma_{solute} \to 1$ as $x_{solute} \to 0$. This scale is preferred over volume based scales due to its independence on temperature and pressure, while the mole fraction basis tends to unnecessarily complicate the models (for example see Pitzer (1991), Ch.3, Appendix. I). Furthermore, common practice is to select a standard state as a 1 mol/kg, ideal, hypothetical solution, $m^0 = 1$ mol/kg with $\gamma = 1$, and this will be adopted throughout this work.

Thus, it is apparent that the chemical potential of a species in solution is given by a reference potential and the activity of the species within the solution and that knowledge of these quantities would allow the solution problem to be solved.

Individual ion activity coefficients cannot be directly measured due to electroneutrality limitations, and thus the mean activity coefficient which can be experimentally measured is defined as:

$$\gamma_{\pm} = \left(\gamma_M^{\nu_1}\gamma_X^{\nu_2}\right)^{1/(\nu_1+\nu_2)} \tag{2.3.13}$$

This represents a primary constraint in the calibration of thermodynamic models, especially those that consider complex formation, as the individual ion activity coefficients are merely convenient representations that are, at best, thermodynamically feasible. The water activity, a_w, is often measured via experimental methods which involve measurement of the water vapour pressure, which can be related to the water activity and osmotic coefficient by the following well known expression:

$$\ln a_w = \ln \frac{p_w}{p_w^0} = \frac{-\phi}{\Omega}\sum_i m_i \tag{2.3.14}$$

Where p_w/p_w^0 is the fraction of water vapour pressures measured in an electrolyte system and that of pure water, ϕ is the osmotic coefficient and $\Omega = 1000/MW_w = 55.508$. Evident from the above expression that the osmotic coefficient depends on the sum of the molalities of all the solution species in the system.

Lastly, the water activity (or osmotic coefficient) and the activity coefficient are directly related to the excess contribution to the partial molar Gibbs free energy of the system through the following derivatives:

$$\ln \gamma_i = \left[\frac{\partial G^{ex}/n_w RT}{\partial m_i}\right]_{n_w} \tag{2.3.15}$$

$$\phi - 1 = \frac{-\left[\partial G^{ex}/\partial n_w\right]_{n_w}}{RT\sum m_i} \tag{2.3.16}$$

2.3.4 Inner and outer sphere complexes

In reality, the association of ions to contact ion pairs (CIP), as described in Reaction 2.3.5, occurs in a stepwise association mechanism through doubly-separated (2SIP) and singly-separated (SIP) outer-sphere complexes by the progressive expulsion of water (Eigen and Tamm, 1962; Marcus, 2006) as shown generically below:

$$K_{i,1}: \quad \mathrm{M}^{\mathrm{m}+}_{(\mathrm{aq})} + \mathrm{X}^{\mathrm{x}-}_{(\mathrm{aq})} \rightleftharpoons [\mathrm{M}^{\mathrm{m}+}(\mathrm{H_2O})(\mathrm{H_2O})\mathrm{X}^{\mathrm{x}-}]_{(\mathrm{aq})} \tag{2.3.17}$$

$$K_{i,2}: \quad [\mathrm{M}^{\mathrm{m}+}(\mathrm{H_2O})(\mathrm{H_2O})\mathrm{X}^{\mathrm{x}-}]_{(\mathrm{aq})} \rightleftharpoons [\mathrm{M}^{\mathrm{m}+}(\mathrm{H_2O})\mathrm{X}^{\mathrm{x}-}]_{(\mathrm{aq})} + \mathrm{H_2O} \tag{2.3.18}$$

$$K_{i,3}: \quad [\mathrm{M}^{\mathrm{m}+}(\mathrm{H_2O})\mathrm{X}^{\mathrm{x}-}]_{(\mathrm{aq})} \rightleftharpoons [\mathrm{MX}]^{(\mathrm{m}-\mathrm{x})}_{(\mathrm{aq})} + \mathrm{H_2O} \tag{2.3.19}$$

Importantly, the *hydration* of the overall complex species in Equation 2.3.6 measured by traditional thermodynamic means is typically not considered and the resulting equilibrium constant, thus includes all contributions from 2SIP's, SIP's and CIP's, i.e., $K_{i,1-3}$ above.

Certain techniques, such as Raman spectroscopy, are only sensitive to the detection of CIPs, where a direct chemical bond between metal and ligands exist. As a result, equilibrium constants derived from Raman spectroscopic data are not directly comparable to those measured using techniques that include outer-sphere complexes (Hefter, 2006). Formally, the equilibrium constant derived from such methods are of the form[2]:

$$\mathrm{M}^{\mathrm{m+}}_{(\mathrm{aq})} + \mathrm{X}^{\mathrm{x-}}_{(\mathrm{aq})} + [\mathrm{M}^{\mathrm{m+}}(\mathrm{H_2O})(\mathrm{H_2O})\mathrm{X}^{\mathrm{x-}}]_{(\mathrm{aq})} + [\mathrm{M}^{\mathrm{m+}}(\mathrm{H_2O})\mathrm{X}^{\mathrm{x-}}]_{(\mathrm{aq})} \rightleftharpoons [\mathrm{MX}]^{(\mathrm{m-x})}_{(\mathrm{aq})} \tag{2.3.20}$$

In instances where outer-sphere complexation is significant, the equilibrium constants that describe the K_{Raman} process above will not be directly comparable to literature values obtained by thermodynamic means. Certain techniques, such as ultrasonic and dielectric absorption spectroscopy (Hefter, 2006) are sensitive for these hydrated ion pairs, however, data are typically scarce. Besides, while knowledge of the total inner- and outer-sphere species may be important for certain applications, the formation of contact ion pairs can generally be considered most important for the interpretation of kinetic processes such as reactions, transport phenomenon and precipitation as the strong metal-ligand interactions in CIPs typically, but not exclusively, dominate the solution chemistry. Indeed, modelling studies have often characterised the behaviour of complex electrolyte systems by assuming that the effects of outer-sphere complexes are captured in the behaviour of the dissociated ions, that is, included in the electrostatic and short-range interaction terms of the *free* ions (Papangelakis et al., 1994; Liu and Papangelakis, 2005; Steyl, 2012).

2.4 S(IV) aqueous chemistry

Sulfur dioxide gas exhibits a high solubility in aqueous solutions, in comparison with other common gases such as O_2, N_2, CO_2 which is reflected in a low Henry's law constant of 82.9-88.7 kPa.kg.mol^{-1} (Rodriguez-Sevilla et al., 2002) that is nearly three orders of magnitude smaller than for example O_2 with $H_{O_2} = 7.77 \times 10^4$ kPa.kg.mol^{-1} (Perry

[2]Note that this expression is unbalanced and is intended to show that the stability constant measured by Raman is formed from the free and outer-sphere complexed ions which are usually undetectable by this technique.

et al., 1997) . This is primarily due to the slight polar charge distribution of the SO_2 molecule which interacts strongly with the water dipole. As a result of this interaction, the acid-dissociation of aquated sulfur dioxide must be considered in aqueous systems:

$$SO_{2(g)} \rightleftharpoons SO_{2(aq)} \tag{2.4.1}$$

$$SO_{2(aq)} + H_2O \rightleftharpoons H^+ + HSO_3^- \tag{2.4.2}$$

$$HSO_3^- \rightleftharpoons H^+ + SO_3^{2-} \tag{2.4.3}$$

These equilibria highlight the importance of mass transfer as well as the strong pH dependence of S(IV) speciation in aqueous systems. It has been shown that the second dissociation of sulphurous acid (Reaction 2.4.3) only becomes important above ca. pH 5 at 25°C (Pourbaix and Pourbaix, 1992).

Solubility data for SO_2 presented in Figure 2.4 show the SO_2 solubility in pure water as a function of temperature as well several data of the solubility in various $H_2SO_{4(aq)}$ solutions up to ca. 65% (m/m) H_2SO_4 (Kuznetsov, 1941). These data indicate that the solubility of SO_2 is a strong function of temperature, but weakly dependent on the concentration of H_2SO_4. Interestingly, above 85% H_2SO_4 (50% mol/mol) the solubility of SO_2 drastically increases due to the solution species comprising primarily of oleum ($SO_3 \cdot xH_2O$).

Additional SO_2 solubility data in several non-reactive sulfate and chloride solutions over a wide range of partial pressures, presented in Figures 2.5 and 2.6, also show strong temperature dependence and a largely insensitive relationship with ionic strength. For example, variation in concentration of Na_2SO_4 from 0.5 mol/kg to 4 mol/kg realises a variation in SO_2 solubility of approximately 0.25 mol/kg, where as a temperature increase from 60 to 90 °C results in a change in solubility of about 1.5 mol/kg (at P_{SO_2} = 6 bar). The concentration effect is more pronounced in chloride media, specifically NH_4Cl and NaCl, potentially due to the known affinity for SO_2 to form solution complexes such as SO_2Cl^- (Krissmann et al., 1997, 2000). However, for practical purposes, and at atmospheric pressures, the effects of SO_2 partial pressure and temperature can be considered significantly more important than the ionic strength effects for SO_2 solubility.

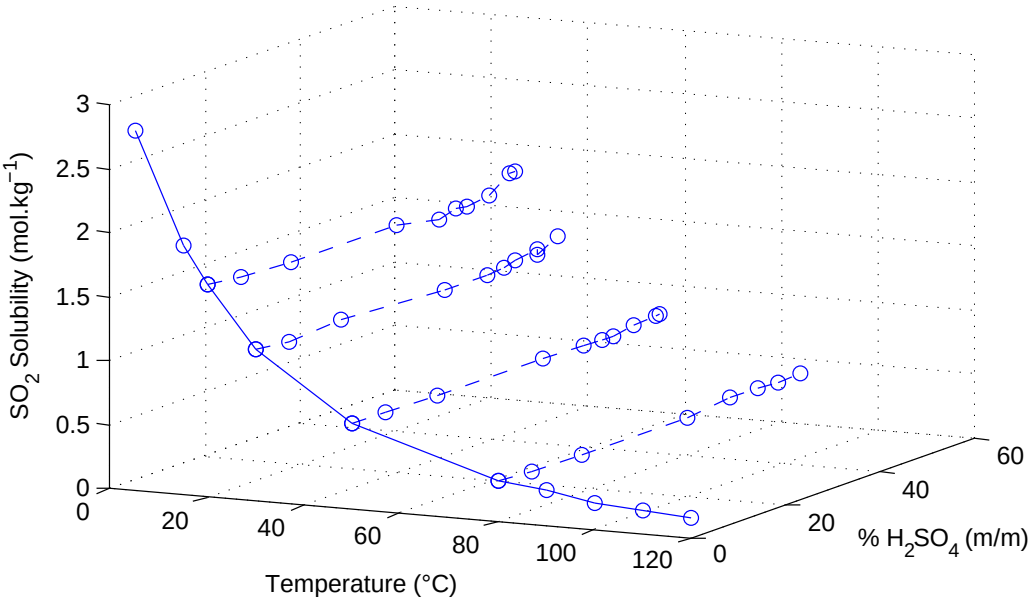

Figure 2.4: SO_2 solubility in water and solutions of sulphuric acid. SO_2 solubility in water is shown by the solid line and at various $H_2SO_{4(aq)}$ concentrations up to 65% (m/m). Data from Kuznetsov (1941).

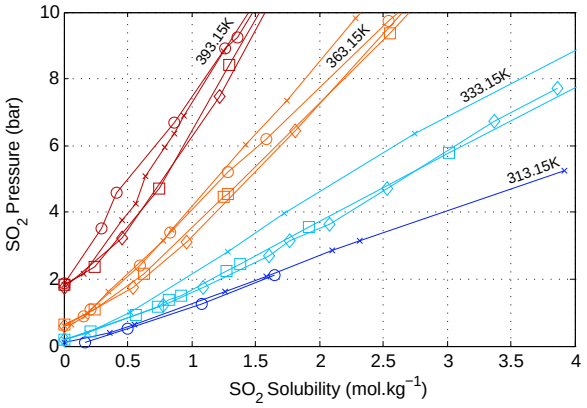

Figure 2.5: SO_2 solubility in $Na_2SO_{4(aq)}$ solutions. Na_2SO_4 concentrations: ○: 0.5M, ×: 1M,□: 2M, ◇: 4M. (Rumpf and Maurer, 1993)

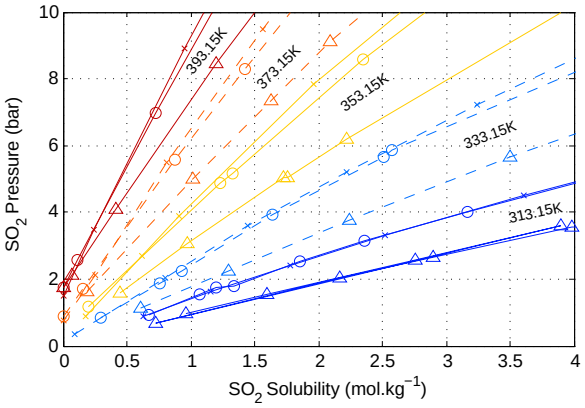

Figure 2.6: SO_2 solubility in $NaCl_{(aq)}$ and $NH_4Cl_{(aq)}$ solutions. NaCl conc.: ○: 2M, ×: 4M. NH_4Cl conc. △: 4M (Xia et al., 1999)

2.5 Fe^{2+} aqueous chemistry

2.5.1 Hydrolysis

Significant differences can be expected in the behaviour of Fe(II) and Fe(III) ions in solution based on their differing electronic structure and ionic radii. Ferrous ion adopts a closed-shell [Ar]$3d^6$ electronic configuration and a typical ionic radii of 0.78 Å in a high-spin ligand field, compared to the open-shell [Ar]$3d^5$ configuration and 0.645 Å radius of ferric (Shannon, 1976). Among other factors, this results in ferrous ion generally having a lower tendency to form solution complexes. This is exemplified when comparing the magnitude of stability constants for the first hydrolysis product of Fe(II) and Fe(III) in Tables 2.1 and 2.3. According to a rigorous analysis of available data and magnetite (Fe_3O_4) solubility, Sweeton and Baes Jr. (1970) suggest that the most reliable estimate for the formation of the $FeOH^+$ species, via Reaction 2.5.1, is $\log_{10} K^0 = -9.3$, i.e. approximately seven orders of magnitude smaller than the equivalent Fe(III) hydroxyl species.

$$Fe^{2+} + H_2O \rightleftharpoons FeOH^+ + H^+ \tag{2.5.1}$$

Table 2.1: Thermodynamic constants for Fe^{2+} hydrolysis at 25 °C taken from Sweeton and Baes Jr. (1970)

Temperature	Ionic Strength	System	$\log_{10}$K
20 °C	0.25, 0.5 M	CH_3COOH	-7.9
20 °C	0 (corr.)	$Fe(ClO_4)_2$	-5.9
25 °C	1 M	$NaClO_4$	-9.5 ± 0.2
25 °C	0 (corr.)	$Fe(OH)_2$ solubility	-8.3 ± 0.2
25 °C	0.5 M	KCl	-7.17
25 °C	dilute	$FeCl_2$	-7.92
25 °C	0.5-2 M	$NaClO_4$	-6.74 ± 0.09
25 °C	very dilute	Fe_3O_4 solubility	-9.3 ± 0.5
25 °C	dilute	$FeCl_2$	-9.58 ± 0.08

The importance of Fe(II) hydrolysis products for solution modelling purposes in multi-electrolyte solutions, particularly when acid is present, is regarded so small that many authors have neglected these complexes for practical modelling applications (Stipp, 1990; Liu et al., 2003; Papangelakis et al., 1994). In the context of this case-study system in this work, i.e., concentrated and acidic $Fe_2(SO_4)_3$ solutions, the same approach is to be

adopted and, this assumption validated on the basis of the ability to explain experimental observations.

2.5.2 Fe^{2+}-SO_4^{2-} speciation

The tendency for Fe(II) contact ion pairs in sulfate solutions is also expected to be significantly lower than that of Fe(III). A Mössbauer spectroscopy study of quenched Fe(II) solutions with perchlorate, sulfate and chloride counter-ions reported strikingly similar radial distribution functions for the three ligands (Kalman et al., 1988). Since perchlorate is known to be a non-complexing ligand, this highlights the weak affinity for contact ion pairing in this system, at room temperature. Water and sulfate coordination numbers to the ferrous ion of 5.8 and 0.2 respectively were measured in this study, emphasising that the hydrated $Fe(H_2O)_{6(aq)}^{2+}$ species is dominant in solution. Additionally, Raman studies of $FeSO_4$ solutions highlighted that the $FeSO_4^0$ contact ion pair was only formed to a minor extent at room temperature and hydrated $Fe(H_2O)_6^{2+}$ dominated the solution speciation (Rudolph et al., 1997; Sobron et al., 2007). While these studies are relatively limited in their *quantification* of CIP concentrations in $FeSO_4$ solutions, a significant amount of spectroscopic studies have been carried out for other divalent sulfate solutions such as $MgSO_4$ (Rudolph et al., 2003; Buchner et al., 2004; Akilan et al., 2006b), $CuSO_4$ (Akilan et al., 2006a), $ZnSO_4$ (Rudolph et al., 1999), $CdSO_4$ (Rudolph and Irmer, 1994), $BeSO_4$ (Rudolph, 2010), $NiSO_4$ and $CoSO_4$ (Chen et al., 2005). These studies have highlighted the formation of contact, solvent separated and doubly solvent separated ion pairs in these solutions, albeit with generally large uncertainties due to the difficult nature of these measurements.

In addition, divalent sulfate systems have been rigorously modelled using a variety of thermodynamic models (Pitzer and Mayorga, 1974b; Pitzer, 1975; Reardon and Beckie, 1987; Archer and Rard, 1998; Balarew et al., 2001; Casas et al., 2005; Liu and Papangelakis, 2005; Kobylin et al., 2007; Ninkovic et al., 2007; Jones et al., 2009). Typically, these studies do not take cognisance of solution species and adopt only an ion-interaction approach. Recently however, Steyl (2012) highlighted the benefits of including the $FeSO_4^0$ contact ion pair within a modelling framework to properly account for the kinetic interactions of sulfate in ferrous oxidation and iron precipitation at elevated temperatures. In the present study, due to the high sulfate background and elevated temperatures, and it is likely that the capturing of Fe(II) ions into a neutral species may be significant for the description of the kinetic processes during ferric reduction and it is thus proposed to include the effects of the $FeSO_4^0$ CIP within the model.

While some thermodynamic data for the $FeSO_4$ system is available in the open literature, relatively little is known about the chemical nature of the $FeSO_4^0$ contact ion pair, especially at elevated temperatures. Rudolph et al. (1997) used Raman spectroscopy to study a 1.95 mol/kg $FeSO_4$ solution up to 303°C and estimated the association to the $FeSO_4^0$ contact ion pair to be 13%, 25% and 36% at 25, 95 and 150 °C respectively. In order to model divalent sulfates in metallurgical solutions, it has been proposed to use the $MgSO_4$ aqueous system as surrogate system as substantially more thermodynamic data are available in open literature (Steyl, 2012). The basis for this approach is two-fold, firstly, the lack of thermodynamic data for these systems, especially in multi-electrolyte systems, demands that some means of simplification is required in order to produce meaningful analyses of real systems for engineering purposes. Secondly, there is a remarkable similarity in the thermodynamic properties, such as overall equilibrium constants (see Table 2.2) and mean activity coefficients, between $MgSO_4$ and other divalent transition metal-sulfates, such as copper, zinc, iron and nickel sulfate (Steyl, 2009). Furthermore, measured speciation data of $MgSO_4^0$ at 25 °C agrees well with the data of Rudolph et al. (1997) for $FeSO_4^0$ under similar conditions (Hefter, 2006).

Association constants of CIPs are typically significantly lower than the overall stability constants in systems where outer-sphere interactions are important. In a thorough review of divalent metal sulfate systems, and supporting static quantum calculations, Steyl (2012) proposed a value of $\log_{10} K^0 = 1.5$ for the association of $MgSO_4^0$ and this value was adopted in this study and not the value of 2.2 typically taken for total speciation studies, shown in Table 2.2. Furthermore, the DRS study of Akilan et al. (2006b) facilitated estimation of the individual contributions of 2SIP, SIP and CIP's to the association of $MgSO_4^0$ and they estimated that ΔH^0_{CIP} = 19 kJ/mol with no contribution from $\Delta C^0_{p,CIP}$.

Table 2.2: $\log_{10}K^0$, ΔH° values for divalent metal sulfate CIP formation at 25 °C (Martell and Smith, 1976)

Overall Association	$\log_{10}K^0$	ΔH^0 (kCal/mol)
$Mg^{2+} + SO_4^{2-} \rightleftharpoons MgSO^0_{4(aq)}$	2.23 ± 0.07	0.51 ± 0.03
$Fe^{2+} + SO_4^{2-} \rightleftharpoons FeSO^0_{4(aq)}$	2.20 ± 0.06	0.56 ± 0.02
$Cu^{2+} + SO_4^{2-} \rightleftharpoons CuSO^0_{4(aq)}$	2.26 ± 0.07	1.22 ± 0.03
$Zn^{2+} + SO_4^{2-} \rightleftharpoons ZnSO^0_{4(aq)}$	2.49 ± 0.04	0.63 ± 0.02
$Ni^{2+} + SO_4^{2-} \rightleftharpoons NiSO^0_{4(aq)}$	2.81 ± 0.09	0.41 ± 0.02

2.6 Fe^{3+} aqueous chemistry

2.6.1 Hydrolysis

Aqueous ferric systems have a strong tendency to hydrolyse at even relatively low pH values, i.e., pH 2-3, and can form an array of aqueous hydrolytic species, the form of which is influenced by the Fe(III) concentration, background media and temperature. While most of the solutions important to this work contain added acid, in contrast to the Fe(II) systems, it was nevertheless required to take cognisance of hydrolysis which becomes increasingly important at elevated temperatures. The most common hydrolysed Fe(III) aqueous species reported in the literature include: Fe^{3+}, $FeOH^{2+}$, $Fe(OH)_2^+$ and $Fe_2(OH)_2^{4+}$ (Flynn, 1984). Rapid increases in pH of Fe(III) solutions at room temperature typically cause the precipitation of a red hydrolytic polymer, which can vary in structure and composition substantially depending conditions; ultimately forming a variety of iron precipitates, i.e., goethite (FeOOH), hematite (Fe_2O_3), magnetite (Fe_3O_4) or, more commonly, polymorphic Fe-(hydroxy)oxide compounds. Precipitation processes are exceedingly complex due the contributions of both thermodynamic aspects, i.e., solution speciation and solubility limits, and kinetic aspects that are influenced by supersaturation ratios and the crystallisation regime of the system. Despite this, many commercial hydrometallurgical processes utilise pH adjustment as a means of rejecting Fe(III) and, as such, many studies have attempted to build chemical models of these processes to characterise Fe(II) oxidation kinetics, Fe(III) solubility and precipitation under industrial conditions (Dutrizac and Monhemius, 1986; Steyl, 2012).

The hydrolysis products for several commonly reported ferric hydroxyl aqueous species are presented in Table 2.3. Obviously, as with other metal systems, these hydrolytic species become increasingly important at higher pH and temperature, i.e., typically entropically driven (Stefansson and Seward, 2008). However, the general lack of reliable data of these species typically limits the number of Fe(III) hydroxyl species to $FeOH^{2+}$ and $Fe(OH)_2^+$ in geochemical models containing acid (Stipp, 1990).

The experimental quantification of metal ion hydrolysis is typically performed in an inert media such that dissociated OH^- species are the only assumed complexing ligands available to the metal ions. While this technique can provide high quality estimates of the thermodynamic parameters of the species, these solutions represent an oversimplification of *real* solutions as short range intermolecular forces are typically small compared to the electrostatic effects. Direct utilisation of the ionic strength dependence of the equilibrium constants, while providing some indication into the electrostatic effects, does not accurately capture the solution interactions in more complex systems, where other com-

Table 2.3: Thermodynamic hydrolysis products of Fe(III)-OH_n species at 25 °C

Reaction	$\log_{10}\beta^\circ$	Reference
$Fe^{3+} + H_2O \rightleftharpoons FeOH^{2+} + H^+$	-2.18	Wagman et al. (1982)
	-2.19	Liu et al. (2003)
	-2.17	Papangelakis et al. (1994)
	-2.19	Stipp (1990)
	-2.2	Flynn (1984)
	-2.19	Martell and Smith (1976)
$2\,Fe^{3+} + 2\,H_2O \rightleftharpoons Fe_2(OH)_2^{4+} + 2\,H^+$	-2.91	Papangelakis et al. (1994)
	-2.9	Flynn (1984)
	-2.90	Martell and Smith (1976)
$Fe^{3+} + 2\,H_2O \rightleftharpoons Fe(OH)_2^+ + 2\,H^+$	-7.19	Wagman et al. (1982)
	-6.89	Liu et al. (2003)
	-5.70	Papangelakis et al. (1994)
	-5.69	Stipp (1990)
	-5.7	Flynn (1984)
	-5.70	Martell and Smith (1976)
$Fe^{3+} + 3\,H_2O \rightleftharpoons Fe(OH)_3^0 + 3\,H^+$	-9.84	Papangelakis et al. (1994)
	-11.7	Flynn (1984)
$Fe^{3+} + 4\,H_2O \rightleftharpoons Fe(OH)_4^- + 4\,H^+$	-21.60	Papangelakis et al. (1994)
	-21.7	Flynn (1984)

plexing components are present. Extrapolation of such data to real solutions, especially at elevated temperatures where data becomes even more scarce, must be treated with care. In this study, while a range of Fe(III) hydroxyl species may be present in solution, these species are not expected to dominate the solution environment (see Sections 2.6.2 and 5.5) and only the most relevant CIP will be considered to pragmatically reduce model complexity, while not sacrificing an adequate description of available experimental data.

2.6.2 Fe^{3+}-SO_4^{2-} speciation

In addition to the hydrolytic Fe(III) species that may exist in $Fe_2(SO_4)_3$ solutions at even low pH, a number of ferric sulfato species have been reported in the literature. However, due to the complexities associated with $Fe_2(SO_4)_3$ systems, supporting molecular information for the existence and the structure of these complexes are generally not considered in modelling studies (Majzlan and Myneni, 2005). Usually, convenient stoichiometries are assumed that capture (albeit sometimes artificially) the trends observed in experimental data such as solubility, pH and conductivity. Within the framework of this

Table 2.4: Thermodynamic data for $Fe(SO_4)_n^{3-2n}$ species. All data are with reference to the conventional unsymmetrical standard state at 25 °C.

Reaction	ΔG^0 (kJ/mol)	ΔH^0 (kJ/mol)	S^0 (J/mol.K)	ΔC_p^0 (J/mol.K)	$\log_{10}\beta^0$	Ref.
$Fe^{3+} + SO_4^{2-} \rightleftharpoons FeSO_4^+$	-23.74	26.32	167.37	453.79	4.160	(a)
	-23.57	25.90	166.12	335.01	4.129	(b)
	-23.47	25.97	165.80	-	4.112	(c)
$Fe^{3+} + 2\,SO_4^{2-} \rightleftharpoons Fe(SO_4)_2^-$	-31.14	39.28	235.17	781.62†	5.456	(a)
	-30.79	38.46	232.67	781.62†	5.394	(b)

(a): Liu et al. (2003), (b) Papangelakis et al. (1994), (c) Wagman et al. (1982)
†Calculated from BLCM reaction, see Section 5.5

study, a review of Fe_3^+-SO_4^{2-} species was necessary, with the aim of selecting the most important, experimentally verified contact ion pairs that are expected under the conditions of this study.

Stipp (1990) reviewed the $Fe^{2+}-Fe^{3+}-H^+-SO_4^{2-}$ system and collated the most notable studies published since the 1950's. It was suggested that, in "*geochemical models for acid, high iron-sulfate waters*", two contact ion pairs can be considered are most important, namely; $FeSO_4^+$ and $Fe(SO_4)_2^-$. Thermodynamic stability constants as a function of ionic strength for these species are presented in Figure 2.7, where they have been linearised according to the method proposed by Grenthe et al. (2000) for the extrapolation of measured stability constants to infinite dilution; data was taken from Martell and Smith (1976). Stipp (1990) recommends the values $\log_{10}\beta_1^0 = 4.04\pm0.1$ and $\log_{10}\beta_2^0 = 5.38\pm1.0$ for the mono- and di-sulfato complexes of Fe(III) respectively, which are close to those calculated in Figure 2.7, viz., 4.05 and 5.45 respectively as well as those from more recent studies presented in Table 2.4.

An interesting and important trend can be inferred from the slope of the robust linear fits to the stability constant function for both sulfate complexes in Figure 2.7, which are almost identical. This highlights that the electrostatic interactions of the these species with the non-complexing perchlorate medium are very similar. Thus, despite their significant differences in stoichiometry and thermodynamic stability, their long range interactions are strikingly similar, which is an important point for the consideration of these species in the modelling framework developed in this study. Additionally, the few data that are available at temperatures other than 25 °C suggest that the stability constants for both sulfato species increases with increasing temperature. This is in agreement with reported enthalpies and entropies of formation for these species presented in Table 2.4.

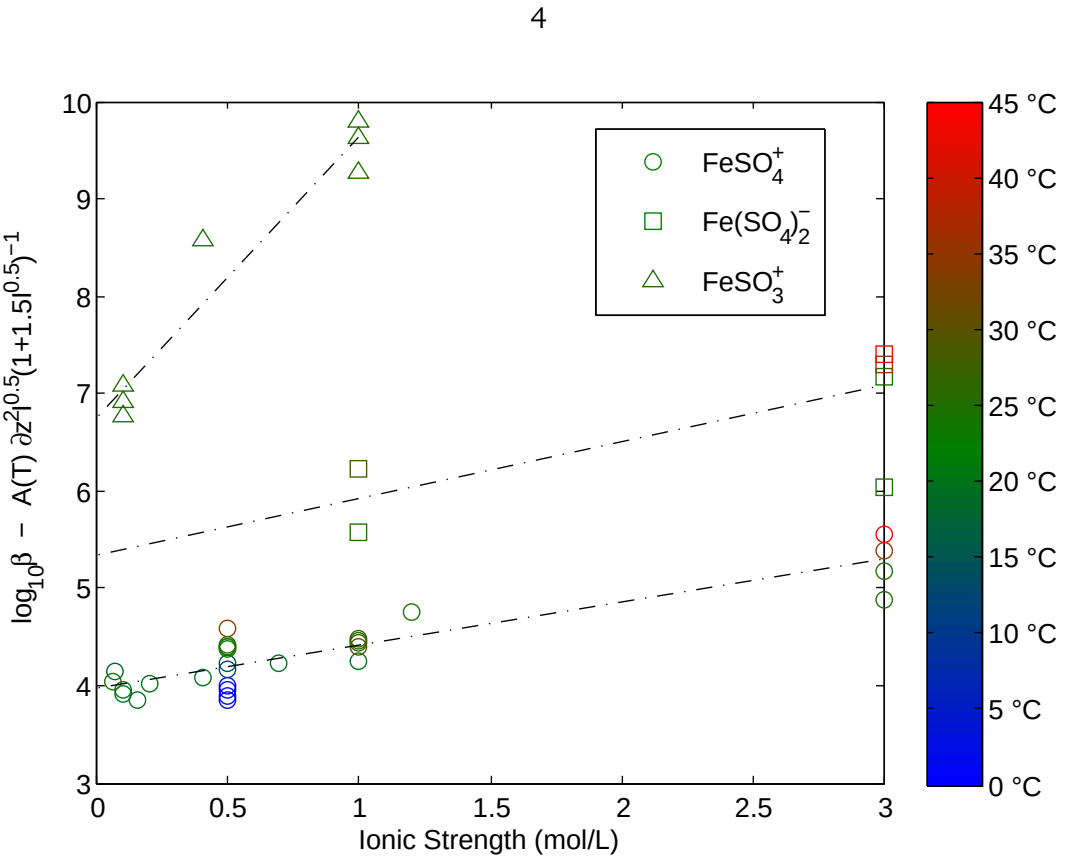

Figure 2.7: Fe(III)-S(IV) and Fe(III)-S(VI) stability constants as a function of ionic strength. Data are plotted as $\log_{10}\beta(I,T) - \frac{A(T)\Delta z^2\sqrt{I}}{1+1.5\sqrt{I}}$ vs. I for the extrapolation to zero ionic strength (see Grenthe et al. (2000) for details). Data from Martell and Smith (1976); Hogfeldt (1982); Kuo et al. (2006).

In addition to these species, others have also been proposed. Recently, $Fe_2(SO_4)_3$ speciation was investigated in H_2SO_4 solutions ($H_2SO_4 \approx 2.2$ mol/kg), primarily through pH and conductivity changes with Fe(III) concentration at 25 and 50°C (Casas et al., 2005). Raman spectroscopy was used to motivate for the inclusion of a neutral, previously unreported $FeH(SO_4)_2^0$ species in their model of concentrated acidic solution on the basis of Raman bands in the 242-282 cm^{-1} region. This species depletes free protons and decreases the calculated ionic strength of the solution, thereby capturing the decrease in measured solution conductivity (dominated by the mobile proton) with increasing Fe(III) concentrations. Furthermore, Liu and Papangelakis (2005) regressed thermodynamic parameters for $Fe_2(SO_4)_3^0$ and $Fe(OH)_2SO_4^-$ in order to model solubility in multi-component electrolytes at elevated temperatures, despite not providing any fundamental supporting

evidence for these species.

In another study, Majzlan and Myneni (2005) investigated the chemistry of the $Fe_2(SO_4)_3$ system in order to rationalise the solubility of Fe(III) in acid mine drainage and estimated that only about 10% of the total sulphate in (very) dilute solution forms inner-sphere complexes ($[Fe^{3+}]_{max}$ = 50 mmol/kg, T = 25°C). They suggested that the reasonably large association constants for $[Fe(SO_4)_n]^{3-2n}$ complexes are not *solely* attributable to inner-sphere complexes, but due to the presence of extensive hydrogen-bonded networks in dilute $Fe_2(SO_4)_3$ solutions. These effects can be expected to become more pronounced at increased ionic strengths, as solvent-solute interactions become progressively more important. Solution phase X-ray diffraction measurements of more concentrated $Fe_2(SO_4)_3$ solutions at ambient temperatures support this. Magini and Radnai (1979) calculated peaks in the radial distribution function associated with the second-order interactions between Fe, S and the second hydration sphere occurring at 4.34-4.39 Å. In addition, these data further suggested a coordination number of sulfate between 1-1.3 which supports the presence of both 1:1 and 1:2 Fe(III)-SO_4 species as recommended by Stipp (1990).

Despite the widespread evidence for the strong affinity for CIP formation in $Fe_2(SO_4)_3$ solutions, attempts have been made to model the system using the traditional ion-interaction approach of Pitzer (1973). Tosca et al. (2007) used an extended Pitzer model to correlate available isopiestic data in the $Fe_2(SO_4)_3$-H_2SO_4-H_2O system. Interestingly, the $\beta^{(1)}$ parameters from their optimisations are large, having the effect of countering the dramatic rapid decrease in activity coefficients at low ionic strength associated with the Debye-Huckel limiting slope of a trivalent charged ion. This suggests that, while the ion-interaction model is capable of accurately capturing water activity data in this system, it does not quantify the inherent solution chemistry of the system, which could prove significant for understanding kinetic processes involving $Fe_2(SO_4)_3$.

2.6.3 Fe^{3+}-S(IV) speciation

Ferric ion has a significantly greater affinity to form solution complexes with S(IV) ions in comparison to SO_4^{2-}, clearly observed from the magnitude of the limited number of stability constants available in the literature, as compiled in Figure 2.7 (Martell and Smith, 1976). This has been suggested to result from the stabilization due to partial electron transfer from the S(IV) to the metal centre and has also been observed for other metals such as Cu(II) and Hg(II) (Lente and Fabian, 2002). Some discrepancy exists in the literature as to whether S(IV) ligands are bonded to the metal centre via sulfur or oxygen. Conklin and Hoffmann (1988a) identified a Raman band at 938 cm^{-1} and attributed it

to the Fe−OSO_2 stretching mode, suggesting that it was oxygen-bonded. In contrast, Kraft and Van Eldik (1989b) interpreted the 1330 cm^{-1} absorption in the FT-IR spectrum of Fe(III)-S(IV) solutions as an S-bonded metal sulfite complex. The transient nature of this system significantly complicates its study via experimental means but nevertheless, there is general agreement in the literature that, depending on the pH, Fe(III) and S(IV) concentrations a number of $[Fe(SO_3)_n]^{3-2n}$ or $[Fe(OH)_m(SO_3)_n]^{3-2n-m}$ contact ion pairs exist in solution (Kuo et al., 2006).

The importance of the metal-catalysed oxidation of S(IV) to atmospheric-related processes, such as acid rain production, has resulted in a large number of studies into the chemistry. Conditions in natural systems are typically characterised by a large excess of O_2 and 0.001-100 ppm levels of S(IV) and metal ions (Brandt and van Eldik, 1995). Much of the literature detailing the transient chemistry of the Fe(III)-S(IV) system have been performed at S(IV) excess; graphically presented in Figure 2.8. This figure stresses that only a limited number of studies have been carried out under conditions of metal ion excess.

It is generally accepted that the time scale for the formation of Fe(III)-S(IV) complexes is established within the first 200 ms after mixing; mono-sulfito complexes being established first, followed by those involving three or more constituents (Kuo et al. (2006) and references within). Conklin and Hoffmann (1988a) highlighted that since, at pH 2, Fe(III) = 0.5-5 mmol/L, S(IV) = 5-20 mmol/L, HSO_3^- is the dominant S(IV) solution complex and $FeOH^{2+}$ is the most labile Fe(III) species, the $Fe(OH)SO_3^0$ species would be the dominant Fe(III)-S(IV) solution complex. Kraft and Van Eldik (1989b) reported similar findings, but identified the mono-, bis- and tris(sulfito) species along with hydroxosulfito analogues. A number of other authors report the formation of species involving more than one sulfite ligand and report that the reactivity of these species apparently increases due to the trans-labilization effect (Prinsloo et al., 1997; Bassett and Parker, 1951; Kraft and Van Eldik, 1989b). The 1:1 complex formation has been suggested to have a half-life corresponding to $\tau_{1/2} \approx 3$ ms (Conklin and Hoffmann, 1988a; Kraft and Van Eldik, 1989b). The formation of 1:2 complexes and, subsequently, 1:3 complexes, are reported to occur in a second step with a half-life of $\tau_{1/2} \approx 30$ ms. A further complexity was highlighted by the suggestion of a simultaneous process of linkage-isomerisation between S-bonded and O-bonded structures (Conklin and Hoffmann, 1988a). However this has not been rigorously confirmed. Other investigations only report the presence of a single 1:1 species but the approaches used were not able to elucidate the individual contributions of the complex formation within the first 200 ms of reaction (Karraker, 1963; Carlyle, 1971; Betterton, 1993).

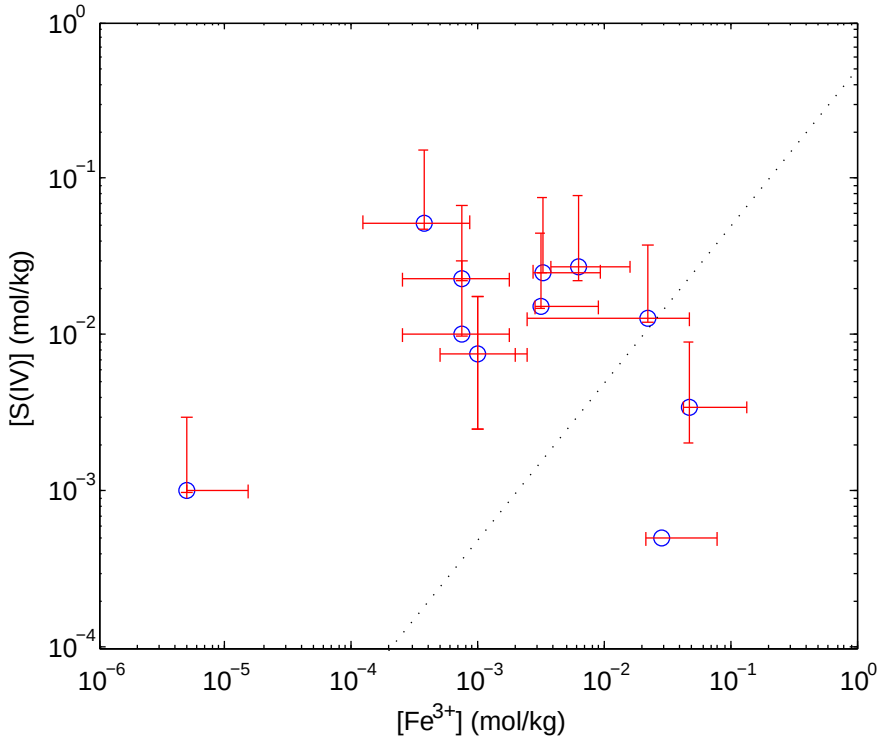

Figure 2.8: Summary of previous studies' Fe(III)-S(IV) concentration ranges shown by the red bars. Dotted line represents the stoichiometric Fe(III):S(IV) ratio of 1:2 according to reaction 1.1.1. Data from: Conklin and Hoffmann (1988a); Dasgupta et al. (1979); Fuzzi (1978); Karraker (1963); Kraft and Van Eldik (1989b,a); Lente and Fabian (2002, 1998); Prinsloo et al. (1997)

Importantly, the above mentioned studies have focused on typically occurring environmental conditions; where S(IV) and (generally) oxygen were in excess. To attempt to avoid the complex kinetics associated with the formation and decomposition of a number of sulfito complexes Lente and Fabian (1998; 2002) considered this system at Fe(III) excess, albeit at similar dilute concentrations. They highlighted the potential to form a number of poly-metallic ferric sulfito species, but concluded that the $FeSO_3^+$ species played a central role in the reaction mechanism, discussed further in the following section.

For this work, it is critical to note that very limited experimental data is available for the Fe(III)-S(IV) system, particularly under conditions of Fe(III) excess and, in line with the general focus on atmospheric systems, no fundamental studies in concentrated systems could be found in the open literature.

2.7 Reaction in the Fe(III)-S(IV)-O_2 system

Transition metal catalysed autoxidation of S(IV) has been well studied in the literature due to its central role in the treatment of industrial plume gases and the production of acid rain (Brandt and van Eldik, 1995; Lente and Fabian, 1998). Trace amounts of transition metals such as Fe^{3+}, Mn^{2+}, Cu^{2+}, Co^{2+} and Ni^{2+} in the atmosphere from industrial and natural processes can catalyse the reaction of S(IV) and oxygen to produce acid and a number of S(VI) products. Throughout the literature, there have been contradictory reports, specifically regarding the nature of the participating species in the autoxidation pathways. Furthermore, S(IV) systems have much wider application, particularly in hydrometallurgy where it can act as a cheap reductant or, when combined with oxygen, a powerful oxidant capable of oxidizing relatively stable species such as Mn^{2+}. (Kao, 1979; Zhang et al., 2000a; Schulze-Messing et al., 2007).

Various mechanisms have been proposed for the metal catalysed autoxidation of S(IV) in the Fe(III)-S(IV)-O_2 system over a wide range of concentrations, pH and O_2 partial pressures. Brandt and van Eldik (1995) summarize these into three main groups: (1) free-radical based mechanism, (2) inner-sphere electron transfer within Fe(III)-S(IV) complexes, and (3) mixed mechanisms of (1) and (2). Comparisons between studies of different authors becomes complicated by substantial variation in experimental conditions under which this system was studied; most notably Fe(III) and S(IV) concentrations (see Figure 2.8) and pH. However, much of the disagreement regarding the *oxidative* mechanism surrounds the interaction of oxygen with Fe(III) and S(IV) species and it's ultimate electron acceptance. For example, Zhang et al. (2000a) proposed a mechanism for Fe^{2+} oxidation with SO_2/O_2 mixtures, summarized schematically in Table 2.5. In this mechanism, the $SO_3^{\bullet-}$ radical emerging from the decomposition of $FeSO_3^+$ directly interacts with oxygen to form peroxo-monosulfate intermediates that are suggested to be responsible for the strong oxidizing power of SO_2/O_2 systems. The main difference between such mechanisms and those which don't involve radical species is in the form of the inner-sphere electron transfer, which, for example Freiberg (1975) suggests the mechanism presented in Table 2.6.

Much of the disagreement between the proposed reaction mechanisms can likely be ascribed to the conditions over which specific studies were focused as well as the difficulties of categorically identifying the presence of radical species in these systems since the addition radical scavengers (mild reducing agents) may affect the speciation-type mechanism as well. It is however generally accepted that the initial stages of the reaction involve the formation of Fe(III)-S(IV) complexes discussed in the previous sections. The

decomposition of these inner-sphere complexes are suggested to be comparatively slow and represent the rate-limiting step in the overall reaction mechanism (Kuo et al., 2006).

Table 2.5: Schematic Fe^{3+} mediated SO_2/O_2 oxidation mechanism proposed by Zhang et al. (2000a)

Initiation	$SO_{2(aq)} + H_2O \rightleftharpoons H^+ + HSO_3^-$
	$HSO_3^- \rightleftharpoons H^+ + SO_3^{2-}$
	$Fe^{3+} + SO_3^{2-} \rightleftharpoons FeSO_3^+$
	$FeSO_3^+ \longrightarrow Fe^{2+} + SO_3^{\cdot-}$
$SO_5^{\cdot-}$ Formation	$SO_3^{\cdot-} + O_2 \longrightarrow SO_5^{\cdot-}$
Propagation	$SO_5^{\cdot-} \longrightarrow HSO_5^- \rightleftharpoons FeSO_5^+$
Oxidation	$Fe^{2+} + (SO_5^{\cdot-}, HSO_5^-, FeSO_5^+) \longrightarrow Fe^{3+} + SO_4^{2-} + H_2O$
Termination	$2\,(SO_n^{\cdot-})_{n=3,5} \longrightarrow S_2O_6^{2-}$

Table 2.6: Fe^{3+} mediated SO_2/O_2 oxidation mechanism proposed by Freiberg (1975)

Equilibria	$SO_{2(aq)} + H_2O \rightleftharpoons H^+ + HSO_3^-$
	$HSO_3^- \rightleftharpoons H^+ + SO_3^{2-}$
	$Fe^{3+} + H_2O \rightleftharpoons FeOH^{2+}$
	$Fe^{3+} + HSO_3^- \rightleftharpoons FeHSO_3^{2+}$
Rate determining step	$FeHSO_3^{2+} + SO_3^{2-} \rightleftharpoons Fe(HSO_3)(SO_3)^0$
Species' oxidation	$Fe(HSO_3)(SO_3)^0 + O_2 + H_2O \longrightarrow FeOH^{2+} + 2\,HSO_4^-$
	$Fe(HSO_3)(SO_3)^0 + Fe^{3+} + H_2O \longrightarrow 2\,Fe^{2+} + HSO_4^- + HSO_3^- + H^+$

Most relevant to this study, Lente and Fabian (1998, 2002) studied the reaction between Fe(III) in both oxygenated and deoxygenated solutions where Fe(III) was in excess, clearly identified in Figure 2.8. Their stopped-flow experiments showed that the initial UV absorbance changes ($<$ 50 ms) upon mixing Fe(III) and S(IV) differed, depending on whether the solutions where at the same or differing pH (at pH 1.68). These spectral changes were reasoned to result not necessarily from Fe(III)-S(IV) equilibria, which were expected to be complete within the dead-time of the mixer, but rather from the dimerization reaction of two $FeOH^{2+}$ species to form $Fe_2(OH)_2^{4+}$. This process was reported to be completed in approximately 50 s and would obviously be influenced predominantly by the solution pH, Fe(III) and ligand concentrations in the solution.

More importantly, they noted an approximate first order decay in the absorbance spectra behaviour under these conditions, consistent with the decomposition of a Fe(III)-S(IV) contact ion pair. Deviations from this behaviour in the first 200 ms however suggested

that there was more than one contributing Fe(III)-S(IV) species. Based on the observed differences depending on the pH jump during mixing, they proposed that, after the formation of $FeSO_3^+$, the $Fe_2(OH)_2^{4+}$ species played a role in the formation of a polynuclear sulfite species. In a later publication, Lente and Fabian (2002) clarified their claims of two ferric sulfito species, which included the polynuclear ferric sulfito species with stoichiometry $Fe_2(SO_3)(OH)(H_2O)_8^{3+}$. However, in their reaction modelling they highlighted that the formation of this species was a "*dead end*" reaction as it does not participate in the electron transfer process between Fe(III) and S(IV). This highlighted the $FeSO_3^+$ monosulfito complex as the primary species involved in the redox process determining the main kinetic effects at long (> 200 s) reaction times.

Additionally, Lente and Fabian (2002) showed in that oxygen saturated solutions produced nearly identical kinetic traces to oxygen free solutions, suggesting that the efficient oxidation pathway through the SO_5^- radical (see Table 2.6) does not take place in large Fe(III) excess. From this it was reasoned that, in conditions of excess Fe(III), the SO_3^- radical is rapidly oxidised by Fe^{3+} even when O_2 is present in solution. Their reaction model also confirmed other reports that suggest the slow inner-sphere electron transfer within the $FeSO_3^+$ complex is the rate determining step within the reaction mechanism. In fact, *and critical to this study*, they suggest that for prolonged reaction times, i.e., greater than 200 s, a simplified model that includes only the $FeSO_3^+$ decomposition characterises the system well (Lente and Fabian, 2002).

In agreement with the findings above, Kuo et al. (2006) collected reported rate constants for various kinetic process that most authors converged towards and generally included in reaction mechanisms in the Fe(III)-S(IV)-O_2 system, presented in Table 2.7. Specifically, the decomposition of the monosulfito ferric complex to form radical species is reported to be orders of magnitude slower than the other equilibria and kinetic processes. These data exemplify the importance of the $FeSO_3^+$ species within the mechanism and suggest that the stability of this complex, at the prevailing conditions, will be a primary determinant of the overall reaction rate. This is critical for the development of a reaction mechanism for Fe(III) reduction using SO_2 in this work as it suggests that the trends noted in dilute, atmospheric systems may be applicable to the concentrated, highly reductive system characteristic of the case study system.

Table 2.7: Reported rate constants at 25°C for selected reactions in atmospheric systems (See Kuo et al. (2006), Appendix C, for original sources)

Reaction	$k_{\rightarrow}$	$k_{\leftarrow}$
$SO_2 + H_2O \rightleftharpoons HSO_3^- + H^+$	$6.3 \times 10^4\ M^{-1}s^{-1}$	$2.0 \times 10^8\ M^{-1}s^{-1}$
	$1.0 \times 10^8\ M^{-1}s^{-1}$	$2.5 \times 10^9\ M^{-1}s^{-1}$
$HSO_3^- \rightleftharpoons SO_3^{2-} + H^+$	$3.1 \times 10^{10}\ s^{-1}$	$5.0 \times 10^{10}\ s^{-1}$
$Fe^{3+} + SO_3^{2-} \rightleftharpoons FeSO_3^+$	$5.0 \times 10^{10}\ M^{-1}s^{-1}$	$6.9 \times 10^3\ M^{-1}s^{-1}$
$FeSO_3^+ \longrightarrow Fe^{2+} + SO_3^-$	$\mathbf{2.1 \times 10^{-3}\ s^{-1}}$	
	$\mathbf{1.4 \times 10^{-1}\ s^{-1}}$	
	$\mathbf{1.9 \times 10^{-1}\ s^{-1}}$	
	$\mathbf{2.0 \times 10^{-1}\ s^{-1}}$	
$Fe^{3+} + SO_3^- + H_2O \longrightarrow Fe^{2+} + SO_4^{2-} + 2\,H^+$	$1.5 \times 10^7\ M^{-1}s^{-1}$	

2.8 Solution modelling

Solution modelling of electrolyte solutions is a powerful tool that enables the extrapolation of various experimentally measured data, usually to areas of interest where little supporting data is available or is difficult to measure, provided the model has been correctly calibrated. Broadly, there are three types of solution modelling classes which vary in their treatment of the electrolyte entities : (a) no electrolyte dissociation occurs, which is typically applicable to high temperature systems (T > 300 °C), (b) complete dissociation of electrolytes occurs, which is typically only valid for very dilute systems or strong electrolytes, and (c) speciation-type models which include association equilibria and have been shown to produce superior results, particularly when the electrolyte systems are known to strongly interact (Anderko et al., 2002; Liu and Papangelakis, 2005).

As outlined in Chapter 1, the focus of this study will be on the development of a speciation-type model in the $Fe_2(SO_4)_3$-$FeSO_4$-H_2SO_4-SO_2-H_2O reactive system. While this model aims to make explicit recognition of important contact ion pairs, considerable advantages regarding the model structure and parameters is facilitated by embedding this approach into the more traditional, ion-interaction framework. The details regarding this approach are presented in the following subsections.

2.8.1 Activity coefficient modelling

There are numerous methods of characterising activity coefficients in electrolyte solutions, although many of these methods are limited to dilute solutions (< 0.1 mol/kg), where interactions are largely electrostatic and the solvent approximates a dielectric continuum. With increasing ionic strength, the interactions between solution species, can significantly alter the activity coefficients from only there electrostatic effects and their estimation becomes more difficult. Moreover, data on which to calibrate models to account for these interactions is generally scarce and often necessitates a simplified approach.

The selection of an appropriate modelling framework for concentrated electrolyte systems becomes quite arbitrary and often, the most common frameworks are selected from their prevalence in commercially available simulation packages. Common means of accounting for activity coefficients involve extended Debye-Hückel models, such as in Casas et al. (2005), however these simple models have serious drawbacks when used out of their range of compositional reliability, typically below 0.1 mol/kg. In recent years, the mixed-solvent electrolyte (MSE) model (Wang et al., 2004) has received significant attention due to its ability to include explicit solvent effects as well as successfully modelling a wide number of systems and forms the basis of the OLI systems software pack-

age. However, typically applications of this model are highly parametrised and rely on an abundance of experimental data.

A complete discussion of the development of activity coefficient modelling theory, while important for understanding the advantages and short-comings of various models, is not central to the objectives of this study and is detailed in Appendix E. The findings of this review highlighted several key benefits of the use of the Pitzer model (Pitzer, 1991) for speciation-type solution modelling. This model, like the MSE model, is also grounded in fundamental electrolyte theory and often permits high quality interpolation and even extrapolation of experimental data, even when they are sparsely distributed over various conditions. The most basic form of the Pitzer model, in terms of the excess contribution to the Gibbs free energy is shown below:

$$\frac{G^{ex}}{n_w RT} = f(I) + \sum_i \sum_j m_i m_j \lambda_{ij}(I) + \sum_i \sum_j \sum_k m_i m_j m_k \mu_{ijk} + \dots \tag{2.8.1}$$

where, $f(I)$ is a function of ionic strength that characterises the long-range electrostatic interactions among ions in solution, $\lambda_{ij}(I)$ is a coefficient matrix of binary interactions between alike solute species i and j which is dependent on ionic strength and μ_{ijk} is a coefficient matrix of ternary interactions between alike solute species.

Some of the most important benefits of the Pitzer modelling framework are the well defined and theoretically meaningful interaction parameters as well as a virial-coefficient structure (seen in Equation 2.8.1) that is grounded in fundamental statistical-mechanical theory of electrolyte systems (McMillan and Mayer, 1945). This offers some restraints for the model in its prediction of activity coefficients, which often facilitates the use of a minimum number of parameters as well as a high confidence in the underlying validity of the interactions. Another significant advantage of the Pitzer model stems from its definition in terms of the excess Gibbs free energy in Equation 2.8.1. Most activity coefficient models are defined to characterise the activity coefficient directly, which makes calculation of the excess Gibbs free energy, or more importantly, the water activity difficult, if not impossible; i.e, through the integration of Equation 2.3.15 and the derivative of Equation 2.3.16. However, forms of the Pitzer model (by the appropriate derivatives of Equation 2.8.1) can be obtained from the direct calculation of activity and osmotic coefficients can be obtained and thus, extensively available water activity data can be used to calibrate interaction parameters.

However, the Pitzer framework does have several important limitations that must be considered which are summarised below:

- The model is semi-empirical and while this does often facilitate extrapolation outside regions that have been calibrated (Pitzer, 1991), this must be performed with caution as the deviations with extrapolation may be extreme.
- The model is limited by the fact that the virial expansion of interaction terms is commonly truncated at ternary interactions among anion-cation pairs, C_{MX}, and thus ignores all higher-order interactions among the solute components.
- The model is typically only valid to concentrations below 6 mol/kg, above which higher-order effects, not included in the model, are not quantified.
- The model does not have inherent dependence on temperature and inclusion of such dependence rapidly increases the number of model parameters.
- Several model parameters, such as the b parameter in the Pitzer-Debye-Huckel term, do not have any associated theoretical significance but are empirical in nature.

Considering the benefits and short-comings of the Pitzer model, the ion-interaction approach, which can be easily extended to include the explicit recognition of contact ion pairs was deemed very beneficial for this study. Additionally, the shortcomings are mainly attributable to the maximum concentration range which is above that expected in this work and thus this modelling framework was adopted. Recently, Bea et al. (2010) published an efficient matrix-based implementation of the Pitzer model which, facilitates the direct calculation of all activity coefficients by matrix algebra, avoiding the need for highly nested loops which become time consuming when the number of species increases. The main equations for the activity and osmotic coefficients, in matrix notation, are reproduced below:

$$\ln \gamma_{\mathbf{aq}} = (\ln \gamma_{DH} + q')\mathbf{z_2} + q^c\mathbf{z} + (2\mathbf{Q} + Z\mathbf{C})\mathbf{m} + \mathbf{m^t T m} \tag{2.8.2}$$

$$\phi = \frac{2}{M}(\ln \gamma'_{DH} + q^\phi + Zq^c + q^L + t) + 1 \tag{2.8.3}$$

Where $\gamma_{\mathbf{aq}}$, $\mathbf{m}$,$\mathbf{z}$ and $\mathbf{z_2}$ are vectors of the activity coefficient, molality, species' charge and the square of the charge respectively, $\mathbf{Q}$ and $\mathbf{C}$ are square, symmetric matrices ($N_{aq} \times N_{aq}$) of second ($\beta^{(0)}_{ca}, \beta^{(1)}_{ca}, L_{cn,an}, \Phi_{aa,cc}$) and ternary ($C_{ca}$) third virial interaction coefficients respectively. Tensor $\mathbf{T}$ includes the higher-order mixing terms ($\psi_{cca,aac}$). A complete description of this approach is detailed in Bea et al. (2010) and not repeated here. The details of the computational solving of the speciation code is included in Appendix A.3.1.

2.9 Summary

This review chapter has highlighted the specific regions of interest for this study, mainly pertaining to the ARFe system. Furthermore, in reviewing the state of knowledge regarding the various sub-systems in that system, the complexities of iron containing solutions was clearly highlighted. Despite their prevalence throughout industrial and environmental systems, we still have a relatively poor understanding of their inherent chemistry. One of the primary limitations to our understanding of these systems is the scarcity of reliable experimental data on which to develop meaningful models that we can use to investigate the system chemistry.

For the $Fe_2(SO_4)_3$ aqueous system specifically, a lack of direct evidence for the nature and prevalence of ferric sulfato solution complexes remains a major hurdle for the accurate modelling of this system. Available evidence does suggest that, even at low concentrations and at room temperature, numerous solution complexes are formed and are likely responsible for the largely non-ideal behaviour of these systems. This further highlights that, in order to test the hypothesis of this study, quantification of solution speciation in common $Fe_2(SO_4)_3$ containing systems is essential and thus represents a primary objective of this work.

Importantly though, the modelling of aqueous iron systems can be somewhat simplified in acidic solutions by eliminating the dominance of the myriad of potential hydroxyl species; mostly applicable to the hydrometallurgical process from which the current study originates. However, even in these solutions many authors have included experimentally unverified species or manipulated equilibrium constants to achieve acceptable descriptions of specific properties they were targeting, i.e., solubility, conductance, pH, redox, etc. While acceptable for such objectives, this does not provide useful information about the chemical nature of these solutions. This underpins the objectives of this study, i.e. to shed light on the behaviour of ferric in concentrated sulfate solutions and to determine the importance of solution speciation in developing a kinetic model of ferric reduction with SO_2.

Obviously, it is unlikely that the complete complexity of these systems can be quantified given our current levels of understanding and a pragmatic approach to quantifying the most important solution species and their interactions is required. Thus, a dominant theme in this study is the development of a minimum-parameter-minimum-species approach that is focused on including only experimentally verified solution complexes in a framework capable of explaining observed trends in available experimental measurements and the engineering implications which this facilitates.

Chapter 3

Experimental

As mentioned in Chapter 1, the primary objective of this work is the development of a solution model for Fe(III) reduction with SO_2 in concentrated sulfate solutions. However, as noted in the previous chapter, reaction kinetics and thermodynamic speciation in this system are not well characterised in the open literature and their experimental measurement forms a core component of this work. The aim of this section is to outline the experimental apparatus and techniques used in these measurements. Additionally, certain methods applicable to the experimental work that are not directly relevant to later discussions are detailed here to facilitate a greater focus on the experimental results in subsequent chapters.

3.1 Mass transfer coefficient measurements

3.1.1 Direct method

The direct method, while easily implemented and not relying on any chemical reaction that may exhibit mass transfer enhancement, does rely on the combination of dynamic responses attributed to mass transfer and the DO electrode itself. If not properly accounted for, this will result in an underestimation of mass transfer coefficients determined via this method (Gourich et al., 2008). Additionally, the DO electrodes are also limited to below 50-60°C. In this work, the direct method was used to measure mass transfer coefficients using an optical dissolved oxygen (DO) electrode (Mettler-Toledo, InPro6800i) to measure gassing and degassing rates of oxygen in water medium.

In this work, for each experimental condition, a cycle of gassing and degassing was carried at least twice resulting in four independent measurement of the k_La for each condition. A kinetic model of gas-liquid mass transfer was used to extract the k_La coef-

Table 3.1: Bound constraints imposed on Equation 3.1.1 during parameter optimisation

Parameter	Lower bound	Upper bound
k_La [min^{-1}]	0	20
t_0 [min]	0	0.25
$\hat{C}^{sat}$ [mg O_2/L]	10	50

ficients from the measured DO content of the solution under each condition. The model included the effects of electrode dynamics and transient hydrodynamic and gas mixing effects and had the following form (Gourich et al., 2008):

$$C(t) = \hat{C}^{sat} \cdot \left(1 - \frac{1}{k_p - k_La}\left[k_p \cdot \exp\left[-k_La(t-t_0)\right] + k_La \cdot \exp\left[-k_p(t-t_0)\right]\right]\right) \quad (3.1.1)$$

Where $\hat{C}^{sat}$ is the estimated saturation concentration of oxygen in the solution, k_La is the mass transfer coefficient (units of min^{-1}), t_0 is a time delay to account for potential hydrodynamic and gas mixing delays in the system and k_p is the response of the electrode (units of min^{-1}). While $\hat{C}^{sat}$ could be estimated via various common methods it was not deemed beneficial in this analysis and was considered as a regression parameter, i.e., $\hat{C}^{sat}$ reduced to a normalisation factor. The probe response was determined to be 3.96$\pm$0.09 min^{-1} and 5.82$\pm$0.12 min^{-1} at 25 and 50°C respectively by rapidly transferring the probe between N_2 and O_2 saturated water solutions at constant temperature. The oxygen-time data of these measurements are shown in Figure 3.1.

The procedure of parameter optimisation involved the following. Commencement of gassing or degassing was set as the start of gas addition into the system and O_2 saturation or removal was distinguished arbitrarily by the achievement of 97% of the maximum (or minimum) value. The degassing measurements were then mathematically inverted to a monotonically increasing concentration profile to match the gassing measurements. The DO reading at commencement of each run was subtracted from the data set to avoid additional parametrisation of the model (Gourich et al., 2008). The k_La, t_0 and $\hat{C}^{sat}$ parameters were then optimised to fit Equation 3.1.1 to the measured data in a least-squares sense. The interior-point constrained optimisation algorithm (MATLAB, 2014) was used to facilitate lower and upper bounds on the parameters to ensure physical meaning was preserved; the bounds are presented in Table 3.1.

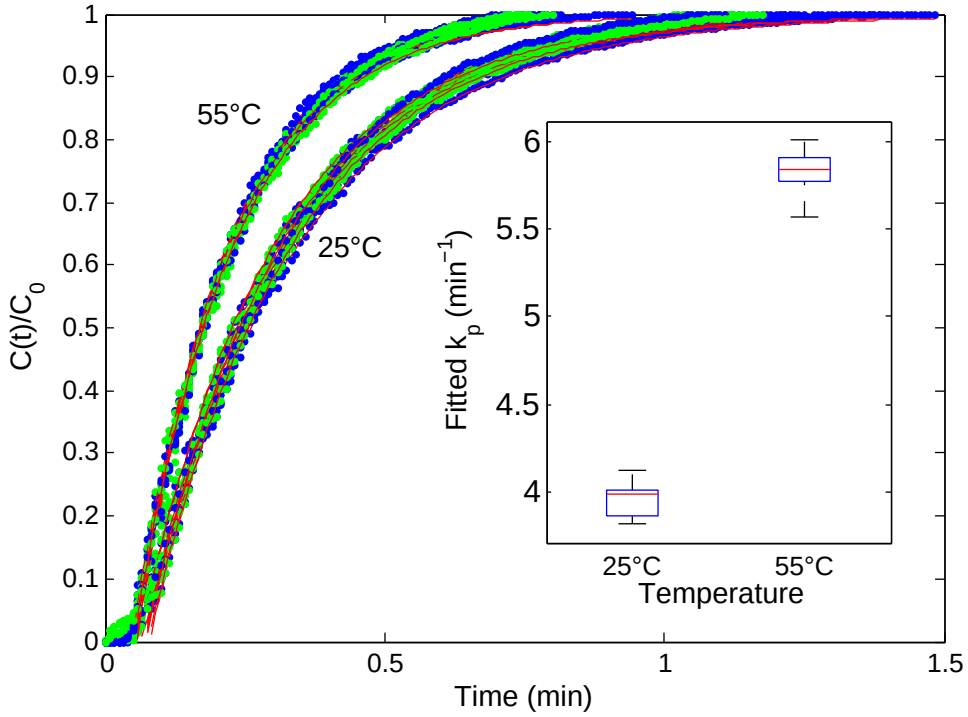

Figure 3.1: Dissolved oxygen electrode response measurements for the probe response in water sparged with O_2 and N_2. Concentrations have been normalised. The insert boxplots represent the calculated first order rate constant for the electrode, k_p, from a simple exponential model regression of the responses show in the figure (red lines).

3.1.2 Indirect method

The indirect method of k_La measurement is one of the most common means of measuring mass transfer coefficients and does overcome many of the limitations of the direct method. However, the method is limited in that a concentrated sodium sulfite solution is the only permissible electrolyte and the method can be quite sensitive to catalyst concentration. Since the sulfite oxidation reaction is relatively slow when uncatalysed, a small amount of catalyst is required to ensure the reaction is not limiting (i.e. to ensure $[O_2]_{\text{bulk}} \approx 0$). However, too much catalyst can significantly accelerate the oxidation reaction, causing reaction in the gas-liquid boundary layer and significantly enhancing overall mass transfer. In addition, heat generated during the oxidation of sulfite ($\Delta H^0 = -547.3$ kJ/mol (Roine, 2002)) in solution can increase the temperature at the gas-liquid interface and enhance mass transfer. Thus, the experimental effects, specifically the ease in which

the reaction can be enhanced, associated with the indirect method typically provides an upper limit on the mass transfer coefficient of a particular system.

It has been shown that by the addition of oxygen into a 1.1 - 1.3 mol/L Na_2SO_3 solution containing 1.5 $\times$ 10^{-5} mol/L $CoSO_4$, the reaction is pseudo-zero-order in sulfite concentration as well as negligible enhancement due to chemical reaction in the boundary layer (Linek and Vacek, 1981). Thus, given the reaction stoichiometry and the arguments above the mass transfer coefficient can be calculated from the rate of sulfite consumption in the following way:

$$\mathrm{SO_3^{2-}} + \tfrac{1}{2}\,\mathrm{O_{2(aq)}} \xrightarrow{Co^{2+}} \mathrm{SO_4^2-} \tag{3.1.2}$$

$$\frac{dC_{O_2}}{dt} = \Phi \cdot k_L a \left(C_{O_2}^{sat} - C_{O_2}\right) = 2\frac{dC_{SO_3^{2-}}}{dt} \tag{3.1.3}$$

$$\text{with:} \quad \phi \approx 1 \quad \& \quad \mathrm{C_{O_2}} \approx 0 \tag{3.1.4}$$

$$\therefore k_L a = \frac{2}{C_{O_2}^{sat}} \cdot \frac{dC_{SO_3}}{dt} \tag{3.1.5}$$

Equation 3.1.5 thus permits the calculation of the mass transfer coefficient from the slope of the sulfite concentration (and the calculation of the oxygen solubility) with time which, by the assumptions above, should be linear.

3.2 Kinetic tests

3.2.1 Batch and continuous test setup

As presented in Figure 3.2, SO_2 absorption tests were performed in a 2000 mL jacketed, glass reaction vessel equipped with temperature, pH and ORP measurement (if required) as well as a gas system capable of supplying the reactor with SO_2, O_2 and/or N_2 via independent mass-flow controllers (Bronkhorst High-Tech, LOW-ΔP-FLOW). Agitation was provided via a 75 W overhead stirrer (Heidolph) fitted with a Halar-coated 45° pitch-bladed dual-impeller; having two sets of four blades (⌀60 mm, spaced 60 mm apart). Reactor internals were fabricated from polypropylene and consisted of four baffles and a draught-tube, diving a cross-section of the reactor into equal flow areas, which were supported from the lid of the reactor. The impeller seal was fabricated from a 1" male SS316 coupler with graphite impregnated PTFE seal packing. Gases were sparged below the surface of the solution, between the agitator blades. The reactor temperature was controlled via a 3 kW oil bath (Julabo, ML-12) circulating through the jacket of the reactor. Counter-cooling was achieved with a 2 kW water chiller (Julabo, FL 1703), to

improve the controllability of the oil temperature which was set via a digital PI controller hosted on a process controller (ABB, AC 800F). For continuous tests, an overflow reactor of identical dimensions to the batch reactor was used to ensure mass transfer and bulk mixing was consistent. Solution addition into the reactor was performed using a peristaltic pump (Watson-Marlow, R220) from a bulk container of initial solution. An overflow solution seal was used to ensure no SO_2 gas escaped from the reactor.

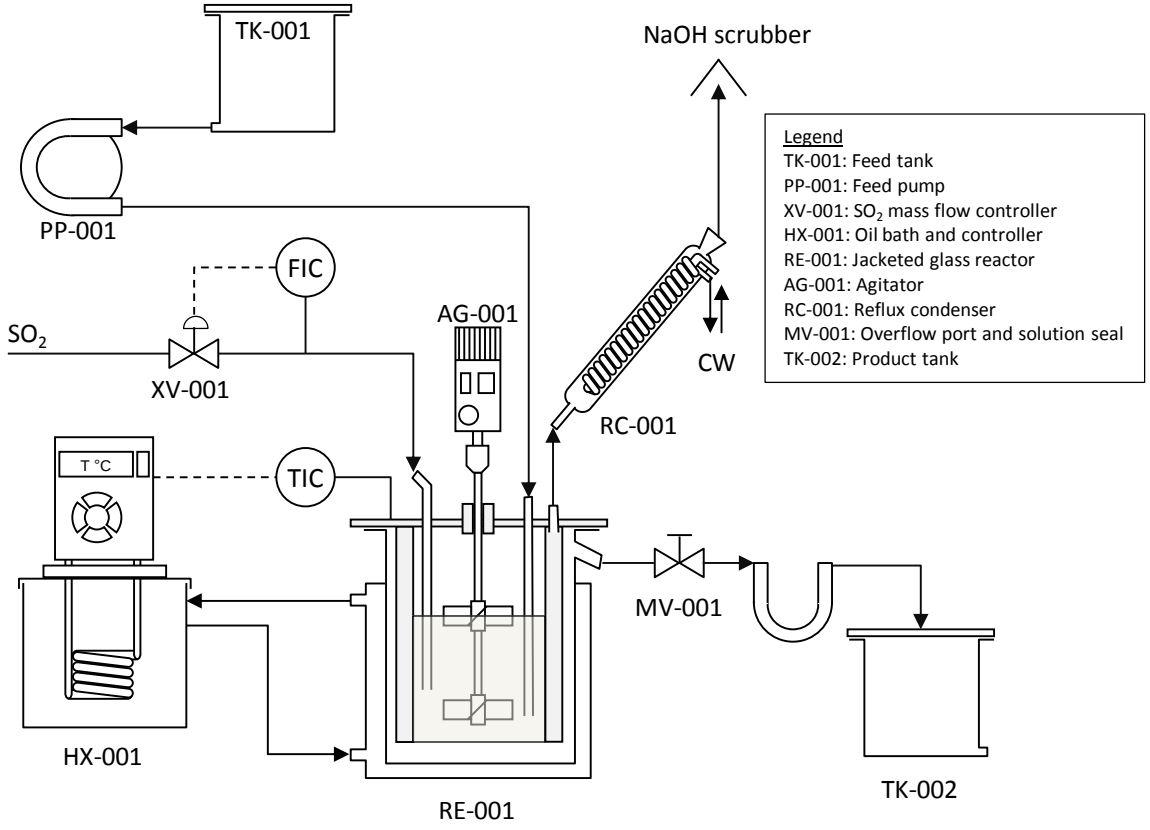

Figure 3.2: Kinetic tests experimental setup for batch and continuous tests. Internal draft tube, supported from the lid of the reactor is shown transparent for clarity.

For each of the kinetic tests, the following procedure was adopted:

Preparation and start-up

- The amounts of reagents required to achieve 1900 mL at the desired concentrations were calculated based on the chemical analyses of each of the reagents as well as the aqueous density model of Laliberte and Cooper (2004).
- All solid reagents were added into a 2000 mL beaker and their masses recorded.
- The water was first added into a separate 2000 mL beaker and its mass recorded, before concentrated sulfuric acid added slowly via a solution dropper to the specified mass.
- The solid reagents were transferred into the clean reaction vessel and the beaker washed several times with the acidic water to ensure all solids were transferred into the vessel.
- The reactor internals were lowered into the vessel which was then sealed and agitated slowly (ca. 500 rev/min) while the oil jacket temperature was ramped up.
- Cooling water was fed through the condenser to ensure evaporation was kept to a minimum.
- Once the vessel had reached the desired temperature a head sample was taken (procedure below) and the test was started by increasing agitation to 1800 rpm and feeding SO_2 into the reactor at 1 L/min (STP).

Sampling

- At the required time, a sample was extracted from the reaction vessel using a syringe and flushing the sample tube several times before extracting a sample.
- The sample was then transferred to a sample bottle and it's mass recorded. Cool dilution water at pH 2 was then added to the sample bottle to achieve approximately a 1:1 dilution and its mass recorded. This effectively quenched the reaction.
- A sample aliquot of approximately 1-4 g from the diluted sample was then taken to determine ferrous ion by titration (refer to the procedure in Section 3.5.3).

- The remaining sample was then retained for submission for ferrous, multi-element ICP-OES and acid analysis. (Immediate titrations and those performed later with the ICP-OES analyses showed little differences, suggesting the reaction was quenched after sampling)

Shut-down

- After the final sample was taken, the SO_2 addition into the reactor and agitation was stopped and the contents allowed to cool.

- The remaining solution was then discarded into a waste container and the reaction vessel cleaned for the next use.

3.3 Raman spectroscopy

Solution spectra were measured with a Jobin-Yvon T64000 Raman spectrometer operated in single spectrograph mode with a liquid nitrogen cooled CCD (1024 $\times$ 256 pixels). The spectrometer was attached to an Olympus BX40 microscope for sample acquisition. The 514.5 nm line of an argon ion gas laser was used throughout and a 20X long-working-distance (WD = 12.0 mm) objective (Olympus, LMPLFLN20X) was used to focus the laser on the sample, at which approximately 1.5 mW of laser power was applied to a spot size of approximately 1 μm. A slit width of 65 μm to optimise throughput and a 1800 lines/mm grating was selected. Individual spectra were compiled from two acquisitions centred at 520 and 1000 cm^{-1} respectively in order to obtain Raman intensities over the range 200-1300 cm^{-1}.

Solution samples were prepared from analytical grade chemicals gravimetrically and their composition validated by ICP-OES for metal ions, ferrous titration (where applicable) and H^+ titration as described in Section 3.5. Each solution was added into a shortened borosilicate NMR tube (Wilmad, Economy) of 5 mm diameter and approximately 40 mm in length. The open end was sealed with PTFE tape and a polypropylene NMR tube lid. These tubes were inserted horizontally into a specially manufactured copper cell (isometric cross-section is presented in Figure 3.3), though which heating fluid from a circulator (Julabo, F12-ED) maintained the required measurement temperature. The temperature at the sample was measured by a type-K thermocouple attached to a Fluke multimeter. The copper cell was mounted on the microscope stage to facilitate accurate and repeatable focusing on the sample. Optimal Raman intensity with the 20X LWD ob-

jective was observed when the laser was focused 600 μm below the surface of the glass tube, perpendicular to a tangential plane.

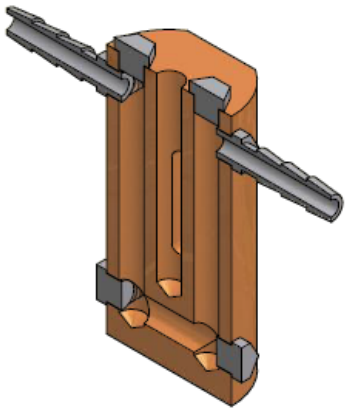

Figure 3.3: Isometric cross-section of Raman temperature cell. A cut-off 5 mm borosilicate NMR tube containing the samples fits tightly into the top of the cell and the slots permit focussing of the laser into the sample using a LWD objective. Total height is 50 mm. Detailed design drawing is attached in Appendix B

.

Solutions were maintained at the required temperature for at least 30 minutes prior to measurement by a sample holder that was submerged in the circulating heater. Sample tubes were inserted into the copper cell and the microscope was focused at the optimal position. A temperature measurement was taken before and after each acquisition and was found to vary no more that 0.3 °C. The 981 cm^{-1} peak of a $(NH_4)_2SO_4$ solution was used as an external standard, and its spectrum was acquired every fifth spectra to track instrumental drift. In all cases this was insignificant and no correction of the measured spectra was necessary.

3.3.1 Treatment of Raman spectra

Measured Raman spectra were converted into a reduced format (R-spectra) by adjusting the measured Raman intensity for temperature and the excitation wavelength of the laser used in each measurement (Brooker et al., 1988). The measured Raman intensity, $I(\nu)$, is given by the following function

$$I(\nu) \quad = \sum_i K \frac{(\nu_0 - \nu_i)^4}{\nu(1 - e^{-hv/kT})} \cdot m_i Si \tag{3.3.1}$$

$$\text{Where:} \qquad S_i \propto \left(\frac{\partial \alpha}{\partial \mathbf{Q}}\right)^2 \tag{3.3.2}$$

Here K is an instrument parameter, associated with the selection of slit width, instrument optics and collection angle as well as sample properties such as absorption due to colour, ν_0 is the frequency of the exciting laser, ν is the measured Raman shift, the Boltzmann distribution is an approximated temperature factor related to excited states and m_i and S_i are the specific scattering activity of the ith species respectively. The specific scattering activity (Equation 3.3.2) is directly proportionality to the square of the partial derivative of the polarizability tensor, α, along each of the normal co-ordinates, $\mathbf{Q}$, which is of primary interest in Raman studies. By rearranging Equation 3.3.1 the reduced spectra, which are directly related to scattering activity, can be obtained via Equation 3.3.3. This equation is valid under the double harmonic approximation assumptions; that is, that the normal coordinates are harmonic and the polarizability expansion is only taken to include first-order effects (Rudolph and Mason, 2001).

$$R(\nu) = I(\nu)\frac{\nu(1 - e^{-hv/kT})}{(\nu_0 - \nu)^4} \tag{3.3.3}$$

In this study, the resulting R-spectra from Equation 3.3.3 were (arbitrarily) scaled to have intensities between 0 and 1000. The R-spectra were then background corrected using a simple piece-wise cubic polynomial function which was fitted through sections of the spectra that exhibited no Raman bands; typically at ca. 200, 700 and 1200 cm^{-1}. Figure 3.4 presents an example of the R-spectra conversion and background fitting. This simple background subtraction method was adopted to avoid the introduction of any systematic errors into the analysis by more complex background shapes. Curve fitting of the background corrected R-spectra was performed by fitting a sum of Gaussian-Lorenzian curves by least squares in a custom-built Matlab (MATLAB, 2014) GUI. Detailes of the curve-fitting application are detailed in Appendix B.1.1 but briefly, the fitting process involved the following:

- Approximate band locations and maximum intensities were manually selected and initialised in the curve fitting routine
- The Gaussian and Lorenzian band widths were initialised at 10 and 100 cm^{-1} respectively.

- Parameters were optimised by bounded least-squares regression using the *lsqnonlin* function (MATLAB, 2014)

- The optimised parameters for all sets of measurements were analysed together and the curve-fitting procedure repeated with manually constrained parameters to ensure the trends in parameters were not erratic. This was particularly important for situations where bands were highly convoluted.

3.4 UV-vis spectroscopy

All UV-vis spectra were measured using a Varian 100 double-beam spectrophotometer, used in single-beam mode, over the region 190 - 400 nm using a tungsten UV source. Spectra were corrected for the effects of the cell and the solvent by measuring a blank prior to any experimental measurements.

The UV-vis experimental rig for steady-state measurements, shown schematically in Figure 3.5a, consisted of a reagent tank from which solution was recirculated by means of a multi-roller peristaltic pump, through a short-path-length quartz flow cuvette (Starna, 584.4/Q/0.001/Z15, l = 10 μm) that was housed in a specially designed copper cell. The reagent tank was jacketed and the copper cell had channels through which a temperature controlled fluid was circulated to maintain the temperature within 0.2 °C of the set point. A 0.45 μm HTTP syringe filter was attached to the feed side of the pump and submerged in the tank solution, which was agitated by a magnetic stirrer. The temperature of the cell, inside the UV-vis instrument was taken by a Type-K thermocouple attached to a multimeter (Fluke, 289). Solutions of known composition were made up gravimetrically into the reagent tank and continuously fed through the flow cuvette. The system was allowed to equilibrate for a period of time until at least three coincident spectra were obtained.

In order to make quantitative measurements from UV spectra, the Beer-Lambert law is typically employed. This law describes the relationship between light absorbance and concentration of species and is typically written as:

$$A(\lambda) = -\log_{10}\left(\frac{I(\lambda)}{I_0(\lambda)}\right) = \epsilon_i(\lambda) l c_i \tag{3.4.1}$$

where $A(\lambda)$ is the absorbance measured at wavelength λ, $\epsilon_i(\lambda)$ the molar extinction coefficient of species i at wavelength λ in [L/mol.cm], l is the optical path length in [cm] and c_i is the concentration of species i in the analysed solution in [mol/L]. Typically,

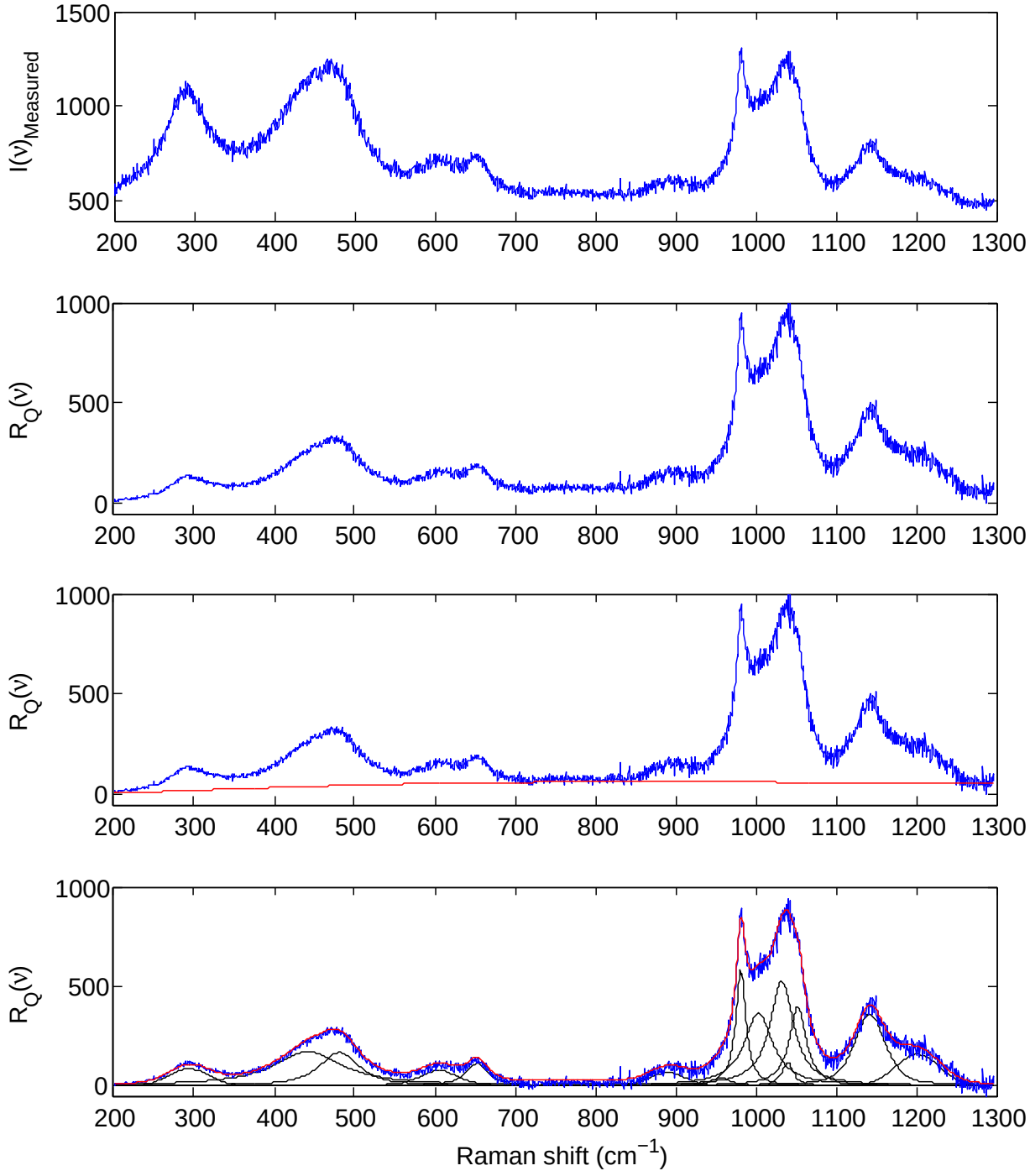

Figure 3.4: Example of (from top to bottom) (a) raw measured Raman spectra, (b) spectra converted to R-format using Equation 3.3.3, (c) background correction using selected points at ca. 200, 750 and 1300 cm^{-1}, and (d) resolved component bands (black) and overall fit of the spectrum (red).

for unknown solution speciation, both $\epsilon_i(\lambda)$ and c_i are unknown and must be estimated simultaneously; this is ideally suited to multivariate spectral analysis.

Many methods exist for the deconvolution and interpretation of multidimensional spectral data (Brown et al., 2009). The spectra obtained in the steady-state experiments were treated via Multivariate Curve Resolution by Alternating Least Squares (MCR-ALS) using the Matlab (MATLAB, 2014) implementation of Jaumot et al. (2005). This method has the advantage that closure and non-negativity constraints can be easily implemented in the ALS algorithm to ensure physical constraints are met and is highly effective for spectroscopic data. A complete review of this method is not important for the objectives of this study and the reader is referred to Jaumot et al. (2005) and the references therein for a comprehensive review of the technique. The details of the experimental and MCR-ALS treatment are included in Appendix B.2.

For kinetic measurements a different experimental rig was used, shown schematically in Figure 3.5b. Reagents were rapidly mixed by injecting solutions simultaneously from two glass syringes (Socorex, 10 ml) into a small-dead-volume HPLC tee mixer (Upchurch) via 0.5 mm OD tubing. The mixed solution was then transferred into a quartz flow cuvette (Starna, 584.4/Q/1/Z15, l = 1 mm), that was temperature controlled as described above, and then to a waste beaker. Once a steady-flow of solution was obtained through the cell, the inlet and outlet tubes to the cuvette were clamped off to prevent any back-diffusion of reagents and spectra were collected at timed intervals, typically only at a single wavelength.

3.5 Reagents and chemical analyses

3.5.1 Reagents: Kinetic tests

All reagents for the batch kinetic tests (ferric sulfate hydrate (AR), sulfuric acid (AR)) were AR grade and sourced from Associated Chemical Enterprises (PTY) LTD. Additional reagents included potassium dichromate (ampoule, Associated Chemical Enterprises), sodium hydroxide (Merck). No further purification of the reagents was performed.

Continuous tests required substantially more reagen quantities and for these tests reagent grade ferric sulfate (Associated Chemical Enterprises) was used, as received.

3.5.2 Reagents: Equilibrium tests

The Raman and UV-vis experiments were prepared with high grade reagents. Ferric sulfate (AR, Sigma-Aldrich), ferrous sulfate (AR, Sigma-Aldrich), sodium perchlorate (AR,

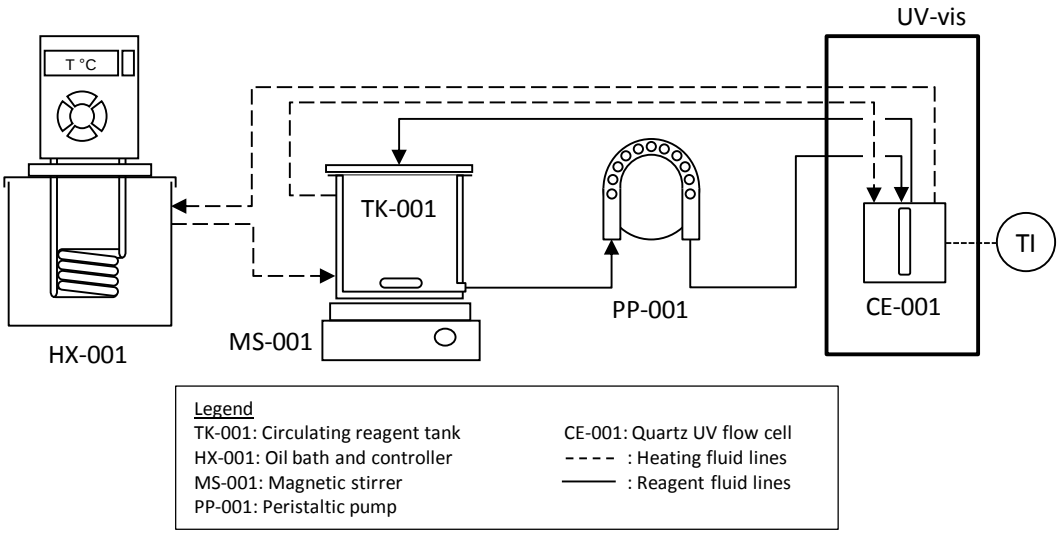

(a) Setup for steady-state UV measurements. The pump is used to recycle solution through the temperature controlled cell continuously.

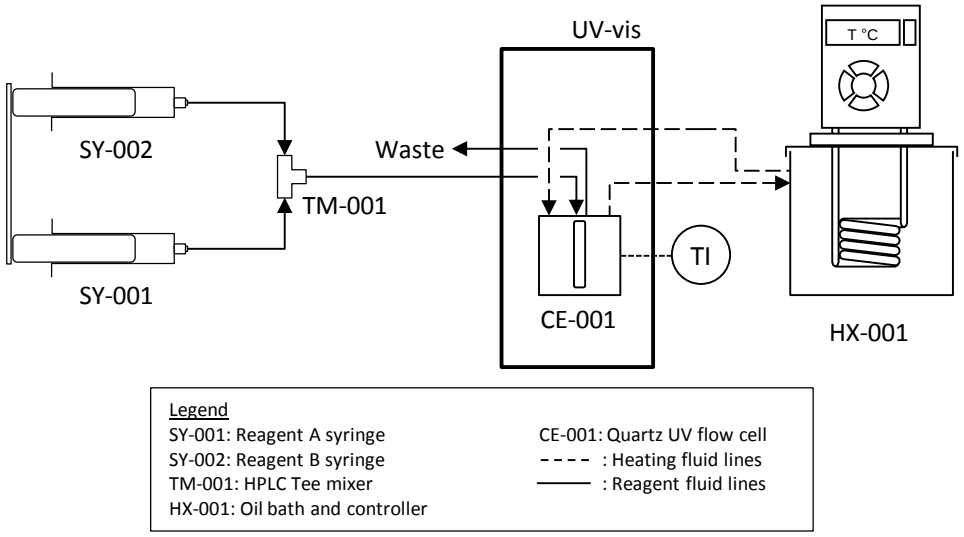

(b) Setup for Kinetic measurements: A simple stopped flow device, utiliting a low volme HPLC mixing tee to inject the solution into a temperature controlled cell.

Figure 3.5: Schematic representation of UV-vis experimental setup

Sigma-Aldrich), perchloric acid (AR, Associated Chemical Enterprises), ferric perchlorate (AR, Sigma-Aldrich) and ammonium sulfate (AR, Sigma-Aldrich) were all used with no further purification.

3.5.3 Fe(II) determination

Determination of ferrous ions by dichromate titration (Bazhko, 2009) was selected as the primary means of monitoring the reaction kinetics, primarily as the analyses could be performed rapidly. The reaction between ferrous and dichromate ions in solution is presented below however, dichromate is also capable of oxidizing sulfite in the sample solution according to the following reaction:

$$6\,Fe^{2+} + Cr_2O_7^{2-} + 14\,H^+ \longrightarrow 6\,Fe^{3+} + 2\,Cr^{3+} + 7\,H_2O \tag{3.5.1}$$

$$3\,SO_3^{2-} + Cr_2O_7^{2-} + 8\,H^+ \longrightarrow 3\,SO_4^{2-} + 2\,Cr^{3+} + 4\,H_2O \tag{3.5.2}$$

The solution potential rises sharply as Fe(II) and SO_3^{2-} are oxidised which facilitates determination via an ORP electrode. In order to minimise interactions from background ferric ion and provide sufficient acid for the reactions above, the titration is performed in an acidic medium of sulphuric acid and orthophosphoric acid (complexing agent for Fe(III)) (Bazhko, 2009). From the reactions above, dissolved sulfite may enhance the ferrous ion concentration should it not be considered during the titration. However, since the $SO_{2(aq)}$ solubility is small at temperatures near the atmospheric boiling point, the concentration of sulfite in solution samples is expected to be significantly lower than the Fe(II) concentration and induce negligible error. In order to validate this assumption, the complete procedure described in Bazhko (2009) was performed on a single sample which includes an EDTA titration for Fe^{3+} and subsequent calculation of dissolved sulphite indirectly. This procedure produced a sulfite concentration of zero within experimental error. Thus, the effect of dissolved SO_2 in the samples taken near the solution boiling point for the determination of ferrous ion was neglected. Indeed, due to the significant increase in the SO_2 solubility at lower temperature these effect must be corrected. In these cases, diluted samples were sparged with N_2 to strip SO_2 from the solution before the titration. N_2 was fed at 1 L/min (STP) until the Fe(II) titration analyses was constant (within experimental error) over three successive samples.

The titration procedure involved the following: Firstly, ca. 10 ml of a mixture of 98% H_2SO_4 and 85% H_3PO_4 (60% H_3PO_4(v/v)) was diluted with approximately 50 ml of deionized water. An accurately weighed aliquot of the reactor liquor sample was then

added to the acid solution and titrated with a standardised solution of 0.1N (0.0166M) $K_2Cr_2O_7$ in an auto-titrator fitted with an ORP electrode. The amount of Fe^{2+} per mass reactor solution in the i^{th} sample, $\hat{c}^{(i)}$, is given by the following relationship according to the stoichiometry of Reaction 3.5.1 and the normality of the $K_2Cr_2O_7$ solution:

$$\hat{c}^{(i)} = \frac{0.1 \cdot V_{titration}}{M_{aliquot}} \text{ [mol Fe(II)/kg soln.]} \tag{3.5.3}$$

Since the molality scale was adopted in this study, conversion from mol Fe(II)/kg Soln. to mol Fe(II)/kg H_2O was then performed. Since the reactor was operated in a semi-batch mode with SO_2 added with time, this conversion required an iterative solution as the amount of SO_2 added is directly calculated from the concentration of Fe(II). The total reactor mass was calculated from the following mass balance:

$$M^{(i)}_{reactor} = M_{init} - \sum_{j=1}^{i} M^{(j)}_{sample} + M^{(i)}_{\mathrm{SO_2}added} \quad \text{[kg]} \tag{3.5.4}$$

Then, the approximate number of moles of Fe(II) can be obtained from:

$$n^{(i)}_{\mathrm{Fe^{2+}}} = \hat{c}^{(i)} m^{(i)}_{reactor} \quad \text{[mol]} \tag{3.5.5}$$

By assuming that the amount of Fe(II) in the reactor was related to the amount of SO_2 absorbed into the solution before sample i through the stoichiometry of the overall reduction reaction (Reaction 1.1.1), the mass of SO_2 required in Equation 3.5.4 could be estimated and the above steps iterated until convergence. With the amount of Fe(II) in the reactor solution estimated, the mass of H_2O could be obtained from the initial mass less that reacted according to the overall reaction stoichiometry. The molality of Fe(II) is then given by the ratio of these quantities:

$$m^{(i)}_{\mathrm{Fe^{2+}}} = n^{(i)}_{\mathrm{Fe^{2+}}} / M^{(i)}_{\mathrm{H_2O}} \quad \text{[mol Fe(II)/kg } \mathrm{H_2O}\text{]} \tag{3.5.6}$$

Fe(II) titrations were performed in duplicate, on separate samples and the average difference in analytical results were 0.017 mol/kg (4.5% relative error, $n = 128$). Additionally, utilisation of SO_2 gas was not carried out in this work as initial tests highlighted that the presence of a SO_2 scrubber affected the partial pressure of SO_2 in the reactor and was removed from the experimental setup.

3.5.4 Multi-element chemical analysis

In order to confirm metal ion concentrations, solutions were also analysed by inductively coupled plasma with optical emission spectroscopy (ICP-OES). Samples were typically diluted (mass basis) with water or pH 2 solution, depending on the sample acidity. The density of the diluted samples was taken using a portable density meter (Anton-Paar, DMA 35) in order to facilitate the conversion between volume and mass based units. The calculation of ionic molalities was carried out in the following way. Firstly, the mass of each component in the diluted sample, M_i, could be calculated from:

$$M_i = \frac{x_i \cdot M_{dil}}{10^3 \cdot 10^3 \cdot \rho_{dil}} \qquad \frac{[\text{mg/L}] \cdot [\text{g}]}{[\text{ml/L}] \cdot [\text{mg/g}] \cdot [\text{g/ml}]} \tag{3.5.7}$$

Then the water fraction in the undiluted sample was obtained from the difference between sample mass and the sum of the analysed cation and anion masses, it was assumed that sulfate was the only anionic species:

$$f_{H_2O} = \frac{M_{sample} - \sum_i M_i}{M_{sample}} \qquad [\text{kg } H_2O/\text{kg}] \tag{3.5.8}$$

This then permits the direct calculation of the molality (mol/kg) of each species in solution via the following:

$$m_i = \frac{10^3 \cdot M_i}{M_{sample} \cdot MW_i \cdot f_{H_2O}} \qquad \frac{[\text{g}] \cdot [\text{g/kg}]}{[\text{g}] \cdot [\text{g/mol}] \cdot [\text{kg } H_2O/\text{kg}]} \tag{3.5.9}$$

Calibrations for the ICP-OES analyses were performed using TATI multi-analyte calibration solutions and all analyses were carried out at Anglo American Technical Solutions: Research (SANAS accredited).

3.5.5 H_2SO_4 determination

Acid determination in the sample solutions was performed by titration with 0.1N NaOH on an auto-titrator fitted with a pH electrode. A standard method of preventing easily hydrolysable metals from forming basic salts or hydroxides at increased pH, metal cations were complexed with 10 ml saturated potassium oxalate (ca. 2 mol/L) before titrating to the positive inflection point.

3.5.6 SO_3^{2-} determination

For the indirect mass transfer and SO_2 solubility tests, discussed later, sulfite concentration were determined by the standard iodine-back-titration method (Jeffery et al., 1961).

The chemical reactions occurring during the titration involve, firstly, the formation of the highly soluble tri-iodide ion when iodine is dissolved in excess iodide solution (Reaction 3.5.10). The addition of sulfite into this solution results in its oxidation to sulfate according to reaction 3.5.11. The remaining iodine is then reduced by the rapid reaction with thiosulfate ($S_2O_3^{2-}$), with the end-point determined by titration.

$$I_2 + I^- \longrightarrow I_3^- \tag{3.5.10}$$

$$SO_3^{2-} + I_3^- + H_2O \longrightarrow SO_4^{2-} + 2\,H^+ + 3\,I^- \tag{3.5.11}$$

$$6\,S_2O_3^{2-} + 3\,I_3- \longrightarrow 3\,S_4O_6^{2-} + 9\,I^- \tag{3.5.12}$$

The resulting concentration of sulfite in the sample can then be calculated by difference between the amount of I_2 added initially and that determined by titration assuming the stoichiometry in the above reactions.

The procedure for the titrations involved the following: First, a 0.05 mol/L solution of iodine in excess potassium iodide was prepared according to the method outlined in Jeffery et al. (1961). Then, a standard solution of 0.1 N sodium thiosulfate ($Na_2S_2O_3$) from an ampoule and deionised water was prepared and used to standardize the iodine solution. The titration procedure then in involved the following:

- A 100 ml polypropylene titration cup was filled with ca. 30 g of standardized iodine solution (accurately weighed) and 10 g of 2 mol/L HCl solution.
- A sulfite containing sample of approximately 1 g (accurately weighed) was added to the acidic iodine solution which was in excess, gently mixed, covered with a watch glass to prevent I_2 loss and left in the dark for approximately 10 minutes.
- The resulting iodine solution was titrated against standard 0.1 N sodium thiosulfate solution using an auto-titrator fitted with an ORP electrode. A sharp increase in solution ORP occurs as I_2 is depleted from solution and is easily detected as the titration end-point.

Masses were taken with an analytical balance and densities recorded with a portable density meter (Anton-Paar, DMA 35). This approach was deemed more reliable than volumetric determinations.

3.5.7 Na^+ determination

Sodium ion in solution was used to determine the perchlorate concentration in standardised Raman samples. All perchlorate was added as AR grade $NaClO_4$ and analyses

were performed by atomic absorption spectroscopy (AAS). A spectrometer with an air-acetylene support and fuel was used with a 589.5 nm hollow cathode lamp. All analyses were performed at Anglo American Technical Solutions: Research (SANAS accredited).

Chapter 4

Equilibrium Systems: Spectroscopic and DFT Analysis

This chapter involves the study of the various binary, ternary and multi-component systems applicable to the reduction of Fe(III) using SO_2 in concentrated sulfate solutions, i.e., the context of the ARFe process conditions. Raman and UV-vis spectroscopic measurements were used to generate previously unavailable solution speciation data for the $Fe_2(SO_4)_3$-H_2SO_4-H_2O system, which were rationalised on the basis of previous literature findings and quantum calculations.

4.1 Computational chemistry calculations

Clearly, from the literature review in Chapter 2, there remains large uncertainty in the exact nature of the Fe(III)-SO_4^{2-} solution species. In this context, it was deemed necessary to investigate the plausible aqueous species from first principles to attempt to highlight their likely molecular structures and indicate the main features of their vibrational spectra. The primary aim of this section is to calculate species geometries using density functional theory (DFT) and subsequent time-dependent DFT calculations to generate vibrational spectra of the important solution species in order to assist the interpretation of spectral analyses presented later in this chapter.

Solution speciation is an inherently dynamic phenomenon and is the culmination of large number of interactions among solutes and the solvent medium that are influenced by concentration and temperature effects, among others. Given the aims of the computation calculations in this study, it was thus elected to a adopt static approach to the quantum modelling, and to not exhaustively attempt to quantify the affect of basis set,

exchange-correlation (XC) potential and relativistic effects selection.

4.1.1 Computational methodology

All quantum calculations were performed using Amsterdam Density Functional (ADF) software (Fonseca Guerra et al., 1998; te Velde et al., 2001; SCM, 2013) by implementing the density functional theory (DFT) formalism via a self-consistent Kohn-Sham procedure (Kohn and Sham, 1965). The generalized gradient approximation (GGA) approach was adopted to include the effects of first-order changes in the local electron density. The OPBE exchange-correlation (XC) energy functional, a combination of Handy's optimized exchange (Handy and Cohen, 2001) with the PBE correlation (Perdew et al., 1996), was selected for all systems investigated in this study. This XC functional has shown good performance and computational efficiency in predicting the geometry and zero-point vibrational energies for small molecules (Swart et al., 2004a) as well as the spin-states for various Fe-complexes applicable to biochemical reactions (Swart et al., 2004b). The basis sets employed throughout were high quality all-electron, double-zeta core, triple-zeta valence, doubly polarized basis sets (TZ2P). Several more elaborate basis sets (i.e., ATZ2P, QZ4P and those with extra diffuse functions) were investigated for several of the species, but geometries and vibrational spectra were not significantly different and since the focus of this section was to indicate trends rather than absolute values, the increased computational time associated with the larger basis sets could not be justified.

As ion solvation plays a vital role in the coordination and stability of aqueous solution species, the first hydration sphere was treated by the explicit recognition of water molecules that were directly bonded to the metal centres. For simplicity, and computational ease, subsequent solvent molecules were treated by a dielectric continuum model; the Conductor-like Screening Model (COSMO) (Pye and Ziegler, 1999; Klamt, 2005). Within this framework the water dielectric constant, ϵ, was taken as 78.39 and the radius of spherical solvent molecules, from which the solvent cavity is constructed, was taken at 1.93 Å, the defaults in the ADF software (Fonseca Guerra et al., 1998; te Velde et al., 2001; SCM, 2013).

Vibrational energies of the optimised structures can be readily determined by the calculation of the Hessian matrix with respect to the normal modes of the optimized geometry. Moreover, the Hessian matrix also provides invaluable information regarding the potential energy optima. Negative vibrational frequencies, resulting from complex roots of the Hessian matrix, indicate a saddle point in the energy surface, signifying that the geometry is not optimal. In all cases, *important* vibrational modes showed positive frequencies and, in some instances where negative roots were found, were associated

with small modes of the coordinated water molecules. These are common when modelling aqueous species and are associated with the static DFT approach and the use of the continuum dielectric models (Jarzecki et al., 2004). Consideration of additional effects attributed to the COSMO model must be made when calculating vibrational energies and to this end, calculations were repeated at successively finer numerical differentiation tolerances until the vibrational energies were independent of the tolerance (SCM, 2013). In all cases there was a negligible shift in the calculated energies (see Appendix D.2).

4.1.2 Sulfate species

The structure of free sulfate in solution has been recently shown to be highly solvated in a hydrogen bonded network of 8 to 14 water molecules (Vchirawongkwin et al., 2007). These authors modelled the sulfate-water system dynamically using quantum mechanical charge field (QMCF) molecular dynamics with mixed quantum and classical regions and highlighted the weak structure making ability of the molecule. In addition, X-ray scattering measurements highlighted the S-O bond distance in aqueous sulfate to be 1.495(6) Å (Vchirawongkwin et al., 2007) and 1.481-1.493 Å (Magini and Radnai, 1979). In the current study, static optimisations of aqueous sulfate, using the COSMO solvation model, produced S-O bond distances of 1.492 Å which are in excellent agreement with experimental measurements. The optimised T_d geometry of the SO_4^{2-} molecule is presented in Figure 4.1. For unassociated sulfate, the nine characteristic T_d modes of vibration present as four distinct modes due to bending mode degeneracies; resulting in the representation: $\Gamma_{vib}(T_d) = a_1 + e + 2f_2$ (Pye and Rudolph, 2001). The symmetric S-O stretching mode is important for the Raman spectra and speciation results later in this chapter, and was calculated via TDDFT calculations to be 957 cm^{-1}, highlighted bold in Figure 4.3. The calculated frequency is slightly lower than the experimentally measured mode of sulfate, which is known to occur at 981 cm^{-1} (Meyer et al., 1980).

The bisulfate molecule was also modelled computationally due to its importance to acidic sulfate solutions. The most stable static structure for bisulfate occurred with the proton located in a plane with the two oxygen atoms, resulting in C_s symmetry, presented in Figure 4.2. However, due to the negligible expected coupling between OH modes and those of O'-SO_3 as well as the variable proton position in average solution geometry, the bisulfate ion is commonly considered to have C_{3v} symmetry (Rudolph, 1996; Vchirawongkwin et al., 2010). Calculations show that the protonation of sulfate distorts its tetrahedral unit and extends the HO-S bond to 1.629 Å and slightly shortens the other S-O bonds to 1.463 Å, i.e., by 0.029 Å. The H-O bond length was calculated at 0.97 Å. These results are in good agreement with similar static and dynamic treatments in the

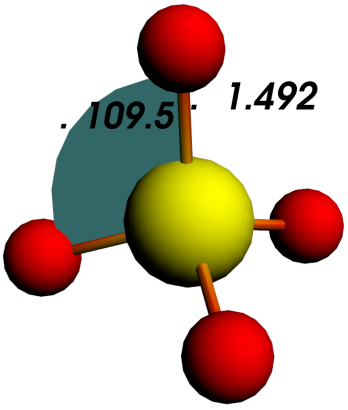

Figure 4.1: Optimised geometry of SO_4^{2-} ion in aqueous solution using the COSMO model for solvent effects. Key geometry for the T_d symmetry shown.

literature of 0.969 - 0.993 Å (Vchirawongkwin et al., 2010). In addition to the bond length changes, the SO_3 unit is flattened by protonation, i.e., by decreasing the HO-S-O angle and increasing the O-S-O angle to 113.3° compared to the tetrahedral angle of 109.5°. This distortion, and the associated electron density variation, results in a significant change to the vibrational mode of the SO_3 stretch, which was calculated at 1046 cm^{-1} via TDDFT calculations. This is in good agreement with the well known experimentally measured mode at 1050 cm^{-1} (Meyer et al., 1980).

The accurate calculation of the equilibrium geometry and vibrational spectra of the simple $[H_nSO_4(H_2O)_m]^{n-2}$ species, known to be present in acidic sulfate systems, provided a validation of the computational approach to obtaining indicative trends in the vibrational spectrum.

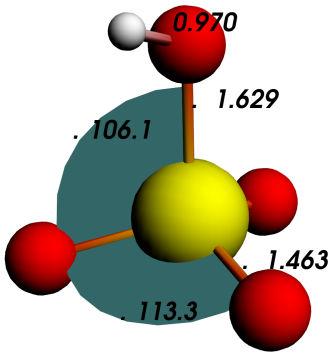

Figure 4.2: Optimised geometry of HSO_4^- ion in aqueous solution using the COSMO model for solvent effects. Key geometry for the C_s symmetry shown. Symmetry was reduced from C_{3v} to prevent the labile proton moving to local minima.

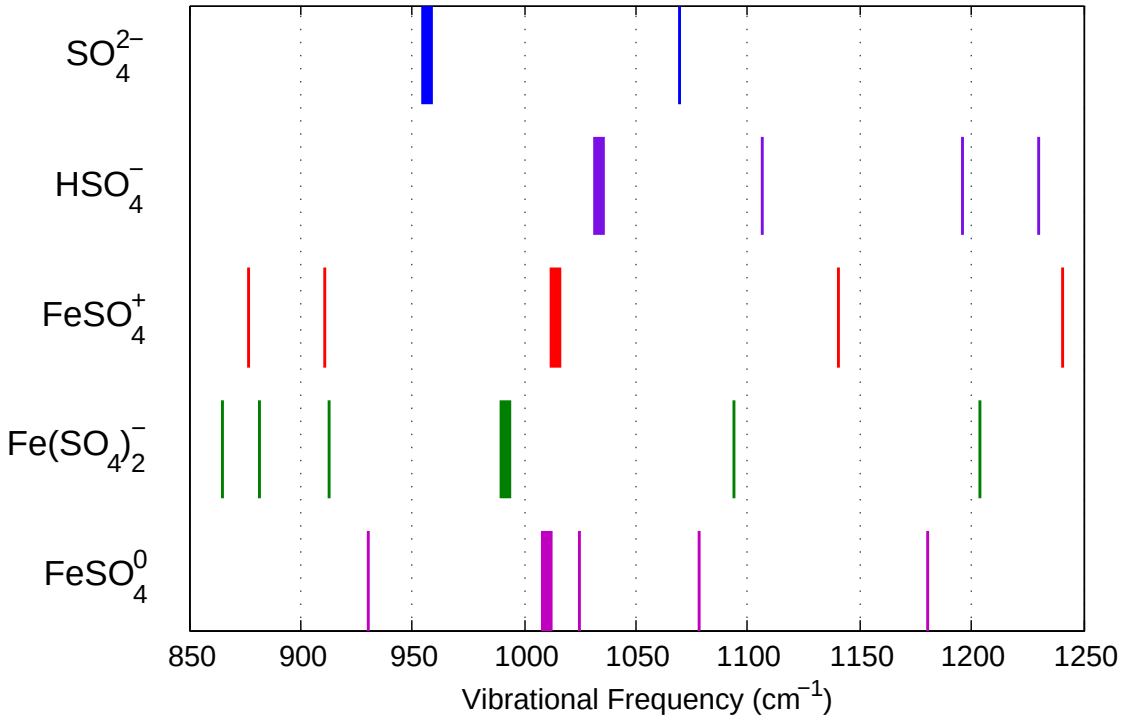

Figure 4.3: Calculated vibrational modes of SO_4^{2-}, HSO_4^-, $FeSO_4^0$ and $Fe(SO_4)_n^{3-2n}$ species. Bold lines indicate the ν_1-SO_3 stretch for each molecule. Also visible is the reduction in degeneracy associated with the ca. 1075 cm^{-1} band of SO_4^{2-} from the resulting ion pairing

4.1.3 Ferrous species

Ferrous hexaaquo ion, $Fe(H_2O)^{2+}_{6(aq)}$, is known to be a predominant species in even concentrated $FeSO_4$ solutions, with comparatively minor association to the ferrous sulfate contact ion pair, $FeSO^0_{4(aq)}$ at ambient temperatures (Rudolph et al., 1997). Recently, aquated ferrous ion was investigated computationally and showed that a dielectric solvent model combined with the B3LYP level of theory reproduced experimentally determined structures and vibrational modes (Jarzecki et al., 2004). The inclusion of continuum models in geometry optimisations does complicate the procedure due to small rotation and tilting modes of water flattening the energy surface. To account for this, gas phase optimisation of the ferrous hexaaquo species was first performed with C_i symmetry to facilitate Jahn-Teller effects from the d^6 configuration of Fe^{2+}. The optimised gas phase geometry was then used as the initial geometry with the COSMO solvation model included and the symmetry again fixed to C_i. The Fe-O distances in the ferrous hexaaquo species were calculated at 1.984 Å and 1.985 Å, slightly contracted from the gas phase calculations of 2.009 Å and 2.014 Å respectively.

It was deemed unnecessary to consider any hydroxyl species of Fe(II) due to the relative instability these species compared to those of Fe(III) ($\log_{10} K^0_{Fe(OH)^{2+}} = 11.81$ *cf.* $\log_{10} K^0_{Fe(OH)^{+}} = 4.5$). Furthermore, in the reactive systems in this study, there is expected to always be sufficient acid to prevent formation of significant amounts of $Fe(OH)^{2-n}_n$ species.

However, the ferrous sulfato CIP is present in appreciable concentrations in relatively concentrated solutions and could not be ignored (Rudolph et al., 1997). The $FeSO^0_4$ CIP was constructed by replacing an inner sphere water with sulfate, initially in approximate C_{3v} symmetry (ignoring the remaining inner sphere water molecules). During geometry optimisation, strong hydrogen between oxygen atoms in the sulfate molecule and the coordinated water resulted in a tilting of the sulfate molecule to an approximate included angle of 121.9°. Both mono- and bi-dentate configurations for the $FeSO^0_4$ CIP were considered, although the bidentate species were found to have significant overlap between ferrous and sulfur, which would not be stable. Further support for the monodentate bonding of sulfate is the lack of evidence of bidentate bonding in the structure of the common hydrates of $FeSO_4$, melanterite and szomolnokite, which have been identified in the P2/c and C2/c space groups by X-ray diffraction respectively (Wildner and Giester, 1991; Baur, 1964). While the sulfate molecule is also likely to be somewhat hydrated in the CIP, no additional water molecules were included and all hydration effects were were assumed to be captured by the solvation model. The most stable structure of the CIP is presented in Figure 4.4a. Like the bisulfate case, the O-SO_3 bond length is lengthened to

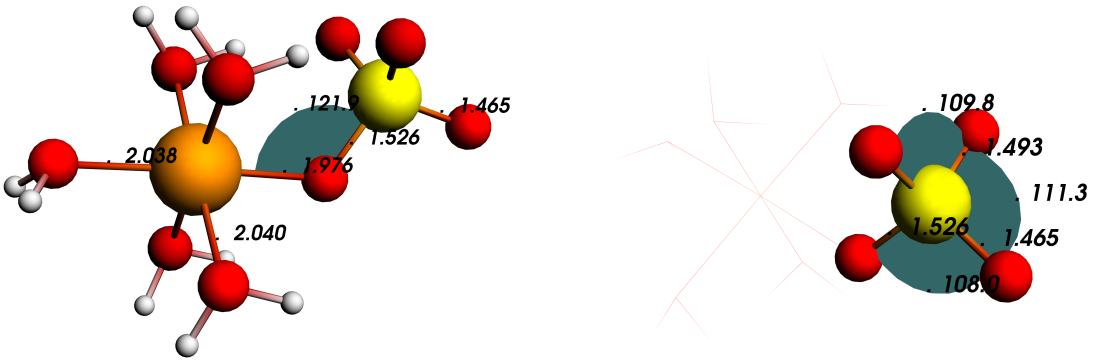

(a) $FeSO_4^0$ species geometry showing important values. (b) Highlighted SO_4^{2-} geometry in the $FeSO_4^0$ species

Figure 4.4: Optimised geometry of $FeSO_4^0$ ion in aqueous solution with enforced C_s symmetry.

1.524 Å and the distribution of S-O distances is altered, primarily due to hydrogen bonding effects with the water molecules in the inner coordination sphere. Slight variations in the positions of the water molecules from the highly symmetrical $Fe(H_2O)_6^{2+}$ species and a slight lengthening of the Fe-OH_2 lengths to 2.038 Å and 2.040 Å for the *trans* and *cis* water molecules respectively.

The calculated vibrational spectrum of the $FeSO_4^0$ species is also presented in Figure 4.3 where the ν_1-SO_3 band is calculated at 1010 cm^{-1}. This positive shift in energy is associated with the broadening of the SO_3 unit in the CIP, clearly visible in Figure 4.4b. In comparison with the ν_1-SO_3 frequencies at which the other species calculated in this study and a previous Raman investigation into this system (Rudolph et al., 1997), the calculated energy of the $FeSO_4^0$ band is larger than expected. However, considering the simplicity at which the static quantum calculations are performed and the different numerical routines used for open- and closed-shell molecules, such a discrepancy is not unexpected. Importantly, the shift in the energy of this stretch is consistent with the variation in sulfate geometry and confirms that the energy of the ν_1-SO_3 stretch in the $FeSO_4^0$ CIP occurs at a slightly larger energy than that of free sulfate but not as large as HSO_4^-, consistent with experimental measurements in the literature and in this study.

4.1.4 Ferric species

Ferric ion has $3d^5$ valence electron configuration, facilitating multiple spin states that are influenced by the ligand type and symmetry during complex formation. In this study, sulfate and water constitute the primary ligands, which both can be classified as weak field ligands, i.e. facilitate a large $\Delta_{oct.}$ energy in octahedral symmetry. This results in high-spin complexes generally being the most stable. This was confirmed by modelling the octahedral $Fe(OH_2)_6^{3+}$ species with T_h symmetry for the doublet, quartet and sextet spin states. Table 4.1 shows that the calculated hydrated ferric ion is most stable in a high spin configuration, confirming similar calculations in the open literature (Harris et al., 1997). Furthermore, the Fe-O distance of 2.02 Å is in good agreement with several sources at 1.97-2.10 Å (See references in Harris et al. (1997)). The slight difference in the Fe-O bonds shown in Figure 4.5 result from a reduction in the T_h symmetry to D_{2h} by the ADF program suite.

Table 4.1: Spin state optimisation of $Fe(OH_2)_6^{3+}$ with T_h symmetry

Multiplicity	Spin Number (S)	Fe-O Bond (Å)	Energy (a.u.)
Doublet	$1/2$	1.919	-2.93437
Quartet	$3/2$	2.065	-2.94906
Sextet	$5/2$	2.020	-2.99826

Ground-state geometries and spin-states of the various $[Fe(OH)_n(H_2O)_m]^{3-n}$ species have recently been calculated using DFT (Avelino De Abreu et al., 2006). In agreement with the calculations detailed in Table 4.1, the sextet (high spin) electron configuration was found to have the lowest potential energy and was accepted as the ground state for $Fe(H_2O)^{3+}$. Avelino De Abreu et al. (2006) calculated Fe-O bond lengths in this molecule of 2.067 using the PBE/TZVP level of theory, which is slightly longer than the calculations of this study, but within the range of experimental determinations. Since the focus of this DFT investigation was to quantify Raman bands in concentrated sulfate solutions, the $[Fe(OH)_n(H_2O)_m]^{3-n}$ which are poor Raman scatterers (Murata et al., 1989) and will be of minor importance in acidic solutions, no quantum modelling of these species was performed.

From the guidance of Section 2.6.2, the most important $Fe(SO_4)n^{3-2n}$ species in aqueous solution are the $FeSO_4^+$ and $Fe(SO_4)_2^-$ species, and relatively little is known about their structure. In similar manner to the ferrous sulfato CIP above, the $FeSO_4^+$ CIP was constructed by replacing an inner sphere water with sulfate. Similarly, strong hydrogen

bonding between the sulfate and coordinate water was observed, the resulting included angle of sulfate was 132.2° with the symmetry reduced to C_s. Both the monodentate and bidentate structures were investigated, however, as with the ferrous species, the bidentate molecule was unstable (i.e. Fe-S overlap) from several starting geometries and not considered to be realistic[1]. The $Fe(SO_4)_2^-$ CIP was optimised in the same way, with monodentate and bidentate as well as cis- and trans- configurations investigated. The bidentate species again proved to be unstable and monodentate bonding was adopted with the symmetry raised to C_i to account for the inversion point about the Fe atom, facilitating hydrogen bonding between the sulfate molecules and different inner sphere waters, see Figure 4.7a. This symmetry also facilitates maximum separation between the sulfate anions and is reasonable to assume this configuration dominates in real solutions.

The geometry of the $Fe(SO_4)n^{3-2n}$ CIPs is presented in Table 4.2 for comparison. The included angle between the sulfate tetrahedron and the iron octahedron of the CIPs are in good agreement with the X-ray study of Magini (1979) who determined angles in the range 134.7-135.1 ° in three $Fe_2(SO_4)_3$ solutions by least squares fitting of the radial distribution function. The slightly lower angle calculated in this study may be partially due to the COSMO model approximation of the waters molecules surrounding the sulfate anion. Moreover, the calculated Fe-O bond lengths in the CIPs are elongated from the $Fe(H_2O)_6^{3+}$ species. This is not unexpected and due to the partial charge transfer away from the metal centre to the sulfate anions, confirmed by the enhanced effect in the $FeSO_4^+$ complex, i.e., with lower symmetry. Interestingly, the Fe-O and S-O bond lengths reported by Magini (1979) more closely resemble those calculated for the free $Fe(H_2O)_6^+$ and SO_4^{2-} species. This is probably due to the fact that, under the conditions where the X-ray data was collected, a significant portion of the ferric remained uncomplexed and, by the nature of radial distribution fitting, the parameters represent averages over the entire solution.

The calculated vibrational frequencies of the $FeSO_4^+$ and $Fe(SO_4)_2^-$ species were presented in Figure 4.3 and show that the ν_1-SO_3 of the $FeSO_4^+$ species occurs at an energy higher than that of the $Fe(SO_4)_2^-$ species. This can be attributed to the increased distortion of the sulfate tetrahedron in the $FeSO_4^+$ species due to the unsymmetrical charge distribution resulting in considerably more charge transfer between the Fe and sulfate molecules. In comparison with the HSO_4^- molecule, where the small size of the proton facilitates a large transfer of charge towards itself and significantly distorts the SO_4^{2-} tetrahedron (see Figure 4.2), it is expected that the lack of a symmetrical sulfate anion in the

[1]Several additional geometry optimisations with explicit water molecules surrounding the sulfate molecule were tested but this did not improve the stability of the bidentate CIP.

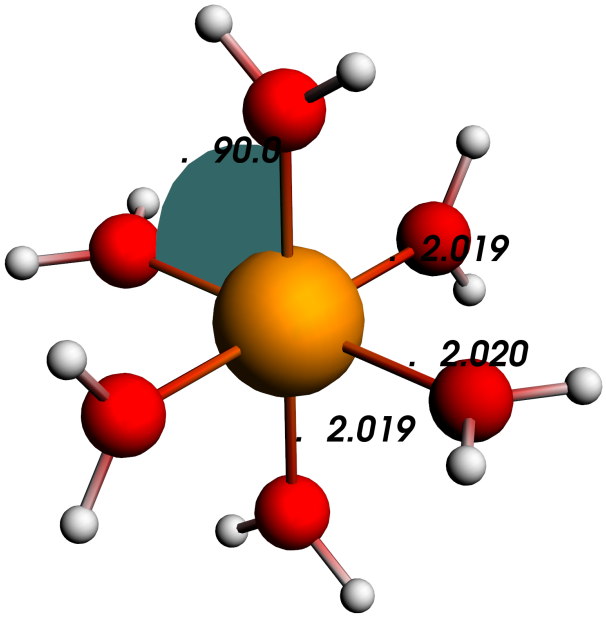

Figure 4.5: Optimised geometry of sextet configuration of the $Fe(OH_2)_6^{3+}$ ion in aqueous solution.

$FeSO_4^+$ species to distribute charge equally will result in a more significant vibrational energy shift than the $Fe(SO_4)_2^-$ species.

Table 4.2: Comparison of $Fe(SO_4)_n^{3-2n}$ species geometry

Species	Dimension	SO_4^{2-}	$Fe(H_2O)_6^{3+}$	$FeSO_4^+$	$Fe(SO_4)_2^-$	Literature†
$Fe(SO_4)_n^{3-2n}$	n	-	0	1	2	0.95 - 1.27
	$\alpha_{FeO-S-O}$ (°)	-	-	132.2	130.2	134.7 - 135.5
$Fe(H_2O)_{6-n}(O)_n$	r_{Fe-H_2O} (Å)	-	2.020	2.124	2.114	2.006 - 2.018
SO_4^{2-}	r_{S-OFe} (Å)	-	-	1.584	1.549	1.486 - 1.493
	r_{S-O_3} (Å)	1.492	-	1.448 - 1.474	1.457 - 1.483	

† Magini (1979)

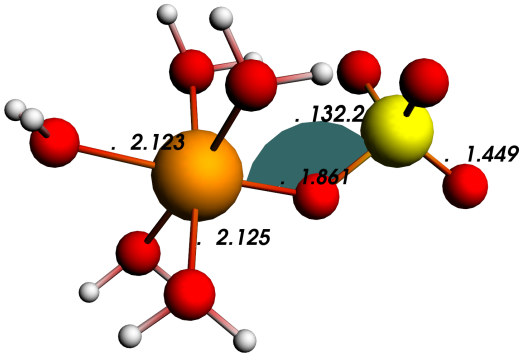

(a) Optimised geometry of $FeSO_4^+$ species showing important values.

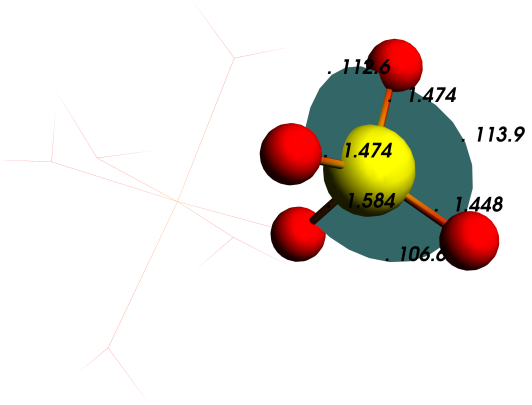

(b) Highlighted geometry of SO_4^{2-} in $FeSO_4^+$ species

Figure 4.6: Optimised geometry of the $FeSO_4^+$ species with enforced C_s symmetry. Cartesian co-ordinates are attached in Appendix D.1.

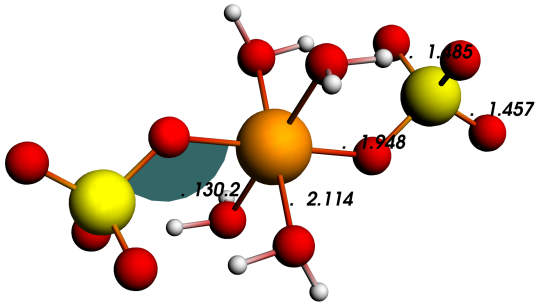

(a) $Fe(SO_4)_2^-$ species geometry showing important values

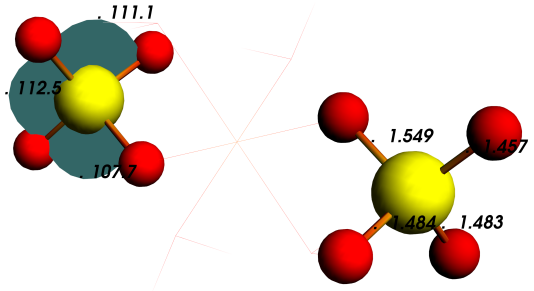

(b) Highlighted eometry of SO_4^{2-} in $Fe(SO_4)_2^-$ species

Figure 4.7: Optimised geometry of the $Fe(SO_4)_2^-$ species with enforced C_i symmetry. Cartesian co-ordinates are attached in Appendix D.1.

4.1.5 Computational chemistry summary

On the basis of the review in Chapter 2 a number of important sulfate species pertinent to the $Fe_2(SO_4)_3$-$FeSO_4$-H_2SO_4-H_2O system were investigated by static DFT and TDDFT analyses. Where available, calculated geometry and vibrational spectra were compared to experimental determinations and generally showed acceptable accuracy, considering the simplified approach. Critically, the geometry of the sulfate moiety in each of the solution species was observed to vary significantly and as a result, affected the spectral position of the intense ν_1-SO_3 stretching mode. Figure 4.8 presents the relationship between the excluded O-S-O angle, i.e., opposite the hydrogen bonds between sulfate-oxygens and coordinated water-hydrogens, and the calculated and measured ν_1-SO_3 stretching frequency of the various species (discussed in the following section). The ultimate usefulness of the

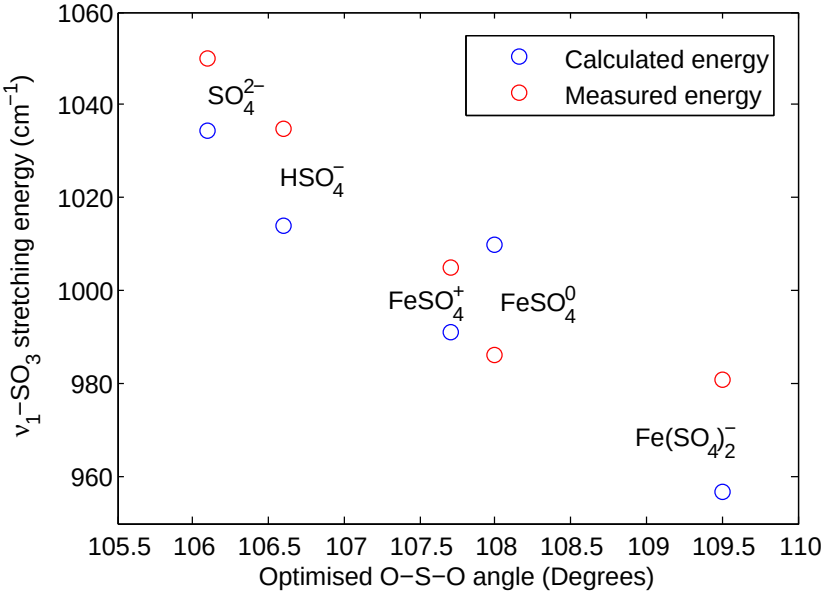

Figure 4.8: Calculated and measured vibrational energies of the ν_1-SO_3 mode as a function og optimised O-S-O angle and frequencies of sulfate moiety in each species. This clearly highlights that the *primary* cause of shift in the vibrational energy of this mode is the distortion of the T_d symmetry of sulfate within the CIPs.

DFT analysis in this study was to aid in the identification of the various species contributing to the Raman spectra presented in the following section. This indicates that the subtle changes in the structure of sulfate within each of the contact ion pairs is responsible, in part, for the variation in the vibrational bands observed in real solutions and provides an excellent basis on which to interpret the Raman spectral information.

4.2 Raman spectroscopy

The general lack of speciation data in the open literature for the $Fe_2(SO_4)_3$-$FeSO_4$-H_2SO_4-H_2O system warranted further investigation in order to develop a realistic modelling framework for the system. Raman spectroscopy has been used extensively to determine CIP formation in sulfate systems (Davis and Smith, 1962; Rudolph et al., 1997; Rudolph and Pye, 1999; Zhang et al., 2000a; Rudolph and Mason, 2001; Rudolph et al., 2003), and has been cross-validated by other experimental methods such as XAS (Magini and Caminiti, 1977; Magini and Radnai, 1979), DRS (Akilan et al., 2006b; Buchner et al., 2004), FTIR (Majzlan and Myneni, 2005) and UV-vis (Sapieszko et al., 1977; De Laat and Le, 2005; Kormanyos et al., 2008).

Importantly, as discussed in Chapter 2, ferric systems typically undergo hydrolysis at reasonably low pH, meaning that the study of these systems is not possible without the presence of acid. A number of sulfate systems were thus selected for analysis via Raman spectroscopy to develop a platform on which quantitative CIP determinations in $Fe_2(SO_4)_3$ systems could be achieved. This basis would then be used to interpret kinetics phenomena in the reactive Fe(III) reduction system with $SO_{2(g)}$.

The sulfate anion is characterised by the high-symmetry $\mathbf{T}_d$ point group (Nakamoto, 1997) and the symmetrical stretching mode, ν_1, has a strong Raman intensity. Furthermore, the SO_4^{2-} species is known to bond to metal ions via a number of mechanisms, forming an array of monodentate and bidentate complexes that distort the symmetry of the sulfate tetrahedron and shift the Raman bands from those of free sulfate (Rudolph et al., 2003). However, since these changes are generally relatively minor, and sulfate still retains its general structure, the molal scattering coefficient, i.e., the relationship between Raman intensity and concentration, of free and associated sulfate is generally quite similar; shown categorically for the $CdSO_4$ system (Rudolph and Irmer, 1994). Generally speaking, the formation of divalent metal sulfate CIP's does not result in a significant energy shift in the ν_1-SO_4^{2-} band for unassociated sulfate and, in such cases, CIP formation is quantified by the relative integrated intensity of this shoulder to that of unassociated sulfate, i.e., internal standardisation is not necessarily required (Rudolph et al., 1997, 2003). However, where more marked changes in the structure of sulfate are noted (viz. HSO_4^-) the molal scattering coefficients can deviate significantly (Irish and Chen, 1970; Rudolph, 1996; Lund Myhre et al., 2003). Appropriate calibration of such systems is thus required to determine each species' scattering activity and facilitate the measurement of species concentrations from their Raman response. In this study, the majority of spectra were obtained without any internal standardization and a subset of solutions were re-

analysed with added $NaClO_4$ to facilitate determination of the effective molal scattering coefficients.

The solution compositions analysed by Raman spectrometry in this study are detailed in Table 4.3.

Table 4.3: Analysed molal concentrations of solutions analysed by Raman spectroscopy

Sample Set	Sample Name	Fe(III)	H^+	Fe(II) (mol/kg)	SO_4^{2-}	$ClO_4^{-\dagger}$
$(NH_4)_2SO_4$	S1				0.30	
	S2				0.79	
	S3				1.86	
	S4				4.08	
H_2SO_4	H1		0.50		0.23	
	H2		1.03		0.53	
	H3		2.13		1.10	
	H4		4.27		2.15	
$FeSO_4$	E1			0.21	0.23	
	E2			0.40	0.42	
	E3			0.80	0.74	
	E4			1.76	1.53	
$Fe_2(SO_4)_3$	A1	0.20			0.30	
	A2	0.39			0.64	
	A3	0.78			1.20	
	A4	1.50			2.21	
	A5	3.20			4.97	
$Fe_2(SO_4)_3+H_2SO_4$	C1	0.58	0.57		1.13	
	C2	0.54	0.96		1.10	
	C3	0.56	1.62		1.60	
	C4	2.24	0.46		3.57	
	C5	2.27	0.96		3.86	
	C6	2.38	1.52		4.30	
$Fe_2(SO_4)_3+H_2SO_4+FeSO_4$	D1		0.37	1.69	1.79	
	D2	0.35	0.40	1.39	1.89	
	D3	0.77	0.39	0.92	1.99	
	D4	1.20	0.36	0.46	2.07	
	D5	1.61	0.70	0.00	2.22	
$NaClO_4$	LA3	0.73			1.16	0.50
	LA4	1.44			2.21	0.48
	LA5	2.81			4.26	0.47
	LS3				1.68	0.45
	LS4				3.82	0.41
	LH3		2.83		0.92	0.47
	LH4		4.80		1.85	0.47
	LC3	0.53	1.69		1.52	0.48
	LC6	2.14	1.76		3.97	0.47

† Inferred from Na analysis by AAS.

4.2.1 Solution speciation from Raman bands

Appropriate treatment of measured Raman spectra can permit the extraction of speciation trends. The relationship between measured Raman intensity and species concentration is non-trivial and depends on the magnitude of the various components of the polarisability tensor for each normal mode. Thus, practically, the conversion from intensity to concentration is typically performed using an inert internal standard (usually perchlorate) to which *relative* molal scattering coefficients can be measured, defined by:

$$J_{i,\mathrm{ClO_4}} = \frac{A_i}{m_i} \cdot \frac{m_{\mathrm{ClO_4}}}{A_{\mathrm{ClO_4}}} \tag{4.2.1}$$

where A_i and m_i are the integrated band area and concentration attributed to species i respectively. Provided that the internal standard is added to the analysed solution in a known quantity and the concentration of the species of interest is known, the J-values can be calculated as above. In the sulfate systems pertinent to this study, as the sulfate S-O bonds are not broken during CIP formation, and all forms of CIPs in the systems of interest are Raman active, the relative intensities of the ν_1-SO_3 bands can be used to characterise solution speciation without an internal standard, provided that each of the species J-values are known (Rudolph and Irmer, 1994).

In this study, relative molal scattering coefficients, relative to the 935 cm^{-1} ν_1-ClO_4 band for SO_4^{2-}, HSO_4^- and $Fe(SO_4)_n^{3-2n}$ species have been calculated from several solutions containing added $NaClO_4$. Solutions of $(NH_4)_2SO_4$ and H_2SO_4 with ca. 0.5 mol/kg added $NaClO_4$ were analysed to determine the relative molal scattering coefficients of SO_4^{2-} and HSO_4^- respectively. In order to obtain the best estimates for $J_{\mathrm{HSO_4^-}}$ an excess of 1 mol/kg HCl was added to minimise the amount of unassociated sulfate. Determination of J-values for the Fe(III)-S(VI) CIP's had to be performed simultaneously from the Raman spectra of $Fe_2(SO_4)_3$-H_2SO_4 solutions with added $NaClO_4$ due to the inability of isolating these species in solutions. A complete account of the calculation of J-values from standardized solutions is included in Appendix B.1.2.

The calculated J-values, relative to perchlorate, for the various species of interest to this study are presented in Table 4.4. Differences between the J-values calculated in this study and those in the literature can be attributed to the temperature and laser frequency correction techniques (Rudolph et al., 1997), concentration range of the calibration, background solution media as well as the concentration and cation of the perchlorate salt used as internal standard (Lewis and Edwards, 2001). However, the expected trends in the J-values are consistent with theoretical arguments. For instance, the J-values for SO_4^{2-} and $FeSO_4^+$ are strikingly similar, suggesting that minimal distortion of the SO_4

Table 4.4: Calculated J-values from perchlorate internal standardisation

Aqueous species	J_{i,ClO_4^-}	Reference
SO_4^{2-}	0.785	This work
	0.637	Dawson et al. (1986)
	0.778	Rudolph (1996)
	0.788	Rudolph (2010)
	0.792	Eysel et al. (1988)
HSO_4^-	0.690	This work
	0.589	Rudolph (1996)
	0.655	Dawson et al. (1986)
	0.676	Lund Myhre et al. (2003)
$FeSO_4^0$	0.785†	Rudolph et al. (1997)
$FeSO_4^+$	0.787	This work
$Fe(SO_4)_2^-$	0.974	This work

† Assumed equivalent to sulfate

tetrahedron occurs in the CIP. Rudolph et al. (1997) also assumed that the J-value of the $FeSO_4^0$ relative to perchlorate was equal to that of sulfate. The bisulfate J-value was found to be lower than that of SO_4^{2-}, which is also expected from the more significant distortion of the SO_4^{2-} tetrahedra than for the metal monosulfato complexes. Lastly, the increased J-value calculated for the $Fe(SO_4)_2^-$ is expected due to the two sulfate molecules contained per CIP molecule. However, due to the significantly different charge distribution and symmetry as compared to the other species, the variation in J-values is not expected to be linear, as calculated.

In the subsequent sections, the J-values presented in Table 4.4 are used to calculate species concentrations from measured Raman spectra that do not have internal standards. In an attempt to analyse the sensitivities of the calculated J-values, a sensitivity analysis for the ferric sulfato species was performed. The J-values for $FeSO_4^+$ and $Fe(SO_4)_2^-$ were varied up to 20% of their values in Table 4.4 and the effect on the solution speciation determined. The findings of this analysis shows that a 20% variance in J-values has approximately the same effect as the estimated variance on the experimental measurements, determined from repeated analyses, detailed in the following sections. The variation in calculated speciation during this sensitivity analysis is included in Appendix B.

4.2.2 Unassociated SO_4^{2-} Raman spectra

Ammonium sulfate solutions were analysed to characterise the Raman spectrum of unassociated sulfate, as no evidence has been found for NH_4^+-SO_4^{2-} CIP formation (Rudolph et al., 2003). Figure 4.9 presents the measured Raman spectra of four $(NH_4)_2SO_4$ solutions at 25°C where the four Raman bands are visible in the 4.80 mol/kg $(NH_4)_2SO_4$ solution: $\nu_1(a_1)$ at 981 cm^{-1}, $\nu_3(f_2)$ at 1110 cm^{-1}, $\nu_4(f_2)$ at 619 cm^{-1} and $\nu_2(e)$ at 452 cm^{-1}. These bands are in excellent agreement with those extensively reported in the literature (Pye and Rudolph, 2001; Rudolph et al., 2003). There is a slight shift to lower frequency and an increase in the FWHH of the ν_1-SO_4^{2-} band with increasing concentration visible from the inset in Figure 4.9 and as has been previously noted by Rudolph et al. (2003).

The solution of 1.90 mol/kg $(NH_4)_2SO_4$ solution was used as an external standard during all measurements to facilitate monitoring of instrumental drift. In all cases the variation in the 981 cm^{-1} band of this solution were insignificant over the measurements and no normalisation of the experimental measurement was deemed necessary.

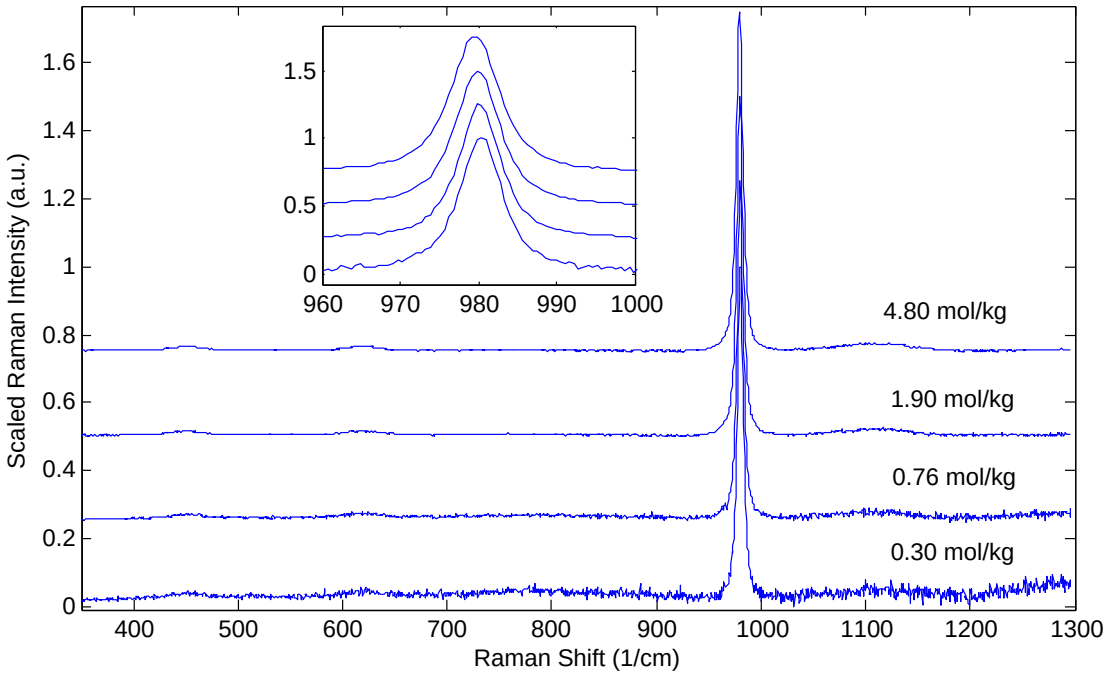

Figure 4.9: $(NH_4)_2SO_4$ Raman spectra in R-format at 25°C and 0.3, 0.76, 1.90 and 4.80 mol/kg. The inset shows a close-up of the ν_1-SO_4^{2-} mode highlighting the slight shift in the band with sulfate concentration.

4.2.3 H_2SO_4 system Raman spectra and speciation

Solutions of sulfuric acid were measured to characterise the bands associated with the bisulfite species, HSO_4^-, and, since speciation in this system has been extensively studied by Raman spectroscopy (Lindstrom and Wirth, 1969; Irish and Chen, 1970; Chen and Irish, 1971; Rudolph, 1996; Lund Myhre et al., 2003; Knopf et al., 2003), to validate the approach of calculating solution speciation. The formation of HSO_4^- causes a strong deviation, particularity of the ν_1-SO_4^{2-} bands primarily due to a reduction of the sulfate T_d symmetry by strong O-H interactions as was suggested by DFT calculations in the previous section.

Figure 4.10a presents Raman spectra of several sulfuric acid solutions of 0.10-2.13 mol/kg H_2SO_4 at 25, 50 and 90°C. Clearly visible in the low temperature spectra are the 981 cm^{-1} peaks of unassociated sulfate. The intense ν_1-SO_3 stretching mode of HSO_4^- is detected at 1051 cm^{-1} and shows a pronounced low-frequency shoulder at 1035-1040 cm^{-1}. This shoulder is attributed to differing hydration states of HSO_4^- (Turner, 1972) and the two band components are typically considered together in quantitative Raman analyses (Dawson et al., 1986; Rudolph, 1996; Lund Myhre et al., 2003). The significant increase in the frequency of the ν_1-SO_3 mode in HSO_4^- from the 981 cm^{-1} band of sulfate (i.e., 69 cm^{-1}) can be attributed to the significant change in the S-O bonds due to the association of the hydrogen ion. Furthermore, the 880-900 cm^{-1} band is a result of ν-S(OH) stretches and shifts to lower frequency with temperature and higher frequency with concentration, this can be clearly seen from the supplementary information in Appendix B.1.4. This is related to extensive hydrogen bonding networks (Rudolph, 1996) and emphasizes the chemical complexity of these solutions. In addition, the ν_2(e) and $\nu_4(f_2)$ modes of HSO_4^- at 436 and 595 cm^{-1} (not shown) were also clearly visible in the H_2SO_4 spectra.

Figure 4.10a and (especially) Figure 4.11, shows a marked decrease in the intensity of the ν_1-SO_4^{2-} band with temperature. However, there is clearly a near-constant relative intensity of this band with increasing concentration at the same temperature, presented in Figure 4.10a. This can be explained by the known rapid association of H^+ and SO_4^{2-} at low H_2SO_4 concentration, followed by relatively constant fraction of associated HSO_4^- with increasing concentration (see Figure 4.12 and references cited). This can be interpreted as resulting from a constant H^+:SO_4^{2-} ratios in H_2SO_4 solutions. However, in strongly concentrated solutions of H_2SO_4, i.e. above 30 wt%, the fraction of HSO_4^- increases approximately linearly with concentration up to 80 wt% (Lund Myhre et al., 2003).

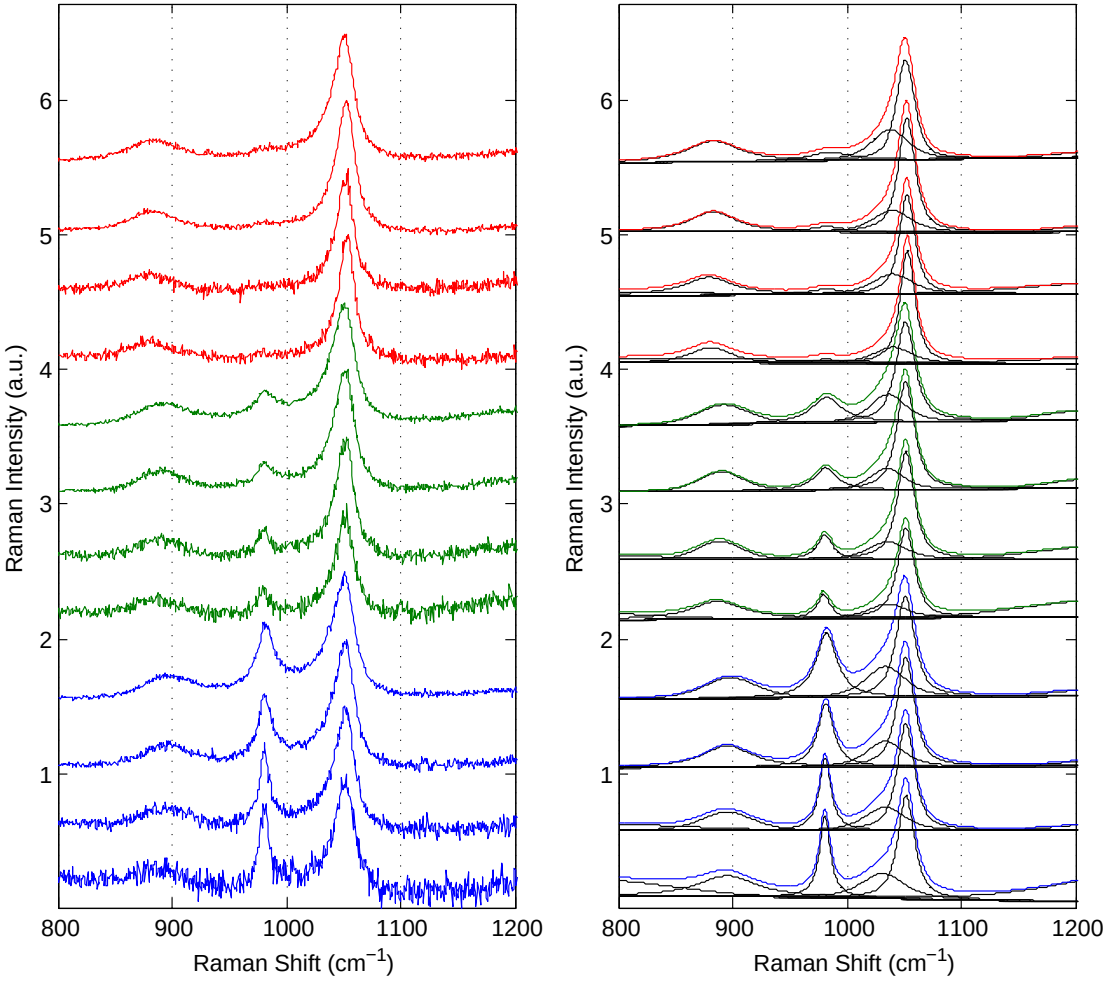

(a) Measured Raman spectra

(b) Fitted component bands

Figure 4.10: Raman spectra (R-format) of H_2SO_4 solutions at 25 (blue), 50 (green) and 90°C (red) at concentrations of 0.10, 0.52, 1.07 and 2.13 mol/kg H_2SO_4 stacked vertically. Fitted component bands are shown in (b) for ν_1-SO_4^{2-} (981 cm^{-1}), ν_1-HSO_4^- (1040/1050 cm^{-1}) and ν_2-HSO_4^- (S-OH, 890 cm^{-1})

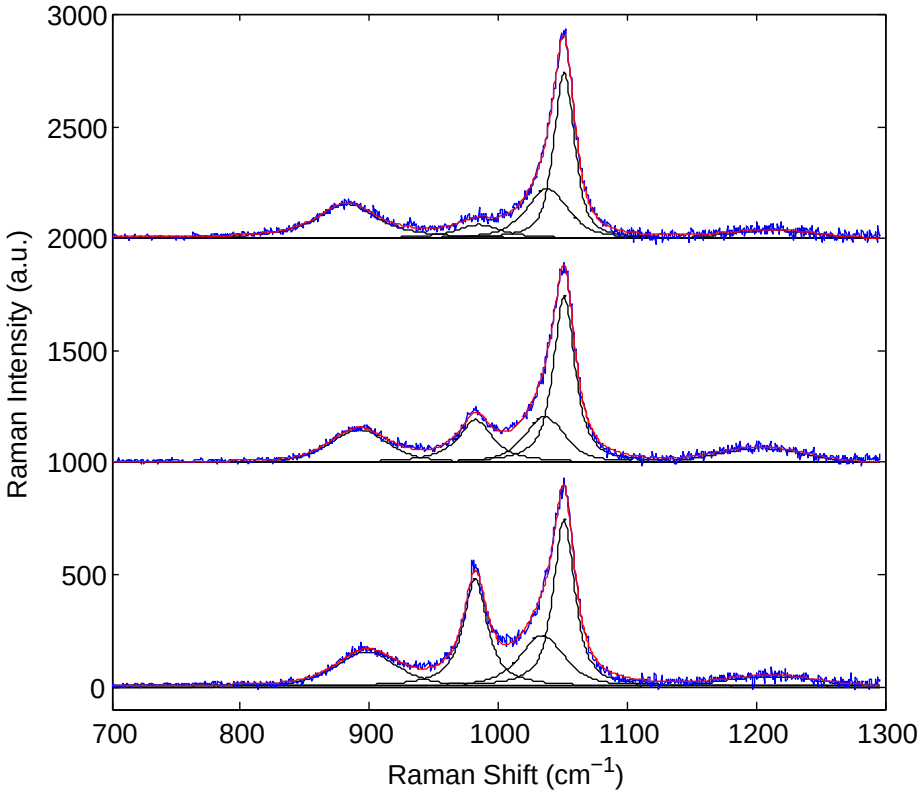

Figure 4.11: Fitted component bands of 2.13 mol/kg H_2SO_4 solution at 25 °C, 50 °C and 90 °C (bottom to top). These spectra clearly show the temperature dependence of the 981 cm^{-1} band of SO_4^{2-} and the S-OH stretching mode of HSO_4^- at 890 cm^{-1}

The calculated fraction of free sulfate, $\alpha_{SO_4^{2-}}$, which is commonly used to quantify bisulfite association, was calculated using the integrated intensities of the composite 1040/1050 cm^{-1} band of HSO_4^- relative to that of the 981 cm^{-1} band of SO_4^{2-}:

$$\alpha_{SO_4^{2-}} = \frac{A_{SO_4^{2-}} \cdot J^{-1}_{SO_4^{2-}}}{A_{SO_4^{2-}} \cdot J^{-1}_{SO_4^{2-}} + A_{HSO_4^-} \cdot J^{-1}_{HSO_4^-}} \tag{4.2.2}$$

The calculated free sulfate fraction for four H_2SO_4 solutions at 25, 50 and 90 °C is presented in Figure 4.12; the data are also tabulated in Table B.1 in Appendix B. A comparison between the results obtained in this study and those data available in the literature show good agreement. Furthermore, several reported solution models (Clegg et al., 1994; Clegg and Brimblecombe, 1995; Holmes and Mesmer, 1992), which have been calibrated on numerous available thermodynamic parameters also agree with the

speciation measurements of this study. These agreements serve to increase confidence in the overall approach of speciation characterisation in this study.

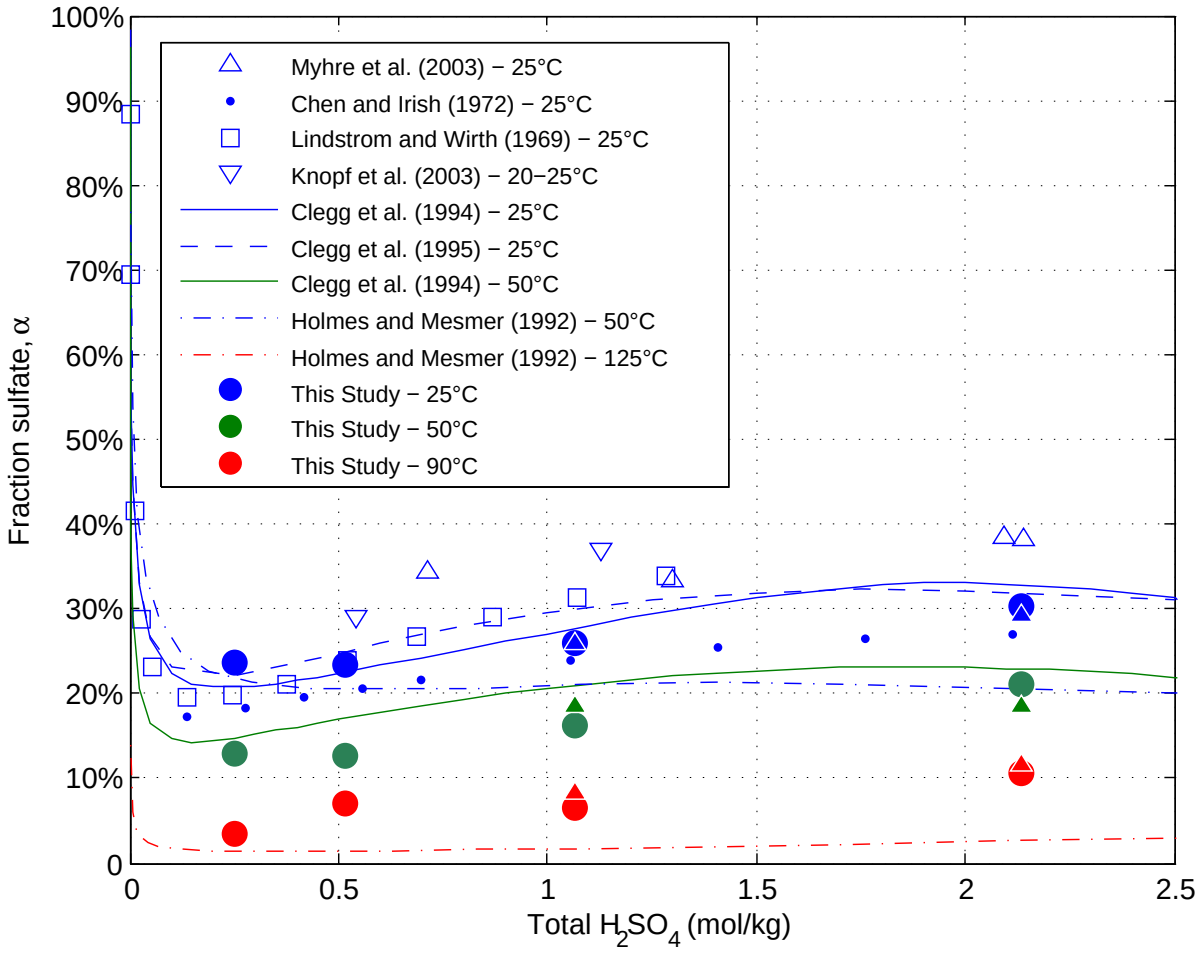

Figure 4.12: Association of HSO_4 in H_2SO_4 solutions as a function of concentration at 25, 50 and 90 °C (Blue, green and red data respectively). Filled data points were measured in this study: • = H1-H4, △ = LH3 and LH4 (See Table 4.3). Various measurements from the literature have been included for comparison (Knopf et al., 2003; Lindstrom and Wirth, 1969; Chen and Irish, 1971; Clegg et al., 1994; Clegg and Brimblecombe, 1995; Holmes and Mesmer, 1992). Data are also tabulated in Table B.1 in Appendix B

4.2.4 $FeSO_4$ system Raman spectra and speciation

This system has been studied previously by Raman spectroscopy and it has been shown that the dominant solution species below 100 °C is the ferrous hexaaqua ion, $Fe(H_2O)_6^{2+}$ (Rudolph et al., 1997; Sobron et al., 2007). The ferrous sulfate CIP, $FeSO^0_{4(aq)}$, is however known to exist at appreciable concentrations in $FeSO_{4(aq)}$ solutions and it was deemed necessary to account for this within the modelling framework. Several spectra in pure $FeSO_4$ solutions were recorded to provide additional information regarding the association to $FeSO^0_4$ as a function of concentration and temperature. It was noted that solutions of $FeSO_4$ were not stable with time and oxidized within several days, forming characteristic Fe(III)-hydroxide colloidal solids Flynn (1984). All measured spectra in the $FeSO_4$ system were thus taken using solutions that were made up and analysed the same day. Raman spectra (in R-format) of a 1.76 mol/kg $FeSO_4$ solution at temperatures from 25 – 90 °C are presented in Figure 4.13.

The intense ν_1-SO^{2-}_4 band of unassociated sulfate at 981 cm^{-1} was dominant in all spectra suggesting that hydrated Fe^{2+}-hexaaquo ions were the dominant solution species. Additionally, weak Fe-O stretches of the these species were detected at 366 cm^{-1}. This is considerably closer to the frequencies measured in nitrate solutions (viz. 370 cm^{-1}) as compared to the results of (Rudolph et al., 1997) in sulfate solutions perhaps due to the concentration differences between the solutions. As with $(NH_4)_2SO_4$ solutions, the 981 cm^{-1} band decreased in frequency with increasing temperature. The high frequency shoulder at 988 cm^{-1} has been previously ascribed to the $FeSO^0_4$ CIP (Rudolph et al., 1997) in accordance with other divalent sulfate aqueous systems: $MgSO_4$ (Rudolph et al., 2003; Zhang et al., 2009), $ZnSO_4$ (Rudolph and Pye, 1999), $CdSO_4$ (Rudolph and Irmer, 1994). The contribution of the 988 cm^{-1} band increases with increasing temperature as expected from the entropy of formation of the $FeSO^0_4$, estimated by calorimetry to be 50.1±0.8 J/mol.K (Izatt et al., 1969), which albeit include effects from outer-sphere complexes.

The FWHH of the sulfate band was similar to that measured in the $(NH_4)_2SO_4$ solutions at 7-8 cm^{-1}, while the high frequency shoulder had a FWHH between 15-17.5 cm^{-1} and became progressively more Lorenzian with increasing temperature.

Furthermore, although not visible in Figure 4.13, a very weak band at 1050 cm^{-1} was detected at 90 °C and was attributed to a small degree of formation of HSO^-_4 via Fe^{2+} hydrolysis, which is known to be favoured with increasing temperature.

The J-value for the $FeSO^0_4$ CIP was assumed equal to that of sulfate on the basis that the vibrational energy of the sulfate band is only shifted a small amount (i.e., about 7 cm^{-1}), when compared to the bisulfate and ferric sulfato species (i.e., up to about 70

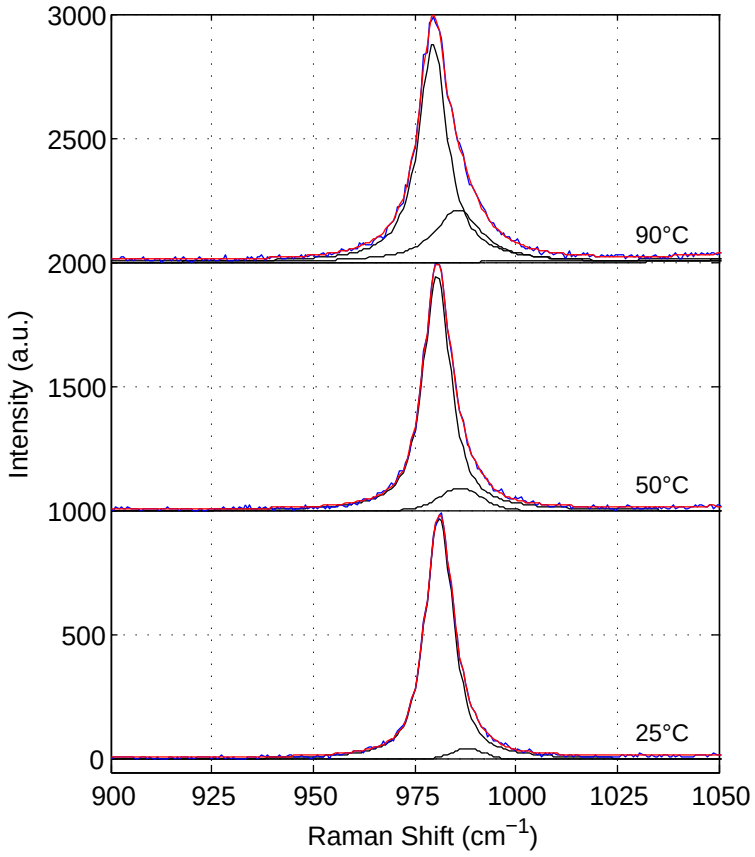

Figure 4.13: Raman spectra of a 1.76 mol/kg $FeSO_4$ solution at 25, 50 and 90 °C. Fitted component bands (black) highlight the increasing stability of the CIP with temperature.

cm^{-1}). Additionally, previous studies have highlighted that divalent transition metal systems impart only relatively weak distortions of the sulfate molecule during CIP formation and have similar J-values to that of free sulfate (see discussion in Rudolph and Irmer (1994)).

From the relative integrated intensities of the 981 cm^{-1} band of unassociated sulfate and the 983-986 cm^{-1} band of the $FeSO_4^0$ CIP, the fraction of the sulfate bound as CIP in $FeSO_4$ solutions could be calculated using Equation 4.2.3 and are presented in Figure 4.14; data are also tabulated in Table B.2 in Appendix B. The limited available speciation for this system is also included in the figure, along with measured Raman and DRS data for the $MgSO_4^0$ CIP (Rudolph et al., 2003).

$$\alpha_{FeSO_4^0} = \frac{A_{FeSO_4^0} \cdot J^{-1}_{FeSO_4^0}}{A_{SO_4^{2-}} \cdot J^{-1}_{SO_4^{2-}} + A_{FeSO_4^0} \cdot J^{-1}_{FeSO_4^0}} = \frac{A_{FeSO_4^0}}{A_{SO_4^{2-}} + A_{FeSO_4^0}} \tag{4.2.3}$$

These data show that there is an excellent agreement between the speciation measurements of the $FeSO_4$ and $MgSO_4$ systems, similar to their thermodynamic properties (see Section 5.3). This further validates the approach of using a $MgSO_4$-surrogate approach (Steyl, 2012) for the modelling of $FeSO_4$ systems, for which comparatively more data are available.

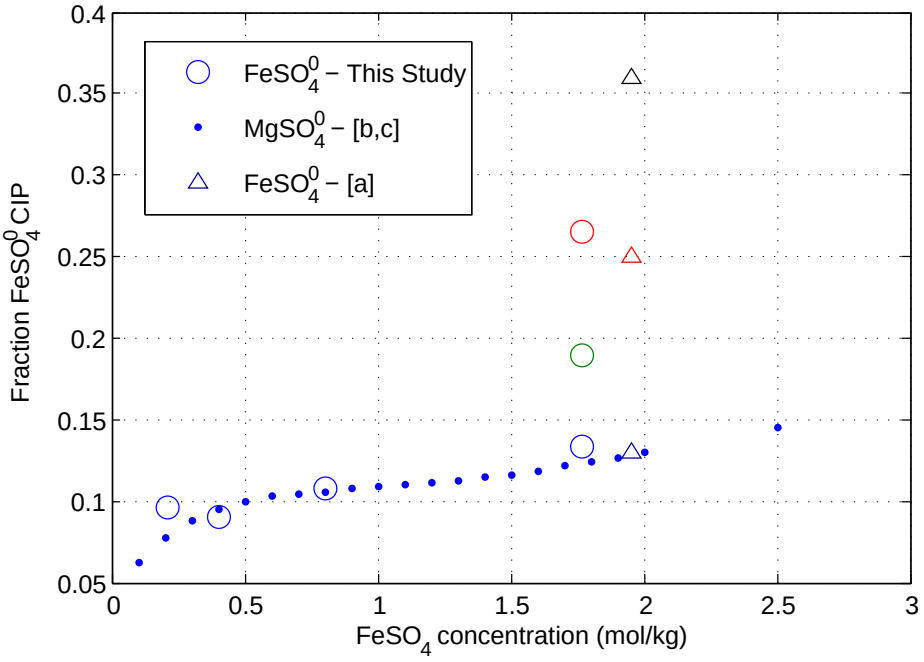

Figure 4.14: $FeSO_4^0$ CIP formation in $FeSO_4$ solutions as a function of concentration and temperature. Measurements of this study are blue, green and red at 25, 50 and 90 °C respectively. References: [a]: Rudolph et al. (1997) (T = 25 (blue), 95 (red), 125 (black) °C), [b]: Rudolph et al. (2003) (T = 25 °C (blue)), [c]: Buchner et al. (2004) (T = 25 °C) (blue). Data are also tabulated in Table B.2 in Appendix B.

4.2.5 $Fe_2(SO_4)_3$ system Raman spectra and speciation

Raman spectra, in R-format, of five $Fe_2(SO_4)_3$ solutions at 25 – 90 °C are presented in Figure 4.15a; a close up of the 800-1200 cm^{-1} region, with fitted component bands is also presented in Figure 4.16. Clearly, the 800-1200 cm^{-1} spectral region is significantly more complex than the $(NH_4)_2SO_4$, H_2SO_4 and $FeSO_4$ systems, with several additional bands being detected. Deconvolution of the bands in this region is challenging due to the unknown number of species present as well as the high correlation of the bands. The time-dependent quantum-level calculations from Section 4.1, UV-vis measurements (Section 4.3) and available information from open literature were used to assign the bands. However, the overlapping bands resulted in ill-conditioned curve fitting and the number of adjustable parameters required reduction. This was done by assuming all bands in the 800-1200 cm^{-1} region has no Gaussian component, i.e., Lorenzian bands were assumed. Given the accuracy of the measurement and the data treatment technique, it is expected that this induced a negligible influence on the speciation trends and significantly improved the robustness of the regression by reducing a degree of freedom.

4.2.5.1 High frequency: 800-1200 cm^{-1} region

The band assignments of the 981 cm^{-1} and 1040/1050 cm^{-1} bands was relatively easy based on the extensive study of neutral and acidic sulfate system in the open literature.

Firstly, the prominent 981 cm^{-1} ν_1-SO_4^{2-} band of unassociated sulfate is visible in all $Fe_2(SO_4)_3$ spectra, however, the relative intensity of this band decreases with increasing temperature and, to a lesser extent, concentration. The relatively weak concentration dependence of the 981 cm^{-1} band intensity, as compared to the other bands in the 800-1200 cm^{-1} region, is not expected from the similar Fe(III):SO_4^{2-} ratios in these solutions; as with the H_2SO_4 and $FeSO_4$ systems. Typically extreme ligand:metal ratios are required to shift the dominance of the solution species to one main solutions species (Murata et al., 1989). The FWHH of the 981 cm^{-1} band was observed to broaden with increasing concentration and temperature, which is in line with that noted by others in different sulfate systems (Fujita and Kimura, 1981; Rudolph, 1996).

Secondly, two composite bands in the 1040-1050 cm^{-1} region are assigned to the ν_3-HSO_4^- modes (assuming average C_{3v} symmetry in solution). The presence of bisulfate is expected, due to both the strong tendency of Fe(III) to hydrolyse as well as small quantities of H_2SO_4 being entrained in the $Fe_2(SO_4)_3 \cdot xH_2O_{(s)}$ reagent. However, the significant contribution of these bands in $Fe(SO_4)_3$ solutions can not be explained solely by entrained acid and, as will be discussed Section 4.2.1, must have originated from the

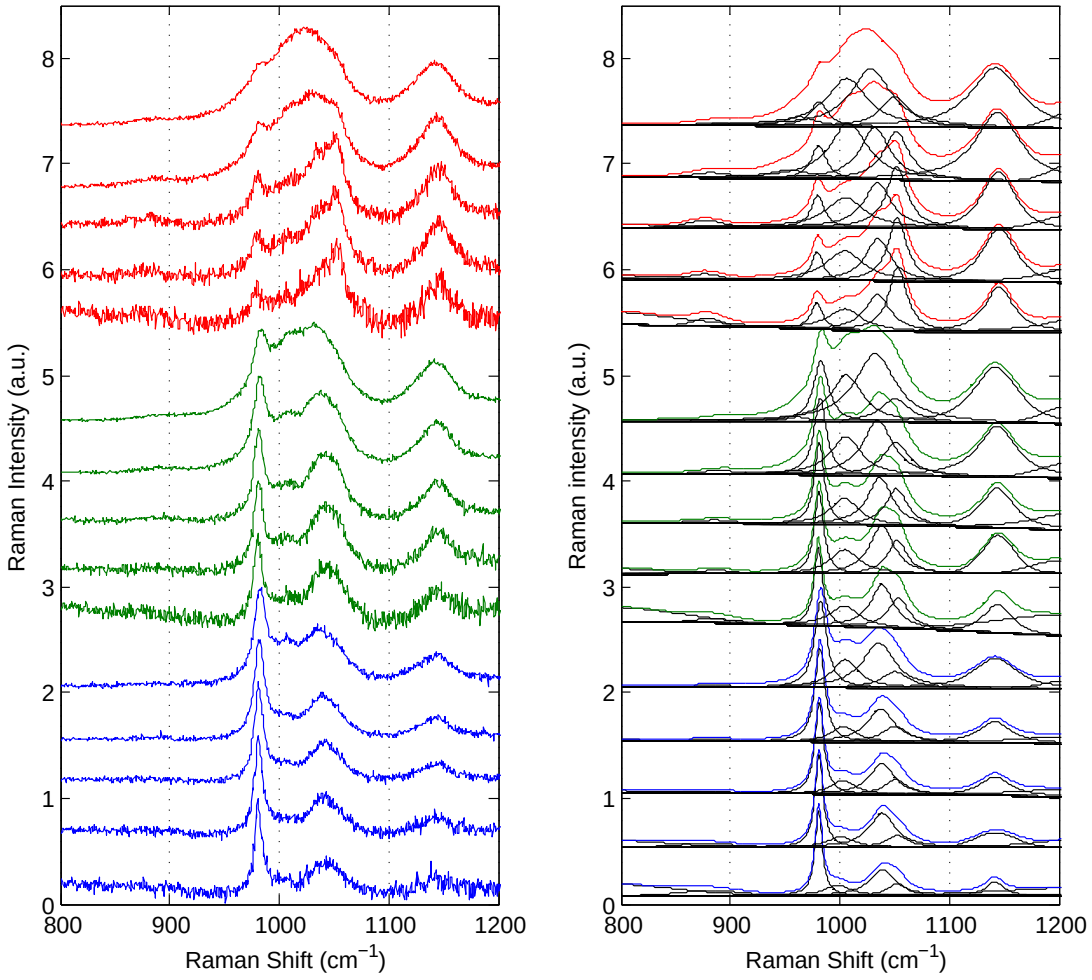

(a) Measured Raman spectra

(b) Fitted component bands

Figure 4.15: Measured and fitted $Fe_2(SO_4)_3$ Raman spectra at 25 (blue), 50 (green) and 90°C (red) at concentrations from 0.10, 0.19, 0.39, 0.75 and 1.60 mol/kg (stacked with increasing concentration). Spectra are presented in R-format and have been scaled to have a identical maximum intensities

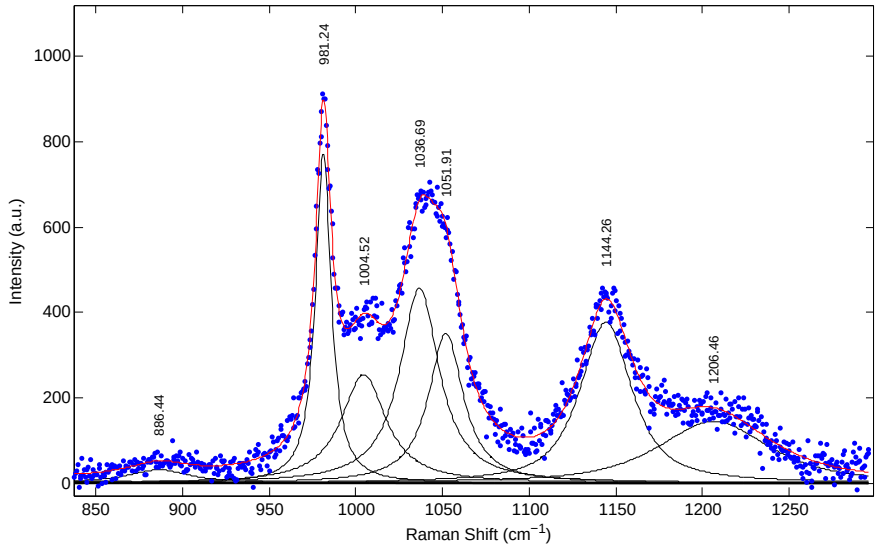

Figure 4.16: Enlargement of the measured and fitted Raman spectra of 0.75 mol/kg $Fe_2(SO_4)_3$ at 50°C over the 850-1300 cm^{-1} region. Individual component bands and centre wavenumbers are shown.

hydrolysis of Fe(III) to one or more of the $Fe(OH)_n^{3-n}$ species. Raman spectral evidence for these hydroxyl species was not deteceded since these species have comparatively weak Raman intensities of the Fe-OH modes which are known to occur in the 300-450 cm^{-1} region; for example see Figure 1 in Murata et al. (1989).

The H_2SO_4 system the results of Lund Myhre et al. (2003), as well as those in this study suggested that the 1040 cm^{-1} band was consistently of lower intensity to the 1050 cm^{-1} band, and that the band widths were approximately equivalent. Interestingly, some divergence from this trend was noted in the $Fe_2(SO_4)_3$ system, with the 1040 cm^{-1} band occasionally having a larger intensity than the 0.18:1 ratio reported by Lund Myhre et al. (2003). Besides, both bands were observed to shift to lower wavenumbers with increasing concentration, while only the 1040 cm^{-1} band shifted significantly with increasing temperature, in accordance with previous findings (Dawson et al., 1986). In $Fe_2(SO_4)_3$ solutions another band at 1030-1035 cm^{-1} makes the true deconvolution of the the 1040 cm^{-1} band of HSO_4^- difficult. Several $Fe_2(SO_4)_3$ solutions containing added H_2SO_4 (C1-C6 in Table 4.3) were thus also analysed in order to increase the contributions of HSO_4^- and aid in the deconvolution of bands in this region, several spectra from these solutions are presented in Figure 4.17a. Indeed, particularly at lower Fe(III) concentrations, the 1040/1050 cm^{-1} bands were dominant in the 800-1200 cm^{-1} spectral region, while the contributions of the 1030 cm^{-1} band were still detectable.

As discussed in Section 2.6.2, a number of ferric complexes that include protonated species have been proposed in the literature, such as $FeH(SO_4)_2^0$ (Casas et al., 2005). While no structures of these complexes have been directly proposed, however the labile proton is stabilised, one can expect the structure of the associated sulfate would not be similar to the HSO_4^- species. This is reasoned from the fact that the proton would likely not be closely associated with the metal core and probably (weakly) bonded to one of the sulfate species. The structure of sulfate in such a species would likely not resemble the HSO_4^- moiety and thus would be expected to have a unique Raman band. Moreover, the proposal of this species by Casas et al. (2005) was based largely on conductivity measurements and the requirement of decreasing free proton concentration in order to successfully model experimental measurements. However, it must also be noted that while the Raman analysis in this study does suggest that none of these species are present in large concentrations below 90 °C, their existence cannot be completely discarded and will likely become important at higher temperatures, for instance as a precursor to jarosite precipitation (Majzlan and Myneni, 2005).

The two remaining bands in the 981-1050 cm^{-1} region are observed only with the addition of Fe(III) into the acidic sulfate system and are assigned to Fe(III)-SO_4^{2-} CIP's. In conjunction with the noted decrease in the free sulfate band at 981 cm^{-1}, these bands provide direct evidence for the extensive formation of Fe(III)-SO_4^{2-} CIP's in $Fe_2(SO_4)_3$ solutions. A number of explicit Fe(III)-SO_4^{2-} species have been suggested in the literature (Stipp, 1990), generally to best model specifically measured solution properties, however few studies have directly probed their exact chemical nature.

The most simple $Fe_2(SO_4)_3$ CIP is the 1:1 $FeSO_{4(aq)}^+$ complex. The DFT analysis in the previous section suggested that the vibration energy of the ν_1-SO_3 stretch occurs at a higher frequency than unassociated sulfate, but lower than that of HSO_4^-, which is in agreement with the two remaining unassigned bands. Another recent study of Fe(III) solutions by Raman showed that, apart from the 981 cm^{-1} band, the most significant contribution in this region in solutions containing much higher Fe(III):SO_4^{2-} ratios (i.e., of about 11) was a band at 1040 cm^{-1} (Sobron et al., 2007). This band cannot solely be attributed to the formation of HSO_4^- due to the much weaker band at 1055 cm^{-1} and must have originated from a "low-sulfate" CIP, such as $FeSO_4^+$. Furthermore, a Raman spectroscopic study of CIP formation in $Al_2(SO_4)_3$ solutions highlighted that the $AlSO_4^+$ CIP exhibited a ν_1-SO_3 stretch at 1010 cm^{-1} (Rudolph and Mason, 2001). The 1035 cm^{-1} band in $Fe_2(SO_4)_3$ solutions is thus assigned to the $FeSO_{4(aq)}^+$ CIP.

The additional band in the 918-1050 cm^{-1} region, at 1005 cm^{-1}, showed significantly larger temperature dependence and is assigned to the anionic $Fe(SO_4)_2^-$ complex. Several

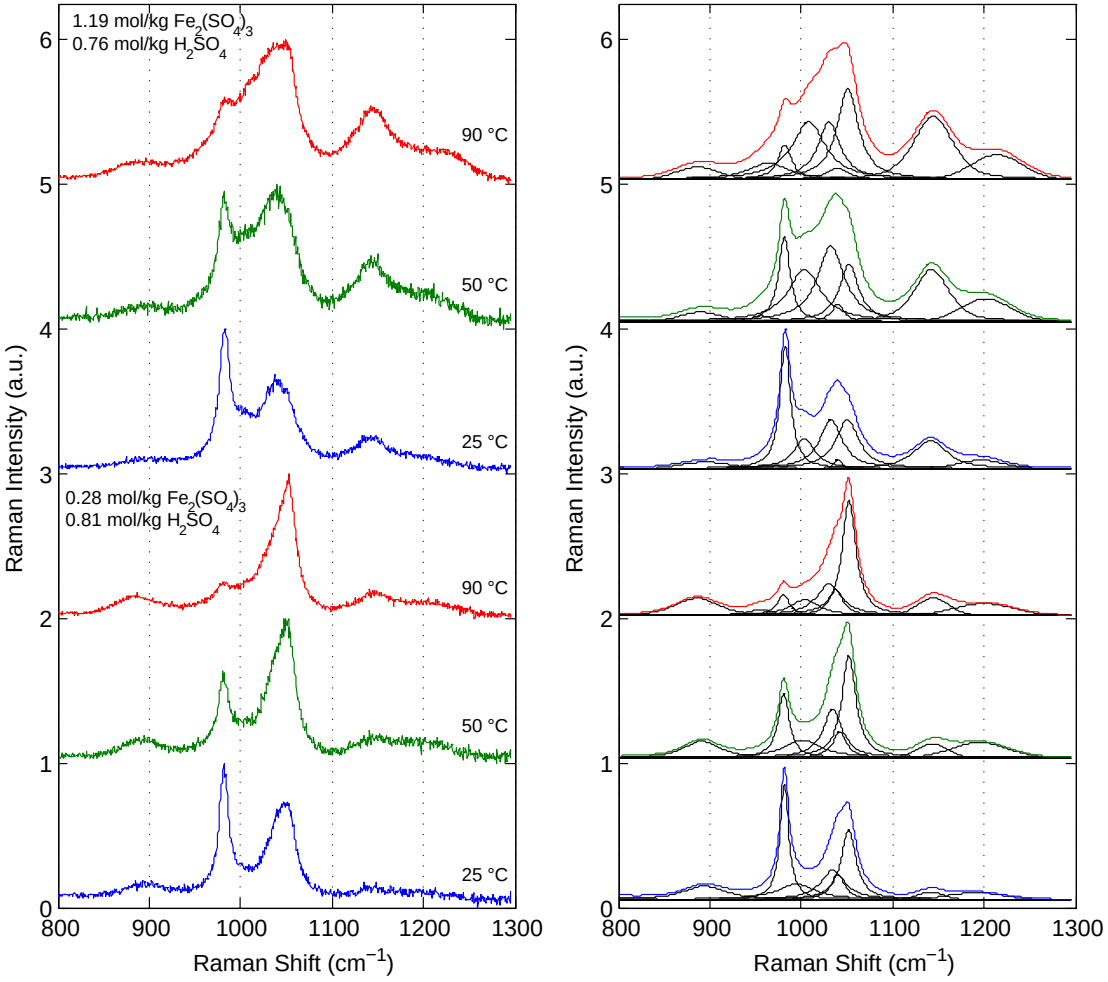

(a) Measured Raman spectra

(b) Fitted component bands

Figure 4.17: Measured and fitted Raman spectra (R-Format) of two $Fe_2(SO_4)_3$ + H_2SO_4 solutions at 25, 50 and 90 °C. The fitted bands in figure (b) highlight the strong response of HSO_4^- (1050 cm^{-1}), particularly at low Fe(III), while the $Fe(SO_4)_2^-$ species (1005 cm^{-1}) is dominant at higher Fe(III).

arguments can be made for this assignment. Firstly, the charge distribution around the trans-$Fe(SO_4)_2^-$ CIP likely results in the FeO-S bonds being slightly longer than the equivalent $FeSO_4^+$ and HSO_4^- complexes and more closely resembling that of unassociated sulfate (see DFT calculations in the previous section). This has the effect of decreasing the vibration energy of the ν-SO_3 band and it can be expected to lie between the SO_4^{2-} and $FeSO_4^+$ ν-SO_3 bands. Secondly, the strong temperature dependence of this band suggests that the entropy of formation is larger, as would be expected from the release of two water molecules from the Fe(III) octahedron during formation of the $Fe(SO_4)_2^-$ species. Indeed, the available data do suggest the ΔS^0 to be of the order of 232-275 J/mol.K compared to 165-167 J/mol.K for $FeSO_4^+$ formation, although these do include outer-sphere contributions due to their measurement technique (Wagman et al., 1982; Papangelakis et al., 1994; Liu et al., 2003). Additional support for this assignment can be taken from the previous study of Sobron et al. (2007), where an analysis of low Fe(III):SO_4^{2-} ratio's produced only a weak, but detectable, band at 1005 cm^{-1} while the band at 1035 cm^{-1} was clearly evident (see Figure 1 in Sobron et al. (2007)). In stoichiometric solutions, such as those presented in Figure 4.15a, the 1005 and 1035 cm^{-1} bands have similar relative intensities. However, at the low relative sulfate concentrations, one would expect the concentration of $Fe(SO_4)_2^-$ to be significantly lower than that of the $FeSO_4^+$ species. The assignment of these ν_1-SO_3 bands to the two Fe(III)-SO_4^{2-} CIP's is further validated by concentrated UV-vis spectroscopy in the following section.

Lastly, two high frequency bands at 1144 and 1206 cm^{-1} are visible in all the measured spectra and both increase in intensity with increasing $Fe_2(SO_4)_3$ concentration and temperature. These bands originate from the ν_3-SO_3 modes of the various ligated species. However, the lack of any significant bands in H_2SO_4 and $FeSO_4$ solution spectra highlight that these peaks are primarily attributed to the ferric sulfate ion pairs and are likely due to splitting of the antisymmetric stretching modes within the complex. Similar bands at 1154 cm^{-1} were observed in $Al_2(SO_4)_3$ solutions, albeit at significantly lower intensities (Rudolph and Mason, 2001). Specifically, the 1144 cm^{-1} band intensity was found to be highly correlated to that of the 1005 and 1035 cm^{-1} bands, as presented in Figure 4.18. There appeared to be a greater correlation between the 1005 and 1144 cm^{-1} bands, however, from the data measured in this study, the interaction of the 1035 cm^{-1} band could not be ruled out. Nevertheless, since speciation calculations in the next paragraph were focused on the ν_1-SO_3 modes, beyond providing further evidence for direct Fe(III)-SO_4^{2-} interaction, these bands were not considered further.

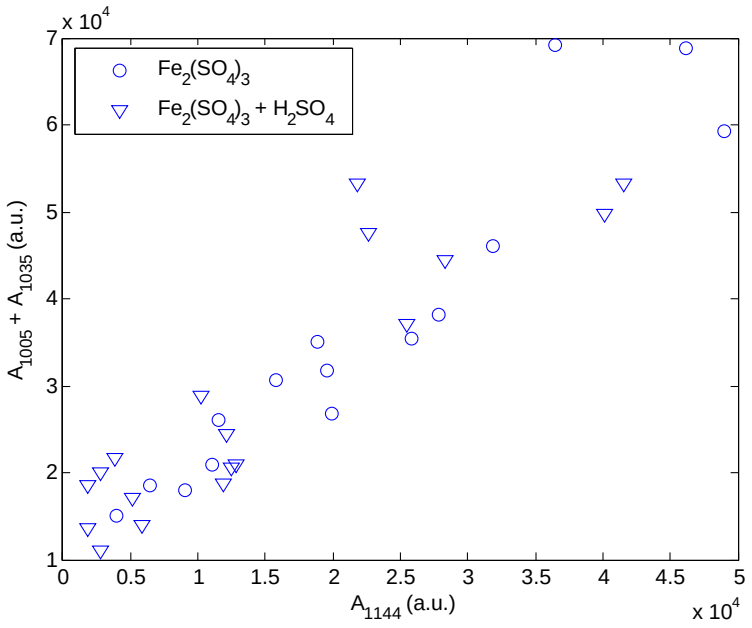

Figure 4.18: Correlation of 1144 cm^{-1} and 1005 + 1035 cm^{-1} bands in $Fe_2(SO_4)_3$ and $Fe_2(SO_4)_3$+H_2SO_4 solutions

4.2.5.2 Low frequency: 200-700 cm^{-1} region

The low frequency region of the Raman spectra also highlight some important features, which add validity to the previous paragraph's assignments and are presented in Figure 4.19. The most distinguishing band, in comparison to those spectra of the $(NH_4)_2SO_4$, H_2SO_4 and $FeSO_4$ solutions, is the intense band at 293 cm^{-1}, which increases in intensity with temperature and, to a lesser extent, concentration. This band is attributed to the low frequency Fe-OSO_3 stretch within the $Fe(SO_4)_n^{3-2n}$ CIP's and provides further direct evidence for the presence of these solution species. Given the similarity of the calculated geometry of the $FeSO_4^+$ and $Fe(SO_4)_2^-$ species, with respect to the Fe-O-S bonds, highlighted in Section 4.1, it is unlikely that their individual contributions to the 293 cm^{-1} band would be detectable. Thus, it was accepted that this band contained contributions from all ferric sulfato contact ion pairs.

Also evident from the low frequency spectra is the splitting of the sulfate deformational modes, measured at $\nu_4(f_2)$ at 619 cm^{-1} and $\nu_2(e)$ at 452 cm^{-1} respectively. In these $Fe_2(SO_4)_3$ solutions, the $\nu_2(e)$ band was split to approximately 445 and 483 cm^{-1} and the $\nu_4(f_2)$ band was split to approximately 610 and 655 cm^{-1} respectively. In both instances the higher frequency component appeared to be have a smaller FWHH, while

the lower frequency component widened significantly with temperature and concentration. In reality, this lower frequency band, likely represents the contributions from the various CIP's. However, given the similar Fe(III):SO_4^{2-} ratios in these solutions, there is not sufficient variability to distinguish their individual contributions.

Another band, at approximately 560 cm^{-1}, was observed in the 50 and 90 °C spectra. It is known that the $Fe(OH)_n^{3-2n}$ hydroxyl species have their dominant Fe-O stretches in the 300-450 cm^{-1} region (Murata et al., 1989), while those of $Fe(H_2O)_6^{3+}$ are known to occur in the region of 510 cm^{-1} (Kanno, 1988) to 523 cm^{-1} (Jarzecki et al., 2004) and known to be quite weak. Thus, these bands cannot be conclusively excluded from any $[Fe(OH)_n(H_2O)_m]^{3-2n}$ species, particularly as these bands were not clearly visible in solutions with added H_2SO_4. However, the lack of direct evidence of these species does not prevent the use of the high frequency data to determine the *sulfate* species distribution, from which the remaining species can be calculated by a mass balance with several simplifying assumptions, discussed in the following section.

4.2.5.3 Speciation

With the various Raman bands assigned to the appropriate species, the calculated fractions of SO_4^{2-}, HSO_4^-, $FeSO_4^+$ and $Fe(SO_4)_2^-$ were determined from integrated intensity ratios of the ν_1-SO_3 band from $Fe_2(SO_4)_3$ and $Fe_2(SO_4)_3 + H_2SO_4$ solutions. The J-values for the ferric species were estimated simultaneously from a mass-balance-constrained fit of measured Raman intensities of solutions containing added $NaClO_4$ as an internal standard and are presented in Table 4.4. The details of this standardisation procedure are deferred to Appendix B.1.2 for continuity. Using these J-values, and those calculated for sulfate and bisulfate, the resulting distribution of sulfate among SO_4^{2-}, HSO_4^-, $FeSO_4^+$ and $Fe(SO_4)_2^-$ could be calculated easily and are presented in Figure 4.20 for $Fe_2(SO_4)_3$ solutions; the data are also tabulated in Tables B.3 and B.4 in Appendix B.

In order to build confidence in the methodology, the speciation calculated from those solutions with added $NaClO_4$ are also included in Figure 4.20 and were used to estimate the variance associated with the measurement and data treatment of the Raman data to extract speciation trends in these solutions. The error bars represent the maximum standard deviation of each set of measurements at each temperature and, since they are calculated from only two measurements, are indicative only. Given the nature of such measurements, the significant scatter is not unexpected and the reasonably similar estimates of the species' concentration from the samples with and without $NaClO_4$ standard confirms the standardization approach.

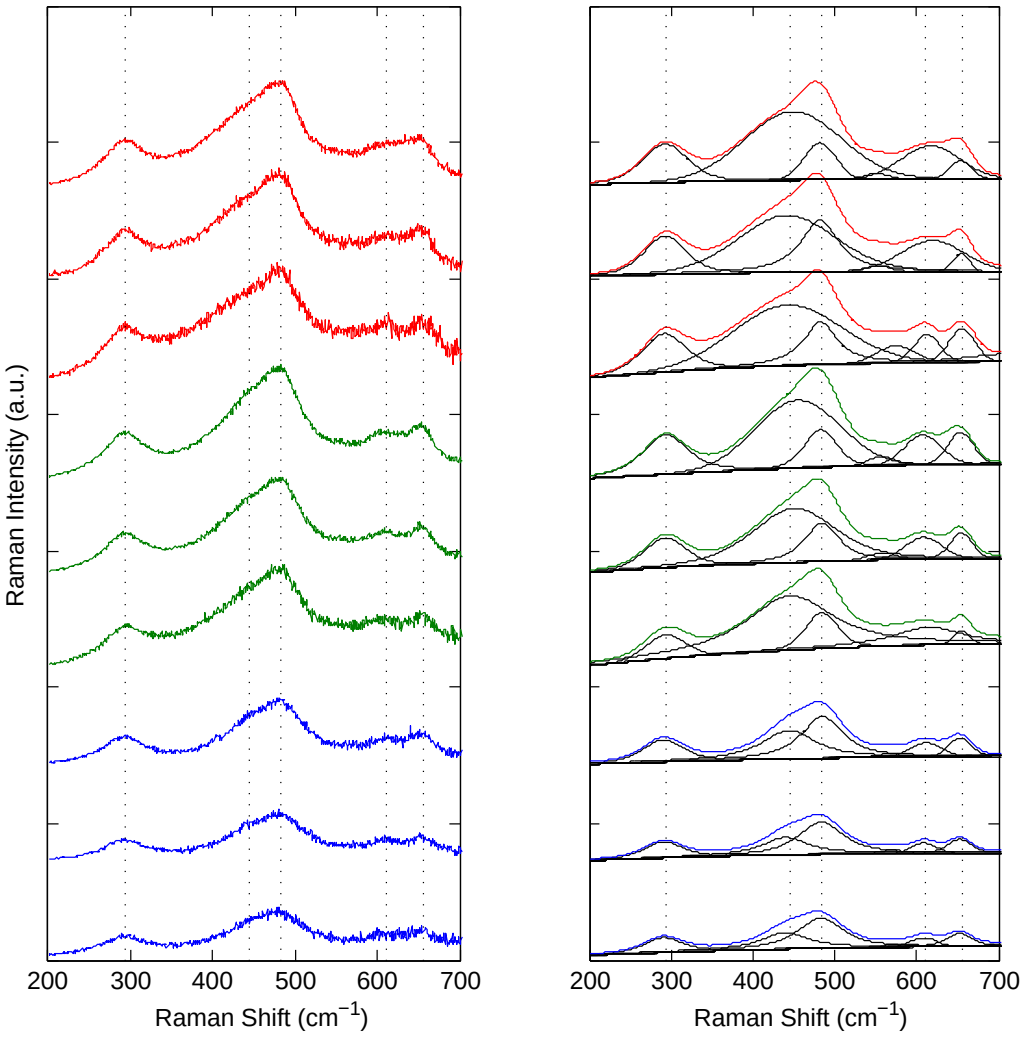

Figure 4.19: Low frequency measured and fitted $Fe_2(SO_4)_3$ Raman spectra at 25 (blue), 50 (green) and 90 °C (red) at concentrations from 0.39, 0.75 and 1.6 mol/kg $Fe_2(SO_4)_3$ (stacked with increasing concentration). Spectra are presented in R-format and have been scaled to have a identical maximum intensities

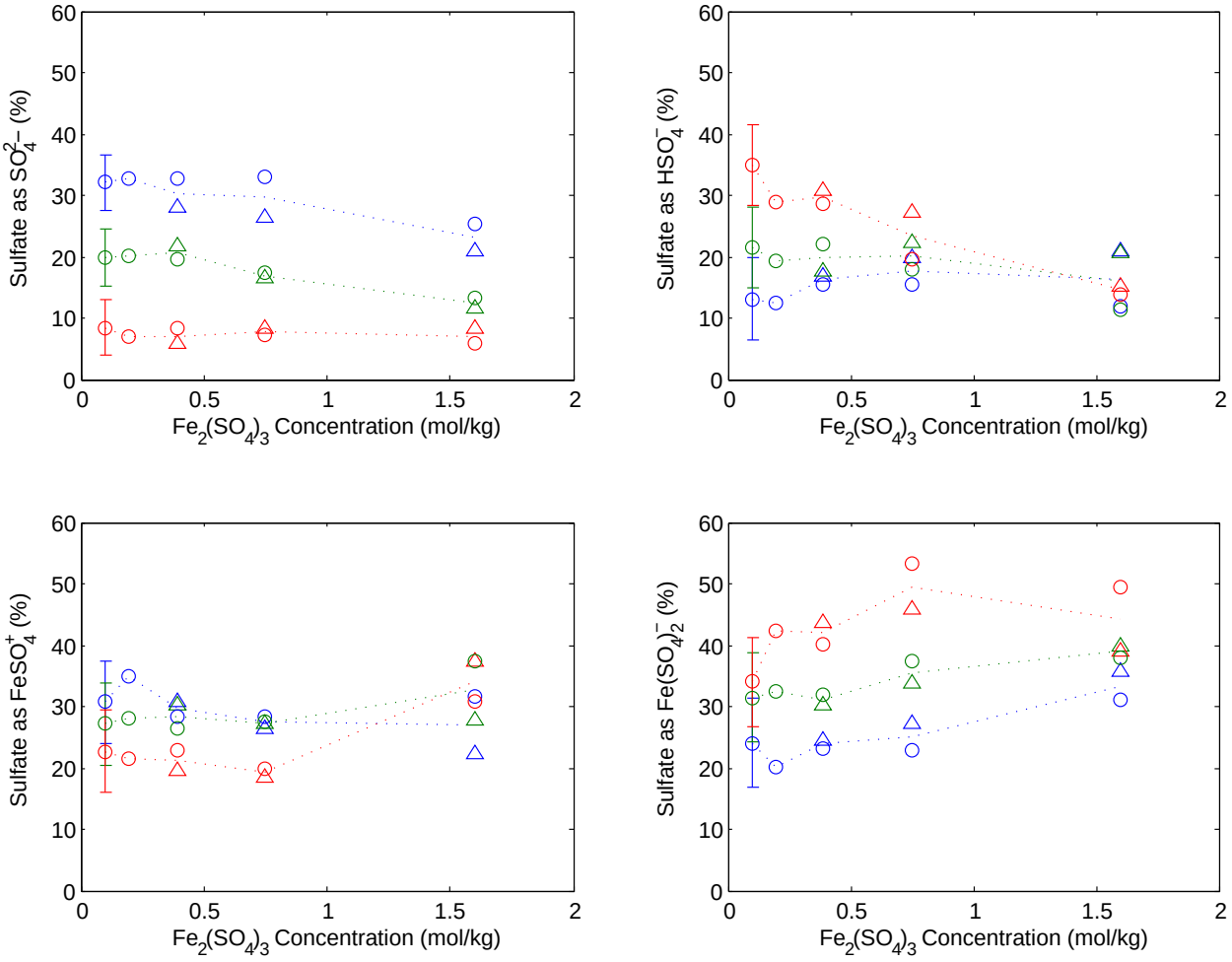

Figure 4.20: Ferric sulfato speciation in $Fe_2(SO_4)_3$ solutions as a function of concentration at 25, 50 and 90 °C. Circles represent pure $Fe_2(SO_4)_3$ solutions and triangles represent solutions with 0.5 mol/kg $NaClO_4$ added as internal standard. Error bars illustrate experimental and data treatment variance from two independent measurements

The trends in speciation conform to the expected trend with an increasing tendency to form contact ion pairs with increasing temperature (entropically drive) and a detectable, but less intense effect of concentration. Perhaps the most interesting features produced from this analysis is the near constant fraction of sulfate associated as $FeSO_4^+$ and the significant concentration changes occurring between the HSO_4^- and $Fe(SO_4)_2^-$ species, particularly at elevated temperatures. Clearly, at lower concentrations, the formation of HSO_4^- is dominant. However as the solution becomes more concentrated in $Fe_2(SO_4)_3$, the $Fe(SO_4)_2^-$ species becomes increasingly more stable. Despite this, if one considers the distribution of iron species, the solution is clearly dominated by the $FeSO_4^+$ species. From this data alone, it is difficult to determine the fraction of Fe^{3+} and $Fe(OH)_2^+$ species because the H^+ concentration is also not known explicitly. Thus, the iron species distribution is deferred to Section 5.5 where the solution model, calibrated on these speciation measurements, is used to determine the complete iron species distribution.

A further interesting interpretation of the solution speciation can be taken from the mixed $Fe_2(SO_4)_3$-H_2SO_4 solutions, presented in Figure 4.21, which also indicate the average values taken from the $Fe_2(SO_4)_3$ solutions only for comparison. Importantly, a significant increase in the solution acidity, i.e., a variation of 1.5 mol/kg total H^+, produces the greatest variation in the HSO_4^- species predominance. The HSO_4^- concentrations are significantly larger in solutions with added acid, while the fraction SO_4^{2-} remains essentially unchanged. The sulfate species distribution thus appears to shift towards HSO_4^- at the expense of $FeSO_4^+$ and, at lower $Fe_2(SO_4)_3$ concentrations, $Fe(SO_4)_2^-$. This trend is critical and provides further evidence for the species present in solution. As discussed above, some have included polycationic species in their modelling frameworks, specifically the $FeH(SO_4)_2^0$ and $FeHSO_4^{2+}$ species (Dry and Bryson, 1988; Liu et al., 2003; Casas et al., 2005; Yue et al., 2014). If the bands attributed to $Fe(SO_4)_2^-$ species in this work were in fact one of these polycationic species, one would expect its predominance to increase with added H_2SO_4. However, the spectroscopic results presented here indicate that the fraction of sulfate associated at the $Fe(SO_4)_2^-$ species is *lower* in the presence of H_2SO_4 and the most significant effect of added acid is a large increase in the HSO_4^- concentration. This is critical since no direct experimental evidence has been reported for the structure of such polycationic species, which, as pointed out above, would likely have a significantly different Raman spectrum, in $Fe_2(SO_4)_3$ solutions and supports the selection of only the minimum number of solution species identified in this work.

These speciation results also reveal the strong tendency for CIP formation in $Fe_2(SO_4)_3$ solutions. Figure 4.22 presents the fraction of total Fe(III) in the solution that is associated in the $FeSO_4^+$ and $Fe(SO_4)_2^-$ contact ion pairs. The average values over these mea-

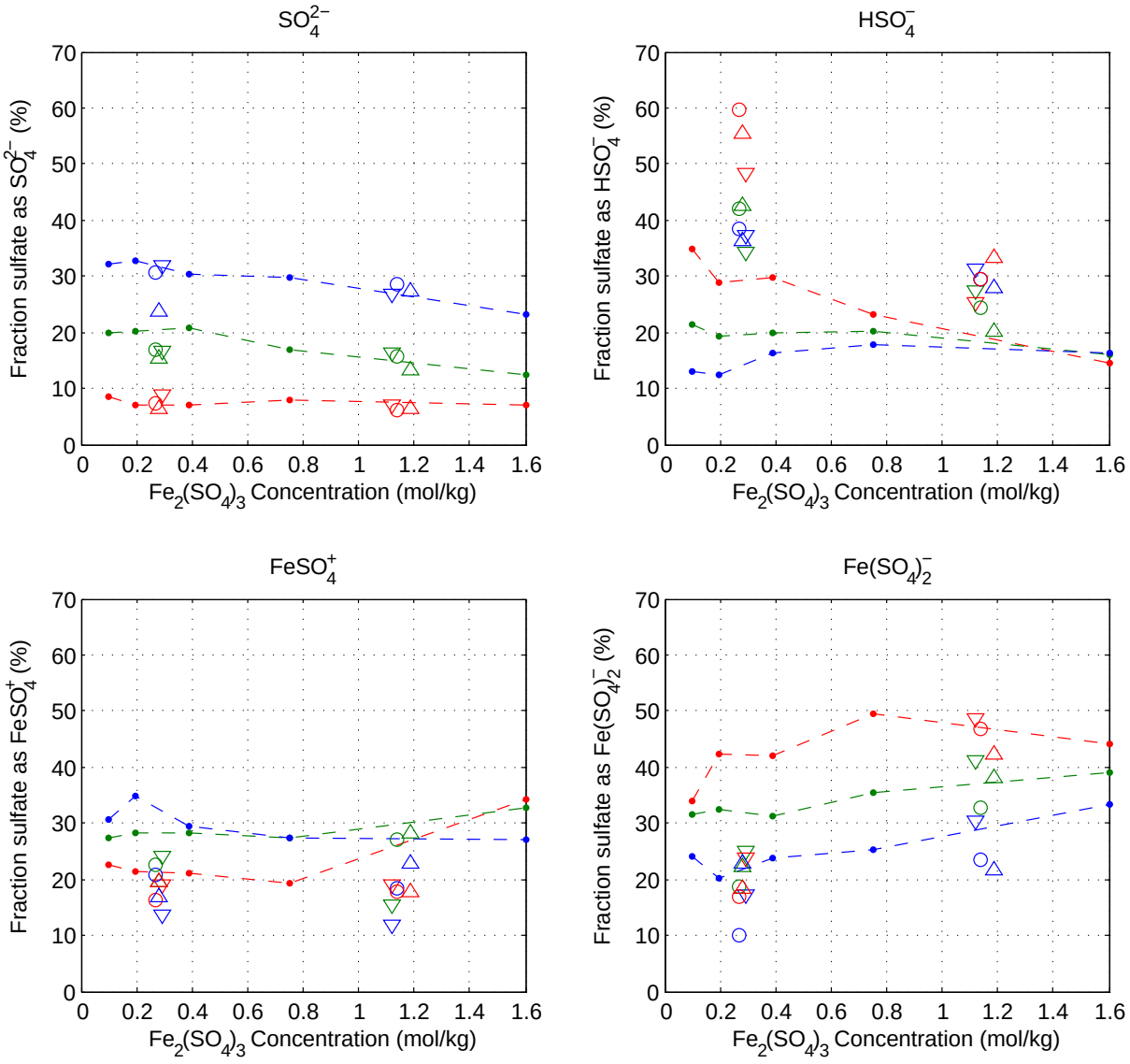

Figure 4.21: Solution speciation in $Fe_2(SO_4)_3$ + H_2SO_4 solutions as a function of concentration at 25, 50 and 90 °C. Acid concentrations: ▽ = 0.5 mol/kg H^+, ◯ = 1.0 mol/kg H^+, △ = 1.5 mol/kg H^+. Temperature: 25 (blue), 50 (green) and 90 °C (red). Dots (and joining dashed lines) represent the speciation with no added acid, i.e., from Figure 4.20, for comparison of the effect of added acid. Data are also tabulated in Tables B.3 and B.4 in Appendix B

surements is 68% at 25 °C and 71% at 90 °C, which is significantly larger than other di- and tri-valent systems that have been studied by Raman and DRS in the literature, clearly depicted in the figure. This increased tendency of Fe(III) to form contact ion pairs in sulfate solutions can be attributed to several factors. The Fe^{3+} ion is highly charged and relatively small (d_{ion} = 1.28 Å (Marcus, 1988)) and, while comparable to the Al^{3+} ion, has partially filled 3^d-orbitals, which have much greater interaction with ligands than the fully filled 2p-orbitals of Al^{3+}. Furthermore, ferric ion is well known to only be stable in acidic solutions and to precipitate from solution at pH 2-3 (whereas Al^{3+} is not). This emphasizes its increased tendency to form hydroxyl CIPs, compared to other tri- and di-valent metals which are stable to higher pH. By analogy, it is not unexpected that ferric exhibits a similar tendency with sulfate, particularly in solutions with stoichiometric ferric:sulfate ratios and the natural intense electrostatic attraction between 3-2 charged species.

Moreover, an important implication for the high fraction of sulfate co-ordinated as ferric sulfato ion pairs, provides supporting evidence that at least one of these species must be negatively charged. The calculation of the fraction iron complexes in Figure 4.22 can be done independent of the J-values of the ferric sulfato species in solutions with an added internal standard and can be achieved using only the J-values of sulfate and bisulfate, which have been widely reported in the literature. Given that the amount of complexed sulfate is of the order of 70%, a simple charge balance emphasizes that, in order to maintain electroneutrality, an anionic ferric sulfato species, such as $Fe(SO_4)_2^-$ must have formed, further supporting the band assignments made in the previous paragraphs.

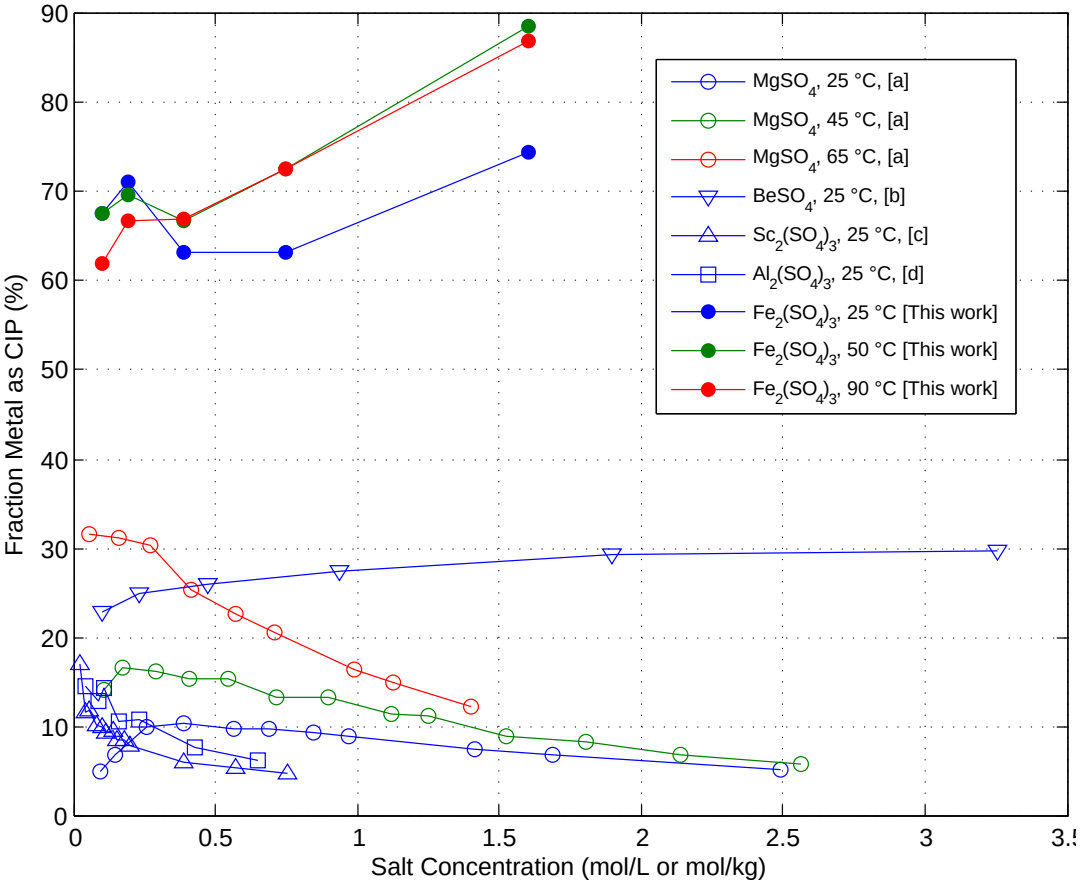

Figure 4.22: Comparison of measured and reported fractions of CIP's for several di- and tri-valent sulfate systems. [a]: Akilan et al. (2006b), [b]: Rudolph (2010), [c]: Schrodle et al. (2008), [d]: Schrodle et al. (2007)

4.3 UV-vis spectroscopy

UV-vis spectroscopy has been previously used to identify $Fe(SO_4)_n^{3-2n}$ species in dilute solutions and information regarding the molar absorption coefficients for the $FeSO_4^+$ and $Fe(SO_4)^{2-}$ species are available in the open literature (Whiteker and Davidson, 1953; Davis and Smith, 1962; Sapieszko et al., 1977; Benkelberg and Warneck, 1995; De Laat and Le, 2005; Kormanyos et al., 2008). These studies have shown that although these coefficients have broad and strikingly similar features, this method can be used to distinguish the mono- and di-sulfato ferric aqueous species. Thus, UV-vis spectroscopy of $Fe_2(SO_4)_3$ solutions can facilitate an independent means of verifying the Raman analysis in the previous section.

UV-vis spectroscopy is typically limited to low analyte concentrations to ensure total absorption of the incident light does not occur. In this study, to investigate solutions of similar concentrations to those investigated by Raman spectra, a short path-length flow cuvette (0.01mm, quartz, Starna Scientific) was used to limit the volume exposed to the light path and allow concentrated solutions to be analysed. The experimental setup is described in Section 3.4. During the experiment, a solution of 0.4 mol/kg $Fe(ClO_4)_3$, acidified with 0.25 mol/kg $HClO_4$ was circulated through the flow cuvette and controlled at 25 °C. The step-wise formation of ferric sulfato species was then investigated by the step-wise addition of $(NH_4)_2SO_4$ into the solution. Three spectra were acquired at each composition and the mean used for all calculations; these data are presented in Figure 4.23 and represent SO_4^{2-}:Fe^{3+} ratios from 0-4.5.

Clearly evident from Figure 4.23 are the three *almost* isobestic points at 196, 232 and 265 nm as well as increasing intensities in the 215 and 300 nm regions and decreasing intensity in the 240 nm region with increasing sulfate concentration. The three points of approximately constant intensity are observed to all shift with added sulfate, suggesting that there are (at least) three absorbing species in the solution. Moreover, the relatively small magnitude of this shift suggests that two components have very similar molar absorption coefficients.

The insert in Figure 4.23 (10X magnification) highlights the very weak shoulder in the region of 340 nm which is attributed to the $Fe(OH)_2^+$ species. This species has been shown experimentally and theoretically to have an absorption maximum at 335 nm (Lopes et al., 2002; Stefansson, 2007). The minor intensity associated with this species, in comparison to the major peak of Fe^{3+} at about 240 nm, suggests that minimal hydrolysis had occurred in the background of $HClO_4$ and the effects of these species could probably be excluded from the analysis. However, the identification of the $Fe(OH)_2^{2+}$ species in this solution

is significant and likely due to the relatively concentrated nature of the solution, i.e., 0.4 mol/kg Fe(III). Typically, $Fe(OH)n^{3-n}$ speciation is reported at low concentration, as a function of pH where n gradually increases from 0 to 4 over the range pH 0 - 12 (Stefansson, 2007). While the presence of $FeOH^{2+}$ ($n = 1$) cannot be excluded from these spectroscopic data, the detection of the $Fe(OH)_2^+$ species in acidic solution highlights that the high concentration of Fe(III) may favour higher-coordination's of ferric hydroxyl species. This has important implications for the handling of the $Fe(OH)n^{3-n}$ within the modelling framework developed in Chapter 5.

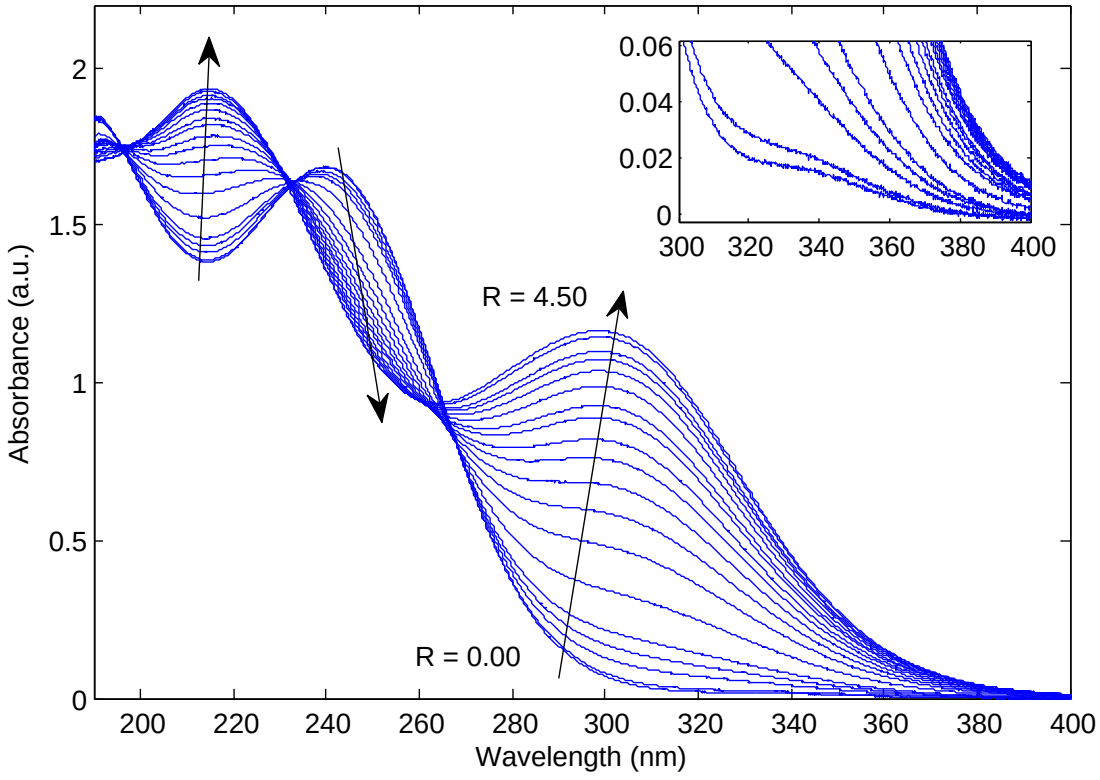

Figure 4.23: UV-vis spectra of 0.4 mol/kg $Fe(ClO_4)_3$ solutions with increasing SO_4^{2-} concentration at 25 °C. Spectra were taken at constant Fe(III) molality with sulfate to ferric ratios (R) from 0.00 - 4.50. Insert shows a small shoulder at 340 nm in the solution with R = 0.00 attributed to the $Fe(OH)_2^+$ species.

In order to further investigate the UV-spectra in this series, singular value decomposition (SVD) of the path-length corrected absorbance matrix was performed in order to

determine the number of absorbing species. Figure 4.24 presents the calculated singular values as well as the first four concentration loadings. The change in gradient with increasing singular values, signalling a loss of significant variance, appears to occur between three and four components. the concentration loadings are in agreement with this and confirm that the fourth component (dotted blue line) is likely not physically meaningful as it does not conform to a smooth trend as expected from the series of measurements. These analyses suggest that only three absorbing species are contributing to the measured spectra over the concentration range examined.

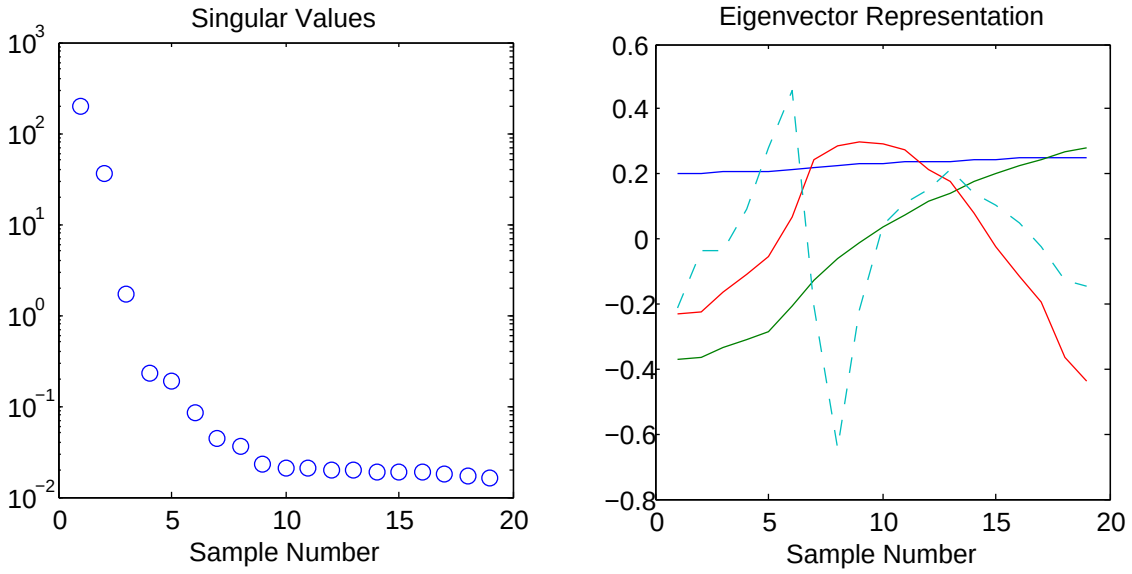

Figure 4.24: Singular values and the corresponding first four concentration eigenvectors of path-length corrected absorbance matrix. Three large singular-values (associated with the amount of variance explained) and the lack of a smooth profile of the fourth component suggests only three components are contributing to the measured spectra.

The high-quality spectra in Figure 4.23 facilitate a deeper analysis into the molar absorption coefficients and concentrations of each of the species in the solution. Multivariate Curve Resolution by Alternating Least Squares (MCR-ALS) was used to estimate concentrations an molar extinction coefficients simultaneously from the spectral data (Jaumot et al., 2005). The resulting molar extinction coefficients are presented in Figure 4.23 and are in excellent agreement with those reported in the literature (see references in Figure 4.25), despite the ferric concentrations in this study being *two to three orders of magnitude larger*. This tentatively validates the short path-length method for the analysis

of concentrated solutions. See Appendix B.2 for the complete details of the MCR-ALS procedure.

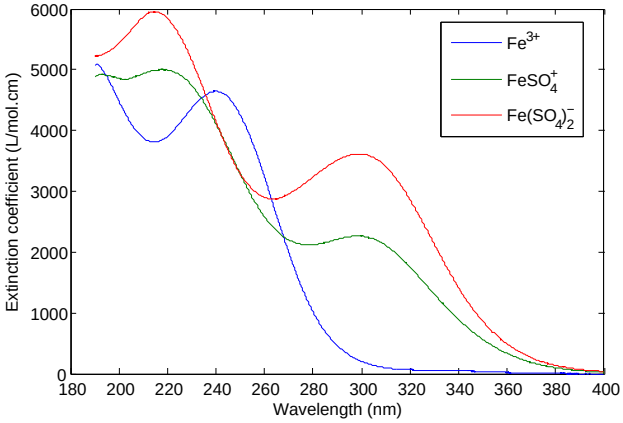

(a) Calculated molar extinction coefficients from the MCR-ALS algorithm

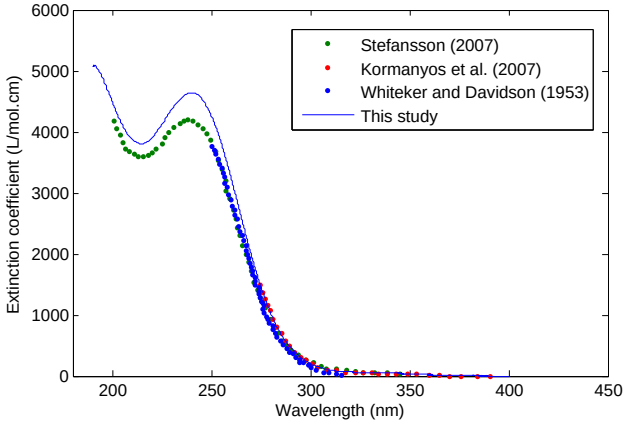

(b) Literature comparison between the molar extinction coefficient of Fe^{3+}

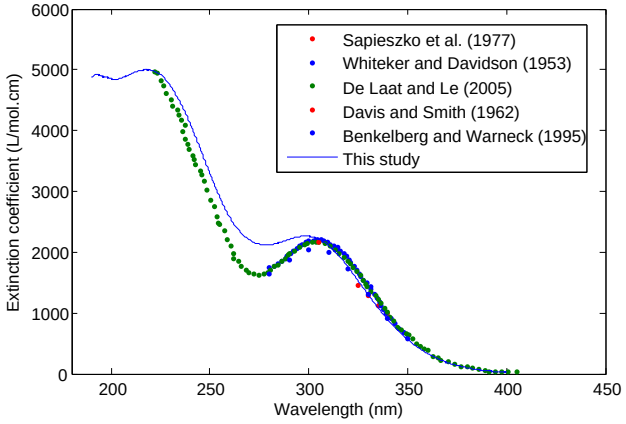

(c) Literature comparison between the molar extinction coefficient of $FeSO_4^+$

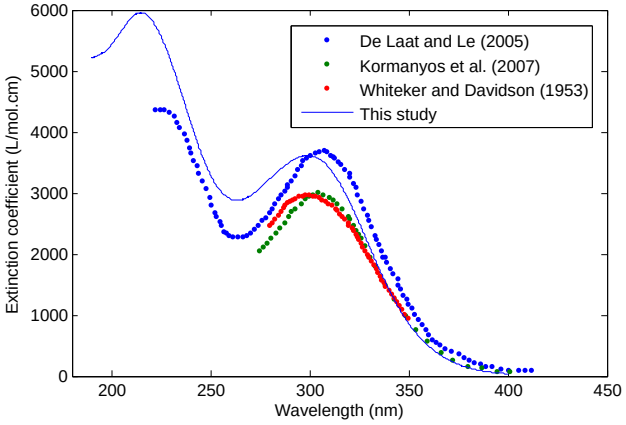

(d) Literature comparison between the molar extinction coefficient of $Fe(SO_4)_2^-$

Figure 4.25: Calculated UV-vis molar extinction coefficients from solutions of 0.4 mol/kg $Fe(ClO_4)_3$ and variable $(NH_4)_2SO_4$ at 25 °C.

The concentration profiles for these three components calculated from the MCR-ALS procedure are presented in Figure 4.26 and confirm that along with unassociated Fe^{3+}, or perhaps Fe^{3+} present in outer-sphere complexes which UV-vis is also not sensitive to,

two ferric sulfato contact ion pairs are present in solutions with SO_4^{2-}:Fe^{3+} = 1.5. The Raman analysis in the previous section highlighted that in pure $Fe_2(SO_4)_3$ solutions (i.e., SO_4^{2-}:Fe^{3+} = 1.5) the $FeSO_4^+$ and $Fe(SO_4)_2^-$ species were always present simultaneously and the amount of free sulfate suggested that Fe^{3+} was also present. These results confirm the simultaneous presence of these three species in acidic perchlorate solutions at the same SO_4^{2-}:Fe^{3+} ratio.

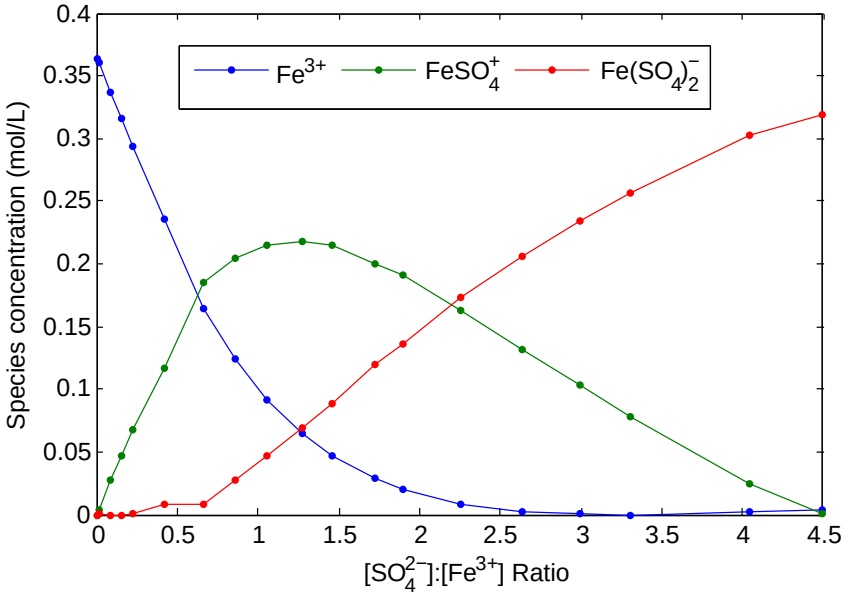

Figure 4.26: Calculated ferric sulfato species concentrations from UV-vis measurements of $Fe(ClO_4)_3$-$(NH_4)_2SO_4$ solutions at 25 °C, showing successively larger sulfate association with SO_4^{2-}:Fe(III) ratios. These concentrations were calculated using the molar extinction coefficients in Figure 4.25a and Equation 3.4.1.

Given the excellent agreement between the calculated molar scattering coefficients and those in the literature (Figure 4.25) and the resulting species concentrations, which are in agreement with the results of the Raman analysis, the UV-vis analysis unequivocally confirms the presence of the Fe^{3+}, $FeSO_4^+$ and $Fe(SO_4)_2^-$ species in 0.4 mol/kg $Fe_2(SO_4)_3$ solution at 25 °C. Additionally, this analysis significantly enhances the confidence in the Raman band assignments for the $FeSO_4^+$ and $Fe(SO_4)_2^-$ species previously made on the basis of concentration and temperature dependence of the Raman bands as well as qualitative TDDFT calculations.

4.4 Summary

This chapter has provided a detailed view of the nature of acidic $Fe_2(SO_4)_3$ systems as well other systems commonly associated with soluble ferric ion, i.e., H_2SO_4-H_2O and $FeSO_4$-H_2SO_4-H_2O. Static DFT calculations were used to optimise equilibrium geometry of the SO_4^{2-}, HSO_4^-, $FeSO_4^0$, $FeSO_4^+$ and $Fe(SO_4)_2^-$ solution species, and subsequently estimate their vibrational spectrum, with particular focus on the intense ν_1-SO_3 band. There was a significant correlation between the included O-S-O angle in the sulfate moiety and the spectral position of the sulfate stretching mode.

Spectroscopic measurements over a fairly wide concentration (0.1 – 1.6 mol/kg Fe(III)) and temperature range (25 – 90 °C) highlighted significant spectral changes in these systems. Bands were assigned to the dominant species and rationalised based on the DFT calculations, supporting literature and theoretical arguments.

Internal standardisation of the Raman spectra permitted the estimation of species concentration in each of the solutions and facilitated previously unavailable quantitative measurements of solution speciation in the $Fe_2(SO_4)_3$-H_2SO_4-H_2O system. Importantly, the findings highlighted that approximately 70% of Fe(III) in $Fe_2(SO_4)_3$ solutions is complexed in ferric sulfato contact ion pairs, emphasizing the criticality of considering speciation in this system in concentrated solutions, which become increasing stable at elevated temperatures.

Critically, for hydrometallurgical systems, the effects of added H_2SO_4 on the solution speciation in $Fe_2(SO_4)_3$ solutions was quantified. It was shown that, at $Fe_2(SO_4)_3$ concentrations of about 0.3 mol/kg, added acid reduces the concentrations of ferric sulfato CIP's slightly and significantly increases the fraction of HSO_4^- species. At higher $Fe_2(SO_4)_3$ concentration, the increased total sulfate concentration tended to stabilise the $Fe(SO_4)_2^-$ species, while still increasing the HSO_4^- above those solutions without added acid. A further important inference from this work was the lack of explicit evidence for other polycationic $FeH(SO_4)_n^{4-2n}$ or $Fe(OH)_n(SO_4)_m^{3-n-2m}$ species in solution and while they cannot be completely ruled out, their presence under the conditions of this study is unlikely.

In summary, the findings of this chapter have provided a good experimental and theoretical basis, previously unavailable in the open literature, for the development of a robust solution modelling framework for $Fe_2(SO_4)_3$-containing systems detailed in the following chapter.

Chapter 5

Equilibrium Systems: Modelling

The findings of Chapter 4 have made a significant contribution to the understanding of ferric in concentrated sulfate solutions and provide an excellent basis on which to develop a solution modelling framework for the $Fe_2(SO_4)_3$-H_2SO_4-H_2O system.

The primary objective of this chapter is to develop a self-consistent thermodynamic model of the various sub-systems applicable to the $Fe_2(SO_4)_3$-$FeSO_4$-H_2SO_4-SO_2-H_2O reactive system on which the kinetics of Fe(III) reduction with $SO_{2(g)}$ can be interpreted. Of primary importance to the modelling of kinetic processes are the aqueous species present in the system and thus the primary focus of the model developed in this chapter is to provide an adequate description of the solution speciation in this system on the basis of the spectroscopic measurements in the previous chapter.

Critically however, it is the aim of this section to develop a simplified model, which is capable of capturing the dominant trends in the systems' speciation. Within this approach, only experimentally verified species are to be considered and a minimum number of parameters used to capture the solution chemistry effectively. While it is acknowledged that only a simplified representation of the underlying chemistry will be captured by such a model, given the stringent constraints imposed on a thermodynamic framework by the subsequent requirement of modelling reaction kinetics, the absolute errors between the model and measured data are expected to be larger than typically observed in thermodynamic modelling studies. Ultimately, since the primary objective of this model is the characterisation of kinetic processes, errors in the thermodynamic model will be absorbed into the kinetic model parameters. However, this approach facilitates a reliable basis on which to develop, mechanistically, the important aspects of the reaction steps.

5.1 Solution model structure

The selection of a minimum number of solution species to adequately describe the thermodynamic behaviour of each of the sub-systems is not trivial, particularly considering the general lack of data describing these species. Furthermore, the selection of only a limited number of species, can artificially constrain the solution model due to specific stoichiometries and the requirement of mass and charge balancing. On the basis of the literature review and equilibrium spectroscopic measurements in previous chapters, a good basis for the selection of the most important species in the various sub-systems has been developed. As detailed in Table 5.1, the sulfate and bisulfate components were important to consider in all systems. Besides the obvious primary species, for systems containing $Fe_2(SO_4)_3$, it is expected that both the $FeSO_4^+$ and $Fe(SO_4)_2^-$ species require consideration, while for the $FeSO_4$ systems, only the $FeSO_4^0$ CIP is expected in appreciable concentration. Additionally, in ferric systems, the effect of hydrolysis is certainly required and it is suggested that a single surrogate $Fe(OH)_n^{3-n}$ species is included in the model to account for such effects. Lastly, in systems containing sulfite, the acid speciation is known to be important, i.e., HSO_3^- and $SO(OH)_2^0$ species, but critically for this study, the ferric sulfito complexes need to be considered. The lack of thermodynamic data for this species, particularly due to its transient nature, warrants special treatment in the kinetic solution model and is deferred to Chapter 7.

Table 5.1: Model sub-system structure and primary and secondary species

Reagent	Primary Species		Secondary Species
H_2SO_4	H^+	SO_4^{2-}	HSO_4^-
$FeSO_4$	Fe^{2+}		$FeSO_4^0$
$Fe_2(SO_4)_3$	Fe^{3+}		$FeSO_4^+$
			$Fe(SO_4)_2^-$
		H_2O	$Fe(OH)_n^{3-n}$
		SO_3^{2-}	$FeSO_3^+$
SO_2	H^+		HSO_3^-
			$SO(OH)_2^0$

The Pitzer equations, rigorously detailed in Section E.4, were implemented to the various sub-systems applicable to the $Fe_2(SO_4)_3$-$FeSO_4$-H_2SO_4-H_2O system in which binary and ternary model parameters could be regressed as independently as possible. Additionally, the SO_2-H_2O system was examined to facilitate the inclusion of the reducing agent within the reaction model. A key focus of this exercise was to try and reduce the number

of variable model parameters as much as possible to avoid over-parametrisation and improve the extrapolation capability of the model. Thus, parameters were either allowed to vary linearly with temperature or fixed, over the region of 25 – 95 °C according to Equation 5.1.1, where $T_{\text{ref}} = 298.15\text{K}$ and $n \leq 2$.

$$Par_{Pitzer}(T) = \sum_{i=1}^{n} p_{i-1}(T - T_{ref})^{i-1} \tag{5.1.1}$$

Another important consideration in the adopted modelling approach is that equilibrium constants typically reported in the literature are derived from total solution measurements such as potentiometry, titrations and calorimetry and represent the total contribution of contact ion pairs, solvent-separated ion pairs and doubly-solvent-separated ion pairs, i.e., outer-sphere complexes. In the solution modelling approach of this study, only the explicit contact ion pairs are of direct interest due to their distinct chemical differences from the outer-sphere complexes. Since these species are also directly measured by Raman spectroscopy, such experimental data can be considered directly applicable for calibrating parameters in such an approach.

5.2 H_2SO_4-H_2O system

The first dissociation of H_2SO_4 (Reaction 5.2.1) is essentially complete in aqueous solutions ($<$ 40 mol/kg) at room temperature (Clegg et al., 1994) and the $H_2SO_4^0$ only constitutes a minor component above 100°C (Steyl, 2012). However, the second dissociation (Reaction 5.2.2) is not complete and must be incorporated when modelling the thermodynamics of this system. Fortunately, this system has been reasonably well characterised due to its widespread importance and a variety of reliable thermodynamic data exist, especially at temperatures below 60°C. There are several reported solution models for the system (Pitzer et al., 1977; Clegg et al., 1994; Clegg and Brimblecombe, 1995) and the isopiestic study of Holmes and Mesmer (1992) include water activity data up to 200 °C, from which other thermodynamic properties were calculated.

$$K_1^\circ : \mathrm{H_2SO_4} \rightleftharpoons \mathrm{H^+ + HSO_4^-} \tag{5.2.1}$$

$$K_2^\circ : \mathrm{HSO_4^-} \rightleftharpoons \mathrm{H^+ + SO_4^{2-}} \tag{5.2.2}$$

The departure point for the H_2SO_4 model follows from Steyl (2012) who presented a minimum-parameter Pitzer approach to model this system up to 1 mol/kg and 200°C for use in multicomponent metal-sulfate systems. In that study, a careful evaluation of

stability constants of the HSO_4^- equilibrium (Reaction 5.2.1) suggested that the expression of Dickson et al. (1990) was accurate over a wide temperature range and was thus also adopted in this study; Equation 5.2.3 with parameters in Table 5.2.

$$\log_{10} K^0 = q_1 + q_2/T + q_3 \ln T + q_4 T + q_5 T^2 \tag{5.2.3}$$

The excellent performance of the Pitzer model with the use of the overall thermodynamic association constant for HSO_4^- highlights the unimportance of outer-sphere complexes in this system (See discussion in Section 2.3.2). This can be further rationalised by the high mobility of the proton in aqueous solution, which likely results in outer-sphere complexes involving H^+ being unstable.

Table 5.2: HSO_4^- equilibrium constant parameters for Equation 5.2.3 (Dickson et al., 1990)

Parameter	Value
q_1	562.7097
q_2	-13273.75
q_3	-102.5154
q_4	0.2477538
q_5	-1.117033 $\times$ 10^{-4}

As this study was focused on temperatures below 100°C, solute and water activity data as well as published and experimentally measured speciation in this system was included in the overall parameter optimisation. All permutations of Pitzer interaction parameters between H^+, SO_4^{2-} and HSO_4^- were trialled and the most important parameters were found by a simple sensitivity analysis to be $\beta^{(0)}$ and $\beta^{(1)}$ parameters for proton-sulfate and proton-bisulfate interactions. Thermodynamic data (i.e., $\gamma_\pm$, ϕ, α) for this system were taken from the literature and the measured HSO_4^- association from Section 4.2.1 were also included in the parameter regression.

Optimised parameters for this system are presented in Table 5.3 and result in a corresponding total AARD of 2.75 %. The model residuals showed a slight deviation from normal distribution, but the low AARD did not warrant the inclusion of additional model parameters.

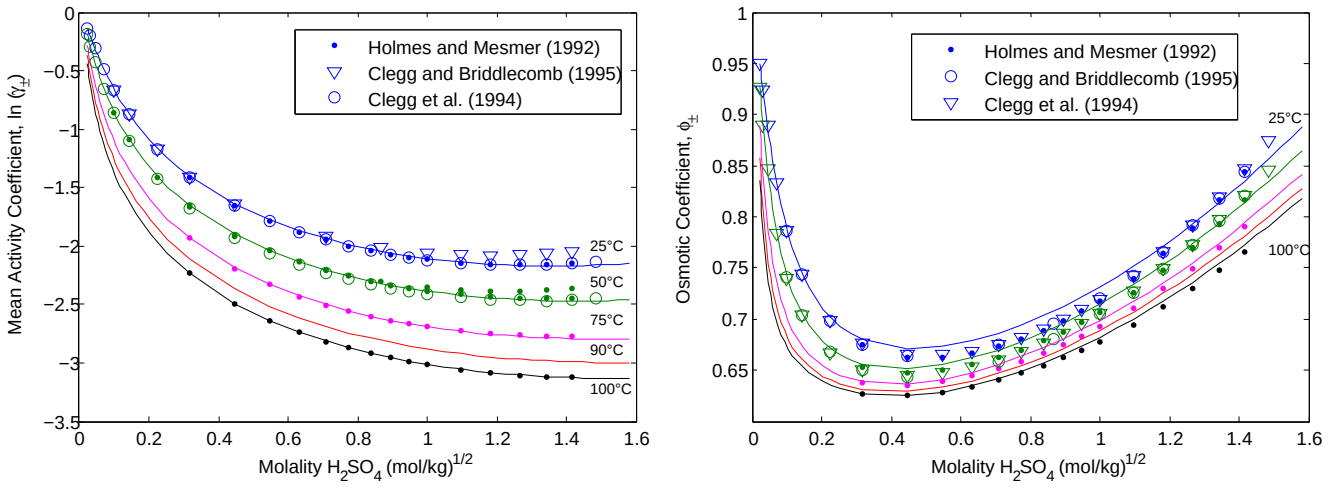

(a) Reported and calculated H_2SO_4 mean activity coefficients from 25-100 °C. Note logarithmic and square root of molality scale.

(b) Reported and calculated H_2SO_4 osmotic coefficients from 25-100 °C. Note square root of molality scale.

Figure 5.1: Model characterisation of available H_2SO_4 thermodynamic data in the open literature from 25 – 100 °C.

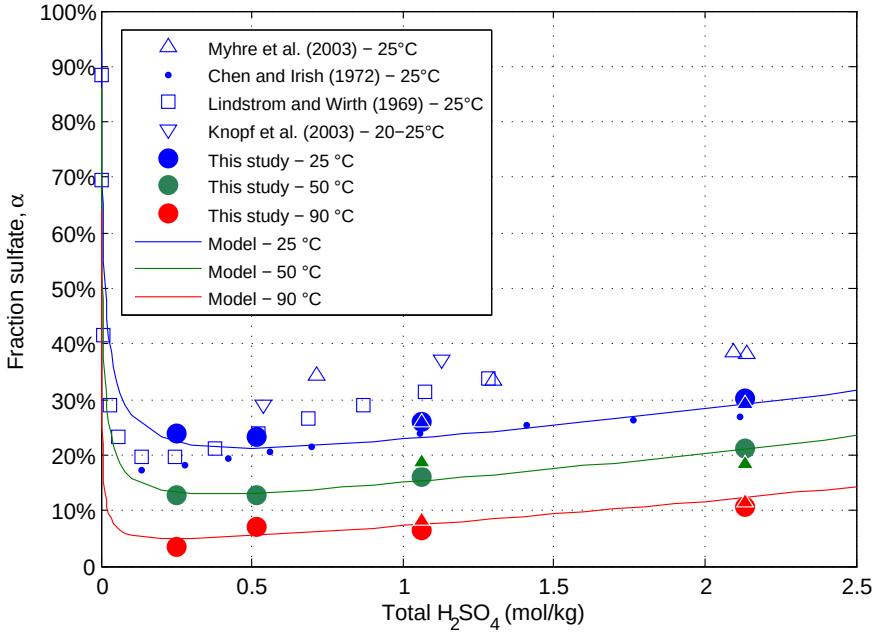

Figure 5.2: Model characterisation of measured and reported association of HSO_4^- in H_2SO_4 solutions, presented as fraction free SO_4^{2-}. Large closed circles and triangles represent the Raman measurements of this work, previously presented in Figure 4.12

Table 5.3: H_2SO_4-H_2O interaction parameters

Parameter	Interaction	p_0	$10^3 \cdot p_1$
$\beta^{(0)}_{HS}$	H^+-$SO^{2}_{4}-$	0.028578	-1.0244
$\beta^{(1)}_{HS}$	H^+-$SO^{2}_{4}-$	0.20502	-8.0561
$\beta^{(0)}_{HB}$	H^+-HSO^{-}_{4}	0.22109	-0.30535
$\beta^{(1)}_{HB}$	H^+-HSO^{-}_{4}	0.48515	-1.7541

Fit Statistic	Value
$AARD_{\alpha}$	6.116%
$AARD_{\gamma_{\pm}}$	1.51 %
$AARD_{\phi}$	0.892 %
AARD	2.57 %

Note: p_i parameters refer to Equation 5.1.1

5.3 $FeSO_4$-H_2O system

Using the $MgSO_4$ surrogate approach, discussed in Section 2.5, parameters in the $FeSO_4$-H_2O system were optimised to activity coefficient data for $FeSO_4$ at 25°C from 0-2 mol/kg (Oykova and Balarew, 1974), estimates of the $FeSO^0_4$ concentration at 1.95 mol/kg at 25 and 90°C (Rudolph, 1996), osmotic and activity coefficient data for $MgSO_4$ at 40-100 °C and 0-2 mol/kg (Archer and Wood, 1985). Additionally, given the similarity of the available $FeSO^0_4$ and $MgSO^0_4$ concentrations that are available at higher concentrations, the DRS and Raman (Buchner et al., 2004; Rudolph et al., 2003) measurements of $MgSO^0_4$ concentrations at 25°C were also included in the optimisation of the $FeSO^0_4$ system.

As discussed in Section 2.5.2, a recent review of divalent metal sulfate CIP's highlighted that a good estimate for the stability constant of the first CIP is $\log_{10}\beta^{\circ} = 1.5$, significantly lower than the overall stability constant typically reported for these species (Steyl, 2012). This value was adopted in this study and fixed during parameter optimisation. Additionally, the reaction heat of the CIP formation, necessary for the extrapolation of the stability constant with temperature, has been reported to be of the order of 10-15 kJ/mol (Steyl, 2012; Rudolph et al., 1997). The most reliable estimate for the $FeSO_4$ system is study of Rudolph et al. (1997) who reported fractions of the CIP at several temperatures and, by assuming a simple approach for the activity coefficients, suggested that the $\Delta H^0 = 15$ kJ/mol, and this value was adopted in this study. The change in heat capacity of the CIP formation reaction is not available in the literature and was thus optimised in this study.

The typical parameters[1] for the $FeSO_4$ system are the $\beta^{(0)}_{MS}$, $\beta^{(1)}_{MS}$ and C^{ϕ}_{MS} parameters and these were included, with linear temperature dependence. In order to prevent underestimation of the $FeSO^0_4$ CIP with increasing concentration and temperature the neutral interaction parameter, λ_{MN}, was required. Typically, for 2-2 electrolytes, the $\beta^{(2)}_{MS}$ parameter is set at a value of -32 to account for ion association in the dilute region (Pitzer and Mayorga, 1974a). Although this study explicitly recognises the formation of CIP's, the $\beta^{(2)}_{MS}$ parameter was found to improve the fit of the experimental data, particularly at higher temperature, and was thus included as a fixed model parameter.

Due to the greater uncertainty in the speciation measurements, these were weighted lower during parameter optimisation, the resulting objective function being:

$$\min F_{\mathrm{FeSO_4}} = \sum_i \Delta^2(\phi_{i,stoich.}) + \Delta^2(\gamma_{i,stoich.}) + \frac{1}{4}\Delta^2(\alpha_i) \tag{5.3.1}$$

$$\text{where:} \quad \Delta(x) = \frac{x_{calc} - x_{meas}}{x_{meas}} \tag{5.3.2}$$

This function was minimised using a Nelder-Mead algorithm (Lagarias et al., 1998) in Matlab (MATLAB, 2014) and the resulting optimal parameters are presented in Table 5.4 and the fit of the experimental data presented in Figures 5.3 and 5.4. The descriptive statistics of this fit are AARD = 3.19 % with a median absolute deviation of 2.27×10^{-3}. Also shown in Table 5.4 is the AARD of the speciation data, which is considerably higher than the corresponding thermodynamic properties. This reflects the reduced weighting of the experimental data and is further influenced by the low concentration $MgSO^0_4$ data. Furthermore, is clear that the fit of the osmotic coefficient data at higher concentration shows the most pronounced deviations. This results from a trade-off between the osmotic coefficient interaction parameters and the neutral CIP, which does not significantly contribute to this property. Additional parametrisation of the model would be required to obtain an improved fit of the data however, this was not considered valuable in the context of this study.

An extensive set of solubility data is available for the $FeSO_4$-H_2O and $FeSO_4$-H_2SO_4-H_2O systems (Linke and Seidell, 1965), which were used to quantify the interaction between ferrous and sulfuric acid species. First, using the optimised Pitzer parameters for $FeSO_4$−H_2O, solubility product constants (K_{sp}) for the formation of melanterite ($FeSO_4 \cdot 7\,H_2O$) and szomolnokite ($FeSO_4 \cdot H_2O$) were determined in this system as a function of temperature. A typically employed temperature dependence function for solubility

[1] Subscripts are M: Fe^{2+}, S: SO^{2-}_4, N: $FeSO^0_4$, H: H^+

Table 5.4: $FeSO_4$-H_2O speciation model parameters and descriptive statistics

Parameter	Interaction	p_0	$10^3 \cdot p_1$
$\beta^{(0)}_{MS}$	Fe^{2+}-SO_4^{2-}	0.18995	-2.0163
$\beta^{(1)}_{MS}$	Fe^{2+}-SO_4^{2-}	3.4302	15.047
$\beta^{(2)}_{MS}$	Fe^{2+}-SO_4^{2-}	-32†	-
C^{ϕ}_{MS}	Fe^{2+}-SO_4^{2-}	0.075016	1.3897
λ_{MN}	Fe^{2+}-$FeSO_4^0$	0.035811	-1.3943
$\log K^0$		-	1.50†
ΔH^{CIP} (kJ/mol)		-	15†
ΔC_p^{CIP} (J/mol.K)		-	376.58

Fit Statistic	Value
$AARD_{\alpha}$	12.79%
$AARD_{\gamma_{\pm}}$	1.86 %
$AARD_{\phi}$	1.83 %
AARD	3.19 %

†Fixed during optimisation, see text.
Note: p_i parameters refer to Equation 5.1.1

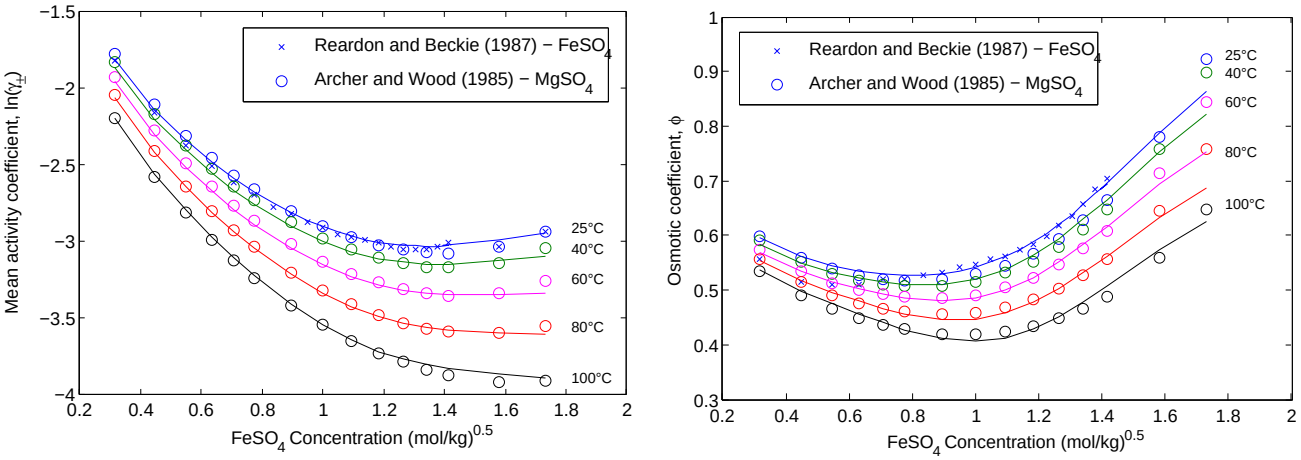

(a) $FeSO_4$ mean activity coefficient

(b) $FeSO_4$ osmotic coefficients

Figure 5.3: Model characterisation of $FeSO_4$ and surrogate $MgSO_4$ thermodynamic data from 25-100 °C. Note the square root of concentration and logarithmic scale for the activity coefficients. Crosses represent $FeSO_4$ data and circles $MgSO_4$ data.

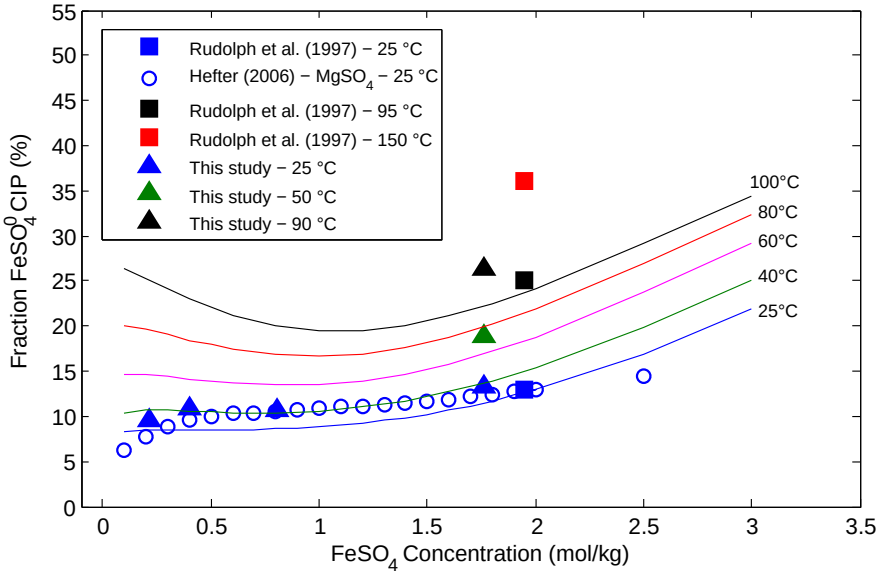

Figure 5.4: Model characterisation of fraction of the $FeSO_4^0$ CIP in $FeSO_4$ solutions as a function of temperature (25 – 125 °C) and concentration (0.1-3 mol/kg). Open circles represent reported $MgSO_4^0$ concentration fractions for comparison between the $MgSO_4$-H_2O and $FeSO_4$-H_2O systems.

products (Reardon and Beckie, 1987) was used:

$$\ln K_{sp}(T) = w_0 + w_1 \cdot T + w_2 \cdot T^{-2} \tag{5.3.3}$$

However, due to the speciation approach adopted in this study, the calculated K_{sp} values are not directly comparable to those reported in the literature due to the form of the solubility product relationships below. In this study, the solubility products for $FeSO_4$ crystal products were compiled from the $FeSO_4^0$ CIP and not, as typically done, from the free ions, i.e., Fe^{2+} and SO_4^{2-}. The form of the liquid-solid equilibria in this study are:

$$\mathrm{FeSO^0_{4(aq)}} + 7\,\mathrm{H_2O} \rightleftharpoons \mathrm{FeSO_4 \cdot 7\,H_2O_{(s)}} \tag{5.3.4}$$

$$\mathrm{FeSO^0_{4(aq)}} + \mathrm{H_2O} \rightleftharpoons \mathrm{FeSO_4 \cdot H_2O_{(s)}} \tag{5.3.5}$$

An additional phase, rozenite ($FeSO_4 \cdot 4\,H_2O$), is also known to exist near the maximum solubility limit. However, given that it is only stable over a small region of temperatures, it was not deemed valuable to include in the model. Figure 5.5 presents the optimised model fit of $FeSO_4$ solubility in water as a function of temperature and the corresponding K_{sp} parameters are presented in Table 5.5.

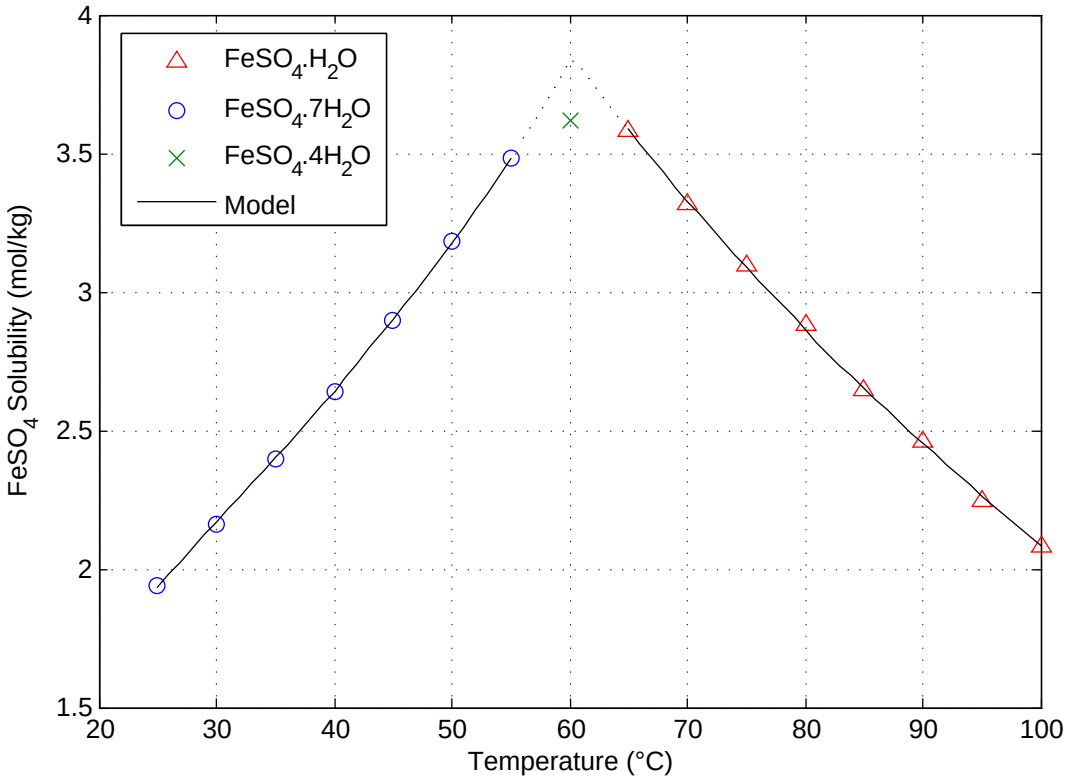

Figure 5.5: $FeSO_4-H_2O$ system solubility as a function of temperature. Data points represent compiled data from Linke and Seidell (1965), lines show the model characterisation of the two common phases, melanterite ($FeSO_4 \cdot 7\,H_2O$) and szomolnokite ($FeSO_4 \cdot H_2O$) with dotted regions representing areas of metastability, i.e, rozenite ($FeSO_4 \cdot 4\,H_2O$) stability region which was not included in this model.

Table 5.5: $FeSO_4$-H_2O solubility product parameters for Equation 5.3.3

Salt	w_0	$w_1 \cdot 10^3$	$w_2 \cdot 10^{-5}$
$FeSO_4 \cdot 7\,H_2O$	23.9438	-41.7097	-11.6801
$FeSO_4 \cdot 1\,H_2O$	7.7552	-24.6195	0.72803

5.4 $FeSO_4$-H_2SO_4-H_2O system

Data on which to optimise interaction parameters in the $FeSO_4$-H_2SO_4-H_2O system above 25 °C are scarce and essentially limited to solubility data, of which a reasonably extensive collection exists (Linke and Seidell, 1965). A high quality isopiestic study of the $MgSO_4-H_2SO_4-H_2O$ system at 25 °C (Rard and Clegg, 1999) does facilitate the evaluation of interaction parameters using a surrogate approach, similar to the previous section.

Using the $FeSO_4-H_2O$ Pitzer model and K_{sp} parameters from the previous section, an additional four parameters were required to accurately model the suppression of $FeSO_4$ solubility with H_2SO_4 concentration over 0 – 2 mol/kg and 25 – 100 °C. The most influential interaction parameters in this system are the $\beta^{(0)}_{Fe^{2+},HSO_4-}$, $\beta^{(1)}_{Fe^{2+},HSO_4-}$ and $C^{\phi}_{Fe^{2+},HSO_4-}$ parameters. However, the inclusion of the neutral species interaction parameter, $\lambda_{H^+,FeSO^0_4}$ significantly improved the description of the experimental data, due to its direct involvement in the solubility product expressions, and was thus included in the optimisation. Solubility data was also limited to below 2 mol/kg H_2SO_4 as higher acidities were not as important in the context of this study.

It was found that the temperature dependence of the interaction parameters had little effect on the objective function, since only a limited amount of solubility data was available above 60 °C and much of the temperature variation was already captured in the K_{sp} equations. Thus, all temperature dependence terms were maintained at zero. The optimised parameters are presented in Table 5.6 the resulting solubility and water activity surfaces are presented in Figure 5.6.

Table 5.6: $FeSO_4$-H_2SO_4 interaction parameters and descriptive statistics

Parameter	Interaction	p_0	$10^3 \cdot p_1$
$\beta^{(0)}_{MS}$	Fe^{2+}-HSO^-_4	0.26900	-
$\beta^{(1)}_{MS}$	Fe^{2+}-HSO^-_4	0.98649	-
C^{ϕ}_{MS}	Fe^{2+}-HSO^-_4	0.27526	-
λ_{NH}	$FeSO^0_4$-H^+	-0.042489	-
Fit Statistic		Value	
$AARD_{solub.}$		3.81 %	
$AARD_{a_w}$		0.35 %	
AARD		1.79 %	

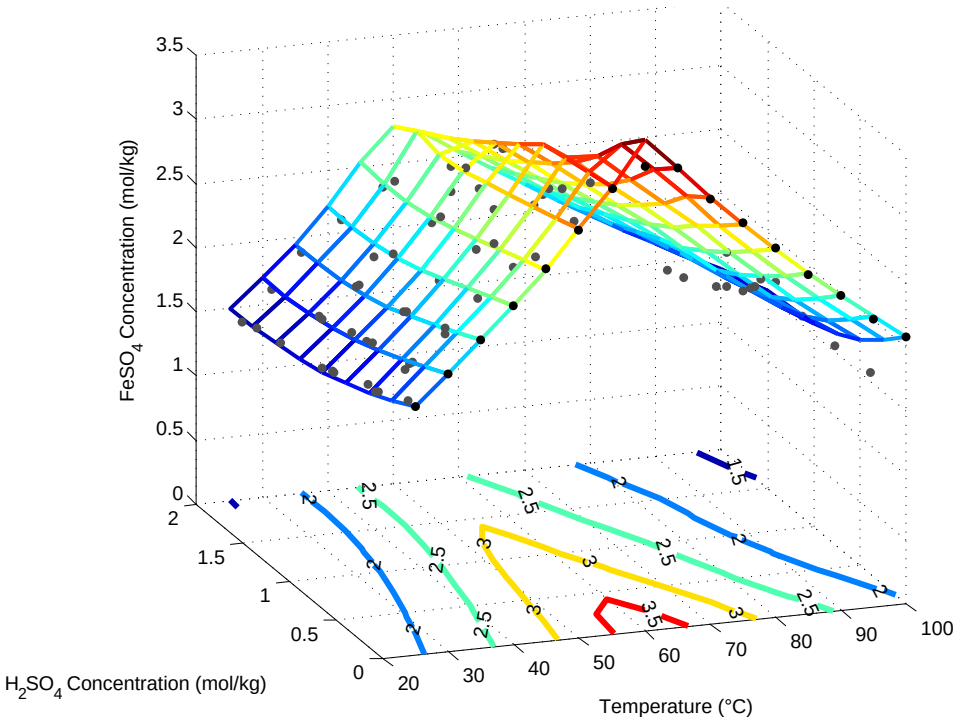

(a) Model characterisation of solubility in the $FeSO_4$-H_2SO_4-H_2O system. Experimental data are from various sources and reported in Linke and Seidell (1965)

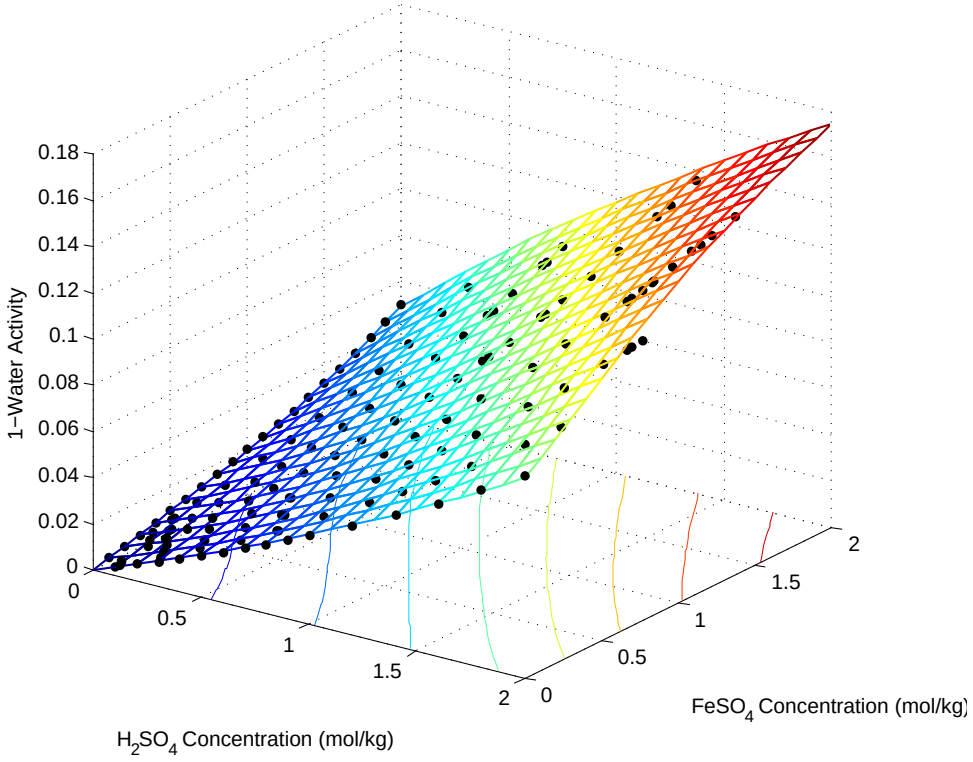

(b) Water activity characterisation for the $MgSO_4$-H_2SO_4-H_2O system as a surrogate for the equivalent Fe^{2+} system. Experimental data is taken from Rard and Clegg (1999).

Figure 5.6: Solubility and water activity model fit in the $FeSO_4$-H_2SO_4-H_2O system

5.5 $Fe_2(SO_4)_3$-H_2SO_4-H_2O system

Recently, extensive and reliable water activity data of this system have been measured by separate authors up to reasonably high concentrations at 25 and 50 °C (Rumyantsev et al., 2004; Velazquez-Rivera et al., 2006) and has been correlated using an extended Pitzer ion-interaction model containing 12 adjustable parameters (Tosca et al., 2007), although speciation was not considered in their study. The magnitude of the interaction parameters regressed in this study are indicative of a system with a high degree of non-ideality and complex formation, i.e., $\beta^{(1)}_{Fe^{3+},SO_4^{2-}} = 11.968$, $\beta^{(1)}_{Fe^{3+},HSO_4^-} = 7.519$ at 25 °C, which are significantly larger than, for example, divalent metal systems.

Indicative above, this system is notoriously difficult to model due to several complicating factors. Firstly, due to the strong tendency of Fe(III) ion to hydrolyse (Flynn, 1984), the pure $Fe_2(SO_4)_3$-H_2O system cannot be practically studied and ternary systems, the simplest of which includes only H_2SO_4, must be considered practically. Secondly, as outlined in Chapter 2, the aqueous behaviour of Fe(III) systems are complicated by the large number of potential species that can co-exist in solution. Thirdly, the chemical behaviour of Fe(III), i.e., a small, highly charged cation, is complex and interacts strongly with the solution environment. Resultantly, when modelling this system, particularly when adopting a speciation approach, the system requires simplification in order to obtain meaningful predictive ability.

In adopting a speciation approach to modelling this system, the possible number of species becomes large and permutations of interaction parameters rapidly increase. With the knowledge of the two ferric sulfato CIP's developed in the previous chapter, a minimum number of species were selected for inclusion in the model. Also from the preceding chapter, it is clear that the unassociated sulfate and bisulfate species also will need to be included in the model. Furthermore, although not directly observed in the Raman spectra, free (or more likely outer-sphere complexed) Fe^{3+} is expected to be present from the amount of unassociated sulfate observed in the solutions, in agreement with X-ray diffraction data (Magini, 1979) . Additionally, the presence of significant HSO_4^- in the $Fe_2(SO_4)_3$ solutions suggests that hydrolysis must have occurred and, in order to replicate the experimental measurements accurately, the hydrolysis products clearly needed to be included.

To avoid unnecessary complication, a simple surrogate approach for Fe(III) hydrolysis was adopted in which only a single $Fe(OH)_n^{3-n}$ species was included in the framework. The ultimate engineering application in this study is in a system where acid is always present and hydrolysis products are expected to not be dominant. The selection of an

appropriate ferric hydroxyl species was performed iteratively. The simplest hydrolysis product of Fe(III), $Fe(OH)^{2+}$, produced inconsistent speciation trends and the model consistently underestimated the HSO_4^- concentration. Much improved estimates of the HSO_4^- speciation were achieved by considering only the $Fe(OH)_2^+$ species in the solution model. In reality, both these ferric hydroxyl species, and potentially others, are present in solution, although, in the interest of developing a simplified model of the system, the consideration of the major species was most important. The UV-vis spectra, presented in Section 4.3, confirmed the presence of $Fe(OH)_2^+$ in 0.4 mol/kg $Fe(ClO_4)_3$ solution with added $HClO_4$ and this was attributed to the relatively high Fe(III) concentration. Thus, in concentrated $Fe_2(SO_4)_3$ solutions, it is *reasonable* to assume that the $Fe(OH)_2^+$ species may characterise the dominant ferric hydroxyl species.

The resulting model for the $Fe_2(SO_4)_3$-H_2SO_4-H_2O system thus contains a total of seven species, summarised in Table 5.7. Additional species, reported in the literature (Stipp, 1990; Casas et al., 2005; Papangelakis et al., 1994; Liu et al., 2003), such as $Fe(OH)SO_4^0$ or $FeH(SO_4)_2^0$, were not considered in this framework as there is little supporting evidence for their existence beyond the (somewhat arbitrary) flexibility they facilitate for modelling specific experimental measurements, such as pH, conductivity and solubility. Additionally, the substitution of these polycationic species instead of the simpler CIP's discussed above can unnecessarily constrain the stoichiometry of the model, i.e., exactly one proton is removed from the system per two sulfates if the $FeH(SO_4)_2^0$ is included over the $Fe(SO_4)_2^-$ species. Such a relationship cannot be justified on the basis of the experimental data presented in the previous chapter.

Table 5.7: Solution species in the $Fe_2(SO_4)_3$-H_2SO_4-H_2O system

	Cations	Anions
Primary Species	H^+ Fe^{3+}	SO_4^{2-}
Secondary Species	$Fe(OH)_2^+$ $FeSO_4^+$	HSO_4^- $Fe(SO_4)_2^-$

The HSO_4^- species stability constant and optimised interaction parameters for the H_2SO_4-H_2O system were taken from Section 5.2. The selection of stability constants for the ferric sulfato CIP's are somewhat arbitrary as no experimental data exist for these quantities and they must be inferred by the *overall association* constant reported in the literature, i.e., that accounting for both inner- and outer-sphere complexes. However,

guidance from the Raman results presented in the previous chapter suggests that the majority of Fe(III) in $Fe_2(SO_4)_3$ solutions of moderate concentration are associated as the CIP; that is, CIP's account for the majority of species in these solutions. This would mean that the CIP contribution to the overall K_{ass} parameter would dominate and serious errors would likely not be induced by assuming the reported K_{ass} values for these species. Additionally, since there is a large number of unknown parameters in the model, variations arising from this assumption would be absorbed into the interaction parameters during optimisation.

The Density model (Equation A.2.2) was used to extrapolate the $FeSO_4^+$ species stability constant using the standard value recommended by Stipp (1990) and the ΔH^0 and ΔC_p^0 values recommended by Liu et al. (2003) (see Table 2.4 and calculations attached in Appendix A.2.3). The temperature dependence of the $Fe(SO_4)_2^-$ species' stability constant is not well known, primarily due to the difficulties in studying this species in isolation. For this species, the BLCM method for the following isocoulombic reaction was used to determine the ΔC_p^0 value of the $Fe(SO_4)_2^-$ formation reaction presented in Table 2.4.

$$FeSO_4^+ + HSO_4^- \rightleftharpoons Fe(SO_4)_2^- + H^+ \tag{5.5.1}$$

The full details of this calculation are included in Appendix A.2.4. An average value of the ΔH^0 term from Liu et al. (2003) and Papangelakis et al. (1994) was used in the extrapolation and the standard stability constant of this species was taken as that recommended by Stipp (1990). For the hydrolysis product, an empirical approach was required as the species was a surrogate for the array of potential $Fe(OH)_n^{3-n}$ species. The $\log K^0$ and ΔH^0 parameters for the species with stoichiometry n=2 was allowed to vary during the optimisation; the ΔC_p^0 for this species was fixed at zero to prevent over-parametrisation of the model.

The seven species selected in the $Fe_2(SO_4)_3$-H_2SO_4-H_2O model can have up to 74 individual Pitzer model parameters, excluding temperature dependent terms. In order to simplify the parameter optimisation, a manual scan of the most common model parameters (i.e., $\beta^{(0)}$, $\beta^{(1)}$ and C^{ϕ}) was performed. This scan highlighted that the interaction parameters between Fe^{3+} and the various anions were important. This is due to Fe(III) being directly involved in mass action expressions for all the ferric species. Interestingly, interaction parameters involving the $Fe(OH)_2^+$ species were much less important, validating the surrogate approach, albeit somewhat artificially.

Unfortunately, even by increasing the number of model parameters, the measured trends in water activity could not be reproduced above approximately 0.5 mol/kg $Fe_2(SO_4)_3$. The variations in water activity with concentration of electrolytes is a net result of all in-

teractions between the solution species and the solvent. In multi-electrolyte models, particularly with the explicit recognition of solution complexes, the number of interactions are large and difficult to independently quantify. However, speciation is not affected by the absolute quantity of the species' interactions, that is, the magnitude of the interaction parameters, but rather by the *ratios* of activity coefficients (see Equation 2.3.7). Thus, it is possible to correctly capture the speciation trends by incorporating realistic activity coefficient ratios, while not correctly accounting for their individual magnitudes. Moreover, both the Raman and UV-vis measurements (Chapter 4) highlighted that there are significant quantities of hydrated Fe^{3+} in these $Fe_2(SO_4)_3$ solutions, even in the presence of acid. These ions would obviously be strongly solvated and likely characterised by an extensive, structured hydrogen bonded network of solvent and outer-sphere complexed molecules (Majzlan and Myneni, 2005). Such networks would certainly, and largely, affect the water activity in a way that only explicit recognition of outer-sphere complexes would be able to model. Since the focus of the thermodynamic framework in this study is to develop a basis on which to interpret kinetic processes, the speciation, particularly of Fe(III) is centrally important and the water activity can be considered a secondary objective. Thus, while it is acknowledged that the minimum parameter model presented here does not correctly account for the water activity, the inclusion of additional parameters to do so was not warranted.

In the parameter regression, the objective function was composed from the following function, where $\Delta\alpha_x$ represents the difference between the calculated and measured fractions of sulfate contained in each of the species. Since no mass balance constraints were imposed on the concentrations of species during *fitting* of the Raman spectra, it was deemed necessary to include all sulfate species in the regression. The solutions containing only $Fe_2(SO_4)_3$ were weighted higher than those containing both $Fe_2(SO_4)_3$ and H_2SO_4 due to increased confidence in the band deconvolution in these samples. In addition, the fraction sulfate was weighted higher than the other species due to the relative ease in which the 981 cm^{-1} band could be characterised during curve fitting.

$$\begin{aligned} F =& 2\left(2\Delta\alpha_{SO_4^{2-}} + \Delta\alpha_{HSO_4^-} + \Delta\alpha_{FeSO_4^+} + \Delta\alpha_{Fe(SO_4)_2^-}\right)_{Fe_2(SO_4)_3} + \\ & \left(2\Delta\alpha_{SO_4^{2-}} + \Delta\alpha_{HSO_4^-} + \Delta\alpha_{FeSO_4^+} + \Delta\alpha_{Fe(SO_4)_2^-}\right)_{Fe_2(SO_4)_3+H_2SO_4} \end{aligned} \tag{5.5.2}$$

The optimised parameters for this system are presented in Table 5.8. It was observed that the $\beta^{(1)}$ and $C^{(\phi)}$ parameters involving Fe(III) interactions between the HSO_4^- and $Fe(SO_4)_2^-$ species were insensitive to the predictions of the model and were maintained

at zero. Indeed, the $\beta^{(0)}$ parameter for these interactions, ultimately the value of the binary interaction at high ionic strength, was significant and required inclusion. However, the inclusion of the $\beta^{(2)}$ parameters in the optimisation had little affect on the fit of the experimental data, particularly since the α_2 parameter was maintained at 12 as recommended by Pitzer (1991). In the form of the second-virial coefficient in the Pitzer model (presented in Equation E.4.6), of which the $\beta^{(n)}$ parameters are present, the α_n terms appear inside the exponential terms, as the coefficient of $I^{0.5}$. Thus, large values of α_2 result in the contribution of the $\beta^{(2)}$ term being focused at low ionic strength; primarily to account for speciation effects in an ion-interaction approach (Pitzer, 1991). In this application, the focus on higher ionic strengths and the explicit recognition of solution phase ion pairs results in the $\beta^{(2)}$ parameter has a low sensitivity to the model output and was thus not included.

Table 5.8: $Fe_2(SO_4)_3$-H_2SO_4-H_2O speciation model parameters

Parameter	Interaction	p_0 mol/kg	$10^3 \cdot p_1$ mol/kg
$\beta^{(0)}_{MS}$	Fe^{3+}-SO_4^{2-}	1.0962	-28.677
$\beta^{(1)}_{MS}$	Fe^{3+}-SO_4^{2-}	6.2122	-
C^{ϕ}_{MS}	Fe^{3+}-SO_4^{2-}	-0.18496	-20.860
$\beta^{(0)}_{MB}$	Fe^{3+}-HSO_4^{-}	0.43885	-
$\beta^{(0)}_{MC_2}$	Fe^{3+}-$Fe(SO_4)_2^{-}$	0.53151	-
$\log K^0$	$Fe(OH)_2^{+\,(a)}$	-2.8476$^{(b)}$	-
ΔH^0	$Fe(OH)_2^{+\,(a)}$	15.326$^{(c)}$	-
ΔC_p^0	$Fe(OH)_2^{+\,(a)}$	0	-
AAD†		0.1205 mol/kg	

[a] Surrogate hydrolysis species
[b] Dimensionless
[c] Units of kJ/mol
† with reference to Equation 5.5.2

The model fit of the measured solution speciation for this system is presented in Figure 5.7 for solutions without added H_2SO_4 and in Figure 5.9 with added H_2SO_4. While there are several significant deviations between the measured speciation and the model predictions, given the complexity of the system and the comparative simplicity of the model, the capturing of the trends in speciation is good. The resulting AARD of this fit in Figure 5.7 is 23.68%, emphasising the variation. However, despite this, the solution model does effectively capture the trends in speciation from the Raman measurements

of the previous section and the nine interaction parameters do effectively capture the temperature and concentration effects.

The ability of the model to quantify, to reasonable accuracy, the sulfate and bisulfate speciation highlights that the majority of the uncertainty lies in the quantification of the ferric sulfato complexes. Based on the spectroscopic evidence in Chapter 4.2.5, only two *dominant* ferric sulfato species exist in solution, although many other authors have included additional ferric species such as $FeHSO_4^+$ and $FeH(SO_4)_2^0$ in their modelling frameworks under various conditions (Liu et al., 2003; Papangelakis et al., 1994; Steyl, 2012). However, these species have not been rigorously studied and they have not been unequivocally identified in solution. It is plausible to reason that it is not possible to distinguish these species from the $FeSO_4^+$ and $Fe(SO_4)_2^-$ species from the measurements in the previous chapter. While the addition of additional species may improve the model fit of the measured data it, was not considered valuable in the context of this study, for which the speciation *trends* with experimental conditions (i.e., temperature and concentrations) can be considered more important.

Several important aspects of the model description of the system can be taken from the fits presented in Figures 5.7 to 5.9. Firstly, at very low concentrations ($\leq$ 0.05 m) the $FeSO_4^+$ and $Fe(SO_4)_2^-$ species predominance decreases significantly, while the sulfate and bisulfate species' increases. Ultimately, as the concentration approaches an infinitely dilute solution, one expects that the free ions, such as SO_4^{2-} and Fe(III), should dominate. It is observed from the distribution of iron species, presented in Figure 5.8, that the $Fe(OH)_2^+$ species becomes increasingly stable at lower concentrations. It is well-known that a large number of ferric hydroxyl species exist, particularly in dilute solutions where Fe(III)-H_2O interactions should be more prevalent than Fe(III)-SO_4^{2-} interactions (Byrne and Kester, 1976; Flynn, 1984). Since the model developed in this study was not focused on the low concentration regions, the dominant $Fe(OH)n^{3-n}$ speciation is likely not well characterised. However, with reference to the low-sulfate UV-vis measurements in Section 4.3, the indication that the sulfate speciation is minor and that the $Fe(OH)_2^+$ is present does suggest that the model predictions do reflect reality. Ultimately, if speciation data could be extended to more dilute solutions, an improved description of these species may be included in the modelling framework.

A second important point is the fairly constant profile of the $FeSO_4^+$ species, in comparison to the $Fe(SO_4)_2^-$ species, which is observed to increase significantly with temperature and concentration. The root of this behaviour lies in the Fe^{3+}-$Fe(SO_4)_2^-$ interaction parameter, without which the dominance of $FeSO_4^+$ decreases with concentration and the $Fe(SO_4)_2^-$ dominance increases. This parameter thus can be interpreted as capturing the

buffering effect of the $FeSO_4^+$ species in these solutions. Obviously, as shown by the UV-vis spectra, significantly different Fe(III):SO_4^{2-} ratios will alter the dominance of the ferric sulfato species, but, in solutions where this ratio is close to 1.5, the $FeSO_4^+$ complex is dominant and has a relatively constant fractional concentration.

Thirdly, from the model characterisation of solutions with added H_2SO_4 (Figure 5.9), it is clear that the main effect of added H_2SO_4 is a significant increase in the fractional concentration of the HSO_4^- species as well as the low-concentration abundance of the ferric sulfato CIP's. While added H_2SO_4 does decrease the relative Fe(III):SO_4^{2-} ratio, tending to promote CIP formation, the increase in total H^+ in the system has a significantly greater effect and results in a shift in the HSO_4^- equilibrium to capture free proton's from solution. The model quantification of the HSO_4^- concentration at high H_2SO_4:$Fe_2(SO_4)_3$ ratios is significantly larger than the experimental measurements. This may be due to the presence of additional species containing protons (i.e., $FeHSO_4^+$ or $FeH(SO_4)_2^0$) or simply that the model does not have sufficient flexibility in its minimal-parameter form to account for the changes accurately. However, since the *trends* in the speciation are considered most important for the engineering modelling objectives of this study and given the reasonably large variance in the speciation measurements, the inclusion of additional model parameters to improved on the fit of the data was not considered valuable.

An additional interesting aspect of the model calculation is the relativity large fraction of *free* Fe^{3+} predicted in concentrated $Fe_2(SO_4)_3$ solutions, i.e., 10-25% of the total Fe(III). This prediction is a similar order of magnitude as the recent calculations of Yue et al. (2014) ($Fe^{3+} \approx 5\%$ at 0.18 mol/kg Fe(III), 25°C) although they did not include any experimental verification of their modelling results. Moreover, the even larger calculated fraction of Fe^{3+} ions in solutions containing added acid, particularly at low ferric concentrations is attributed to the strong association of HSO_4^- determined by Raman spectroscopy. It is observed in Figure 5.8 that as the Fe(III) concentration and the temperature are increased, the stability of the ferric sulfato complexes increases in line with experimental observations.

Given the large net charge on the Fe^{3+} ion, it is expected that only low concentrations of this species would exist in concentrated solution, particularly at elevated temperatures. The high confidence in the sulfate bands and corresponding J-value is sufficient to prove that there must be significant uncomplexed sulfate, and correspondingly Fe^{3+}. In addition, the sensitivity analysis on the ferric sulfato species' J-values (Section B.1.2.3) showed the speciation measurement to be relatively insensitive to these and thus there is high confidence in the model calibration data, and thus the resulting trends speciation calculated from the model.

Obviously though, uncomplexed Fe^{3+} would be in the form of outer-sphere-complexes (SIP and SSIP's) with the surrounding anions; likely in a highly structured aqueous environment considering the considerable charge on the ferric ion. Significant outer-sphere complexation was suggested by Majzlan and Myneni (2005) in dilute $Fe_2(SO_4)_3$ solutions. Since such species are not detected by Raman spectroscopy, and no theoretical methods exist for their explicit consideration in a thermodynamic model, no further consideration of these species are made. However, for the objectives of this study, and particularly in the context of the reactive system, inner sphere coordination and competition is considered the most important aspect and hence the focus of this modelling exercise.

Thus, the calibrated model of the $Fe_2(SO_4)_3$-H_2SO_4-H_2O system has been shown to effectively model the measured speciation trends of the main species present in these solutions from 25 - 90 °C.

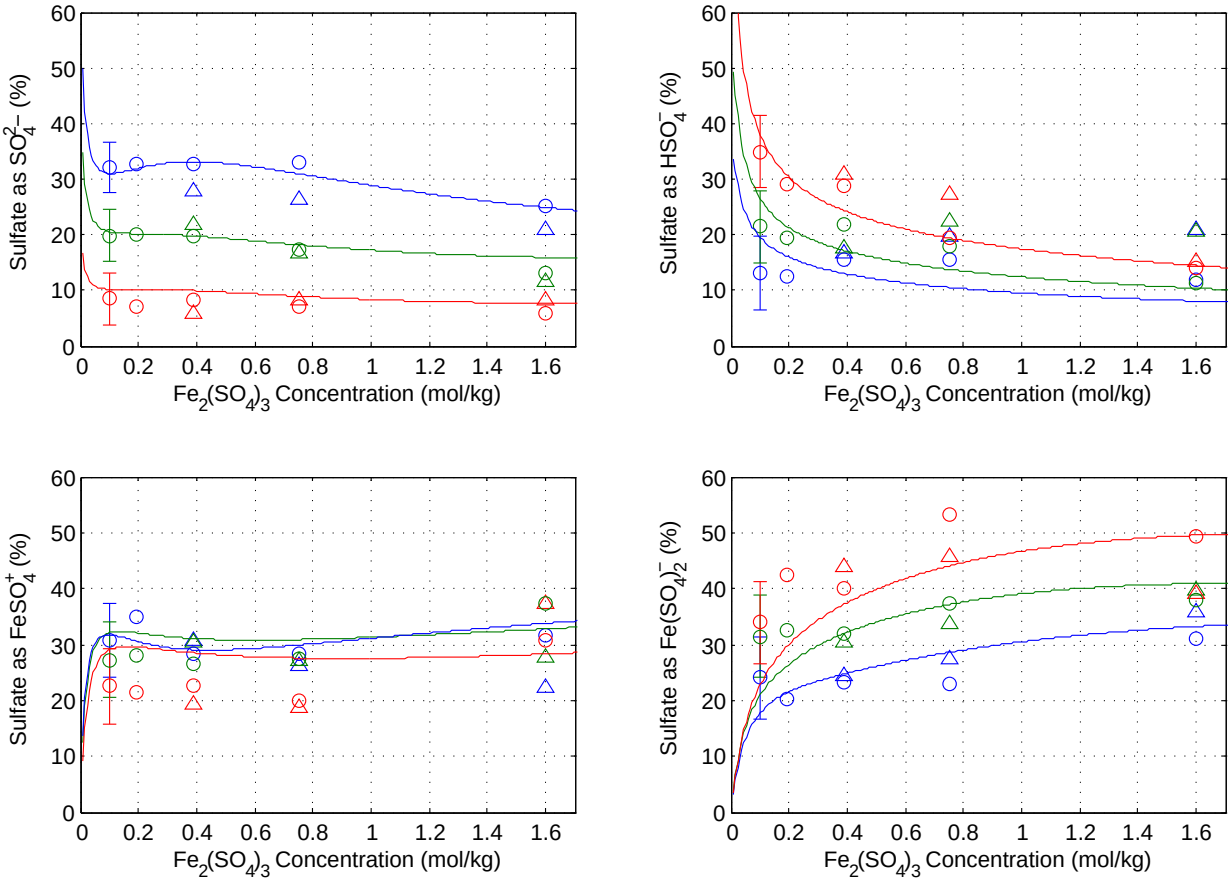

Figure 5.7: Measured $Fe_2(SO_4)_3$ speciation and fit of Pitzer model at 25, 50 and 90 °C without added acid. △: 0.5 mol/kg $NaClO_4$ internal standard, ○: no added $NaClO_4$. Error bars were established from maximum deviation between repeated measurement with and without internal standards.

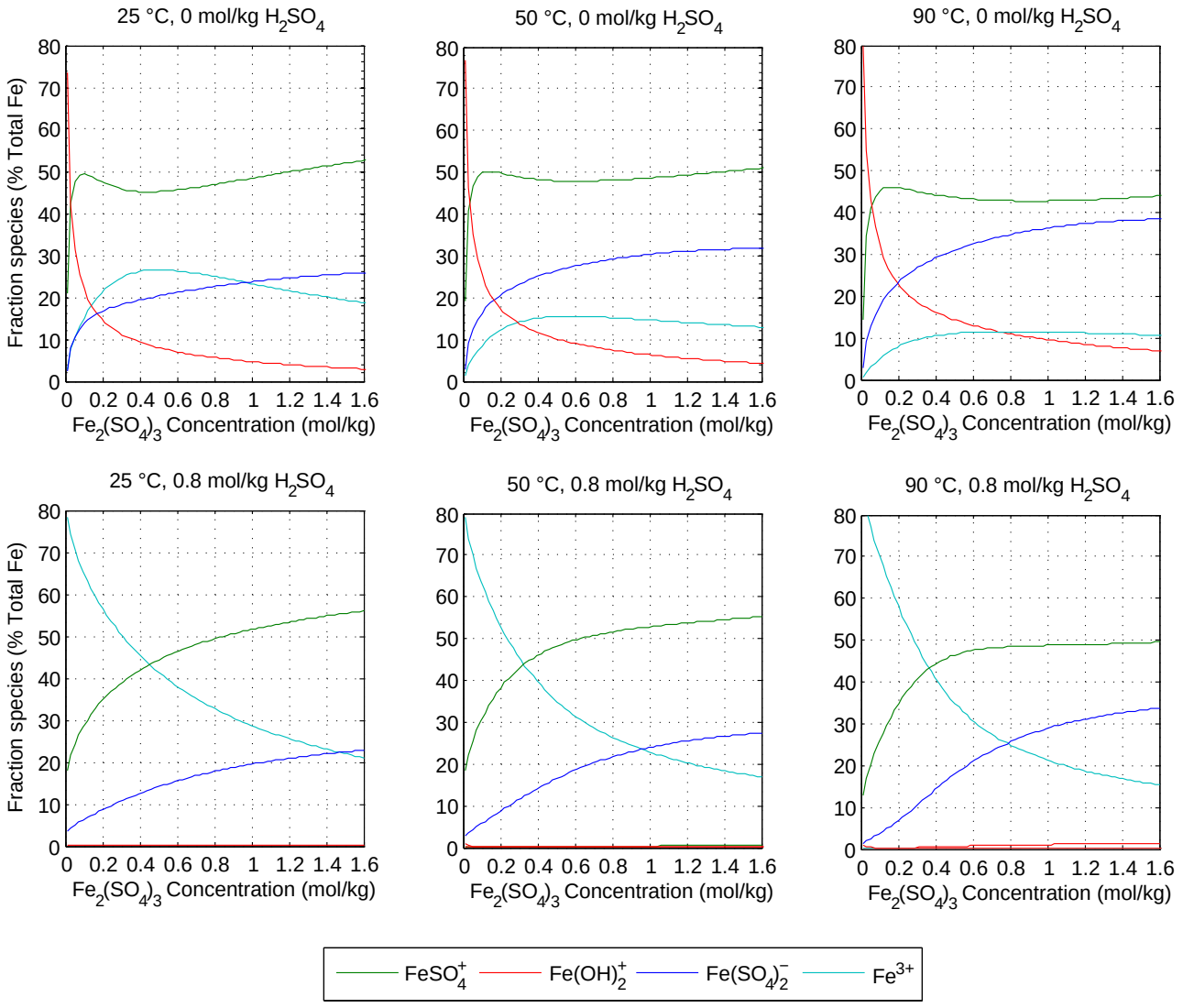

Figure 5.8: Calculated Fe-species distribution in $Fe_2(SO_4)_3$ solutions with and without added H_2SO_4. Species fractions are calculated at species concentration of total iron concentration.

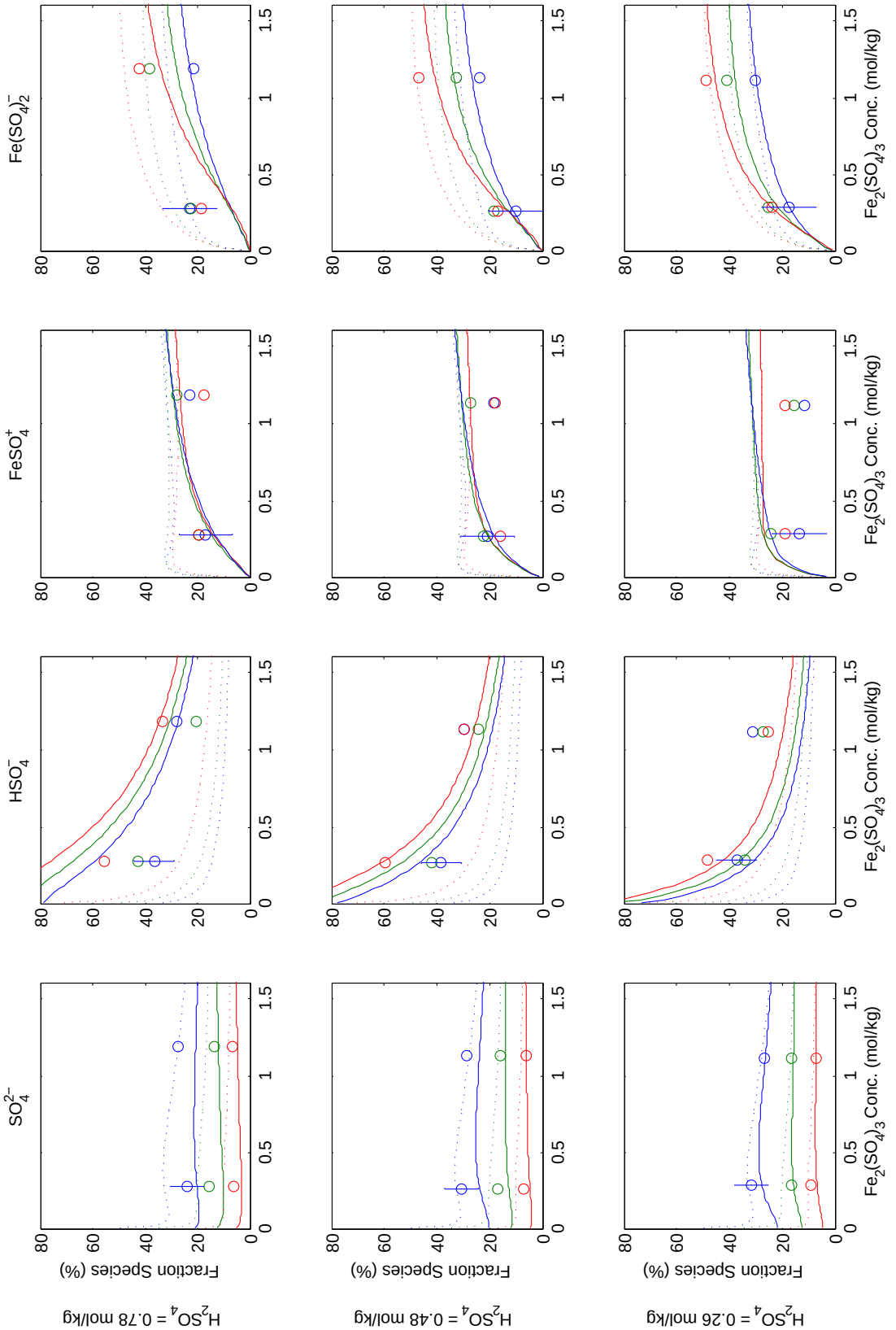

Figure 5.9: Measured speciation in the $Fe_2(SO_4)_3$-H_2SO_4 system and Pitzer model at 25, 50 and 90 °C. Dotted lines represent the calculated speciation in the $Fe_2(SO_4)_3$ system without added acid. Error bars indicate expected uncertainty in the experimentally measured values.

5.6 $Fe_2(SO_4)_3$-$FeSO_4$-H_2SO_4-H_2O system

In addition to the $Fe_2(SO_4)_3$-H_2SO_4-H_2O and $FeSO_4$-H_2O systems analysed by Raman spectroscopy in the previous chapter, a set of solutions containing $FeSO_4$ and $Fe_2(SO_4)_3$ were also analysed. Speciation from these solutions was extracted and used to validate the solution model in a mixed system. Thus, none of the speciation measurements from these solutions were included in the parameter optimisations in the preceding sections and serve only to analyse the predictive capability of the model in a mixed system.

The extraction of speciation trends in this mixed system is more challenging due to the number of convoluted bands in the ν_1-SO_3 mode of all relevant sulfate CIPs. Thus, an approach to fix all peak locations and widths from the individual systems was taken and the resulting speciation determined. As such, the confidence of individual measurements in this series is lower than that of the individual systems presented in the previous system, reflected in the estimated error bars in Figure 5.10. The concentrations for this set of solutions were established to vary the Fe(III):Fe(II) ratio at constant total iron of about 1.6 mol/kg in a background of 0.2 mol/kg H_2SO_4 (see Table 4.3).

The speciation measurements extracted from the Raman spectra as well as those calculated from the calibrated thermodynamic model of the system are presented in Figure 5.10. Generally, the fit of the model is good, with the majority of the variance associated with the concentrations of HSO_4^- and $Fe(SO_4)_2^-$, i.e., similar to the $Fe_2(SO_4)_3$ sub-system model. However, given the uncertainties in this analysis and that these measurements were not used in the parameter optimisation, the quantification of solution speciation in these solutions is excellent. This performance of the model can likely be attributed to the negligible interaction between Fe(II) and Fe(III) species, for which no parameters were explicitly included. Considering the literature regarding these systems' thermodynamics this is unsurprising as the natural tendency for both Fe^{2+} and Fe^{3+} to interact with sulfate is likely orders of magnitude stronger than with each other. Thus, the Pitzer model's consideration of the electrostatic effects of the presence of both cations through the total ionic strength is sufficient to capture the dominant thermodynamic behaviour in the system.

Furthermore, since the solubility of SO_2 decreases rapidly at elevated temperature, this mixed system provides a good estimate of that expected in the kinetic tests presented in the following chapter. Thus, these solutions provide an ideal basis on which the predictions of the solution model can be validated and the quality of fit shown in Figure 5.10 emphasize the validity of the model in the mixed system and provide good confidence in the use of this model as a basis for the reactive system in Chapter 7.

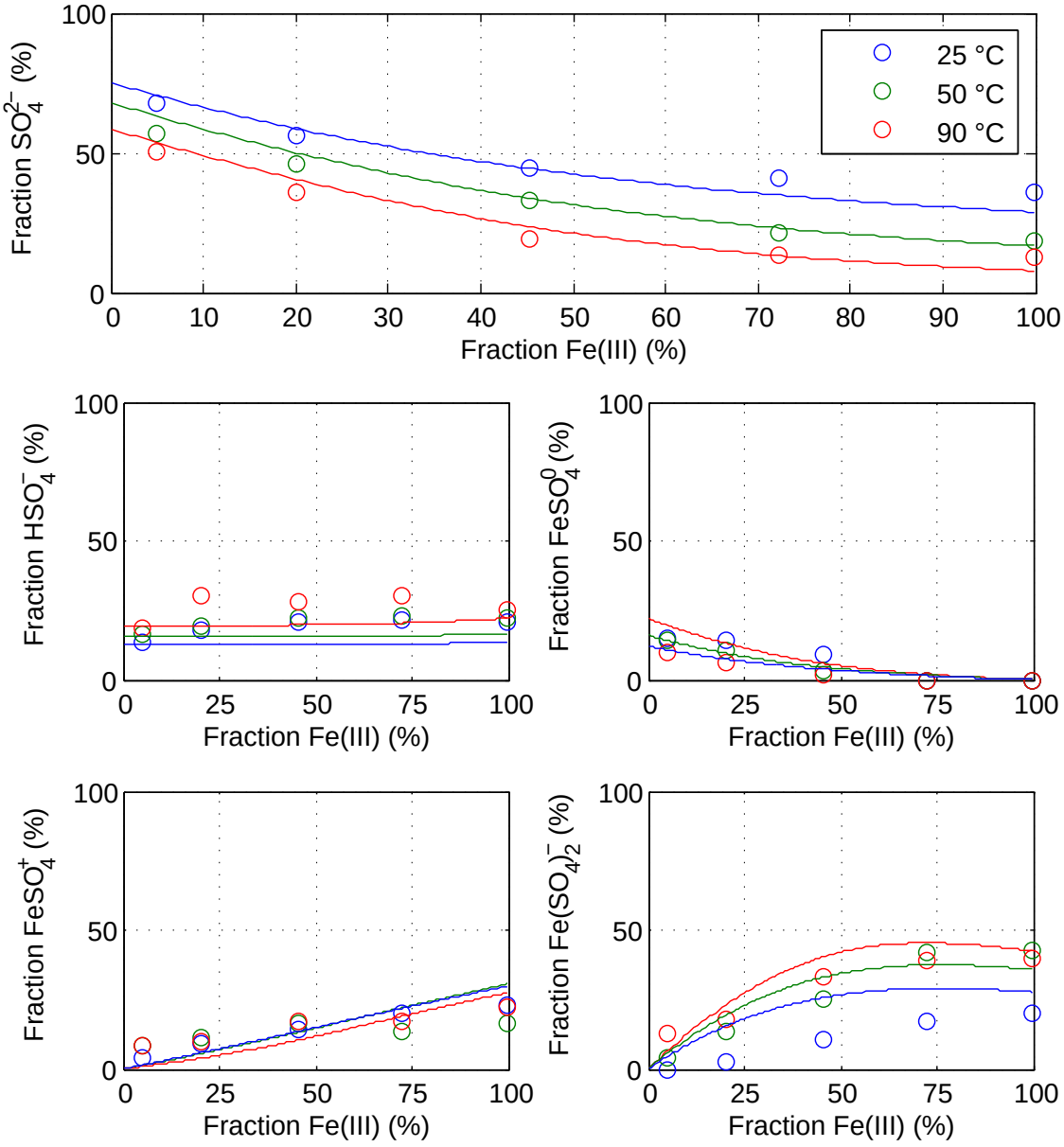

Figure 5.10: Measurements and model characterisation of total sulfate associated as each CIP species in mixed $Fe_2(SO_4)_3$-$FeSO_4$-H_2SO_4-H_2O solutions at 25, 50 and 90 °C. All solutions contained a total iron concentration (Fe(III) + Fe(II)) of 1.6 mol/kg, made up with different fractions of $Fe_2(SO_4)_3$ and $FeSO_4$ in a background of 0.2 mol/kg H_2SO_4. These data were not used in the calibration of model parameters and highlight the excellent predictive ability of the solution model. These data are also tabulated in Table B.5 in Appendix B

5.7 Sulfite systems

5.7.1 SO_2-H_2O system

The S(IV)-acid dissociation equilibria were calculated using enthalpy and heat capacity data taken from Wagman et al. (1982), Shock et al. (1997) and Goldberg and Parker (1985). Given the amount and diversity of data (heat capacities, enthalpies of solution, equilibrium constants, entropies, solubilities and partial and total vapour pressure measurements) on which the self-consistent set of standard state thermodynamic parameters for this system were based, the values (Goldberg and Parker, 1985) were accepted as the most accurate and were included in the chemical model; these parameters are presented in Table 5.9.

Reported speciation in this system is scarce, probably due to the volatility of SO_2 which complicates experimental measurements. However, successful modelling studies of this system have been carried out using a simple Debye-Hückel model up to 1 mol/kg $SO(OH)_2$ to consolidate extensive calorimetric data and some limited speciation data measured spectroscopically (Goldberg and Parker, 1985). Additionally, solubility of SO_2 in sulfate solutions has been modelled using a Pitzer ion interaction framework (Hunger et al., 1990). The largest source of uncertainty regarding the sulfite systems in this study involves the Fe(III)-S(IV) interactions. Ultimately, since errors induced by an oversimplification of the SO_2-H_2O chemistry will be captured in the other equilibrium and kinetic parameters, a simple approach was adopted to characterise this system. Several authors have had good success in modelling this system using interaction parameters for H^+-HSO_3^- suggested by Rosenblatt (1981) and these were adopted in this study and are also presented in Table 5.9. The resulting model provided an excellent description of speciation data contained in Goldberg and Parker (1985) up to 1 mol/kg sulfite as presented in Figure 5.11.

5.7.2 Fe^{3+}-S(IV)-H_2O system

Comparatively little is known about the thermodynamics of the Fe^{3+}-S(IV)-H_2O system, primarily due to its transient nature, which makes it inherently more difficult to study than the other systems already discussed. From the extensive review of the available literature by Kuo et al. (2006), it is known that a number of Fe(III)-S(IV) species have been proposed under varying experimental conditions. The simplest species, common to most studies is the $FeSO_3^+$ CIP and while other $Fe(SO_3)_n(OH)_m^{3-2n-m}$ species have been reported, in the conditions present in this study, *viz.* large Fe(III) excess, elevated tem-

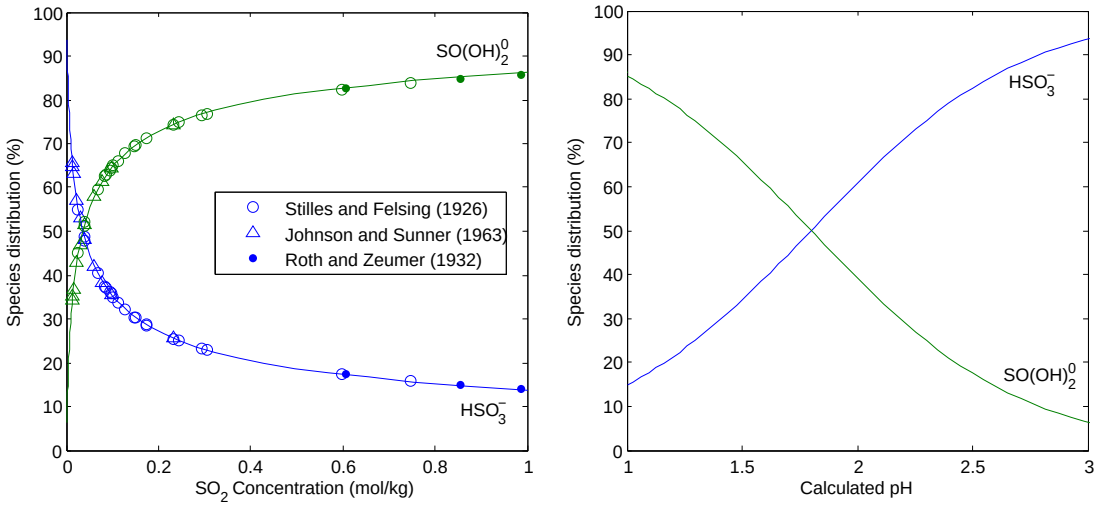

(a) Calculated SO_2-H_2O species distribution with concentration

(b) Calculated SO_2-H_2O species distribution with pH

Figure 5.11: Calculated SO_2-H_2O speciation as a function of (a) stoichiometric SO_2 concentration and (b) calculated pH , i.e., $-\log_{10}(m_{H^+}\gamma_{H^+})$

peratures, highly acidic solutions, it is expected that the monosulfito species is expected to be most dominant (Lente and Fabian, 1998, 2002). The formation equilibria of this species is given by:

$$Fe^{3+} + SO_3^{2-} \rightleftharpoons FeSO_3^+ \tag{5.7.1}$$

Several studies have reported the stability constant of the $FeSO_3^+$ species at various ionic strengths (refer to Figure 2.7) and extrapolation of these reported values to zero

Table 5.9: SO_2-H_2O thermodynamic and speciation model parameters

Species	$\log_{10}$ K^0	ΔH^0 [kJ/mol]	ΔC_p^0 [J/mol.K]	Source
$SO(OH)_2$	9.3373	21.45	534	Goldberg and Parker (1985)
HSO_3^-	7.1745	3.65	262	Goldberg and Parker (1985)

Parameter	p_0	p_1	Source
$\beta^{(0)}_{H^+-HSO_3^-}$	0.15	-	Hunger et al. (1990)
$\beta^{(1)}_{H^+-HSO_3^-}$	0.40	-	Hunger et al. (1990)

ionic strength results in an estimated value of $\log_{10} K^0 = 6.807$ (See Appendix A.2.5) for calculations details, which is in agreement with that reported by Betterton (1993), i.e., $\log_{10} K^0 = 6.845$. Given the difficulties in working with the transient system, the value of Betterton (1993) was deemed the most reliable and accepted for Reaction 5.7.1.

No reported values for the equilibrium constant at temperatures above 25 °C are available and a simplified approach was necessitated. Lente and Fabian (1998; 2002) reported stability constants for the reaction between Fe^{3+} and HSO_3^- to form $FeSO_3^+$ at 10 and 25 °C. Using the van't Hoff equation (Equation A.2.1) to extrapolate between these values, i.e., assuming $\Delta C_p^0 = 0$, the heat of reaction is calculated as 40.2 kJ/mol. This results in a calculated formation enthalpy of -635.58 kJ/mol for the $FeSO_3^+$ species using the reported formation heats collected in Table A.5. This value then permits a calculated heat of reaction for Reaction 5.7.1 at 25 °C of 49.50 kJ/mol. Unfortunately, these limited data do not permit the estimation of the heat capacity term and it was selected to maintain this as a variable in the model optimisation.

The transient nature of the Fe^{3+}-S(IV)-H_2O system excludes traditional thermodynamic data (activity and osmotic coefficients), since such data would not have real meaning, i.e., true equilibrium conditions could not be achieved. The most reliable data on which to calibrate this system would be high-resolution stopped-flow spectrophotometric experiments that could accurately determine the relevant species' concentrations immediately upon mixing. This is beyond the scope of this study and a simplified approach was adopted. A minimum number of interaction parameters among the species in this system were required, to be determined from measured kinetic data and reported in the following chapter. The calibration of thermodynamic model parameters in order to fit kinetic data is ill-defined, but by careful selection of a minimum number of interaction parameters and validation of the meaning of such parameters, a reasonable degree of confidence in the simplification methodology can be developed. A complete discussion of this is thus deferred to Section 7.2.

5.8 Summary

This chapter has detailed the development and calibration of a self-consistent minimum-parameter thermodynamic basis required to describe the $Fe_2(SO_4)_3$-$FeSO_4$-H_2SO_4-H_2O system over 25 – 90 °C and up to 1.6 mol/kg $Fe_2(SO_4)_3$, 2 mol/kg H_2SO_4. The Pitzer formalism for quantifying activity coefficients was used and a systematic approach was adopted by considering the binary and ternary systems individually and calibrating their respective parameters based on available thermodynamic and non-thermodynamic data,

with a specific focus on the speciation measurements made in Chapter 4.

While the model developed in this chapter quantifies the main solution speciation in the various sub-systems, the necessary simplified approach model is approximate and does not attempt to quantify *all* species in concentrated solutions, i.e., only experimentally verified species were considered in the model. The model could be improved by obtaining further spectroscopic data over a wider range of solution compositions (including other ligands) to build up an improved framework for the speciation. Such data would likely provide the necessary variation in speciation for the more accurate determination of interaction parameters for the various species, and ultimately facilitate total solution properties, i.e., the water activity data, to be reconciled with true speciation measurements.

Nevertheless, the minimum-parameter solution model does accurately quantify measured and reported speciation and activities in the H_2SO_4-H_2O systems, activities, speciation and solubility in the $FeSO_4$-H_2O and $FeSO_4$-H_2SO_4-H_2O as well as measured speciation in the $Fe_2(SO_4)_3$-H_2SO_4-H_2O system. Model overparameterisation was avoided by confirming the significance of model parameters by systematically removing model parameters and noting the lack of fit of the model. Additionally, the model was validated in the mixed $Fe_2(SO_4)_3$-$FeSO_4$-H_2SO_4-H_2O system by independent Raman speciation measurements that were not included in the parameter optimisation, highlighting that extrapolation of the model outside its calibration range provided reliable and consistent predictions. This validation also highlights the applicability of using this solution model in the reactive system detailed in the following chapters. The complete set of resulting model parameters are detailed in Appendix A.3.7.

Chapter 6

Reaction Kinetics and Mechanism

Reaction kinetics data are often even more scarce than thermodynamic data due to the large number of permutations that exist. No meaningful kinetic data for the reduction of ferric using SO_2 in concentrated sulfate solutions at elevated temperatures could be found in the literature and thus, its characterisation is a primary objective of this study.

This chapter presents a study of the kinetics of ferric reduction in concentrated aqueous solutions using SO_2 gas as reductant. The main objectives of this chapter are to characterise the rate and achievable conversion of ferric reduction under conditions relevant to the ARFe process and to highlight the most influential factors for these measurements. The experimental results presented in this chapter form the basis for a proposed reaction mechanism and data on which a reaction model, developed in the following chapter, can be calibrated.

6.1 Mass transfer considerations

Quantification of mass transfer limitations is essential in laboratory tests to ensure experimentally measured properties are not influenced by physical limitations which may distort any interpretation of the derived results. Accurately determining mass transfer coefficients in reacting systems is difficult and, in this study, several approaches were adopted. Firstly, the mass transfer rates of oxygen into water and sodium sulfite solutions were measured under various conditions in the reactor. Secondly, the effect of agitation speed on the initial rate of ferric reduction was used to highlight mass transfer effects under conditions expected during the kinetic measurements.

6.1.1 Mass transfer coefficient determination

The direct method (DO Electrode) was used at 25 and 55°C in water, according to the method described in Section 3.1, to measure the mass transfer coefficient of the reactor system as a function of agitation rate and temperature. Additionally, as the direct method is prone to underestimation of the true k_La, especially when it is of a similar order of magnitude as the DO electrode response (Gourich et al., 2008), the indirect sulfite oxidation method, was also used to determine the mass transfer coefficient at 90°C as a function of agitation speed.

The measured mass transfer coefficients are presented in Figure 6.1. The direct method showed an increase in k_La from 1.55 to 3.68 min^{-1} in pure water and an increase from 0.36 to 1.48 min^{-1} in 0.5 mol/kg $Fe_2(SO_4)_3$ over 25 – 55 °C when agitated at 1800 rpm. The significant decrease in mass transfer coefficient in $Fe_2(SO_4)_3$ solution is likely due to the significantly more viscous solution as compared to water, which is known to negatively influence the mass transfer coefficient (Garcia-Ochoa and Gomez, 2004). The indirect method at 90 °C and 1600 rev/min agitation[1] produced a k_La of 37.48 min^{-1} (1.3 mol/kg Na_2SO_3 solution). The reasonably large error bars for the indirect test are shown in Figure 6.1 due to the difficulty in accurately determining the oxygen partial pressure in an open system near the solution boiling point. In this analysis the water pressure was estimated at 70 kPa at 90 °C (Kell, 1975) and all details associated with these tests are included in Appendix C.1.

Despite the significant concentration of sulfite in the indirect method tests, the measured coefficients could be reconciled using a typical approach via Equation 6.1.1, with θ =1.047. The DO electrode measurements at 55 °C are overestimated by the model, but this could result from differences in the behaviour of water and sodium sulfite/sufate solutions and was considered reasonable for practical purposes. The temperature dependence parameter is slightly larger than the generally accepted value of θ =1.024 (Stenstrom and Gilbert, 1981), although values in the range 1.01-1.09 have been reported (Steyl, 2012).

$$k_La_{(T)} = k_La_{(T_{ref})} \cdot \theta^{(T-T_{ref})} \tag{6.1.1}$$

Applying the same θ-value for solutions of $Fe_2(SO_4)_3$ showed good quantification of the mass transfer coefficient determined at 55 °C using the DO electrode and resulted in an extrapolated value of the $k_La =$ at 8.92 min^{-1} at 95 °C . However, it must be considered that the θ-value is related to the macroscopic solution properties of the solute and

[1]Note that 1800 rev/min agitation of this solution produced excessive foaming in these solutions

not the reactor setup. For instance, measured kinematic viscosities of $Fe_2(SO_4)_3$ solutions are observed to have a much stronger temperature dependence than water and Na_2SO_3-Na_2SO_4 solutions. This was confirmed by several Ostwald tube measurements and data available in the literature (see details in Appendix C.1). Given this effect, it is expected that the temperature dependence of the mass transfer coefficient in $Fe_2(SO_4)_3$ solutions is greater than that of water and Na_2SO_3-Na_2SO_4 solutions, which would suggest that the extrapolation over temperature presented by the dashed line in Figure 6.1 and the resulting k_La at 95 °C, represents a *lower expected limit*.

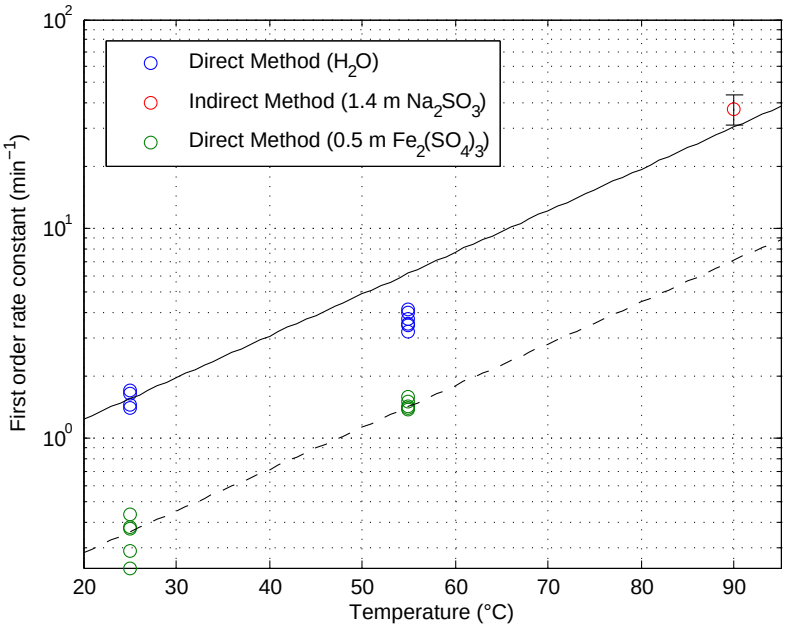

Figure 6.1: First order rate constant for mass transfer via direct and indirect means (described in Section 3.1) at 1800 rev/min. Equation 6.1.1 was fitted to the water and sulfite test data and is represented by the solid and dashed lines. The extrapolated value for $Fe_2(SO_4)_3$ at 95 °C is 8.92 min^-1.

In spite of the results above, which measured mass transfer rates in (essentially) non-reactive media, i.e., with negligible enhancement due to chemical reaction in the gas-liquid interface, these methods have limited applicability to the Fe(III)-$SO_{2(g)}$ system, where such effects could be significant. These tests did not facilitate the quantification of the mass transfer enhancement due to reaction in the boundary layer and a further analysis was required to investigate these effects in the system of interest.

6.1.2 Reactive system mass transfer effects

The most important aspect of mass transfer in this work is to ensure that no physical limitations are present during reaction, such that the observed reduction rate is representative of the true chemical reaction rate. In order to highlight mass transfer effects in the reactive system, several tests in 0.5 mol/kg $Fe_2(SO_4)_3$ solutions were conducted at 95 °C with various gas addition rates and agitation speeds. In the absence of mass transfer limitations, the rate of Fe(III) reduction would be expected to be independent of agitation and lower than the stoichiometric rate of supplied of gas.

The initial rate of Fe(III) reduction over the first 5 minutes of reaction was used to investigate the effects of mass transfer on the reactive system and the results of this analysis are presented in Figure 6.2. It is clear that higher agitation rates increase the rate of Fe(III) reduction, suggesting that mass transfer limitations are presented at lower rates. Additionally, at lower SO_2 gas flow rates, the reaction appeared to be limited by the supply of SO_2 into the reactor. At 1 L/min (STP), it is observed that the rate of Fe(III) reduction is ca. 80% of the stoichiometric SO_2 feed into the reactor and, neglecting any significant bypassing of SO_2, it is reasonable to assume that gas supply into the reactor was not limiting the reaction rate.

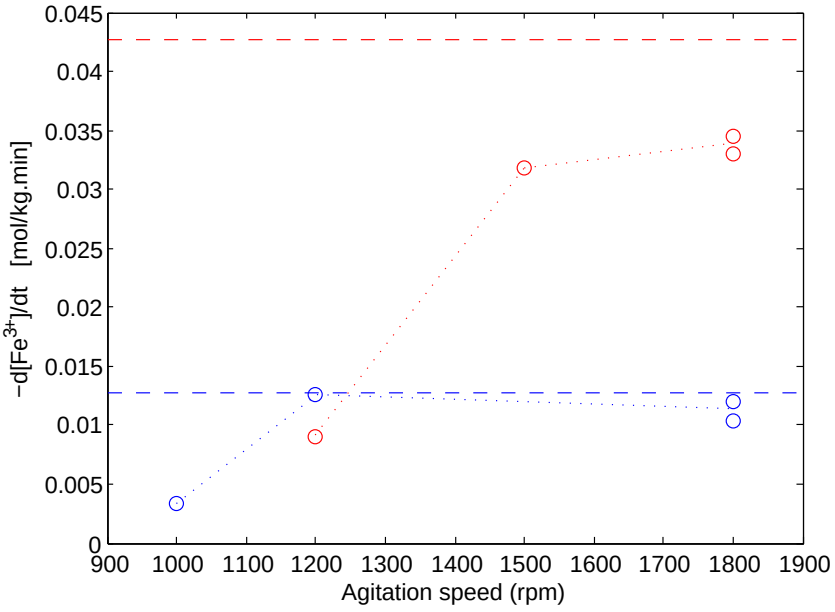

Figure 6.2: Initial rate of ferric reduction as a function of agitation speed and SO_2 gas flow rate. Red and blue points are at 1 and 0.3 L/min SO_2 (STP) respectively. The horizontal lines represent 100% SO_2 utilisation at each gas flow rate, i.e., limed by the supply of gas to the system.

6.1.3 SO_2 solubility

Accurate quantification of overall gas-liquid mass transfer rates also require the solubility of the gas in the solution to be known. The solubility of SO_2 in water and several salt solutions is well quantified (see Section 2.4). In this study, as the focus of the kinetic test work is near the solution boiling point and at atmospheric conditions, the water vapour pressure is significant. All tests were fed continuously with SO_2, resulting in the "batch" tests actually being semi-batch with respect to SO_2, and since a reflux condenser maintained the water balance of the tests, the determination of the SO_2 partial pressure is not trivial. An energy balance of the reactor during semi-batch or continuous operation is given as:

$$\dot{H}_{feed} + \dot{H}_{SO_2,in} + \Delta\dot{H}_{rxn.} + \dot{Q}_{in} = \dot{H}_{product} + \dot{H}_{SO_2,out} + \Delta\dot{H}_{vap} + \dot{Q}_{loss} \qquad (6.1.2)$$

Where $\dot{H}$ of the feed and products refer to the solution entering and exiting the reactor, which fall away under batch conditions. The constant temperature operation of the reactor would result in the above equation balancing and the time-derivatives (over-dot notation) cancelling in Equation 6.1.2. At the solution boiling point, any excess heat input would be balanced by the evaporation of water. Thus, at a constant feed of SO_2, the rate of heat addition into the reactor will determine the SO_2 partial pressure in the head space and the resulting solubility in the solution. In an attempt to quantify the partial pressure of SO_2 in the reactor under these conditions, SO_2 was fed continuously (1 L/min (STP)) into a water solution and iodine-thiosulfite back-titrations (Section 3.5.6) were used to quantify the steady SO_2 concentration. The reactor temperature that was achieved in these tests was lower than in the kinetic tests due to the boiling point elevation experienced in the $Fe_2(SO_4)_3$ solutions. In order to observe the effect of varying heat addition into the system, two jacket temperature set points and the results are summarised in Table 6.1. Details of the SO_2 solubility experiment are attached in Appendix C.2.

Under these conditions, the equilibrium partial pressure of SO_2 was calculated at 16-19 kPa. The determination of SO_2 solubility in Fe(III) solutions is further complicated by the strong affinity of these ions as discussed in Section 2.7 and the solubility is likely to be larger than that in pure water or *inert* electrolytes. However, since these compounds react together, their solubility cannot be measured by conventional means. From this analysis, it was deemed that a *minimum* solubility of 30-40 mmol/kg was expected in $Fe_2(SO_4)_3$ media near the solution boiling point while feeding SO_2 at 1 L/min (STP).

Table 6.1: Equilibrium SO_2 partial pressure determination in water media in semi-batch configuration

Oil Temp. (°C)	Reactor Temp. (°C)	SO_2 Flow (l/min STP)	SO_2 solubility (RSD) [mmol/kg]	Estimated $P^c_{SO_2}$ (bar)
120±0.1	90.6±0.2	1.0	37.8 (4.3%)[a]	0.192
125±0.1	91.4±0.2	1.0	31.5 (0.4%)[a]	0.163
80±0.5	75.0±0.5	1.0	180.0 (3.2%)[b]	0.622

[a] $n = 3$, [b] $n = 9$, [c] using Henry's law relationship of Goldberg and Parker (1985)

6.1.4 Mass transfer summary

In summary, mass transfer limitations may exist in this system, particularly when there is insufficient agitation for intimate gas-liquid mixing. Additionally, the supply of SO_2 gas and the supply (or generation) of heat during reaction has the potential to significantly affect the rate and extent of reaction, where water vapour pressure may suppress the solubility of SO_2. For the purposes of this study, mass transfer and physical limitations are to be avoided in order to provide real information about the chemical reaction kinetics.

Thus, for all kinetic tests SO_2 was fed at 1 1 L/min (STP), agitation at 1800 rev/min was maintained throughout and the reactor jacket temperature was minimised while controlling the reactor at 95 °C to avoid excessive water evaporation.

6.2 Reaction stoichiometry

The overall reaction stoichiometry of Fe(III) reduction with sulfur dioxide was first investigated to determine if Reaction 6.2.1 is applicable. This can be partially confirmed from the data in Figure 6.3, which compares the experimentally determined ferrous concentrations with the equivalent concentration of acid produced by the reaction, i.e., $H_2SO_{4,t} - H_2SO_{4,t=0}$. For the mass transfer tests, in which no initial acid was added into the solutions and the $Fe_2(SO_4)_3$ concentration was reasonably low at ca. 0.25 mol/kg, the reaction stoichiometry was calculated as 0.95 mol H_2SO_4 per mol Fe^{2+}. Other kinetic tests, at increased acid and ferric concentrations, showed significantly larger variance in the stoichiometry with a resulting slope of 0.94 when all data were included in the fit. Despite the large scatter, these data do suggest that reaction stoichiometry below is representative of the overall reaction under the conditions of these tests.

$$2\,Fe^{3+} + SO_{2(g)} + 2\,H_2O \longrightarrow 2\,Fe^{2+} + SO_4^{2-} + 4\,H^+ \tag{6.2.1}$$

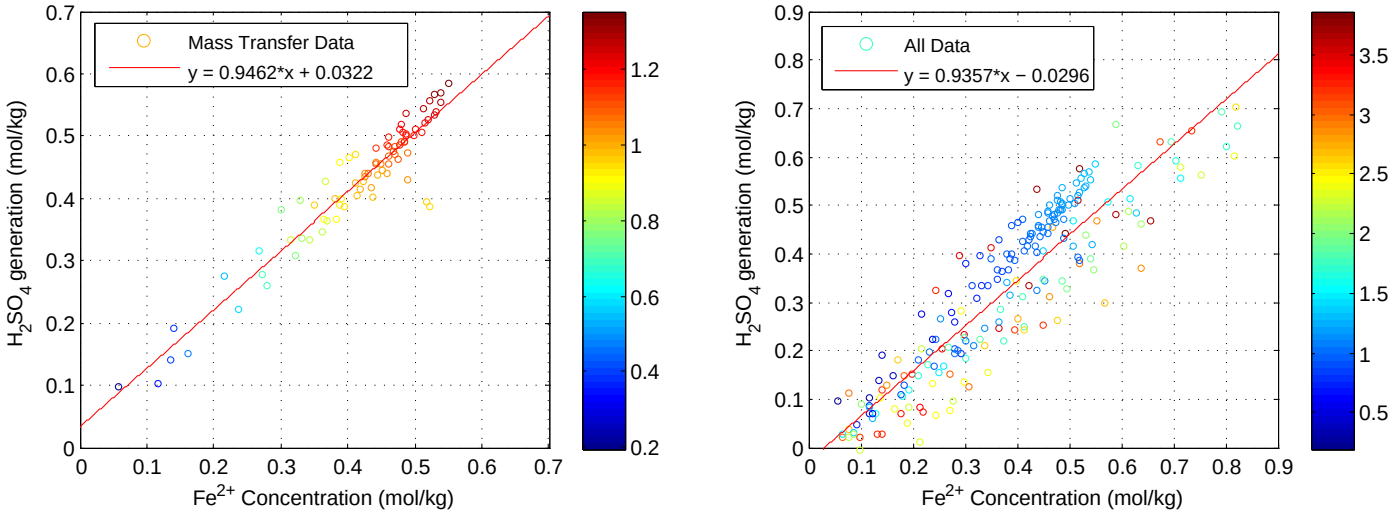

(a) Mass transfer batch test data from Figure 6.2

(b) All batch test kinetic data

Figure 6.3: Relationship between Fe(II) and H_2SO_4 produced during batch tests in order to test the reaction stoichiometry. Data points are coloured according to their total H_2SO_4 concentration. The red lines are linear robust fits of the data with equations shown in each legend.

As a further confirmation of the reaction stoichiometry, the oxidation state of sulfur after reaction was confirmed to be sulfate by Raman spectroscopy. Incomplete sulfur oxidation has been reported in systems utilising SO_2/O_2 mixtures at 40 °C where dithionate, $S_2O_6^{2-}$, was observed, i.e., sulfur in the +5 oxidation state. A Raman spectrum of a solution sample immediately after reaction with SO_2 at 95°C for 180 minutes, presented in Figure 6.4 shows no bands at 1092 cm^{-1}, attributable to dithionate. While this does not rule out its presence *during* reaction, the identification of ditionate during the room temperature reduction of $Fe_2(SO_4)_3$ by Na_2SO_3, presented in Figure 6.15a does suggest complete sulfur oxidation does occur at 95 °C. This is in agreement with other studies that report that dithionate is unstable above about 60 °C (Zhang et al., 2000b).

6.3 Effect of $Fe_2(SO_4)_3$ and H_2SO_4 concentrations

A preliminary set of ferric reduction tests were performed using only $Fe_2(SO_4)_3$ and although these tests were initially limited by mass transfer, shown by the coincidence of all Fe(II) concentrations up to one hour reaction time in Figure 6.5, a clear relationship between increasing ferric concentration and decreasing conversion was observed. This is

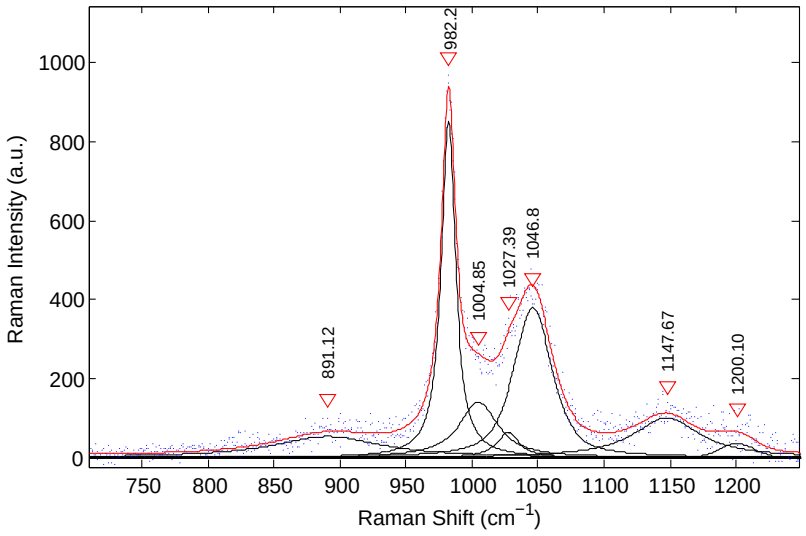

Figure 6.4: Raman spectrum of 0.5 mol/kg $Fe_2(SO_4)_3$ solution after reaction with SO_2 for 3 hours. No bands attributable to dithionate at 1092 cm^{-1} can be observed

not intuitive from the overall reaction stoichiometry and suggests that a reaction product may be limiting the rate of reaction and hence the achievable conversion in a reasonable residence time. In these tests, while conversion decreases with increasing initial $Fe_2(SO_4)_3$ concentration, the absolute concentration of Fe(II) produced over 3 hours increases with added Fe(III), concurrent with a product-limited controlling reaction. However, since the $Fe_2(SO_4)_3$ reagent contains a significant amount of included H_2SO_4 these tests were not sufficient to determine the individual contributions of $Fe_2(SO_4)_3$ and H_2SO_4.

A more elaborate set of tests were thus conducted where $Fe_2(SO_4)_3$ and H_2SO_4 was varied between ca. 0.25 and 1.5 mol/kg and 0.3 and 1.5 mol/kg respectively in four increments. The results of these tests are presented in Figure 6.6 which show the variation in conversion-time profiles for each batch test. Clearly, the effects of both ferric and acid are important for the rate of reaction and achievable conversion. Conversion after 3 hours approximately halves as the acid concentration was raised from 0.3 to 1.5 mol/kg H_2SO_4 for $Fe_2(SO_4)_3$ concentrations in the range 0.25 - 1.5 mol/kg $Fe_2(SO_4)_3$. The relationship between the achieved conversion and the initial acid and ferric concentrations is however influenced by the overall reaction stoichiometry, i.e., increased molar Fe(III) reduction will produce additional acid. This effect is highlighted in Figure 6.7a where the empirical interpolating surface indicates that the conversion achieved after 3 hours is clearly a function of both variables and consistent with a decrease in conversion with

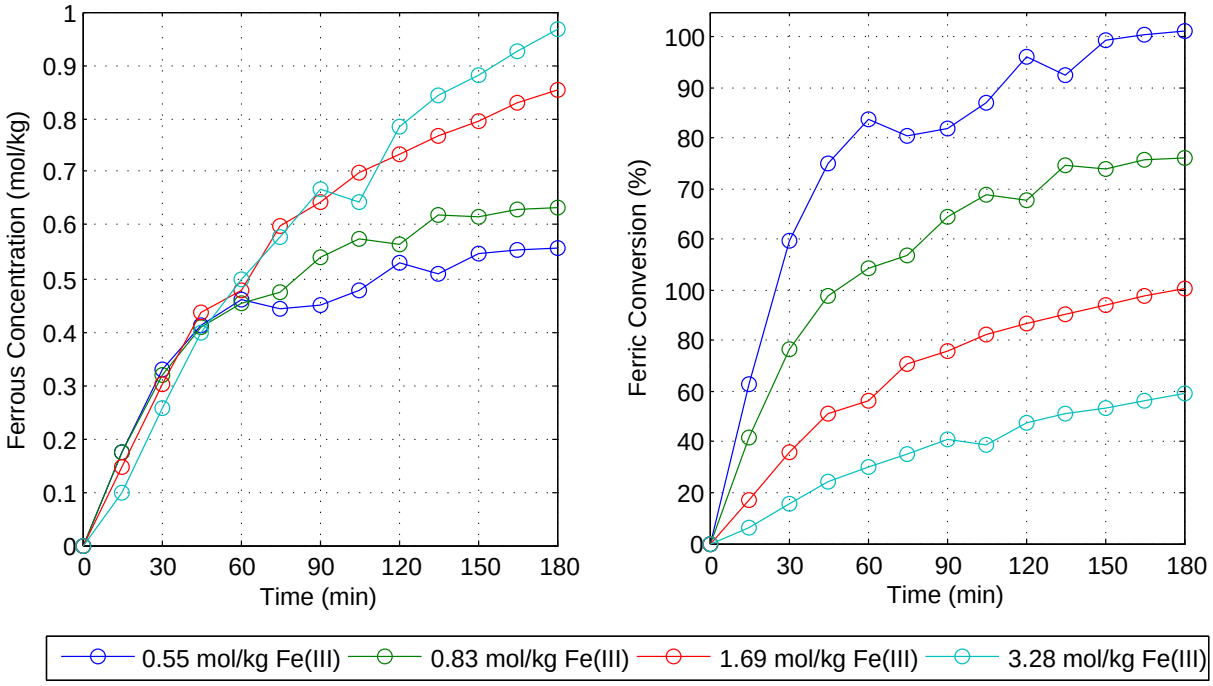

Figure 6.5: Ferrous concentration and conversion kinetic profiles of pure $Fe_2(SO_4)_3$ solutions. Tests were mass transfer limited over the period 0 - 50 minutes due to a SO_2 flow rate of 0.3 L/min (STP). Data points are jointed with lines only for clarity.

increased acid, added initially or generated during reaction.

The average rate over the first 5 minutes of reaction, albeit sensitive to errors in the first Fe(II) analysis, increased significantly with Fe(III) concentration, as presented in Figure 6.7b. Except for the low acid tests, the initial reaction rate approximately doubled when increasing the $Fe_2(SO_4)_3$ concentration. Thus, while increased $Fe_2(SO_4)_3$ concentrations limit the overall conversion achieved, the rate of reaction was observed to increase significantly. These results suggest, not unexpectedly, that a significant primary driving force for the reaction is the $Fe_2(SO_4)_3$ concentration. Figure 6.7b also highlights that the rate of addition of SO_2 into the reactor was not limiting as the stoichiometric equivalent rate of Fe(II) generation for absorption of 1 L/min (STP) SO_2 is estimated at 0.049 mol/kg.min, i.e., more than twice the equivalent average reaction rate over the first 5 minutes. This is in agreement with the reactive mass transfer tests performed in Section 6.1.2.

The importance of the effect of total acid concentration is most effectively highlighted in Figure 6.8 which presents the relationship between the initial and final acid concentra-

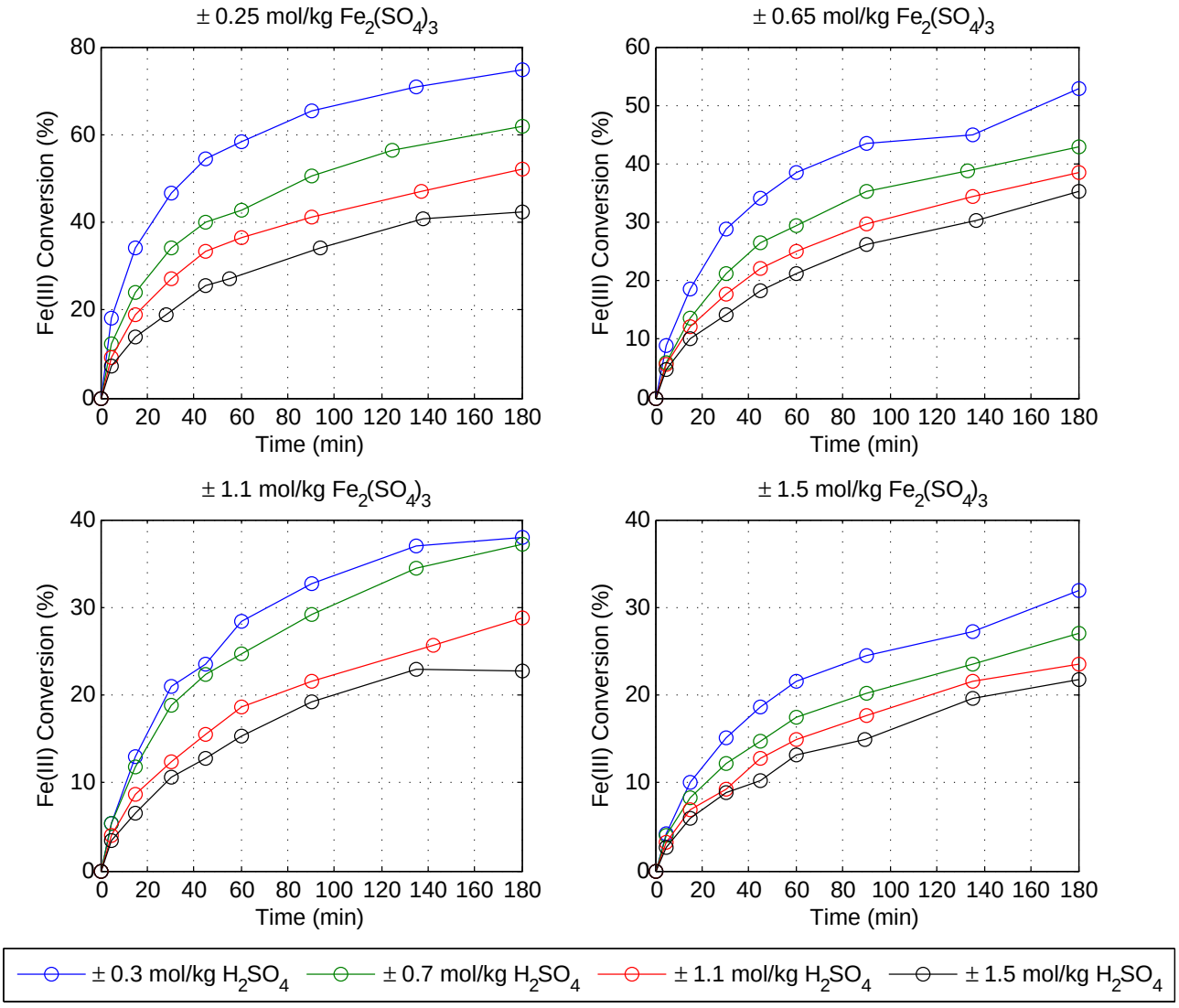

Figure 6.6: Conversion profiles of kinetic tests as a function of Fe(III) and H_2SO_4 concentrations. Data points are jointed with lines only for clarity.

tions for the four Fe(III) concentrations in this experimental set. The slopes of the points in this figure, at each Fe(III) concentration, are approximately the same, highlighting that the same overall reaction stoichiometry is achieved at each acid concentration, i.e., H_2SO_4 per mole of Fe(II). However, the relatively small vertical offset (i.e., ca. 0.375 mol/kg H_2SO_4) of the best-fit line for the various $Fe_2(SO_4)_3$ concentrations highlights that a significantly lower conversion was achieved at increased $Fe_2(SO_4)_3$ concentrations. In other words, despite the significantly larger Fe(III) driving force in the most

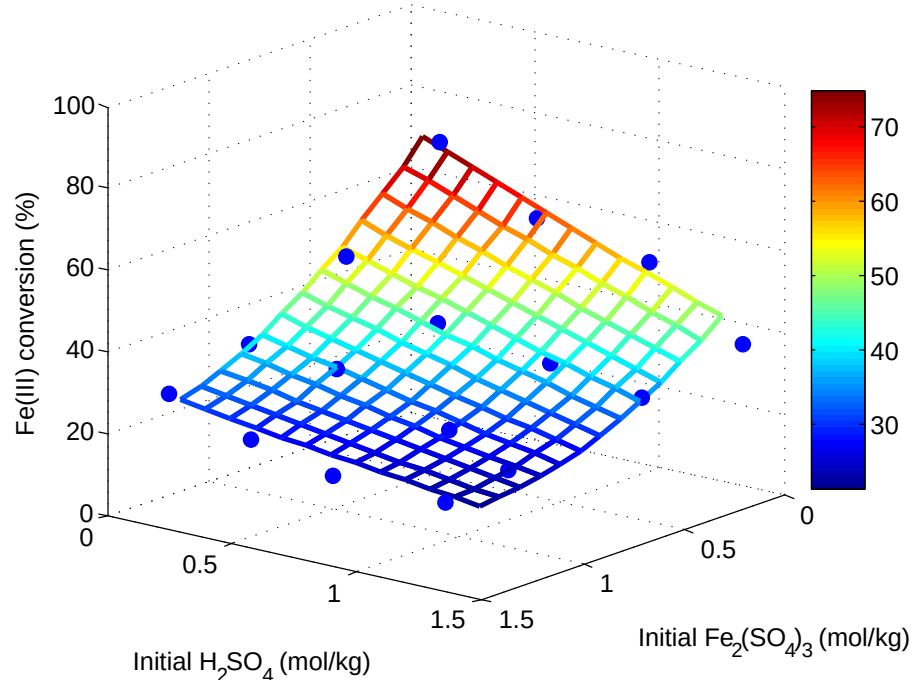

(a) Ferric conversion after 180 minutes of reaction.

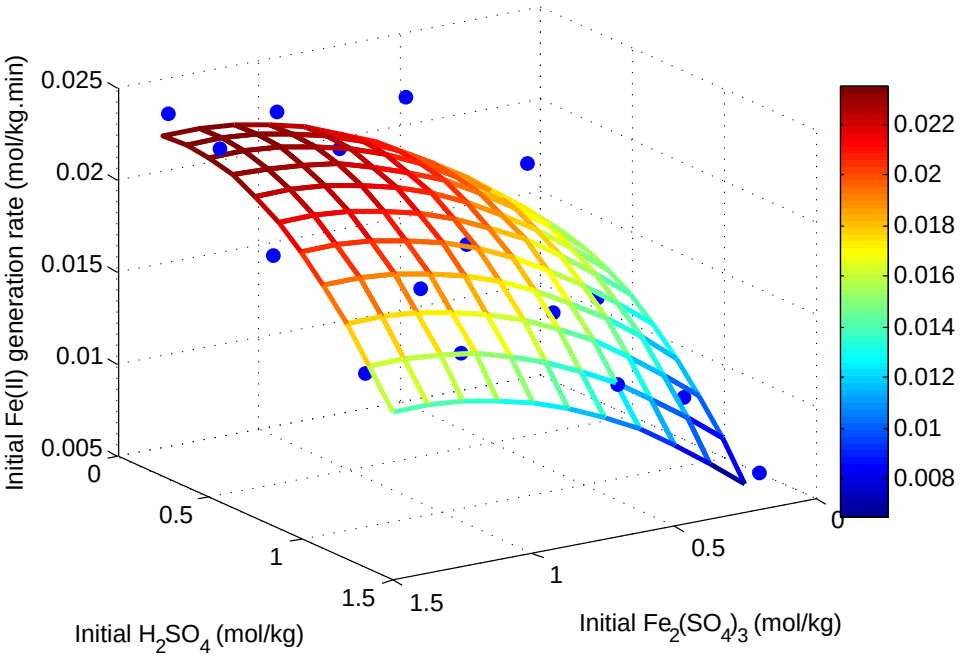

(b) Initial rate of Fe(II) generation

Figure 6.7: Final conversion and initial rate summary plots of kinetic tests in $Fe_2(SO_4)_3$–H_2SO_4 solutions. *Note: Surfaces represent a simple quadratic model that was fitted to the data in order to highlight the general trends with concentration.*

concentrated tests, the total amount of acid generated at low conversion was comparable to those at lower $Fe_2(SO_4)_3$ concentrations.

These findings are concurrent with a reaction mechanism that is driven by Fe(III) but retarded by the presence of acid during the reaction. In order to further validate this, several additional batch tests were carried out with 0.45 mol/kg $Fe_2(SO_4)_3$ solutions containing no added H_2SO_4. In one of these tests, 1 mol of NaOH was added to the reactor after 90 minutes. This neutralised approximately 37% of the acid produced by the reaction. The resulting conversion of Fe(III), presented in Figure 6.9, shows a marked increase in the rate of ferric reduction, immediately after the neutralisation, and a corresponding increase of ca. 10% after 3 hours. The instantaneous increase in reaction rate was not comparable to the initial rate, probably due to the depletion of ca. 65% of the available Fe(III) prior to the addition of NaOH and the still significant H_2SO_4:$Fe_2(SO_4)_3$ ratio.

This test highlights the absolute importance of acid concentration for limiting the rate of the rate-limiting step in the reaction mechanism.

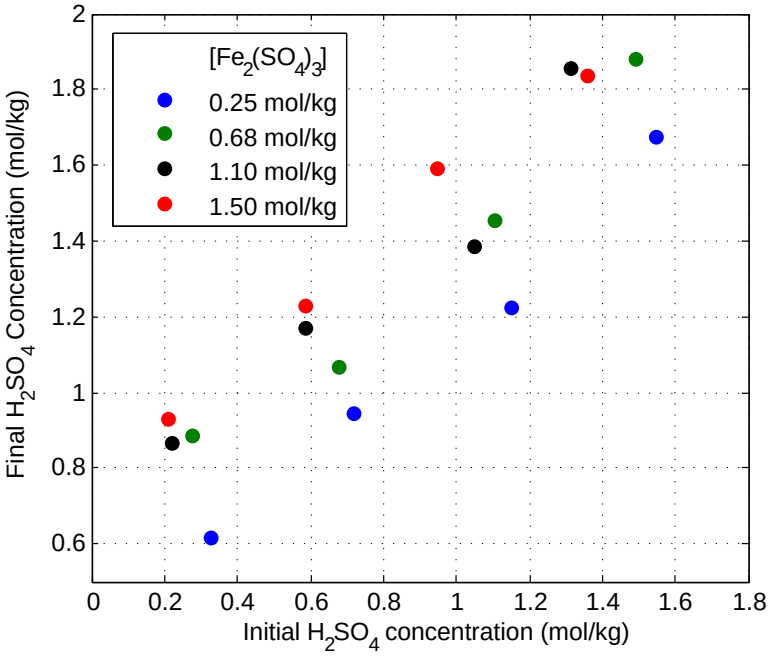

Figure 6.8: Relationship between initial and final acid concentrations for batch tests

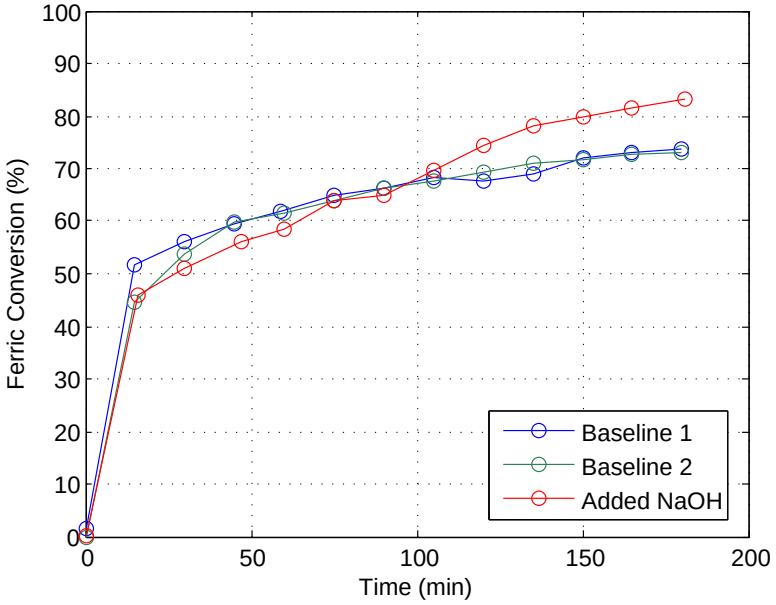

Figure 6.9: Effect of added NaOH on ferric conversion. Red data points: 40 g $NaOH_{(s)}$ added at 90 min. Data points are jointed with lines only for clarity.

6.4 Effect of temperature

The temperature profiles, presented in Figure 6.10, had a trend that showed an initial increase in temperature from 95 $\pm$ 1 °C to up to 97 °C followed by a decrease in the reactor temperature to below 94 °C, that was slowly rectified by the temperature controller. The initial rise in reactor temperature was attributed to the generation of heat in the initial phase of the batch reaction, i.e., the fastest rate of reaction. Since the reduction reaction is exothermic with a calculated reaction enthalpy of -162.90 kJ/mol (Reaction 6.2.1 at 95 °C) (Roine, 2002)) the considerable generation of Fe(II) in the initial stages of the reaction would generate a considerable amount of heat. As the reaction rate slowed, the enthalpy associated with heating the SO_2 gas supplied to the reactor (from ambient temperature) and the water evaporation associated with the gas flow was in excess of the reaction heat generation and the reactor temperature dropped. The temperature controller attempted to rectify this, but the slow time constant associated with the oil bath and jacketed reactor setup, made the precise control of the reactor temperature difficult and the resulting temperature profiles were observed.

In order to account for these significant temperature variations, the temperature profiles for each tests, and thus their effect on the kinetic rate constants and thermodynamic equilibria were used in the reaction modelling in the following chapter.

Despite this temperature variation during the batch tests, it was also desired to investigate the rate and extent of ferric reduction at 75 °C. While the focus of the this study was near the boiling point of the solution, primarily due to energy balance constraints for atmospheric laterite leaching with added SO_2 (see Section 2.1) an enhanced analysis of the reaction mechanism could be facilitated by investigating the effect of temperature. It has been confirmed in another study, that incomplete SO_2 oxidation to sulfate is achieved at temperatures below 60 °C in SO_2/O_2 mixtures (Zhang et al., 2000c). Incomplete sulfite oxidation would limit the acid generating capacity of the reaction, which would be undesirable for commercial applications and it was thus selected to operate above this temperature. Figure 6.11 presents two tests carried out with the same feed composition (0.26 mol/kg $Fe_2(SO_4)_3$, 0.3 mol/kg H_2SO_4) at 75 and 95 °C.

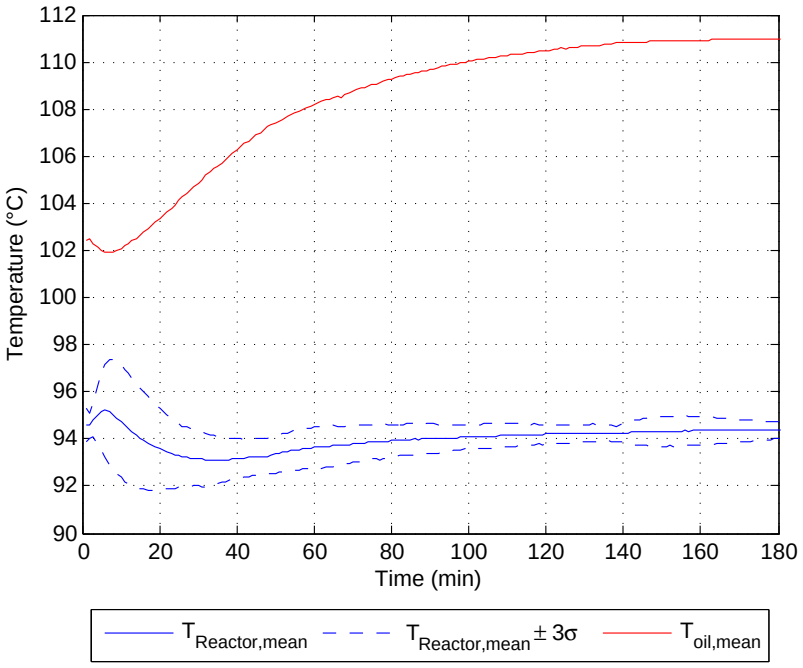

Figure 6.10: Mean reactor and oil temperature profiles for the batch kinetic tests presented in Section 6.3

The noted insensitivity to the reaction to temperature can be attributed to competing thermodynamic and kinetic effects. The solubility of SO_2 increases about three fold at 75 °C compared to 95 °C due to the increased SO_2 partial pressure, viz. a lower water vapour pressure, as well as the solubility relationship which SO_2 has with temperature

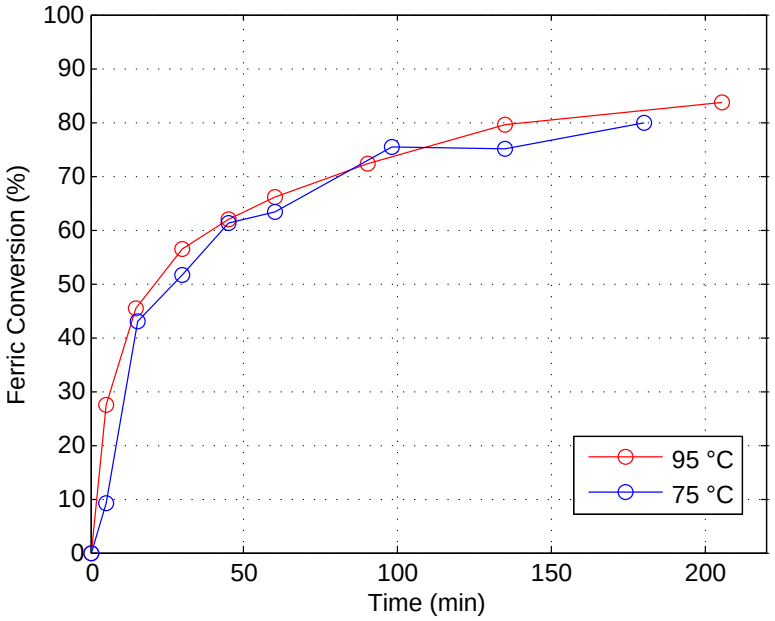

Figure 6.11: Conversion time profiles at the same initial concentrations at 75 and 95 °C

in aqueous solutions (see Section 2.4). At 95 °C the solubility of SO_2 is estimated at 0.03 mol/kg , whereas at 75 °C the solubility is approximately 0.18 mol/kg (See Table 6.1). In order to accurately account for the amount of dissolved SO_2 in the reactor solution during the low temperature test, which is significant, the solution was sparged with N_2 at 1 L/min STP to strip residual SO_2 from the solution. Ferrous titration (by $K_2Cr_2O_7$) of regular samples during N_2 sparging indicated that the solution contained 0.13 mol/kg dissolved SO_2. Sparging was ceased when the Fe(II) analysis by titration was statistically identical in three successive analyses. The SO_2 solubility was subtracted from all preceding Fe(II) analyses to give the profile presented in Figure 6.11. This inherently assumed that the SO_2 solubility was constant throughout the test, but was considered acceptable considering the significantly stronger trend with temperature than ionic strength (see Figure 2.4).

The similarity of the batch conversion profiles at 75 and 95 °C highlights that the increases solubility of SO_2 is appropriately cancelled by the decrease in chemical reaction rate. As such, the calculation of the limiting reaction activation energy is not trivial and is confounded by thermodynamic, i.e., solubility and speciation, changes. Thus, further consideration of the temperature effect on the reaction is deferred to the reaction modelling section in the next chapter.

6.5 Continuous ferric reduction tests

The kinetic experimental work reported thus far was carried out in 2000 mL (semi-) batch reactors, due to the ease in which bulk kinetic data can be obtained. However, industrial applications would likely be operated in continuous reactor trains, where the steady-state solution compositions do not change with time. Significant differences between batch and continuous reactions can occur should the solution background, which is transient in batch systems, have a significant kinetic contribution. It was thus also necessary to validate the batch findings in continuous operation.

The continuous reactor setup was essentially identical to the batch case as described in Section 3.2. All continuous tests were allowed to reach steady-state, which was typically reached within three residence times, determined by an unchanging Fe(II) concentration in the reactor. Slight differences in the working volume of the reactor, induced by the goose-neck overflow, were accounted for by measuring the volume in the reactor directly after the test. Furthermore, a residence time distribution tracer test showed that the CSTR used in this study can be accepted as a perfect CSTR for practical residence times (refer to Section C.4.1 for the experimental details).

As expected from theory, all single-CSTR tests showed a significant decrease in conversion compared to the batch tests under the similar experimental conditions. The results of the continuous tests are presented in Figure 6.12. This decrease is primarily due to the fact that a significant portion of the CSTR residence time distribution (RTD) lies below the mean residence time (Fogler, 2006).

The conversion achieved in a single CSTR, $\bar{X}$, can be calculated from the following equation:

$$\bar{X} = \int_0^\infty X(t) \cdot E(t) dt \tag{6.5.1}$$

where $X(t)$ is the conversion achieved in a batch configuration and $E(t)$ is the residence time distribution, for which a perfectly mixed CSTR has the form shown in the first part of Equation 6.5.2. For the purpose of this analysis, it was found that an empirical rate law of the form shown in Equation 6.5.2 accurately fitted the measured batch conversion-time profiles from the above section. While this rate law is not extremely useful in the development of a reaction model of the system, it can be used to investigate if indeed the same prevailing reaction mechanism is applicable for both batch and continuous reactions.

$$E(t) = \frac{1}{\tau} \exp\left(\frac{-t}{\tau}\right), \qquad X(t) = \frac{p_1 t}{1 + p_2 t + p_3 t^{0.5}} \tag{6.5.2}$$

The empirical rate law was fitted to the batch test profiles in Figure 6.12 (blue lines) using non-linear least squares regression (MATLAB, 2014). By substituting the empirical correlation and the ideal CSTR residence time distribution into Equation 6.5.1 one obtains Equation 6.5.3 and the resulting single CSTR conversion as a function of residence time can be calculated by integration.

$$\bar{X} = \int_0^\infty \frac{p_1 \frac{t}{\tau} \exp\left(\frac{-t}{\tau}\right)}{1 + p_2 t + p_3 t^{0.5}} dt \tag{6.5.3}$$

Figure 6.12 also shows how the measured conversions for a single CSTR are in good agreement with those calculated from the fitted batch curves and the equation above. The constantly changing solution background, in batch tests, thus has little effect on the rate limiting reaction, which must be significantly slower than the changes in solution phase equilibria. Thus, in the time-scale of the limiting reaction, the system is effectively in a pseudo-equilibrium, meaning that modelling of this system need only consider the kinetic effects of the rate limiting process. These CSTR tests also emphasize the applicability of kinetic measurements made in batch, laboratory tests in this system to continuous operation that would be more closely related to industrial applications.

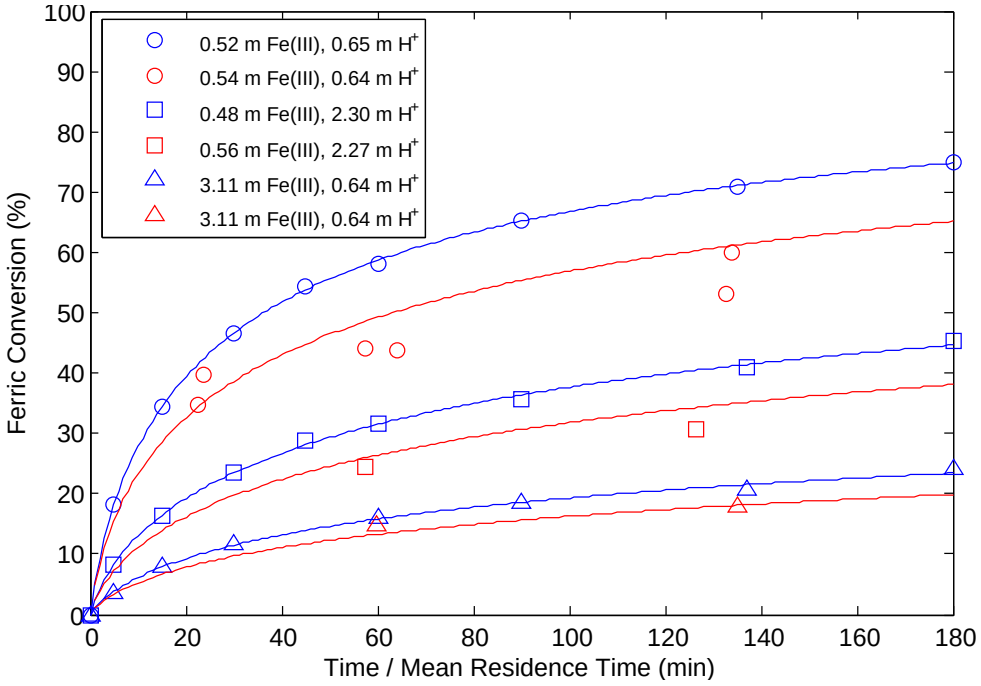

Figure 6.12: Comparison of batch and continuous Fe(III) conversion tests. Batch conversion profiles are the blue data points and individual continuous tests are shown in red. The blue and red curves represent fitted Equations 6.5.2 and 6.5.3.

6.6 Proposed mechanism of Fe^{3+} reduction with SO_2

From the results presented above, several important relationships between the input variables and the observed kinetic effects are apparent and provide some insights into the controlling reaction mechanism.

Firstly, the reaction rate increases with increasing Fe(III) at constant acid concentration and decreases with increasing acidity at constant Fe(III) concentration. This is consistent with a reaction mechanism that is driven by a pathway involving Fe(III) and hindered by the presence of acid (either initial or generated via reaction). Additionally, the impact of acid generation is critical, since 4 protons are generated per sulfate, i.e., above the stoichiometric ratio of H_2SO_4, which would tend to increase the overall H^+ activity as the reaction proceeds.

Secondly, the response of the reaction rate to added neutralising agent suggests that the rate is retarded by acid rather than Fe(II) or sulfate. The addition of NaOH, while increasing the total ionic strength of the solution, most notably effects the free acid concentration in solution. This suggests that the product limiting the reaction rate can exclusively be attributed to acid and is in further agreement with the significant decrease in conversion observed at high acid and Fe(III) concentrations.

Thirdly, the insensitivity of the reaction rate to temperature highlights that the rate-limiting kinetic step is directly influenced by thermodynamic effects. These effects may be exclusively the increased P_{SO_2} and SO_2 solubility at decreased temperatures or a more intricate involvement in the solution phase equilibria.

The proposed mechanism for Fe(III) reduction in this study is largely based on that previously reported in the literature for the Fe(III) catalysed oxidation of SO_2 in the presence of oxygen as discussed in Section 2.7. The primary difference between the previously reported systems and this study is the presence of oxygen. Fortunately, many of the disagreements within the literature of the proposed mechanisms of sulfite oxidation involving oxygen are focused on the specific activity of oxygen and how it is involved in the chemistry as the final electron acceptor (Brandt and van Eldik, 1995). The resulting reaction mechanism is presented in Table 6.2 and involves four main kinetic processes.

Firstly, SO_2 in the gas phase is absorbed into solution via mass transfer through a gas-liquid boundary layer where it is aquated to form the solution $SO(OH)_2^0$ species (or H_2SO_3). The rate of mass transfer into solution, r_1, is controlled by the concentration gradient across the gas-liquid interface as well as the resistance to mass transfer and the interfacial area (k_La) in the usual way as discussed in Section 2.2.

Secondly, the solution phase speciation is established according to reactions r_2-r_9,

Table 6.2: Proposed ferric reduction mechanism using $SO_{2(g)}$

SO_2 absorption	r_1:	$SO_{2(g)}(+H_2O) \overset{k_La}{\rightleftharpoons} SO(OH)_2^0$
Solution speciation	r_2:	$H^+ + HSO_3^- \rightleftharpoons SO(OH)_2^0$
	r_3:	$H^+ + SO_3^{2-} \rightleftharpoons HSO_3^-$
	r_4:	$H^+ + SO_4^{2-} \rightleftharpoons HSO_4^-$
	r_5:	$Fe^{3+} + nH_2O \rightleftharpoons Fe(OH)_n^{3-n} + nH^+$
	r_6:	$Fe^{3+} + SO_4^{2-} \rightleftharpoons FeSO_4^+$
	r_7:	$Fe^{3+} + 2\,SO_4^{2-} \rightleftharpoons Fe(SO_4)_2^-$
	r_8:	$Fe^{2+} + SO_4^{2-} \rightleftharpoons FeSO_4^0$
	r_9:	$Fe^{3+} + SO_3^{2-} \rightleftharpoons FeSO_3^+$
Inner sphere e^- transfer	r_{10}:	$FeSO_3^+ \xrightarrow{k_1} Fe^{2+} + SO_3^{\cdot-}$
Radical termination	r_{11}:	$SO_3^{\cdot-} + Fe^{3+} \xrightarrow{k_2} Fe^{2+} + SO_3^0$
	r_{12}:	$2\,SO_3^{\cdot-} \xrightarrow{k_3} S_2O_6^{2-}$
Rapid hydration	r_{13}:	$SO_3^0 + H_2O \xrightarrow{k_4} HSO_4^- + H^+$

Note: All equilibria are shown as association reactions

where, specifically $SO(OH)_2^0$ dissociates according to equilibria r_2 and r_3. In acidic conditions, this dissociation will be largely incomplete and $SO(OH)_2^0$ will be the dominant acidic S(IV) species (see Figure 5.11). The bisulfate species as well as ferric hydroxyl and sulfato species will also form according to the appropriate equilibrium reactions. The time scale for solution phase speciation is expected to be very rapid, i.e., complete within the order of milliseconds (Kuo et al., 2006), and the distribution of these species will govern the overall properties of the solution. Since these reaction rates are orders of magnitude faster than the limiting reaction, they can be approximated as pseudo-equilibria that reach equilibrium conditions instantaneously, confirmed by the continuous tests.

On the basis of the experimental evidence presented in the next section and the findings of stopped-flow experiments of Lente and Fabian (2002, 1998) at metal ion excess, the formation of the $FeSO_3^+$ CIP is central to the proposed reaction mechanism and the rate-limiting step is suggested to be the inner-sphere electron transfer from S(IV) to Fe(III). In fact, they only included this species in their reaction modelling of sulfite oxidation at long reaction times, i.e. those most relevant to this study. The proposed rate-limiting decomposition of the $FeSO_3^+$ CIP and subsequent reactions are presented schematically in Figure 6.13.

The first process presented in Figure 6.13, Process (a), involves the slow inner sphere electron transfer across the Fe(III)-S(IV) bond which produces a hydrated Fe(II) ion and

an electron deficient S(V) radical, $SO_3^{\bullet-}$ that dissociates (Process (b)). The radical is likely highly reactive and, with excess Fe(III) in solution, particularly at elevated temperatures, rapidly co-ordinates to another Fe(III) ion in solution in Process (c). This implies that the reaction is second order in Fe(III), but due to the large difference in rate constants associated with the first and second electron transfer and the controlling mechanism being the decompositions of the $FeSO_3^+$ species, the observed reaction is pseudo-first-order according to Reaction r_{10}.

At elevated temperatures, it was confirmed by Raman spectroscopy that the decomposition of two S(V) radicals to form dithionate (Reaction r_{12}) does not readily occur. However, the dithionate species may provide a transient, stabilising role for the $SO_3^{\bullet-}$ radical, particularly at low Fe(III) concentrations. This aspect is less important for this study, as the electron transfer from S(V) to Fe(III) is known to occur from the demonstrated stoichiometry of the overall reaction. It is thus uncertain from the results of this study as to the exact nature of how electron transfer between the S(V) and Fe(III) occurs, and it is hypothesized in Figure 6.13 that an inner-sphere co-ordination exists. Process (c) results in the production of the second Fe(II) ion and the highly unstable $SO^0_{3(aq)}$ species. In aqueous solution, this species will be rapidly hydrated (Process (e)) and subsequently dissociates to achieve H^+/HSO_4^- equilibrium determined by the solution conditions (Process (f)).

This mechanism, although simplistic and not exceedingly important for the interpretation of observed kinetic trends, which are likely equivalent to the rate of process (a), does provide a plausible explanation for the fast kinetic processes (Reactions r_{11}-r_{13}), which produce the required overall stoichiometry of the reaction. In order to make firm conclusions regarding this mechanism further, more detailed kinetic tests are required.

6.7 Rationalisation of proposed mechanism

From the findings of Section 6.3, the effect of acid was observed to significantly retard the rate of ferric reduction, confirmed by tests with added NaOH during reaction. The proposed reaction mechanism in Table 6.2 encapsulates the effect of acid within thermodynamic relationships. The formation of the $FeSO_3^+$ contact ion pair is written from the primary species, Fe^{3+} and SO_3^{2-}, however since all sulfite in this study originated from $SO_{2(g)}$, the overall reaction to form the $FeSO_3^+$ CIP can be written as follows, i.e., a combination of r_2, r_3 and r_9 above:

$$Fe^{3+} + SO(OH)_2 \rightleftharpoons FeSO_3^+ + 2\,H^+ \tag{6.7.1}$$

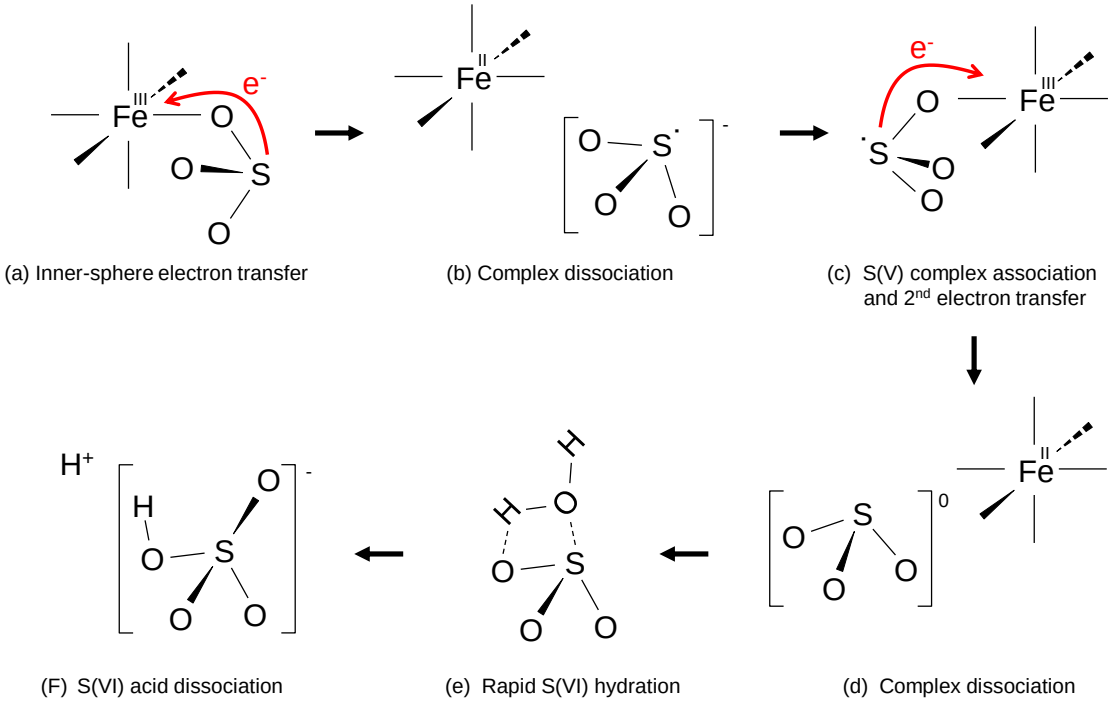

Figure 6.13: Plausible schematic representation of rate-limiting and subsequent reactions. Inner-sphere water molecules not shown for clarity.

From this equilibria, it is clear that increased proton activity will shift the equilibrium to the left and lower the stability of the $FeSO_3^+$ CIP. Since the inner-sphere electron transfer in this CIP is proposed as the rate limiting step, lower concentrations of the CIP would result in a decrease in the observed reaction rate, which is in agreement with experimental observations. This highlights the value of combining thermodynamic considerations within a kinetic modelling framework and avoids the necessity for non-physical rate laws that contain species concentrations in the denominators. Obviously however, the thermodynamic interaction parameters of the $FeSO_3^+$ CIP will directly affect its calculated concentrations and hence the observed reaction rate.

Additional support for the proposed reaction model can be taken from visible and spectroscopic observations of batch reactions between $Fe_2(SO_4)_3$ and Na_2SO_3. Sodium sulfite was selected as the source of sulfite for these tests rather than SO_2 to simplify the experimental procedure and the quantification of the added reagents. In the first confirmatory test, a solution of 0.1 mol/kg $Fe_2(SO_4)_3$ was mixed with sufficient solid Na_2SO_3 to reduce approximately 30% of the Fe(III) in solution according to stoichiometry. Mixing was performed at ambient temperatures by adding the solids into a 100 mL Schott bottle

and shaking vigorously for about 40 seconds until no solid Na_2SO_3 was observed. The reaction was monitored by video camera for a period of 2 hours and frames from the video, at specified times, are presented in Figure 6.14.

Figure 6.14: Colorimetric progression of reaction between $Fe_2(SO_4)_3$ and Na_2SO_3. Sufficient Na_2SO_3 for 10 % conversion was mixed with a 0.1 mol/kg $Fe_2(SO_4)_3$ solution and the solution monitored by video camera over the reaction.

Immediately after mixing, the Fe(III) solution became a dark red/orange colour that gradually faded in intensity with time and approached the colour of the initial solution, albeit slightly darker. Firstly, the observed colour change upon addition of sulfite into the $Fe_2(SO_4)_3$ solution suggests that distinct Fe(III)-SO_3^{2-} complexes were formed. Intra-complex electronic transitions, typically ligand-to-metal charge transfers, are dominant during the UV-vis excitation of ionic complexes and, in this case, can be attributed to transitions between the Fe(III) and S(IV) in the solution complexes. Secondly, it has been reported in the literature that the complex or complexes involved with the reaction between Fe(III) and S(IV) in dilute solutions have a visible red/orange colour (Conklin

and Hoffmann, 1988b) and further that the these complexes have an absorption shoulder maxima at approximately 430 nm (Kraft and Van Eldik, 1989b,a; Lente and Fabian, 1998, 2002) which would result in red-shifted colour.

This evidence also supports the direct role in which the CIP responsible for the red colour shift is involved in the mechanism. For instance, it is well-known that acid and ferric sulfato species would equilibrate rapidly upon mixing: $k_f\left(\mathrm{HSO_4^-}\right) >= 1.5 \times 10^6 \;\; M^{-1}.s^{-1}$, $k_f\left(\mathrm{FeSO_4^+}\right) = 4.4 \times 10^3 \;\; M^{-1}.s^{-1}$, $k_f\left(\mathrm{Fe(SO_4)_2^-}\right) = 1.12 \times 10^3 \;\; M^{-1}.s^{-1}$ (Kormanyos et al., 2008). By comparing these to the slow decay associated with the Fe(III)-S(IV) decomposition suggested by the changing colour of the solution, this straightforward experiment provides proof that the equilibria are established much faster than the rate-limiting charge transfer reaction.

6.7.1 Raman spectroscopy kinetics

The results of the simple colour change test prompted a deeper investigation into the kinetics between $Fe_2(SO_4)_3$ and Na_2SO_3. Another similar test was conducted and the solution of Fe(III) and S(IV) was analysed by Raman spectroscopy with time. A solution of 0.4 mol/kg $Fe_2(SO_4)_3$ solution was mixed with sufficient sulfite for 10% conversion of Fe(III) in a 50 mL Schotte bottle and injected into a 5 mm diameter borosilicate NMR tube. Raman spectra were taken over a period of 113 minutes at ambient temperature (ca. 20 °C, not controlled) and are presented in R-format in Figure 6.15a.

A new band at 935 cm^{-1}, not present in solutions without added sulfite, was clearly observed and found to decay with time. The position of this band is in good agreement with the 938 cm^{-1} band identified by Conklin and Hoffmann (1988b) in $FeCl_3$ media with added sulfite, to which they attributed to the $FeSO_3^+$ species. The emergence of this transient band provides direct evidence for the formation of at least one $Fe_n^{(III)}(SO_3)_m$ complex, which decays with time as the reaction proceeds. Given that Fe(III) is in excess in this solution and only a single band was observed to form, the band at 935 cm^{-1} attributed to the ferric monosulfito, $FeSO_3^+$, complex, in line with the suggestions of Lente and Fabian (2002) in dilute solutions with excess Fe(III). The Raman spectrum of sulfite (SO_3^{2-}) has two modes in the region around 930 cm^{-1}, specifically, the ν_1 stretching mode at 966 cm^{-1} and ν_1 mode at 933 cm^{-1} (Meyer et al., 1980). These bands would be expected to be shifted by the complexation of sulfite with Fe(III) and the distortion of the sulfite moiety in analogy with the sulfate system discussed previously.

The integrated intensities of the various bands as a function of reaction time are presented in Figure 6.15b. These show that as the concentration of the $FeSO_3^+$ species decreased, the concentrations of sulfate and dithionate (981 and 1092 cm^{-1} respectively)

increased. It is known that, at temperatures below 60 °C, the oxidation of sulfite is incomplete and dithionate is formed (Zhang, 2000).

This test provides an independent and direct confirmation of the role in which the ferric sulfito complex plays in the reaction mechanism and, the observed slow decay of the band associated with this complex to form reaction products is consistent with the proposed rate-liming step being the inner-sphere electron transfer between S(IV) and Fe(III) in the $FeSO_3^+$ CIP. Unfortunately, with the difficulties associated with the calibration of concentrations from Raman spectroscopy and the use of SO_2 as a reagent in these tests, kinetic parameters could not be extracted from the data. However, the confirmation of the main kinetic step within the reaction mechanism was considered sufficient in the context of this study.

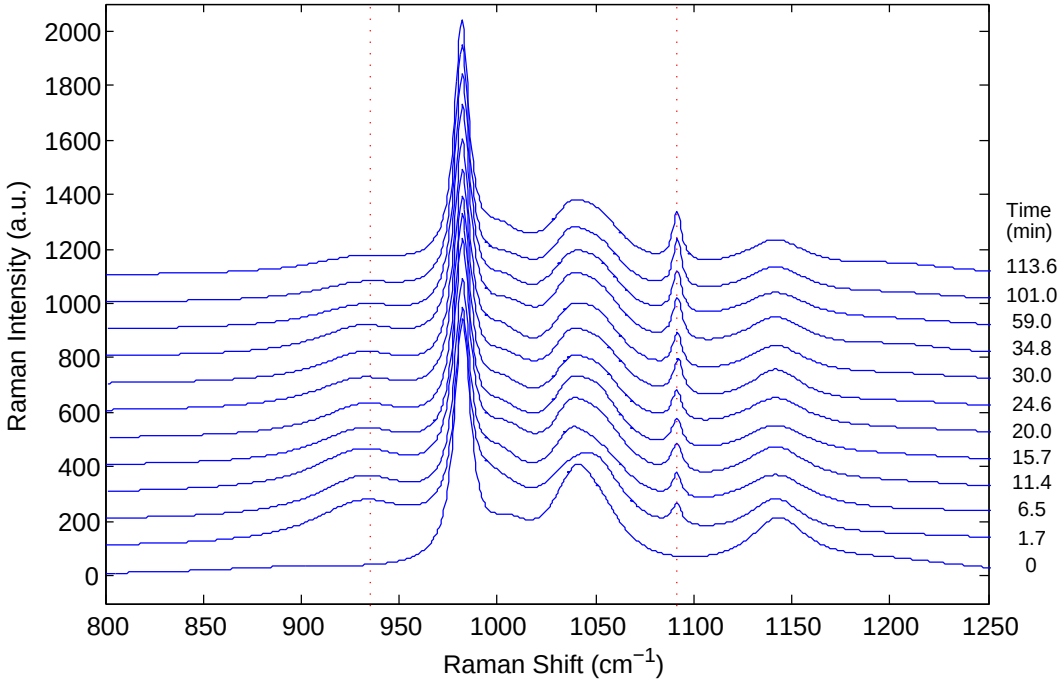

(a) Fitted Raman spectra of 0.4 mol/kg $Fe_2(SO_4)_3$ + Na_2SO_3 as a function of time since mixing in R-format. Sufficient Na_2SO_3 was added for 10% ferric conversion. Dotted lines show the bands at 935 and 1091 cm^{-1}.

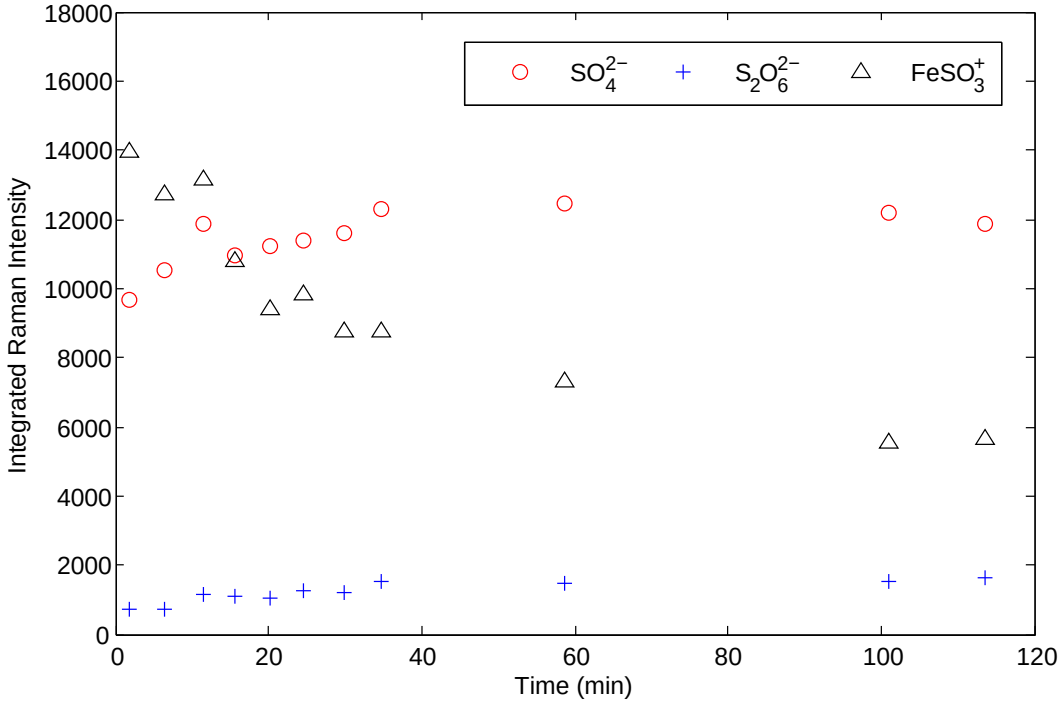

(b) Integrated intensity of sulfate, dithionate and Fe(III)-S(IV) complex bands from Figure 6.15a

Figure 6.15: Fitted transient Raman spectra of a $Fe_2(SO_4)_3$ + Na_2SO_3 solution during reaction at room temperature. The depletion of the 938 cm^{-1} band and increase of the sulfate and dithionate bands highlights the progress of the batch reaction with time.

6.7.2 UV-vis spectroscopy kinetics

In order to confirm the analyses above as well as the effect of acid concentration on the formation of the proposed $FeSO_3^+$ complex, a series of transient UV-vis experiments were conducted using a simple stopped flow apparatus (See Figure 3.5b). Solutions of Na_2SO_3 and $Fe_2(SO_4)_3$ were made up to concentrations such that, when mixed, the Fe(III) concentration was ca. 0.5 mol/kg and the sulfite concentration was ca. 25 mmol/kg, i.e., sufficient for 10% Fe(III) conversion. These solutions were fed into 10 mL glass syringes and attached to a small-volume HPLC tee mixer via 0.5 mm internal diameter tubing and then into a 1 mm flow cuvette, held at 25 °C via the cuvette holder described previously. The solutions were then rapidly mixed by discharging the syringes manually through the flow cuvette at the same rate. After approximately 8 mL of each solution was fed thorough the flow cuvette, the cell was manually isolated using pipe clamps and the reaction monitored via UV-vis absorption.

As mentioned previously, the Fe(III)-S(IV) species are known to have an absorption shoulder at 430 nm and this wavelength was analysed exclusively during the kinetic experiments. The absorbance-time measurements of four tests, at various acid concentrations, are presented in Figure 6.16. Similar to the 935 cm^{-1} band during the transient Raman test, the absorbance at 430 nm rapidly increases upon mixing before slowly decaying over 3 hours of reaction time. These results are in direct agreement with more advanced stopped-flow measurements that were focused on the quantification of the formation of the $Fe_n(SO_3)_m$ species, i.e., within milliseconds of mixing, rather than their slow decay (Lente and Fabian, 1998; Kraft and Van Eldik, 1989b). The primitive nature of the stopped-flow device used in this study did not permit the analysis of such short reaction times.

The effect of acid on the initial absorbance upon mixing agrees with the earlier argument that increased acid concentrations will decrease the stability of the Fe(III)-S(IV) species, i.e., via Reaction 6.7.1. The linear variation in initial absorbance at 430 nm with acid concentration can be interpreted as a linear decrease in the concentration of the $FeSO_3^+$ species, if the molar extinction coefficient of $FeSO_3^+$ is constant over the conditions of these tests and that it is the only additional absorbing species. In these solutions, S(IV) is added into the system as Na_2SO_3 and not $SO_{2(g)}$ as with the larger scale kinetic experiments which will decrease the net amount of acid formed per mole of sulfite in solution. However, upon mixing of the Na_2SO_3 solution with an acidic solution, the $SO(OH)_2$ species would be most stable (see Figure 5.11) and the overall reaction to form $FeSO_3^+$ (Reaction 6.7.1) would still be applicable. Furthermore, the flow cuvette was isolated shortly after mixing to prevent the evolution of SO_2 gas from solution.

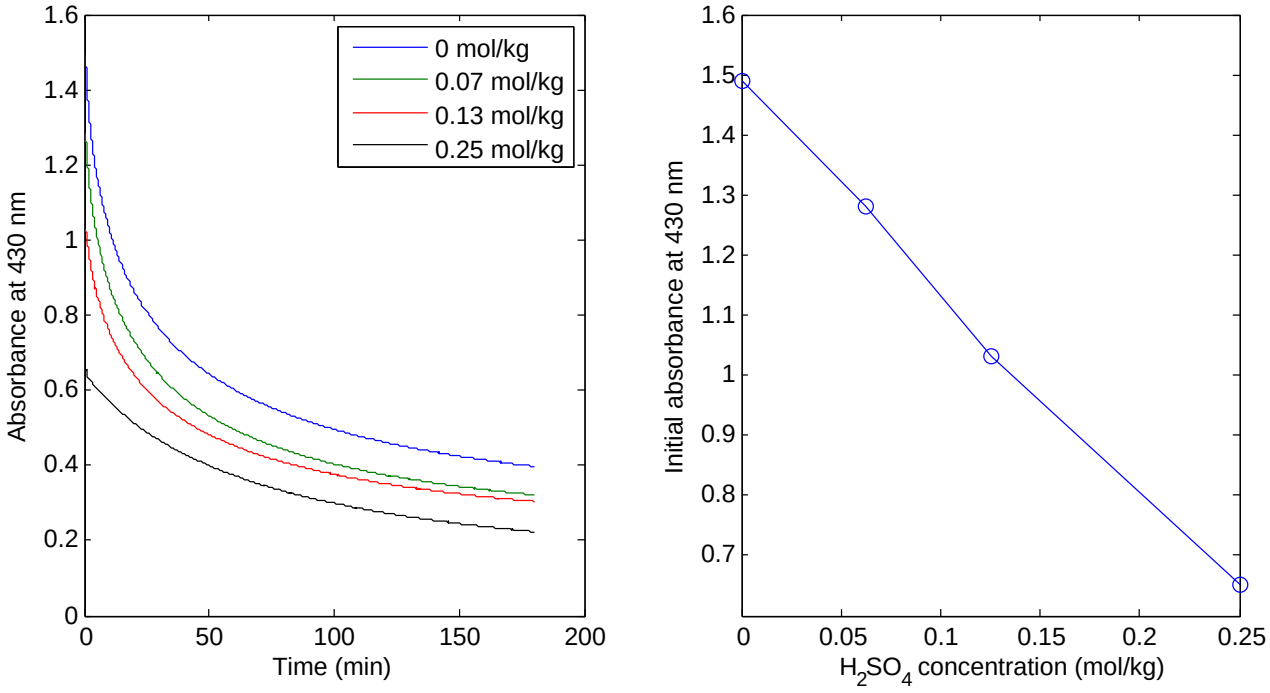

Figure 6.16: Absorbance profiles at 430 nm, for the reaction between $Fe_2(SO_4)_3$ and Na_2SO_3 with various acid concentrations controlled at 25 °C. All tests were at 1.0 mol/kg Fe(III) and sufficient sulfite added initially for 10% Fe(III) conversion. The initial absorbance was observed to be almost linear with acid concentration, showing the retardation effect of initial acid on the formation of $FeSO_3^+$, the primary absorbing species at 430 nm.

Attempts to linearise the absorbance-time data to extract rate constants were unsuccessful as the profiles did not conform to pseudo first (or second) order kinetics, i.e., plots of $\ln A$ and $1/A$ with time were non-linear. These effects were attributed to the variation in solution speciation with time as the reaction proceeded, i.e., with even low conversion producing sufficient acid to decrease the $FeSO_3^+$ concentration. In an attempt to limit these effects and obtain a rough indication of the pseudo first order rate constant, the gradient of the logarithm of 15 absorbance points (30 seconds) immediately after the turbulence during mixing was determined for each of the tests. These absorbance profiles were well approximated by linear functions with high R^2 statistics and the resulting pseudo-first-order rate constants are presented in Table 6.3. The data to which these constants were fitted is attached in Appendix B.2.2.

In agreement with the proposed reaction mechanism and the decreasing stability of $FeSO_3^+$ with acid concentration, the observed rate constant was also found to decrease

with increasing acidity. Interestingly, while using a relatively crude method of stopped-flow spectroscopy, the rate of decay of the $FeSO_3^+$ agrees well with that reported by Conklin and Hoffmann (1988b), i.e., $2.0 \cdot 10^{-3} s^{-1}$, and is approximately two orders of magnitude slower than those reported by others (Kraft and Van Eldik, 1989a; Brandt et al., 1994; Lente and Fabian, 2002). This difference may be due to their experimental methodologies, which permitted measurement of the rate of $FeSO_3^+$ in significantly shorter time-scales after mixing than permitted in this study.

Table 6.3: Pseudo-first-order observed rate constants for $FeSO_3^+$ decomposition

$[H_2SO_4]$ (mol/kg)	$\hat{k}$ (s^{-1})	R^2 (t vs. $\ln A$)
0	$1.96 \cdot 10^{-3}$	0.9965
0.07	$1.70 \cdot 10^{-3}$	0.9930
0.13	$1.05 \cdot 10^{-3}$	0.9938
0.25	$8.25 \cdot 10^{-4}$	0.9794

These values were fitted over the first 30 s of measurements

6.7.3 Quantum calculations

In a further attempt to rationalise the proposed reaction mechanism, the electronic structure of the $FeSO_3^+$ contact ion pair was analysed by static DFT calculation in a similar manner as in Section 4.1. As discussed, there is some discrepancy in the literature regarding whether sulfite bonds to Fe(III) via the sulfur or oxygen atom in the $FeSO_3^+$. In this study, all configurations of the S-bonded complex proved to be unstable during the geometry optimisation and the O-bonded form was thus maintained. The optimised geometry of the $FeSO_3^+$ complex using the GGA:OPBE XC functional and the TZ2P basis set (see Section 4.1 for details) is presented in Figure 6.17. After an initial manual scan of the geometry potential energy surface, the molecular symmetry was fixed at C_s.

After optimisation, the DFT calculation was subsequently divided up into molecular fragments for iron, sulfite and the various water molecules which permitted an interpretation of the molecular orbitals. This highlights that the highest-occupied-molecular-orbital (HOMO) is composed largely of the sulfite p-orbitals with 83.53% of the orbital being attributed to the SO_3^{2-} ligand; clearly visible in Figure 6.18a. The lowest-unoccupied-molecular-orbital (LUMO) is composed largely of the iron 3d-orbitals with 88.87% being attributed to the iron core; presented in Figure 6.18b. In the context of Reaction 10 in the proposed mechanism, the single inner sphere electron transfer within this complex is

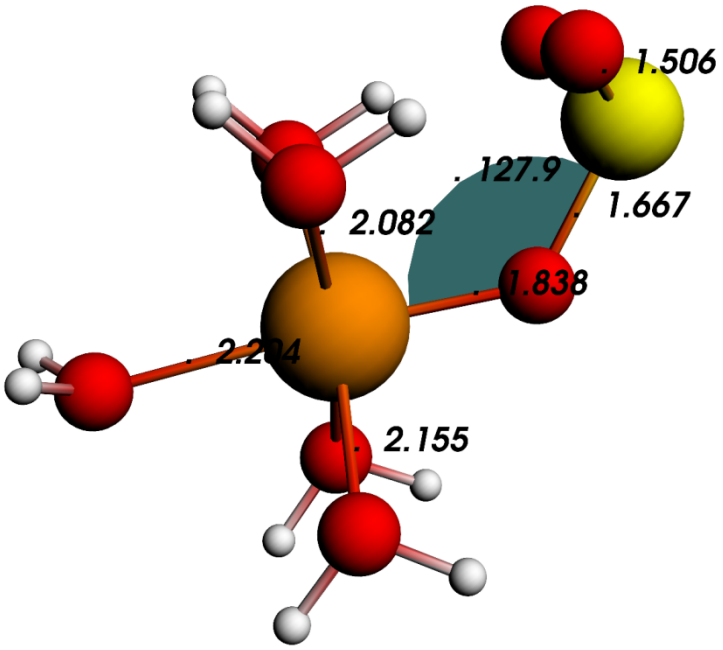

Figure 6.17: Optimised geometry of the $FeSO_3^+$ species

suggested to be extremely slow and rate limiting. It is reasonable to assume that the first electron transfer from the S(IV) ligand to the Fe(III) ion occurs between the HOMO and LUMO orbitals highlighted in Figure 6.18 and the small degree of overlap between these orbitals is concurrent with a decreased probability of electron transfer and a resulting slow kinetic process. Moreover, the poor overlap between these orbitals, preventing reaction, is likely responsible for the stabilisation of this complex and resulting in its generally large equilibrium constant in comparison to the ferric sulfato complexes (See Figure 2.7).

While this analysis is exceedingly simplified and no quantitative insights of the rate-limiting reaction are made, the calculations do strongly support the experimental findings of Lente and Fabian (2002) at long reaction times, where the assertion that the $FeSO_3^+$ decomposition was the rate-limiting kinetic process at metal ion excess. While their analysis did highlight the feasibility of te formation of additional ferric sulfito complexes, the monosulfito complex was considered most important for the characterisation of the reaction, especially at long reaction times. On this basis, and in line with the minimum-species approach in this study, the $FeSO_3^+$ complex can be considered as the most important sulfite species in the context of ferric reduction with SO_2.

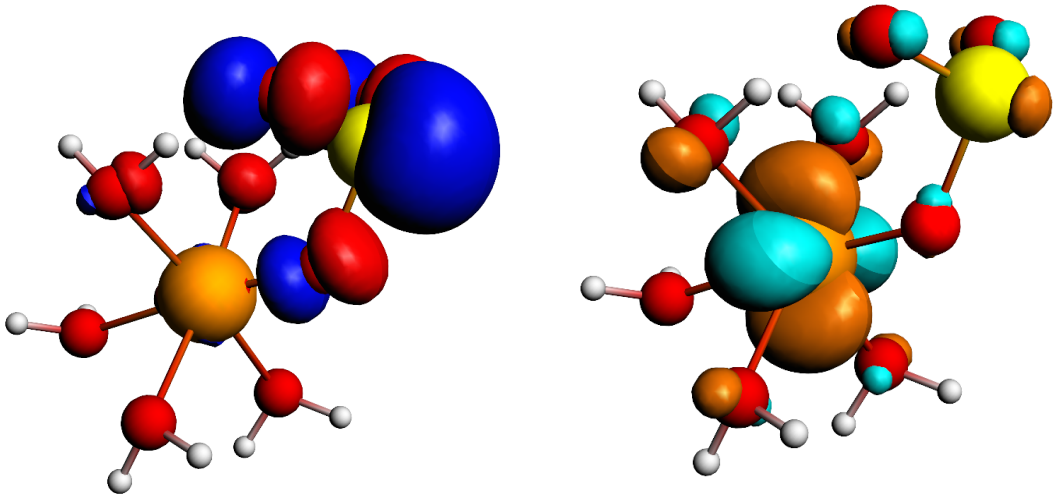

(a) $FeSO_3^+$ species HOMO (b) $FeSO_3^+$ species LUMO

Figure 6.18: Calculated $FeSO_3^+$ highest occupied (HOMO) and lowest unoccupied (LUMO) molecular orbitals emphasising the poor overlap which can contribute to the slow rate of the inner-sphere electron transfer between S(IV) and Fe(III).

6.8 Implications for the ARFe process

As detailed in the introductory chapters, the overarching context of this study is the ARFe process concept, with particular focus on the atmospheric leaching operation. The findings of the investigation into the kinetics of ferric reduction detailed in this chapter have several significant implications for the ARFe circuit.

Several leaching configurations have been considered for the ARFe circuit and two options with separate and combined ferric reduction and laterite leaching were the focus (Biley et al., 2013). Combined laterite leaching and ferric reduction involves two competing kinetic processes, which are respectively enhanced and retarded by increased acid activities. Thus, in-situ ferric reduction while leaching facilitates the simultaneous generation and consumption of acid in the leaching reactors. However, given the findings presented above, the steady-state acid concentration achieved under continuous leaching will significantly affect the rate of ferric reduction and, obviously, the amount of acid available for leaching. As detailed in Section 2.1, the transport of iron from the leaching to the value-recovery circuit depends on Fe(II) solubility in the leach liquor and low levels of Fe(III) reduction will result in considerably larger circuits due to the much greater solubility of $Fe_2(SO_4)_3$. The optimal operation of the leaching unit in this circuit thus relies on the balance between the inherent rate of acid attack of the laterite minerals and

the capability to absorb and react SO_2 with available ferric in solution. Ultimately, for a specific laterite ore, the leaching conditions (i.e., temperature, acid and ferric concentrations, SO_2 partial pressure) need to be optimised to ensure the optimal use of SO_2 and maximum simultaneous ferric reduction and leaching takes place.

Additionally, the strong, deleterious effect of acid on the rate of ferric reduction suggests that, even for low acid backgrounds, complete reduction of ferric is unlikely and the circuit must be able to effectively manage high levels of ferric in the primary leaching circuit. Technically, this has been shown to be possible in the operation of a continuous piloting campaign, however deleterious effects are expected based on the known suppression of ferrous sulfate solubility in the presence of ferric ion (Biley et al., 2013). This recycling of iron around the leaching circuit may present economic constraints for the scale of commercial operations as well as technical constraints as the solution density and viscosity will increase markedly with increased Fe(III) in the leaching liquor. Moreover, it is known that the maximum solubility of Fe(II) decreases with increasing Fe(III) in sulfate media (Linke and Seidell, 1965) and thus excessive Fe(III) levels in the leaching circuit will decrease the single pass removal of $FeSO_4 \cdot 7\,H_2O$ in the crude crystallisation step and resultantly increase the net amount of total iron (Fe(III) + Fe(II)) recycling around the leaching section. This will require larger flows and impact both capital and operational expenditure.

Also, the ferric reduction test operated at 75 °C, highlighted the significant effect of SO_2 solubility as a driving force for ferric reduction. It is well-known that the rate of laterite mineral dissolution decreases with decreasing temperature (McDonald and Whittington, 2008) so, in the ARFe concept, a potentially feasible means of increasing the efficiency of ferric reduction is to operate under SO_2 overpressure where the benefits of both fast leaching kinetics and enhanced ferric reduction may facilitate a reduction in the required size of the leaching operation. This will undoubtedly drive up capital costs and needs to be carefully considered in the context of a rigorous economic study. Also related to this, is the challenge of producing a high-strength SO_2 stream from the off-gas of ferrous sulfate thermal decomposition which is expected to contain about 10% SO_2, i.e., typical of that fed to a sulfuric acid plant.

Most importantly, the findings of this study highlight that, while the key process chemistry for the ARFe leaching circuit is technically feasible, the practical window of operation is significantly smaller and careful optimisation of the leaching section, one of the major cost-drivers of the circuit, is required. The results indicate that the competing effects of fast laterite leaching at high acidities cannot be achieved while simultaneously absorbing SO_2 as an acid source for leaching during ferric reduction. Obviously, another

means of directly bypassing the requirement for SO_2 absorption in the leaching section would be to feed SO_2 generated in the pyrometallurgical section directly to an acid plant where H_2SO_4 can be generated and could be fed directly into the leaching section. The ARFe concept relies on the removal of value metals and impurites from a solution containing only minor amounts of Fe(III) and, if SO_2 is not used in the leaching section, it will have to be used in the recovery section where acid will need to be neutralised at high cost, i.e., not with the feed ore. Additionally, the nett acid generated in an acid plant versus in-situ ferric reduction would be considerably more expensive as sulfur units do not produce equivalent amounts of acid. The overall reaction, Reaction 1.1.1 shows that 4 mol H^+ are produced per mole of SO_2, whereas an acid plant will only facilitate 2 mol H^+ per mole of SO_2.

Thus, the use of SO_2 in the leaching section as a reduction and a lixiviant source is central to the ARFe concept and the findings of this work provide direct and informative insights to the respective chemical trade-offs that must be made in configuring the circuit. Again, these insights will prove most valuable as part of greater mass-and-energy balance model of the circuit that is capable of estimating circuits capital and operating cost requirements.

6.9 Summary

This chapter has presented the results of several kinetic measurements of Fe(III) reduction with SO_2 in concentrated sulfate solutions; one of the main objectives of this study.

Firstly, mass transfer effects were investigated on the experimental rig and conditions identified such that these effects would not influence the measured reaction rates. Subsequently, a systematic set of batch tests where the initial Fe(III) and H_2SO_4 concentrations were varied clearly highlighted the importance of acid concentration for the rate of reduction, with higher concentrations significantly decreasing the achievable extent of reduction at fixed reaction time. This effect was confirmed by a test where in-situ neutralisation was performed, showing an instantaneous increase in reaction rate and the overall achieved conversion. Moreover, the effect of temperature and continuous operation provided further insights into the reaction chemistry and highlighted the importance of SO_2 solubility and the independence of the rate-limiting reaction to the changing solution background in batch operation; a critical point for the development of a reaction model of the system in the following chapter.

The noted effects on the reaction rate and extent were consolidated by the proposal of a mechanism that is consistent with published reaction pathways and feasibly ex-

plains the observed kinetic trends. This mechanism was then rationalised by a series of spectroscopic measurements and DFT calculations. Direct evidence was provided for the formation and slow-decay of a Fe(III)-S(IV) solution species, that was rationalised to be the mono-sulfito $FeSO_3^+$ through various theoretical arguments. Further evidence was generated to show that the inner-sphere electron transfer in this CIP represents the rate-limiting step in the mechanism and is significantly affected by the presence of acid.

The findings in this chapter highlight the complex and interconnected nature of the system thermodynamics and kinetics. The measured kinetic data and supporting spectroscopic and DFT evidence enforce the proposed reaction mechanism and provide an excellent basis for the development of a reaction model of the system.

Chapter 7

Reaction Modelling

The preceding two chapters have presented a thermodynamic framework for the $Fe_2(SO_4)_3$-$FeSO_4$-H_2SO_4-H_2O system as well as characterised ferric reduction kinetics with SO_2. The true value of these investigations can be obtained by combining them in a consistent reaction model of the system, such that the rate and extent of ferric reduction with SO_2 can be predicted under various conditions of interest.

This chapter details the development of a reaction model of the system, based on the proposed mechanism in the last chapter. This model is calibrated using all available data and validated against independent tests.

7.1 Reaction model equations

7.1.1 Mass transfer equations

The first aspect of the kinetic model involves the quantification of mass transfer of SO_2 from the gas phase into solution. In addition to the mass transfer across the boundary layer, the total gas flow of SO_2 could also potentially be limiting the reaction. Thus, the effective mass transfer of SO_2 into solution is given as:

$$\dot{N}_{\mathrm{SO_{2(g)}}} = \begin{cases} F_{\mathrm{SO_2}}, & \text{if } F_{\mathrm{SO_2}} < F_{MT} \\ F_{MT} = \Phi k_L a \left(m^{sat}_{\mathrm{SO_{2(aq)}}} - m_{\mathrm{SO_{2(aq)}}} \right) \cdot M_{\mathrm{H_2O}} & \text{otherwise} \end{cases} \tag{7.1.1}$$

where $N_{\mathrm{SO_2}}$ is the molar amount SO_2 transferred into solution from the gas phase, $F_{\mathrm{SO_2}}$ is the molar flow rate of SO_2 gas into the reactor, $M_{\mathrm{H_2O}}$ is the total mass of water in the system and the mass transfer expression as defined in Equation 2.2.1. It is expected, in acidic solutions, that the $SO_{2(aq)}$ (or $SO(OH)_2$) species would be the dominant

solution species (Pourbaix and Pourbaix, 1992), and since the methods for SO_2 solubility measurements typically are of the total sulfite, i.e., via vapour pressure measurement (Kuznetsov, 1941), the molal saturation concentration, $m^{sat}_{SO_{2(aq)}}$, in the above equation refers to the total amount of S(IV) present in the solution. The thermodynamic calculation of sulfite solubility via vapour-liquid equilibrium, i.e., equivalence of $SO_{2(aq)}$ activity and $SO_{2(g)}$ fugacity, was therefore not performed in this analysis.

A further simplifying approach was adopted in quantifying the mass transfer coefficient and the enhancement factor in Equation 7.1.1. As discussed in Section 6.1.1, the k_La determined by extrapolation of the measured mass transfer rates by the direct method at 25 and 55 °C to 95 °C probably represent a minimum value. This was primarily due to the significant reduction in solution viscosity of $Fe_2(SO_4)_3$ solutions with temperature, as compared to water or Na_2SO_3/Na_2SO_4. The minimum value of k_La = 8.92 min^{-1}, which is extrapolated from the direct measurements in $Fe_2(SO_4)_3$ solutions between 25 and 55 °C, was included in the model (see page 133). For the enhancement factor, the conventional treatment via the Ha number is not well defined in this case primarily due to the uncertainties associated with the molar diffusivity and solution phase mass transfer resistance in concentrated solutions at elevated temperatures. A conservative approach was adopted by fixing the enhancement factor at unity, i.e. typical for negligible reaction occurring with in the gas-liquid boundary layer, which would result in a *lower limit* on the rate of mass transfer. A sensitivity analysis on the effect of this parameter on the model calculations is detailed in Section 7.3.4.

Moreover, the absorption of SO_2 into solution influences the sulfite, proton and water concentrations through the hydration and subsequent dissociation of SO_2 (Reactions r_1 to r_3 in Table 6.2 on page 150). This is important for the quantification of the total amounts of each species in solution at each time step. Thus, for each molecule of SO_2 transferred into solution by the above mass transfer equation, one water molecule is consumed and two protons and one sulfite molecule are produced; this is included in Equations 7.1.10 to 7.1.14 in the following section.

7.1.2 Rate-limiting reaction equations

In the mechanism detailed in Table 6.2 and from the compilation of forward and backward reaction rates from Kuo et al. (2006) at 25 °C (see Table 2.7), the rates of acid and sulfate equilibria are orders of magnitude faster than the proposed rate limiting reaction, even in the reactive system at 95 °C; assuming conventional limits for the activation energies. This large difference in rates facilitates a simplification of the kinetic model equations since the observed reaction rate will only be a function of the rate lim-

iting step. Thus, the thermodynamic equilibria, assumed to reach a pseudo-equilibrium instantaneously, can be combined with the kinetic processes through a rate-limiting approach, given the prevailing solution conditions at that instant. Furthermore, irreversible processes such as r_{11}, r_{12} and r_{13} (Table 6.2) are also significantly faster than the rate limiting step (Kuo et al., 2006) and can thus also be assumed to occur instantaneously in the context of the reaction model.

The rate of the inner-sphere electron transfer in the $FeSO_3^+$ species, resulting in its decomposition to form Fe^{2+} and $SO_3^{\cdot-}$, was proposed as the rate-limiting reaction in the mechanism. This reaction was assumed to be elementary and hence a function only of its own concentration, such that the change in $FeSO_3^+$ concentration with time is given by:

$$r_{10} = \frac{d[FeSO_3^+]}{dt} = -k_1[FeSO_3^+] \tag{7.1.2}$$

Where k_1 is the first order rate constant with units of min^{-1}. This reaction can be related to the rate of ferric reduction, or equivalently ferrous generation, via the irreversible reactions, r_{11} and r_{13}. Since the conditions in this study are at reasonably large Fe(III) concentrations, with an excess of S(IV), it can be assumed that the reactive radical species' concentration will be small compared to that of Fe(III). This allows the second electron transfer reaction (r_{11}) to be approximated by a pseudo-first order reaction, with different rate constant $\hat{k_2}$, given by:

$$r_{11} = k_2[Fe^{3+}][SO_3^{\cdot-}] \approx \hat{k_2}[SO_3^{\cdot-}] \quad \text{when} \quad [SO_3^{\cdot-}] \ll [Fe^{3+}] \tag{7.1.3}$$

Then, by considering the radical species generation and consumption reactions, Reactions r_{10} and r_{11} respectively, the steady-state approximation (SSA) could be applied to eliminate the radical species from the rate expressions (Fogler, 2006).

$$\frac{d[SO_3^{\cdot-}]}{dt} = r_{10} - r_{11} = k_1[FeSO_3^+] - \hat{k_2}[SO_3^{\cdot-}] = 0 \quad \text{(via SSA)} \tag{7.1.4}$$

$$\therefore \quad [SO_3^{\cdot-}] = \frac{k_1}{\hat{k_2}}[FeSO_3^+] \tag{7.1.5}$$

Furthermore, the SO_3^0 is known to be highly unstable in aqueous solution (Meijer and Sprik, 1998), and will be rapidly hydrated according to Reaction r_{13} (Table 6.2). Similarly to the above treatment, a simplified expression can be derived via the steady-state approximation:

$$\frac{d[SO_3^0]}{dt} = r_{11} - r_{13} = k_1[FeSO_3^+] - \hat{k_4}[SO_3^0] = 0 \quad \text{(via SSA)} \tag{7.1.6}$$

$$\therefore \quad [SO_3^0] = \frac{k_1}{\hat{k_4}}[FeSO_3^+] \tag{7.1.7}$$

By substituting Equations 7.1.5 and 7.1.7 into the rate expression for Reaction r_{11} and r_{13}, we obtain that $r_{10} = r_{11} = r_{13}$ (Table 6.2) as expected, i.e., all reaction rates are equal to the rate-limiting reaction rate, and the following expression for the rate of ferric reduction can be obtained:

$$\frac{d[Fe^{3+}]}{dt} = -r_{10} - r_{11} = -k_1[FeSO_3^+] - \hat{k_2}[SO_3^{\cdot -}] \tag{7.1.8}$$

$$= -2k_1[FeSO_3^+] \tag{7.1.9}$$

Subsequently, for each of the remaining total, formal concentrations in the system, namely H^+, Fe^{2+}, SO_4^{2-} and SO_3^{2-}, the rate of production (in mol/kg.min) can be written in terms of the limiting reaction equation above.

$$\frac{d[H^+]}{dt} = 2r_{11} + 2\dot{N}_{SO_{2(g)}} = 2k_1[FeSO_3^+] + 2\dot{N}_{SO_{2(g)}}/M_w \tag{7.1.10}$$

$$\frac{d[Fe^{2+}]}{dt} = r_{10} + r_{11} = 2k_1[FeSO_3^+] \tag{7.1.11}$$

$$\frac{d[SO_4^{2-}]}{dt} = r_{13} = r_{11} = k_1[FeSO_3^+] \tag{7.1.12}$$

$$\frac{d[SO_3^{2-}]}{dt} = -r_{10} + \dot{N}_{SO_{2(g)}}/M_w = -k_1[FeSO_3^+] + \dot{N}_{SO_{2(g)}}/M_w \tag{7.1.13}$$

$$\frac{d[H_2O]}{dt} = -r_{11} - \dot{N}_{SO_{2(g)}}/M_w = -k_1[FeSO_3^+] - \dot{N}_{SO_{2(g)}}/M_w \tag{7.1.14}$$

Where $\dot{N}_{SO_{2(g)}}$ is the molar flow rate (mol/min) of SO_2 into solution, according to Equation 7.1.1 and M_w is the total mass of water in the solution (kg).

Thus, as suggested by the reaction mechanism, the rate of production (or consumption) of all total species in the system is determined almost exclusively, with the exception of mass transfer effects, by the rate of decomposition of the $FeSO_3^+$ species. This is critical as it stresses the importance of the consideration of both thermodynamic and kinetic aspects within the solution model. Specifically, the solution speciation that reaches a pseudo-thermodynamic-equilibrium in the time scale of the rate-limiting decomposition reaction, directly determines the observed reaction rate of ferric reduction. Thus, the

effect of external variables such as acid concentration, is captured fundamentally in the thermodynamic speciation calculations and avoids the complication of the basic rate law expression.

7.1.3 Reaction heat effects

As discussed in the Section 6.4, the generation of heat during the initial stages of the batch tests and the subsequent cooling of the reactor by the sensible heating of the SO_2 gas feed had a measurable effect on the reactor temperature. For accurate modelling of these batch tests, these effects required consideration.

The measured temperature-time profiles in each of the tests were used to interpolate the reactor temperature at each time step in solving the system of differential equations presented above. The thermodynamic speciation and the first-order rate constant of the rate-limiting process are expected to vary with temperature, with the former having a significantly smaller effect; already captured within the stability constant extrapolation and the interaction parameter temperature dependence (where applicable). In order to account for the changes in rate constant with temperature, a typical Arrhenius equation was used (Fogler, 2006):

$$k_1\left(T\right) = A \exp\left(\frac{-E_a}{R_g T}\right) \tag{7.1.15}$$

where the pre-exponential factor, A, and the activation energy, E_a, were determined from values of k_1 at two temperatures. The assumption of Arrhenius behaviour for inner-sphere electron transfer is in accordance with Marcus' theory of electron transfer (Marcus, 1964). The recommended value of $k_1 = 0.12$ min^{-1} at 25 °C (Conklin and Hoffmann, 1988b) was used and the value at 95 °C was treated as a variable parameter and permitted calculation of parameters A and E_a in order to interpolate k_1 over temperature. Additionally, the SO_2 solubility is known to be a strong function of temperature however, given the inherent uncertainty in the solubility in $Fe_2(SO_4)_3$ solutions, it was deemed inappropriate to adjust the gas solubility parameter as a function of temperature for the variation during tests. However, the significant increase in solubility of SO_2 at 75 °C (see Figure 2.4) was considered and the measured values in Table 6.1 were used. Errors induced by using these constant values will ultimately be absorbed into the optimised value of the rate constant; discussed further below.

7.2 Parameter optimisation methodology

The optimisation of Pitzer thermodynamic interaction parameters to fit measured kinetic data is necessitated by the inherent transient nature of the Fe(III)-S(IV) system. This unconventional treatment can be justified by the following arguments.

To reiterate the previous findings in the literature and the further support developed in the previous paragraphs, a reasonable reaction mechanism was proposed which involves several important processes, specifically: (a) mass-transfer effects; (b) thermodynamic speciation; (c) rate-limiting electron transfer, and (d) rapid oxidation of radical species in excess Fe(III). This mechanism reduces the focus of the kinetic modelling to a single, elementary kinetic process, i.e., the decomposition of the $FeSO_3^+$ CIP. Naturally, this rate-limiting reaction is thus controlled by the concentration of $FeSO_3^+$ in the solution, which is inherently and directly related to the thermodynamic speciation of the system. Thus, the interaction parameters which affect the stability of the $FeSO_3^+$ complex have an unambiguous effect on the reaction kinetics within the assumptions on which the mechanism was proposed. Furthermore, since the Pitzer interaction parameters have a well-defined and theoretically-based impact on calculated activity coefficients, they can be considered to capture important interactions within the solution and are not merely arbitrary fitting parameters.

Since the primary aim of this study is the development of a solution model for characterising rates and extents of ferric reduction with SO_2 under various conditions, considering these arguments, the validity of optimising thermodynamic interaction parameters involving the $FeSO_3^+$ complex to fit observed kinetic data can be considered reasonable.

7.2.1 $FeSO_3^+$ stability and kinetic parameters

Several key uncertainties in the development of the solution model exist, particularly related to the values of the $FeSO_3^+$ stability and kinetic parameters and a special treatment during the parameter optimisation was required. The first-order rate constant of the $FeSO_3^+$ decomposition reaction, k_1, the value of the equilibrium constant of the $FeSO_3^+$ species at 95 °C and the solubility of SO_2 in the $Fe_2(SO_4)_3$ solutions all have a significant effect on the resulting reaction kinetics through Equation 7.1.9 and are not explicitly known at the reaction conditions. Additionally, the effects of these parameters on the regression of the experimentally measured kinetic data are not independent from one another and thus their values could not be uniquely determined solely from the data measured in this study.

As detailed in Section 5.7.2, there is reasonable confidence in the $FeSO_3^+$ formation

constant at 25 °C of $\log_{10} K^0 = 6.897$, and one study indicated that the reaction heat[1] between 10 and 25 °C was 49.50 kJ/mol (detailed in Appendix A.2.5). However, there is still large uncertainty in using this data to extrapolate the stability constant to 95 °C, especially since the change in heat capacity for $FeSO_3^+$ formation is not known. For extrapolation of stability constants using the Density model (Equation A.2.2), variations in both ΔH^0 and ΔC_p^0 have a linear relationship with the calculated $\log_{10} K$ values, however, the value of $\log_{10} K$ is over 5 times more sensitive to relative variations in ΔH^0 compared to ΔC_p^0. Thus, given the uncertainty in this system, ΔC_p^0 was set to zero and the ΔH^0 term was fixed at the recommended value of 49.50 kJ/mol. This induced an error in the model however, these effects would be counteracted by the optimisation of the rate law constant without rendering the system underspecified.

Another key sensitivity in the modelling framework is that the solubility of SO_2 in $Fe_2(SO_4)_3$ solutions is not explicitly known. It has been observed that SO_2 solubility is enhanced by the formation of solution complexes, such as the SO_2Cl^- species observed in dilute chloride solutions (Krissmann et al., 1997), and the formation of $FeSO_3^+$, and other potential solution species, may result in an increase in the total S(IV) solubility in solution. This effect is difficult to quantify, especially in concentrated solutions, due to the transient nature of the system and further detailed experimental work is required to determine these effects. This was considered beyond the scope of this study and the total S(IV) solubility was assumed to be equivalent to that in water, which is well characterised. Again, the errors induced by this assumption would be absorbed into the optimised value of the rate constant.

Thus, these simplifying assumptions essentially involve the fixing of the $FeSO_3^+$ stability constant and the S(IV) solubility at reasonable, but experimentally unverified, values and first order rate constant optimised to fit measured experimental data. Critically, should improved estimates of these estimated values become available, the kinetic and thermodynamics interaction parameters optimised in this study could be easily be re-evaluated.

7.2.2 Thermodynamic interaction parameters

From the experimental evidence presented in Chapter 6 it is evident that one of the most important factors for the kinetics of ferric reduction is the acid concentration. Clearly, from Reaction 6.7.1 the formation of the $FeSO_3^+$ complex releases acid from the hydrated SO_2 species and, in a thermodynamic sense, the effect of acid is inherently captured in

[1] Referring to Reaction r_9 in Table 6.2 on page 150

this by destabilising $FeSO_3^+$ with increasing acidity. However, an initial analysis of the model predictions without any additional interactions parameters highlighted that the effect of acid concentration was not accurately captured and that interaction parameters needed to be considered.

A maximum of 72 potential parameters involving the $FeSO_3^+$ species can exist in the solution model and careful selection of the most important parameters is essential. Currently, no theoretical means for the optimal selection of interaction parameters in thermodynamic models exists and an iterative approach is required. The simplest, binary interaction parameters were investigated first and the effect of the $\beta_{ca}^{(0)}$, $\beta_{ca}^{(1)}$, C_{ca}^{ϕ}, $\phi_{aa'}$ and $\phi_{cc'}$ parameters highlighted that several were highly insensitive. For example, the low concentrations of HSO_3^- and SO_3^{2-} as well as the large background of SO_4^{2-} resulted in the interaction parameters involving these species either producing insignificant effects on the resulting conversion-time profiles or the inability to capture the effects of Fe(III) and acid noted in Chapter 6. However, in accordance with expectations, the binary interaction parameters between H^+, HSO_4^- and $FeSO_3^+$ showed a significant effect on the model predictions and were necessary to include.

7.2.3 Objective function

Given the large number of potential parameters, the optimisation scale was reduced to include only a subset of the experimental measurements, which captured the important trends and significantly increased the speed of calculations. The subset included the highest and lowest acid concentrations at each ferric concentration as well as the test at 75 °C, which reduced the total number of calculations by 50%. Once parameters were partially optimised on this subset, all tests were included in the objective function for the final optimisation. The overall objective function was constructed from the sum-of-squared difference in measured and calculated ferrous concentrations according to Equation 7.2.1. Relative errors were not considered in order to prevent excessive error contributions from small ferrous analyses and, furthermore, despite the reasonably large various in the initial Fe(III) concentrations

$$\min F = \sum_i \left([Fe^{2+}]_{calc} - [Fe^{2+}]_{exp}\right)_i^2 \tag{7.2.1}$$

7.3 Model evaluation and validation

The selection and optimisation of the solution model parameters was carried out iteratively in order to develop a minimum-parameter model for the system. In addition to the rate-limiting reaction rate constant, other parameters all pertained to the $FeSO_3^+$ species which occupies a central role in the reaction mechanism. Interactions with this complex and the other solution components can not be evaluated at equilibrium due to the inherent reaction that takes place and must be derived from kinetic data. The final optimised solution model parameters are presented in Table 7.1. Discussion of the method of selecting these parameter is presented in the following subsection along with the model description of the measured experimental data.

Table 7.1: Optimised solution model parameters

Parameter	Interaction	p_0	Units
$k_1\,(368.15K)$	-	87.9976	min^{-1}
C_{ca}^{ϕ}	$FeSO_3^+$-HSO_4^-	0.22756	kg/mol
$\beta_{ca}^{(0)}$	$FeSO_3^+$-$Fe(SO_4)_2^-$	2.02891	kg/mol
C_{ca}^{ϕ}	$FeSO_3^+$-$Fe(SO_4)_2^-$	-0.85376	kg/mol
ϕ_{cc}	$FeSO_3^+$-H^+	-0.86513	kg/mol
ϕ_{cc}	$FeSO_3^+$-Fe^{3+}	-1.00577	kg/mol

Fit Statistic	Value
AARD†	9.33 %
AAD†	0.0194 mol/kg

† with reference to Equation 7.2.1

Following from the discussion regarding the independence of the first-order rate constant, the stability constant of the $FeSO_3^+$ and the S(IV) solubility in the previous sections a sensitivity analysis on the optimised value of k_1 was deemed necessary. From the value for the $k_1\,(298.15K)$ parameter, taken from Conklin and Hoffmann (1988b), and the regressed value at 95 °C, the activation energy[2] for the inner-sphere electron transfer reaction in the $FeSO_3^+$ CIP is calculated at 86.01 kJ/mol. However, given the assumptions regarding the fixing of the $FeSO_3^+$ stability constant and the SO_2 solubility parameters at their *lowest* expected values, the kinetic parameter was obviously artificially inflated during the optimization. To further validate this assumption, the ΔC_p^0 term for the $FeSO_3^+$ formation was assumed to be 400 J/mol.K (i.e., equivalent to the $FeSO_4^+$ CIP) and the

[2]Assuming: $\log_{10} K^0$ = 6.897, ΔH^0 = 49.5 kJ/mol, ΔC_p^0 = 0 J/mol.K and $m_{S(IV)}^{sat.}$ = 0.031 mol/kg

optimisation routine reinitialised. This resulted in all thermodynamic interaction parameters remaining essentially unchanged, with a maximum relative differences of 0.9%, whereas the $k_1\,(398.15K)$ term was optimised to a value of 45.75 min^{-1} with a corresponding activation energy of 77.27 kJ/mol. This confirms the direct dependence of the stability and kinetic parameters and supports the inclusion of only one of these parameters in the optimisation to avoid model over-parametrisation. The value of the ΔC_p^0 term for $FeSO_3^+$ formation was thus maintained at zero.

7.3.1 Effect of $Fe_2(SO_4)_3$ and H_2SO_4

The 6 optimised interaction parameters presented in Table 7.1 provide an excellent description of the measured effects of the initial Fe(III) and acid concentrations on the achievable rate and extent of ferric reduction over the range 0.25 – 1.5 mol/kg $Fe_2(SO_4)_3$ and H_2SO_4 at 95 °C; clearly shown in Figure 7.1.

In addition to the stability and kinetic parameters already discussed, the $\beta^{(0)}$($FeSO_3^+$-HSO_4^-), C^{ϕ}($FeSO_3^+$-HSO_4^-) and ϕ($FeSO_3^+$-H^+) parameters were sufficient to capture the *predominant* trends in the kinetic profiles of the batch tests. Importantly, for the effect of acid concentration, the calculated solution speciation varies substantially between those tests at 0.25 mol/kg $Fe_2(SO_4)_3$ and those at higher total ferric concentrations. This variation is primarily attributed to the distribution of acid species, which is presented in Figure 7.2. At low $Fe_2(SO_4)_3$ concentration, the comparatively small total sulfate concentration results in a considerable fraction of free H^+ in the solution which manifests in the decreasing of the stability of the $FeSO_3^+$ complex through the overall formation equilibrium in Reaction 6.7.1. To ensure the correct quantification of the reaction profiles over the entire range of Fe(III) concentrations, a reasonably large negative term was required for the ϕ($FeSO_3^+ - H^+$) parameter to counteract the (unrealistic) destabilising of the active species. However, a positive value for the C^{ϕ}($FeSO_3^+ - H^+$) parameter was necessary to capture the effect of acid at higher Fe(III) concentrations, where the increased sulfate background promotes the formation of HSO_4^-. Lastly, the $\beta^{(1)}$($FeSO_3^+ - HSO_4^-$) parameter was also found to have a measurable effect on the calculated kinetic profiles, although it did not improve the description of the experimental data sufficiently to warrant its inclusion in the framework and was thus maintained at zero.

The primary deviations of the model with the consideration of only these (H^+,HSO_4^-)-$FeSO_3^+$ parameters were; (a) the lack of a general trend with increasing total Fe(III) and (b) an underestimation of the reaction conversion at elevated acid concentrations. In an attempt to quantify these effects, two additional binary interaction parameters were included: $\beta^{(0)}$($FeSO_3^+ - Fe(SO_4)_2^-$) and C^{ϕ}($FeSO_3^+ - Fe(SO_4)_2^-$) for interactions of the $FeSO_3^+$

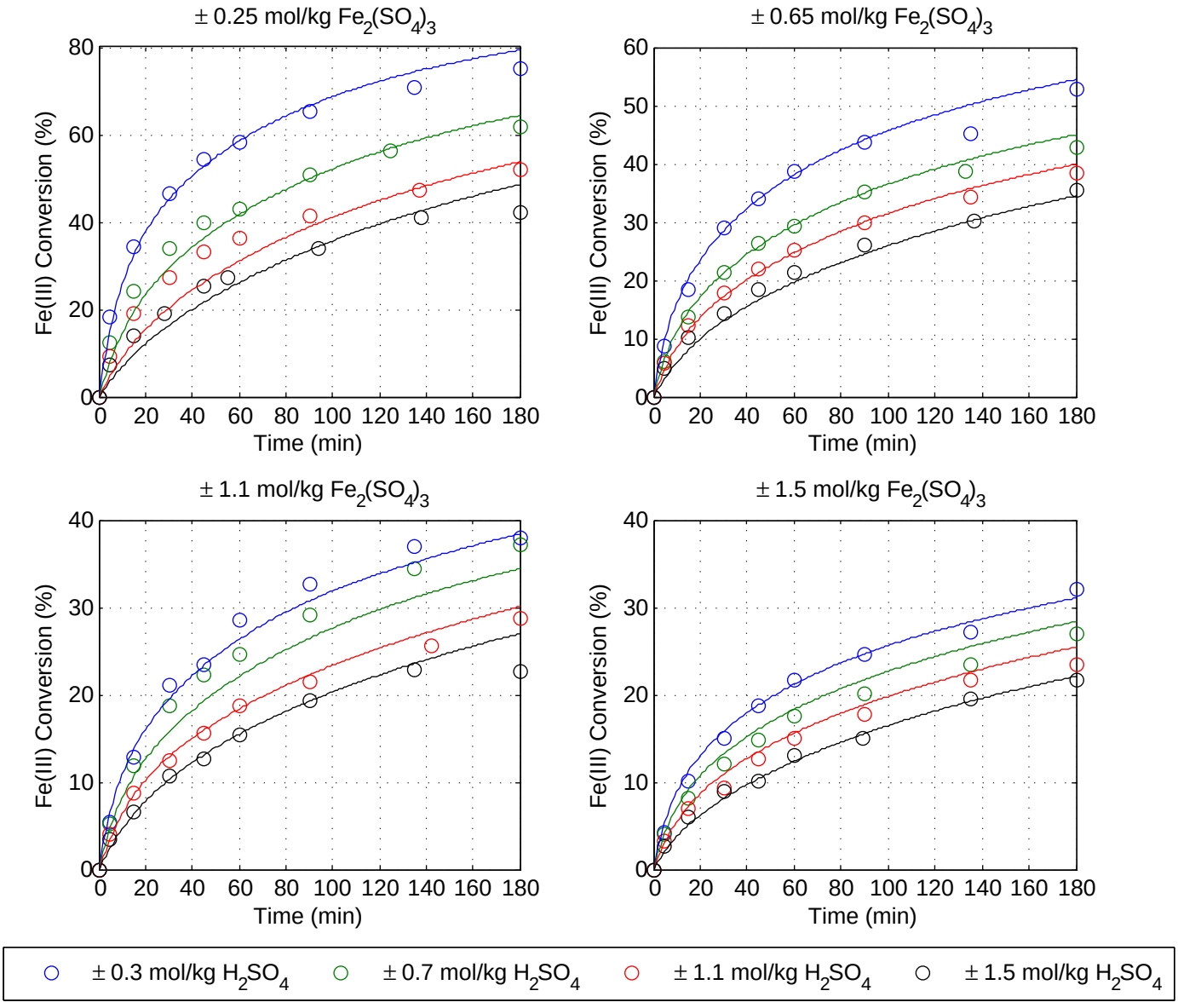

Figure 7.1: Measured and calculated Fe(III) conversion profiles as a function of initial total $Fe_2(SO_4)_3$ and H_2SO_4 concentrations. Solid lines are the calculated conversion profiles from the overall solution model and include the effects of mass transfer, thermodynamics and kinetics. Note the variation in scales between low and high acid tests.

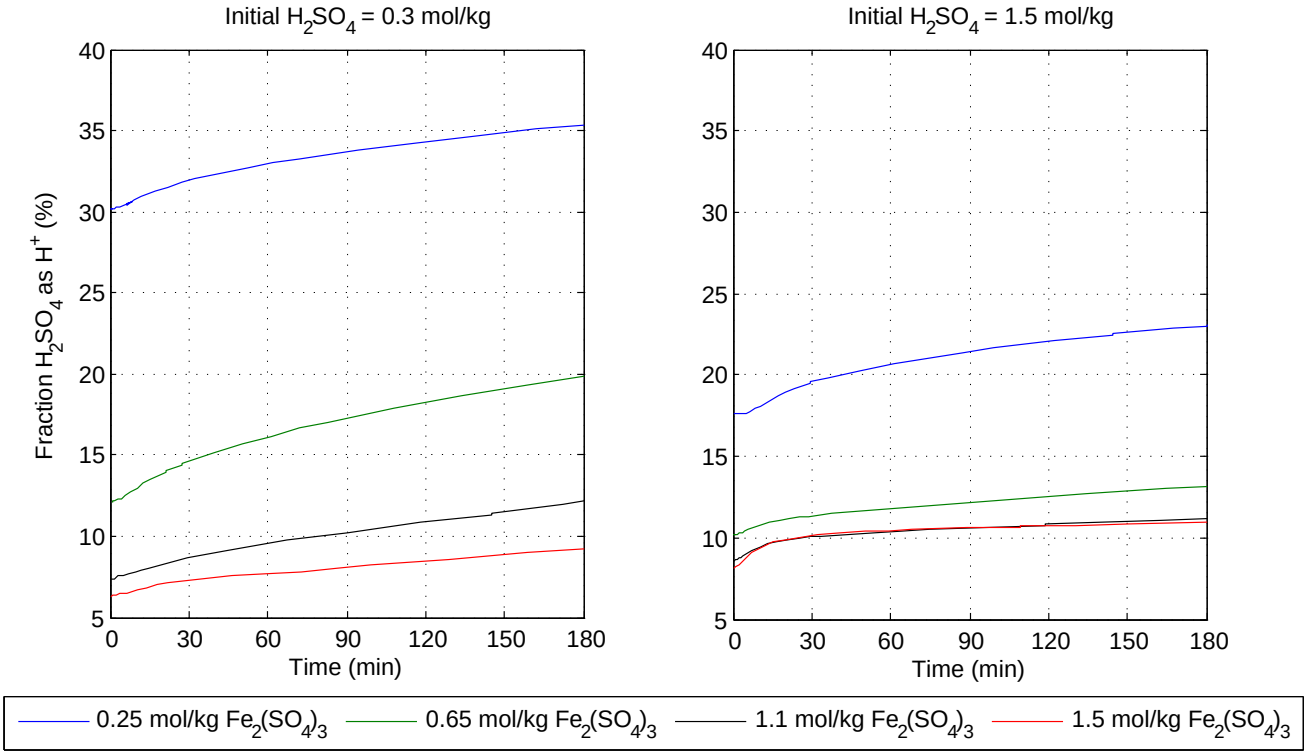

Figure 7.2: Fraction free H^+ of total H_2SO_4 during Fe(III) reduction between 0.25–1.5 mol/kg $Fe_2(SO_4)_3$ and 0.30–1.5 mol/kg H_2SO_4. Only the smallest and largest initial sulfuric acid concentrations are presented for clarity.

complex with the $Fe(SO_4)_2^-$ CIP. These parameters were essential for the accurate capturing of the non-linear relationship of decreasing conversion with increasing Fe(III) concentrations which is most clearly presented in Figure 7.3a where the conversion decreases by approximately 30% for an increase in $Fe_2(SO_4)_3$ concentration from 0.25 mol/kg to 0.65 mol/kg.

However, even with the inclusion of these parameters, the remaining model residuals were not randomly distributed and showed a systematic deviation with a slight underestimation of the conversion at reaction times below about 60 minutes and an overestimation thereafter. Clearly, from the reaction profiles in Figure 7.1, the conversion is still increasing with time in all instances, and the reaction has not reached an equilibrium, but appears to be continuing at a near-linear rate with time. By adjusting only the $FeSO_3^+$–$Fe(SO_4)_2^-$ interaction parameters, these vastly different rates could not be reproduced by the model and a further interaction with a species that changes with time was required. From interpretation of the mechanism, and the known strong affinity to form

$FeSO_3^+$ in this system, it is unlikely that the presence of initial Fe(II) would significantly affect the ferric conversion. This excluded the Fe^{2+}-$FeSO_3^+$ or $FeSO_4^0$-$FeSO_3^+$ interaction parameters from consideration in the model. Instead, the $\phi(FeSO_3^+ - Fe^{3+})$ parameter was included to effect the reduction in availability of Fe(III) as the reaction progressed. As discussed above, the significant complexation of sulfate in the HSO_4^- species at high acid backgrounds results in a considerable fraction of the unassociated Fe^{3+} ion in solution, clearly shown in Figure 7.4a. The negative optimised value for this interaction parameter produces in a reduction in the $FeSO_3^+$ species concentration as Fe(III) is removed from the system by the reaction. However, this parameter also facilitates the *enhancement* of the $FeSO_3^+$ stability at high acidities. Critically, the noted retardation of the reaction rate by increasing acid concentration without this parameter is severe and required correction via a large negative value of $\beta^{(0)}(FeSO_3^+ - HSO_4^-)$. By including it in the framework it captured, simultaneously, the correct variation in reaction rate as a function of time as well as enhanced the stability of $FeSO_3^+$ at higher acidity through interaction with the more stable Fe^{3+} ion under these conditions and facilitated an excellent description of the observed kinetic profiles. Moreover, by the inclusion of this parameter, the optimised value of $\beta^{(0)}(FeSO_3^+, HSO_4^-)$ was close to zero and thus removed from the model framework.

The noted variation in the calculated reaction rate surface compared to that measured experimentally (Figure 7.3b) is particularly significant at lower Fe(III) concentrations. The visible decrease in the reaction rate at lower Fe(III) is due to the formation of $FeSO_3^+$ being retarded through the overall formation reaction (Reaction 6.7.1). From inspection of the reaction mechanism, the decreased concentration of $FeSO_3^+$ will directly decrease the rate of Fe(II) generation. Indeed, better fitting of the *initial* reaction rate could potentially have been achieved by including the model residuals highlighted in Figure 7.3b in the overall objective function during parameter optimisation. However, in an industrial context, such short residence times are of little importance compared to the achievable conversion in reaction times of the order of a few hours.

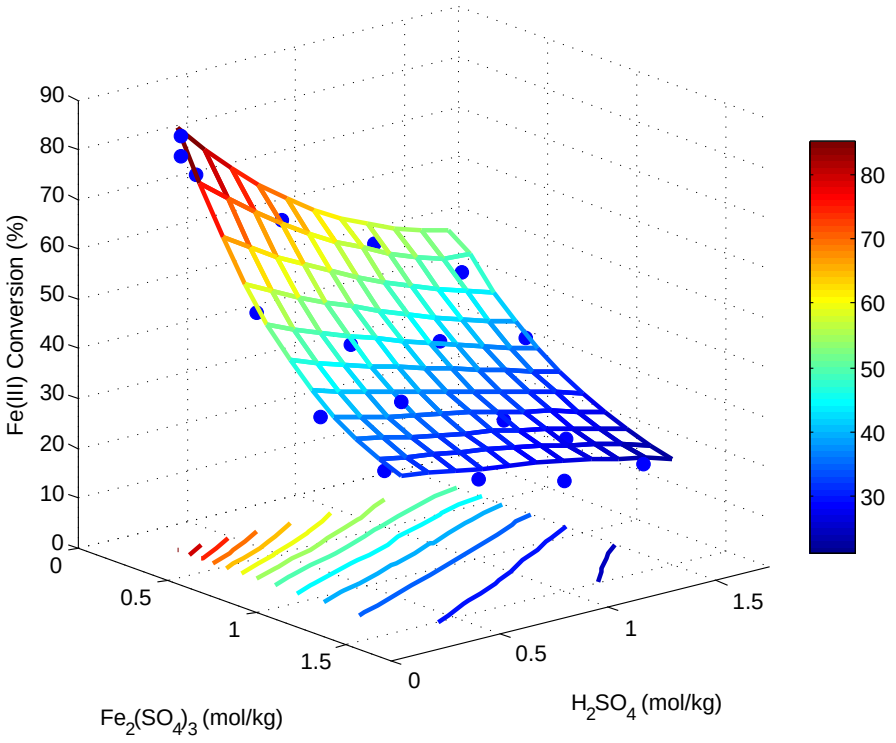

(a) Measured and calculated Fe(III) conversion after 180 min as a function of Fe(III) and acid concentrations. The surface was calculated using the calibrated solution model.

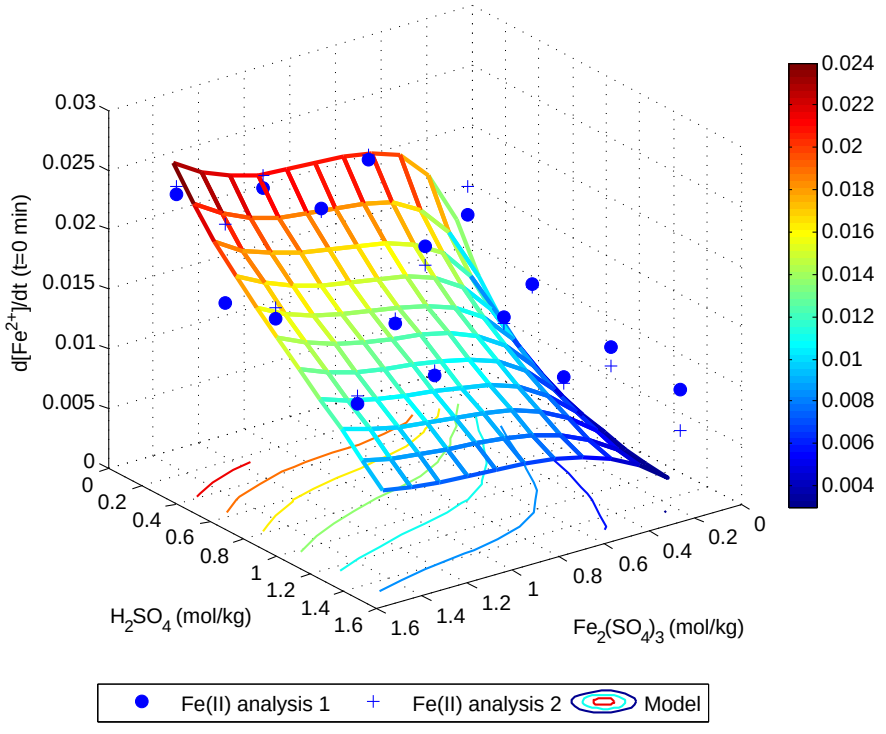

(b) Measured and calculated average reduction rate over first 5 minutes of reaction. The surface was calculated using the extent of reaction after 5 minutes calcualted by the solution model. Duplicate Fe(II) analyses, taken directly after sample extraction and as part of the multi-element analysis are presented to emphasise the sensitivity to the analytical results.

Figure 7.3: Measured and calculated conversion after 180 min and average reduction rate over first 5 minutes of reaction.

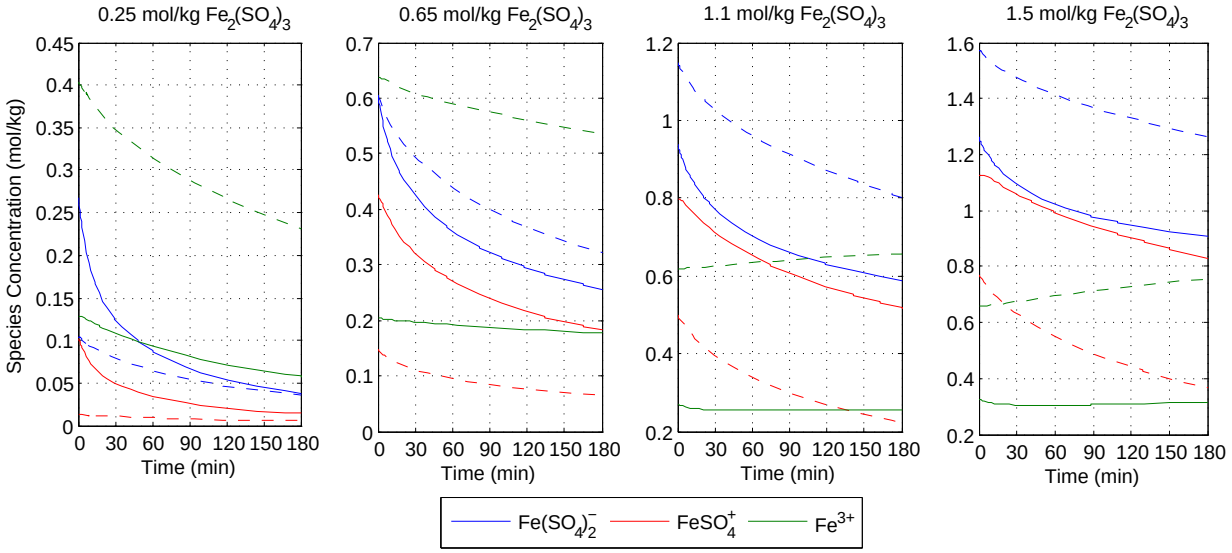

(a) Calculated ferric speciation during Fe(III) reduction. Blue, red and green represent the $Fe(SO_4)_2^-$, $FeSO_4^+$ and Fe^{3+} species respectively. Solid lines represent speciation at 0.3 mol/kg initial H_2SO_4 and dotted lines at 1.5 mol/kg initial H_2SO_4, T = 95 °C

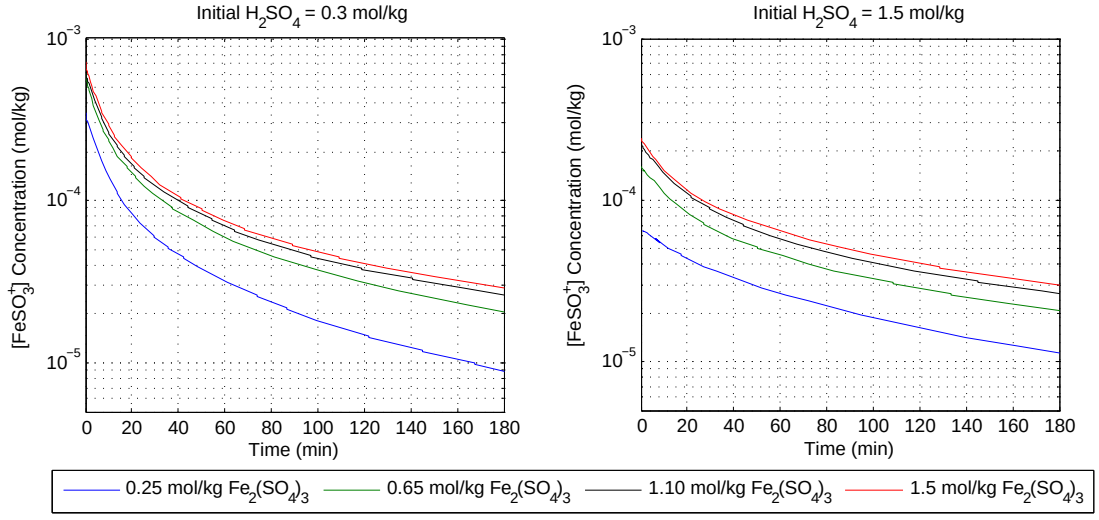

(b) Calculated $FeSO_3^+$ concentrations during reaction at $Fe_2(SO_4)_3$ = 0.25–1.5 mol/kg and H_2SO_4 = 0.3–1.5 mol/kg, T = 95 °C. These clearly emphasise the retardation effect of acid on the rate-limiting reagent concentration. Note the logarithmic scale.

Figure 7.4: Calculated concentrations of the various ferric species and CIPs during reaction with SO_2 at a range of initial $Fe_2(SO_4)_3$ and H_2SO_4 concentrations

7.3.2 Effect of temperature

Another important feature of the optimised model is the ability to accurately quantify the measured kinetic data at 75 °C, presented in Figure 7.5. As discussed in Section 6.4, the reduction in rate of chemical reaction was proposed to have been compensated by the increase in SO_2 solubility, thereby driving the formation of the $FeSO_3^+$ species. Under the assumptions on which the model was based, namely: (a) the accepted parameters for the extrapolation of the $FeSO_3^+$ stability constant with temperature, (b) the fixed SO_2 solubility at 75 and 95 °C (Table 6.1), and (c) the Arrhenius-type extrapolation of the rate constant, the modelling results confirm this assertion.

Again, it must be stressed that the solubility of SO_2 is not explicitly known in $Fe_2(SO_4)_3$ solutions, and the formation of the $FeSO_3^+$ complex may increase the solubility. However, from the speciation calculations[3] during reaction presented in Figure 7.4b which suggested that the concentration of $FeSO_3^+$ is of the order of 10^{-4} to 10^{-3} mol/kg. This would obviously not contribute significantly to the overall soluble S(IV) and tentatively validates the assumption that the solubility of SO_2 in $Fe_2(SO_4)_3$ is equivalent to that in water; albeit artificially. The effect of temperature increases the initial calculated concentration of $FeSO_3^+$ at 75 °C to approximately 3.8 times the concentration calculated at 95 °C, shown in Figure 7.4b, which appears sufficient, in addition the thermodynamic speciation changes built into the model in Chapter 5, to counteract the decrease in rate constant approximately 3-fold via the Arrhenius relationship.

This is a crucial finding from this work and highlights the significant effect that the SO_2 partial pressure, and hence solubility, can have on the reduction kinetics of this system. While the effect of temperature on the kinetics is obviously also significant, in the context of the ARFe leach process, other factors such as the inherent rate of laterite leaching and the $FeSO_4$ solubility relationships (directly related to the heating and cooling duty required in the process) also vary with temperature and must be simultaneously optimised. However, the SO_2 solubility can be varied *independently* of temperature, i.e., in a pressure vessel, and the findings of this study suggest that the optimal rate and extent of ferric reduction and acid generation in the ARFe leaching operation can be engineered by the appropriate reactor design.

Moreover, the model developed in this chapter can be incorporated into an integrated mass and energy balance model of the ARFe circuit and used to investigate CAPEX and OPEX trade-offs associated with the temperature and SO_2 partial pressure which the leaching unit is operated.

[3] Assuming the SO_2 solubility in pure water and the respective thermodynamic parameters outlined in Section 7.2.1

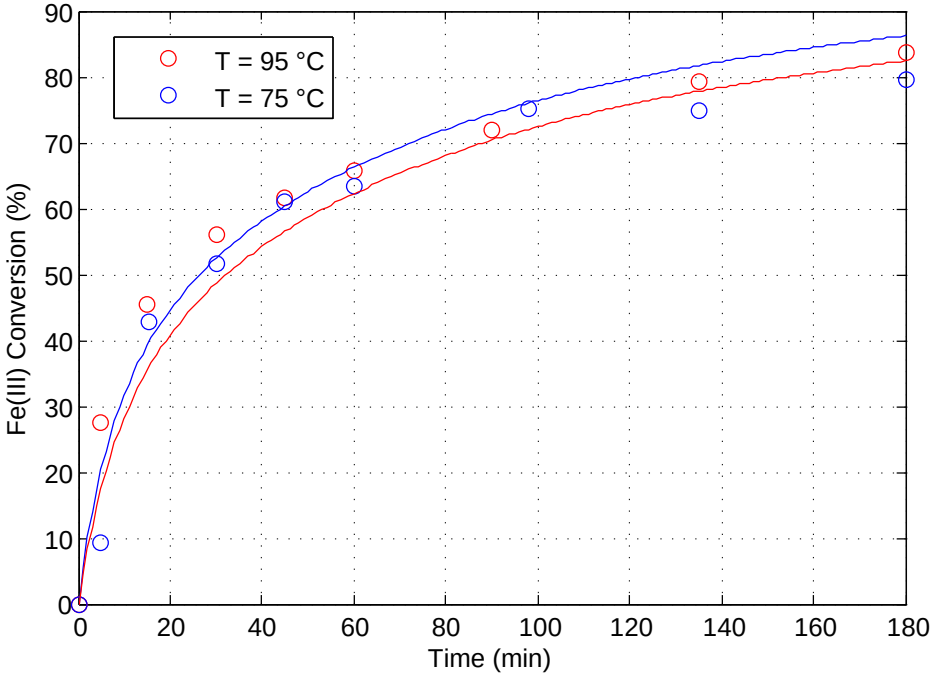

Figure 7.5: Measured and calculated Fe(III) conversion profiles for tests at 75 and 95 °C using the identical experimental setup and adjusting measured Fe(II) concentrations for the significantly higher concentration of $SO_{2(aq)}$ at lower temperature.

7.3.3 Effect of in-situ neutralisation

An important validation of the reaction mechanism was suggested by the noted observation of a significant increase in Fe(III) conversion upon addition of NaOH into the reactor. These tests were not included in the parameter optimisation and were thus used for validation. The tests were characterised by no initial acid addition and only a small amount of acid, inherent in the $Fe_2(SO_4)_3 \cdot xH_2O$ reagent was present.

The addition of 40 g NaOH into the reactor (H_2O basis: 1900 g) resulted in a decrease in the concentration of 0.26 mol/kg H_2SO_4 by neutralisation. This was included in the system of differential equations as a negative impulse in the computed derivatives of the total H^+ and SO_4^{2-} after 95 minutes of reaction. The magnitude of this impulse was adjusted iteratively to achieve a decrease of 0.26 mol/kg H_2SO_4 at this time. Since no consideration of Na^+ ions was included in the model, the reduction in total acid necessitated a simultaneous reduction in the sulfate concentration to maintain charge balance. However, given the significant effect of acid in comparison to the total ionic strength of the solution, this simplification did not likely contribute to significant error.

The results of this simulation are presented in Figure 7.6 where the quantification of the effect of neutralisation is excellent and captures the overall effect well. It is however noted that the predicted conversion profiles for these tests over the first 60 minutes of reaction is underestimated. This is likely due to the fact that model parameters were not calibrated in solutions with such low initial acidities and, given the increasingly non-linear relationship with acid at low acidities (see Figure 7.3a), the effect on the reaction kinetics not completely captured by the minimum parameter approach. However, after 90 minutes of reaction, when solution conditions are representative of those on which the model was calibrated, the increase in conversion is accurately characterised.

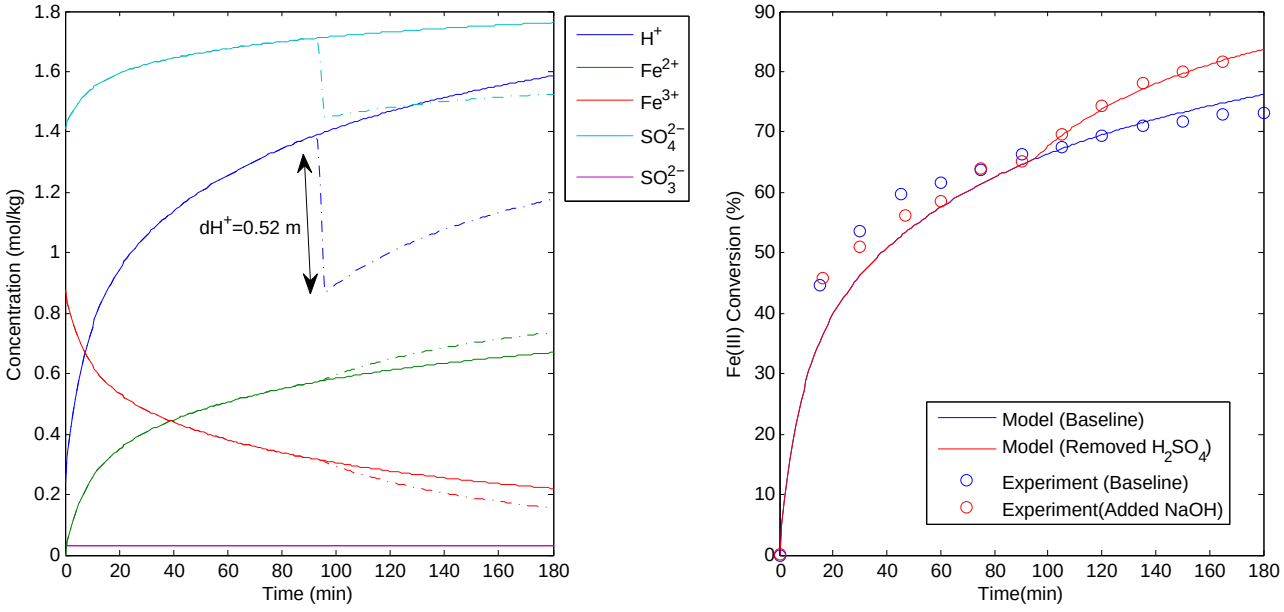

Figure 7.6: Model characterisation of artificial in-situ neutralisation and comparison to experiment with added NaOH. Dotted lines show the impulse effect of decreasing the total H_2SO_4 concentration at 90 minutes in the model. Conditions: $Fe_2(SO_4)_3$ = 0.44 mol/kg, H_2SO_4 = 0.09 mol/kg, T = 95 °C.

7.3.4 Mass transfer evaluation and sensitivity analysis

From the mass transfer analysis in Section 6.1, the findings suggested that the mass transfer coefficient measurements via the direct and indirect methods provided only an indication of the *lower* limit of the k_La based on the variation in $Fe_2(SO_4)_3$ viscosity as compared to that of water and sodium sulfite/sulfate solutions as well as the possible enhancement of mass transfer during ferric reduction with SO_2. The k_La was set at 8.92 min^{-1} in the reaction model and the enhancement factor, ϕ, was set at unity however, the sensitivity of this assumption needed to be validated.

For this analysis, the enhancement factor was varied over two orders of magnitude, i.e., from 0.1 to 10, corresponding to an overall mass transfer coefficient, $\phi \cdot k_La$, between 0.89 - 71.4 min^{-1}. This range covers nearly the entire range of Figure 6.1 (page 134) and it is highly likely that the actual mass transfer coefficient lies within this range. The sensitivity of the total S(IV) concentration and the Fe(III) conversion profiles were investigated. The laboratory test with the largest measured reaction rate in the experimental set, i.e., initial concentrations of 3.0 mol/kg Fe(III) and 0.3 mol/kg H_2SO_4, was selected for this analysis and the results are presented in Figure 7.7.

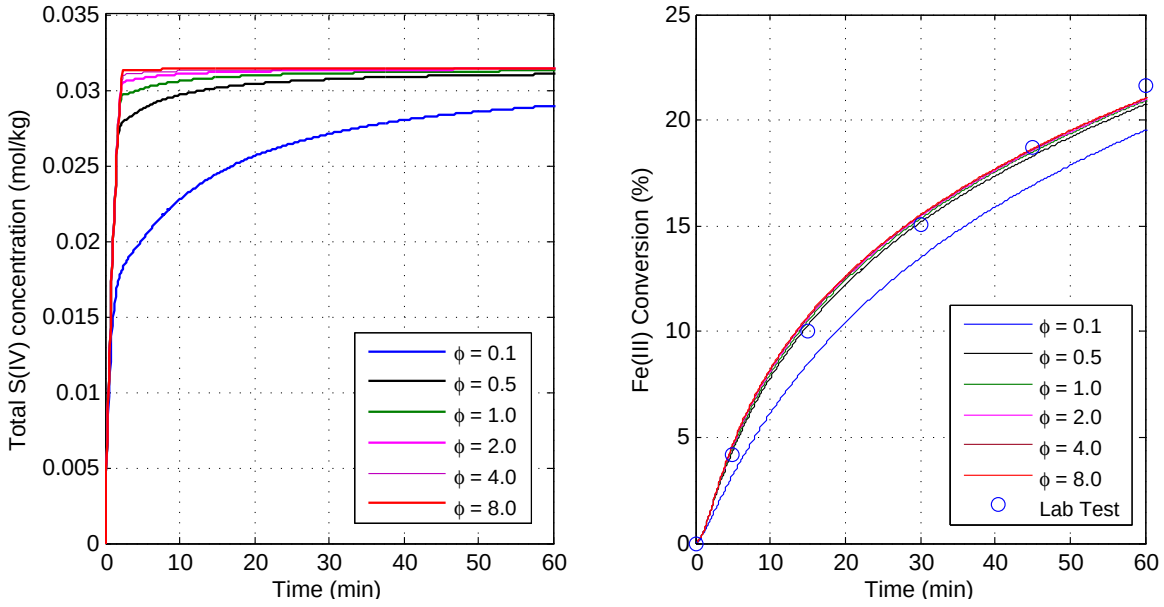

Figure 7.7: Sensitivity analysis over the first 60 minutes of reaction on the mass transfer coefficient by variation of the enhancement factor, ϕ, at a fixed k_La of 8.92 min^{-1}. This produced total effective k_La's up to 71.4 $min^{-}1$. The data points correspond to the ferric reduction batch test at 1.5 mol/kg $Fe_2(SO_4)_3$ and 0.3 mol/kg H_2SO_4, i.e. the fastest experimentally measured rate in the set.

This sensitivity analysis highlight that the mass transfer coefficient is essentially unimportant for the quantification of the kinetic profiles above an overall mass transfer coefficient of about 4.5 min^{-1}, corresponding to $\phi = 0.5$. Importantly, this suggests that the expected *lower* limit of the k_La of 8.92 min^{-1} facilitates gas-liquid mass transfer well in excess of that required by the reaction. Moreover, for modelling purposes, this analysis has highlighted that the assumption of the selected mass transfer coefficient and the fixing of the enhancement factor at unity is reasonable.

7.4 Summary

This chapter details a self-consistent, minimum-parameter solution model of ferric reduction with SO_2 in concentrated sulfate solutions, which was able to accurately capture the complex effects of Fe(III) and H_2SO_4 concentration on the observed reduction kinetics of this complex, multi-phase system.

The reaction model is comprised of a thermodynamic framework with the explicit recognition of 13 solution species, which was calibrated largely from the various subsystems that comprise the $Fe_2(SO_4)_3-FeSO_4-H_2SO_4-SO_2-H_2O$ system in Chapter 5. A system of differential equations, representing the rate-limiting kinetic process, was incorporated into this thermodynamic framework in order to characterise the observed reaction kinetics. The *thermodynamic* behaviour of the $FeSO_3^+$ species is central to the observed reaction kinetics through its direct involvement in the rate-limiting kinetic process.

Importantly, this approach required the regression of thermodynamic interaction parameters to observed kinetic data. This approach was justified by the rigorous theoretical framework on which the Pitzer solution model is based and the supporting evidence for the reaction mechanism that highlights the pivotal role which $FeSO_3^+$ plays in the rate-limiting kinetic process. By combining this comparatively simple decomposition reaction with a set of pseudo-equilibria for the remaining solution species, the complex behaviour of the reaction could be captured within the thermodynamic framework in a consistent and structured way. This aspect stresses the great value of making thermodynamic considerations in the development of a practical kinetic model and facilitates not only insights into the inherent chemistry of the system, but a simple and intuitive kinetic model.

The insight into the important trade-off between temperature and SO_2 partial pressure was highlighted by the accurate modelling of the reaction at 95 and 75 °C. This suggested that the most significant leverage for enhancing ferric reduction rates is the

manipulation of the SO_2 partial pressure through the most appropriate reactor vessel design and operation. Additionally, the confirmatory test with added NaOH was also accurately modelled, despite not being included in the parameter regression. This provides strong support for the reaction mechanism and the modelling approach and assumptions.

Lastly, the key uncertainties in the model remain the parameters influencing the stability, and rate of decay, of the $FeSO_3^+$ species. Specifically, in this approach, the ΔH^0 term was fixed at 49.5 kJ/mol on the basis of reported measurements at 25 °C and the ΔC_p^0 term was set to zero due to a lack of data. The first order rate constant, k_1, for the inner-sphere electron transfer in the $FeSO_3^+$ CIP was included in the model parameter optimisation to prevent overparametrisation. It was further shown that, for a value of $\Delta C_p^0 = 400$ J/mol.K, only the optimised value of the k_1 parameter was observed to change significantly. Should further detailed tests on the rate of this process be reported, the model parameters can be easily re-evaluated.

Chapter 8

Conclusions

Many kinetic studies in hydrometallurgy often solely focus on the phenomenological effects of variables such as concentrations, pressures and temperatures on the observable properties of one or more reactions. While this is useful for developing empirical reaction models and optimising processes, development of fundamental understanding into the underlying reaction mechanism is often overlooked. The ultimate engineering objective of this work is the development of a kinetic model of ferric reduction with SO_2 in concentrated sulfate solutions at elevated temperature. The primary contribution of this work highlights that the careful consideration of the fundamental solution chemistry of the $Fe_2(SO_4)_3$ systems, with appropriate contextual simplifications, permits an enhanced analysis and description of Fe(III) reduction under these conditions. The approach of integrating a kinetic model of the rate-limiting processes into a rigorous thermodynamic framework has shown to capturing of complex kinetic behaviour in a structured and natural way.

This chapter outlines the principal results of this study, differentiated into thermodynamic and kinetic aspects of ferric reduction and their resulting implications for industrial implementations, with particular reference to the Iron Focused Laterite Process (ARFe) case study.

8.1 Thermodynamics of $Fe_2(SO_4)_3$ solution systems

A thorough review of available literature detailing the thermodynamics of $Fe_2(SO_4)_3$ solutions highlighted the existence of several of the important contact ion pairs, but a general lack of experimental data confirming the actual speciation in solution; even at dilute concentrations. In contrast to many divalent metal-sulfate systems, such as $MgSO_4$

or $CaSO_4$, and despite the prevalence of ferric sulfate systems throughout industry and the environment, a limited amount of thermodynamic data have been reported. This is undoubtedly due to the significant complexities associated with strong interactions with ligand and solvent species and the resulting large tendency for hydrolysis.

One of the key contributions of this work is the use of Raman and UV-vis spectroscopic measurements, rationalised by static DFT calculations, to highlight the sulfate speciation in the $Fe_2(SO_4)_3$-$FeSO_4$-H_2SO_4-H_2O system, through the investigation of the binary and ternary component systems. This resulted in the direct, quantitative characterisation of at least two ferric sulfato species, namely $FeSO_4^+$ and $Fe(SO_4)_2^-$, in addition to unassociated sulfate and bisulfate in solutions up to 1.6 mol/kg $Fe_2(SO_4)_3$ and 3.0 mol/kg H_2SO_4 at 25 to 90 °C. The presence of significant quantities of outer-sphere complexed Fe^{3+} was also indicated from the amount of unassociated[1] sulfate under these conditions. These measurements provide insights into $Fe_2(SO_4)_3$ that are unavailable in the open literature and are widely applicable to an array of industrial and environmental ferric containing systems.

These newly available speciation measurements facilitated the development of a minimum-species, minimum-parameter thermodynamic solution model for the various subsystems within the $Fe_2(SO_4)_3$-$FeSO_4$-H_2SO_4-H_2O system. The well known Pitzer ion-interaction framework was used with the explicit recognition of the important, verified solution species. A pragmatic surrogate approach was adopted to account for Fe(III) hydrolysis to reduce model complexity without sacrificing reliability. The model was calibrated using available speciation, water activity, activity coefficient and solubility data and was validated using speciation measurements in the mixed system that were not used during parameter optimisation. The model was shown to be capable of accurately predicting the major speciation trends in the multicomponent system as well as quantifying available data well. A key limitations of this model, namely, the inability to reconcile measured water activity data in the $Fe_2(SO_4)_3$-H_2SO_4-H_2O system and the simplified manner in which ferric hydrolysis products were treated. However, considering the ultimate application of modelling kinetic processes, the model provides a robust and realistic basis on which kinetic aspects can be incorporated.

Additionally, given the significant number of natural and industrial systems that contain soluble ferric ion, the ability to make reliable estimates of speciation in aggressive, concentrated solutions have significant wider-reaching implications. For instance, these data can directly support modelling applications in refractory sulfide pressure leaching and matte-sulfide base metal refining circuits, treatment of steel pickling liquor waste and

[1] i.e., in a contact ion pair sense

the evaluation of the impacts and potential remediation of acid mine drainage instances.

8.2 Fe(III) reduction kinetics and modelling

Ferric reduction kinetics in concentrated sulfate solutions ($m_{SO_4^{2-}}$ = 1.0 - 6.6 mol/kg) at 75 - 95 °C were determined in several systematic batch and continuous laboratory tests. Confirmation of the expected reaction stoichiometry and a rigorous investigation of mass transfer effects was performed, which highlighted the validity of the experimental approach as well as ensuring observed measurements were not influenced by physical effects.

The impact of $Fe_2(SO_4)_3$ and H_2SO_4 concentrations were found to decrease reaction conversion with increasing concentration of both reagents, while the initial reaction rate was observed to increase with $Fe_2(SO_4)_3$ concentration. The individual effect of acid was isolated by the in-situ neutralisation of acid produced during reaction, which increased batch conversion by ca. 10% after 180 minutes. A key outcome of these tests highlighted that acid, either added externally or generated during reaction, was the most critical factor for the achievable Fe(III) conversion at fixed residence time. Additionally, the effect of temperature showed negligible difference in the observed reaction kinetics. This was attributed to the decrease in intrinsic reaction rate being compensated by the known increase in solubility of SO_2 at lower temperature.

Similar reaction conversions measured in batch and continuous operation, when corrected for residence time effects, highlighted that the reaction kinetics were not influenced by the time-variant compositions during batch tests. Critically, this confirmed that the time-scale of the rate limiting step in the reaction mechanism was significantly slower than that of the solution speciation, which could thus be effectively considered as a set of pseudo-equilibria, i.e., that reach equilibria instantaneously.

Based on the findings of these kinetic tests and a thorough analyses of metal catalysed sulfite oxidation mechanisms, most often studied in dilute solutions, i.e., [Fe(III)] = 1 mmol/kg, [S(IV)] = 10 mmol/kg], available in the open literature, a reaction mechanism was proposed. The rate-limiting reaction was identified as the inner-sphere electron transfer within the transient ferric sulfito species, $FeSO_3^+$, as has been noted by others (Lente and Fabian, 1998, 2002; Kuo et al., 2006). This specific reaction was monitored by time-resolved Raman and UV-vis spectroscopy at 25 °C where the presence of the $FeSO_3^+$ contact ion pair was confirmed and observed to slowly decompose at a rate comparable to those reported in the literature. Furthermore, static DFT calculations of the $FeSO_3^+$ complex highlighted poor overlap between HOMO and LUMO orbitals that were largely

centred on the sulfite and ferric atoms respectively. This provides additional support for the identified kinetically unfavourable inner-sphere electron transfer.

Through various simplifications, using experimental evidence and published data for the rates of various equilibria and reactions in the proposed reaction mechanism, a system of differential equations was developed, which characterised the reaction system according to the rate-limiting step, while also including the effects of gas-liquid mass transfer. These equations were superimposed on the thermodynamic framework developed previously into a self-consistent reaction model for Fe(III) reduction with SO_2. The kinetic and interaction parameters that could not be determined in isolated systems were optimised by regression to the measured kinetic data. The resulting calibrated solution model showed an excellent ability to capture the observed variation in extent of Fe(III) reduction up to 1.5 mol/kg $Fe_2(SO_4)_3$ and 1.5 mol/kg H_2SO_4 (as initial concentrations) which was observed to vary from 85 % to 21 % over this concentration range. This was achieved with only a single rate-limiting kinetic expression corresponding to the decomposition of the $FeSO_3^+$:

$$\frac{d[\mathrm{Fe}^{3+}]}{dt} = -2k_1[\mathrm{FeSO}_3^+] \tag{8.2.1}$$

The effects of acid and Fe(III) concentrations and temperature are captured in the thermodynamic treatment of the stability of the $FeSO_3^+$ which directly influences the calculated reaction rate via the above expression. This exemplifies the key benefit of considering both thermodynamic and kinetic aspects in a unified model of reacting systems and the manner in which chemical effects can be incorporated in a consistent and natural way.

8.3 Implications of this work

One of the most important engineering implications of this work is the improved understanding of the key drivers of the Fe(III) reduction reaction. Specifically, since the concentration of $FeSO_3^+$ species is solely responsible for the overall rate of ferric reduction (through Reaction 8.2.1) factors that directly affect the stability of this CIP will be most influential for the achievable rate and extent of reaction. As discussed, the effect of acid is a primary factor which has limited scope for being optimised in the context of the ARFe circuit, i.e., the inherent rate of laterite leaching which will set the steady-state acid concentration recycling around the leaching circuit (see Figure 2.2). However, the modelling insights and experimental evidence developed in this work suggests that the rate of ferric reduction can be significantly increased by raising the SO_2 partial pressure and thereby increasing the total S(IV) solubility in solution.

Practically, this could be achieved by the use of closed, pressurised reaction vessels, or the use of high-aspect-ratio reactors that would generate significant hydrostatic pressures at the base of the reactors where SO_2 could be injected. Obviously, such processes would increase capital and operating requirements of the circuit through more elaborate reactors and associated infrastructure required by large-scale pressure leaching, albeit mild in comparison to high-pressure acid leaching (HPAL) circuits. The reaction model developed in this study can be easily incorporated into mass-and-energy-balance models of the ARFe conceptual circuit to facilitate the enhanced evaluation and optimisation of the various circuit conditions and configurations.

Apart from the model's direct applicability to the ARFe process, the fundamental insights into speciation in the $Fe_2(SO_4)_3$-H_2SO_4-H_2O system have significantly wider implications. Firstly, the description of the primary species in acidic ferric sulfate systems has been simplified in comparison to other reported speciation models in the open literature, with only two ferric sulfato species being explicitly considered as opposed to several polycationic species reported by others (see Section 2.6). Indeed, additional aqueous species that are precursors to the multitude of iron precipitates, i.e., ferrihydrate, goethite, hematite, jarosite, etc., must be formed at higher temperatures (and pH), but below the solution boiling point in acidic solutions, these species can be accepted as a minority on the basis of the experimental findings of this work.

Lastly, this work has further emphasised the important role which engineering studies have in generating unavailable chemical data on which to develop phenomenological models that can be used for practical applications. The vast complexity of industrial hydrometallurgical systems will nearly always result in a lack of specific experimental data on which to develop models. In such instances, it is extremely valuable and necessary to develop of make use of existing techniques to measure these unknown data and, in adopting a carefully thought-out engineering approach, sufficiently simplify the system and the model such that maximum value can be derived from such measurements in a pragmatic way.

8.4 Recommendations for future work

8.4.1 ARFe process development

On the basis of the findings of this work, several key focus areas for the continued development of the ARFe process can be recommended, specifically, these are:

1. Extend the context of the reaction modelling framework to include laterite leaching

models (Senanayake et al., 2011) and, potentially, ferrous oxidation (Steyl, 2009, 2012) to consider the entire suite of chemical processes applicable to the ARFe leaching operation.

2. Given the significant importance of SO_2 solubility in this system, it is recommended to develop an explicit calculation of SO_2 vapour-liquid equilibrium in the modelling framework.

3. Incorporate the reaction model into the available mass-and-energy balance model of the ARFe process (Biley, 2011) concept to facilitate an enhanced analysis of the capital and operational costs of the ARFe hydrometallurgical circuit.

8.4.2 $Fe_2(SO_4)_3$ system thermodynamics

This study further highlights that, despite the numerous studies and industrial applications of iron-containing systems, there is still a poor understanding of the thermodynamics of these systems. This severely limits the extent to which truly predictive models can be developed. To this end, it is recommended that further work be conducted in the following specific focus areas:

1. Further extend the currently available thermodynamic data of the $Fe_2(SO_4)_3$-$FeSO_4$-H_2SO_4-H_2O system through experimental measurements, such as isopiestic, EMF and speciation measurements, in binary, ternary and multi-electrolyte systems to elevated temperatures.

2. Extend the ferric speciation study to conditions that are directly applicable to existing industrial applications. Of particular interest is the behaviour of soluble ferric and precipitation of a range of iron products during medium and high pressure leaching (Papangelakis et al., 1994; Liu et al., 2003; Liu and Papangelakis, 2005; Steyl, 2012).

Appendices

Appendix A

Thermodynamics

A.1 Standard thermodynamic values

Table A.1 contains a list of standard heats of formation for the solution species applicable to this study. These values are standardized by the convention where the hydrated proton at infinite dilution has zero values. Many of the values in this collection have significant variation in their reported values which emphasizes the difficulties in measuring such quantities. From an rigorous analysis of the reported valued, the bold values in Table A.1 are considered most reliable and were selected in this study based on their ability to characterise the stability constants of interest most effectively and produce the best results under extrapolation.

Table A.1: Standard aqueous species heats of formation

Aqueous Species	ΔG_f^0 (kJ/mol)	ΔH_f^0 (kJ/mol)	S^0 J/mol.K	C_p^0 J/mol.K	Kelley-A	Kelley-B	Kelley-C	Reference
$Fe(OH)_2^+$	-452.29	-559.78	2.4	-155.30				Liu et al. (2003)
$Fe(OH)_2^+$	-446.40	-543.80	-29.29	229.59				Papangelakis et al. (1994)
$Fe(OH)_2^+$	-438.00							Wagman et al. (1982)
$Fe(OH)_2^+$	-446.40	-543.8	-29.29					Papangelakis et al. (1994)
$Fe(SO_4)_2^-$	**-1537.30**	**-1829.50**	**-4.57**					**Liu et al. (2003)**
$Fe(SO_4)_2^-$	-1524.65	-1828.40	-43.07					Papangelakis et al. (1994)
$Fe(SO_4)_2^-$	-1524.50							Wagman et al. (1982)
Fe^{2+}	-78.90	-89.10	-137.70					Wagman et al. (1982)
Fe^{3+}	**-17.23**	**-49.50**	**-277.40**	**-142.67**				**Liu et al. (2003)**
Fe^{3+}	-4.60	-48.50	-315.90	31.01	79.09	-219.35	15.40	Papangelakis et al. (1994)
Fe^{3+}	-4.70	-48.50	-315.90					Wagman et al. (1982)
$FeOH^{2+}$	-241.93	-334.42	-115.10	-114.50				Liu et al. (2003)
$FeOH^{2+}$	-229.41	-290.80	-142.00	46.15	19.40	-21.22	29.40	Papangelakis et al. (1994)
$FeOH^{2+}$	-241.60	-292.60	-106.20	-34.31				Shock et al. (1997)
$FeOH^{2+}$	-229.41	-290.8	-142					Wagman et al. (1982)
$FeSO_4^0$	**-823.43**	**-998.30**	**-117.60**					**Wagman et al. (1982)**
$FeSO_4^+$	**-785.44**	**-932.86**	**-91.20**	**41.75**				**Liu et al. (2003)**
$FeSO_4^+$	-772.80	-931.78	-129.70	131.02	37.70	316.78	-1.00	Papangelakis et al. (1994)
$FeSO_4^+$	-772.70	-931.80	-130.00					Wagman et al. (1982)
H_2O	**-237.18**	**-285.85**	**69.96**	**75.35**				**Liu et al. (2003)**
H_2SO_3	-537.81	-608.81	232.2					Wagman et al. (1982)
H_2SO_3	-537.74	-609.61	229.43	270.00				Goldberg and Parker (1985)
HSO_3^-	-527.73	-626.22	139.7					Wagman et al. (1982)
HSO_3^-	-527.14	-627.41	134.17	-2.00				Goldberg and Parker (1985)
HSO_4^-	**-755.76**	**-889.10**	**125.52**	**22.18**				**Liu et al. (2003); Shock and Helgeson (1988)**
HSO_4^-	-756.01	-887.01	131.80	152.97	-547.29	1342.10	266.78	Papangelakis et al. (1994)
HSO_4^-	-755.91	-887.34	131.80	-84.00				Wagman et al. (1982)
$SO_{2(g)}$	**-300.03**	**-296.81**	**248.223**	**39.84**				**Goldberg and Parker (1985)**
SO_2	-300.68	-322.98	161.9					Wagman et al. (1982)
SO_2	-300.68	-322.98	161.90					Wagman et al. (1982)
SO_2	-300.6	-323.78	159.48	195.00				Goldberg and Parker (1985)
SO_3^{2-}	-486.50	-635.5	29					Wagman et al. (1982)
SO_3^{2-}	**-486.2**	**-631.06**	**-15.4**	**-264.00**				**Goldberg and Parker (1985)**
SO_4^{2-}	**-744.46**	**-909.60**	**18.83**	**-269.37**				**Liu et al. (2003); Shock and Helgeson (1988)**
SO_4^{2-}	-744.63	-909.18	20.08	-235.00	874.60	-1759.70	-519.98	Papangelakis et al. (1994)
SO_4^{2-}	-744.53	-909.27	20.10	-293.00				Wagman et al. (1982)

Note: Values in bold were selected for use in this study

A.2 Temperature extrapolation of complex stability constants

A.2.1 Extrapolation method

Several methods for correlating and extrapolating these constants exist, with approaches generally limited by the amount of reliable data present. The most basic approach, requiring only a single experimental parameter (ΔH^0) is the van't Hoff equation (Thomsen, 2008), but is typically only valid over a small range of temperature:

$$\ln \beta_i (T) = \ln \beta_i(T_0) - \frac{\Delta H^0}{R_g}\left(\frac{1}{T} - \frac{1}{T_0}\right) \tag{A.2.1}$$

Conversely, the 7-parameter semi-empirical model of Shock and Helgeson (1988) is exceptionally accurate however model parameters are only available for the most common solution components. Anderson et al. (1991) report significantly simpler model based on the uncanny, near-linear relationship between $\ln \beta_i$ and $\ln \rho_w$, presented in Equation A.2.2. This model only relies on the heats of formation and heat capacities of the involved components at a reference temperature and is remarkably accurate given its simplicity.

$$\begin{aligned}\ln \beta_i (T) = \ln \beta_i^0 &- \frac{\Delta H_i^0}{R}\left(\frac{1}{T} - \frac{1}{T_{ref}}\right) \\ &+ \frac{\Delta C_p^0}{RT_{ref}(\partial \alpha_w / \partial T)_{P_{ref}}}\left(\frac{1}{T}\ln\frac{\rho_{w,ref}}{\rho_w} - \frac{\alpha_{ref}}{T}(T - T_{ref})\right)\end{aligned} \tag{A.2.2}$$

where α_w and ρ_w are the coefficient of thermal expansion and density of water respectively. In this study, water density was calculated from the model of Kell (1975) up to 150 °C:

$$\rho_w = \frac{((((p_1 T + p_2)T + p_3)T + p_4)T + p_5)T + p_6}{1 + p_7 T} \tag{A.2.3}$$

where $p_{\rho_w} = [-2.8054253e-10;\ 1.0556302e-7;\ -4.6170461e-5;\ -0.0079870401;\ 16.945176;\ 999.83952;\ 0.01687985]$ and T is in degrees Celsius. The thermal expansion of water, and its derivative, were calculated by a polynomial expansion fitted to the measured data of Anderson et al. (1991), after centring and scaling:

$$\alpha_w, \frac{d\alpha}{dT} = \sum_n p_n \left(\frac{T - \mu}{\sigma}\right)^{n-1} \tag{A.2.4}$$

Where, $p_{\alpha_w} = [9.142334e-06;\ 6.366965e-06;\ 4.390408e-05;\ 5.527157e-05;\ 4.288124e-04;\ 9.540176e-04]$, μ_{α_w} =$4.106500e+02$, $\sigma_{\alpha_w} = 7.569126e+01]$, $p_{\partial\alpha_w}$ =

$[-4.917182e{-}07; 9.988829e{-}07; 8.164462e{-}07; -9.999799e{-}07; -2.214362e{-}07; 2.960373e{-}06; 1.026225e-06; 5.435641e-06]$, $\mu_{\partial\alpha_w} = 3.981500e+02$, $\sigma_{\partial\alpha_w} = 8.291562e+01$ and T is in Kelvin. The goodness of fit over the range 25-250 °C of these polynomials is presented in Figure A.1.

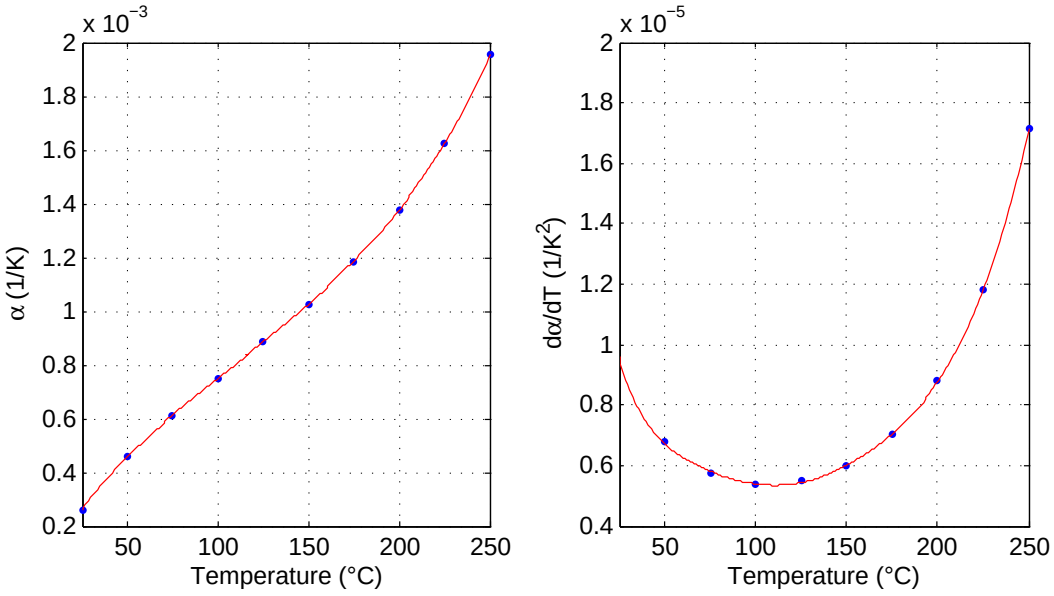

Figure A.1: Thermal expansion of water and its temperature derivative over 25-250 °C. Data is from Anderson et al. (1991), fit is from Equation A.2.4 and used in this study.

A.2.2 HSO_4^- species

The HSO_4^- species has been extensively studied in the literature and a number of stability constants over 25 - 200 °C have been reported. The rigorous study of Steyl (2012) collected a number of stability constant parameters for this species and selected the model of Dickson et al. (1990) for quantification of the stability constant over temperature. The details of this were covered in Section 5.2. This approach was adopted in this study, as discussed in the text, and as shown in Figure A.2, characterises the observed temperature effect well to 200 °C despite the large variance in experimental measurements.

A.2.3 $FeSO_4^+$ species

The $FeSO_4^+$ species has been quite thoroughly studied at 25 °C and there is a reasonable degree of confidence in the value of the stability constant. Although Papangelakis et al.

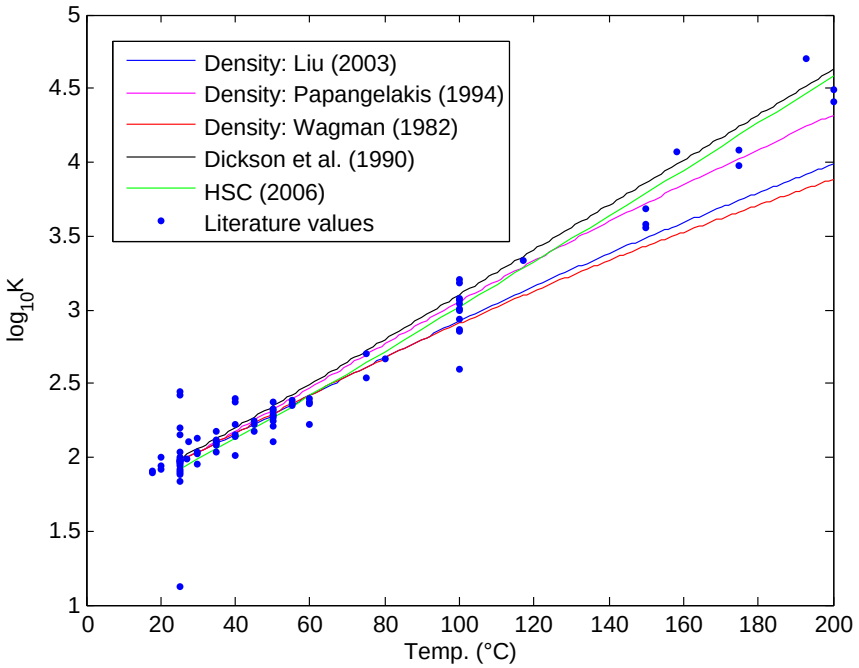

Figure A.2: Extrapolation of HSO_4^- stability constant using various available thermodynamic parameters and models in the literature. All literature data points were taken from Steyl (2012)

(1994), Liu et al. (2003) and Wagman et al. (1982) suggest slightly higher values, Stipp (1990) recommends a value of log_{10}K = 4.04 from a thorough survey of available data and was thus adopted in this study. Reported values for the heat of reaction and heat capacity data for this reaction are in reasonable agreement and, for this study, the average values of Liu et al. (2003) and Papangelakis et al. (1994) were used, specifically: ΔH_{rxn} = 26.11 kJ/mol and ΔC_p^0 = 394.4 J/mol.K. The extrapolation of these values and those reported in the literature are compared in Figure A.3 using the Density model for extrapolation.

A.2.4 $Fe(SO_4)_2^-$ species

Due to the limited amount of thermodynamic data for the $Fe(SO_4)_2^-$ species, particularly at higher temperatures, the balanced like charge method (BLCM) was used to estimate the reaction enthalpy and heat capacity. The BLCM assumes that the heat capacity is zero for isocoulombic reactions, for which the $Fe(SO_4)_2^-$ can be achieved as such:

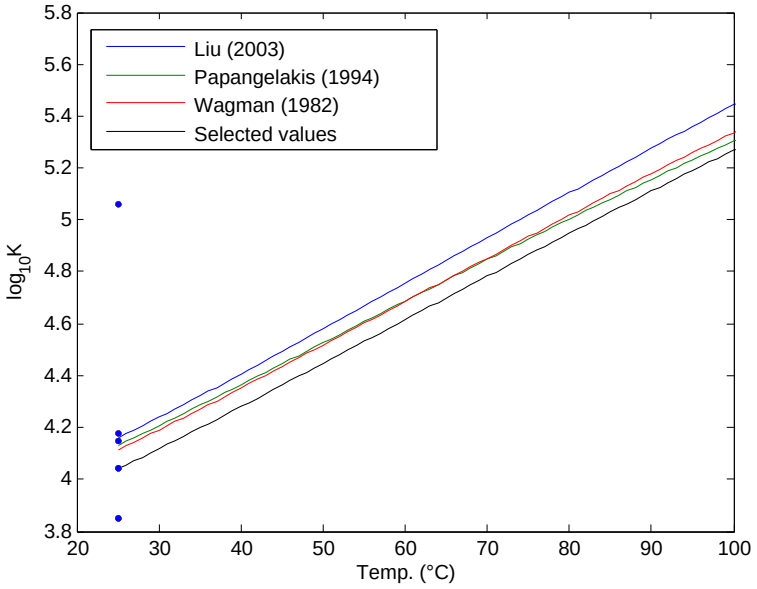

Figure A.3: Extrapolation of the $FeSO_4^+$ stability constant using various available thermodynamic parameters and models in the literature. Experimental data taken from Martell and Smith (1976).

$$FeSO_4^+ \rightleftharpoons Fe^{3+} + SO_4^2- \tag{A.2.5}$$

$$HSO_4^+ \rightleftharpoons H^+ + SO_4^2- \tag{A.2.6}$$

$$Fe^{3+} + 2\,SO_4^2- \rightleftharpoons Fe(SO_4)_2^- \tag{A.2.7}$$

$$\therefore \quad FeSO_4^+ + HSO_4^- \rightleftharpoons Fe(SO_4)_2^- + H^+ \tag{A.2.8}$$

On the basis of recommendations by Stipp (1990), the equilibrium constant was selected to be $\log_{10} K = 5.38$ and ΔH^0 was estimated from the formation enthalpies in Table A.1, the above BLCM reaction could be calculated and is presented in Table A.2. The isocoulombic reaction could then be easily extrapolated over temperature with $\Delta C^0_{p,BLCM} = 0$, and the resulting equilibrium constants used to back-calculate the ΔC^0_p for the formation of $Fe(SO_4)_2^-$ from Fe^{3+} and SO_4^{2-}. This method produced $\Delta C^0_p = 781.62$ J/mol.K using the data from both Liu et al. (2003) and Papangelakis et al. (1994) and the resulting temperature extrapolation is presented in Figure A.4.

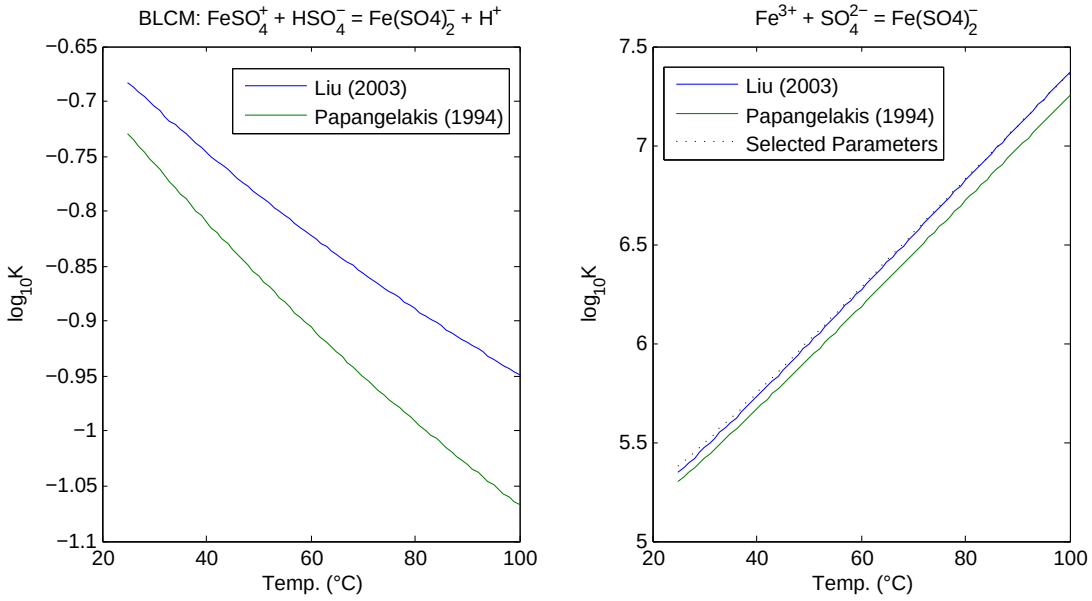

Figure A.4: BLCM method of extrapolating $Fe(SO_4)_2^-$ stability constant. Thermodynamic data from Liu et al. (2003) and Papangelakis et al. (1994) were used for comparisons. The selected value of $\log_{10}K = 5.38$ was used in the final selected values (Stipp, 1990).

Table A.2: Thermodynamic values for BLCM reaction involving $Fe(SO_4)_2^-$

Equilibrium	$\log_{10} K^0$	ΔH^0	Reference
$FeSO_4^+ + HSO_4^- \rightleftharpoons Fe(SO_4)_2^- + H^+$	-0.6825	-7.54	Liu et al. (2003)
	-0.7288	-9.61	Papangelakis et al. (1994)

A.2.5 $FeSO_3^+$ species

Only a limited amount of information regarding the $FeSO_3^+$ species thermodynamic values could be found in the literature, primarily at 25 °C, detailed in Table A.6. The standard state stability constant for $FeSO_3^+$ was extrapolated to zero ionic strength from data reported in various sources using the extrapolation method detailed in Grenthe et al. (2000) and presented in Table A.3. The resulting value of $\log_{10} K = 6.807$ was accepted as the equilibrium constant in this study. The formation heat of the $FeSO_3^+$ species has not been previously reported in the literature and was estimated using van't Hoff extrapolation of the stability constants reported by Lente and Fabian (2002) at 10 and 25 °C and the accepted values in Table A.5. The extrapolation and resulting value of $\Delta H^0_{FeSO_3^+}$ = -635.58 kJ/mol is presented in Table A.4. Unfortunately, no data on which to estimate ΔC_p^0 was available and necessitated estimation of this property in the model parameter optimisation.

Table A.3: Extrapolation of reported $FeSO_3^+$ stability constants to zero ionic strength using the method recommended by Grenthe et al. (2000)

Δz^2	-12
$\log_{10} K^0$	6.807
$\Delta\epsilon$	2.83

I (mol/kg)	$\log_{10} K$	$D = \frac{A_\phi I^{0.5}}{1 + 1.5 \cdot I^{0.5}}$	$\log_{10} K - \Delta z^2 \cdot D$	Reference
0	6.8451	0.0000	6.8451	Betterton (1993)
0.4	6.5999	0.1652	8.5827	Conklin and Hoffmann (1988a)
1	7.1931	0.2036	9.6368	Kao (1979)
1	7.3536	0.2036	9.7973	Lente and Fabian (2002)
0.1	5.4705	0.1092	6.7809	Prinsloo et al. (1997)
0.1	5.7771	0.1092	7.0875	Prinsloo et al. (1997)
0.1	5.6203	0.1092	6.9306	Kraft and Van Eldik (1989b)
1	6.8256	0.2036	9.2693	Carlyle (1971)

Table A.4: Estimation of $FeSO_3^+$ formation heat from data in Lente and Fabian (2002)

$Fe^{3+} + HSO_3^- \rightleftharpoons FeSO_3^+ + H^+$		
T (°C)	10.00	25.00
$\log K$	-0.2433	0.1300
$\ln K$	-0.5601	0.2993
T (K)	283.15	298.15
R_g(J/mol.K)	8.314	
ΔH^{rxn} (kJ/mol)	40.21572153	
$\Delta H^0_{FeSO_3^+}$ (kJ/mol)	-635.58†	

† using reported thermodynamic values in Table A.5

Table A.5: Selected values of thermodynamic heats of formation for $FeSO_3^+$ reactions

Species	ΔG_f^0 (kJ/mol)	ΔH_f^0 (kJ/mol)	C_p^0 (J/mol.K)	Reference
Fe^{3+}	-17.24	-49.58	-142.67	Liu et al. (2003)
H_2O	-237.18	-285.85	75.35	Liu et al. (2003)
H_2SO_3	-537.81	-608.81		Wagman et al. (1982)
SO_3^{2-}	-486.50	-635.5		Wagman et al. (1982)
HSO_3^-	-527.73	-626.22		Wagman et al. (1982)
$FeOH^{2+}$	-229.41	-290.80	46.15	Papangelakis et al. (1994)

A.3 Reaction model: Computational details, parameters and structure

A.3.1 Speciation model computational methodology

The calculation of solution speciation according to each species' thermodynamic equilibrium constants and activity coefficient parameters involves the solution of a set of non-linear mass action equations. The following iterative procedure, an adaptation of that proposed by Filippou et al. (1995), was adopted in order to solve the solution speciation equations. This procedure is summarised schematically in the inner section of Figure A.5. Firstly, all species are divided into primary and secondary species, with secondary species representing complexes formed from two or more primary species. Mass-action expressions are written for each of the secondary species in the form:

$$K^0_{j,sec} = \gamma_j m_j \prod_{i,pri} \gamma_i^{\nu_i} m_i^{\nu_i} \tag{A.3.1}$$

Table A.6: Summary of thermodynamic data for the $FeSO_3^+$ species

Temp. (°C)	I (mol/kg)	K	$\log_{10}$K	lnK	ΔG_r (kJ/mol)	Medium	$\Delta G_f(FeSO_3^+)$ (kJ/mol)	Reference
					$Fe^{3+} + SO_3^{2-} \rightleftharpoons FeSO_3^+$			
25	0	7.000E+06	6.845	15.761	-39.07	$NaClO_4$+$HClO_4$	-542.81	Betterton (1993)
25	0.4	3.980E+06	6.600	15.197	-37.67	$NaClO_4$+$HClO_4$	-541.41	Conklin and Hoffmann (1988a)
25	1	1.560E+07	7.193	16.563	-41.06	Not specified	-544.79	Kao (1979)
25	1	2.257E+07	7.354	16.932	-41.97	$NaClO_4$+$HClO_4$	-545.71	Lente and Fabian (2002)
25	0.1	2.955E+05	5.471	12.596	-31.22	$NaClO_4$+$HClO_4$	-534.96	Prinsloo et al. (1997)
25	0.1	5.986E+05	5.777	13.302	-32.97	$NaClO_4$+$HClO_4$	-536.71	Prinsloo et al. (1997)
25	0.1	4.171E+05	5.620	12.941	-32.08	$NaClO_4$+$HClO_4$	-535.82	Kraft and Van Eldik (1989b)
25	1	6.693E+06	6.826	15.717	-38.96	$NaClO_4$+$HClO_4$	-542.70	Carlyle (1971)
					$Fe^{3+} + HSO_3^- \rightleftharpoons FeSO_3^+ + H^+$			
Temp (°C)	I (mol/kg)	K	$\log_{10}$K	lnK	ΔG_r (kJ/mol)	Medium	$\Delta G_f(FeSO_3^+)$ (kJ/mol)	Reference
25	1	1.349E+00	0.130	0.299	-0.742	$NaClO_4$+$HClO_4$	-545.71	Lente and Fabian (2002)
25	1	4.000E-01	-0.398	-0.916	2.271319	$NaClO_4$+$HClO_4$	-542.70	Carlyle (1971)
10	1	5.711E-01	-0.243	-0.560	1.318593	$NaClO_4$+$HClO_4$	-543.65	Lente and Fabian (2002)
					$FeOH^{2+} + HSO_3^- \rightleftharpoons FeSO_3^+ + H_2O$			
Temp (°C)	I (mol/kg)	K	$\log_{10}$K	lnK	ΔG_r (kJ/mol)	Medium	$\Delta G_f(FeSO_3^+)$ (kJ/mol)	Reference
25	0.1	4.250E+02	2.628	6.052	-15.002	$NaClO_4$+$HClO_4$	-534.96	Prinsloo et al. (1997)
25	0.1	8.610E+02	2.935	6.758	-16.7521	$NaClO_4$+$HClO_4$	-536.71	Prinsloo et al. (1997)
25	0.1	6.000E+02	2.778	6.397	-15.8568	$NaClO_4$+$HClO_4$	-535.82	Kraft and Van Eldik (1989b)

These can be simply rearranged to give the molality of all secondary species as a function of primary species:

$$m_{j,sec} = K_j^0 \Gamma_j \prod_{i=pri} m_i^{\nu_i} \tag{A.3.2}$$

Here, Γ is the product of activity coefficients, obtained from the activity coefficient model, and is a function of all species' molalities and the prevailing solution conditions:

$$\Gamma_i = \prod_i \gamma_i^{\nu_i} = f\left(T, m_{pri}, m_{sec}\right) \tag{A.3.3}$$

Γ is initialized at an appropriate value and an inner iteration loop initiated. This involves a total mass balance for each anion and cation, which are usually the selected primary species:

$$m_{total} - \sum_{i=pri} \nu_i m_i - \sum_{j=sec} \nu_j m_j = 0 \tag{A.3.4}$$

$$m_{k,total} - \sum_{i,pri} \nu_i m_i - \sum_{j,sec} K_j^0 \Gamma_j \prod_{i,pri} m_i^{\nu_i} = \mathbf{F}\left[k\right] \tag{A.3.5}$$

The mass balance is then solved by a suitable non-linear equation solver (Equation A.3.6) by assuming that Γ does not vary with m_{pri} during the inner iteration loop, i.e. m_{pri} are the only variables in the optimisation. Since Γ is constant, the gradient of the objective function can easily be calculated from Equation A.3.5, detailed for the case study system in Section A.3.5, which makes the non-linear solver extremely efficient:

$$\min_{m_{pri}} \|\mathbf{F}\| \tag{A.3.6}$$

Once a solution is found in the inner iteration, m_{pri}^*, the secondary species molalities are calculated from their mass action equations (Equation A.3.2) and an updated value for Γ calculated using Equation A.3.3 and the inner loop re-initiated. The solution to the speciation problem at a given set of m_{total} concentrations is reached when the change in m_{pri}^* between successive outer iterations is below a set tolerance:

$$\|m_{pri,n}^* - m_{pri,n-1}^*\| < tol \tag{A.3.7}$$

At this solution to Equation A.3.5, the secondary species concentrations, and hence total solution speciation, can be calculated trivially from the mass-action expressions and the calculated activity coefficients. The Matlab implementation for solving the speciation calculations are detailed in the following subsections.

A.3.2 Kinetic model computational methodology

Once the thermodynamic speciation basis has been established, the kinetic aspects can be evaluated; these are represented by the outer section of the schematic in Figure A.5. The resulting solution species distribution is used to evaluate the mass transfer of $SO_{2(g)}$ into the solution phase and lastly to obtain a vector of the change in mole amounts of each of the total primary species. This rate of change of the total number of moles of each component is subsequently used to update the total primary species concentrations in each time step and is handles by a suitable ODE integration solver.

For the case study in this work, best results were obtained with the *ode15s* variable-order, multi-step, stiff solver with the maximum order reduced to 2 and all concentrations constrained to be non-negative. It was also necessary to reduce the relative tolerance on the solution to 1.5% (default is 0.1%) to prevent numerical noise originating from the non-linear speciation calculations causing significant deviations in the time dependent calculations. Final solutions at specific times were re-sampled from the ODE solution by polynomial interpolation.

Solving the system of mass action equations, with activity coefficients, is relatively time-consuming and sensitive to the initial speciation guess. To improve performance, the total primary species concentration, the resulting speciation and activity coefficients were stored in a database at each time-step and used to calibrate an empirical model of the system to aid in initial speciation guesses; discussed in Section A.3.8.

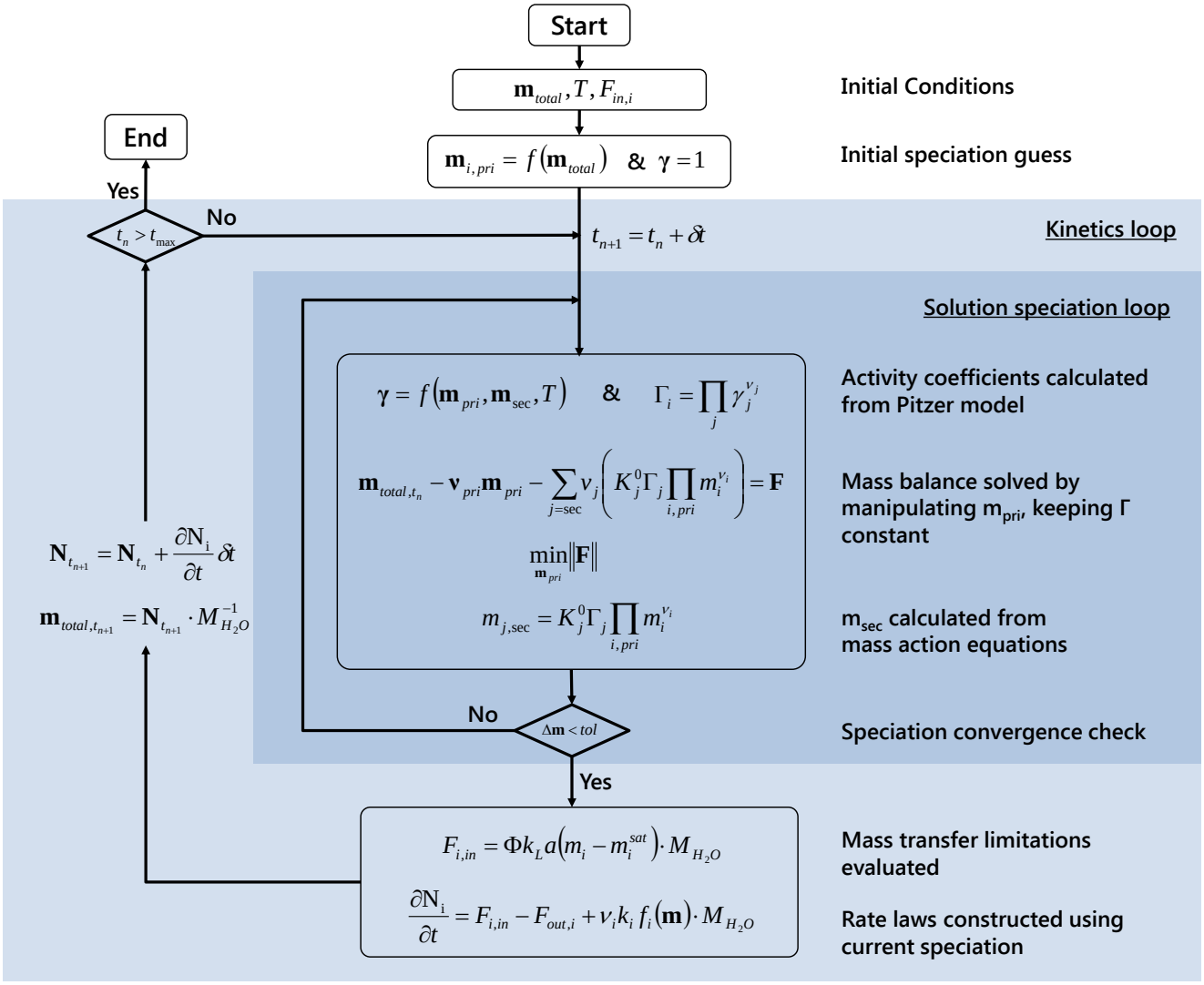

Figure A.5: Reaction model calculation methodology flow diagram. The inner speciation loop calculates the solution speciation for a specified total solution composition at temperature. The outer loop implements the differential equations derived from the reaction mechanism (including mass transfer) and updates the total solution composition via an appropriate ODE solver.

A.3.3 An efficient implementation of Pitzer's equations: pitzermodel.m

This code implements an efficient application of Pitzer's equations developed by Bea et al. (2010). A *pitzerModel* object is created by calling the following function with a file name to an Excel sheet containing all speciation data and parameters; presented in Section A.3.7.

A.3.4 Calculation of equilibrium quotients: equilib.m

This file is a helper function to *pitserModel.m* which creates *equilib* objects that contain information about each equilibria in the speciation system. This approach facilitates rapid analysis of the equilibrium constant at a specified solution composition and temperature through the activity coefficient model and the temperature extrapolation method specified in the corresponding *speciesInfo.xlsx* database file.

A.3.5 Mass action expressions: massActionEquilibFe3-H-SO4.m

While *equilib.m* above calculates the effective equilibrium quotients , required to estimate Equation A.3.2, this function cannot set up the overall mass balance, i.e., Equation A.3.5. In order to facilitate the optimal solving of the mass balance equations, the derivative with respect to speciation molality is required (assuming constant activity coefficients in the inner loop). This mass balance, and the respective derivatives were hard-coded into the *massActionEquilibFe3-H-SO4.m* function.

A.3.6 Speciation solving algorithm: solveSpeciation.m

This function implements the solving of a system of mass action expressions using the *pitzerModel* class object and a function handle to the system of mass action expressions (specified in the previous function). The function makes use of a nested non-linear solving routine, implementing the Levenberg-Marquardt (Levenberg, 1944) algorithm, inside a modified direct substitution iteration that terminated when the change in primary species molalities falls below a set tolerance.

A built-in timer is included to catch situations that do not converge within 10 seconds.

A.3.7 Species database: speciesInfo.xlsx

This Excel file database contains all species information (primary/secondary, charges) separated into cations, anions and neutral species. The list of addresses at the top of the file is used by *pitzerModel.m* to allocate parameters correctly into the appropriate matrices

to facilitate calculation of the activity coefficients. Moreover, *equilib.m* creates *equilib* objects for each equilibrium, which facilitates the calculation of equilibrium coefficients, K, at any solution composition and temperature.

numCat	6
numAn	5
numNeu	2
SPECIES	17
BINMAT	35
NEUtMAT	43
NEUaMAT	47
PHtcMAT	52
PHtaMAT	60
PStcMAT	68
PStaMAT	77
OFFSETn0n1	55

ParamTFun	dBT.n0.n1\n0 + n1.*(T-298.15)\1000

SPECIES	Charge	1*/2*	Position	Other
!H+	1	1	1	0.3
!Fe2+	2	1	2	0.3
!Fe3+	3	1	3	0.1
!Fe(OH)2+	1	0	4	0.1
!FeSO3+	1	0	5	0.3
!FeSO4+	1	0	6	1
!SO4)2-	-2	1	7	0.05
!HSO4)-	-1	0	8	0.6
!Fe(SO4)2)-	-1	0	9	2
!HSO3)-	-1	0	10	0.3
!SO3)2-	-2	1	11	0.3
!FeSO4)0	0	0	12	0.3
!SO(OH)2)0	0	0	13	0.3

Color Legend

Fe2(SO4)3-H2SO4-H2O = Measured Speciation Data
FeSO4 - gamma, phi, alpha (with MgSO4)
H2SO4-H2O - gamma, phi, alpha
SO2 - Reported in literature
FeSO4-H2SO4-H2O - Solubility
FeSO3+ - Reactive system

n0 - Parameter at 25°C

BINMAT	beta0 !SO4)2-	!HSO4)-	!Fe(SO4)2)-	!HSO3)-	!SO3)2-	beta1 !SO4)2-	!HSO4)-	!Fe(SO4)2)-	!HSO3)-	!SO3)2-	C !SO4)2-	!HSO4)-	!Fe(SO4)2)-	!HSO3)-	!SO3)2-	beta2 !SO4)2-	!HSO4)-	!Fe(SO4)2	!HSO3)-	!SO3)2-	alpha1 !SO4)2-	!HSO4)-	!Fe(SO4)2	!HSO3)-	!SO3)2-	alpha2 !SO4)2-	!HSO4)-	!Fe(SO4)2)!	!HSO3)-	!SO3)2-
!H+	0.07858	0.27109	0.00000	0.15000	0	-0.28603	-0.84615	0	0	0	0	0	0	0	0	0	0	0	0	0	2	2	2	2	2	12	12	12	12	12
!Fe2+	0.18995	0.26900	0	0	0	3.43023	1	0	0	2	0.07502	0	0	0	0	-12	0	0	0	0	1	2	2	2	2	12	12	12	12	12
!Fe3+	1.09620	0.43885	0.53151	0	0	6.21222	0	0	0	0	-0.18496	0	0	0	0	0	0	0	0	0	2	2	2	2	2	12	12	12	12	12
!Fe(OH)2+	0	0	0	0	0	0	0	0	0	0	0	0	0	0	0	0	0	0	0	0	2	2	2	2	2	12	12	12	12	12
!FeSO3)+	0	0	-2.02881	0	0	0	0	0	0	0	0	-0.22760	-0.85376	0	0	0	0	0	0	0	2	2	2	2	2	12	12	12	12	12
!FeSO4)+	0	0	0	0	0	0	0	0	0	0	0	0	0	0	0	0	0	0	0	0	2	2	2	2	2	12	12	12	12	12

NEUtMAT	!H+	!Fe2+	!Fe3+	!Fe(OH)2+	!FeSO3)+	!FeSO4)+
!FeSO4)0	-0.04249	0.03581	0	0	0	0
!SO(OH)2)0	0	0	0	0	0	0

	!SO4)2-	!HSO4)-	!Fe(SO4)2)-	!HSO3)-	!SO3)2-
!FeSO4)0	0	0	0	0	0
!SO(OH)2)0	0	0	0	0	0

PHtcMAT	!H+	!Fe2+	!Fe3+	!Fe(OH)2+	!FeSO3)+	!FeSO4)+
!H+		0	0	0	-0.86513	0
!Fe2+	0		0	0	0	0
!Fe3+	0	0		0	-1.00577	0
!Fe(OH)2+	0	0	0		0	0
!FeSO3)+	-0.86513	0	-1.00577	0		0
!FeSO4)+	0	0	0	0	0	

PHtaMAT	!SO4)2-	!HSO4)-	!Fe(SO4)2)-	!HSO3)-	!SO3)2-
!SO4)2-		0	0	0	0
!HSO4)-	0		0	0	0
!Fe(SO4)2)-	0	0		0	0
!HSO3)-	0	0	0		0
!SO3)2-	0	0	0	0	

PStcMAT	SO4)2- !H+	!Fe2+	!Fe3+	!Fe(OH)2+	!FeSO3)+	!FeSO4)+	HSO4)- !H+	!Fe2+	!Fe3+	!Fe(OH)2+	!FeSO3)+	!FeSO4)+	!Fe(SO4)2)- !H+	!Fe2+	!Fe3+	!Fe(OH)2+	!FeSO3)+	!FeSO4)+	!HSO3)- !H+	!Fe2+	!Fe3+	!Fe(OH)2+	!FeSO3)+	!FeSO4)+	!SO3)2- !H+	!Fe2+	!Fe3+	!Fe(OH)2+	!FeSO3)+	!FeSO4)+
!H+		0	0	0	0	0		0	0	0	0	0		0	0	0	0	0		0	0	0	0	0		0	0	0	0	0
!Fe2+	0		0	0	0	0	0		0	0	0	0	0		0	0	0	0	0		0	0	0	0	0		0	0	0	0
!Fe3+	0	0		0	0	0	0	0		0	0	0	0	0		0	0	0	0	0		0	0	0	0	0		0	0	0
!Fe(OH)2+	0	0	0		0	0	0	0	0		0	0	0	0	0		0	0	0	0	0		0	0	0	0	0		0	0
!FeSO3)+	0	0	0	0		0	0	0	0	0		0	0	0	0	0		0	0	0	0	0		0	0	0	0	0		0
!FeSO4)+	0	0	0	0	0		0	0	0	0	0		0	0	0	0	0		0	0	0	0	0		0	0	0	0	0	

PStaMAT	!H+ !SO4)2-	!HSO4)-	!Fe(SO4)2)-	!HSO3)-	!SO3)2-	!Fe2+ !SO4)2-	!HSO4)-	!Fe(SO4)2)-	!HSO3)-	!SO3)2-	!Fe3+ !SO4)2-	!HSO4)-	!Fe(SO4)2)-	!HSO3)-	!SO3)2-	!Fe(OH)2+ !SO4)2-	!HSO4)-	!Fe(SO4)2	!HSO3)-	!SO3)2-	!FeSO3)+ !SO4)2-	!HSO4)-	!Fe(SO4)2	!HSO3)-	!SO3)2-	!FeSO4)+ !SO4)2-	!HSO4)-	!Fe(SO4)2)!	!HSO3)-	!SO3)2-
!SO4)2-		0	0	0	0		0	0	0	0		0	0	0	0		0	0	0	0		0	0	0	0		0	0	0	0
!HSO4)-	0		0	0	0	0		0	0	0	0		0	0	0	0		0	0	0	0		0	0	0	0		0	0	0	0
!Fe(SO4)2)-	0	0		0	0	0	0		0	0	0	0		0	0	0	0		0	0	0	0	0		0	0	0	0	0		0	0
!HSO3)-	0	0	0		0	0	0	0		0	0	0	0		0	0	0	0		0	0	0	0	0		0	0	0	0		0
!SO3)2-	0	0	0	0		0	0	0	0		0	0	0	0		0	0	0	0		0	0	0	0		0	0	0	0		

n1 - 1000 x dP/dT

BINMAT	beta0 !SO4)2-	!HSO4)-	!Fe(SO4)2)-	!HSO3)-	!SO3)2-	beta1 !SO4)2-	!HSO4)-	!Fe(SO4)2)-	!HSO3)-	!SO3)2-	C !SO4)2-	!HSO4)-	!Fe(SO4)2)-	!HSO3)-	!SO3)2-	beta2 !SO4)2-	!HSO4)-	!Fe(SO4)2	!HSO3)-	!SO3)2-	alpha1 !SO4)2-	!HSO4)-	!Fe(SO4)2	!HSO3)-	!SO3)2-	alpha2 !SO4)2-	!HSO4)-	!Fe(SO4)2)!	!HSO3)-	!SO3)2-
!H+	-1.07436	-0.30035	0	0	0	-6.09603	-1.75405	0	0	0	0	0	0	0	0	0	0	0	0	0	0	0	0	0	0	0	0	0	0	0
!Fe2+	-2.01634	0.00000	0	0	0	15.04693	0	0	0	0	1.38974	0	0	0	0	0	0	0	0	0	0	0	0	0	0	0	0	0	0	0
!Fe3+	28.67722	0	0	0	0	0	0	0	0	0	-20.85999	0	0	0	0	0	0	0	0	0	0	0	0	0	0	0	0	0	0	0
!Fe(OH)2+	0	0	0	0	0	0	0	0	0	0	0	0	0	0	0	0	0	0	0	0	0	0	0	0	0	0	0	0	0	0
!FeSO3)+	0	0	0	0	0	0	0	0	0	0	0	0	0	0	0	0	0	0	0	0	0	0	0	0	0	0	0	0	0	0
!FeSO4)+	0	0	0	0	0	0	0	0	0	0	0	0	0	0	0	0	0	0	0	0	0	0	0	0	0	0	0	0	0	0

NEUtMAT	!H+	!Fe2+	!Fe3+	!Fe(OH)2+	!FeSO3)+	!FeSO4)+
!FeSO4)0	0	-1.39431	0	0	0	0
!SO(OH)2)0	0	0	0	0	0	0

	!SO4)2-	!HSO4)-	!Fe(SO4)2)-	!HSO3)-	!SO3)2-
!FeSO4)0	0	0	0	0	0
!SO(OH)2)0	0	0	0	0	0

PHtcMAT	!H+	!Fe2+	!Fe3+	!Fe(OH)2+	!FeSO3)+	!FeSO4)+
!H+		0	0	0	0	0
!Fe2+	0		0	0	0	0
!Fe3+	0	0		0	0	0
!Fe(OH)2+	0	0	0		0	0
!FeSO3)+	0	0	0	0		0
!FeSO4)+	0	0	0	0	0	

PHtaMAT	!SO4)2-	!HSO4)-	!Fe(SO4)2)-	!HSO3)-	!SO3)2-
!SO4)2-		0	0	0	0
!HSO4)-	0		0	0	0
!Fe(SO4)2)-	0	0		0	0
!HSO3)-	0	0	0		0
!SO3)2-	0	0	0	0	

PStcMAT	SO4)2- !H+	!Fe2+	!Fe3+	!Fe(OH)2+	!FeSO3)+	!FeSO4)+	HSO4)- !H+	!Fe2+	!Fe3+	!Fe(OH)2+	!FeSO3)+	!FeSO4)+	!Fe(SO4)2)- !H+	!Fe2+	!Fe3+	!Fe(OH)2+	!FeSO3)+	!FeSO4)+	!HSO3)- !H+	!Fe2+	!Fe3+	!Fe(OH)2+	!FeSO3)+	!FeSO4)+	!SO3)2- !H+	!Fe2+	!Fe3+	!Fe(OH)2+	!FeSO3)+	!FeSO4)+
!H+		0	0	0	0	0		0	0	0	0	0		0	0	0	0	0		0	0	0	0	0		0	0	0	0	0
!Fe2+	0		0	0	0	0	0		0	0	0	0	0		0	0	0	0	0		0	0	0	0	0		0	0	0	0
!Fe3+	0	0		0	0	0	0	0		0	0	0	0	0		0	0	0	0	0		0	0	0	0	0		0	0	0
!Fe(OH)2+	0	0	0		0	0	0	0	0		0	0	0	0	0		0	0	0	0	0		0	0	0	0	0		0	0
!FeSO3)+	0	0	0	0		0	0	0	0	0		0	0	0	0	0		0	0	0	0	0		0	0	0	0	0		0
!FeSO4)+	0	0	0	0	0		0	0	0	0	0		0	0	0	0	0		0	0	0	0	0		0	0	0	0	0	

PStaMAT	!H+ !SO4)2-	!HSO4)-	!Fe(SO4)2)-	!HSO3)-	!SO3)2-	!Fe2+ !SO4)2-	!HSO4)-	!Fe(SO4)2)-	!HSO3)-	!SO3)2-	!Fe3+ !SO4)2-	!HSO4)-	!Fe(SO4)2)-	!HSO3)-	!SO3)2-	!Fe(OH)2+ !SO4)2-	!HSO4)-	!Fe(SO4)2	!HSO3)-	!SO3)2-	!FeSO3)+ !SO4)2-	!HSO4)-	!Fe(SO4)2	!HSO3)-	!SO3)2-	!FeSO4)+ !SO4)2-	!HSO4)-	!Fe(SO4)2)!	!HSO3)-	!SO3)2-
!SO4)2-		0	0	0	0		0	0	0	0		0	0	0	0		0	0	0	0		0	0	0	0		0	0	0	0
!HSO4)-	0		0	0	0	0		0	0	0	0		0	0	0	0		0	0	0	0		0	0	0	0		0	0	0	0
!Fe(SO4)2)-	0	0		0	0	0	0		0	0	0	0		0	0	0	0		0	0	0	0	0		0	0	0	0	0		0	0
!HSO3)-	0	0	0		0	0	0	0		0	0	0	0		0	0	0	0		0	0	0	0	0		0	0	0	0		0
!SO3)2-	0	0	0	0		0	0	0	0		0	0	0	0		0	0	0	0		0	0	0	0		0	0	0	0		

Num Equilibria	10
Start	6
Length	9

Equilibria #1	1	2	6		
Equation	**[H]+ + [SO4]2- = [HSO4]-**				
Numerator	8				
Denominator	1	7			
NumeratorPwr	1				
DenominatorPwr	1	1			
lnK0Equation	@(T,p) log(10.^(-(p(1) + p(2)./T + p(3).*log(T) + p(4).*T + p(5).*T.^2)))				
lnK0Pars	5.6271E+02	-1.3274E+04	-1.0252E+02	2.4775E-01	-1.1170E-04

Equilibria #2	2	3	3		
Equation	**[Fe]3+ + [SO42-] = [FeSO4]+**				
Numerator	6				
Denominator	3	7			
NumeratorPwr	1				
DenominatorPwr	1	1			
lnK0Equation	@(T,p) densityModel(p(1),p(2),p(3),298.15,T)				
lnK0Pars	9.30244	26.11000	394.40000		

Equilibria #3	1	2	3		
Equation	**[Fe]3+ + 2[SO42-] = [Fe(SO4)2]-**				
Numerator	9				
Denominator	3	7			
NumeratorPwr	1				
DenominatorPwr	1	2			
lnK0Equation	@(T,p) densityModel(p(1),p(2),p(3),298.15,T)				
lnK0Pars	12.324	38.872	781.625		

Equilibria #4	2	2	3		
Equation	**[Fe]3+ + 2H2O = [Fe(OH)2]+ + 2[H]+**				
Numerator	4	1			
Denominator	3	-1			
NumeratorPwr	1	2			
DenominatorPwr	1	2			
lnK0Equation	@(T,p) densityModel(p(1),p(2),p(3),298.15,T)				
lnK0Pars	-2.8476	15.3258	0.0000		

Equilibria #5	2	2	3		
Equation	**[SO3]2- + 2[H]+ = [H2O.SO2]**				
Numerator	13	-1			
Denominator	11	1			
NumeratorPwr	1	1			
DenominatorPwr	1	2			
lnK0Equation	@(T,p) densityModel(p(1),p(2),p(3),298.15,T)				
lnK0Pars	20.790	21.450	534.000		

Equilibria #6	1	2	3		
Equation	**[SO3]2- + [H]+ = [HSO3]-**				
Numerator	10				
Denominator	11	1			
NumeratorPwr	1				
DenominatorPwr	1	1			
lnK0Equation	@(T,p) densityModel(p(1),p(2),p(3),298.15,T)				
lnK0Pars	16.520	3.650	262.000		

Equilibria #7	1	2	3		
Equation	**[Fe]3+ + [SO3]2- = [FeSO3]+**				
Numerator	5				
Denominator	11	3			
NumeratorPwr	1				
DenominatorPwr	1	1			
lnK0Equation	@(T,p) densityModel(p(1),p(2),p(3),298.15,T)				
lnK0Pars	21.500	42.600	150.390		

Equilibria #8	1	2	3		
Equation	**[Fe]2+ + [SO4]2- = [FeSO4]0**				
Numerator	12				
Denominator	2	7			
NumeratorPwr	1				
DenominatorPwr	1	1			
lnK0Equation	@(T,p) densityModel(p(1),p(2),p(3),298.15,T)				
lnK0Pars	3.4539	15.0000	376.58		

Equilibria #9	2	1	3		
Equation	**[FeSO4]0 + 7H2O = FeSO4.7H2O(s)**				
Numerator	12	-1			
Denominator	7				
NumeratorPwr	1	7			
DenominatorPwr	0	0			
lnK0Equation	@(T,p) p(1) + p(2)/1000.*T + p(3)*100000.*T.^-2				
lnK0Pars	23.9438	-41.7097	-11.6801		

Equilibria #10	2	1	3		
Equation	**[FeSO4]0 + H2O = FeSO4.H2O(s)**				
Numerator	12	-1			
Denominator	7				
NumeratorPwr	1	1			
DenominatorPwr	0	0			
lnK0Equation	@(T,p) p(1) + p(2)/1000.*T + p(3)*100000.*T.^-2				
lnK0Pars	7.7552	-24.6195	0.72803		

A.3.8 Initial guess function: mPriInitNN.m

This function represents a Neural Network that facilitates an approximate, initial guess of the primary species concentration and all species' activity coefficients by accepting an input consisting of a vector of the system temperature and total component concentrations, represented by the following expression:

$$[\vec{m_{pri}}, \vec{\gamma}] = f_{NN}\left(\left[T, [\mathrm{H}^+]_{tot.}, [\mathrm{Fe}^{2+}]_{tot.}, [\mathrm{Fe}^{3+}]_{tot.}, [\mathrm{SO}_4^{2}-]_{tot.}, [\mathrm{SO}_3^{2}-]_{tot.}\right]\right) \tag{A.3.8}$$

A feed-forward neural network, f_{NN}, comprising of 6 input neurons (temperature and the 5 total species concentrations) and 18 output neurons (5 primary species and 13 activity coefficients) was selected due to its flexible structure. It was found that a hidden layer comprising of 7 neurons provided an excellent fit of the speciation data without significant over-fitting. The network weights and biases were optimised using the Levenberg-Marquardt algorithm (Levenberg, 1944) with Bayesian Regularisation (MATLAB, 2014). This function was calibrated iteratively from the results of the thermodynamic and kinetic model, initially assuming constant initial guesses, and provides an excellent and robust means of initialising the speciation of the system and significantly decreases the computational time of solving the complex system of equations.

A.3.9 Kinetic model equations: feIIIRedBatch.m

The final computational aspect, representing the outer loop in Figure A.5, involves the evaluation of the rate-limiting step and the corresponding gradient in the total moles in the system, i.e., Equations 7.1.11 to 7.1.14. Given the initial conditions, an appropriate numerical ODE solver then solves the system over time.

Appendix B

Spectroscopy

B.1 Raman spectroscopy

B.1.1 Raman curve fitting

Figure B.1 presents a screen-shot of the Matlab implemented GUI for subtracting Raman backgrounds using various methods and fitting a series of Gaussian-Lorenzian curves to measured Raman spectra. The application also facilities the constraint of various band parameters to enable expert user intervention.

Typically, for the spectra obtained in this study, Piecewise Cubic Hermite Interpolating Polynomials (PCHIP) (MATLAB, 2014) were used to model the Raman background, shown green in Figure B.1. Parts of the spectra, with no visible bands, i.e., 200 cm^{-1}, 700-800 cm^{-1} and 1300 cm^{-1} were manually selected for the and used to fit the PCHIP function.

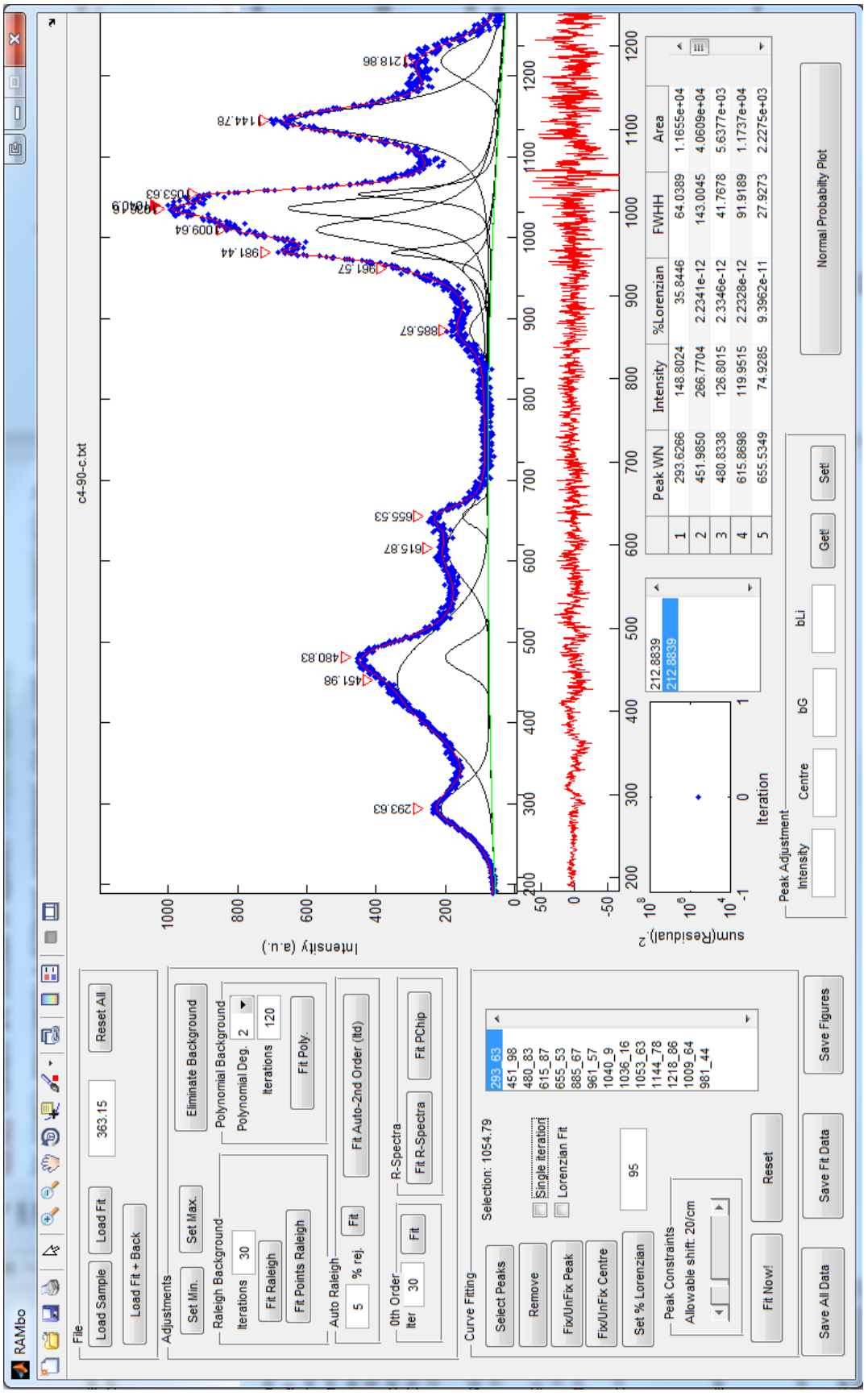

Figure B.1: Screenshot of Matlab Curve-fitting GUI

B.1.2 Calculation of relative molal scattering coefficients

Relative molal scattering coefficients (or J-values) to a common, inert species, permit the calculation of species concentrations from the integrated intensities of the Raman bands and are defined as:

$$J_{i,\mathrm{ClO_4}} = \frac{A_i}{m_i} \cdot \frac{m_{\mathrm{ClO_4}}}{A_{\mathrm{ClO_4}}} \tag{B.1.1}$$

where A_i and m_i are the integrated area and concentration of the band attributed to species i respectively. These J-values account for the variation in polarizability tensors for different molecules' normal modes and physically, with reference to the sulfate molecule, the greater the structural difference from the tetrahedral SO_4^{2-} moiety due to CIP formation, the greater the expected variation in J-value from that of unassociated sulfate. Typically, provided that perchlorate is added to the analysed solution in a known quantity, the concentration of solution species can be obtained from the integrated Raman intensity of peaks associated with a particular vibration of a particular species. However, since all forms of sulfate (associated and unassociated) have a Raman response, internal standardisation is unnecessary if all J-values are known since all perchlorate terms disappear in expressions for the fraction of sulfate in each species.

Figure B.2 shows the Raman spectrum of pure $NaClO_4$ with its characteristic four bands, including a low-frequency shoulder of the ν_1-ClO_4^- mode. In all instances, the integrated area of the perchlorate band was taken as the sum of the main ν_1 band at ca. 933 cm^{-1} and the low-frequency shoulder at ca. 925 cm^{-1}.

B.1.2.1 Sulfate and bisulfate J-values

For the calculation of sulfate and bisulfate J-values, several solutions of $(NH_4)_2SO_4$ and H_2SO_4 were used. The J-value for sulfate was determined to be 0.7852 from spectra of a 1.68 mol/kg $(NH_4)_2SO_4$ solution at 25, 50 and 90 °C. This similar to J-values for sulfate in the literature of 0.637 (Dawson et al., 1986), 0.778 (Rudolph, 1996) and 0.792 (Eysel et al., 1988). A Raman spectrum of the solution is shown in the lower part of Figure B.3. The bisulfate J-value was determined from two solutions containing H_2SO_4 with added HCl to minimise the sulfate content. The best results were observed at 90 °C where sulfate was only present in minor quantities. The resulting J-value for bisulfate was found to be 0.7012 which is similar to reported values, namely, 0.655 (Dawson et al., 1986), 0.676 (Lund Myhre et al., 2003) and 0.589 (Rudolph, 1996). Differences in these cases can likely be attributed to the use of ammonium hydrogen sulfate instead of sulfuric acid as well as different concentrations used in each of the studies.

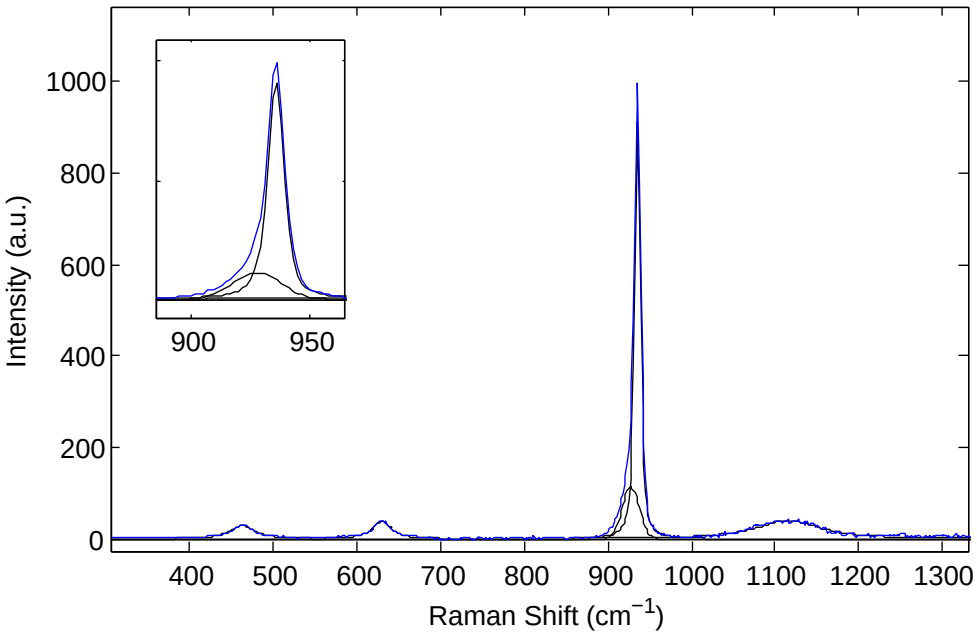

Figure B.2: Raman spectra of 1.5 mol/kg $NaClO_4$ at 25°C. Inset shows the low frequency perchlorate shoulder

B.1.2.2 Ferric species J-values

From the quantum calculations and UV spectra in the text (Chapter 4), it was determined that at least two ferric sulfato CIP species are present in the $Fe_2(SO_4)_3$ solutions analysed in this study, $FeSO_4^+$ and $Fe(SO_4)_2^-$. Since these species cannot be completely isolated from one another in pure sulfate solutions, the estimation of their J-values had to be performed simultaneously from solutions of $Fe_2(SO_4)_3$ with added $NaClO_4$. Three solutions of pure $Fe_2(SO_4)_3$ and two solutions with added H_2SO_4 (i.e., similar to solutions A3, A4 and A5 and C3 and C6 from the perchlorate free spectra) were used to determine J-values of the two ferric sulfato species.

The total sulfate complexed with Fe(III) was calculated by difference between the total sulfate and concentrations of sulfate and bisulfate determined using their known J-values from the previous paragraph.

$$[SO_4]_{Fe\cdot CIP} = [SO_4^{2-}{}_{Total}] - [SO_4^{2-}] - [HSO_4^-] \tag{B.1.2}$$

The ferric sulfato species' J-values were then determined by a constrained minimisation of the function F (Equation B.1.5). A total iron mass balance was imposed using an

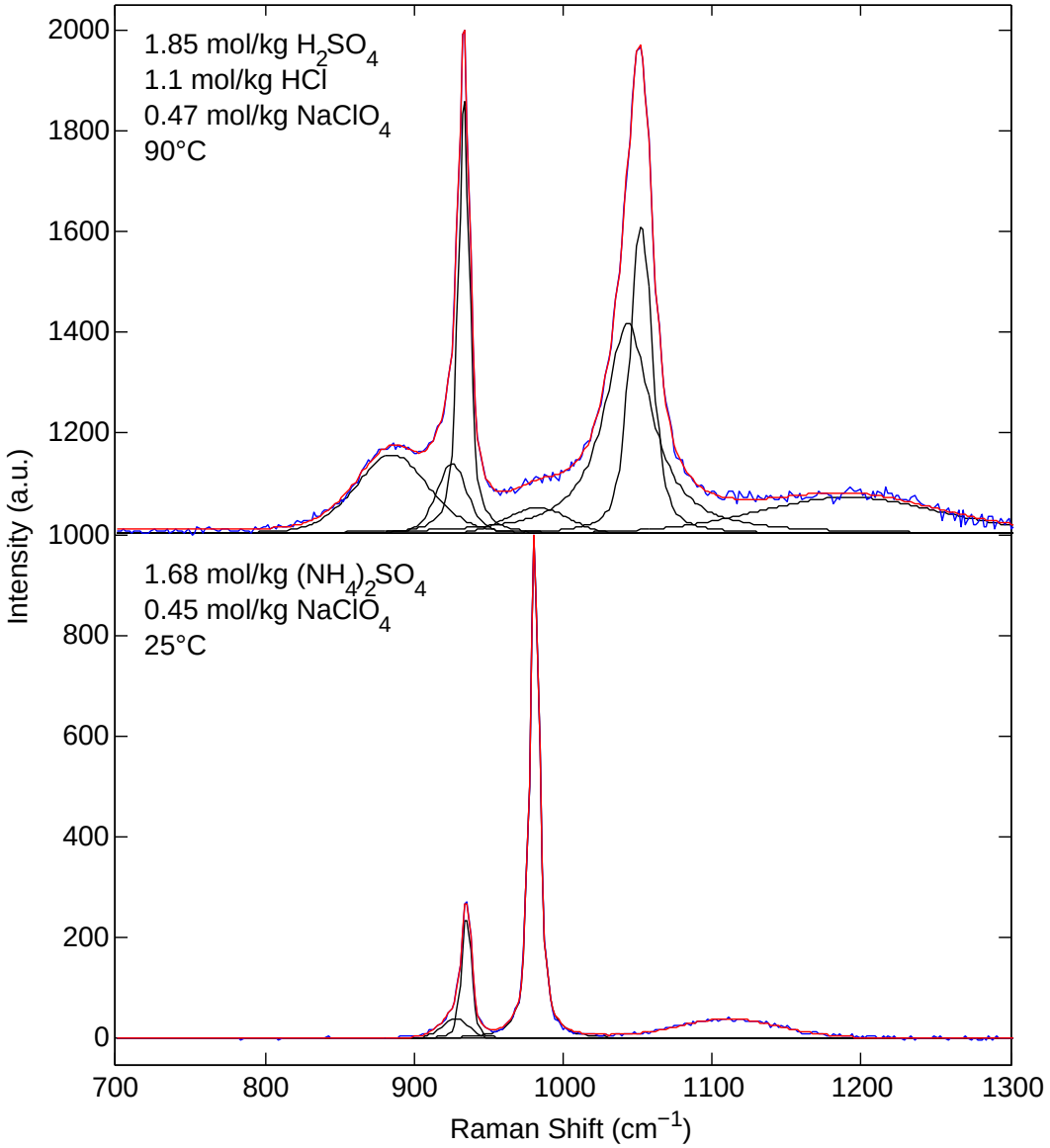

Figure B.3: Raman spectra of $(NH_4)_2SO_4$ and H_2SO_4 solutions with added $NaClO_4$

inequality (Equation B.1.5) to account for the fact that neither the concentrations of $Fe^{3+}_{(aq)}$ nor $Fe(OH)^{3-n}_{n(aq)}$ could be directly extracted from the Raman data. In this formulation, the ferric sulfato species' J-values represent a plane in the scaled-integrated-intensity-space of the 1005 cm^{-1} and 1035 cm^{-1} bands. This optimal plane is shown in Figure B.4.

$$\min \sum_i F_i^2 \tag{B.1.3}$$

$$F_i = [SO_4]_{Fe \cdot CIP} - \left[\frac{A_{FeSO_4^+}}{J_{FeSO_4^+}} \cdot -2 \frac{A_{Fe(SO_4)_2^-}}{J_{Fe(SO_4)_2^-}} \right] \cdot \frac{m_{ClO_4-}}{A_{ClO_4-}} \tag{B.1.4}$$

$$\text{s.t. } [Fe^{3+}]_{Total} \geq [FeSO_4^+] + [Fe(SO_4)_2^-] \tag{B.1.5}$$

$$\tag{B.1.6}$$

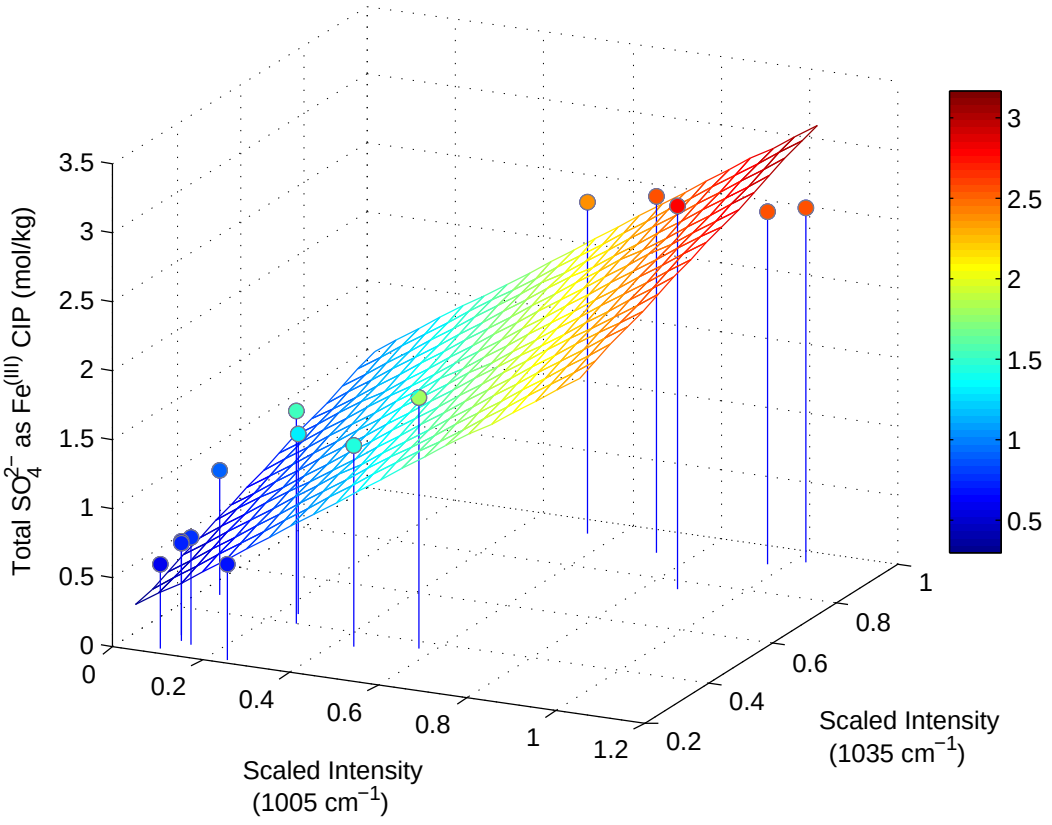

Figure B.4: Ferric sulfato J-value determination. Integrated intensities have been scaled by the ratio of perchlorate peak area to perchlorate concentration in each solution. The 1035 cm^{-1} and 1035 cm^{-1} bands represent the $FeSO_4^+$ and $Fe(SO_4)_2^-$ species respectively

B.1.2.3 Sensitivity analysis of J-values

Given the approach in calibrating the ferric sulfato species' J-values using solutions with added $NaClO_4$ as an internal standard, it was necessary to determine the sensitivity of the calculated values. To this end, a sensitivity analysis was performed where all combinations of the $J_{FeSO_4^+}$ and $J_{Fe(SO_4)_2^-}$ were varied by 20% of their calculated values and the resulting speciation determined. This analysis is presented in Figure B.5. This shows that the variation on overall speciation is significantly less than the 20 % variation on the input and the main speciation trends are still present. This lack of sensitivity provides a good confidence in the selected J-values and the method in which they were calculated.

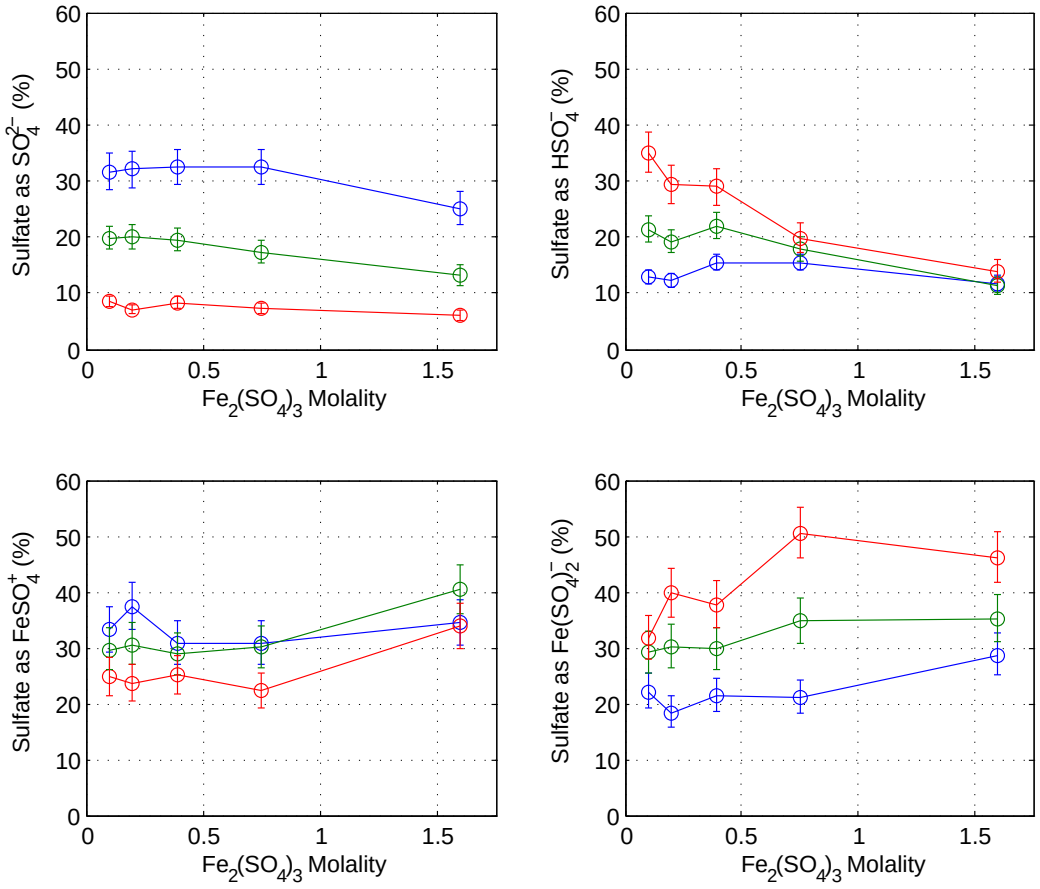

Figure B.5: Sensitivity analysis on $FeSO_4^+$ and $Fe(SO_4)_2^-$ species J-value. Both the $J_{FeSO_4^+}$ and $J_{Fe(SO_4)_2^-}$ were varied up to $\pm$20% of their calculated values and the error bar limits represent the *maximum* variation in the resulting speciation calculations.

B.1.3 Tabulated measured speciation data

Tables B.1 - B.5 present the measured speciation data from the Raman spectra measured in this study and the appropriate data treatment discussed in the text. J-values as per Table 4.4 were used and these data are presented graphically in the various figures in the text.

Table B.1: Sulfate speciation in H_2SO_4 solutions - Samples H1-H4

Sample	Temperature °C	H_2SO_4 mol/kg	$NaClO_4$ mol/kg	$\alpha_{SO_4^{2-}}$
H1	25	0.50	0.00	0.235
H2	25	1.03	0.00	0.231
H3	25	2.13	0.00	0.255
H4	25	4.27	0.00	0.299
H1	50	0.50	0.00	0.127
H2	50	1.03	0.00	0.125
H3	50	2.13	0.00	0.159
H4	50	4.27	0.00	0.210
H1	90	0.50	0.00	0.035
H2	90	1.03	0.00	0.069
H3	90	2.13	0.00	0.065
H4	90	4.27	0.00	0.106
LH3	25	2.13	0.47	0.257
LH4	25	4.27	0.47	0.288
LH3	50	2.13	0.47	0.184
LH4	50	4.27	0.47	0.182
LH3	90	2.13	0.47	0.083
LH4	90	4.27	0.47	0.115

Table B.2: Sulfate speciation in $FeSO_4$ solutions - Samples E1-E4

Sample	Temperature °C	$FeSO_4$ mol/kg	$NaClO_4$ mol/kg	$\alpha_{FeSO_4^0}$
E1	25	0.21	0.00	0.096
E2	25	0.40	0.00	0.090
E3	25	0.80	0.00	0.108
E4	25	1.76	0.00	0.134
E4	50	1.76	0.00	0.190
E4	90	1.76	0.00	0.265

Table B.3: Sulfate speciation in $Fe_2(SO_4)_3$ solutions - Samples A1-A5

Sample	Temp. °C	$Fe_2(SO_4)_3$ mol/kg	$NaClO_4$ mol/kg	$\alpha_{SO_4^{2-}}$	$\alpha_{HSO_4^-}$	$\alpha_{FeSO_4^+}$	$\alpha_{Fe(SO_4)_2^-}$
A1	25	0.10	0.00	0.316	0.132	0.331	0.221
A2	25	0.20	0.00	0.320	0.124	0.373	0.184
A3	25	0.39	0.00	0.324	0.157	0.306	0.213
A4	25	0.75	0.00	0.325	0.157	0.307	0.211
A5	25	1.60	0.00	0.251	0.120	0.343	0.286
A1	50	0.10	0.00	0.197	0.216	0.296	0.291
A2	50	0.20	0.00	0.199	0.195	0.305	0.300
A3	50	0.39	0.00	0.195	0.222	0.287	0.296
A4	50	0.75	0.00	0.172	0.181	0.300	0.347
A5	50	1.60	0.00	0.131	0.114	0.404	0.351
A1	90	0.10	0.00	0.084	0.354	0.246	0.316
A2	90	0.20	0.00	0.071	0.296	0.236	0.397
A3	90	0.39	0.00	0.083	0.293	0.249	0.375
A4	90	0.75	0.00	0.073	0.201	0.222	0.504
A5	90	1.60	0.00	0.059	0.142	0.338	0.461
LA3	25	0.39	0.50	0.276	0.165	0.332	0.226
LA4	25	0.75	0.48	0.263	0.197	0.286	0.253
LA5	25	1.60	0.47	0.194	0.204	0.276	0.326
LA3	50	0.39	0.50	0.215	0.174	0.330	0.281
LA4	50	0.75	0.48	0.166	0.223	0.296	0.315
LA5	50	1.60	0.47	0.116	0.207	0.305	0.372
LA3	90	0.39	0.50	0.060	0.312	0.215	0.413
LA4	90	0.75	0.48	0.086	0.275	0.206	0.433
LA5	90	1.60	0.47	0.082	0.151	0.406	0.361

Table B.4: Sulfate speciation in $Fe_2(SO_4)_3$-H_2SO_4 solutions - Samples C1-C6

Sample	Temperature °C	$Fe_2(SO_4)_3$ mol/kg	H_2SO_4 mol/kg	$NaClO_4$ mol/kg	$\alpha_{SO_4^{2-}}$	$\alpha_{HSO_4^-}$	$\alpha_{FeSO_4^+}$	$\alpha_{Fe(SO_4)_2^-}$
C1	25	0.29	0.28	0.00	0.318	0.372	0.137	0.173
C2	25	0.27	0.48	0.00	0.307	0.383	0.209	0.101
C3	25	0.28	0.81	0.00	0.239	0.364	0.168	0.228
C4	25	1.12	0.23	0.00	0.267	0.313	0.117	0.303
C5	25	1.14	0.48	0.00	0.285	0.295	0.184	0.236
C6	25	1.19	0.76	0.00	0.275	0.279	0.230	0.216
C1	50	0.29	0.28	0.00	0.166	0.342	0.241	0.251
C2	50	0.27	0.48	0.00	0.168	0.421	0.225	0.186
C3	50	0.28	0.81	0.00	0.155	0.427	0.195	0.222
C4	50	1.12	0.23	0.00	0.162	0.273	0.154	0.411
C5	50	1.14	0.48	0.00	0.158	0.244	0.271	0.327
C6	50	1.19	0.76	0.00	0.134	0.203	0.281	0.381
C1	90	0.29	0.28	0.00	0.089	0.484	0.190	0.237
C2	90	0.27	0.48	0.00	0.073	0.596	0.162	0.170
C3	90	0.28	0.81	0.00	0.063	0.556	0.197	0.184
C4	90	1.12	0.23	0.00	0.071	0.253	0.190	0.486
C5	90	1.14	0.48	0.00	0.060	0.296	0.177	0.467
C6	90	1.19	0.76	0.00	0.065	0.334	0.177	0.424
LC3	25	0.27	0.85	0.48	0.267	0.367	0.243	0.123
LC6	25	1.07	0.88	0.47	0.186	0.387	0.124	0.303
LC3	50	0.27	0.85	0.48	0.174	0.517	0.183	0.126
LC6	50	1.07	0.88	0.47	0.151	0.255	0.310	0.284
LC3	90	0.27	0.85	0.48	0.109	0.508	0.328	0.055
LC6	90	1.07	0.88	0.47	0.067	0.235	0.247	0.451

Table B.5: Sulfate speciation in $Fe_2(SO_4)_3$-$FeSO_4$-H_2SO_4 solutions - Samples D1-D5

Sample	Temperature °C	$Fe_2(SO_4)_3$ mol/kg	H_2SO_4 mol/kg	$FeSO_4$ mol/kg	$NaClO_4$ mol/kg	$\alpha_{SO_4^{2-}}$	$\alpha_{HSO_4^-}$	$\alpha_{FeSO_4^+}$	$\alpha_{Fe(SO_4)_2^-}$	$\alpha_{FeSO_4^0}$
D1	25	0.00	0.19	1.69	0.00	0.674	0.136	0.042	0.000	0.148
D2	25	0.18	0.20	1.39	0.00	0.561	0.181	0.089	0.028	0.141
D3	25	0.39	0.20	0.92	0.00	0.444	0.214	0.144	0.106	0.092
D4	25	0.60	0.18	0.46	0.00	0.411	0.220	0.197	0.172	0.000
D5	25	0.81	0.35	0.00	0.00	0.356	0.212	0.230	0.202	0.000
D1	50	0.00	0.19	1.69	0.00	0.568	0.163	0.084	0.040	0.145
D2	50	0.18	0.20	1.39	0.00	0.455	0.196	0.110	0.133	0.106
D3	50	0.39	0.20	0.92	0.00	0.327	0.226	0.162	0.251	0.034
D4	50	0.60	0.18	0.46	0.00	0.211	0.233	0.138	0.418	0.000
D5	50	0.81	0.35	0.00	0.00	0.187	0.227	0.161	0.425	0.000
D1	90	0.00	0.19	1.69	0.00	0.499	0.191	0.082	0.128	0.099
D2	90	0.18	0.20	1.39	0.00	0.355	0.307	0.096	0.177	0.064
D3	90	0.39	0.20	0.92	0.00	0.189	0.286	0.174	0.334	0.017
D4	90	0.60	0.18	0.46	0.00	0.131	0.310	0.174	0.386	0.000
D5	90	0.81	0.35	0.00	0.00	0.125	0.257	0.222	0.396	0.000

B.1.4 Fitted Raman band component parameters

Figures B.6 - B.9 present the fitted band parameters, i.e., centre wavenumbers and FWHH, as a function of temperature and concentration for the H_2SO_4, $FeSO_4$, $Fe_2(SO_4)_3$ and $Fe_2(SO_4)_3$-H_2SO_4 systems respectively.

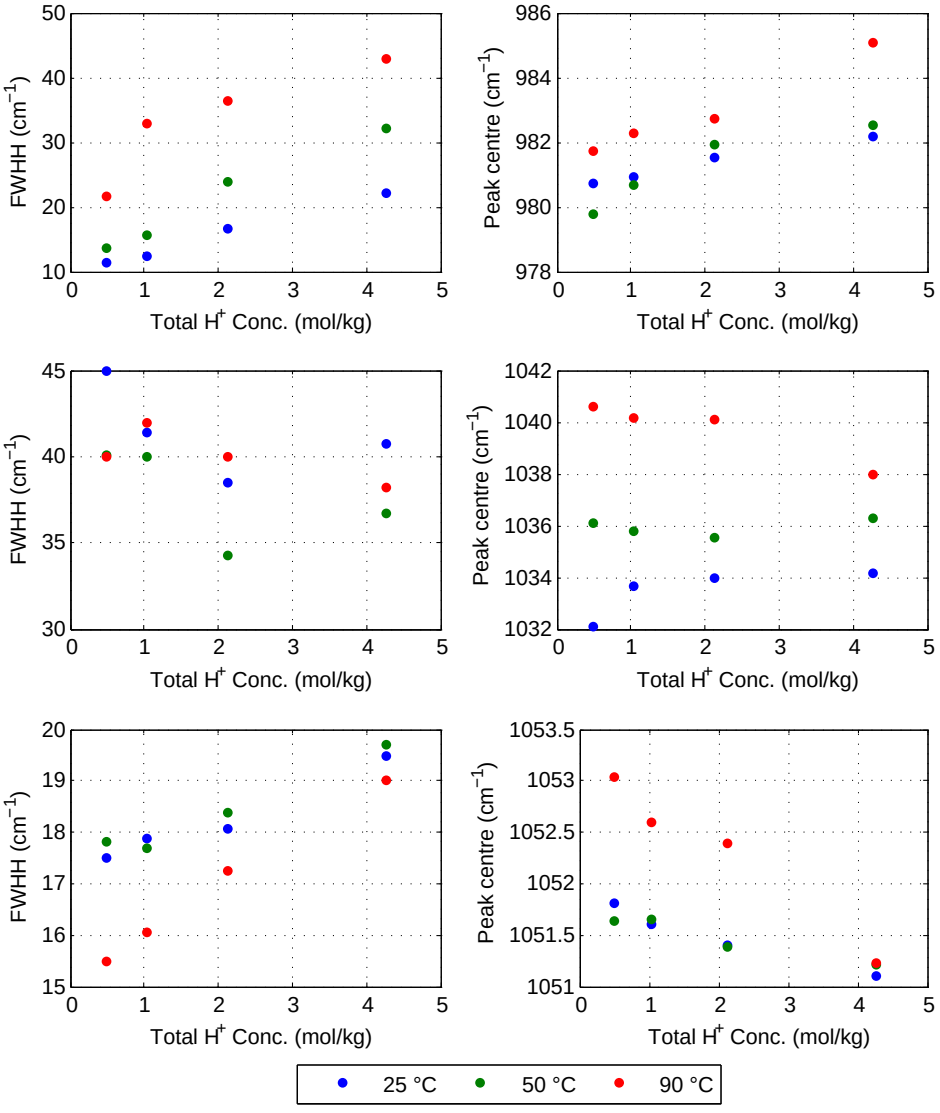

Figure B.6: Variation in peak centres and FWHH for H_2SO_4 solution Raman spectra as a function of concentration and temperature. Solution labels are H1-H4 for reference with Table 4.3

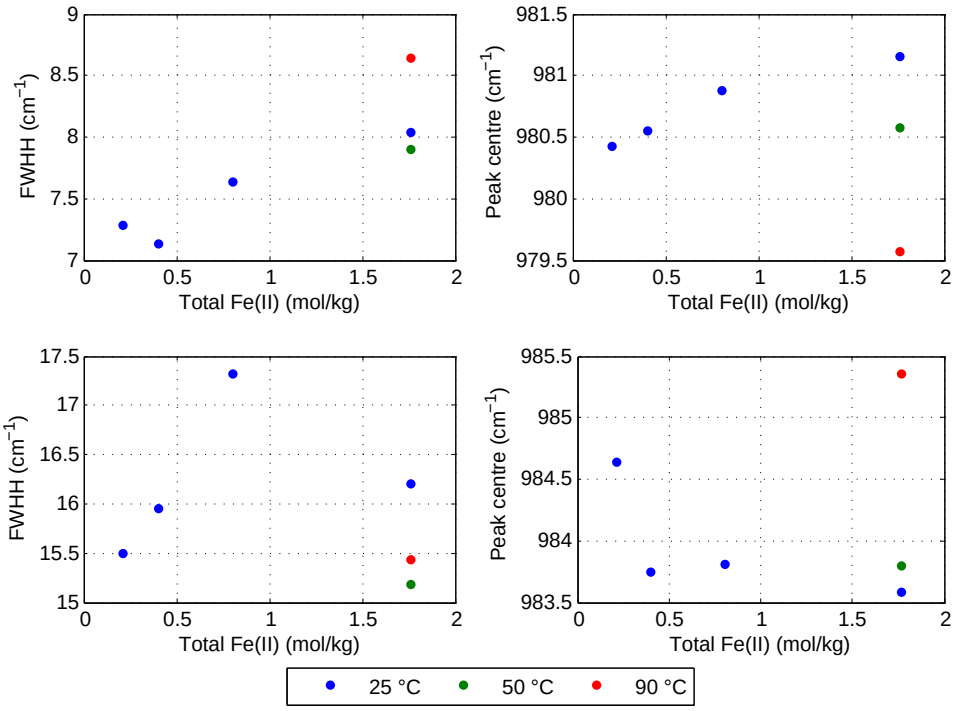

Figure B.7: Variation in peak centres and FWHH for $FeSO_4$ solution Raman spectra as a function of concentration and temperature. Solution labels are E1-E4 for reference with Table 4.3

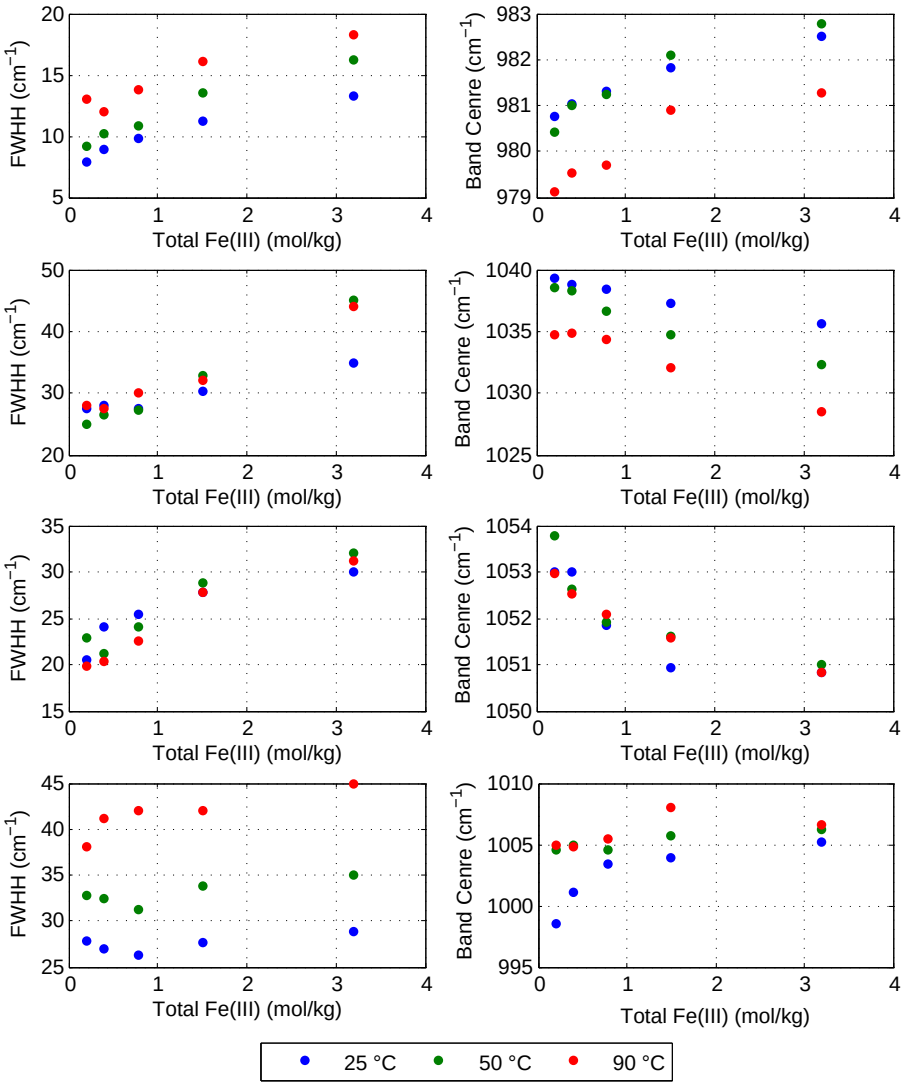

Figure B.8: Variation in peak centres and FWHH for $Fe_2(SO_4)_3$ solution Raman spectra as a function of concentration and temperature. Solution labels are A1-A5 for reference with Table 4.3

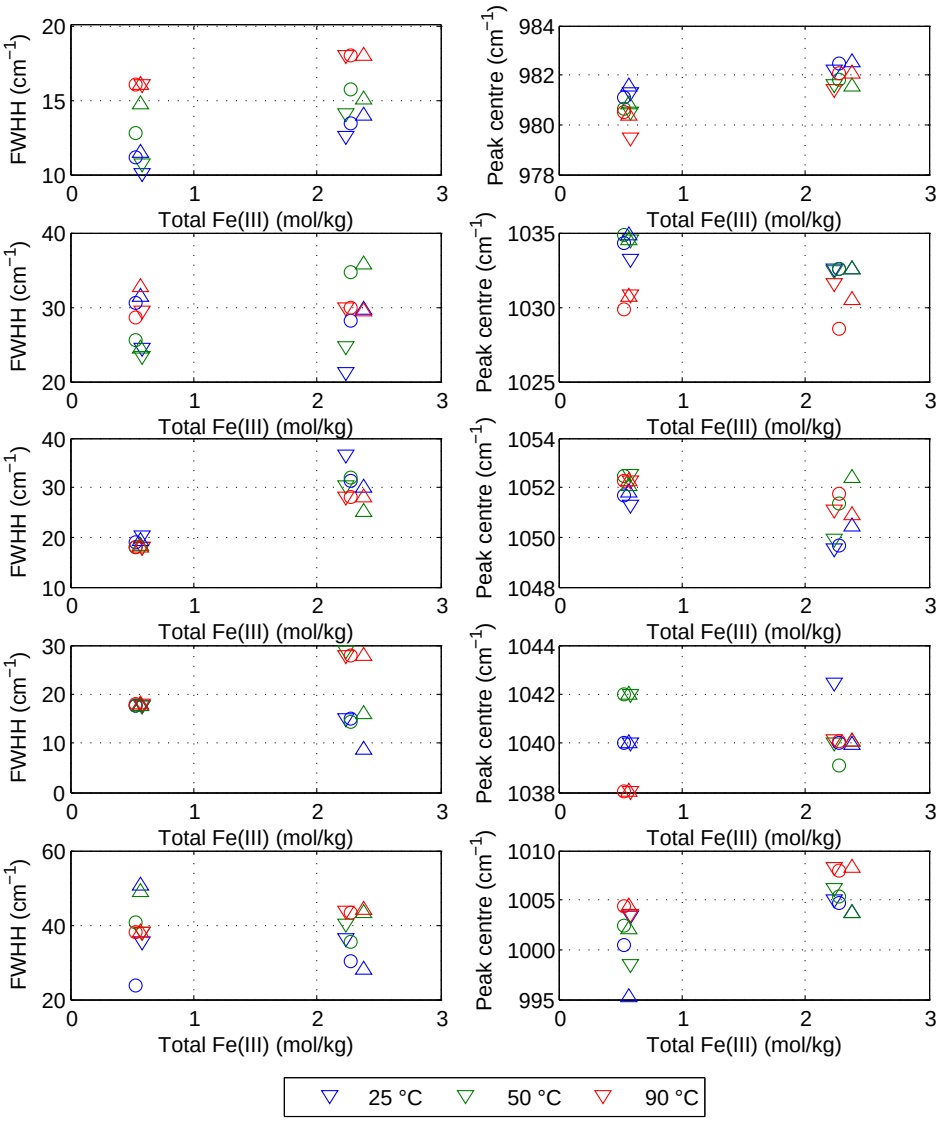

Figure B.9: Variation in peak centres and FWHH for $Fe_2(SO_4)_3$-H_2SO_4 solution Raman spectra as a function of concentration and temperature. Solution labels are C1-C6 for reference with Table 4.3. Acid concentrations: $\bigtriangledown$ = 0.5 mol/kg H^+, $\bigcirc$ = 1.0 mol/kg H^+, $\bigtriangleup$ = 1.5 mol/kg H^+.

B.1.5 Raman temperature cell design drawing

A detailed design drawing for the Raman temperature cell is presented below.

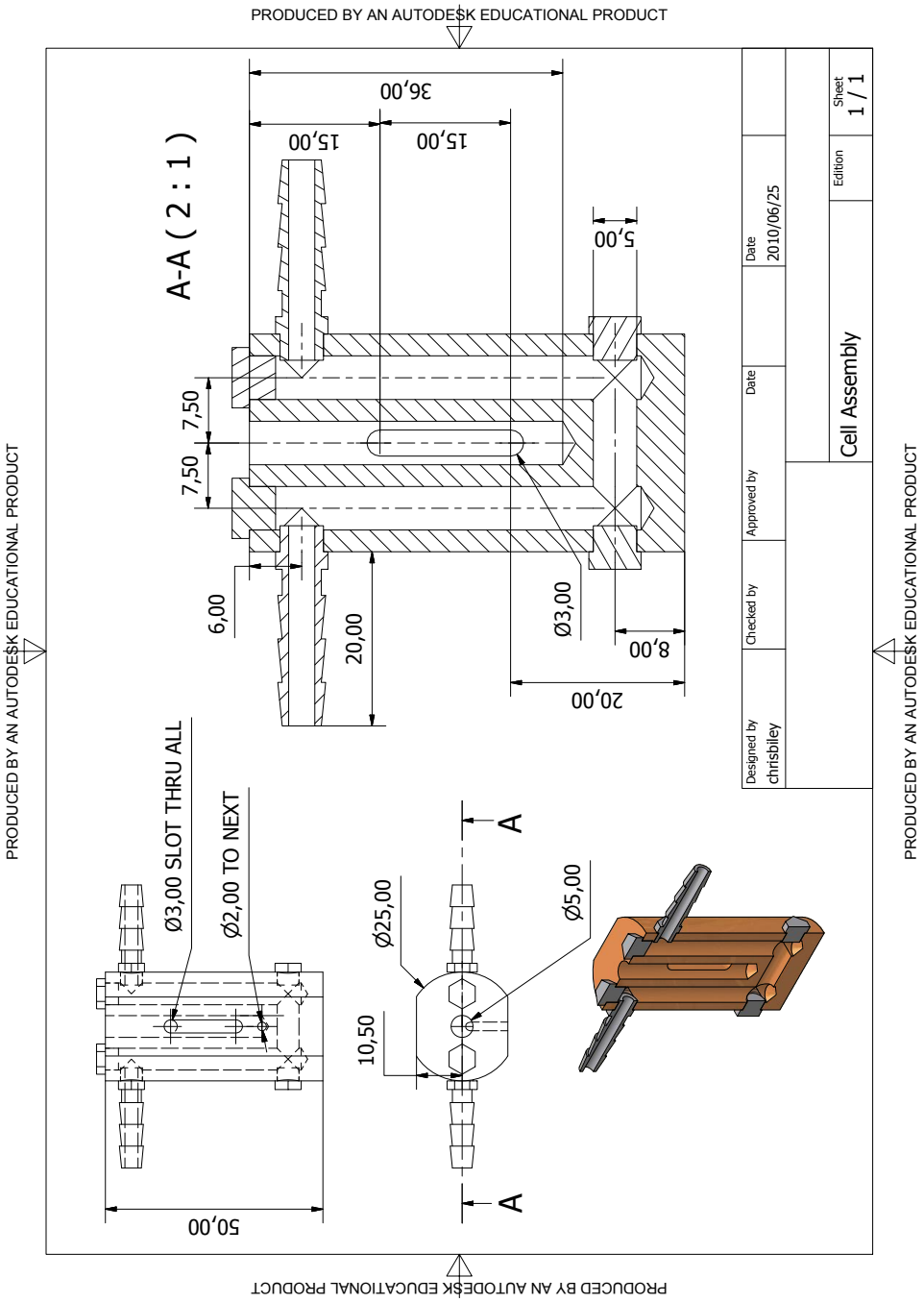

B.2 UV-vis spectroscopy

B.2.1 Equilibrium measurements

In this study, density and concentration basis considerations are required for the analysis of concentrated solutions. In the series of $Fe(ClO_4)_3 + (NH_4)_2SO_4$ solutions analysed by UV-vis to determine the step-wise formation of Fe(III)-S(VI) CIP's the variation in density and fractional amount of water resulted in a variation in the molar concentration of Fe^{3+} at constant molal concentration. In order to obtain the most accurate analysis of the spectra, the density of these solutions and the final solution composition were measured.

The density of $Fe(ClO_4)_3 + (NH_4)_2SO_4$ solutions as a function of total sulfate molality (calculated gravimetrically) were determined for a 0.40 mol/kg $Fe(ClO_4)_3$ solution by the step-wise addition of solid $(NH_4)_2SO_4$. These data are presented in Figure B.10 and were correlated using a simple quadratic polynomial with $\rho = -0.006111[SO_4^{2-}]^2 + 0.05197[SO_4^{2-}] + 1.1037$.

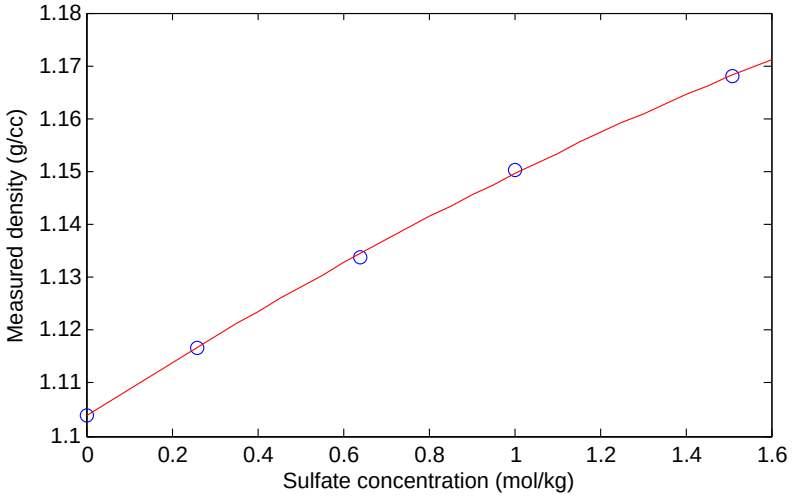

Figure B.10: Measured Density of 0.4 mol/kg $Fe(ClO_4)_3$ as a function of added $(NH_4)_2SO_4$. Data points are laboratory measurement with an Anton-Paar hand-held instrument and the line represents a second order polynomial (see text) fit to the data.

The final solution in the $Fe(ClO_4)_3 + (NH_4)_2SO_4$ series was analysed by ICP-OES and titration and the concentrations of ferric, sulfate and acid were determined as 0.38, 1.72 and 0.25 mol/kg respectively, with 72% H_2O. This analysis, combined with the density correlation were used to calculate the molar concentration of Fe^{3+} as a function of added

$(NH_4)_2SO_4$ and is detailed in Table B.6. These concentration were used in the MCR-ALS procedure to ensure the calculated concentrations of each species summed to the total iron concentration.

The MCR-ALS procedure was implemented using the Matlab code published by Jaumot et al. (2005). The following settings were implemented in their code in calculating the species' concentrations and molar extinction coefficients Presented in Figures 4.25 to 4.26:

- Scaling: All absorbance data was multiplied by 1^{-3} cm to account for the flow cell cuvette path-length of 10 μm.
- Closure constraints: The sum of the three selected components' concentrations were forced to equal the calculated total Fe(III) concentration calculated in Table B.6.
- Both the concentration and extinction coefficient vectors were forced to be non-negative.

Table B.6: Calculation of molar concentrations in $Fe(ClO_4)_3 + (NH_4)_2SO_4$ solutions

Solution	$(NH_4)_2SO_4$ Added (g)	$(NH_4)_2SO_4$ Total (g)	Sulfate mol	Sulfate mol/kg	SO_4^{2-}:Fe^{3+}	Density g/ml	Fraction H_2O (%)	Fe^{3+} mol/L	H^+) mol/L	SO_4^{2-} mol/L
1	0.0000	0.0000	0.000	0.000	0.00	1.1038	86.1%	0.3642	0.2411	0.0000
2	0.0780	0.0780	0.001	0.006	0.02	1.1041	86.1%	0.3640	0.2410	0.0056
3	0.3562	0.4342	0.003	0.033	0.09	1.1055	85.8%	0.3634	0.2405	0.0312
4	0.3123	0.7465	0.006	0.057	0.15	1.1067	85.6%	0.3628	0.2401	0.0536
5	0.3579	1.1044	0.008	0.084	0.22	1.1081	85.3%	0.3621	0.2397	0.0792
6	1.0044	2.1088	0.016	0.160	0.42	1.1119	84.6%	0.3603	0.2385	0.1504
7	1.2020	3.3108	0.025	0.251	0.66	1.1164	83.7%	0.3581	0.2370	0.2347
8	1.0425	4.3533	0.033	0.330	0.86	1.1203	83.0%	0.3562	0.2358	0.3070
9	1.0048	5.3581	0.041	0.406	1.06	1.1239	82.3%	0.3544	0.2346	0.3759
10	1.0842	6.4423	0.049	0.489	1.28	1.1277	81.6%	0.3525	0.2333	0.4495
11	0.9569	7.3992	0.056	0.561	1.46	1.1310	81.0%	0.3507	0.2322	0.5137
12	1.3213	8.7205	0.066	0.661	1.73	1.1354	80.1%	0.3484	0.2306	0.6014
13	0.8897	9.6102	0.073	0.729	1.90	1.1384	79.5%	0.3468	0.2296	0.6598
14	1.8111	11.4213	0.086	0.866	2.26	1.1442	78.4%	0.3436	0.2275	0.7769
15	1.9104	13.3317	0.101	1.011	2.64	1.1500	77.2%	0.3403	0.2252	0.8980
16	1.7757	15.1074	0.114	1.146	2.99	1.1552	76.2%	0.3372	0.2232	1.0084
17	1.6152	16.7226	0.127	1.268	3.31	1.1598	75.3%	0.3344	0.2213	1.1069
18	3.7440	20.4666	0.155	1.552	4.05	1.1696	73.2%	0.3280	0.2171	1.3287
19	2.2510	22.7176	0.172	1.723	4.50	1.1750	72.0%	0.3241	0.2146	1.4576

B.2.2 UV kinetic measurements

The determination of pseusdo-first order rate constants from the absorbance time profiles were carried out over the 30 seconds of the measured data which are highlighted in Figure B.11 by the round data points. The dotted line represent linear fits to this data, the slope of which gives the first order rate constant. Only the initial data was used as deviations from first order behaviour were noted at longer times, attributed to the changing speciation with continued reaction.

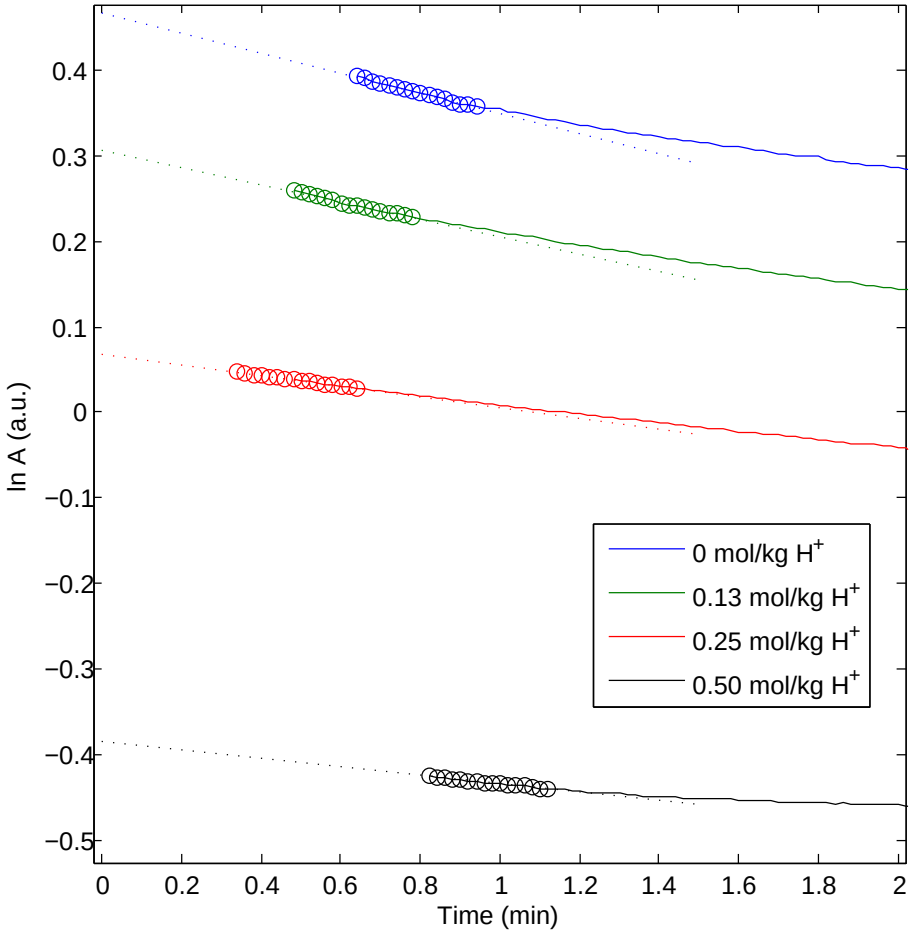

Figure B.11: Selection of sub-set of initial absorbance time data for pseudo-first order rate constant determination. The first 30 seconds of stable measurement were use to estimate the first order decay, shown by the straight dotted line. The open circles represent the data to which the first-order decay functions were fitted.

Appendix C

Kinetics

C.1 Mass transfer measurements

The dissolved oxygen electrode responses to step changes in the gas feed of either N_2 or O_2 is presented in Figure C.1 where the [O_2] response was normalised by the steady-state O_2 concentration. The red lines in this figure show the fitted model and the regressed k_La parameters at 25 and 50 °C.

The sulfite titration test sheets, detailing the reaction of a sulfite solution in contact with oxygen in the reactor setup, tracked by the titrations detailed in Section 3.5. The test sheets are included below and Figure C.2 compares the calculated amount of oxygen reacted with time for agitation at 1000 and 1600 rpm. The resulting k_La from these tests are 15.16 and 37.48 min^{-1} respectively.

Moreover, the influence of viscosity on mass transfer coefficients are well-known (Garcia-Ochoa and Gomez, 2004). Several viscosity measurements of water ferric sulfate solutions were conducted and are presented in Figure C.3 along with several available measurement in the literature. It is clear that there is a considerably stronger temperature dependence of viscosity in ferric sulfate solutions as compared to water or sodium sulfate solutions. Thus, the temperature extrapolation of mass transfer coefficients using the conventional means in different media is questionable given this significant difference.

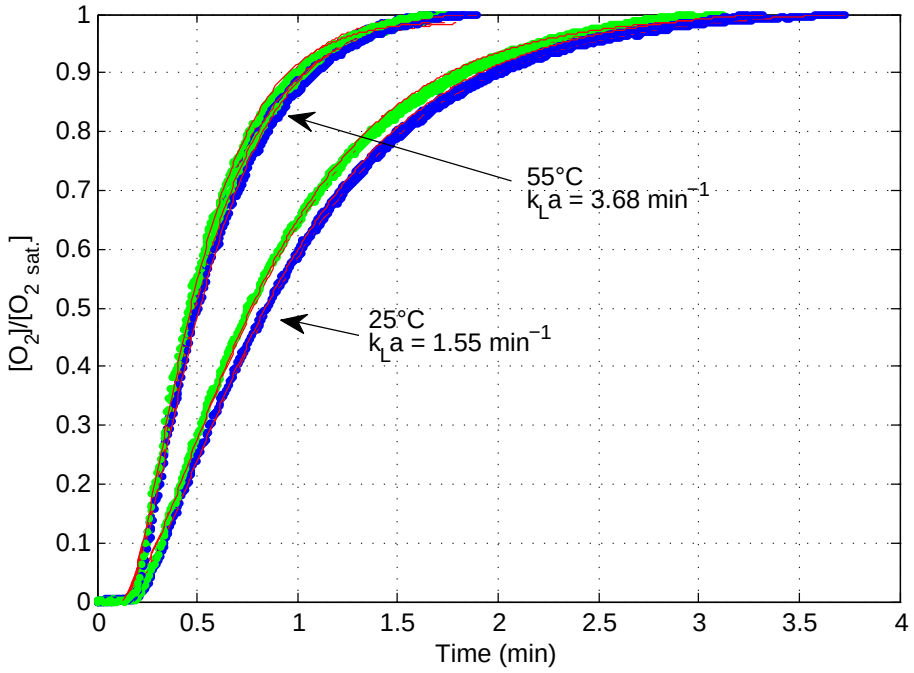

Figure C.1: Direct method of k_La determination at 25 and 55 °C in water. Blue data points are gassing measurements (O_2 sparge), green data points are degassing measurements (N_2 sparge) and red lines represent Equation 3.1.1.

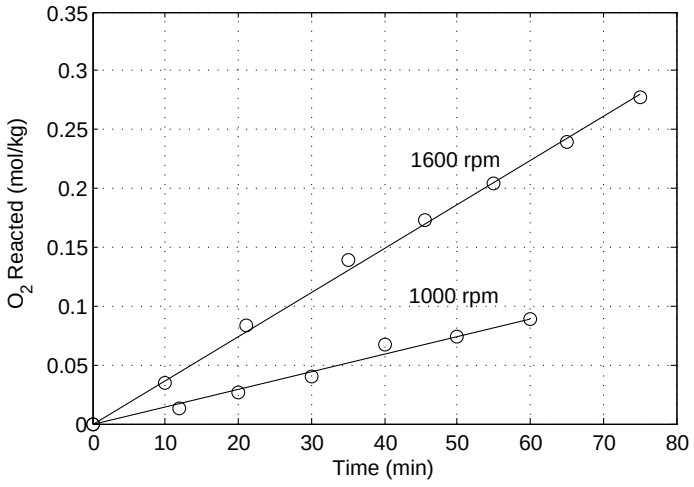

Figure C.2: Oxygen-time plots from sulfite oxidation method of mass transfer measurement. Solid line represent robust linear fits fo the experimental measurement, constants were fixed at zero.

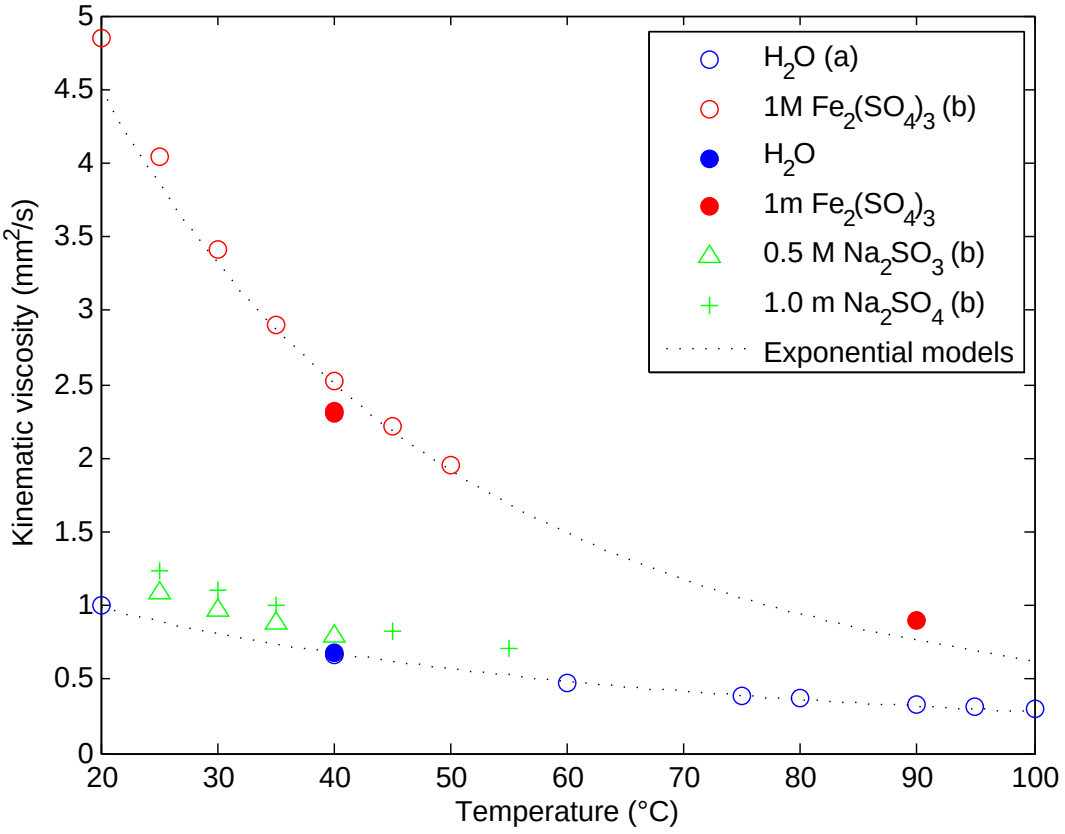

Figure C.3: Viscosity-temperature dependence of H_2O, $Fe_2(SO_4)_3$, Na_2SO_3 and Na_2SO_4. References: (a) Kestin et al. (1978), (b) Laliberte and Cooper (2004)

Sulfite Oxidation Testwork Sheet

Date	12-Mar-13
Temperature	90
Agitation Rate	1000
O_2 Flow Rate	1.00 SLPM

0.0409 mol/min

Reagents

Na_2SO_3	305.71 g
H_2O	1849.11 g
$CoSO_4$ Solution	16.29 g

Fraction H_2O	85.92%

Estimated Concentrations

SO_3^{2-}	1.300 mol/kg
Co^{2+}	1.310E-07 mol/kg
Solution Density	1.1130 g/ml

CoSO4 Solution

Concentration	1.500E-05 mol/L

I_2 Solution

Concentration	0.049 mol/L
Density	1.0234 g/ml

Thiosulfate Solution

Concentration	0.100 mol/L

Oxygen Solubility - Water Parameters (Tromans, 1998)

p1	0.046
p2	203.35
p3	299.378
p4	0.092
p5	20591

Oxygen Solubility

$(K_H)_{O2,H2O}$	0.000780693	(mol/kg.atm)

Oxygen Solublity - Electrolyte Parameters (Tromans, 1998)

	K	y	n
Na_2SO_4	0.629498	0.911841	1.440175
Electrolyte Par.	0.440		

$(K_H)_{O2,Electrolyte}$	0.000343828	(mol/kg.atm)
Total Pressure	1	atm
Water Pressure	70.06	kPa
O_2 Solubility	3.29	mg/kg
	0.000102937	mol/kg

Titration Log

Sample	Time	Mass SO_3^{2-} Sample	Mass I_2 Solution	Volume $S_2O_3^{2-}$	SO_3^{2-} Concentration	Conversion	O2 Reacted	Slope	k_La (min^{-1})	$1-R^2$	O2 Fed
1	0	1.00 g	29.61 g	6.795 ml	1.242 mol/kg	0%	0.000 mol/kg	0.00156	15.16	1.43E-02	0.000 mol/kg
2	12	1.03 g	32.40 g	9.240 ml	1.218 mol/kg	2%	0.012 mol/kg				0.265 mol/kg
3	20	1.13 g	29.65 g	5.093 ml	1.189 mol/kg	4%	0.027 mol/kg				0.442 mol/kg
4	30	1.03 g	30.33 g	8.278 ml	1.161 mol/kg	7%	0.041 mol/kg				0.663 mol/kg
5	40	1.02 g	30.23 g	9.311 ml	1.108 mol/kg	11%	0.067 mol/kg				0.884 mol/kg
6	50	0.94 g	30.34 g	11.156 ml	1.095 mol/kg	12%	0.074 mol/kg				1.105 mol/kg
7	60	1.11 g	31.27 g	9.428 ml	1.064 mol/kg	14%	0.089 mol/kg				1.326 mol/kg

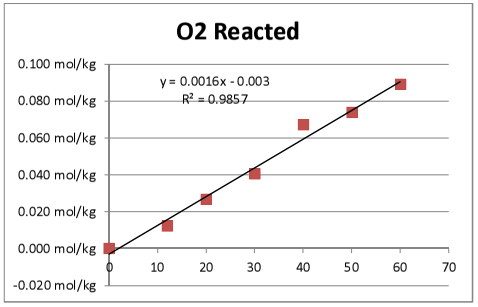

Sulfite Oxidation Testwork Sheet

Date	15-Mar-13
Temperature	90
Agitation Rate	1800
O_2 Flow Rate	1.00 SLPM

0.0409 mol/min

Reagents

Na_2SO_3	282.20 g
H_2O	1707.48 g
$CoSO_4$ Solution	14.94 g

Fraction H_2O	85.92%

Estimated Concentrations

SO_3^{2-}	1.300 mol/kg
Co^{2+}	1.301E-07 mol/kg
Solution Density	1.1130 g/ml

CoSO4 Solution

Concentration	1.500E-05 mol/L

I_2 Solution

Concentration	0.053 mol/L
Density	1.0234 g/ml

Thiosulfate Solution

Concentration	0.100 mol/L

Oxygen Solubility - Water Parameters (Tromans, 1998)

p1	0.046
p2	203.35
p3	299.378
p4	0.092
p5	20591

Oxygen Solubility

$(K_H)_{O2,H2O}$	0.000780693	(mol/kg.atm)

Oxygen Solublity - Electrolyte Parameters (Tromans, 1998)

	K	y	n
Na_2SO_4	0.629498	0.911841	1.440175
Electrolyte Par.	0.409		

$(K_H)_{O2,Electrolyte}$	0.000319537	(mol/kg.atm)
Total Pressure	1.00	atm
Water Pressure	70.06	kPa
O_2 Solubility	3.06	mg/kg
	9.85922E-05	mol/kg

Titration Log

Sample	Time	Mass SO_3^{2-} Sample	Mass I_2 Solution	Volume $S_2O_3^{2-}$	SO_3^{2-} Concentration	Conversion	O2 Reacted	Slope	k_La (min^{-1})	$1-R^2$	O2 Fed
1	0	1.1106 g	30.6705 g	4.619 ml	1.407 mol/kg	0%	0.000 mol/kg	0.00370	37.48	1.77E-03	0.000 mol/kg
2	10	1.1066 g	30.5459 g	5.884 ml	1.339 mol/kg	5%	0.034 mol/kg				0.239 mol/kg
3	21	1.0822 g	30.6286 g	8.347 ml	1.241 mol/kg	12%	0.083 mol/kg				0.503 mol/kg
4	35	1.1053 g	30.6273 g	9.992 ml	1.129 mol/kg	20%	0.139 mol/kg				0.838 mol/kg
5	45.5	1.1059 g	30.6876 g	11.328 ml	1.061 mol/kg	25%	0.173 mol/kg				1.089 mol/kg
6	55	1.0851 g	30.7318 g	12.913 ml	0.999 mol/kg	29%	0.204 mol/kg				1.317 mol/kg
7	65	1.0713 g	30.6715 g	14.390 ml	0.928 mol/kg	34%	0.240 mol/kg				1.556 mol/kg
8	75	1.1088 g	30.6378 g	15.200 ml	0.852 mol/kg	39%	0.277 mol/kg				1.795 mol/kg

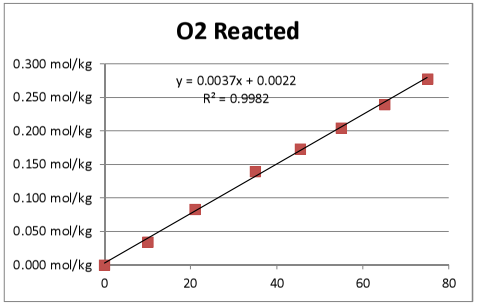

C.2 Sulfite solubility in reactor system

Table C.1: Determination of SO_2 solubility in H_2O during steady SO_2 flow at 1 SLPM - ca. 90 °C measurements

$Na_2S_2O_3$	0.100	mol/L									
Mass I_2 (g)	I_2 Density (g/cc)	Vol. I_2 (ml)	Vol. $S_2O_3^{2-}$ (ml)	I_2 Conc. (mol/L)	Mean (mol/L)						
9.4501		9.236	8.960	0.04851							
4.0198	1.0232	3.929	3.810	0.04849	0.04855						
5.4390		5.316	5.172	0.04865							
Oil °C	Reactor °C	I_2 Mass g	Sample g	Vol $S_2O_3^{2-}$ ml	I_2 Tot. (mol)	I_2 by $S_2O_{32}^-$ (mol)	SO_2 (g)	H_2O (g)	SO_2 (mol/kg)	Mean (mol/kg)	RSD (%)	P_{SO_2} (bar)
120	90.6	5.9416	4.5548	2.053	2.82E-04	1.03E-04	1.15E-02	4.5433	0.0395			0.201
120	90.7	5.3560	5.1564	1.356	2.54E-04	6.78E-05	1.19E-02	5.1445	0.0362	0.0378	4.3%	0.185
120	90.6	5.7336	4.1425	2.326	2.72E-04	1.16E-04	9.98E-03	4.1325	0.0377			0.192
125	91.4	7.6480	5.6842	3.673	3.63E-04	1.84E-04	1.15E-02	5.6727	0.0316			0.164
125	91.4	8.7405	6.7014	4.087	4.15E-04	2.04E-04	1.35E-02	6.6879	0.0315	0.0315	0.4%	0.163
125	91.4	6.2016	6.7746	1.644	2.94E-04	8.22E-05	1.36E-02	6.7610	0.0314			0.163

Table C.2: Determination of SO_2 solubility in H_2O during steady SO_2 flow at 1 SLPM - ca. 75 °C measurements

$Na_2S_2O_3$	0.100	mol/L											
Mass I_2 (g)	I_2 Density (g/cc)	Vol. I_2 (ml)	I_2 Mass g	Vol. $S_2O_3^{2-}$ (ml)	Sample g	I2 Conc. (mol/L)	Vol $S_2O_3^{2-}$ ml	Mean (mol/L)	RSD (%)	I_2 Tot. (mol)	I_2 by $S_2O_{32}^{-}$ (mol)	SO_2 (g)	H_2O (g)	SO_2 (mol/kg)	Mean (mol/kg)	RSD (%)	P_{SO_2} (bar)
2.9893		2.855		1.447		0.05061											
6.9997		6.685		3.406		0.05088		0.05083	0.30%								
9.9843	1.047	9.536		4.866		0.05096											
7.3862		7.054		3.595		0.05089											
Oil °C	Reactor °C	I_2 Mass g		Sample g		Vol $S_2O_3^{2-}$ ml		I_2 Tot. (mol)	I_2 by $S_2O_{32}^{-}$ (mol)	SO_2 (g)	H_2O (g)	SO_2 (mol/kg)	Mean (mol/kg)	RSD (%)	P_{SO_2} (bar)		
80.25	75.05	7.6354		0.9223		2.056		3.71E-04	2.06E-04	1.06E-02	0.9117	0.1811			0.628		
80.25	75.1	8.2112		0.6856		2.766		3.99E-04	2.77E-04	7.82E-03	0.6778	0.1801			0.625		
80.25	75.05	10.2054		0.7932		3.506		4.95E-04	3.51E-04	9.28E-03	0.7839	0.1848			0.641		
80.25	74.6	4.4448		0.5677		1.151		2.16E-04	1.15E-04	6.45E-03	0.5612	0.1794			0.615		
80.25	74.7	4.7709		0.2249		1.922		2.32E-04	1.92E-04	2.53E-03	0.2224	0.1773	0.1800	3.16%	0.609		
80.25	74.8	4.9808		0.4413		1.598		2.42E-04	1.60E-04	5.25E-03	0.4360	0.1881			0.648		
80.25	74.9	4.7957		0.271		1.870		2.33E-04	1.87E-04	2.94E-03	0.2681	0.1710			0.591		
80.25	75	17.4578		1.5766		5.778		8.48E-04	5.78E-04	1.73E-02	1.5593	0.1730			0.599		
80.25	75.05	13.2560		1.4064		3.856		6.44E-04	3.86E-04	1.65E-02	1.3899	0.1856			0.644		

C.3 Batch test logsheets

Exp. Number	1-1
Test Name	FERRED-1-1
Conditions	
Temperature	95°C
SO2	1.00 l/min
O2	0.00 l/min
Agitation	1800 rpm
[Fe3+]	0.50 mol/kg
[Fe2+]	0.00 mol/kg
[H+]	0.63 mol/kg

Date	22 March 2012
Initial Reactor Mass	2142.28 g
Final Mass	
Solids	
H_2O Basis	1894.00 g
Repeat	0.00

Experimental Measurements

Time (planned)	Time (actual)	Total Sample Mass	Total Diluted	Density (20°C)	Titrator Dil. Sample	Volume $K_2Cr_2O_7$
0 min	0 min	35.75 g	72.66 g	1.0502 g/ml	2.32 g	0.087 ml
5 min	5 min	29.81 g	61.73 g	1.0498 g/ml	1.82 g	0.722 ml
15 min	15 min	27.26 g	55.28 g	1.0519 g/ml	1.83 g	1.504 ml
30 min	30 min	28.45 g	56.76 g	1.0536 g/ml	1.91 g	2.150 ml
45 min	45 min	30.33 g	60.58 g	1.0539 g/ml	2.10 g	2.701 ml
60 min	60 min	29.73 g	60.34 g	1.0534 g/ml	1.56 g	2.100 ml
90 min	90 min	29.75 g	59.39 g	1.0547 g/ml	1.57 g	2.379 ml
135 min	135 min	28.18 g	56.13 g	1.0547 g/ml	1.81 g	3.000 ml
180 min	180 min	28.01 g	56.93 g	1.0534 g/ml	1.71 g	2.999 ml

Titration Calculations

Time (planned)	Est. Reactor Mass	Fe^{2+} (mol/kg Soln.)	Total Fe^{2}	Total SO_2 added	Total H2O	Fe^{2+} Molality
0 min	2106.53 g	0.01 mol/kgsln	0.02 mol	0.00 g	1893.71 g	0.01 mol/kg
5 min	2082.20 g	0.08 mol/kgsln	0.17 mol	5.48 g	1890.92 g	0.09 mol/kg
15 min	2065.97 g	0.17 mol/kgsln	0.34 mol	11.03 g	1887.80 g	0.18 mol/kg
30 min	2052.28 g	0.22 mol/kgsln	0.46 mol	14.76 g	1885.70 g	0.24 mol/kg
45 min	2038.72 g	0.26 mol/kgsln	0.52 mol	16.77 g	1884.56 g	0.28 mol/kg
60 min	2026.73 g	0.27 mol/kgsln	0.55 mol	17.73 g	1884.02 g	0.29 mol/kg
90 min	2016.51 g	0.30 mol/kgsln	0.61 mol	19.54 g	1883.01 g	0.32 mol/kg
135 min	2009.58 g	0.33 mol/kgsln	0.66 mol	21.25 g	1882.05 g	0.35 mol/kg
180 min	2004.45 g	0.36 mol/kgsln	0.71 mol	22.88 g	1881.13 g	0.38 mol/kg

Lab Sample Analysis

Time (planned)	Volume	Fe2+	Fe(T)	H+	S	SO4	H2O
0 min	69.19 ml	0.00 g	0.93 g	0.02 g	1.12 g	3.35 g	31.46 g
5 min	58.80 ml	0.14 g	0.73 g	0.02 g	0.89 g	2.66 g	26.40 g
15 min	52.55 ml	0.24 g	0.67 g	0.02 g	0.90 g	2.68 g	23.88 g
30 min	53.87 ml	0.33 g	0.71 g	0.02 g	0.98 g	2.93 g	24.78 g
45 min	57.48 ml	0.41 g	0.79 g	0.03 g	1.09 g	3.26 g	26.26 g
60 min	57.28 ml	0.43 g	0.72 g	0.03 g	1.02 g	3.06 g	25.92 g
90 min	56.31 ml	0.49 g	0.73 g	0.03 g	1.04 g	3.11 g	25.88 g
135 min	53.22 ml	0.50 g	0.75 g	0.03 g	1.05 g	3.16 g	24.24 g
180 min	54.04 ml	0.52 g	0.70 g	0.03 g	1.01 g	3.04 g	24.24 g

Lab Sample Molalities

Time (planned)	%H2O	Fe2+	Fe(T)	H+	SO4	X (Fe^{2+}/avg(Fe_T))
0 min	88%	0.00 mol/kg	0.53 mol/kg	0.65 mol/kg	1.11 mol/kg	0.00%
5 min	89%	0.09 mol/kg	0.50 mol/kg	0.75 mol/kg	1.05 mol/kg	18.15%
15 min	88%	0.18 mol/kg	0.51 mol/kg	0.87 mol/kg	1.17 mol/kg	34.34%
30 min	87%	0.24 mol/kg	0.51 mol/kg	0.99 mol/kg	1.23 mol/kg	46.51%
45 min	87%	0.28 mol/kg	0.54 mol/kg	1.04 mol/kg	1.29 mol/kg	54.35%
60 min	87%	0.30 mol/kg	0.50 mol/kg	1.10 mol/kg	1.23 mol/kg	58.17%
90 min	87%	0.34 mol/kg	0.50 mol/kg	1.14 mol/kg	1.25 mol/kg	65.41%
135 min	86%	0.37 mol/kg	0.55 mol/kg	1.18 mol/kg	1.35 mol/kg	70.94%
180 min	87%	0.39 mol/kg	0.52 mol/kg	1.28 mol/kg	1.30 mol/kg	74.91%

Analytical Results

Time (planned)	Fe2+_g/l	Fe_mg/l	H+_g/L	S_mg/l
0 min	0	13398	0.3	16146
5 min	2.35	12425	0.34	15109
15 min	4.5	12825	0.4	17035
30 min	6.17	13134	0.46	18181
45 min	7.16	13669	0.48	18904
60 min	7.59	12611	0.5	17846
90 min	8.67	12894	0.53	18435
135 min	9.32	14116	0.54	19790
180 min	9.69	12912	0.58	18768

Exp. Number	1-2
Test Name	FERRED-1-2
Conditions	
Temperature	95°C
SO2	1.00 l/min
O2	0.00 l/min
Agitation	1800 rpm
[Fe3+]	1.33 mol/kg
[Fe2+]	0.00 mol/kg
[H+]	0.63 mol/kg

Date	03 April 2012
Initial Reactor Mass	2378.44 g
Final Mass	
Solids	
H_2O Basis	1833.00 g
Repeat	0.00

Experimental Measurements

Time (planned)	Time (actual)	Total Sample Mass	Total Diluted	Density (20°C)	Titrator Dil. Sample	Volume $K_2Cr_2O_7$
0 min	0 min	33.25 g	68.62 g	1.1055 g/ml	2.37 g	0.000 ml
5 min	5 min	33.60 g	67.29 g	1.1109 g/ml	2.39 g	1.070 ml
15 min	15 min	29.25 g	59.51 g	1.1104 g/ml	2.43 g	2.408 ml
30 min	30 min	30.27 g	60.25 g	1.1144 g/ml	2.71 g	4.154 ml
45 min	45 min	30.87 g	62.87 g	1.1123 g/ml	2.16 g	3.815 ml
60 min	60 min	30.38 g	60.56 g	1.1156 g/ml	2.43 g	4.852 ml
90 min	90 min	29.43 g	60.18 g	1.1131 g/ml	2.27 g	5.001 ml
135 min	135 min	32.25 g	64.85 g	1.1156 g/ml	2.29 g	5.672 ml
180 min	180 min	31.84 g	64.45 g	1.1154 g/ml	2.16 g	5.699 ml

Titration Calculations

Time (planned)	Est. Reactor Mass	Fe^{2+} (mol/kg Soln.)	Total Fe^2	Total SO_2 added	Total H2O	Fe^{2+} Molality
0 min	2345.19 g	0.00 mol/kgsln	0.00 mol	0.00 g	1833.00 g	0.00 mol/kg
5 min	2318.25 g	0.09 mol/kgsln	0.21 mol	6.66 g	1829.26 g	0.11 mol/kg
15 min	2303.87 g	0.20 mol/kgsln	0.46 mol	14.88 g	1824.63 g	0.25 mol/kg
30 min	2296.04 g	0.31 mol/kgsln	0.70 mol	22.44 g	1820.38 g	0.38 mol/kg
45 min	2291.57 g	0.36 mol/kgsln	0.82 mol	26.40 g	1818.15 g	0.45 mol/kg
60 min	2290.39 g	0.40 mol/kgsln	0.91 mol	29.20 g	1816.58 g	0.50 mol/kg
90 min	2294.05 g	0.45 mol/kgsln	1.03 mol	33.10 g	1814.38 g	0.57 mol/kg
135 min	2298.47 g	0.50 mol/kgsln	1.14 mol	36.66 g	1812.38 g	0.63 mol/kg
180 min	2306.07 g	0.53 mol/kgsln	1.23 mol	39.44 g	1810.81 g	0.68 mol/kg

Lab Sample Analysis

Time (planned)	Volume	Fe2+	Fe(T)	H+	S	SO4	H2O
0 min	62.07 ml	0.00 g	1.92 g	0.01 g	1.89 g	5.67 g	25.65 g
5 min	60.57 ml	0.17 g	1.96 g	0.02 g	1.96 g	5.86 g	25.76 g
15 min	53.59 ml	0.30 g	1.67 g	0.02 g	1.74 g	5.21 g	22.35 g
30 min	54.06 ml	0.49 g	1.70 g	0.03 g	1.84 g	5.50 g	23.04 g
45 min	56.52 ml	0.60 g	1.70 g	0.03 g	1.75 g	5.25 g	23.89 g
60 min	54.28 ml	0.66 g	1.65 g	0.03 g	1.84 g	5.52 g	23.18 g
90 min	54.07 ml	0.71 g	1.63 g	0.04 g	1.83 g	5.48 g	22.29 g
135 min	58.13 ml	0.80 g	1.78 g	0.04 g	2.07 g	6.19 g	24.24 g
180 min	57.78 ml	0.93 g	1.76 g	0.04 g	2.02 g	6.05 g	23.99 g

Lab Sample Molalities

Time (planned)	%H2O	Fe2+	Fe(T)	H+	SO4	X (Fe^{2+}/avg(Fe_T)
0 min	77%	0.00 mol/kg	1.34 mol/kg	0.55 mol/kg	2.30 mol/kg	0.00%
5 min	77%	0.12 mol/kg	1.36 mol/kg	0.72 mol/kg	2.37 mol/kg	8.79%
15 min	76%	0.24 mol/kg	1.34 mol/kg	1.00 mol/kg	2.42 mol/kg	18.46%
30 min	76%	0.38 mol/kg	1.32 mol/kg	1.23 mol/kg	2.49 mol/kg	28.94%
45 min	77%	0.45 mol/kg	1.27 mol/kg	1.36 mol/kg	2.29 mol/kg	34.11%
60 min	76%	0.51 mol/kg	1.28 mol/kg	1.49 mol/kg	2.48 mol/kg	38.54%
90 min	76%	0.57 mol/kg	1.31 mol/kg	1.56 mol/kg	2.56 mol/kg	43.55%
135 min	75%	0.63 mol/kg	1.32 mol/kg	1.71 mol/kg	2.66 mol/kg	47.98%
180 min	75%	0.69 mol/kg	1.32 mol/kg	1.82 mol/kg	2.62 mol/kg	52.75%

Analytical Results

Time (planned)	Fe2+_g/l	Fe_mg/l	H+_g/L	S_mg/l
0 min	0	30870	0.23	30466
5 min	2.75	32302	0.31	32303
15 min	5.66	31191	0.42	32421
30 min	9.07	31397	0.53	33968
45 min	10.6	30053	0.58	31004
60 min	12.1	30426	0.64	33924
90 min	13.2	30157	0.65	33819
135 min	13.8	30689	0.72	35534
180 min	16.1	30520	0.76	34923

Exp. Number	1-3
Test Name	FERRED-1-3
Conditions	
Temperature	95°C
SO2	1.00 l/min
O2	0.00 l/min
Agitation	1800 rpm
[Fe3+]	2.17 mol/kg
[Fe2+]	0.00 mol/kg
[H+]	0.63 mol/kg

Date	11 April 2012
Initial Reactor Mass	2587.91 g
Final Mass	
Solids	
H_2O Basis	1768.00 g
Repeat	0.00

Experimental Measurements

Time (planned)	Time (actual)	Total Sample Mass	Total Diluted	Density (20°C)	Titrator Dil. Sample	Volume $K_2Cr_2O_7$
0 min	0 min	36.82 g	76.87 g	1.1496 g/ml	2.30 g	0.005 ml
5 min	5 min	39.58 g	79.69 g	1.1570 g/ml	2.03 g	0.793 ml
15 min	15 min	37.11 g	74.91 g	1.1583 g/ml	2.07 g	2.005 ml
30 min	30 min	28.90 g	58.09 g	1.1604 g/ml	1.97 g	3.000 ml
45 min	45 min	32.95 g	66.79 g	1.1598 g/ml	2.02 g	3.638 ml
60 min	60 min	30.65 g	62.24 g	1.1603 g/ml	2.06 g	4.157 ml
90 min	90 min	36.99 g	74.27 g	1.1629 g/ml	2.04 g	4.877 ml
135 min	135 min	37.44 g	76.47 g	1.1606 g/ml	2.01 g	5.316 ml
180 min	180 min	35.01 g	70.60 g	1.1628 g/ml	2.19 g	6.366 ml

Titration Calculations

Time (planned)	Est. Reactor Mass	Fe^{2+} (mol/kg Soln.)	Total Fe^2	Total SO_2 added	Total H2O	Fe^{2+} Molality
0 min	2551.09 g	0.00 mol/kgsln	0.00 mol	0.00 g	1767.98 g	0.00 mol/kg
5 min	2517.85 g	0.08 mol/kgsln	0.20 mol	6.34 g	1764.43 g	0.11 mol/kg
15 min	2496.37 g	0.20 mol/kgsln	0.49 mol	15.63 g	1759.21 g	0.28 mol/kg
30 min	2491.90 g	0.31 mol/kgsln	0.76 mol	24.43 g	1754.26 g	0.43 mol/kg
45 min	2488.04 g	0.37 mol/kgsln	0.91 mol	29.09 g	1751.64 g	0.52 mol/kg
60 min	2490.07 g	0.41 mol/kgsln	1.02 mol	32.68 g	1749.62 g	0.58 mol/kg
90 min	2491.38 g	0.48 mol/kgsln	1.20 mol	38.30 g	1746.46 g	0.68 mol/kg
135 min	2497.15 g	0.54 mol/kgsln	1.35 mol	43.20 g	1743.70 g	0.77 mol/kg
180 min	2509.24 g	0.59 mol/kgsln	1.47 mol	47.11 g	1741.50 g	0.84 mol/kg

Lab Sample Analysis

Time (planned)	Volume	Fe2+	Fe(T)	H+	S	SO4	H2O
0 min	66.87 ml	0.00 g	3.00 g	0.01 g	2.82 g	8.46 g	25.35 g
5 min	68.88 ml	0.17 g	3.37 g	0.02 g	3.15 g	9.44 g	26.76 g
15 min	64.67 ml	0.40 g	2.97 g	0.02 g	2.84 g	8.50 g	25.62 g
30 min	50.06 ml	0.48 g	2.53 g	0.02 g	2.50 g	7.50 g	18.85 g
45 min	57.59 ml	0.64 g	2.55 g	0.03 g	2.53 g	7.59 g	22.77 g
60 min	53.64 ml	0.70 g	2.57 g	0.03 g	2.60 g	7.78 g	20.28 g
90 min	63.87 ml	0.96 g	3.07 g	0.04 g	3.14 g	9.40 g	24.48 g
135 min	65.89 ml	1.11 g	3.09 g	0.04 g	3.18 g	9.54 g	24.76 g
180 min	60.72 ml	1.12 g	2.52 g	0.04 g	2.66 g	7.97 g	24.48 g

Lab Sample Molalities

Time (planned)	%H2O	Fe2+	Fe(T)	H+	SO4	X (Fe^{2+}/avg(Fe_T))
0 min	69%	0.00 mol/kg	2.12 mol/kg	0.44 mol/kg	3.47 mol/kg	0.00%
5 min	68%	0.12 mol/kg	2.26 mol/kg	0.59 mol/kg	3.67 mol/kg	5.42%
15 min	69%	0.28 mol/kg	2.08 mol/kg	0.85 mol/kg	3.45 mol/kg	12.92%
30 min	65%	0.45 mol/kg	2.41 mol/kg	1.13 mol/kg	4.14 mol/kg	20.99%
45 min	69%	0.51 mol/kg	2.01 mol/kg	1.28 mol/kg	3.47 mol/kg	23.46%
60 min	66%	0.62 mol/kg	2.27 mol/kg	1.47 mol/kg	3.99 mol/kg	28.49%
90 min	66%	0.71 mol/kg	2.24 mol/kg	1.63 mol/kg	4.00 mol/kg	32.63%
135 min	66%	0.80 mol/kg	2.24 mol/kg	1.69 mol/kg	4.01 mol/kg	37.02%
180 min	70%	0.82 mol/kg	1.84 mol/kg	1.77 mol/kg	3.39 mol/kg	38.01%

Analytical Results

Time (planned)	Fe2+_g/l	Fe_mg/l	H+_g/L	S_mg/l
0 min	0	44884	0.17	42210
5 min	2.54	48958	0.23	45729
15 min	6.18	45934	0.34	43870
30 min	9.54	50621	0.43	49987
45 min	11.2	44345	0.51	44019
60 min	13	47832	0.56	48399
90 min	15.1	48022	0.63	49136
135 min	16.8	46961	0.64	48328
180 min	18.5	41470	0.72	43811

Exp. Number	1-4
Test Name	FERRED-1-4
Conditions	
Temperature	95°C
SO2	1.00 l/min
O2	0.00 l/min
Agitation	1800 rpm
[Fe3+]	3.00 mol/kg
[Fe2+]	0.00 mol/kg
[H+]	0.63 mol/kg

Date	20 March 2012
Initial Reactor Mass	2771.96 g
Final Mass	
Solids	
H_2O Basis	1700.00 g
Repeat	0.00

Experimental Measurements

Time (planned)	Time (actual)	Total Sample Mass	Total Diluted	Density (20°C)	Titrator Dil. Sample	Volume $K_2Cr_2O_7$
0 min	0 min	40.67 g	81.10 g	1.1967 g/ml	2.65 g	0.000 ml
5 min	5 min	39.76 g	79.38 g	1.1977 g/ml	2.87 g	1.073 ml
15 min	15 min	32.93 g	66.10 g	1.1964 g/ml	3.02 g	2.675 ml
30 min	30 min	38.59 g	76.93 g	1.2002 g/ml	2.47 g	3.450 ml
45 min	45 min	40.71 g	80.29 g	1.2045 g/ml	2.00 g	3.361 ml
60 min	60 min	36.30 g	73.74 g	1.1986 g/ml	1.93 g	3.585 ml
90 min	90 min	38.32 g	77.56 g	1.1986 g/ml	2.22 g	4.902 ml
135 min	135 min	42.45 g	84.48 g	1.2027 g/ml	1.97 g	5.143 ml
180 min	180 min	39.56 g	79.26 g	1.2004 g/ml	2.15 g	6.081 ml

Titration Calculations

Time (planned)	Est. Reactor Mass	Fe^{2+} (mol/kg Soln.)	Total Fe^2	Total SO_2 added	Total H2O	Fe^{2+} Molality
0 min	2731.29 g	0.00 mol/kgsln	0.00 mol	0.00 g	1700.00 g	0.00 mol/kg
5 min	2697.98 g	0.07 mol/kgsln	0.20 mol	6.45 g	1696.37 g	0.12 mol/kg
15 min	2680.31 g	0.18 mol/kgsln	0.48 mol	15.26 g	1691.41 g	0.28 mol/kg
30 min	2665.49 g	0.28 mol/kgsln	0.74 mol	23.77 g	1686.63 g	0.44 mol/kg
45 min	2652.94 g	0.33 mol/kgsln	0.88 mol	28.16 g	1684.16 g	0.52 mol/kg
60 min	2648.65 g	0.38 mol/kgsln	1.00 mol	32.01 g	1681.99 g	0.59 mol/kg
90 min	2648.24 g	0.45 mol/kgsln	1.18 mol	37.91 g	1678.68 g	0.71 mol/kg
135 min	2649.88 g	0.52 mol/kgsln	1.38 mol	44.09 g	1675.20 g	0.82 mol/kg
180 min	2658.57 g	0.57 mol/kgsln	1.51 mol	48.25 g	1672.86 g	0.90 mol/kg

Lab Sample Analysis

Time (planned)	Volume	Fe2+	Fe(T)	H+	S	SO4	H2O
0 min	67.77 ml	0.00 g	4.04 g	0.01 g	3.62 g	10.86 g	25.77 g
5 min	66.28 ml	0.17 g	3.85 g	0.01 g	3.70 g	11.07 g	24.82 g
15 min	55.25 ml	0.32 g	3.46 g	0.02 g	3.25 g	9.73 g	19.73 g
30 min	64.10 ml	0.57 g	3.95 g	0.02 g	3.77 g	11.30 g	23.32 g
45 min	66.66 ml	0.75 g	3.93 g	0.03 g	4.00 g	12.00 g	24.75 g
60 min	61.52 ml	0.76 g	3.79 g	0.03 g	3.65 g	10.92 g	21.55 g
90 min	64.71 ml	0.94 g	3.64 g	0.04 g	3.71 g	11.12 g	23.52 g
135 min	70.24 ml	1.13 g	4.00 g	0.05 g	4.29 g	12.86 g	25.55 g
180 min	66.03 ml	1.24 g	3.84 g	0.05 g	3.94 g	11.79 g	23.88 g

Lab Sample Molalities

Time (planned)	%H2O	Fe2+	Fe(T)	H+	SO4	X (Fe^{2+}/avg(Fe_T)
0 min	63%	0.00 mol/kg	2.80 mol/kg	0.42 mol/kg	4.39 mol/kg	0.00%
5 min	62%	0.12 mol/kg	2.78 mol/kg	0.56 mol/kg	4.64 mol/kg	4.19%
15 min	60%	0.29 mol/kg	3.14 mol/kg	0.81 mol/kg	5.13 mol/kg	10.02%
30 min	60%	0.44 mol/kg	3.03 mol/kg	1.06 mol/kg	5.04 mol/kg	15.03%
45 min	61%	0.54 mol/kg	2.84 mol/kg	1.26 mol/kg	5.04 mol/kg	18.71%
60 min	59%	0.63 mol/kg	3.15 mol/kg	1.39 mol/kg	5.28 mol/kg	21.59%
90 min	61%	0.71 mol/kg	2.77 mol/kg	1.53 mol/kg	4.92 mol/kg	24.53%
135 min	60%	0.79 mol/kg	2.80 mol/kg	1.80 mol/kg	5.24 mol/kg	27.22%
180 min	60%	0.93 mol/kg	2.88 mol/kg	1.92 mol/kg	5.14 mol/kg	31.97%

Analytical Results

Time (planned)	Fe2+_g/l	Fe_mg/l	H+_g/L	S_mg/l
0 min	0	59543	0.16	53473
5 min	2.55	58121	0.21	55777
15 min	5.82	62615	0.29	58765
30 min	8.89	61600	0.39	58845
45 min	11.3	58917	0.47	60076
60 min	12.3	61675	0.49	59271
90 min	14.5	56310	0.56	57360
135 min	16.1	56906	0.66	61105
180 min	18.8	58177	0.7	59620

Exp. Number	1-5
Test Name	FERRED-1-5
Conditions	
Temperature	95°C
SO2	1.00 l/min
O2	0.00 l/min
Agitation	1800 rpm
[Fe3+]	0.50 mol/kg
[Fe2+]	0.00 mol/kg
[H+]	1.42 mol/kg

Date	10 April 2012
Initial Reactor Mass	2183.61 g
Final Mass	
Solids	
H_2O Basis	1867.00 g
Repeat	0.00

Experimental Measurements

Time (planned)	Time (actual)	Total Sample Mass	Total Diluted	Density (20°C)	Titrator Dil. Sample	Volume $K_2Cr_2O_7$
0 min	0 min	29.60 g	60.97 g	1.0602 g/ml	1.95 g	0.066 ml
5 min	5 min	33.13 g	65.25 g	1.0638 g/ml	2.35 g	0.791 ml
15 min	15 min	33.59 g	66.51 g	1.0641 g/ml	2.27 g	1.360 ml
30 min	30 min	30.21 g	61.33 g	1.0631 g/ml	2.16 g	1.766 ml
45 min	45 min	30.58 g	60.71 g	1.0646 g/ml	2.25 g	2.206 ml
60 min	60 min	28.75 g	58.60 g	1.0636 g/ml	2.00 g	2.007 ml
90 min	90 min	30.64 g	62.32 g	1.0637 g/ml	2.04 g	2.380 ml
135 min	125 min	30.97 g	61.94 g	1.0650 g/ml	1.99 g	2.565 ml
180 min	181 min	38.44 g	76.86 g	1.0653 g/ml	2.22 g	3.075 ml

Titration Calculations

Time (planned)	Est. Reactor Mass	Fe^{2+} (mol/kg Soln.)	Total Fe^2	Total SO_2 added	Total H2O	Fe^{2+} Molality
0 min	2154.01 g	0.01 mol/kgsln	0.02 mol	0.00 g	1866.73 g	0.01 mol/kg
5 min	2125.39 g	0.07 mol/kgsln	0.14 mol	4.51 g	1864.46 g	0.08 mol/kg
15 min	2099.78 g	0.12 mol/kgsln	0.25 mol	7.98 g	1862.51 g	0.13 mol/kg
30 min	2080.63 g	0.17 mol/kgsln	0.35 mol	11.06 g	1860.78 g	0.19 mol/kg
45 min	2062.91 g	0.19 mol/kgsln	0.40 mol	12.86 g	1859.77 g	0.22 mol/kg
60 min	2047.57 g	0.20 mol/kgsln	0.42 mol	13.41 g	1859.46 g	0.23 mol/kg
90 min	2032.38 g	0.24 mol/kgsln	0.48 mol	15.45 g	1858.31 g	0.26 mol/kg
135 min	2018.07 g	0.26 mol/kgsln	0.52 mol	16.66 g	1857.63 g	0.28 mol/kg
180 min	1997.35 g	0.28 mol/kgsln	0.55 mol	17.72 g	1857.03 g	0.30 mol/kg

Lab Sample Analysis

Time (planned)	Volume	Fe2+	Fe(T)	H+	S	SO4	H2O
0 min	57.51 ml	0.00 g	0.79 g	0.04 g	1.26 g	3.76 g	25.01 g
5 min	61.34 ml	0.10 g	0.84 g	0.04 g	1.36 g	4.06 g	28.19 g
15 min	62.50 ml	0.20 g	0.92 g	0.05 g	1.46 g	4.36 g	28.27 g
30 min	57.69 ml	0.26 g	0.73 g	0.04 g	1.24 g	3.73 g	25.71 g
45 min	57.03 ml	0.31 g	0.76 g	0.05 g	1.33 g	3.99 g	25.78 g
60 min	55.10 ml	0.31 g	0.69 g	0.04 g	1.24 g	3.72 g	24.31 g
90 min	58.59 ml	0.39 g	0.77 g	0.05 g	1.37 g	4.12 g	25.71 g
135 min	58.16 ml	0.43 g	0.77 g	0.05 g	1.40 g	4.18 g	25.97 g
180 min	72.15 ml	0.59 g	0.95 g	0.06 g	1.72 g	5.14 g	32.29 g

Lab Sample Molalities

Time (planned)	%H2O	Fe2+	Fe(T)	H+	SO4	X (Fe^{2+}/avg(Fe_T)
0 min	84%	0.00 mol/kg	0.56 mol/kg	1.44 mol/kg	1.57 mol/kg	0.00%
5 min	85%	0.07 mol/kg	0.53 mol/kg	1.49 mol/kg	1.50 mol/kg	12.39%
15 min	84%	0.13 mol/kg	0.58 mol/kg	1.58 mol/kg	1.61 mol/kg	24.07%
30 min	85%	0.18 mol/kg	0.51 mol/kg	1.65 mol/kg	1.51 mol/kg	34.04%
45 min	84%	0.21 mol/kg	0.53 mol/kg	1.73 mol/kg	1.61 mol/kg	39.88%
60 min	85%	0.23 mol/kg	0.51 mol/kg	1.78 mol/kg	1.59 mol/kg	42.78%
90 min	84%	0.27 mol/kg	0.53 mol/kg	1.85 mol/kg	1.67 mol/kg	50.61%
135 min	84%	0.30 mol/kg	0.53 mol/kg	1.89 mol/kg	1.68 mol/kg	56.39%
180 min	84%	0.33 mol/kg	0.53 mol/kg	1.88 mol/kg	1.66 mol/kg	61.68%

Analytical Results

Time (planned)	Fe2+_g/l	Fe_mg/l	H+_g/L	S_mg/l
0 min	0	13700	0.63	21853
5 min	1.69	13690	0.69	22103
15 min	3.23	14681	0.72	23286
30 min	4.5	12725	0.74	21562
45 min	5.35	13354	0.79	23347
60 min	5.6	12442	0.79	22512
90 min	6.59	13080	0.82	23451
135 min	7.47	13268	0.85	24012
180 min	8.19	13203	0.85	23773

Exp. Number	1-6
Test Name	FERRED-1-6
Conditions	
Temperature	95°C
SO2	1.00 l/min
O2	0.00 l/min
Agitation	1800 rpm
[Fe3+]	1.33 mol/kg
[Fe2+]	0.00 mol/kg
[H+]	1.42 mol/kg

Date	26 March 2012
Initial Reactor Mass	2412.23 g
Final Mass	
Solids	
H_2O Basis	1805.00 g
Repeat	0.00

Experimental Measurements

Time (planned)	Time (actual)	Total Sample Mass	Total Diluted	Density (20°C)	Titrator Dil. Sample	Volume $K_2Cr_2O_7$
0 min	0 min	35.67 g	71.15 g	1.1159 g/ml	2.07 g	0.000 ml
5 min	5 min	35.80 g	72.05 g	1.1155 g/ml	1.90 g	0.678 ml
15 min	15 min	33.37 g	66.67 g	1.1174 g/ml	2.28 g	1.672 ml
30 min	30 min	32.22 g	65.97 g	1.1154 g/ml	1.99 g	2.393 ml
45 min	45 min	33.77 g	68.43 g	1.1170 g/ml	2.12 g	2.952 ml
60 min	60 min	33.68 g	66.12 g	1.1215 g/ml	1.77 g	2.796 ml
90 min	90 min	34.01 g	68.08 g	1.1196 g/ml	1.85 g	3.377 ml
135 min	133 min	32.28 g	64.99 g	1.1193 g/ml	1.96 g	4.024 ml
180 min	180 min	32.17 g	65.44 g	1.1183 g/ml	1.88 g	4.185 ml

Titration Calculations

Time (planned)	Est. Reactor Mass	Fe^{2+} (mol/kg Soln.)	Total Fe^2	Total SO_2 added	Total H2O	Fe^{2+} Molality
0 min	2376.56 g	0.00 mol/kgsln	0.00 mol	0.00 g	1805.00 g	0.00 mol/kg
5 min	2346.16 g	0.07 mol/kgsln	0.17 mol	5.40 g	1801.96 g	0.09 mol/kg
15 min	2323.69 g	0.15 mol/kgsln	0.34 mol	10.90 g	1798.87 g	0.19 mol/kg
30 min	2309.68 g	0.25 mol/kgsln	0.57 mol	18.21 g	1794.76 g	0.32 mol/kg
45 min	2296.67 g	0.28 mol/kgsln	0.65 mol	20.75 g	1793.33 g	0.36 mol/kg
60 min	2285.69 g	0.31 mol/kgsln	0.71 mol	22.70 g	1792.23 g	0.40 mol/kg
90 min	2278.34 g	0.37 mol/kgsln	0.83 mol	26.66 g	1790.00 g	0.47 mol/kg
135 min	2276.19 g	0.41 mol/kgsln	0.94 mol	30.13 g	1788.05 g	0.53 mol/kg
180 min	2277.05 g	0.45 mol/kgsln	1.03 mol	33.02 g	1786.42 g	0.58 mol/kg

Lab Sample Analysis

Time (planned)	Volume	Fe2+	Fe(T)	H+	S	SO4	H2O
0 min	63.76 ml	0.00 g	2.18 g	0.04 g	2.44 g	7.30 g	26.16 g
5 min	64.59 ml	0.13 g	2.08 g	0.04 g	2.33 g	6.98 g	26.70 g
15 min	59.67 ml	0.26 g	1.98 g	0.04 g	2.28 g	6.84 g	24.51 g
30 min	59.14 ml	0.40 g	1.83 g	0.04 g	2.17 g	6.51 g	23.83 g
45 min	61.26 ml	0.51 g	1.96 g	0.04 g	2.36 g	7.07 g	24.70 g
60 min	58.96 ml	0.57 g	1.96 g	0.05 g	2.35 g	7.03 g	24.64 g
90 min	60.81 ml	0.68 g	2.00 g	0.05 g	2.45 g	7.35 g	24.62 g
135 min	58.06 ml	0.73 g	1.82 g	0.05 g	2.22 g	6.65 g	23.76 g
180 min	58.52 ml	0.80 g	1.72 g	0.05 g	2.26 g	6.77 g	23.63 g

Lab Sample Molalities

Time (planned)	%H2O	Fe2+	Fe(T)	H+	SO4	X (Fe^{2+}/avg(Fe_T)
0 min	73%	0.00 mol/kg	1.49 mol/kg	1.35 mol/kg	2.90 mol/kg	0.00%
5 min	75%	0.09 mol/kg	1.40 mol/kg	1.42 mol/kg	2.72 mol/kg	6.11%
15 min	73%	0.19 mol/kg	1.45 mol/kg	1.59 mol/kg	2.91 mol/kg	13.67%
30 min	74%	0.30 mol/kg	1.38 mol/kg	1.72 mol/kg	2.84 mol/kg	21.34%
45 min	73%	0.37 mol/kg	1.42 mol/kg	1.80 mol/kg	2.98 mol/kg	26.46%
60 min	73%	0.41 mol/kg	1.43 mol/kg	1.85 mol/kg	2.97 mol/kg	29.41%
90 min	72%	0.50 mol/kg	1.45 mol/kg	2.01 mol/kg	3.11 mol/kg	35.13%
135 min	74%	0.55 mol/kg	1.37 mol/kg	2.09 mol/kg	2.92 mol/kg	38.80%
180 min	73%	0.60 mol/kg	1.30 mol/kg	2.19 mol/kg	2.98 mol/kg	42.77%

Analytical Results

Time (planned)	Fe2+_g/l	Fe_mg/l	H+_g/L	S_mg/l
0 min	0	34223	0.56	38192
5 min	1.99	32251	0.59	36066
15 min	4.42	33186	0.66	38288
30 min	6.77	30986	0.7	36754
45 min	8.4	31973	0.73	38514
60 min	9.68	33294	0.78	39806
90 min	11.2	32842	0.82	40330
135 min	12.5	31372	0.86	38244
180 min	13.6	29392	0.89	38619

Exp. Number	1-7
Test Name	FERRED-1-7
Conditions	
Temperature	95°C
SO2	1.00 l/min
O2	0.00 l/min
Agitation	1800 rpm
[Fe3+]	2.17 mol/kg
[Fe2+]	0.00 mol/kg
[H+]	1.42 mol/kg

Date	27 March 2012
Initial Reactor Mass	2615.05 g
Final Mass	
Solids	
H_2O Basis	1740.00 g
Repeat	0.00

Experimental Measurements

Time (planned)	Time (actual)	Total Sample Mass	Total Diluted	Density (20°C)	Titrator Dil. Sample	Volume $K_2Cr_2O_7$
0 min	0 min	33.92 g	64.95 g	1.1702 g/ml	2.38 g	0.000 ml
5 min	5 min	35.32 g	71.44 g	1.1610 g/ml	2.03 g	0.795 ml
15 min	15 min	36.33 g	74.18 g	1.1602 g/ml	2.10 g	1.783 ml
30 min	30 min	37.59 g	76.89 g	1.1605 g/ml	1.96 g	2.533 ml
45 min	45 min	35.11 g	71.16 g	1.1631 g/ml	2.04 g	3.290 ml
60 min	60 min	37.12 g	75.03 g	1.1643 g/ml	1.96 g	3.529 ml
90 min	90 min	36.80 g	73.34 g	1.1672 g/ml	2.00 g	4.258 ml
135 min	135 min	37.87 g	75.44 g	1.1675 g/ml	1.95 g	4.759 ml
180 min	180 min	37.29 g	75.40 g	1.1652 g/ml	2.55 g	6.676 ml

Titration Calculations

Time (planned)	Est. Reactor Mass	Fe^{2+} (mol/kg Soln.)	Total Fe^{2}	Total SO_2 added	Total H2O	Fe^{2+} Molality
0 min	2581.13 g	0.00 mol/kgsln	0.00 mol	0.00 g	1740.00 g	0.00 mol/kg
5 min	2552.28 g	0.08 mol/kgsln	0.20 mol	6.47 g	1736.36 g	0.12 mol/kg
15 min	2530.00 g	0.17 mol/kgsln	0.44 mol	14.05 g	1732.10 g	0.25 mol/kg
30 min	2513.69 g	0.26 mol/kgsln	0.66 mol	21.28 g	1728.03 g	0.38 mol/kg
45 min	2504.81 g	0.33 mol/kgsln	0.82 mol	26.22 g	1725.25 g	0.47 mol/kg
60 min	2496.79 g	0.36 mol/kgsln	0.91 mol	29.10 g	1723.63 g	0.53 mol/kg
90 min	2493.88 g	0.42 mol/kgsln	1.06 mol	33.89 g	1720.94 g	0.61 mol/kg
135 min	2494.85 g	0.49 mol/kgsln	1.21 mol	38.85 g	1718.15 g	0.71 mol/kg
180 min	2499.95 g	0.53 mol/kgsln	1.32 mol	42.38 g	1716.16 g	0.77 mol/kg

Lab Sample Analysis

Time (planned)	Volume	Fe2+	Fe(T)	H+	S	SO4	H2O
0 min	55.50 ml	0.00 g	2.69 g	0.03 g	2.74 g	8.21 g	23.00 g
5 min	61.53 ml	0.15 g	2.98 g	0.03 g	2.86 g	8.57 g	23.74 g
15 min	63.94 ml	0.35 g	3.00 g	0.04 g	2.96 g	8.86 g	24.43 g
30 min	66.26 ml	0.55 g	3.28 g	0.04 g	3.49 g	10.44 g	23.83 g
45 min	61.18 ml	0.63 g	2.78 g	0.04 g	3.05 g	9.15 g	23.14 g
60 min	64.44 ml	0.74 g	2.91 g	0.05 g	3.21 g	9.62 g	24.54 g
90 min	62.83 ml	0.86 g	2.92 g	0.05 g	3.24 g	9.72 g	24.12 g
135 min	64.62 ml	1.02 g	3.15 g	0.06 g	3.48 g	10.43 g	24.23 g
180 min	64.71 ml	1.11 g	3.02 g	0.06 g	3.31 g	9.91 g	24.30 g

Lab Sample Molalities

Time (planned)	%H2O	Fe2+	Fe(T)	H+	SO4	X (Fe^{2+}/avg(Fe_T)
0 min	68%	0.00 mol/kg	2.09 mol/kg	1.17 mol/kg	3.71 mol/kg	0.00%
5 min	67%	0.12 mol/kg	2.25 mol/kg	1.34 mol/kg	3.76 mol/kg	5.27%
15 min	67%	0.26 mol/kg	2.20 mol/kg	1.51 mol/kg	3.78 mol/kg	11.83%
30 min	63%	0.41 mol/kg	2.46 mol/kg	1.79 mol/kg	4.56 mol/kg	18.77%
45 min	66%	0.49 mol/kg	2.15 mol/kg	1.86 mol/kg	4.12 mol/kg	22.26%
60 min	66%	0.54 mol/kg	2.12 mol/kg	1.95 mol/kg	4.08 mol/kg	24.68%
90 min	66%	0.64 mol/kg	2.16 mol/kg	2.09 mol/kg	4.19 mol/kg	29.17%
135 min	64%	0.75 mol/kg	2.32 mol/kg	2.30 mol/kg	4.48 mol/kg	34.43%
180 min	65%	0.82 mol/kg	2.22 mol/kg	2.38 mol/kg	4.25 mol/kg	37.21%

Analytical Results

Time (planned)	Fe2+_g/l	Fe_mg/l	H+_g/L	S_mg/l
0 min	0	48441	0.49	49352
5 min	2.49	48385	0.52	46499
15 min	5.53	46971	0.58	46270
30 min	8.26	49458	0.65	52616
45 min	10.3	45454	0.71	49918
60 min	11.5	45168	0.75	49832
90 min	13.7	46398	0.81	51627
135 min	15.8	48678	0.87	53899
180 min	17.1	46607	0.9	51145

Exp. Number	1-8
Test Name	FERRED-1-8
Conditions	
Temperature	95°C
SO2	1.00 l/min
O2	0.00 l/min
Agitation	1800 rpm
[Fe3+]	3.00 mol/kg
[Fe2+]	0.00 mol/kg
[H+]	1.42 mol/kg

Date	05 April 2012
Initial Reactor Mass	2813.76 g
Final Mass	
Solids	
H_2O Basis	1647.00 g
Repeat	0.00

Experimental Measurements

Time (planned)	Time (actual)	Total Sample Mass	Total Diluted	Density (20°C)	Titrator Dil. Sample	Volume $K_2Cr_2O_7$
0 min	0 min	39.30 g	80.65 g	1.1976 g/ml	2.30 g	0.235 ml
5 min	5 min	37.24 g	74.51 g	1.2041 g/ml	2.33 g	0.865 ml
15 min	15 min	35.46 g	71.88 g	1.2015 g/ml	2.28 g	1.704 ml
30 min	30 min	41.43 g	82.16 g	1.2075 g/ml	2.16 g	2.411 ml
45 min	45 min	40.70 g	80.97 g	1.2079 g/ml	2.70 g	3.703 ml
60 min	60 min	38.10 g	67.74 g	1.2367 g/ml	2.26 g	3.902 ml
90 min	90 min	37.01 g	74.33 g	1.2063 g/ml	2.12 g	3.886 ml
135 min	135 min	37.95 g	77.42 g	1.2035 g/ml	2.54 g	5.406 ml
180 min	180 min	37.04 g	74.64 g	1.2072 g/ml	2.04 g	4.889 ml

Titration Calculations

Time (planned)	Est. Reactor Mass	Fe^{2+} (mol/kg Soln.)	Total Fe^2	Total SO_2 added	Total H2O	Fe^{2+} Molality
0 min	2774.46 g	0.02 mol/kgsln	0.06 mol	0.00 g	1645.95 g	0.04 mol/kg
5 min	2743.75 g	0.07 mol/kgsln	0.20 mol	6.53 g	1643.33 g	0.12 mol/kg
15 min	2721.49 g	0.15 mol/kgsln	0.41 mol	13.20 g	1639.57 g	0.25 mol/kg
30 min	2699.20 g	0.22 mol/kgsln	0.60 mol	19.14 g	1636.24 g	0.37 mol/kg
45 min	2681.93 g	0.27 mol/kgsln	0.73 mol	23.44 g	1633.82 g	0.45 mol/kg
60 min	2670.08 g	0.31 mol/kgsln	0.82 mol	26.25 g	1632.23 g	0.50 mol/kg
90 min	2664.49 g	0.37 mol/kgsln	0.98 mol	31.42 g	1629.33 g	0.60 mol/kg
135 min	2663.58 g	0.43 mol/kgsln	1.16 mol	37.04 g	1626.17 g	0.71 mol/kg
180 min	2667.80 g	0.48 mol/kgsln	1.29 mol	41.26 g	1623.79 g	0.79 mol/kg

Lab Sample Analysis

Time (planned)	Volume	Fe2+	Fe(T)	H+	S	SO4	H2O
0 min	67.34 ml	0.00 g	4.05 g	0.03 g	4.00 g	11.99 g	23.23 g
5 min	61.88 ml	0.16 g	3.66 g	0.03 g	3.49 g	10.46 g	23.08 g
15 min	59.83 ml	0.30 g	3.62 g	0.03 g	3.45 g	10.33 g	21.48 g
30 min	68.04 ml	0.51 g	4.26 g	0.04 g	4.15 g	12.45 g	24.68 g
45 min	67.03 ml	0.62 g	3.80 g	0.05 g	4.12 g	12.34 g	24.51 g
60 min	54.77 ml	0.65 g	4.15 g	0.05 g	4.00 g	11.97 g	21.93 g
90 min	61.62 ml	0.76 g	3.69 g	0.05 g	3.72 g	11.13 g	22.14 g
135 min	64.33 ml	0.91 g	3.73 g	0.05 g	3.74 g	11.22 g	22.95 g
180 min	61.83 ml	0.99 g	3.86 g	0.06 g	3.85 g	11.53 g	21.60 g

Lab Sample Molalities

Time (planned)	%H2O	Fe2+	Fe(T)	H+	SO4	X (Fe^{2+}/avg(Fe_T)
0 min	59%	0.00 mol/kg	3.12 mol/kg	1.18 mol/kg	5.37 mol/kg	0.00%
5 min	62%	0.12 mol/kg	2.84 mol/kg	1.30 mol/kg	4.72 mol/kg	4.01%
15 min	61%	0.25 mol/kg	3.01 mol/kg	1.49 mol/kg	5.01 mol/kg	8.23%
30 min	60%	0.37 mol/kg	3.09 mol/kg	1.75 mol/kg	5.25 mol/kg	12.11%
45 min	60%	0.45 mol/kg	2.78 mol/kg	1.87 mol/kg	5.24 mol/kg	14.82%
60 min	58%	0.53 mol/kg	3.39 mol/kg	2.06 mol/kg	5.68 mol/kg	17.52%
90 min	60%	0.61 mol/kg	2.99 mol/kg	2.15 mol/kg	5.24 mol/kg	20.18%
135 min	60%	0.71 mol/kg	2.91 mol/kg	2.34 mol/kg	5.09 mol/kg	23.47%
180 min	58%	0.82 mol/kg	3.20 mol/kg	2.58 mol/kg	5.56 mol/kg	27.00%

Analytical Results

Time (planned)	Fe2+_g/l	Fe_mg/l	H+_g/L	S_mg/l
0 min	0	60190	0.41	59441
5 min	2.54	59221	0.49	56431
15 min	5.01	60428	0.54	57645
30 min	7.45	62653	0.64	61057
45 min	9.19	56744	0.69	61463
60 min	11.9	75745	0.83	72962
90 min	12.3	59931	0.78	60309
135 min	14.2	58005	0.84	58210
180 min	16	62378	0.91	62240

Exp. Number	1-9
Test Name	FERRED-1-9
Conditions	
Temperature	95°C
SO2	1.00 l/min
O2	0.00 l/min
Agitation	1800 rpm
[Fe3+]	0.50 mol/kg
[Fe2+]	0.00 mol/kg
[H+]	2.21 mol/kg

Date	16 April 2012
Initial Reactor Mass	2222.98 g
Final Mass	
Solids	
H_2O Basis	1840.00 g
Repeat	0.00

Experimental Measurements

Time (planned)	Time (actual)	Total Sample Mass	Total Diluted	Density (20°C)	Titrator Dil. Sample	Volume $K_2Cr_2O_7$
0 min	0 min	31.73 g	64.44 g	1.0691 g/ml	2.08 g	0.000 ml
5 min	5 min	32.10 g	64.48 g	1.0706 g/ml	2.08 g	0.499 ml
15 min	15 min	32.95 g	65.14 g	1.0723 g/ml	2.05 g	0.973 ml
30 min	30 min	31.13 g	62.46 g	1.0717 g/ml	2.16 g	1.373 ml
45 min	45 min	30.61 g	61.11 g	1.0723 g/ml	2.03 g	1.522 ml
60 min	60 min	30.65 g	60.99 g	1.0728 g/ml	2.15 g	1.761 ml
90 min	90 min	30.00 g	59.95 g	1.0727 g/ml	2.01 g	1.908 ml
135 min	137 min	30.81 g	66.85 g	1.0671 g/ml	2.23 g	2.201 ml
180 min	180 min	32.86 g	66.03 g	1.0729 g/ml	2.16 g	2.483 ml

Titration Calculations

Time (planned)	Est. Reactor Mass	Fe^{2+} (mol/kg Soln.)	Total Fe^2	Total SO_2 added	Total H2O	Fe^{2+} Molality
0 min	2191.25 g	0.00 mol/kgsln	0.00 mol	0.00 g	1840.00 g	0.00 mol/kg
5 min	2162.49 g	0.05 mol/kgsln	0.10 mol	3.34 g	1838.12 g	0.06 mol/kg
15 min	2135.96 g	0.09 mol/kgsln	0.20 mol	6.42 g	1836.39 g	0.11 mol/kg
30 min	2113.46 g	0.13 mol/kgsln	0.27 mol	8.63 g	1835.14 g	0.15 mol/kg
45 min	2092.88 g	0.15 mol/kgsln	0.31 mol	10.03 g	1834.36 g	0.17 mol/kg
60 min	2073.05 g	0.16 mol/kgsln	0.34 mol	10.82 g	1833.91 g	0.18 mol/kg
90 min	2055.54 g	0.19 mol/kgsln	0.39 mol	12.49 g	1832.98 g	0.21 mol/kg
135 min	2038.71 g	0.21 mol/kgsln	0.44 mol	13.98 g	1832.13 g	0.24 mol/kg
180 min	2020.80 g	0.23 mol/kgsln	0.47 mol	14.95 g	1831.59 g	0.25 mol/kg

Lab Sample Analysis

Time (planned)	Volume	Fe2+	Fe(T)	H+	S	SO4	H2O
0 min	60.27 ml	0.00 g	0.79 g	0.06 g	1.90 g	5.69 g	25.19 g
5 min	60.23 ml	0.07 g	0.72 g	0.06 g	1.71 g	5.12 g	26.21 g
15 min	60.75 ml	0.15 g	0.73 g	0.06 g	1.78 g	5.33 g	26.83 g
30 min	58.28 ml	0.20 g	0.67 g	0.06 g	1.71 g	5.14 g	25.26 g
45 min	56.99 ml	0.24 g	0.68 g	0.06 g	1.67 g	5.00 g	24.88 g
60 min	56.85 ml	0.26 g	0.67 g	0.06 g	1.69 g	5.07 g	24.84 g
90 min	55.89 ml	0.30 g	0.65 g	0.06 g	1.43 g	4.29 g	25.01 g
135 min	62.65 ml	0.35 g	0.68 g	0.06 g	1.51 g	4.54 g	25.53 g
180 min	61.54 ml	0.41 g	0.74 g	0.07 g	1.65 g	4.95 g	27.10 g

Lab Sample Molalities

Time (planned)	%H2O	Fe2+	Fe(T)	H+	SO4	X (Fe^{2+}/avg(Fe_T))
0 min	79%	0.00 mol/kg	0.56 mol/kg	2.30 mol/kg	2.35 mol/kg	0.00%
5 min	82%	0.05 mol/kg	0.49 mol/kg	2.23 mol/kg	2.03 mol/kg	10.07%
15 min	81%	0.10 mol/kg	0.48 mol/kg	2.29 mol/kg	2.07 mol/kg	20.35%
30 min	81%	0.14 mol/kg	0.48 mol/kg	2.27 mol/kg	2.12 mol/kg	29.31%
45 min	81%	0.17 mol/kg	0.49 mol/kg	2.27 mol/kg	2.09 mol/kg	35.82%
60 min	81%	0.19 mol/kg	0.49 mol/kg	2.41 mol/kg	2.13 mol/kg	39.19%
90 min	83%	0.21 mol/kg	0.46 mol/kg	2.33 mol/kg	1.78 mol/kg	44.58%
135 min	83%	0.25 mol/kg	0.48 mol/kg	2.43 mol/kg	1.85 mol/kg	50.86%
180 min	82%	0.27 mol/kg	0.49 mol/kg	2.46 mol/kg	1.90 mol/kg	56.27%

Analytical Results

Time (planned)	Fe2+_g/l	Fe_mg/l	H+_g/L	S_mg/l
0 min	0	13134	0.97	31496
5 min	1.18	11881	0.98	28365
15 min	2.42	11953	1.02	29304
30 min	3.42	11570	0.99	29414
45 min	4.21	11858	1	29270
60 min	4.61	11840	1.06	29797
90 min	5.37	11602	1.05	25606
135 min	5.58	10895	1	24167
180 min	6.67	12060	1.09	26853

Exp. Number	1-10
Test Name	FERRED-1-10
Conditions	
Temperature	95°C
SO2	1.00 l/min
O2	0.00 l/min
Agitation	1800 rpm
[Fe3+]	1.33 mol/kg
[Fe2+]	0.00 mol/kg
[H+]	2.21 mol/kg

Date	28 March 2012
Initial Reactor Mass	2444.45 g
Final Mass	
Solids	
H_2O Basis	1778.00 g
Repeat	0.00

Experimental Measurements

Time (planned)	Time (actual)	Total Sample Mass	Total Diluted	Density (20°C)	Titrator Dil. Sample	Volume $K_2Cr_2O_7$
0 min	0 min	34.30 g	69.87 g	1.1234 g/ml	2.49 g	0.000 ml
5 min	5 min	34.10 g	68.57 g	1.1261 g/ml	2.57 g	0.751 ml
15 min	15 min	33.06 g	68.71 g	1.1225 g/ml	1.93 g	1.163 ml
30 min	30 min	36.11 g	72.09 g	1.1285 g/ml	1.99 g	1.812 ml
45 min	45 min	33.85 g	67.10 g	1.1296 g/ml	2.19 g	2.515 ml
60 min	60 min	35.50 g	70.69 g	1.1296 g/ml	2.09 g	2.663 ml
90 min	90 min	34.65 g	69.55 g	1.1289 g/ml	1.88 g	2.754 ml
135 min	135 min	38.09 g	76.80 g	1.1289 g/ml	2.00 g	3.398 ml
180 min	180 min	35.43 g	70.95 g	1.1303 g/ml	2.17 g	4.135 ml

Titration Calculations

Time (planned)	Est. Reactor Mass	Fe^{2+} (mol/kg Soln.)	Total Fe^2	Total SO_2 added	Total H2O	Fe^{2+} Molality
0 min	2410.15 g	0.00 mol/kgsln	0.00 mol	0.00 g	1778.00 g	0.00 mol/kg
5 min	2380.53 g	0.06 mol/kgsln	0.14 mol	4.48 g	1775.48 g	0.08 mol/kg
15 min	2356.92 g	0.13 mol/kgsln	0.30 mol	9.45 g	1772.68 g	0.17 mol/kg
30 min	2334.40 g	0.18 mol/kgsln	0.42 mol	13.59 g	1770.36 g	0.24 mol/kg
45 min	2317.45 g	0.23 mol/kgsln	0.53 mol	16.90 g	1768.50 g	0.30 mol/kg
60 min	2300.65 g	0.25 mol/kgsln	0.58 mol	18.69 g	1767.48 g	0.33 mol/kg
90 min	2287.54 g	0.29 mol/kgsln	0.67 mol	21.54 g	1765.88 g	0.38 mol/kg
135 min	2274.40 g	0.34 mol/kgsln	0.78 mol	24.95 g	1763.96 g	0.44 mol/kg
180 min	2266.67 g	0.38 mol/kgsln	0.86 mol	27.70 g	1762.42 g	0.49 mol/kg

Lab Sample Analysis

Time (planned)	Volume	Fe2+	Fe(T)	H+	S	SO4	H2O
0 min	62.20 ml	0.00 g	1.87 g	0.06 g	2.44 g	7.30 g	25.08 g
5 min	60.89 ml	0.11 g	1.85 g	0.06 g	2.44 g	7.30 g	24.90 g
15 min	61.21 ml	0.22 g	1.80 g	0.06 g	2.39 g	7.15 g	24.05 g
30 min	63.88 ml	0.35 g	1.95 g	0.07 g	2.67 g	8.01 g	26.08 g
45 min	59.40 ml	0.41 g	1.83 g	0.06 g	2.51 g	7.51 g	24.45 g
60 min	62.58 ml	0.48 g	1.93 g	0.07 g	2.68 g	8.03 g	25.47 g
90 min	61.61 ml	0.55 g	1.90 g	0.07 g	2.67 g	7.99 g	24.69 g
135 min	68.03 ml	0.71 g	2.03 g	0.08 g	2.89 g	8.65 g	27.34 g
180 min	62.77 ml	0.73 g	1.96 g	0.08 g	2.75 g	8.24 g	25.15 g

Lab Sample Molalities

Time (planned)	%H2O	Fe2+	Fe(T)	H+	SO4	X (Fe^{2+}/avg(Fe_T)
0 min	73%	0.00 mol/kg	1.33 mol/kg	2.21 mol/kg	3.03 mol/kg	0.00%
5 min	73%	0.08 mol/kg	1.33 mol/kg	2.26 mol/kg	3.05 mol/kg	5.68%
15 min	73%	0.16 mol/kg	1.34 mol/kg	2.37 mol/kg	3.10 mol/kg	12.16%
30 min	72%	0.24 mol/kg	1.34 mol/kg	2.48 mol/kg	3.20 mol/kg	17.66%
45 min	72%	0.30 mol/kg	1.34 mol/kg	2.48 mol/kg	3.20 mol/kg	22.03%
60 min	72%	0.34 mol/kg	1.36 mol/kg	2.63 mol/kg	3.28 mol/kg	25.15%
90 min	71%	0.40 mol/kg	1.38 mol/kg	2.75 mol/kg	3.37 mol/kg	29.82%
135 min	72%	0.46 mol/kg	1.33 mol/kg	2.84 mol/kg	3.29 mol/kg	34.37%
180 min	71%	0.52 mol/kg	1.39 mol/kg	2.97 mol/kg	3.41 mol/kg	38.44%

Analytical Results

Time (planned)	Fe2+_g/l	Fe_mg/l	H+_g/L	S_mg/l
0 min	0	30013	0.9	39164
5 min	1.75	30347	0.93	40014
15 min	3.6	29351	0.94	39003
30 min	5.43	30586	1.02	41844
45 min	6.83	30750	1.03	42221
60 min	7.71	30876	1.08	42833
90 min	9	30867	1.11	43307
135 min	10.4	29808	1.15	42432
180 min	11.6	31169	1.2	43840

Exp. Number	1-11
Test Name	FERRED-1-11
Conditions	
Temperature	95°C
SO2	1.00 l/min
O2	0.00 l/min
Agitation	1800 rpm
[Fe3+]	2.17 mol/kg
[Fe2+]	0.00 mol/kg
[H+]	2.21 mol/kg

Date	20 March 2012
Initial Reactor Mass	2640.95 g
Final Mass	
Solids	
H_2O Basis	1713.00 g
Repeat	0.00

Experimental Measurements

Time (planned)	Time (actual)	Total Sample Mass	Total Diluted	Density (20°C)	Titrator Dil. Sample	Volume $K_2Cr_2O_7$
0 min	0 min	40.41 g	81.69 g	1.1658 g/ml	2.06 g	0.000 ml
5 min	5 min	34.46 g	69.96 g	1.1656 g/ml	2.11 g	0.594 ml
15 min	15 min	32.73 g	65.32 g	1.1694 g/ml	2.02 g	1.289 ml
30 min	30 min	28.28 g	55.72 g	1.1728 g/ml	2.68 g	2.635 ml
45 min	45 min	35.89 g	71.87 g	1.1699 g/ml	2.02 g	2.599 ml
60 min	60 min	28.98 g	61.23 g	1.1607 g/ml	1.98 g	2.486 ml
90 min	90 min	31.70 g	63.08 g	1.1721 g/ml	1.90 g	2.982 ml
135 min	142 min	26.82 g	54.59 g	1.1688 g/ml	1.99 g	3.844 ml
180 min	180 min	38.51 g	78.19 g	1.1696 g/ml	1.71 g	3.472 ml

Titration Calculations

Time (planned)	Est. Reactor Mass	Fe^{2+} (mol/kg Soln.)	Total Fe^2	Total SO_2 added	Total H2O	Fe^{2+} Molality
0 min	2600.54 g	0.00 mol/kgsln	0.00 mol	0.00 g	1713.00 g	0.00 mol/kg
5 min	2570.79 g	0.06 mol/kgsln	0.15 mol	4.71 g	1710.35 g	0.09 mol/kg
15 min	2548.45 g	0.13 mol/kgsln	0.32 mol	10.39 g	1707.15 g	0.19 mol/kg
30 min	2535.90 g	0.19 mol/kgsln	0.49 mol	15.73 g	1704.15 g	0.29 mol/kg
45 min	2520.81 g	0.26 mol/kgsln	0.65 mol	20.80 g	1701.30 g	0.38 mol/kg
60 min	2513.19 g	0.27 mol/kgsln	0.67 mol	21.35 g	1700.99 g	0.39 mol/kg
90 min	2506.56 g	0.31 mol/kgsln	0.78 mol	25.07 g	1698.90 g	0.46 mol/kg
135 min	2511.36 g	0.39 mol/kgsln	0.99 mol	31.62 g	1695.21 g	0.58 mol/kg
180 min	2505.94 g	0.41 mol/kgsln	1.03 mol	33.09 g	1694.39 g	0.61 mol/kg

Lab Sample Analysis

Time (planned)	Volume	Fe2+	Fe(T)	H+	S	SO4	H2O
0 min	70.07 ml	0.00 g	3.49 g	0.05 g	3.78 g	11.33 g	25.53 g
5 min	60.02 ml	0.11 g	2.84 g	0.05 g	3.14 g	9.41 g	22.17 g
15 min	55.86 ml	0.23 g	2.63 g	0.05 g	2.93 g	8.77 g	21.28 g
30 min	47.51 ml	0.29 g	2.13 g	0.04 g	2.45 g	7.34 g	18.76 g
45 min	61.43 ml	0.46 g	2.73 g	0.06 g	3.11 g	9.31 g	23.79 g
60 min	52.75 ml	0.42 g	2.39 g	0.05 g	2.78 g	8.32 g	18.22 g
90 min	53.82 ml	0.54 g	2.57 g	0.05 g	2.91 g	8.72 g	20.36 g
135 min	46.71 ml	0.56 g	2.08 g	0.05 g	2.39 g	7.15 g	17.54 g
180 min	66.85 ml	0.88 g	3.00 g	0.07 g	3.56 g	10.67 g	24.77 g

Lab Sample Molalities

Time (planned)	%H2O	Fe2+	Fe(T)	H+	SO4	X (Fe^{2+}/avg(Fe_T))
0 min	63%	0.00 mol/kg	2.45 mol/kg	2.10 mol/kg	4.62 mol/kg	0.00%
5 min	64%	0.09 mol/kg	2.29 mol/kg	2.15 mol/kg	4.42 mol/kg	3.96%
15 min	65%	0.19 mol/kg	2.21 mol/kg	2.27 mol/kg	4.29 mol/kg	8.69%
30 min	66%	0.28 mol/kg	2.04 mol/kg	2.29 mol/kg	4.07 mol/kg	12.46%
45 min	66%	0.34 mol/kg	2.06 mol/kg	2.41 mol/kg	4.08 mol/kg	15.50%
60 min	63%	0.41 mol/kg	2.35 mol/kg	2.58 mol/kg	4.75 mol/kg	18.64%
90 min	64%	0.48 mol/kg	2.26 mol/kg	2.62 mol/kg	4.46 mol/kg	21.57%
135 min	65%	0.57 mol/kg	2.12 mol/kg	2.69 mol/kg	4.24 mol/kg	25.59%
180 min	64%	0.64 mol/kg	2.17 mol/kg	2.84 mol/kg	4.49 mol/kg	28.78%

Analytical Results

Time (planned)	Fe2+_g/l	Fe_mg/l	H+_g/L	S_mg/l
0 min	0	49850	0.77	53975
5 min	1.81	47267	0.8	52325
15 min	4.1	47094	0.87	52393
30 min	6.09	44932	0.91	51584
45 min	7.43	44498	0.94	50604
60 min	7.97	45267	0.9	52660
90 min	10.1	47801	1	54066
135 min	11.9	44565	1.02	51084
180 min	13.2	44862	1.06	53287

Exp. Number	1-12
Test Name	FERRED-1-12
Conditions	
Temperature	95°C
SO2	1.00 l/min
O2	0.00 l/min
Agitation	1800 rpm
[Fe3+]	3.00 mol/kg
[Fe2+]	0.00 mol/kg
[H+]	2.21 mol/kg

Date	04 April 2012
Initial Reactor Mass	2813.76 g
Final Mass	
Solids	
H_2O Basis	1647.00 g
Repeat	0.00

Experimental Measurements

Time (planned)	Time (actual)	Total Sample Mass	Total Diluted	Density (20°C)	Titrator Dil. Sample	Volume $K_2Cr_2O_7$
0 min	0 min	28.93 g	58.37 g	1.2059 g/ml	1.98 g	0.000 ml
5 min	5 min	32.15 g	65.17 g	1.2058 g/ml	2.17 g	0.618 ml
15 min	15 min	35.11 g	70.00 g	1.2104 g/ml	2.09 g	1.325 ml
30 min	30 min	37.34 g	75.95 g	1.2063 g/ml	2.35 g	2.188 ml
45 min	45 min	38.84 g	78.02 g	1.2097 g/ml	2.83 g	3.310 ml
60 min	60 min	38.41 g	77.02 g	1.2104 g/ml	2.22 g	2.948 ml
90 min	90 min	38.31 g	77.45 g	1.2086 g/ml	2.59 g	4.093 ml
135 min	135 min	35.82 g	71.82 g	1.2116 g/ml	2.33 g	4.460 ml
180 min	180 min	35.87 g	71.34 g	1.2138 g/ml	2.41 g	5.220 ml

Titration Calculations

Time (planned)	Est. Reactor Mass	Fe^{2+} (mol/kg Soln.)	Total Fe^2	Total SO_2 added	Total H2O	Fe^{2+} Molality
0 min	2784.83 g	0.00 mol/kgsln	0.00 mol	0.00 g	1647.00 g	0.00 mol/kg
5 min	2757.78 g	0.06 mol/kgsln	0.16 mol	5.10 g	1644.13 g	0.10 mol/kg
15 min	2733.74 g	0.13 mol/kgsln	0.35 mol	11.07 g	1640.78 g	0.21 mol/kg
30 min	2712.85 g	0.19 mol/kgsln	0.51 mol	16.45 g	1637.74 g	0.31 mol/kg
45 min	2694.28 g	0.23 mol/kgsln	0.63 mol	20.27 g	1635.60 g	0.39 mol/kg
60 min	2678.72 g	0.27 mol/kgsln	0.71 mol	22.84 g	1634.15 g	0.44 mol/kg
90 min	2667.70 g	0.32 mol/kgsln	0.85 mol	27.30 g	1631.65 g	0.52 mol/kg
135 min	2664.64 g	0.38 mol/kgsln	1.02 mol	32.75 g	1628.58 g	0.63 mol/kg
180 min	2665.54 g	0.43 mol/kgsln	1.15 mol	36.78 g	1626.31 g	0.71 mol/kg

Lab Sample Analysis

Time (planned)	Volume	Fe2+	Fe(T)	H+	S	SO4	H2O
0 min	48.40 ml	0.00 g	2.95 g	0.03 g	2.92 g	8.76 g	17.19 g
5 min	54.05 ml	0.11 g	3.29 g	0.04 g	3.24 g	9.72 g	19.11 g
15 min	57.83 ml	0.25 g	3.55 g	0.05 g	3.63 g	10.88 g	20.64 g
30 min	62.96 ml	0.36 g	3.88 g	0.05 g	3.87 g	11.60 g	21.80 g
45 min	64.50 ml	0.50 g	4.10 g	0.06 g	4.06 g	12.18 g	22.51 g
60 min	63.63 ml	0.57 g	4.01 g	0.06 g	4.26 g	12.77 g	21.57 g
90 min	64.08 ml	0.69 g	3.66 g	0.06 g	4.13 g	12.37 g	22.22 g
135 min	59.28 ml	0.76 g	3.62 g	0.06 g	3.96 g	11.86 g	20.28 g
180 min	58.77 ml	0.85 g	3.49 g	0.07 g	3.86 g	11.58 g	20.73 g

Lab Sample Molalities

Time (planned)	%H2O	Fe2+	Fe(T)	H+	SO4	X (Fe^{2+}/avg(Fe_T)
0 min	59%	0.00 mol/kg	3.07 mol/kg	1.90 mol/kg	5.30 mol/kg	0.00%
5 min	59%	0.10 mol/kg	3.08 mol/kg	2.08 mol/kg	5.29 mol/kg	3.24%
15 min	59%	0.22 mol/kg	3.08 mol/kg	2.31 mol/kg	5.49 mol/kg	6.96%
30 min	58%	0.29 mol/kg	3.19 mol/kg	2.46 mol/kg	5.54 mol/kg	9.34%
45 min	58%	0.40 mol/kg	3.26 mol/kg	2.59 mol/kg	5.63 mol/kg	12.69%
60 min	56%	0.47 mol/kg	3.33 mol/kg	2.81 mol/kg	6.16 mol/kg	14.99%
90 min	58%	0.55 mol/kg	2.95 mol/kg	2.83 mol/kg	5.80 mol/kg	17.66%
135 min	57%	0.68 mol/kg	3.20 mol/kg	3.16 mol/kg	6.09 mol/kg	21.57%
180 min	58%	0.74 mol/kg	3.01 mol/kg	3.21 mol/kg	5.81 mol/kg	23.52%

Analytical Results

Time (planned)	Fe2+_g/l	Fe_mg/l	H+_g/L	S_mg/l
0 min	0	60872	0.68	60403
5 min	2	60788	0.74	60016
15 min	4.34	61378	0.83	62782
30 min	5.65	61669	0.86	61510
45 min	7.74	63551	0.91	63021
60 min	8.88	63019	0.96	66974
90 min	10.7	57110	0.99	64436
135 min	12.9	61071	1.09	66760
180 min	14.5	59385	1.14	65759

Exp. Number	1-13
Test Name	FERRED-1-13
Conditions	
Temperature	95°C
SO2	1.00 l/min
O2	0.00 l/min
Agitation	1800 rpm
[Fe3+]	0.50 mol/kg
[Fe2+]	0.00 mol/kg
[H+]	3.00 mol/kg

Date	16 March 2012
Initial Reactor Mass	2260.54 g
Final Mass	
Solids	
H_2O Basis	1813.00 g
Repeat	0.00

Experimental Measurements

Time (planned)	Time (actual)	Total Sample Mass	Total Diluted	Density (20°C)	Titrator Dil. Sample	Volume $K_2Cr_2O_7$
0 min	0 min	25.97 g	52.00 g	1.0809 g/ml	2.40 g	0.000 ml
5 min	5 min	35.05 g	70.08 g	1.0805 g/ml	2.34 g	0.535 ml
15 min	15 min	32.06 g	64.85 g	1.0799 g/ml	2.63 g	0.966 ml
30 min	28 min	34.74 g	69.22 g	1.0816 g/ml	2.84 g	1.398 ml
45 min	45 min	36.60 g	74.17 g	1.0803 g/ml	2.30 g	1.700 ml
60 min	55 min	34.30 g	68.90 g	1.0812 g/ml	2.78 g	2.544 ml
90 min	94 min	34.82 g	71.02 g	1.0803 g/ml	2.08 g	1.579 ml
135 min	138 min	34.31 g	77.02 g	1.0729 g/ml	2.43 g	1.896 ml
180 min	180 min	34.36 g	74.44 g	1.0758 g/ml	2.57 g	2.408 ml

Titration Calculations

Time (planned)	Est. Reactor Mass	Fe^{2+} (mol/kg Soln.)	Total Fe^{2}	Total SO_2 added	Total H2O	Fe^{2+} Molality
0 min	2234.57 g	0.00 mol/kgsln	0.00 mol	0.00 g	1813.00 g	0.00 mol/kg
5 min	2202.74 g	0.05 mol/kgsln	0.10 mol	3.22 g	1811.19 g	0.06 mol/kg
15 min	2175.86 g	0.07 mol/kgsln	0.16 mol	5.18 g	1810.09 g	0.09 mol/kg
30 min	2147.87 g	0.10 mol/kgsln	0.21 mol	6.75 g	1809.20 g	0.12 mol/kg
45 min	2121.45 g	0.15 mol/kgsln	0.32 mol	10.18 g	1807.28 g	0.18 mol/kg
60 min	2099.51 g	0.18 mol/kgsln	0.39 mol	12.36 g	1806.05 g	0.21 mol/kg
90 min	2074.98 g	0.15 mol/kgsln	0.32 mol	10.29 g	1807.21 g	0.18 mol/kg
135 min	2052.18 g	0.18 mol/kgsln	0.36 mol	11.51 g	1806.52 g	0.20 mol/kg
180 min	2031.02 g	0.20 mol/kgsln	0.41 mol	13.20 g	1805.57 g	0.23 mol/kg

Lab Sample Analysis

Time (planned)	Volume	Fe2+	Fe(T)	H+	S	SO4	H2O
0 min	48.11 ml	0.00 g	0.66 g	0.06 g	1.68 g	5.03 g	20.21 g
5 min	64.86 ml	0.06 g	0.75 g	0.09 g	2.02 g	6.06 g	28.15 g
15 min	60.05 ml	0.11 g	0.68 g	0.08 g	1.84 g	5.51 g	25.79 g
30 min	64.00 ml	0.15 g	0.84 g	0.09 g	2.09 g	6.27 g	27.54 g
45 min	68.66 ml	0.22 g	0.89 g	0.09 g	2.22 g	6.65 g	28.96 g
60 min	63.73 ml	0.22 g	0.78 g	0.09 g	2.06 g	6.16 g	27.26 g
90 min	65.74 ml	0.27 g	0.82 g	0.09 g	2.22 g	6.64 g	27.27 g
135 min	71.79 ml	0.32 g	0.79 g	0.09 g	2.15 g	6.44 g	26.99 g
180 min	69.20 ml	0.33 g	0.76 g	0.09 g	2.12 g	6.35 g	27.16 g

Lab Sample Molalities

Time (planned)	%H2O	Fe2+	Fe(T)	H+	SO4	X (Fe^{2+}/avg(Fe_T))
0 min	78%	0.00 mol/kg	0.58 mol/kg	3.19 mol/kg	2.59 mol/kg	0.00%
5 min	80%	0.04 mol/kg	0.48 mol/kg	3.13 mol/kg	2.24 mol/kg	7.25%
15 min	80%	0.07 mol/kg	0.47 mol/kg	3.14 mol/kg	2.22 mol/kg	13.94%
30 min	79%	0.10 mol/kg	0.55 mol/kg	3.23 mol/kg	2.37 mol/kg	18.85%
45 min	79%	0.13 mol/kg	0.55 mol/kg	3.25 mol/kg	2.39 mol/kg	25.47%
60 min	79%	0.14 mol/kg	0.52 mol/kg	3.25 mol/kg	2.35 mol/kg	27.12%
90 min	78%	0.18 mol/kg	0.54 mol/kg	3.33 mol/kg	2.54 mol/kg	34.08%
135 min	79%	0.21 mol/kg	0.52 mol/kg	3.35 mol/kg	2.48 mol/kg	40.83%
180 min	79%	0.22 mol/kg	0.50 mol/kg	3.34 mol/kg	2.43 mol/kg	42.20%

Analytical Results

Time (planned)	Fe2+_g/l	Fe_mg/l	H+_g/L	S_mg/l
0 min	0	13719	1.35	34926
5 min	0.92	11624	1.37	31186
15 min	1.75	11255	1.36	30622
30 min	2.37	13141	1.4	32719
45 min	3.14	12971	1.38	32341
60 min	3.39	12314	1.4	32280
90 min	4.13	12446	1.39	33736
135 min	4.485	11019	1.27	29952
180 min	4.84	10973	1.32	30635

Exp. Number	1-14
Test Name	FERRED-1-14
Conditions	
Temperature	95°C
SO2	1.00 l/min
O2	0.00 l/min
Agitation	1800 rpm
[Fe3+]	1.33 mol/kg
[Fe2+]	0.00 mol/kg
[H+]	3.00 mol/kg

Date	17 April 2012
Initial Reactor Mass	2475.20 g
Final Mass	
Solids	
H_2O Basis	1751.00 g
Repeat	0.00

Experimental Measurements

Time (planned)	Time (actual)	Total Sample Mass	Total Diluted	Density (20°C)	Titrator Dil. Sample	Volume $K_2Cr_2O_7$
0 min	0 min	35.11 g	70.94 g	1.1300 g/ml	2.28 g	0.000 ml
5 min	5 min	32.34 g	64.47 g	1.1324 g/ml	2.10 g	0.525 ml
15 min	15 min	37.66 g	76.12 g	1.1312 g/ml	2.23 g	1.112 ml
30 min	30 min	35.37 g	71.43 g	1.1317 g/ml	2.34 g	1.682 ml
45 min	45 min	32.52 g	65.79 g	1.1317 g/ml	2.14 g	2.000 ml
60 min	60 min	28.37 g	67.90 g	1.3330 g/ml	2.23 g	1.700 ml
90 min	90 min	32.50 g	64.89 g	1.1345 g/ml	2.26 g	2.750 ml
135 min	137 min	35.43 g	70.53 g	1.1351 g/ml	2.25 g	3.185 ml
180 min	180 min	35.05 g	71.97 g	1.1310 g/ml	2.05 g	3.256 ml

Titration Calculations

Time (planned)	Est. Reactor Mass	Fe^{2+} (mol/kg Soln.)	Total Fe^2	Total SO_2 added	Total H2O	Fe^{2+} Molality
0 min	2440.09 g	0.00 mol/kgsln	0.00 mol	0.00 g	1751.00 g	0.00 mol/kg
5 min	2411.60 g	0.05 mol/kgsln	0.12 mol	3.85 g	1748.83 g	0.07 mol/kg
15 min	2381.63 g	0.10 mol/kgsln	0.24 mol	7.69 g	1746.68 g	0.14 mol/kg
30 min	2357.22 g	0.15 mol/kgsln	0.34 mol	10.96 g	1744.84 g	0.20 mol/kg
45 min	2338.86 g	0.19 mol/kgsln	0.44 mol	14.16 g	1743.03 g	0.25 mol/kg
60 min	2324.07 g	0.18 mol/kgsln	0.42 mol	13.58 g	1743.36 g	0.24 mol/kg
90 min	2309.54 g	0.24 mol/kgsln	0.56 mol	17.97 g	1740.89 g	0.32 mol/kg
135 min	2294.82 g	0.28 mol/kgsln	0.65 mol	20.71 g	1739.35 g	0.37 mol/kg
180 min	2283.62 g	0.33 mol/kgsln	0.74 mol	23.85 g	1737.58 g	0.43 mol/kg

Lab Sample Analysis

Time (planned)	Volume	Fe2+	Fe(T)	H+	S	SO4	H2O
0 min	62.78 ml	0.00 g	1.81 g	0.07 g	3.00 g	8.99 g	24.23 g
5 min	56.93 ml	0.08 g	1.65 g	0.07 g	2.74 g	8.22 g	22.40 g
15 min	67.29 ml	0.20 g	2.03 g	0.08 g	3.48 g	10.44 g	25.11 g
30 min	63.12 ml	0.27 g	1.81 g	0.08 g	3.15 g	9.45 g	24.03 g
45 min	58.13 ml	0.31 g	1.74 g	0.07 g	3.03 g	9.09 g	21.62 g
60 min	50.94 ml	0.32 g	1.47 g	0.07 g	2.55 g	7.65 g	19.19 g
90 min	57.20 ml	0.45 g	1.68 g	0.08 g	2.90 g	8.70 g	22.04 g
135 min	62.14 ml	0.56 g	1.80 g	0.09 g	3.30 g	9.90 g	23.65 g
180 min	63.63 ml	0.62 g	1.95 g	0.09 g	3.49 g	10.45 g	22.56 g

Lab Sample Molalities

Time (planned)	%H2O	Fe2+	Fe(T)	H+	SO4	X (Fe^{2+}/avg(Fe_T)
0 min	69%	0.00 mol/kg	1.34 mol/kg	2.98 mol/kg	3.86 mol/kg	0.00%
5 min	69%	0.07 mol/kg	1.32 mol/kg	3.03 mol/kg	3.82 mol/kg	4.72%
15 min	67%	0.14 mol/kg	1.45 mol/kg	3.22 mol/kg	4.33 mol/kg	10.03%
30 min	68%	0.20 mol/kg	1.35 mol/kg	3.28 mol/kg	4.09 mol/kg	14.31%
45 min	66%	0.26 mol/kg	1.44 mol/kg	3.39 mol/kg	4.38 mol/kg	18.42%
60 min	68%	0.30 mol/kg	1.37 mol/kg	3.45 mol/kg	4.15 mol/kg	21.33%
90 min	68%	0.36 mol/kg	1.37 mol/kg	3.48 mol/kg	4.11 mol/kg	26.12%
135 min	67%	0.42 mol/kg	1.36 mol/kg	3.65 mol/kg	4.36 mol/kg	30.26%
180 min	64%	0.49 mol/kg	1.55 mol/kg	3.86 mol/kg	4.82 mol/kg	35.39%

Analytical Results

Time (planned)	Fe2+_g/l	Fe_mg/l	H+_g/L	S_mg/l
0 min	0	28847	1.16	47825
5 min	1.445	28910	1.2	48206
15 min	2.91	30183	1.21	51789
30 min	4.24	28637	1.26	49975
45 min	5.33	29883	1.27	52192
60 min	6.25	28765	1.31	50130
90 min	7.83	29446	1.35	50773
135 min	8.96	28946	1.4	53169
180 min	9.76	30710	1.38	54814

Exp. Number	1-15
Test Name	FERRED-1-15
Conditions	
Temperature	95°C
SO2	1.00 l/min
O2	0.00 l/min
Agitation	1800 rpm
[Fe3+]	2.17 mol/kg
[Fe2+]	0.00 mol/kg
[H+]	3.00 mol/kg

Date	12 April 2012
Initial Reactor Mass	2665.69 g
Final Mass	
Solids	
H_2O Basis	1687.00 g
Repeat	0.00

Experimental Measurements

Time (planned)	Time (actual)	Total Sample Mass	Total Diluted	Density (20°C)	Titrator Dil. Sample	Volume $K_2Cr_2O_7$
0 min	0 min	40.91 g	81.15 g	1.1775 g/ml	2.28 g	0.046 ml
5 min	5 min	35.86 g	72.79 g	1.1736 g/ml	2.46 g	0.636 ml
15 min	15 min	36.17 g	72.27 g	1.1721 g/ml	2.20 g	1.510 ml
30 min	30 min	35.02 g	73.59 g	1.1681 g/ml	2.48 g	2.100 ml
45 min	45 min	38.72 g	78.35 g	1.1757 g/ml	2.94 g	3.000 ml
60 min	60 min	38.33 g	75.59 g	1.1813 g/ml	2.42 g	2.798 ml
90 min	90 min	38.28 g	76.65 g	1.1785 g/ml	2.09 g	2.780 ml
135 min	135 min	40.20 g	80.68 g	1.1784 g/ml	2.52 g	4.010 ml
180 min	180 min	33.48 g	66.10 g	1.1824 g/ml	2.77 g	5.048 ml

Titration Calculations

Time (planned)	Est. Reactor Mass	Fe^{2+} (mol/kg Soln.)	Total Fe^2	Total SO_2 added	Total H2O	Fe^{2+} Molality
0 min	2624.78 g	0.00 mol/kgsln	0.01 mol	0.00 g	1686.81 g	0.01 mol/kg
5 min	2593.28 g	0.05 mol/kgsln	0.14 mol	4.36 g	1684.55 g	0.08 mol/kg
15 min	2568.39 g	0.14 mol/kgsln	0.35 mol	11.28 g	1680.65 g	0.21 mol/kg
30 min	2547.89 g	0.18 mol/kgsln	0.45 mol	14.52 g	1678.83 g	0.27 mol/kg
45 min	2525.87 g	0.21 mol/kgsln	0.52 mol	16.70 g	1677.60 g	0.31 mol/kg
60 min	2505.84 g	0.23 mol/kgsln	0.57 mol	18.30 g	1676.71 g	0.34 mol/kg
90 min	2488.79 g	0.27 mol/kgsln	0.66 mol	21.23 g	1675.06 g	0.40 mol/kg
135 min	2473.90 g	0.32 mol/kgsln	0.79 mol	25.30 g	1672.77 g	0.47 mol/kg
180 min	2468.86 g	0.36 mol/kgsln	0.89 mol	28.45 g	1671.00 g	0.53 mol/kg

Lab Sample Analysis

Time (planned)	Volume	Fe2+	Fe(T)	H+	S	SO4	H2O
0 min	68.92 ml	0.00 g	3.19 g	0.07 g	3.72 g	11.13 g	26.51 g
5 min	62.02 ml	0.10 g	2.82 g	0.06 g	3.27 g	9.79 g	23.19 g
15 min	61.66 ml	0.20 g	2.66 g	0.07 g	3.10 g	9.28 g	24.16 g
30 min	63.00 ml	0.29 g	2.86 g	0.07 g	3.58 g	10.73 g	21.36 g
45 min	66.64 ml	0.38 g	3.23 g	0.08 g	4.01 g	12.02 g	23.39 g
60 min	63.99 ml	0.46 g	3.11 g	0.08 g	3.87 g	11.60 g	23.54 g
90 min	65.04 ml	0.56 g	3.22 g	0.08 g	4.10 g	12.28 g	22.70 g
135 min	68.47 ml	0.70 g	3.21 g	0.09 g	4.28 g	12.82 g	24.08 g
180 min	55.90 ml	0.63 g	2.42 g	0.08 g	3.09 g	9.24 g	21.74 g

Lab Sample Molalities

Time (planned)	%H2O	Fe2+	Fe(T)	H+	SO4	X (Fe^{2+}/avg(Fe_T))
0 min	65%	0.00 mol/kg	2.16 mol/kg	2.63 mol/kg	4.37 mol/kg	0.00%
5 min	65%	0.08 mol/kg	2.18 mol/kg	2.71 mol/kg	4.39 mol/kg	3.39%
15 min	67%	0.15 mol/kg	1.97 mol/kg	2.89 mol/kg	4.00 mol/kg	6.58%
30 min	61%	0.24 mol/kg	2.40 mol/kg	3.28 mol/kg	5.23 mol/kg	10.68%
45 min	60%	0.29 mol/kg	2.48 mol/kg	3.42 mol/kg	5.35 mol/kg	12.70%
60 min	61%	0.35 mol/kg	2.37 mol/kg	3.45 mol/kg	5.13 mol/kg	15.37%
90 min	59%	0.44 mol/kg	2.54 mol/kg	3.70 mol/kg	5.63 mol/kg	19.27%
135 min	60%	0.52 mol/kg	2.39 mol/kg	3.78 mol/kg	5.54 mol/kg	22.83%
180 min	65%	0.52 mol/kg	1.99 mol/kg	3.65 mol/kg	4.43 mol/kg	22.68%

Analytical Results

Time (planned)	Fe2+_g/l	Fe_mg/l	H+_g/L	S_mg/l
0 min	0	46317	1.02	53927
5 min	1.61	45487	1.02	52670
15 min	3.275	43162	1.14	50255
30 min	4.6	45435	1.12	56847
45 min	5.66	48540	1.21	60194
60 min	7.18	48642	1.28	60510
90 min	8.54	49439	1.3	63045
135 min	10.2	46943	1.34	62481
180 min	11.2	43255	1.43	55198

Exp. Number	1-16
Test Name	FERRED-1-16
Conditions	
Temperature	95°C
SO2	1.00 l/min
O2	0.00 l/min
Agitation	1800 rpm
[Fe3+]	3.00 mol/kg
[Fe2+]	0.00 mol/kg
[H+]	3.00 mol/kg

Date	15 March 2012
Initial Reactor Mass	2833.29 g
Final Mass	
Solids	
H_2O Basis	1622.00 g
Repeat	0.00

Experimental Measurements

Time (planned)	Time (actual)	Total Sample Mass	Total Diluted	Density (20°C)	Titrator Dil. Sample	Volume $K_2Cr_2O_7$
0 min	0 min	43.92 g	87.90 g	1.2107 g/ml	2.06 g	0.000 ml
5 min	5 min	44.46 g	89.61 g	1.2107 g/ml	2.36 g	0.513 ml
15 min	15 min	42.64 g	85.95 g	1.2112 g/ml	2.31 g	1.205 ml
30 min	30 min	39.28 g	79.49 g	1.2107 g/ml	2.07 g	1.639 ml
45 min	45 min	41.40 g	84.22 g	1.2096 g/ml	2.07 g	2.200 ml
60 min	60 min	40.24 g	84.42 g	1.2026 g/ml	2.06 g	2.866 ml
90 min	89 min	42.83 g	86.42 g	1.2121 g/ml	2.17 g	2.968 ml
135 min	135 min	40.43 g	81.80 g	1.2124 g/ml	1.90 g	3.192 ml
180 min	180 min	44.10 g	89.99 g	1.2105 g/ml	1.93 g	3.500 ml

Titration Calculations

Time (planned)	Est. Reactor Mass	Fe^{2+} (mol/kg Soln.)	Total Fe^{2}	Total SO_2 added	Total H2O	Fe^{2+} Molality
0 min	2789.37 g	0.00 mol/kgsln	0.00 mol	0.00 g	1622.00 g	0.00 mol/kg
5 min	2748.77 g	0.04 mol/kgsln	0.12 mol	3.86 g	1619.83 g	0.07 mol/kg
15 min	2715.27 g	0.11 mol/kgsln	0.29 mol	9.14 g	1616.86 g	0.18 mol/kg
30 min	2689.79 g	0.16 mol/kgsln	0.43 mol	13.80 g	1614.24 g	0.27 mol/kg
45 min	2666.86 g	0.22 mol/kgsln	0.58 mol	18.47 g	1611.61 g	0.36 mol/kg
60 min	2651.41 g	0.29 mol/kgsln	0.77 mol	24.78 g	1608.06 g	0.48 mol/kg
90 min	2631.84 g	0.28 mol/kgsln	0.73 mol	23.26 g	1608.92 g	0.45 mol/kg
135 min	2619.93 g	0.34 mol/kgsln	0.89 mol	28.52 g	1605.96 g	0.55 mol/kg
180 min	2606.72 g	0.37 mol/kgsln	0.96 mol	30.89 g	1604.62 g	0.60 mol/kg

Lab Sample Analysis

Time (planned)	Volume	Fe2+	Fe(T)	H+	S	SO4	H2O
0 min	72.60 ml	0.00 g	4.32 g	0.07 g	4.72 g	14.15 g	25.39 g
5 min	74.02 ml	0.11 g	4.36 g	0.07 g	5.13 g	15.38 g	24.64 g
15 min	70.96 ml	0.24 g	4.38 g	0.07 g	4.81 g	14.42 g	23.76 g
30 min	65.66 ml	0.33 g	3.61 g	0.07 g	4.48 g	13.43 g	22.18 g
45 min	69.63 ml	0.43 g	3.83 g	0.08 g	4.06 g	12.17 g	25.32 g
60 min	70.20 ml	0.49 g	3.73 g	0.07 g	4.71 g	14.10 g	22.33 g
90 min	71.30 ml	0.63 g	4.04 g	0.08 g	4.51 g	13.52 g	25.19 g
135 min	67.47 ml	0.74 g	3.80 g	0.08 g	4.74 g	14.19 g	22.35 g
180 min	74.34 ml	0.90 g	4.22 g	0.09 g	5.08 g	15.21 g	24.57 g

Lab Sample Molalities

Time (planned)	%H2O	Fe2+	Fe(T)	H+	SO4	X (Fe^{2+}/avg(Fe_T))
0 min	58%	0.00 mol/kg	3.05 mol/kg	2.72 mol/kg	5.80 mol/kg	0.00%
5 min	55%	0.08 mol/kg	3.17 mol/kg	2.95 mol/kg	6.50 mol/kg	2.59%
15 min	56%	0.18 mol/kg	3.30 mol/kg	3.02 mol/kg	6.32 mol/kg	6.05%
30 min	56%	0.27 mol/kg	2.92 mol/kg	3.03 mol/kg	6.30 mol/kg	8.95%
45 min	61%	0.31 mol/kg	2.71 mol/kg	2.97 mol/kg	5.01 mol/kg	10.19%
60 min	55%	0.40 mol/kg	2.99 mol/kg	3.21 mol/kg	6.57 mol/kg	13.12%
90 min	59%	0.45 mol/kg	2.87 mol/kg	3.23 mol/kg	5.59 mol/kg	14.96%
135 min	55%	0.59 mol/kg	3.05 mol/kg	3.68 mol/kg	6.61 mol/kg	19.54%
180 min	56%	0.66 mol/kg	3.08 mol/kg	3.66 mol/kg	6.45 mol/kg	21.74%

Analytical Results

Time (planned)	Fe2+_g/l	Fe_mg/l	H+_g/L	S_mg/l
0 min	0	59492	0.96	65034
5 min	1.45	58958	0.99	69376
15 min	3.41	61744	1.02	67837
30 min	5.09	54995	1.03	68257
45 min	6.24	55068	1.09	58360
60 min	7.03	53206	1.03	67054
90 min	8.9	56674	1.15	63294
135 min	10.9	56363	1.23	70226
180 min	12.1	56828	1.22	68311

C.4 Continuous ferric reduction tests

C.4.1 CSTR residence time distribution

To determine the ideality of the CSTR used for the continuous tests, a residence time distribution test was performed by adding an impulse of 10 ml of 32% HCl into the reactor while operating at steady conditions and tracking the solution conductivity in the overflow. The reactor was operated at ambient temperature, water was fed into the reactor at a rate of 60 ± 5 ml/min and the working volume of the reactor was measured to be 1350 ± 10 ml resulting in a volumetric residence time of 22.7 ± 2 min.

The experimental measurements as well as an ideal CSTR model, time shifted by 80 seconds to account for the slight delay in mixing, are presented in Figure C.4. The mean residence time calculated as $\bar{t} = \int E(t)dt$ =22.32 min. These results suggest that the experimental setup used for the continuous tests in this study can be assumed to operate as an ideal CSTR.

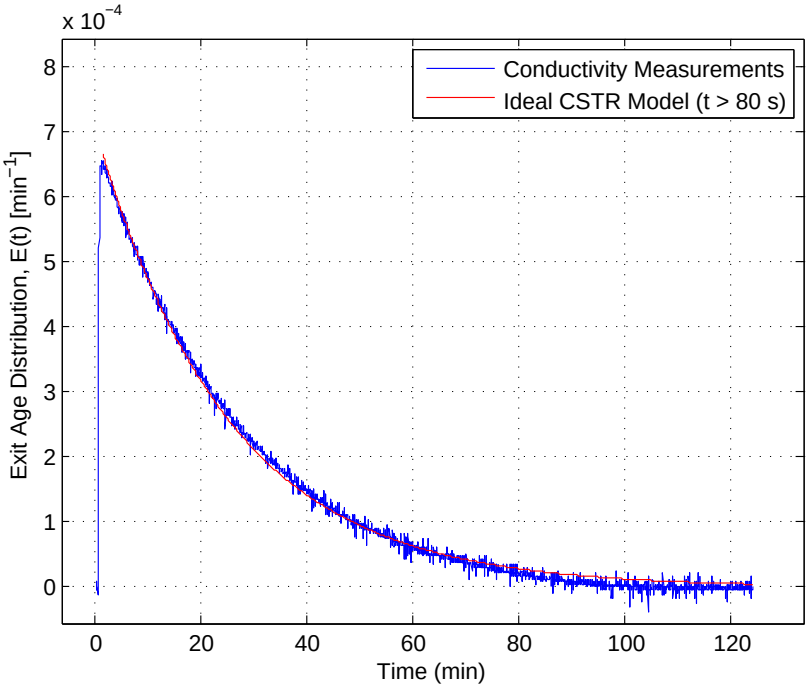

Figure C.4: Residence time distribution of CSTR used for continuous test work. The mean residence time, $\bar{t}$, was calculated to be 22.32 min.

C.4.2 Continuous test logsheets

Continuous Ferric Reduction Tests

Fe(III) Reduction	C1-20	Temperature	95 °C	Residence Time	23 min		Steady Volume	1350 ml
Repeat	0	Duration	-	Flow Rate	59.53 ml/min		Density	1.1050 g/ml
Date	17/07/2013	SO_2	1.00 Nl/min	Mass Flow Rate	65.78 g/min		Steady Mass	1492 g
		Agitation Rate	1800 rpm	Pump Speed	13.1 rpm	4.54 ml/rev		

Reagents

Basis	9715 g	H_2O						
	Concentration				Mass			
Fe^{2+}	0.00 mol/kg			$FeSO_4.7H_2O$	0.00 g	0.00 g		
Fe^{3+}	0.50 mol/kg		0.5435	$Fe_2(SO_4)_3.xH_2O$	1389.78 g	1392.24 g		
H^+	0.63 mol/kg			H_2SO_4 (98%)	255.12 g	254.49 g		
SO_4^{2+}	1.065 mol/kg			H_2O	9341.14 g	9340 g	87%	H_2O (final)
Density (est.)	1.099 g/ml				10986.05 g	10.00 l		

Fe Analytical		
Fe Titration	0.18 mol/kg	
H^+	0.67 mol/kg	0.92 mol/kg

Min SO_2 Flow 0.35 L/min

Sampling

$K_2Cr_2O_7$ Conc.	0.10 N
$K_2Cr_2O_7$ Makeup.	17/07/2013

Time (actual)	Titrator Sample	Volume $K_2Cr_2O_7$	Fe^{2+}	Fe^{2+} mol total	H_2O Mass Total kg	Fe^{2+} molality	X
0	5.0494 g	0.00 ml	0.00 mol/kg soln	0.000 mol	1.3031 kg	0.00 mol/kg	0%
15	5.9875 g	13.44 ml	0.22 mol/kg soln	0.335 mol	1.2970 kg	0.26 mol/kg	48%
30.5	4.2334 g	10.08 ml	0.24 mol/kg soln	0.355 mol	1.2967 kg	0.27 mol/kg	50%
45	4.2282 g	9.02 ml	0.21 mol/kg soln	0.318 mol	1.2973 kg	0.25 mol/kg	45%
60	4.3248 g	8.36 ml	0.19 mol/kg soln	0.288 mol	1.2979 kg	0.22 mol/kg	41%
75	4.4281 g	7.92 ml	0.18 mol/kg soln	0.267 mol	1.2982 kg	0.21 mol/kg	38%
90	4.3718 g	7.72 ml	0.18 mol/kg soln	0.263 mol	1.2983 kg	0.20 mol/kg	37%
105	4.2204 g	7.16 ml	0.17 mol/kg soln	0.253 mol	1.2985 kg	0.19 mol/kg	36%
120	4.2791 g	7.17 ml	0.17 mol/kg soln	0.250 mol	1.2985 kg	0.19 mol/kg	35%
135	4.6214 g	7.66 ml	0.17 mol/kg soln	0.247 mol	1.2986 kg	0.19 mol/kg	35%
140	5.0630 g	8.13 ml	0.16 mol/kg soln	0.240 mol	1.2987 kg	0.18 mol/kg	34%

Selected Conversion 35%

	Sample			Masses					H_2O	Molality				
	Sample Mass	Total Dilution	Density	Fe^{2+}	Fe	SO_4^{2-}	H^+	H_2O	Fraction H2O	Fe^{2+}	Fe	SO_4^{2-}	H^+	Ion Bal.
Initial Sample	10.8096	86.3233	1.0119	0.000 g	0.282 g	0.963 g	0.006 g	9.557 g	88%	0.000 mol/kg	0.529 mol/kg	1.049 mol/kg	0.665 mol/kg	-0.154 mol/kg
Final Sample	10	10	1.1103	0.000 g	0.265 g	0.992 g	0.008 g	8.735 g	87%	0.000 mol/kg	0.543 mol/kg	1.182 mol/kg	0.921 mol/kg	0.035 mol/kg

ICP-OES (mg/L)	Al	Ca	Co	Cr	Cu	Fe	Mg	Mn	Ni	Pb	S	Si	Zn	H^+	Fe^{2+}
Initial Sample	< 5	6.86	< 5	< 5	< 5	3310	< 5	7.1	< 5	< 5	3770	< 5	< 5	0.075133365	
Final Sample	< 5	49.7	< 5	< 5	< 5	29435	14.2	62.9	< 5	< 5	36755	< 5	< 5	0.9	

Continuous Ferric Reduction Tests

Fe(III) Reduction	C1-20	Temperature	95 °C	Residence Time	24 min		Steady Volume	1400 ml
Repeat	1	Duration	-	Flow Rate	59.21 ml/min		Density	1.1050 g/ml
Date	30/07/2013	SO_2	1.00 Nl/min	Mass Flow Rate	65.78 g/min		Steady Mass	1547 g
		Agitation Rate	1800 rpm	Pump Speed	13.1 rpm	4.52 ml/rev		

Reagents

Basis	9715 g	H_2O						
	Concentration				Mass			
Fe^{2+}	0.00 mol/kg		$FeSO_4.7H_2O$	0.00 g				
Fe^{3+}	0.50 mol/kg	0.527552484	$Fe_2(SO_4)_3.xH_2O$	1389.78 g	1390.00 g			
H^+	0.63 mol/kg		H_2SO_4 (98%)	255.12 g	255.91 g			
SO_4^{2+}	1.065 mol/kg		H_2O	9341.14 g	9342 g	87% H_2O (final)		
Density (est.)	1.099 g/ml			10986.05 g	10.00 l			
							Fe Analytical	0.10 mol/kg
							Fe Titration	0.21 mol/kg
Min SO_2 Flow	0.35 L/min						H^+	0.62 mol/kg 0.98 mol/kg

Sampling

$K_2Cr_2O_7$ Conc.	0.10 N
$K_2Cr_2O_7$ Makeup.	

Time (actual)	Titrator Sample	Volume $K_2Cr_2O_7$	Fe^{2+}	Fe^{2+} mol total	H_2O Mass Total kg	Fe^{2+} molality	X
115	4.0984 g	7.43 ml	0.18 mol/kg soln	0.280 mol	1.3461 kg	0.21 mol/kg	39%
145	4.1101 g	7.38 ml	0.18 mol/kg soln	0.278 mol	1.3462 kg	0.21 mol/kg	39%
150	4.3197 g	7.75 ml	0.18 mol/kg soln	0.278 mol	1.3462 kg	0.21 mol/kg	39%
170	4.3439 g	8.12 ml	0.19 mol/kg soln	0.289 mol	1.3459 kg	0.21 mol/kg	41%
180	4.4669 g	8.22 ml	0.18 mol/kg soln	0.285 mol	1.3460 kg	0.21 mol/kg	40%

Selected Conversion 40%

	Sample			Masses					H_2O	Molality				
	Sample Mass	Total Dilution	Density	Fe^{2+}	Fe	SO_4^{2-}	H^+	H_2O	Fraction H2O	Fe^{2+}	Fe	SO_4^{2-}	H^+	Ion Bal.
Initial Sample	10	10	1.1041	0.000 g	0.262 g	0.891 g	0.006 g	8.842 g	88.42%	0.000 mol/kg	0.531 mol/kg	1.049 mol/kg	0.620 mol/kg	0.092 mol/kg
Final Sample	10	10	1.1099	0.100 g	0.257 g	0.997 g	0.009 g	8.737 g	87.37%	0.102 mol/kg	0.528 mol/kg	1.188 mol/kg	0.982 mol/kg	0.022 mol/kg

ICP-OES (mg/L)	Al	Ca	Co	Cr	Cu	Fe	Mg	Mn	Ni	Pb	S	Si	Zn	H^+	Fe^{2+}
Initial Sample	< 5	45.9	< 5	< 5	< 5	28956	13.1	60.2	< 5	< 5	32826	9.02	< 5	0.61	
Final Sample	< 5	44.3	< 5	< 5	< 5	28569	12.5	58.6	< 5	< 5	36937	9.12	< 5	0.96	11.1

Continuous Ferric Reduction Tests

Fe(III) Reduction	C1-60	Temperature	95 °C	Residence Time	64 min		Steady Volume	1400 ml	1575 ml <- original number
Repeat	0	Duration	-	Flow Rate	21.86 ml/min		Density	1.1077 g/ml	
Date	25/10/2013	SO_2	1.00 Nl/min	Mass Flow Rate	24.21 g/min		Steady Mass	1551 g	
		Agitation Rate	1800 rpm	Pump Speed	5.0 rpm	4.37 ml/rev			

Reagents

Basis: 17487 g H_2O

	Concentration			Mass			
Fe^{2+}	0.00 mol/kg		$FeSO_4.7H_2O$	0.00 g	0.00 g		
Fe^{3+}	0.50 mol/kg	0.56550921	$Fe_2(SO_4)_3.xH_2O$	2501.61 g	2780.00 g		
H^+	0.63 mol/kg		H_2SO_4 (98%)	459.22 g	512.65 g		
SO_4^{2+}	1.065 mol/kg		H_2O	16814.06 g	18680 g	87% H_2O	
Density (est.)	1.099 g/ml			19774.89 g		18.00 l	

Fe Analytical	0.13 mol/kg	
Fe Titration	0.25 mol/kg	
H^+	0.63 mol/kg	1.16 mol/kg

Min SO_2 Flow: 0.13 L/min

Sampling

$K_2Cr_2O_7$ Conc.	0.10 N
$K_2Cr_2O_7$ Makeup.	08/10/2013

Time (actual)	Titrator Sample	Volume $K_2Cr_2O_7$	Fe^{2+}	Fe^{2+} mol total	H_2O Mass Total kg	Fe^{2+} molality	X
0	6.2825 g	18.69 ml	0.30 mol/kg soln	0.461 mol	1.3371 kg	0.35 mol/kg	61%
75	4.0147 g	9.09 ml	0.23 mol/kg soln	0.351 mol	1.3391 kg	0.26 mol/kg	46%
120	4.1580 g	9.13 ml	0.22 mol/kg soln	0.341 mol	1.3392 kg	0.25 mol/kg	45%
190	5.6892 g	12.23 ml	0.21 mol/kg soln	0.333 mol	1.3394 kg	0.25 mol/kg	44%
265	4.0230 g	8.52 ml	0.21 mol/kg soln	0.328 mol	1.3395 kg	0.25 mol/kg	43%
360	4.1031 g	8.92 ml	0.22 mol/kg soln	0.337 mol	1.3393 kg	0.25 mol/kg	45%
405	3.8763 g	8.41 ml	0.22 mol/kg soln	0.336 mol	1.3393 kg	0.25 mol/kg	44%
1000	3.9709 g	8.27 ml	0.21 mol/kg soln	0.323 mol	1.3396 kg	0.24 mol/kg	43%
1500	3.9590 g	8.64 ml	0.22 mol/kg soln	0.338 mol	1.3393 kg	0.25 mol/kg	45%

Selected Conversion: 44%

	Sample			Masses					H_2O	Molality				
	Sample Mass	Total Dilution	Density	Fe^{2+}	Fe	SO_4^{2-}	H^+	H_2O	Fraction H2O	Fe^{2+}	Fe	SO_4^{2-}	H^+	Ion Bal.
Initial Sample	10	10	1.104	0.000 g	0.253 g	0.890 g	0.006 g	8.852 g	88.52%	0.000 mol/kg	0.511 mol/kg	1.047 mol/kg	0.629 mol/kg	0.277 mol/kg
Final Sample	10	10	1.1107	0.131 g	0.274 g	1.040 g	0.010 g	8.675 g	86.75%	0.135 mol/kg	0.566 mol/kg	1.248 mol/kg	1.163 mol/kg	-0.118 mol/kg

ICP-OES (mg/L)	Al	Ca	Co	Cr	Cu	Fe	Mg	Mn	Ni	Pb	S	Si	Zn	H^+	Fe^{2+}
Initial Sample	< 5	45.6	< 5	< 5	22	27880	13.5	61.3	< 5	< 5	32804	6.69	< 5	0.62	
Final Sample	< 5	45	< 5	< 5	< 5	30431	13.3	59.8	< 5	< 5	38571	5.8	< 5	1.13	14.5

Continuous Ferric Reduction Tests

Fe(III) Reduction	C1-60	Temperature	95 °C	Residence Time	58 min		Steady Volume	1300 ml
Repeat	1	Duration	-	Flow Rate	22.60 ml/min		Density	1.1077 g/ml
Date	30/10/2013	SO_2	1.00 Nl/min	Mass Flow Rate	0.00 g/min		Steady Mass	1440 g
		Agitation Rate	1800 rpm	Pump Speed	5.0 rpm	4.52 ml/rev		

Reagents

Basis: 17487 g H_2O

	Concentration			Mass			
Fe^{2+}	0.00 mol/kg		$FeSO_4.7H_2O$	0.00 g	0.00 g		
Fe^{3+}	0.50 mol/kg	0.557862722	$Fe_2(SO_4)_3.xH_2O$	2501.61 g	1390.00 g		
H^+	0.63 mol/kg		H_2SO_4 (98%)	459.22 g	255.07 g		
SO_4^{2+}	1.065 mol/kg		H_2O	16814.06 g	9346 g	87% H_2O	
Density (est.)	1.099 g/ml			19774.89 g	18.00 l		

Fe Analytical	0.11 mol/kg	
Fe Titration	0.23 mol/kg	
H^+	0.62 mol/kg	1.01 mol/kg

Min SO_2 Flow: 0.15 L/min

Sampling

$K_2Cr_2O_7$ Conc.: 0.10 N

$K_2Cr_2O_7$ Makeup.: 08/10/2013

Time (actual)	Titrator Sample	Volume $K_2Cr_2O_7$	Fe^{2+}	Fe^{2+} mol total	H_2O Mass Total kg	Fe^{2+} molality	X
65	4.1819 g	8.23 ml	0.20 mol/kg soln	0.283 mol	1.2477 kg	0.23 mol/kg	41%
105	4.2435 g	8.50 ml	0.20 mol/kg soln	0.288 mol	1.2476 kg	0.23 mol/kg	41%
165	4.4252 g	8.95 ml	0.20 mol/kg soln	0.291 mol	1.2476 kg	0.23 mol/kg	42%
178	4.0565 g	8.14 ml	0.20 mol/kg soln	0.289 mol	1.2476 kg	0.23 mol/kg	46%
200	4.5730 g	8.89 ml	0.19 mol/kg soln	0.280 mol	1.2478 kg	0.22 mol/kg	45%

Selected Conversion: 44%

	Sample			Masses					H_2O	Molality				
	Sample Mass	Total Dilution	Density	Fe^{2+}	Fe	SO_4^{2-}	H^+	H_2O	Fraction H2O	Fe^{2+}	Fe	SO_4^{2-}	H^+	Ion Bal.
Initial Sample	10	10	1.104	0.000 g	0.256 g	0.895 g	0.006 g	8.843 g	88.43%	0.000 mol/kg	0.519 mol/kg	1.054 mol/kg	0.620 mol/kg	0.157 mol/kg
Final Sample	10	10	1.1107	0.109 g	0.272 g	0.984 g	0.009 g	8.735 g	87.35%	0.112 mol/kg	0.558 mol/kg	1.173 mol/kg	1.012 mol/kg	-0.116 mol/kg

ICP-OES (mg/L)	Al	Ca	Co	Cr	Cu	Fe	Mg	Mn	Ni	Pb	S	Si	Zn	H^+	Fe^{2+}
Initial Sample	< 5	45.7	< 5	< 5	< 5	28309	12.9	60.6	< 5	< 5	32985	9.47	< 5	0.61	
Final Sample	< 5	45.4	< 5	< 5	< 5	30225	12.8	60.2	< 5	< 5	36485	6.91	< 5	0.99	12.1

Continuous Ferric Reduction Tests

Fe(III) Reduction	C1-135	Temperature	95 °C	Residence Time	134 min		Steady Volume	1370 ml
Repeat	0	Duration	-	Flow Rate	10.22 ml/min		Density	1.1050 g/ml
Date	18/07/2013	SO_2	1.00 Nl/min	Mass Flow Rate	11.29 g/min		Steady Mass	1514 g
		Agitation Rate	1800 rpm	Pump Speed	2.2 rpm	4.65 ml/rev		

Reagents

Basis: 17487 g H_2O

	Concentration			Mass		
Fe^{2+}	0.00 mol/kg		$FeSO_4.7H_2O$	0.00 g		
Fe^{3+}	0.50 mol/kg	0.5312	$Fe_2(SO_4)_3.xH_2O$	2501.61 g	2501.61 g	
H^+	0.63 mol/kg		H_2SO_4 (98%)	459.22 g	459.22 g	
SO_4^{2+}	1.065 mol/kg		H_2O	16814.06 g	87%	H_2O
Density (est.)	1.099 g/ml			19774.89 g	18.00 l	

Fe Analytical		
Fe Titration	0.32 mol/kg	
H^+	0.66 mol/kg	1.08 mol/kg

Min SO_2 Flow: 0.06 L/min

Sampling

$K_2Cr_2O_7$ Conc.	0.10 N
$K_2Cr_2O_7$ Makeup.	17/07/2013

Time (actual)	Titrator Sample	Volume $K_2Cr_2O_7$	Fe^{2+}	Fe^{2+} mol total	H_2O Mass Total kg	Fe^{2+} molality	X
0	4.5930 g	0.00 ml	0.00 mol/kg soln	0.000 mol	1.3239 kg	0.00 mol/kg	0%
15	4.2589 g	4.69 ml	0.11 mol/kg soln	0.167 mol	1.3209 kg	0.13 mol/kg	24%
30	4.2709 g	8.89 ml	0.21 mol/kg soln	0.315 mol	1.3182 kg	0.24 mol/kg	45%
58	4.2427 g	11.71 ml	0.28 mol/kg soln	0.418 mol	1.3164 kg	0.32 mol/kg	60%
90	4.2984 g	12.55 ml	0.29 mol/kg soln	0.442 mol	1.3160 kg	0.34 mol/kg	63%
125	4.2999 g	11.62 ml	0.27 mol/kg soln	0.409 mol	1.3165 kg	0.31 mol/kg	58%
160	4.5854 g	12.71 ml	0.28 mol/kg soln	0.420 mol	1.3164 kg	0.32 mol/kg	60%
182	4.4495 g	12.25 ml	0.28 mol/kg soln	0.417 mol	1.3164 kg	0.32 mol/kg	60%
214	4.2063 g	11.72 ml	0.28 mol/kg soln	0.422 mol	1.3163 kg	0.32 mol/kg	60%
246	4.4054 g	12.08 ml	0.27 mol/kg soln	0.415 mol	1.3164 kg	0.32 mol/kg	59%
266	4.2210 g	11.66 ml	0.28 mol/kg soln	0.418 mol	1.3164 kg	0.32 mol/kg	60%

Selected Conversion: 60%

	Sample			Masses					H_2O	Molality				
	Sample Mass	Total Dilution	Density	Fe^{2+}	Fe	SO_4^{2-}	H^+	H_2O	Fraction H2O	Fe^{2+}	Fe	SO_4^{2-}	H^+	Ion Bal.
Initial Sample	11.0762	85.6355	1.0123		0.269 g	0.900 g	0.007 g	9.901 g	89%		0.487 mol/kg	0.946 mol/kg	0.658 mol/kg	-0.227 mol/kg
Final Sample	10	10	1.1147		0.259 g	0.986 g	0.010 g	8.745 g	87%		0.531 mol/kg	1.173 mol/kg	1.079 mol/kg	0.010 mol/kg

ICP-OES (mg/L)	Al	Ca	Co	Cr	Cu	Fe	Mg	Mn	Ni	Pb	S	Si	Zn	H^+	Fe^{2+}
Initial Sample	< 5	6.62	< 5	< 5	< 5	3183	< 5	6.61	< 5	< 5	3550	< 5	< 5	0.077604732	
Final Sample	< 5	49.9	< 5	142	< 5	28921	15	76.7	68.7	< 5	36676	7.39	< 5	1.06	

Continuous Ferric Reduction Tests

Fe(III) Reduction	C1-135	Temperature	95 °C	Residence Time	133 min		Steady Volume	1200 ml
Repeat	1	Duration	-	Flow Rate	9.03 ml/min		Density	1.1050 g/ml
Date	31/07/2013	SO_2	1.00 Nl/min	Mass Flow Rate	11.29 g/min		Steady Mass	1326 g
		Agitation Rate	1800 rpm	Pump Speed	2.1 rpm	4.30 ml/rev		

Reagents

	Basis	17487 g	H_2O						
		Concentration				Mass			
	Fe^{2+}	0.00 mol/kg			$FeSO_4.7H_2O$	0.00 g			
	Fe^{3+}	0.50 mol/kg		0.5384	$Fe_2(SO_4)_3.xH_2O$	2501.61 g			
	H^+	0.63 mol/kg			H_2SO_4 (98%)	459.22 g			
	SO_4^{2+}	1.065 mol/kg			H_2O	16814.06 g	87%	H_2O	
	Density (est.)	1.099 g/ml				19774.89 g	18.00 l		
	Min SO_2 Flow	0.06 L/min							

Fe Analytical	0.12 mol/kg		
Fe Titration	0.29 mol/kg		
H^+	0.63 mol/kg	1.03 mol/kg	

Sampling

$K_2Cr_2O_7$ Conc.	0.10 N
$K_2Cr_2O_7$ Makeup.	17/07/2013

Time (actual)	Titrator Sample	Volume $K_2Cr_2O_7$		Fe^{2+}	Fe^{2+} mol total	H_2O Mass Total kg	Fe^{2+} molality	X
115	4.1948 g	9.65 ml		0.23 mol/kg soln	0.305 mol	1.1511 kg	0.27 mol/kg	49%
225	4.1898 g	9.38 ml		0.22 mol/kg soln	0.297 mol	1.1512 kg	0.26 mol/kg	48%
300	4.0741 g	9.20 ml		0.23 mol/kg soln	0.299 mol	1.1512 kg	0.26 mol/kg	48%
388	4.5663 g	13.69 ml	batch from 5:12	0.30 mol/kg soln	0.398 mol	1.1494 kg	0.35 mol/kg	64%
479	4.1333 g	10.23 ml	cont. from 6h42	0.25 mol/kg soln	0.328 mol	1.1507 kg	0.29 mol/kg	53%
525	4.0061 g	9.98 ml		0.25 mol/kg soln	0.330 mol	1.1506 kg	0.29 mol/kg	53%

Selected Conversion 53%

	Sample			Masses					H_2O	Molality				
	Sample Mass	Total Dilution	Density	Fe^{2+}	Fe	SO_4^{2-}	H^+	H_2O	Fraction H2O	Fe^{2+}	Fe	SO_4^{2-}	H^+	Ion Bal.
Initial Sample	10	10	1.1064	0.000 g	0.255 g	0.947 g	0.006 g	8.791 g	87.91%	0.000 mol/kg	0.520 mol/kg	1.122 mol/kg	0.632 mol/kg	0.315 mol/kg
Final Sample	10	10	1.1126	0.120 g	0.262 g	1.006 g	0.009 g	8.722 g	87.22%	0.124 mol/kg	0.538 mol/kg	1.201 mol/kg	1.033 mol/kg	0.040 mol/kg

ICP-OES (mg/L)	Al	Ca	Co	Cr	Cu	Fe	Mg	Mn	Ni	Pb	S	Si	Zn	H^+	Fe^{2+}
Initial Sample	< 5	46.8	< 5	< 5	< 5	28264	13.2	62.3	< 5	< 5	34991	< 5	< 5	0.62	
Final Sample	< 5	46.3	< 5	< 5	< 5	29178	12.9	60.7	< 5	< 5	37374	6.35	< 5	1.01	13.4

Continuous Ferric Reduction Tests

Fe(III) Reduction	C2-60	Temperature	95 °C	Residence Time	60 min		Steady Volume	1350 ml
Repeat	0	Duration	-	Flow Rate	22.60 ml/min		Density	1.1077 g/ml
Date	21/11/2013	SO_2	1.00 Nl/min	Mass Flow Rate	24.21 g/min		Steady Mass	1495 g
		Agitation Rate	1800 rpm	Pump Speed	5.0 rpm	4.52 ml/rev		

Reagents

Basis: 16314 g H_2O

	Concentration			Mass		
Fe^{2+}	0.00 mol/kg		$FeSO_4.7H_2O$	0.00 g		
Fe^{3+}	2.17 mol/kg	3.1050	$Fe_2(SO_4)_3.xH_2O$	10128.78 g	8440.00 g	
H^+	0.63 mol/kg		H_2SO_4 (98%)	141.61 g	121.19 g	
SO_4^{2+}	3.570 mol/kg		H_2O	13625.27 g	11349 g	60% H_2O
Density (est.)	1.328 g/ml			23895.66 g	18.00 l	

Min SO_2 Flow: 0.44 L/min

Fe Analytical	0.00 mol/kg	
Fe Titration	0.47 mol/kg	
H^+	0.64 mol/kg	0.00 mol/kg

Sampling

$K_2Cr_2O_7$ Conc.: 0.10 N

$K_2Cr_2O_7$ Makeup.: 19/11/2013

Time (actual)	Titrator Sample	Volume $K_2Cr_2O_7$	Fe^{2+}	Fe^{2+} mol total	H_2O Mass Total kg	Fe^{2+} molality	X
180	3.4609 g	9.48 ml	0.27 mol/kg soln	0.410 mol	0.8951 kg	0.46 mol/kg	15%
228	3.1612 g	8.65 ml	0.27 mol/kg soln	0.409 mol	0.8951 kg	0.46 mol/kg	15%
262	4.5811 g	12.76 ml	0.28 mol/kg soln	0.417 mol	0.8949 kg	0.47 mol/kg	15%

Selected Conversion: 15%

	Sample			Masses					H_2O	Molality				
	Sample Mass	Total Dilution	Density	Fe^{2+}	Fe	SO_4^{2-}	H^+	H_2O	Fraction H2O	Fe^{2+}	Fe	SO_4^{2-}	H^+	Ion Bal.
Initial Sample	10	10	1.1064	0.000 g	1.046 g	2.915 g	0.004 g	6.035 g	60.35%	0.000 mol/kg	3.105 mol/kg	5.028 mol/kg	0.639 mol/kg	0.560 mol/kg

ICP-OES (mg/L)	Al	Ca	Co	Cr	Cu	Fe	Mg	Mn	Ni	Pb	S	Si	Zn	H^+	Fe^{2+}
Initial Sample	15.8	123	< 5	< 5	< 5	115778	32	251	8.6		107651	17.9	< 5	0.43	
Final Sample															

Continuous Ferric Reduction Tests

Fe(III) Reduction	C2-135	Temperature	95 °C	Residence Time	135 min		Steady Volume	1350 ml
Repeat	0	Duration	-	Flow Rate	10.00 ml/min		Density	1.1077 g/ml
Date	21/11/2013	SO_2	1.00 Nl/min	Mass Flow Rate	24.21 g/min		Steady Mass	1495 g
		Agitation Rate	1800 rpm	Pump Speed	2.2 rpm	4.55 ml/rev		

Reagents

Basis	16314 g	H_2O						
	Concentration				Mass			
Fe^{2+}	0.00 mol/kg			$FeSO_4.7H_2O$	0.00 g			
Fe^{3+}	2.17 mol/kg		3.1050	$Fe_2(SO_4)_3.xH_2O$	10128.78 g	8440.00 g		
H^+	0.63 mol/kg			H_2SO_4 (98%)	141.61 g	121.19 g		
SO_4^{2+}	3.570 mol/kg			H_2O	13625.27 g	11349 g	58%	H_2O
Density (est.)	1.328 g/ml				23895.66 g		18.00 l	

Fe Analytical	0.41 mol/kg	
Fe Titration	0.59 mol/kg	
H^+	0.64 mol/kg	1.97 mol/kg

Min SO_2 Flow 0.44 L/min

Sampling

$K_2Cr_2O_7$ Conc. 0.10 N

$K_2Cr_2O_7$ Makeup. 19/11/2013

Time (actual)	Titrator Sample	Volume $K_2Cr_2O_7$	Fe^{2+}	Fe^{2+} mol total	H_2O Mass Total kg	Fe^{2+} molality	X
113	2.8733 g	9.55 ml	0.33 mol/kg soln	0.497 mol	0.8571 kg	0.58 mol/kg	19%
160	3.1921 g	10.71 ml	0.34 mol/kg soln	0.502 mol	0.8570 kg	0.59 mol/kg	19%
189	2.9869 g	10.08 ml	0.34 mol/kg soln	0.505 mol	0.8569 kg	0.59 mol/kg	19%

Selected Conversion 19%

	Sample			Masses					H_2O	Molality				
	Sample Mass	Total Dilution	Density	Fe^{2+}	Fe	SO_4^{2-}	H^+	H_2O	Fraction H2O	Fe^{2+}	Fe	SO_4^{2-}	H^+	Ion Bal.
Initial Sample	10	10	1.1064	0.000 g	1.046 g	2.915 g	0.004 g	6.035 g	60.35%	0.000 mol/kg	3.105 mol/kg	5.028 mol/kg	0.639 mol/kg	0.682 mol/kg
Final Sample	10	10	1.1126	0.268 g	1.064 g	3.133 g	0.012 g	5.791 g	57.91%	0.414 mol/kg	3.290 mol/kg	5.632 mol/kg	1.971 mol/kg	0.011 mol/kg

ICP-OES (mg/L)	Al	Ca	Co	Cr	Cu	Fe	Mg	Mn	Ni	Pb	S	Si	Zn	H^+	Fe^{2+}
Initial Sample	15.8	123	< 5	< 5	< 5	115778	32	251	8.6		107651	17.9	< 5	0.43	
Final Sample	16.1	126	< 5	< 5	< 5	118396	32.9	258	9.14		116359	20.7	< 5	1.28	29.8

Continuous Ferric Reduction Tests

Fe(III) Reduction	C3-60	Temperature	95 °C	Residence Time	58 min		Steady Volume	1300 ml
Repeat	0	Duration	-	Flow Rate	22.60 ml/min		Density	1.1077 g/ml
Date	19/11/2013	SO_2	1.00 Nl/min	Mass Flow Rate	24.21 g/min		Steady Mass	1440 g
		Agitation Rate	1800 rpm	Pump Speed	5.0 rpm	4.52 ml/rev		

Reagents

Basis	16982 g	H_2O						
	Concentration				Mass			
Fe^{2+}	0.00 mol/kg		$FeSO_4.7H_2O$	0.00 g	0.00 g			
Fe^{3+}	0.50 mol/kg	0.5577	$Fe_2(SO_4)_3.xH_2O$	2429.39 g	2040.00 g			
H^+	2.21 mol/kg		H_2SO_4 (98%)	1788.61 g	1490.12 g			
SO_4^{2+}	1.855 mol/kg		H_2O	16301.83 g	13580 g	82% H_2O		
Density (est.)	1.140 g/ml			20519.83 g		18.00 l		
Min SO_2 Flow	0.12 L/min							

Fe Analytical	0.06 mol/kg	
Fe Titration	0.14 mol/kg	
H^+	2.27 mol/kg	2.48 mol/kg

Sampling

$K_2Cr_2O_7$ Conc.	0.10 N
$K_2Cr_2O_7$ Makeup.	19/11/2013

Time (actual)	Titrator Sample	Volume $K_2Cr_2O_7$	Fe^{2+}	Fe^{2+} mol total	H_2O Mass Total kg	Fe^{2+} molality	X
118	4.5481 g	5.91 ml	0.13 mol/kg soln	0.187 mol	1.1794 kg	0.159 mol/kg	28%
155	4.6593 g	5.68 ml	0.12 mol/kg soln	0.176 mol	1.1796 kg	0.149 mol/kg	27%
209	4.5290 g	5.27 ml	0.12 mol/kg soln	0.168 mol	1.1798 kg	0.142 mol/kg	25%
242	4.2679 g	4.78 ml	0.11 mol/kg soln	0.161 mol	1.1799 kg	0.137 mol/kg	25%
341	7.0962 g	7.93 ml	0.11 mol/kg soln	0.161 mol	1.1799 kg	0.136 mol/kg	24%

Selected Conversion 24%

	Sample			Masses					H_2O	Molality				
	Sample Mass	Total Dilution	Density	Fe^{2+}	Fe	SO_4^{2-}	H^+	H_2O	Fraction H2O	Fe^{2+}	Fe	SO_4^{2-}	H^+	Ion Bal.
Initial Sample	10	10	1.1064	0.000 g	0.250 g	1.478 g	0.019 g	8.253 g	82.53%	0.000 mol/kg	0.543 mol/kg	1.864 mol/kg	2.271 mol/kg	-0.014 mol/kg
Final Sample	10	10	1.1126	0.058 g	0.256 g	1.510 g	0.020 g	8.214 g	82.14%	0.063 mol/kg	0.558 mol/kg	1.914 mol/kg	2.475 mol/kg	-0.185 mol/kg

ICP-OES (mg/L)	Al	Ca	Co	Cr	Cu	Fe	Mg	Mn	Ni	Pb	S	Si	Zn	H^+	Fe^{2+}
Initial Sample	< 5	46.5	< 5	< 5	< 5	27702	12.5	60.4	< 5		54576	< 5	< 5	2.09	
Final Sample	< 5	46.7	< 5	< 5	< 5	28460	12.6	61.6	< 5		56073	7.09	< 5	2.28	6.48

Continuous Ferric Reduction Tests

Fe(III) Reduction	C3-135	Temperature	95 °C	Residence Time	126 min		Steady Volume	1200 ml
Repeat	0	Duration	-	Flow Rate	9.50 ml/min		Density	1.1077 g/ml
Date	19/11/2013	SO_2	1.00 Nl/min	Mass Flow Rate	24.21 g/min		Steady Mass	1329 g
		Agitation Rate	1800 rpm	Pump Speed	2.2 rpm	4.32 ml/rev		

Reagents

	Basis	16982 g	H_2O						
		Concentration				Mass			
	Fe^{2+}	0.00 mol/kg			$FeSO_4.7H_2O$	0.00 g	0.00 g		
	Fe^{3+}	0.50 mol/kg		0.5574	$Fe_2(SO_4)_3.xH_2O$	2429.39 g	2040.00 g		
	H^+	2.21 mol/kg			H_2SO_4 (98%)	1788.61 g	1490.12 g		
	SO_4^{2+}	1.855 mol/kg			H_2O	16301.83 g	13580 g	81%	H_2O
	Density (est.)	1.140 g/ml				20519.83 g		18.00 l	
	Min SO_2 Flow	0.12 L/min							

Fe Analytical	0.08 mol/kg	
Fe Titration	0.17 mol/kg	
H^+	2.27 mol/kg	2.63 mol/kg

Sampling

$K_2Cr_2O_7$ Conc.	0.10 N
$K_2Cr_2O_7$ Makeup.	19/11/2013

Time (actual)	Titrator Sample	Volume $K_2Cr_2O_7$	Fe^{2+}	Fe^{2+} mol total	H_2O Mass Total kg	Fe^{2+} molality	X
0	7.0962 g	7.93 ml	0.11 mol/kg soln	0.149 mol	1.0791 kg	0.14 mol/kg	25%
115	5.5581 g	7.24 ml	0.13 mol/kg soln	0.173 mol	1.0787 kg	0.16 mol/kg	29%
145	6.0470 g	7.97 ml	0.13 mol/kg soln	0.175 mol	1.0786 kg	0.16 mol/kg	29%
232	6.1808 g	8.60 ml	0.14 mol/kg soln	0.185 mol	1.0784 kg	0.17 mol/kg	31%
319	6.1573 g	8.55 ml	0.14 mol/kg soln	0.185 mol	1.0784 kg	0.17 mol/kg	31%
379	6.7438 g	9.36 ml	0.14 mol/kg soln	0.184 mol	1.0784 kg	0.17 mol/kg	31%

Selected Conversion 31%

	Sample			Masses					H_2O	Molality				
	Sample Mass	Total Dilution	Density	Fe^{2+}	Fe	SO_4^{2-}	H^+	H_2O	Fraction H2O	Fe^{2+}	Fe	SO_4^{2-}	H^+	Ion Bal.
Initial Sample	10	10	1.1064	0.000 g	0.250 g	1.478 g	0.019 g	8.253 g	82.53%	0.000 mol/kg	0.543 mol/kg	1.864 mol/kg	2.271 mol/kg	-0.035 mol/kg
Final Sample	10	10	1.1126	0.071 g	0.253 g	1.587 g	0.022 g	8.138 g	81.38%	0.078 mol/kg	0.557 mol/kg	2.030 mol/kg	2.630 mol/kg	-0.071 mol/kg

ICP-OES (mg/L)	Al	Ca	Co	Cr	Cu	Fe	Mg	Mn	Ni	Pb	S	Si	Zn	H^+	Fe^{2+}
Initial Sample	< 5	46.5	< 5	< 5	< 5	27702	12.5	60.4	< 5		54576	< 5	< 5	2.09	
Final Sample	< 5	46.3	< 5	6.81	< 5	28185	12.5	61.5	< 5		58932	6.63	< 5	2.4	7.89

Appendix D

DFT Calculations

D.1 ADF Run Files

D.1.1 $Fe(H_2O)_6^{3+}$

```
#! /bin/sh

"$ADFBIN/adf" <<eor
Dependency
ATOMS
1 Fe       0.000000000000       0.000000000000       0.000000000000     R=1.858
2 O        0.000000000000       0.000000000000       1.995225622000     R=1.517
3 O        0.000000000000       1.995323494000       0.000000000000     R=1.517
4 O        1.996472353000       0.000000000000       0.000000000000     R=1.517
5 O        0.000000000000      -1.995323494000       0.000000000000     R=1.517
6 O       -1.996472353000       0.000000000000       0.000000000000     R=1.517
7 O        0.000000000000       0.000000000000      -1.995225622000     R=1.517
8 H        0.000000000000       0.779809781300      -2.561086869000     R=1.350
9 H        0.000000000000      -0.779809781300      -2.561086869000     R=1.350
10 H       0.780231837600      -2.561156439000       0.000000000000     R=1.350
11 H      -0.780231837600      -2.561156439000       0.000000000000     R=1.350
12 H      -2.562129980000       0.000000000000       0.780133191100     R=1.350
13 H      -2.562129980000       0.000000000000      -0.780133191100     R=1.350
14 H       0.780231837600       2.561156439000       0.000000000000     R=1.350
15 H      -0.780231837600       2.561156439000       0.000000000000     R=1.350
16 H       2.562129980000       0.000000000000       0.780133191100     R=1.350
17 H       2.562129980000       0.000000000000      -0.780133191100     R=1.350
18 H       0.000000000000       0.779809781300       2.561086869000     R=1.350
19 H       0.000000000000      -0.779809781300       2.561086869000     R=1.350
END

GUIBONDS
1 1 2 1.0
2 1 3 1.0
3 1 4 1.0
4 1 5 1.0
5 1 6 1.0
6 1 7 1.0
7 2 19 1.0
8 2 18 1.0
9 3 15 1.0
10 3 14 1.0
11 4 16 1.0
```

```
12 4 17 1.0
13 5 10 1.0
14 5 11 1.0
15 6 13 1.0
16 6 12 1.0
17 7 8 1.0
18 7 9 1.0
END

SOLVATION
    Surf Esurf
    Solvent name=Water cav0=0.0 cav1=0.0067639
    Charged method=CONJ
    C-Mat POT
    SCF VAR ALL
    CSMRSP
END

CHARGE 3.0 5.0

UNRESTRICTED

BASIS
type TZ2P
core None
createoutput None
END

XC
GGA OPBE
END

GEOMETRY
    optim Delocalized
END

SAVE  TAPE21 TAPE13

SCF
iterations 200
mixing 0.03
diis  n=30
adiis
END

FULLSCF
INTEGRATION 10

NoBeckeGrid
NOPRINT LOGFILE

eor
```

D.1.2 $Fe(H_2O)_6^{2+}$

```
#! /bin/sh

"$ADFBIN/adf" <<eor
Dependency
ATOMS
1 Fe       0.000000000000       0.000000000000       0.000000000000     R=1.858
2 O      -1.420010000000       1.419680000000       0.000000000000     R=1.517
3 O       0.000000000000       0.000000000000      -2.504390000000     R=1.517
4 O       1.419640000000       1.420050000000       0.000000000000     R=1.517
5 O       0.000000000000       0.000000000000       2.504390000000     R=1.517
6 O      -1.419640000000      -1.420050000000       0.000000000000     R=1.517
```

```
7 O       1.420010000000      −1.419680000000       0.000000000000     R=1.517
8 H       1.814580000000      −1.814110000000      −0.783970000000     R=1.350
9 H       1.814580000000      −1.814110000000       0.783970000000     R=1.350
10 H       0.554270000000       0.554430000000       3.062290000000     R=1.350
11 H      −0.554270000000      −0.554430000000       3.062290000000     R=1.350
12 H      −2.368510000000      −1.260350000000       0.000000000000     R=1.350
13 H      −1.259640000000      −2.368880000000       0.000000000000     R=1.350
14 H       0.554270000000       0.554430000000      −3.062290000000     R=1.350
15 H      −0.554270000000      −0.554430000000      −3.062290000000     R=1.350
16 H       1.259640000000       2.368880000000       0.000000000000     R=1.350
17 H       2.368510000000       1.260350000000       0.000000000000     R=1.350
18 H      −1.814580000000       1.814110000000      −0.783970000000     R=1.350
19 H      −1.814580000000       1.814110000000       0.783970000000     R=1.350
END

GUIBONDS
1 1 2 1.0
2 1 7 1.0
3 1 3 1.0
4 1 5 1.0
5 1 4 1.0
6 1 6 1.0
7 2 19 1.0
8 2 18 1.0
9 3 14 1.0
10 3 15 1.0
11 4 16 1.0
12 4 17 1.0
13 5 11 1.0
14 5 10 1.0
15 6 13 1.0
16 6 12 1.0
17 7 8 1.0
18 7 9 1.0
END

SYMMETRY C(I)

SOLVATION
    Surf Esurf
    Solvent name=Water cav0=0.0 cav1=0.0067639
    Charged method=CONJ
    C—Mat POT
    SCF VAR ALL
    CSMRSP
END

CHARGE 2.0

BASIS
type TZ2P
core None
createoutput None
END

XC
GGA OPBE
END

GEOMETRY
    optim Delocalized
END

SAVE  TAPE21 TAPE13

SCF
iterations 200
mixing 0.03
diis  n=30
```

```
adiis
END

FULLSCF
INTEGRATION 10

NoBeckeGrid
NOPRINT LOGFILE

eor
```

D.1.3 SO_4^{2-}

```
#! /bin/sh

"$ADFBIN/adf" <<eor
Dependency
ATOMS
1 S       0.000000000000       0.000000000000       0.000000000000     R=1.792
2 O      -0.861462146200       0.861462146200       0.861462146200     R=1.517
3 O       0.861462146200      -0.861462146200       0.861462146200     R=1.517
4 O      -0.861462146200      -0.861462146200      -0.861462146200     R=1.517
5 O       0.861462146200       0.861462146200      -0.861462146200     R=1.517
END

GUIBONDS
1 1 4 1.0
2 1 5 1.0
3 1 2 1.0
4 1 3 1.0
END

SYMMETRY T(D)

SOLVATION
    Surf Esurf
    Solvent name=Water cav0=0.0 cav1=0.0067639
    Charged method=CONJ
    C-Mat POT
    SCF VAR ALL
    CSMRSP
END

CHARGE -2.0

BASIS
type TZ2P
core None
createoutput None
END

XC
GGA OPBE
END

GEOMETRY
    optim Delocalized
END

AnalyticalFreq
END

SAVE  TAPE21 TAPE13

FULLSCF
INTEGRATION 10
```

```
NoBeckeGrid
ALLPOINTS
NOPRINT LOGFILE

eor
```

D.1.4 HSO_4^-

```
#! /bin/sh

"$ADFBIN/adf" <<eor
ATOMS
1 O       1.222054349000       0.725550920200       0.661767877500     R=1.517
2 S       0.000000000000      -0.047741096870       0.433159536700     R=1.792
3 O       0.000000000000      -1.370751041000       1.049058299000     R=1.517
4 O      -0.000000000000      -0.429864091700      -1.152560683000     R=1.517
5 O      -1.222054349000       0.725550920200       0.661767877500     R=1.517
6 H      -0.000000000000       0.402977381200      -1.647394720000     R=1.350
END

GUIBONDS
1 1 2 1.0
2 2 3 1.0
3 2 5 1.0
4 2 4 1.0
5 4 6 1.0
END

SOLVATION
    Surf Esurf
    Solvent name=Water cav0=0.0 cav1=0.0067639
    Charged method=CONJ
    C-Mat POT
    SCF VAR ALL
    CSMRSP
END

CHARGE -1.0

BASIS
type TZ2P
core None
createoutput None
END

XC
GGA OPBE
END

SCANFREQ -1000 0

SYMMETRY C(S)

GEOMETRY
    optim Delocalized
END

AnalyticalFreq
END

SAVE  TAPE21 TAPE13

SCF
diis
END
```

```
FULLSCF
INTEGRATION 10

NoBeckeGrid
NOPRINT LOGFILE

eor
```

D.1.5 $Fe(H_2O)_5SO_4^0$

```
#! /bin/sh

"$ADFBIN/adf" <<eor
ATOMS
1 Fe      −0.327334433600      −0.260290792300       0.000000000000     R=1.858
2 O        1.647241206000      −0.218823469400       0.000000000000     R=1.517
3 O       −0.162116312400      −1.654086790000      −1.480084628000     R=1.517
4 O       −0.162116312400      −1.654086790000       1.480084628000     R=1.517
5 O       −0.445961000600       1.111800412000       1.458521660000     R=1.517
6 O       −0.445961000600       1.111800412000      −1.458521660000     R=1.517
7 O       −2.357758447000      −0.399048567200       0.000000000000     R=1.517
8 H       −2.734911339000      −0.852826238700      −0.765002247500     R=1.350
9 H       −2.734911339000      −0.852826238700       0.765002247500     R=1.350
10 H      −1.048799525000       1.839927662000       1.260519070000     R=1.350
11 H       0.476015189600       1.513864704000       1.454534114000     R=1.350
12 H       0.476015189600       1.513864704000      −1.454534114000     R=1.350
13 H      −1.048799525000       1.839927662000      −1.260519070000     R=1.350
14 H       0.784563511300      −1.809039396000      −1.610214923000     R=1.350
15 H      −0.525352822400      −2.528079959000      −1.285076184000     R=1.350
16 H       0.784563511300      −1.809039396000       1.610214923000     R=1.350
17 H      −0.525352822400      −2.528079959000       1.285076184000     R=1.350
18 S       2.425881760000       1.091568445000       0.000000000000     R=1.792
19 O       2.043258355000       1.859185425000       1.220911747000     R=1.517
20 O       2.043258355000       1.859185425000      −1.220911747000     R=1.517
21 O       3.853942329000       0.767863306000       0.000000000000     R=1.517
END

GUIBONDS
1 1 2 1.0
2 1 5 1.0
3 1 6 1.0
4 1 7 1.0
5 1 3 1.0
6 1 4 1.0
7 2 18 1.0
8 3 14 1.0
9 3 15 1.0
10 4 16 1.0
11 4 17 1.0
12 5 10 1.0
13 5 11 1.0
14 6 13 1.0
15 6 12 1.0
16 7 8 1.0
17 7 9 1.0
18 18 21 1.0
19 18 19 1.0
20 18 20 1.0
END

SOLVATION
    Surf Esurf
    Solvent name=Water cav0=0.0 cav1=0.0067639
    Charged method=CONJ
    C-Mat POT
```

```
    SCF VAR ALL
    CSMRSP
END

BASIS
type TZ2P
core None
createoutput None
END

XC
GGA OPBE
END

SCANFREQ —1000 0

SYMMETRY C(S)

GEOMETRY
    optim Delocalized
END

AnalyticalFreq
END

SAVE  TAPE21 TAPE13

SCF
diis
END

FULLSCF
INTEGRATION 10

NoBeckeGrid
NOPRINT LOGFILE

eor
```

D.1.6 $Fe(H_2O)_5SO_4^+$

```
#! /bin/sh

"$ADFBIN/adf" <<eor
ATOMS
1 Fe      —0.278057112900      —0.335882715700      —0.001097583564     R=1.858
2 O        1.568343572000      —0.103244273300       0.000100057057     R=1.517
3 O       —0.334124665400      —1.821888653000      —1.516785737000     R=1.517
4 O       —0.323516175900      —1.820534311000       1.517872475000     R=1.517
5 O       —0.418236345800       1.089063459000       1.521361580000     R=1.517
6 O       —0.415513897000       1.086112197000      —1.525810045000     R=1.517
7 O       —2.394759121000      —0.494040605700       0.001417189700     R=1.517
8 H       —2.926284018000      —0.255819076000      —0.769277262700     R=1.350
9 H       —2.924960824000      —0.253219087300       0.772171399600     R=1.350
10 H      —1.079169219000       1.791388875000       1.454738009000     R=1.350
11 H       0.472437609200       1.539784389000       1.536092031000     R=1.350
12 H       0.474305191500       1.539034307000      —1.537783314000     R=1.350
13 H      —1.078207630000       1.787368106000      —1.466387673000     R=1.350
14 H       0.521270469400      —2.173928394000      —1.798417859000     R=1.350
15 H      —0.908703426700      —2.592593905000      —1.416713611000     R=1.350
16 H       0.531979143800      —2.181830985000       1.787094284000     R=1.350
17 H      —0.908411869300      —2.584910981000       1.429155172000     R=1.350
18 S       2.478695523000       1.194527075000       0.001214582198     R=1.792
19 O       2.090402444000       1.912873766000       1.228714499000     R=1.517
20 O       2.089398584000       1.915287874000      —1.224680022000     R=1.517
21 O       3.852876987000       0.735851036500      —0.000191713067     R=1.517
```

```
END

GUIBONDS
1 1 2 1.0
2 1 6 1.0
3 1 5 1.0
4 1 7 1.0
5 1 3 1.0
6 1 4 1.0
7 2 18 1.0
8 3 15 1.0
9 3 14 1.0
10 4 17 1.0
11 4 16 1.0
12 5 10 1.0
13 5 11 1.0
14 6 13 1.0
15 6 12 1.0
16 7 9 1.0
17 7 8 1.0
18 18 21 1.0
19 18 19 1.0
20 18 20 1.0
END

SYMMETRY C(S)

SOLVATION
    Surf Esurf
    Solvent name=Water cav0=0.0 cav1=0.0067639
    Charged method=CONJ
    C-Mat POT
    SCF VAR ALL
    CSMRSP
END

CHARGE 1.0 5.0

UNRESTRICTED

BASIS
type TZ2P
core None
createoutput None
END

XC
GGA OPBE
END

GEOMETRY
    optim Delocalized
END

SAVE  TAPE21 TAPE13

SCF
iterations 200
mixing 0.03
diis  n=30
adiis
END

FULLSCF
INTEGRATION 10

NoBeckeGrid
NOPRINT LOGFILE
```

```
eor
```

D.1.7 $Fe(H_2O)_4(SO_4)_2^-$

```
#! /bin/sh

"$ADFBIN/adf" <<eor
DEPENDENCY
ATOMS
1 Fe       0.000000000000       0.000000000000       0.000000000000     R=1.858
2 O      −1.347606711000       1.482957573000       0.674911047400     R=1.517
3 O      −1.329438965000      −1.515727652000       0.705003087600     R=1.517
4 O       1.347606711000      −1.482957573000      −0.674911047400     R=1.517
5 O       1.329438965000       1.515727652000      −0.705003087600     R=1.517
6 H       2.274225521000      −1.377880748000      −0.425343134800     R=1.350
7 H       1.310446649000      −1.445124486000      −1.675943678000     R=1.350
8 H       1.131378626000       1.590176181000      −1.683988703000     R=1.350
9 H       1.154506296000       2.387493030000      −0.328413316100     R=1.350
10 H      −1.310446649000       1.445124486000       1.675943678000     R=1.350
11 H      −2.274225521000       1.377880748000       0.425343134800     R=1.350
12 H      −1.154506296000      −2.387493030000       0.328413316100     R=1.350
13 H      −1.131378626000      −1.590176181000       1.683988703000     R=1.350
14 O      −0.780827375500      −0.074707634990      −1.782787488000     R=1.517
15 S      −0.102998552300      −0.001003422354      −3.176008832000     R=1.792
16 O       0.855780900600      −1.133514908000      −3.226905920000     R=1.517
17 O       0.606351164100       1.301457313000      −3.224157498000     R=1.517
18 O      −1.149886079000      −0.106889184800      −4.183815889000     R=1.517
19 O       0.780827375500       0.074707634990       1.782787488000     R=1.517
20 S       0.102998552300       0.001003422354       3.176008832000     R=1.792
21 O      −0.606351164100      −1.301457313000       3.224157498000     R=1.517
22 O       1.149886079000       0.106889184800       4.183815889000     R=1.517
23 O      −0.855780900600       1.133514908000       3.226905920000     R=1.517
END

GUIBONDS
1 1 14 1.0
2 1 19 1.0
3 1 2 1.0
4 1 4 1.0
5 1 3 1.0
6 1 5 1.0
7 2 11 1.0
8 2 10 1.0
9 3 12 1.0
10 3 13 1.0
11 4 6 1.0
12 4 7 1.0
13 5 9 1.0
14 5 8 1.0
15 14 15 1.0
16 15 18 1.0
17 15 17 1.0
18 15 16 1.0
19 19 20 1.0
20 20 22 1.0
21 20 21 1.0
22 20 23 1.0
END

SYMMETRY C(I)

SOLVATION
    Surf Esurf
    Solvent name=Water cav0=0.0 cav1=0.0067639
    Charged method=CONJ
    C−Mat POT
```

```
    SCF VAR ALL
    CSMRSP
END

CHARGE -1.0 5.0

UNRESTRICTED

BASIS
type TZ2P
core None
createoutput None
END

XC
GGA OPBE
END

GEOMETRY
    optim Delocalized
END

SAVE  TAPE21 TAPE13

SCF
iterations 200
mixing 0.03
diis  n=30
adiis
END

FULLSCF
INTEGRATION 10

NoBeckeGrid
NOPRINT LOGFILE

eor
```

D.1.8 $Fe(H_2O)_5SO_3^+$

```
#! /bin/sh

"$ADFBIN/adf" <<eor
ATOMS
1 Fe       0.192824108300      -0.000000000000      -0.118573100100     R=1.858
2 O        0.998477822300       0.000000000000       1.536056238000     R=1.517
3 O       -1.119785951000      -1.513043952000       0.448021474600     R=1.517
4 O       -1.119785951000       1.513043952000       0.448021474600     R=1.517
5 O        1.463736387000       1.536216321000      -0.939965904100     R=1.517
6 O        1.463736387000      -1.536216321000      -0.939965904100     R=1.517
7 O       -0.665558226200      -0.000000000000      -2.142090518000     R=1.517
8 H       -1.163618748000      -0.766707629000      -2.453658681000     R=1.350
9 H       -1.163618748000       0.766707629000      -2.453658681000     R=1.350
10 H       1.760886977000       1.459575404000      -1.856169922000     R=1.350
11 H       2.261009296000       1.729193275000      -0.428882124100     R=1.350
12 H       2.261009296000      -1.729193275000      -0.428882124100     R=1.350
13 H       1.760886977000      -1.459575404000      -1.856169922000     R=1.350
14 H      -1.050224475000      -1.498356434000       1.461722969000     R=1.350
15 H      -2.058338989000      -1.420763432000       0.237008738800     R=1.350
16 H      -1.050224475000       1.498356434000       1.461722969000     R=1.350
17 H      -2.058338989000       1.420763432000       0.237008738800     R=1.350
18 S       0.265185754000       0.000000000000       3.032151986000     R=1.792
19 O      -0.593914788300       1.234741154000       2.957484375000     R=1.517
20 O      -0.593914788300      -1.234741154000       2.957484375000     R=1.517
END
```

```
GUIBONDS
1 1 2 1.0
2 1 5 1.0
3 1 6 1.0
4 1 3 1.0
5 1 4 1.0
6 1 7 1.0
7 2 18 1.0
8 3 15 1.0
9 3 14 1.0
10 4 17 1.0
11 4 16 1.0
12 5 10 1.0
13 5 11 1.0
14 6 13 1.0
15 6 12 1.0
16 7 8 1.0
17 7 9 1.0
18 18 20 1.0
19 18 19 1.0
END

SYMMETRY C(S)

SOLVATION
    Surf Esurf
    Solvent name=Water cav0=0.0 cav1=0.0067639
    Charged method=CONJ
    C—Mat POT
    SCF VAR ALL
    CSMRSP
END

CHARGE 1.0 5.0

UNRESTRICTED

BASIS
type TZ2P
core None
createoutput None
END

XC
GGA OPBE
END

SCANFREQ —1000 0

GEOMETRY
    optim Delocalized
    iterations 100
END

AnalyticalFreq
END

SAVE  TAPE21 TAPE13

SCF
iterations 100
mixing 0.03
diis  n=30
adiis
END

FULLSCF
INTEGRATION 10
```

```
NoBeckeGrid
NOPRINT LOGFILE

eor
```

D.2 Validation of the COSMO approach

The calculation of vibrational frequencies using the COSMO approach can cause undesired effects associated with the slight expansion and contraction of the conductor surface when the molecule is distorted along its normal modes. In order to investigate the influence of this, the numerical differentiation step size along the normal modes was varied between 0.00125 and 0.04 Å and the resulting calculated vibrational energy for the ν_1-SO_3 stretch of the $FeSO_4^+$ species tracked; this is presented in Figure D.1. It is clear that the frequency increases substantially with increasing step size, and tends towards a fixed value of 1013.8 cm^{-1} at lower step sizes. However, significant reduction in the step size value increases the impact of numerical noise on the calculated frequencies and since the focus of this work was on the trends, it was deemed satisfactory to fix the step size parameter at 0.01 Å, i.e., the ADF default value.

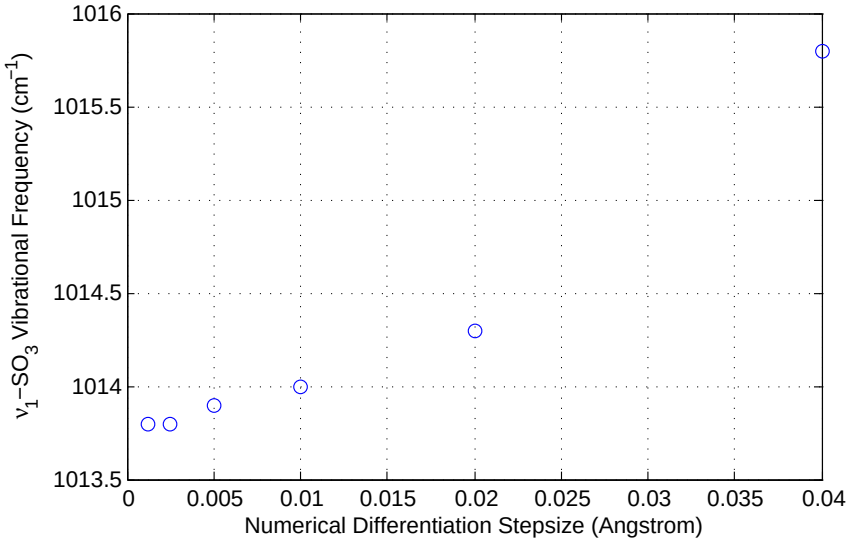

Figure D.1: Variation in calculated ν_1-SO_3 for the $FeSO_4^+$ complex as a function of the numerical differentiation step size. The ADF default is 0.01 Å.

Appendix E

Activity Coefficient Modelling: A Review

E.1 Electrolyte interactions

Some basic solution thermodynamic principles were outlined in the Chapter 2. Extending these into the fundamental origins of the activity coefficient is useful in the context of the development of activity coefficient models and is briefly discussed in the following paragraphs.

E.1.1 Generalised interactions

The most intuitive of the interactions among electrolyte components are of an electrostatic nature and result from the charge differences between anions and cations within a solution. Generally speaking, this is the primary contribution to non-ideality in an electrolyte solution (Wright, 2007). However, there are a number of other interactions that are possible; including ion-dipole, dipole-dipole and molecule-molecule interactions with other ionic species and/or complexes, neutral molecules or the solvent and these may influence the thermodynamic properties of the solution (Thomsen, 2008). These interactions can typically be divided into three broad categories, summarized in Table E.1:

These interactions are not all of the same magnitude and are noticeable depending on the type and concentration of the solute in the system of interest. To give an indication of the ranges over which these interactions become important, it is useful to investigate the change in potential energy with distance from two interacting species, shown in by the approximate dependence of the potential energy with separation distance.

Table E.1: Types of electrolyte interactions (based on Wright (2007))

Solute-Solute	Solute-Solvent	Solvent-Solvent
Long range electrostatic	Ion-dipole	Dipole-dipole
Ion-Induced dipole	Ion-induced dipole	Dipole-induced dipole
Short range interactions		Dispersion/London forces
Hard sphere contact		Dipole-Quadrupole/Higher

Table E.2: Potential energy-approach distance relationships (based on Thomsen (2008))

Interactions	Approx. E_p-r Relationship
Long range electrostatic	r
Ion-dipole	$1/r^2$
Dipole-dipole	$1/r^3$
Molecule-molecule	$1/r^6$

The summary presented in Table E.2 gives a qualitative interpretation of how the effects of the electrolyte interactions are noticeable at different total solute concentrations. In the limit of infinite dilution, an electrolyte solution approaches ideality. In this case, the solute components of the solution lie so far apart that the effects of the higher order interactions are not noticeable. As the solute concentration increases, the number of solute components increases and accordingly, the separation distance decreases. According to Table E.2, the electrostatic interactions are first noticeable and for extremely dilute solutions, consideration of only the electrostatic interactions is usually sufficient to predict their behaviour. At higher concentrations, the individual electrolyte components are forced in closer proximity to one another, and thus, the interactions that are proportional to higher orders of approach distance become more dominant. The presence of the different possible interactions in electrolyte solutions thus depends on the solute concentration range of interest. This conclusion was also suggested by Robinson and Stokes (1970) who claimed that at higher concentrations, ion-solvent interactions dominated and not electrostatic interactions. Despite this, many electrolyte theories do not explicitly recognise solvent species, but consider the solvent as a dielectric continuum, through which charge permeates (Wright, 2007). While this is not precisely theoretically valid, and the explicit solvent interactions are not quantified, this assumption has allowed good results to relatively high concentrations in many systems using a variety of approaches(Pitzer, 1991; Liu and Papangelakis, 2005; Thomsen, 2008). Ion-solvent interactions and their resulting effect on the other interactions within electrolyte systems are being acknowledged

by researchers as being important and considerable new modelling techniques that are rooted in statistical mechanics are treating the solvent explicitly (Wright, 2007).

The total solution concentration has been shown to be important for the presence of the various electrolyte interactions and in order to simplify electrolyte thermodynamic expressions Lewis and Randall (1921) introduced the concept of the ionic strength:

$$I = 0.5 \sum_i m_i z_i^2 \tag{E.1.1}$$

where, m_i and z_i are the molality and charge of species i in the system respectively. The ionic strength is a measure of the total solution concentration and is a common, historical means of correlating electrolyte data. Care must be taken to interpret this quantity within the specific approach adopted in a particular system as the explicit recognition of associated complexes alters the overall solution ionic strength from that case where complete dissociation is assumed.

E.1.2 Potential and distribution functions

While the quantum-statistical mechanics derivation of thermodynamic functions from chemical interactions is beyond the scope of this thesis, considerable insight into the behaviour of electrolytes may be inferred from a basic analysis of several of the resulting equations and this behaviour used to explain trends in model parameters, discussed later. Two predominant features of these equations involve the intermolecular mean force potential and the radial distribution functions. Both of these functions are present in the convenient expression for the osmotic coefficient derived from statistical mechanics, so called the 'pressure equation' (Pitzer, 1973):

$$\phi - 1 = -\left(6ckT\right)^{-1} \sum_i \sum_j c_i c_j \int_0^\infty \left(\frac{\partial u_{ij}(r)}{\partial r}\right) g_{ij}(r) 4\pi r^3 dr \tag{E.1.2}$$

Here, $u_{ij}(r)$ is the intermolecular mean force potential; a function that describes how potential energy (such as electrostatic potential) changes with distance from a central reference ion, j, and $g_{ij}(r)$ is the radial distribution function; a function that describes how the species, i, are arranged around the central reference ion, j. The distribution function is thus a probability function that describes the likelihood of finding an ion i, a specified distance from the reference ion j. It is obvious from this simplified equation that the direct chemical interactions among solute components directly affect the thermodynamic properties - an important consequence for modelling purposes. However, in order to completely account for all interactions, one not only needs to consider the

potentials and distributions between a reference ion and a single ion in the ionic atmosphere, but the great number that realistically exist in a solution. This leads to much more complex equations and requires advanced theoretical means of dealing with them. In order to gain some insight into the behaviour of electrolytes in dilute solutions where Equation E.1.2 may be sufficiently simplified, one may consider the assumptions that: (i) the intermolecular potential may be estimated by the columbic interactions, assumed in the Debye-Huckel theory (discussed later) with an inclusion of hard sphere repulsions; and (ii) a radial Boltzmann distribution of unlike ions in the ionic atmosphere. These assumptions may be considered valid in dilute solutions since the solute ions are not forced close together and unlike charges are most likely to attract each other (and vice versa for like charges). In reality, the intermolecular potential is not given by hard repulsions, but so called 'soft interactions' and the potential and distribution functions are much more complex.

The Boltzmann radial distribution is well-known and given as:

$$g_{ij}(r) = \exp\left(-\frac{z_i e \Psi_{ij}}{kT}\right) = \exp\left(-\frac{\Phi}{kT}\right) \tag{E.1.3}$$

Where Ψ_{ij} is the total potential energy of ion i at distance r from the central ion j and Φ is the potential energy of the interaction between the central ion and the ionic atmosphere. Incorporation of these two binary interaction functions into Equation E.1.2 and transforming for the mathematical anomaly at $r = a$, the following equation is obtained (Pitzer, 1991):

$$\phi - 1 = \frac{e^2 c z^2}{24\epsilon_r \epsilon_0 kT} \int_a^\infty \left[g_{++}(r) - g_{+-}(r)\right] 4\pi r dr + \frac{\pi c a^3}{6} \left[g_{++}(a) - g_{+-}(a)\right] \tag{E.1.4}$$

There are many ways to solve the above equation, which is not important to this discussion, however a qualitative investigation of Equation E.1.4 provides insight into the phenomenon of binary interactions in electrolyte solutions. The first term in Equation E.1.4 is a formulation that incorporates the long range electrostatic forces and can be reduced to generally well understood expressions. However, the second term holds greater theoretical significance as it represents some of the short range binary interactions among like and unlike ions in a solution. This term is clearly dependent on the concentration of the solute in solution and the difference in radial distribution probabilities at hardcore contact, i.e., $r = a$. This bracketed term has been investigated by various authors who report similar findings even for treatment of soft-core ions (Pitzer, 1973); the distribution function for a 1:1 electrolyte as $r \to a$ as a function of ionic strength is presented in Figure E.1.

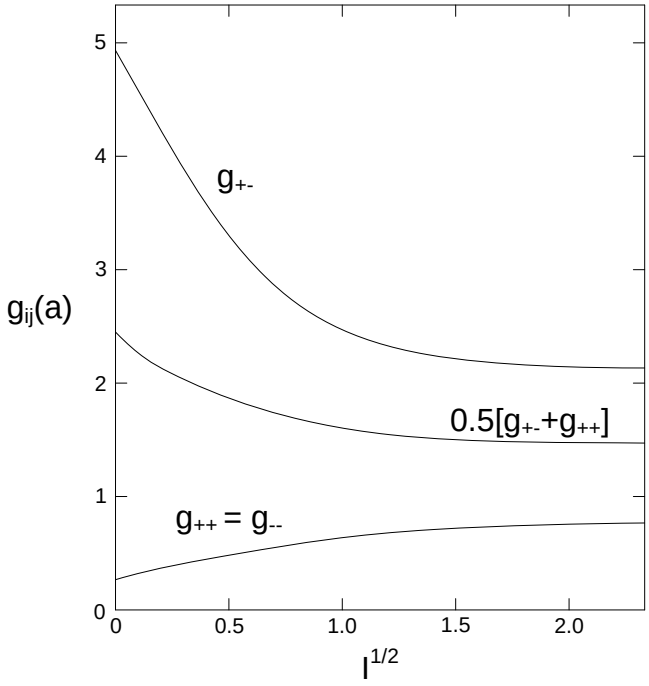

Figure E.1: Distribution functions at contact as a function of ionic strength (1:1 electrolyte) (Redrawn from Pitzer (1991))

The trends in Figure E.1 are critical to the understanding of electrolyte behaviour and shows categorically that the binary interactions among like and unlike charged ions is dependent on the ionic strength; that is, the amount of ion equivalents in solution. At low concentrations, ions are relatively free to move in solution and one expects them to arrange in order to minimise their potential energy, that is, with unlike ions in closer proximity and like ions further apart. This is shown by the larger and smaller relative probabilities in the radial distribution functions at contact for unlike and like ions respectively at low ionic strength.

However, as the ionic strength increases, one notices that the relative probability of finding unlike ions near one another decreases and that of finding like ions near one another increases, with both probabilities tending towards a constant value at higher ionic strength. This phenomenon can be understood if one considers how the solution is becoming more pregnant with ions as the ionic strength increases. Investigating the average of the like and unlike radial distribution functions, one can generalise the behaviour of all ions in the solution. It is clear from Figure E.1 that this average distribution is analogous with the second term to Equation E.1.4 and shows the probability of binary ion interactions decreases with ionic strength. This is initially counter-intuitive since one

would expect the interactions to increase with concentration, but it must be remembered that the distribution functions are multiplied with the concentration in Equation E.1.4 to give the contribution of the short-range forces to the osmotic coefficient. Thus, this investigation emphasises that while overall binary interactions among ions necessarily increases with concentration, the ions are to an extent 'constrained' by their short range forces, observed by the decrease in radial distribution. In other words, the ions ability to locate freely based on their electrostatic potential is generally impaired by the short range interactions among them at high concentrations. An understanding of this variation in the radial distribution function on an ionic level is important to the development of chemical models that are based on the fundamental chemical concepts. Furthermore, this phenomenon has been observed in the analysis of model parameters with measured experimental data (Pitzer, 1973) and is thus considered important for understanding the fundamental basis of the models which are investigated in this study.

E.2 The Debye-Hückel theory

The theory of Debye-Hückel was arguably the beginning of fundamental electrolyte modelling and generally forms the basis of modern electrolyte theories (Wright, 2007). The theory is relatively simple when compared to modern theories and contains many assumptions on the characteristics and behaviour of electrolyte systems. The major assumption of the Debye-Hückel theory was that the most significant interactions, accounting for non-ideality, in electrolyte systems were long range electrostatic interactions among charged, spherical ions. Furthermore, it was assumed that these interactions followed the Coulomb's law of charged particles. These assumptions neglect all short range, higher order and solvent interactions highlighted in Table E.1 and as such the Debye-Hückel theory proved limiting in its description of electrolyte systems.

E.2.1 Theoretical development

The complete derivation of the Debye-Hückel theory is not important to this discussion, although a brief description highlights limitations and the reasons for the model validity only at high dilution. The key development of the Debye-Hückel theory was the quantification of the radial distribution and intermolecular mean force potential via the Boltzmann distribution and Poisson's charge density equations, derived from electrodynamics, respectively. This development resulted in the consideration of only the electrostatic potential surrounding the ions and hence neglected all short range and other forces presented in Table E.1.

The resulting Boltzmann-Poisson equation has no analytical solutions and Debye and Hückel used an appropriate Taylor expansion of the Boltzmann distribution to solve the second order partial differential equation which allowed an approximate solution that was accurate about the expansion point; the limit of small electrical potential which is only present in dilute systems. The solution of the resulting Boltzmann-Poisson equation was then used to determine the excess Helmholtz energy induced by the charging process of an ion in an aqueous solution. Due to the impractical nature of the Helmholtz energy (constant volume) the traditional Debye-Hückel equation has not been used for electrolyte purposes (Thomsen, 2008), but a transformation to the preferred Gibbs energy (constant pressure) is commonly used for dilute solutions and the mean molal activity coefficient is given as:

$$\ln \gamma_{\pm} = \ln x_w - |z_a z_c| \frac{A\sqrt{I}}{1 + Ba\sqrt{I}} \tag{E.2.1}$$

Where B is given as:

$$B = \left(\frac{2e^2 N_A d_0}{\epsilon_r \epsilon_0 kT} \right)^{1/2} \tag{E.2.2}$$

and a is an ion size parameter, often in the range of 3-6 Å (Thomsen, 2008). This expression for the mean activity coefficient and has been observed to give good performance for pure electrolytes up to ionic strengths of approximately 0.1 mol/kg (Thomsen, 2008). This transformation from the original Debye-Hückel equation further includes some additional assumptions that allow the expression to remain relatively simple and thus only applicable to dilute solutions. These are: (i) that the density of the solution may be approximated by that of water; and (ii) the mass and volume of ions in solution is negligible. It should also be noted that the Debye-Hückel equation typically does not include the $\ln x_w$ term as this is often negligible for dilute solutions.

E.2.2 The Debye-Hückel parameter

In this electrostatic framework, and many subsequent theories, the solvent species is considered only to have bulk solution properties and act as a 'dielectric continuum' through which electrostatic charges may permeate (Thomsen, 2008) Debye and Hückel introduced a parameter that quantifies the bulk solvent properties, defined as:

$$A = \left(\frac{2\pi N_A d_{solvent}}{1000} \right)^{1/2} \left(\frac{e^2}{\epsilon_r \epsilon_0 kT} \right)^{3/2} = 3A_{\phi} \tag{E.2.3}$$

Where, N_A is Avogadro's Number, $d_{solvent}$ is the density of the solvent, e is the charge of an electron, $\epsilon_{r,0}$ is the solvent/vacuum permittivity, k is the Boltzmann constant and T is the temperature. This parameter was calculated from the fundamental constants sourced from Mohr et al. (2006). This parameter or a similar form of it is common in many electrolyte modelling frameworks as, in the limit of low dilution, the solvent (usually water) appears to have only bulk solution properties.

E.2.3 Limiting law

In addition to the Debye-Huckel parameter accurately describing the solvent properties, as previously mentioned, the short and intermediate range forces become insignificant at lower dilutions and one of the principle uses of Debye-Hückel theory is the quantification of the excess free energy (or other thermodynamic properties) at high dilution from the so called Debye-Hückel limiting law or Debye-Hückel Slope (Thomsen, 2008). This limiting law is shown for the formulation of the excess free energy in the equation below.

$$\left.\frac{G^{ex}}{n_w RT}\right|_{I\to 0} = -\frac{4}{3}AI^{3/2} \tag{E.2.4}$$

The implication of this equation is that, in limit of high dilution, it is only the long range electrostatic forces that contribute noticeably to the solution non-ideality and that this feature can be adequately expressed by the simple equation. The limiting law represents the slope to which all electrolyte chemical models reduce to at high dilution.

E.2.4 Limitations of the Debye-Hückel theory

The limitations of the Debye-Hückel have been noted by numerous authors (Pitzer, 1991; Thomsen, 2008) and have been neatly summarised by Wright (2007), the most important of which are noted below:

- Additional interactions contributing to non-ideality are not accounted for, such as: (i) short range columbic and quantum-mechanical interactions; (ii) hard and non-hard sphere repulsions; (iii) polarizability; (iv) induced-dipole interactions; (v) specific ion-solvent and solvent-solvent interactions.
- Truncation of the exponential Boltzmann distribution induces mathematical errors in evaluation.
- Unable to account for spherically unsymmetrical ions.
- No account of ion association is considered.

Thus, many assumptions are inherent within the Debye-Hückel theory and the interactions among electrolyte components are treated in an extremely simple manner, in comparison with more modern techniques. The result of this is a model which is only valid at low solute concentrations.

E.3 Extended Debye-Hückel

There are several extensions of the Debye-Hückel theory proposed in the literature which attempt to quantify the short-range interactions between ions in more concentrated solutions, where deviations from the primitive model are observed (Guggenheim and Turgeon, 1955; Davies, 1962; Helgeson, 1969; Bromley, 1973; Zemaitis, 1980). These models typically involve some temperature and ion specific parameters with terms in ionic strength added to the Debye-Hückel equation (Equation E.2.1).

A common equation that is included in several geochemical software packages developed over the years is the B-dot Equation E.3.1 which has a single ion specific parameter, a_i and a temperature dependent slope in ionic strength, $\dot{B}$.

$$\ln \gamma_i = \frac{-Az_i^2\sqrt{I}}{1 + a_i B\sqrt{I}} + \dot{B}I \tag{E.3.1}$$

This model is reported to have validity up to $I_{stoich} = 1$ mol/kg in certain systems (Casas et al., 2005), however the model simplicity could limit it to systems where short-range interactions are not significant. Other extensions, such as Guggenheim and Turgeon (1955) treat the $\dot{B}$ parameter as an ion specific parameter allowing larger concentration ranges to be considered by the model (Thomsen, 2008). In a similar manner, Bromley (1973) suggested an empirical model with individual ion parameters that is capable of modelling multi-component solutions to moderate concentrations. For brevity, only the mean activity coefficient equation is presented here.

$$\ln \gamma_\pm = \frac{-|z_M z_X| A\sqrt{I}}{a + \sqrt{I}} + \ln 10 \left(\frac{(0.06 + 0.6B_{MX})|z_M z_X|\sqrt{I}}{(1 + (1.5/|z_M z_X|)I)^2} + B_{MX} I \right) \tag{E.3.2}$$

Another frequently used extension is the Bromley-Zemaitis extension which adds terms in increasing powers of ionic strength to Equation E.3.2 so that the model may be fit to a wider range of concentrations (Zemaitis, 1980). This model is included in the OLI Systems Software Package (Systems, 2006) and the model parameters, B_{MX},

C, D, can have second order temperature dependence by introducing other parameters, resulting in a maximum of 9 parameters per *interaction*.

$$\ln \gamma_{\pm} = \frac{-|z_M z_X| A\sqrt{I}}{a + \sqrt{I}} + \ln 10 \left(\frac{(0.06 + 0.6 B_{MX})|z_M z_X|\sqrt{I}}{(1 + (1.5/|z_M z_X|)I)^2} + B_{MX} I + C I^2 + D I^3 \right) \tag{E.3.3}$$

The primary drawback to the use of these activity coefficient models is the difficulty in obtaining estimates of the osmotic coefficients, and hence the water activity, in multi-component solutions as integration of the activity coefficient equations is required which becomes extremely cumbersome for higher powers of ionic strength. As a result, the formulation proposed by Meissner and Kusik (1973) or numerical Gibbs-Duhem integration of the activity coefficients are typically employed (Cheng and Li, 2010). As such, these models cannot always fully utilise reliable measurements of the water activity as a means of calibration or validation.

E.4 Pitzer's equations

In a series of papers, Pitzer extended electrolyte theory by combining insights from fundamental theory with a clear focus on model simplicity and empirical effectiveness. Pitzer presented a flexible, semi-empirical model which could be applied to systems having a wide range of species, concentrations and temperatures. The Pitzer equations have been successful in modelling systems to concentrations of typically around 6 mol/kg, although exceptions are noted (Pitzer, 1991). These equations have become a standard means of correlating experimental data and the following section aims to describe the development of Pitzer's equations with reference to the fundamental chemistry on which the equations were based.

A significant advantage of the Pitzer model over other simpler models is the direct calculation of the osmotic coefficient and hence water activity from the model parameters. Additionally, the use of this model has been applied to systems in order to characterise speciation (Steyl, 2009) and while it does become somewhat cumbersome for complex systems, the model does provide some advantages over the more complex models.

E.4.1 Model development

The roots of the Pitzer equations are based on the statistical mechanics framework of the McMillan-Mayer theory; where the specific case of excess solvent is applicable (Pitzer,

1991). In this framework, it has been shown that the thermodynamic properties of an electrolyte system can be related to the interionic mean force potentials, and hence the direct 'interactions' of the solution components. The McMillan-Mayer theory (McMillan and Mayer, 1945) suggested that a solution of neutral molecules, such as a solvent, behaved in a similar manner to an imperfect gas and that the addition of electrolyte particles primarily introduced electrostatic interactions. Developing from these ideas, Pitzer suggested that a model that consisted of an electrostatic term, which is similar to the D-H limiting law, plus a virial coefficient expansion was able to predict electrolyte solution properties while remaining, mathematically, relatively simple (Pitzer, 1973). In this approach, the virial coefficient expansion accounts for shorter range interactions of solute species and the electrostatic term accounts for the long range interactions. In a similar manner to several of the previous models, this modelling approach is based on specific ion interactions and thus solutes are expected to have specific model parameters. In addition to this, one of Pitzer's important theoretical findings was the suggestion that the virial coefficients required a dependence on ionic strength and the incorporation of this into the modelling framework was one of the primary modifications to electrolyte modelling that Pitzer presented. Theoretically, if all of the mean force potentials and distribution functions are known in a specific system, the virial coefficients may be derived from quantum-statistical theory; as has been done for simple, monatomic gases (McQuarrie, 2000). However, the determination of the virial coefficients for liquids is currently not possible due to the much higher concentrations and interactions among them. The simplicity, and empirical nature, of the Pitzer equations resides in the fact that the virial coefficients are left as empirically determined, solute specific parameters instead of being derived from quantum-statistical theory (Pitzer, 1991). This semi-empirical framework allows the model parameters to remain, to an extent, physically meaningful and offer significant advantages for the insight of the fundamental nature of the chemical interactions being investigated. The result of this semi-empirical nature allows the Pitzer model to be highly successful in data interpolation and, to a certain extent, extrapolation.

E.4.2 General model form

The Pitzer model equations have been thoroughly reported throughout literature (Pitzer, 1991) and are a common means of collating experimental data. Thus, only a brief presentation of the equations, relevant to the discussion of this work is made here. The model equations are presented for the unsymmetrical[1], individual-ion activity coefficients of

[1]Pure component reference state for the solvent ($\gamma_{solvent} \rightarrow 1$ as $x_{solvent} \rightarrow 1$) and infinitely dilute reference state for the solute ions ($\gamma_{solute} \rightarrow 1$ as $x_{solute} \rightarrow 0$)

cations (M) and anions (X), using the molality scale and standard state at 1 mol/kg ideal hypothetical solution. The simplest form of the Pitzer model for the total excess Gibbs free energy of an electrolyte system can be written as:

$$\frac{G^{ex}}{n_w RT} = f(I) + \sum_i \sum_j m_i m_j \lambda_{ij}(I) + \sum_i \sum_j \sum_k m_i m_j m_k \mu_{ijk} + \dots \tag{E.4.1}$$

where, $f(I)$ is a function of ionic strength similar to the Debye-Hückel term , $\lambda_{ij}(I)$ is a coefficient matrix of binary interactions between alike solute species i and j which is dependent on ionic strength and μ_{ijk} is a coefficient matrix of ternary interactions between alike solute species. The ternary interactions, theoretically, are also dependent on ionic strength however as previously mentioned no empirical evidence of this has been observed and is usually neglected (Pitzer, 1991).

By taking appropriate derivatives of Equation E.4.1 the individual ion activity coefficients and the osmotic coefficient may be directly obtained:

$$\begin{aligned}\ln \gamma_M = {} & z_M^2 F + \sum_a m_a (2B_{Ma} + ZC_{Ma}) \\ & + z_M \sum_c \sum_a m_c m_a C_{ca} \\ & + \sum_c m_c (2\Phi_{Mc} + \sum_a m_a \Psi_{Mca}) \\ & + \sum_a \sum_{a'} m_a m_{a'} \Psi_{Maa'} \\ & + 2\sum_n m_n \lambda_{Mn} + 3\sum_n m_n^2 \mu_{Mnn} + \cdots\end{aligned} \tag{E.4.2}$$

$$\begin{aligned}\ln \gamma_X = {} & z_X^2 F + \sum_c m_c (2B_{cX} + ZC_{cX}) \\ & + |z_X| \sum_c \sum_a m_c m_a C_{ca} \\ & + \sum_a m_a (2\Phi_{Xa} + \sum_c m_c \Psi_{cXa}) \\ & + \sum_c \sum_{c'} m_c m_{c'} \Psi_{cc'X} \\ & + 2\sum_n m_n \lambda_{Xn} + 3\sum_n m_n^2 \mu_{Xnn} + \cdots\end{aligned} \tag{E.4.3}$$

The osmotic coefficient, a function of the water activity via Equation 2.3.14, may be written as:

$$\begin{aligned}\phi - 1 = (2/\sum_i m_i)[f^\phi I + \sum_c \sum_a m_c m_a (B^\phi_{ca} + Z C_{Ma}) \\ + \sum_c \sum_{c'} (\Phi^\phi_{cc'} + \sum_a m_a \Psi_{cc'a}) \\ + \sum_a \sum_{aa'} (\Phi^\phi_{aa'} + \sum_c m_c \Psi_{caa'}) \\ + \sum_n \sum_c m_n m_c \lambda_{nc} + \sum_n \sum_{nn'} m_n m_{n'} \lambda_{nn'} \\ + \tfrac{1}{2} \sum_n m_n^2 \lambda_{nn} + \cdots\end{aligned} \tag{E.4.4}$$

The subscript i covers all species in solution and the parameters B_{MX} and C_{MX} are the second and third virial coefficients respectively and are defined as:

$$\begin{aligned}B^\phi_{MX} = \beta^{(0)}_{MX} + \beta^{(1)}_{MX} \exp(-\alpha_1 I^{\frac{1}{2}}) \\ + \beta^{(2)}_{MX} \exp(-\alpha_2 I^{\frac{1}{2}})\end{aligned} \tag{E.4.5}$$

$$\begin{aligned}B_{MX} = \beta^{(0)}_{MX} + \beta^{(1)}_{MX} g(-\alpha_1 I^{\frac{1}{2}}) \\ + \beta^{(2)}_{MX} g(-\alpha_2 I^{\frac{1}{2}})\end{aligned} \tag{E.4.6}$$

$$C_{MX} = \frac{C^\phi}{2\sqrt{|z_M z_X|}} \tag{E.4.7}$$

The ancillary functions are defined as:

$$\begin{aligned}F = f^\gamma + \sum_c \sum_a m_c m_a B'_{ca} + \sum_c \sum_{c'} m_c m_{c'} \Psi'_{cc'} \\ + \sum_a \sum_{a'} m_a m_{a'} \Phi'_{aa'}\end{aligned} \tag{E.4.8}$$

$$\begin{aligned}f^\phi &= -A_\phi I^{1/2}/(1 + bI^{1/2}) \\ &= f^\gamma + (2A_\phi/b)\ln(1 + bI^{3/2})\end{aligned} \tag{E.4.9}$$

$$g = \frac{2(1 - (1 + x)\exp(-x)}{x^2} \tag{E.4.10}$$

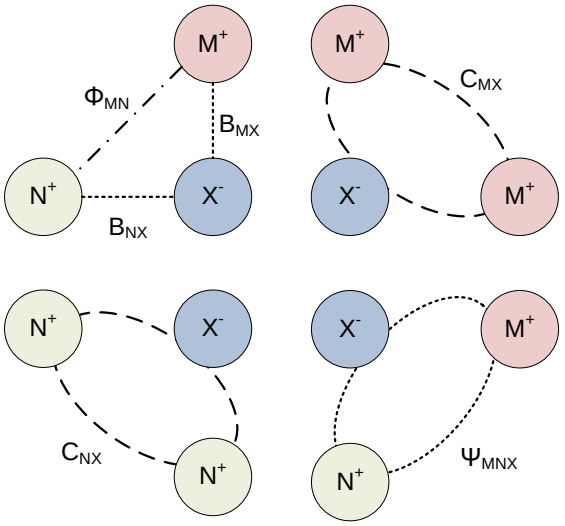

Figure E.2: Diagrammatic representation of Pitzer model parameters in the hypothetical system MX-NX

$$Z = 0.5 \sum_i m_i z_i^2 \tag{E.4.11}$$

$$\gamma_{\pm} = (\gamma_M^{\nu_+} \gamma_X^{\nu_-})^{\frac{1}{\nu_- + \nu_+}} \tag{E.4.12}$$

Where z_i is the charge of ion i, A_ϕ is the usual Debye-Hückel parameter, calculated as 0.39145 kg$^{0.5}$.mol$^{-0.5}$ from fundamental constants sourced from CODATA (Mohr et al., 2006), and b and α_1 are taken as the usual recommended values of 1.2 kg$^{0.5}$.mol$^{-0.5}$ and 2.0 kg$^{0.5}$.mol$^{-0.5}$ respectively (Pitzer, 1973). The primed subscripts indicate all physically distinguishable groups of ions. $\beta^{(0)}_{MX}, \beta^{(1)}_{MX}, \beta^{(2)}_{MX}$ and C_{MX} are the pure component model parameters and $\beta^{(2)}_{MX}$ is conventionally used to account for ion association (Pitzer and Mayorga, 1974b). Φ_{ij} and Ψ_{ijk} are parameters to account for mixing effects in mixed electrolyte systems between binary and ternary ions of different types. The primed B'_{MX}, Ψ'_{ij} and Φ'_{ijk} are the ionic strength derivatives of the model parameters.

E.4.3 Model parameters

Given that the Pitzer modelling approach is based on theoretical insights to electrolyte behaviour, it is important to consider the physical meanings of the model parameters and how these parameters are explicitly defined and related to observed phenomena.

Second virial coefficient As mentioned, the second virial coefficient is transformed into a parameter, B_{MX}, that is more easily interpreted from experimental data. The definition of this transformation is presented below, from (Pitzer, 1973):

$$B^{\phi}_{MX}(I) = \lambda_{MX} + I\lambda_{MX'} + (\nu_M/2\nu_X)\,(\lambda_{MM} + I\lambda_{MM'}) + (\nu_X/2\nu_M)\,(\lambda_{XX} + I\lambda_{XX'}) \tag{E.4.13}$$

It is thus clear that the B_{MX} term is a composite function of the like and unlike binary interactions between cation M and anion X. Due to the fact that one cannot explicitly determine the interactions among like or unlike ions (λ_{ij}) due to electroneutrality constraints the composite function is required for modelling purposes. In order to determine the trend of ionic strength dependence of this composite virial coefficient, it is helpful to recall the analysis of the radial distribution functions ($g_{++}(a), g_{--}(a)$ and $g_{+-}(a)$) at contact for 1:1 electrolytes, shown in Figure E.1. In this figure, the sum of the like and unlike radial distribution functions at contact is observed to decrease rapidly at low ionic strength to a near constant value extending to higher concentrations. In drawing a qualitative analogy between the radial distribution functions at contact and the second virial coefficients in the Pitzer equations one can say that if the probability of two ions coming into close proximity is large, so then is the likely interaction between these ions. Thus, the observed trend in $\lambda_{ij}(I)$, and hence $B_{MX}(I)$, should have the same general features as the ionic strength dependency of the radial distribution functions at contact. This phenomenon has been verified theoretically for a number of 1:1 electrolytes (Pitzer, 1973, 1991).

Based on this fundamental insight into the qualitative behaviour of the second virial coefficient, Pitzer investigated several empirical functions of ionic strength forms that exhibit a similar ionic strength relationship, namely: (i) a finite value at zero ionic strength; (ii) a rapid change approximately linear in $I^{0.5}$ at low concentrations; and (iii) a smooth convergence to a constant value at high concentration (Pitzer, 1973). Pitzer thus proposed the second virial coefficient to have the form shown in Equation E.4.5. This empirical function has been observed to be accurate in quantifying the behaviour of many electrolytes and, since α_1 is usually taken as a constant value of 2.0, the second virial coefficient in the Pitzer model has only two solute-dependent parameters, $\beta^{(0)}_{MX}$ and $\beta^{(1)}_{MX}$, at a given temperature - the additional $\beta^{(2)}_{MX}$ parameter is discussed in the next paragraph.

Inspection of this function of ionic strength shows that the $\beta^{(0)}$ parameter is the limiting value of B_{MX} at high concentrations as the exponential term decays. This is comparable to the effect of both the like and unlike interactions observed in Figure E.1 at higher ionic strengths. Furthermore, at lower ionic strengths the value of the $\beta^{(1)}$ parameter is

most pronounced, suggesting that it is primarily influenced by the interactions of unlike ions in the solution.

While the radial distributions on which Figure E.1 were based were calculated for 1:1 electrolytes, similar qualitative behaviour is expected for other valence types and this has been supported by the ability of the Pitzer model to quantify the behaviour of these electrolytes adequately to moderate concentrations using the same function of ionic strength for the second virial coefficient. Where large charge differences occur however, such as 2:2 electrolytes, additional phenomena such as ion association become potentially important and require considerations. In certain cases, this can be achieved by the inclusion of an additional species (i.e. a speciation approach) or alternatively a more simple approach suggested by Pitzer and Mayorga (1974b) by the inclusion of a $\beta^{(2)}_{MX}$ term in EquationE.4.5.

Pitzer-Debye-Hückel term With the form of the second virial coefficient optimised based on the fundamental insights and empirical effectiveness discussed above, Pitzer considered the precise form of the Debye-Huckel term and suggested a modification of the traditional Debye-Huckel limiting slope. This was done primarily on an empirical basis, initially by the evaluation of a number of plausible functions to experimental data of several 1:1 and 2:1 electrolytes. These functions were either simplified forms of theoretical equations (from statistical mechanics or an ion charging process) or simple empirical formulations. Each of these functions had a single non-linear parameter that was to be optimised in each case and it was desired that this 'empirical' parameter would remain constant for all electrolytes. Pitzer reported that best performing function is that presented in Equation E.4.9 and the optimal value for b in this equation was 1.2 (Pitzer, 1973). These have been successfully implemented in many modelling scenarios with good results and are widely accepted.

The key difference between the traditional Debye-Hückel term and Pitzer's modification is the omission of an explicit parameter that quantifies the difference of closest approach. Pitzer (1973) explains that this effect is included in the second virial coefficient and relieves the model of relying on an explicit difference of closest approach that may be difficult to measure or define. Furthermore, in drawing an analogy between the traditional Debye-Hückel Equation E.2.1 and Equation E.4.9 one notices that the b parameter may account for 'usual' distances of closest approaches as it appears in the same position in the equation.

Higher order coefficients In a similar definition of the composite second virial coefficient, the third virial coefficient used in the Pitzer model is defined below where it can be observed that it is a combination of ternary interactions among cation M and anion X:

$$C^{\phi}_{MX} = \left(3/(\nu_M \nu_X)^{0.5}\right)\left(\nu_M \mu_{MMX} + \nu_X \mu_{MXX}\right) \tag{E.4.14}$$

The Pitzer equations do not consider any ionic strength dependence of this parameter in accordance with experimental observation, although there is no theoretical reason for not doing so (Pitzer, 1991). It should be mentioned here that in certain situations, higher order virial coefficients may be added and are usually assumed independent of ionic strength; however, certain authors have included ionic strength dependence of a similar for to that of the second virial coefficient and described, empirically, the behaviour of complex electrolytes to extremely high concentrations (Archer, 1991; Pitzer, 1991).

Mixed electrolyte parameters The ultimate usefulness of a chemical model is the ability to accurately predict thermodynamic properties in more practical mixed electrolyte systems based on parameters determined from simple pure and common anion electrolyte systems and the incorporation of simple mixing rules. The mixing parameters in the Pitzer model for ions of like charge, Φ_{ij}, and those not of like charge, Ψ_{ijk} are shown in the Pitzer equations presented above and some discussion of their nature is necessary; the exact definition of these mixing parameters can be written:

$$\Phi_{ii'} = \lambda_{ii'} - (z_{i'}/2z_i)/\lambda_{ii} - (z_i/2z_{i}^{'})/\lambda_{i'i'} \tag{E.4.15}$$

$$\Psi_{ii'j} = 6\mu_{ii'j} - (3z_{i'}/z_i)\mu_{iij} - (3z_i/z_{i'})\mu_{i'i'j} \tag{E.4.16}$$

Where i and $i^{'}$ are physically distinguishable pairs of different cations or anions and j is an ion of opposite charge to i. Since the interactions of ions of like charge are expected to be small due to the natural electrostatic tendency to repel one another, the short-range interactions parameters for similarly charged ions are expected to be small. In addition, the interactions of three like ions are completely neglected in the conventional model framework as their interaction is even more unlikely. Thus, from inspection of the above equations, the overall binary mixing parameter is expected to be small in many electrolyte systems, but often necessary to accurately quantify expected behaviour.

This is generally so, however, in cases where significant unsymmetrical mixing occurs[2], there is evidence long range interactions among the like charged ions and further treatment is required. Pitzer quantifies this additional electrostatic effect based on an

[2]When a salt dissociates into cations and anions have differing charge magnitudes

analysis of the expression for the second virial coefficient derived from statistical mechanical arguments (Pitzer, 1991). The key difficulty in evaluating this quantity from theory alone is the precise knowledge of the intermolecular potential; however for this particular case of similarly charges ions, the repulsive forces should sufficiently separate the ions such that the short range potential becomes almost insignificant. In this case, the effect of long range electrostatic forces originating from unsymmetrical mixing may be quantified. Briefly, this treatment involves the integration of an approximate theoretical representation of the second viral coefficient for like charged unsymmetical interactions to obtain an electrostatic term to be added to the empirical term for like charged interactions, shown below:

$$\Phi_{ij} = \theta_{ij} + {}^{E}\theta_{ij}(I) \tag{E.4.17}$$

Where, θ_{ij} represents the estimated model parameter. A complete discussion of this treatment, as well as the estimation of ${}^{E}\theta_{ij}(I)$ by an approximation using Chebyshev polynomials is presented in Pitzer (1991).

The traditional method of determining the mixing parameters in the model involves taking the difference between the measured osmotic or mean activity coefficients in a common anion, mixed electrolyte system (MX-NX) and the respective coefficient calculated via pure electrolyte model parameters. This is useful for optimising parameters from solubility data, however successful results may also be obtained by including the parameters in an overall optimisation to available thermodynamic data of specific relevance (e.g. see Steyl (2009)).

E.4.4 Model limitations

Although the Pitzer model incorporates fundamental insights to electrolyte behaviour, the model remains of a semi-empirical nature and thus the extrapolation out of the range of data on which the parameters were regressed is not theoretically valid and may induce significant errors. Certain cases, where the virial coefficients are not highly variable, acceptable extrapolations have been noted (Pitzer, 1991); however, this must be performed with caution as the deviations with extrapolation may be extreme. This is an important implication for the application of the model as the validity of the model is questionable if experimental data at conditions of interest is not available.

Secondly, the model is limited by the fact that the virial expansion of interaction terms is commonly truncated at ternary interactions among anion-cation pairs, C_{MX}, and thus ignores all higher-order interactions among the solute components. For dilute solutions, this does not introduce significant error since the likelihood of multiple ions (4

or more) coming into close proximity is relatively low. However, for highly concentrated systems, these interactions may become significant and may require explicit recognition. Higher-order interaction considerations have been implemented into the Pitzer equation via fourth and even higher virial coefficients that have successfully modelled complex electrolytes, such as $CaCl_2$ to 11 molal (Pitzer et al., 1999). In such cases, the theoretical validation of model parameters becomes increasingly more complex and one cannot determine the extent to which these parameters are 'theoretically valid' or whether they simply serve as empirical parameters which fit the experimental data. In addition, the inclusion of strict mixing rules for the incorporation of higher order virial coefficients in mixed electrolyte systems is very complex and represents a major drawback of the model; in these cases the most likely higher order interactions are usually selected which typically provides good accuracy.

While a universal upper bound limit on concentration is not possible to quantify since the model performance is system dependent and the model essentially is not limited to any number of parameters, it is suggested with the omission of higher order virial coefficients that model performance will decrease with increasing concentration (Thomsen, 2008). This fact commonly restricts the traditional model to below 6 molal; however, the large variability in electrolyte systems means this is not a strict limitation and may be higher or lower for specific systems.

Thirdly, since the model does not have an inherent dependence on temperature and, as mentioned above, adopts an ion interaction approach, the inclusion of temperature variations or additional solutes has the tendency to rapidly increase the required model parameters. This may result in a large number of required experiments to obtain statistically relevant constants and hence can be considered a limitation of the model.

Although not strictly a model limitation, it was deemed necessary to mention that the b parameter in the Pitzer-Debye-Huckel term does not have any associated theoretical significance. The empirical nature of this term, and subsequent universal definition of its magnitude, is evidence that the term is not rooted entirely in electrolyte theory.

E.5 Beyond Pitzer

While the Pitzer equations have had wide success in describing many electrolyte systems, there have been several directions that electrolyte modelling has progressed since Pitzer first published his models. This section aims to highlight briefly some common additional chemical models which are used to describe electrolyte systems. A compete theoretical analysis of these models is beyond the scope of this study and thus, models are briefly

presented and discussed to place the D-H theory and Pitzer equations of the 1930's and 1970's respectively, in a more modern context.

E.5.1 Mixed solvent electrolyte model

The mixed solvent electrolyte (MSE) model of (Wang et al., 2002), as the name implies, is capable of quantifying systems with multiple solvents such as organic or organic-water solvents. This model has had significant success in modelling numerous systems and boasts quantification of aqueous electrolytes from dilute solutions to fused salts (Systems, 2006). The MSE model separates the excess Gibbs free energy term into three terms, representing long, intermediate and short range interactions respectively. The long range interactions are accounted for using the Pitzer-Debye-Huckel extent ended term, which is usually further extended to account for composition dependence on the density and dielectric constant of the solvent Wang et al. (2002). The Extended UNIQUAC local composition model, discussed below, is used to represent the short range interactions; although other local composition models may also be used. The intermediate range interactions are quantified by a symmetric second virial coefficient type expression that is similar to Pitzer's in that it has ionic strength dependence based similarly on the radial distribution function behaviour discussed previously Thomsen (2008).

The MSE model has recently been incorporated into the OLI Systems software package which incorporates a large database of aqueous electrolyte data and model parameters (Systems, 2006). This framework is furthermore fitted with a built in regression tool for model parameter determination from a variety of experimental data and has been successfully implemented in various systems Liu and Papangelakis (2005). The OLI software boasts simulation capability for electrolyte systems in the following ranges Liu and Papangelakis (2005):

- Temperature: -30 to 300°C
- Pressure: 0 to 1500 bar
- Ionic strength: 0 to 30 molal

Furthermore, the flexibility of the MSE model allows the treatment of electrolytes on associated and dissociated bases as well as true speciation conditions (Systems, 2006) making its implementation into a specific system possible to achieve a number of objectives.

E.5.2 Local composition models

The concept of local composition models was introduced by Wilson in an attempt to quantify the thermodynamic behaviour of non-electrolytes (Wilson, 1964). Local composition models consider the arrangement of species within molecular level 'cell' of the solution in such a way as to minimise their energy and maximise their entropy. In a similar analogy, the Debye-Hückel theory can be considered a local composition theory for electrolytes and for this reason can be implemented into traditional non-electrolyte theories for application to electrolyte systems (Thomsen, 2008). There are two generally well known local composition models of primary interest; the Extended UNIQUAC (Universal Quasi-Chemical Activity Coefficient) and NRTL (Non-Random Two Liquid) models. The Extended UNIQUAC model incorporates the extended Debye-Hückel equation to account for electrostatic interactions and the traditional UNIQUAC contributions to the excess free energy, combinatorial and residual, accounting for entropic and enthalpic contributions respectively. The model parameters in the combinatorial term are traditionally determined form the structure of the system components (volume and surface parameters) however, this has been observed to not produce satisfactory results for electrolyte systems and these are usually left as adjustable model parameters. The residual term contains binary interaction parameters that are temperature dependent (linearly) and are also left as adjustable parameters fitted from experimental data (Thomsen, 2008).

A known advantage of the UNIQUAC framework is the explicit incorporation of temperature dependence in the parameters, allowing an array of thermodynamic properties such as the heat capacity and heat of mixing to be described by the model (Thomsen, 2008). The electrolyte NRTL model is more complex than the UNIQUAC model and contains only an enthalpic term. The significant difference between the NRTL and UNIQUAC electrolyte models is that the NRTL model uses a salt specific approach with appropriate mixing rules, where the UNIQUAC model adopts an ion specific approach. There are other subtle differences between the models but these are not discussed in detain here. This model is conveniently incorporated into the ASPEN simulation package, as the default electrolyte model (Thomsen, 2008).

E.5.3 MSA and electrolyte equations of state

The mean spherical approximation of (Lebowitz and Percus, 1966) is primarily focussed on the electrostatic interactions in electrolyte systems. This model is more theoretically rooted in statistical mechanics and is thus much more complex than the theory of Debye and Hückel despite producing essentially the same numerical results (Thomsen, 2008).

This modelling approach is the preferred choice for researchers attempting to develop electrolyte equations of state (Thomsen, 2008).

The primary additional feature of electrolyte equations of state to the original EOS equations is the incorporation of the pressure effects on the thermodynamic properties of electrolyte solutions. Various electrolyte equations of state have been suggested, including: Furst and Renon (1993), Sako et al. (1989) and Myers et al. (2002). These equations generally contain a conventional cubic EOS with an additional term, usually the mean spherical approximation, to quantify electrostatic interactions. Despite the research in this field, these models are primarily of academic interested and are primitive in the systems they are able to describe (Thomsen, 2008).

A promising direction for electrolyte theory is being permitted by the rapid advances in computer hardware and algorithms. Wright (2007) briefly mentions a statistical mechanical derivation that allows directly the activity coefficient to be derived from distribution functions of two interacting species. With higher order interactions taken into account more accurate descriptions of solution behaviour may be obtained at the expense of extremely complex the equations and solution algorithms. Using high powered computer techniques, this branch of electrolyte system analysis presents "a very powerful theoretical tool, with a realistic expectation of providing considerable insight into the behaviour of electrolyte solutions at the microscopic level" (Wright, 2007).

List of References

Akilan, C., Hefter, G., Rohman, N., Buchner, R., 2006a. Ion association and hydration in aqueous solutions of copper(II) sulfate from 5 to 65 °C by dielectric spectroscopy. The Journal of Physical Chemistry B 110, 14961–14970.

Akilan, C., Rohman, N., Hefter, G., Buchner, R., 2006b. Temperature effects on ion association and hydration in $MgSO_4$ by dielectric spectroscopy. ChemPhysChem 7, 2319–2330.

Anderko, A., Wang, P., Rafal, M., 2002. Electrolyte solutions: From thermodynamic and transport property models to the simulation of industrial processes. Fluid Phase Equilibria 194, 123–142.

Anderson, G., Castet, S., Schott, J., Mesmer, R., 1991. The density model for estimation of thermodynamic parameters of reactions at high temperatures and pressures. Geochimica et Cosmochimica Acta 55, 1769–1779.

Archer, D.G., 1991. Thermodynamic properties of the NaBr-H_2O system. Journal of Physical and Chemical Reference Data 20, 509.

Archer, D.G., Rard, J.A., 1998. Isopiestic investigation of the osmotic and activity coefficients of aqueous $MgSO_4$ and the solubility of $MgSO_4{\cdot}7H_2O$ (cr) at 298.15 K: Thermodynamic properties of the $MgSO_4$+H_2O system to 440 K. Journal of Chemical & Engineering Data 43, 791–806.

Archer, D.G., Wood, R.H., 1985. Chemical equilibrium model applied to aqueous magnesium sulfate solutions. Journal of Solution Chemistry 14, 757–780.

Avelino De Abreu, H., Guimaraes, L., Anderson Duarte, H., 2006. Density-functional theory study of iron(III) hydrolysis in aqueous solution. Journal of Chemical Physics A 110, 7713–7718.

Balarew, C., Tepavitcharova, S., Rabadjieva, D., Voigt, W., 2001. Solubility and crystallization in the system $MgCl_2$-$MgSO_4$-H_2O at 50 and 75 °C. Journal of solution chemistry 30, 815–823.

Baldwin, R., Stauter, J., Terrell, D., 1983. Process for the removal of selenium from aqueous systems. Google Patents. US Patent 4,405,464.

Bassett, H., Parker, W.G., 1951. 352. The oxidation of sulphurous acid. Journal of the Chemical Society (Resumed) , 1540–1560.

Baur, W., 1964. On the crystal chemistry of salt hydrates. III. The determination of the crystal structure of $FeSO_4 \cdot 7H_2O$ (melanterite). Acta Crystallographica 17, 1167–1174.

Bazhko, O., 2009. Application of redox titration techniques for analysis of hydrometallurgical solutions, Hydrometallurgy Conference 2009. pp. 457–464.

Bea, S., Carrera, J., Ayora, C., Batlle, F., 2010. Modeling of concentrated aqueous solutions: Efficient implementation of Pitzer equations in geochemical and reactive transport models. Computers & Geosciences 36, 526–538.

Benkelberg, H.J., Warneck, P., 1995. Photodecomposition of iron(III) hydroxo and sulfato complexes in aqueous solution: Wavelength dependence of OH and SO_4^- quantum yields. The Journal of Physical Chemistry 99, 5214–5221.

Berezowsky, R., Weir, D., 1989. Refractory gold: the role of pressure oxidation, in: Gold Forum on Technology and Practices - World Gold, pp. 295–304.

Berezowsky, R.M.G.S., Collins, M.J., Kerfoot, D.G.E., Torres, N., 1991. The commercial status of pressure leaching technology. JOM 43, 9–15.

Betterton, E.A., 1993. On the pH-dependent formation constants of iron(III)-sulfur(IV) transient complexes. Journal of Atmospheric Chemistry 17, 307–324.

Biley, C., 2011. Iron focussed laterite process (R201104600B: Report 2). Technical Report 2 (R201104600B). Anglo American's Research.

Biley, C., Pelser, M., den Hoed, P., Hove, M., 2013. Development of the iron-focused laterite (ARFe) process, in: SAIMM, Base Metals 2013, Mpumalanga, South Africa.

Brandt, C., van Eldik, R., 1995. Transition metal-catalyzed oxidation of sulfur(IV) oxides. atmospheric-relevant processes and mechanisms. Chemical Reviews 95, 119–190.

Brandt, C., Fabian, I., Van Eldik, R., 1994. Kinetics and mechanism of the iron(III)-catalyzed autoxidation of sulfur(IV) oxides in aqueous solution. Evidence for the redox cycling of iron in the presence of oxygen and modeling of the overall reaction mechanism. Inorganic Chemistry 33, 687–701.

Bromley, L.A., 1973. Thermodynamic properties of strong electrolytes in aqueous solutions. American Institute of Chemical Engineering Journal 19, 313–320.

Brooker, M., Nielsen, O.F., Praestgaard, E., 1988. Assessment of correction procedures for reduction of raman spectra. Journal of Raman spectroscopy 19, 71–78.

Brown, S., Tauler, R., Walczak, B., 2009. Comprehensive chemometrics: Chemical and biochemical data analysis. volume 2. Elsevier, Amsterdam. 1st edition.

Buban, K.R., Collins, M.J., Masters, I.M., 1999. Iron control in zinc pressure leach processes. JOM 51, 23–25.

Buchner, R., Chen, T., Hefter, G., 2004. Complexity in "simple" electrolyte solutions - Ion pairing in $MgSO_4$. The Journal of Physical Chemistry B 108, 2365–2375.

Byrne, R.H., Kester, D.R., 1976. A potentiometric study of ferric ion complexes in synthetic media and seawater. Marine Chemistry 4, 275–287.

Carlyle, D.W., 1971. Kinetic study of the aquation of sulfitoiron (III) ion. Inorganic Chemistry 10, 761—764.

Casas, J., Crisostomo, G., Cifuentes, L., 2005. Speciation of the Fe(II)-Fe(III)-H_2SO_4-H_2O system at 25 and 50 °C. Hydrometallurgy 80, 254–264.

Charpentier, J.C., 1981. Mass transfer rates in gas-liquid absorbers. Advances in chemical engineering 11.

Chen, H., Irish, D., 1971. Raman spectral study of bisulfate-sulfate systems. 3. Salt effects. Journal of Physical Chemistry 75, 2681.

Chen, T., Hefter, G., Buchner, R., 2005. Ion association and hydration in aqueous solutions of nickel(II) and cobalt(II) sulfate. Journal of Solution Chemistry 34, 1045–1066.

Cheng, W., Li, Z., 2010. Nucleation kinetics of nesquehonite ($MgCO_3 \cdot 3H_2O$) in the $MgCl_2$-Na_2CO_3 system. Journal of Crystal Growth 312, 1563–1571.

Clegg, S.L., Brimblecombe, P., 1995. Application of a multicomponent thermodynamic model to activities and thermal properties of 0-40 mol kg-1 aqueous sulfuric acid from< 200 to 328 k. Journal of Chemical and Engineering Data 40, 43–64.

Clegg, S.L., Rard, J.A., Pitzer, K.S., 1994. Thermodynamic properties of 0-6 mol/kg aqueous sulfuric acid from 273.15 to 328.15 K. Journal of the Chemical Society, Faraday Transactions 90, 1875.

Conklin, M.H., Hoffmann, M.R., 1988a. Metal ion-sulfur(IV) chemistry. 2. Kinetic studies of the redox chemistry of copper(II)-sulfur(IV) complexes. Environmental Science & Technology 22, 891–898.

Conklin, M.H., Hoffmann, M.R., 1988b. Metal ion-sulfur(IV) chemistry. 3. Thermodynamics and kinetics of transient iron(III)-sulfur(IV) complexes. Environmental Science & Technology 22, 899–907.

Darling, H., 1964. Conductivity of sulfuric acid solutions. Journal of Chemical & Engineering Data 9, 421–426.

Das, G.K., Anand, S., Das, R., Muir, D., Singh, P., 2000. Sulfur dioxide - a leachant for oxidic materials in aqueous and non-aqueous media. Mineral Processing and Extractive Metallurgy Review 20, 377–407.

Dasgupta, P.K., Mitchell, P.A., West, P.W., 1979. Study of transition metal ion-S(IV) systems. Atmospheric Environment (1967) 13, 775–782.

Davies, C.W., 1962. Ion association. Butterworths, Washington.

Davis, G.G., Smith, W.M., 1962. The kinetics of the formation of the monosulphato complex of iron(III) in aquesous solution. Canadian Journal of Chemistry 40, 1836–1845.

Dawson, B., Irish, D., Toogood, G., 1986. Vibrational spectral studies of solutions at elevated temperatures and pressures. 8. A raman spectral study of ammonium hydrogen sulfate solutions and the hydrogen sulfate-sulfate equilibrium. The Journal of Physical Chemistry 90, 334–341.

De Laat, J., Le, T.G., 2005. Kinetics and modeling of the Fe(III)/H_2O_2 system in the presence of sulfate in acidic aqueous solutions. Environmental Science & Technology 39, 1811–1818.

Dickson, A.G., Wesolowski, D.J., Palmer, D.A., Mesmer, R.E., 1990. Dissociation constant of bisulfate ion in aqueous sodium chloride solutions to 250°C. The Journal of Physical Chemistry 94, 7978–7985.

Dry, M.J., Bryson, A.W., 1988. Prediction of redox potential in concentrated iron sulphate solutions. Hydrometallurgy 21, 59–72.

Dutrizac, J.E., 1981. The dissolution of chalcopyrite in ferric sulfate and ferric chloride media. Metallurgical Transactions B 12, 371–378.

Dutrizac, J.E., Monhemius, A., 1986. Iron control in hydrometallurgy. Toronto, Canada, 19-22 Oct. 1986 , 1986Bibtex: dutrizac1986iron.

Eigen, M., Tamm, K., 1962. Sound absorption in electrolytes as a consequence of chemical relaxation. I. Relaxation theory of stepwise dissociation. Z. Elektrochem 66, 107–121. Bibtex: eigen1962sound.

Eysel, H.H., Lim, K., Oberle, C., 1988. Raman intensities and polarizability parameters (EOPs) of some oxo-anions of group V, VI and VII elements in aqueous solution: general trends. Journal of Molecular Structure 174, 35–40.

Filippou, D., Demopoulos, G.P., Papangelakis, V.G., 1995. Hydrogen ion activities and species distribution in mixed metal sulfate aqueous systems. AIChE Journal 41, 171–184.

Flynn, C.M., 1984. Hydrolysis of inorganic iron(III) salts. Chemical Reviews 84, 31–41.

Fogler, H., 2006. Elements of chemical reaction engineering. Prentice Hall PTR, Upper Saddle River NJ. 4th ed. edition.

Fonseca Guerra, C., Snijders, J.G., te Velde, G., Baerends, E.J., 1998. Towards an order-N DFT method. Theoretical Chemistry Accounts: Theory, Computation, and Modeling (Theoretica Chimica Acta) 99, 391–403.

Freiberg, J., 1975. The mechanism of iron catalyzed oxidation of SO_2 in oxygenated solutions. Atmospheric Environment (1967) 9, 661–672.

Fujita, K., Kimura, M., 1981. The Raman band shape and vibrational relaxation of the ν_1 mode of SO_4^{2-} in Na_2SO_4 and $(NH_4)_2SO_4$ aqueous solutions. Journal of Raman Spectroscopy 11, 108–111.

Furst, W., Renon, H., 1993. Representation of excess properties of electrolyte solutions using a new equation of state. AIChE Journal 39, 335–343.

Fuzzi, S., 1978. Study of iron (III) catalysed sulphur dioxide oxidation in aqueous solution over a wide range of pH. Atmospheric Environment 12, 1439–1442.

Garcia-Ochoa, F., Gomez, E., 2004. Theoretical prediction of gas-liquid mass transfer coefficient, specific area and hold-up in sparged stirred tanks. Chemical Engineering Science 59, 2489–2501.

Goldberg, R.N., Parker, V.B., 1985. Thermodynamics of solution of SO_2(g) in water and of aqueous sulfur dioxide. J. J. Res. Natl. Inst. Stand. Technol. 90, 341–358.

Gourich, B., Vial, C., El Azher, N., Belhaj Soulami, M., Ziyad, M., 2008. Influence of hydrodynamics and probe response on oxygen mass transfer measurements in a high aspect ratio bubble column reactor: Effect of the coalescence behaviour of the liquid phase. Biochemical Engineering Journal 39, 1–14.

Grenthe, I., Wanner, H., Osthols, E., 2000. TDB-2: Guidelines for the extrapolation to zero ionic strength. Nuclear Energy Agency in Organisation for Economic Co-operation and Development (OECD/NEA) .

Guggenheim, E.A., Turgeon, J.C., 1955. Specific interaction of ions. Transactions of the Faraday Society 51, 747.

Hackl, R.P., Dreisinger, D.B., Peters, E., King, J.A., 1995. Passivation of chalcopyrite during oxidative leaching in sulfate media. Hydrometallurgy 39, 25–48.

Handy, N.C., Cohen, A.J., 2001. Left-right correlation energy. Molecular Physics 99, 403–412.

Harris, D., Loew, G.H., Komornicki, A., 1997. Structure and relative spin-state energetics of $Fe(H_2O)_6^{3+}$: A comparison of UHF, Moller-Plesset, Nonlocal DFT, and semiempircal INDOS calculations. The Journal of Physical Chemistry A 101, 3959–3965.

Hefter, G., 2006. When spectroscopy fails - The measurement of ion pairing. Pure and applied chemistry 78, 1571–1586.

Helgeson, H.C., 1969. Thermodynamics of hydrothermal systems at elevated temperatures and pressures. American Journal of Science 267, 729–804.

Hogfeldt, E., 1982. Stability constants of metal-ion complexes : part A: inorganic ligands. International Union of Pure and Applied Chemistry, Pergamon Press, Oxford ;;New York. 1st ed. edition.

Holmes, H., Mesmer, R., 1992. Isopiestic studies of H_2SO_4(aq) at elevated temperatures: Thermodynamic properties. The Journal of Chemical Thermodynamics 24, 317–328.

Hunger, T., Lapicque, F., Storck, A., 1990. Thermodynamic equilibrium of diluted sulfur dioxide absorption into disodium sulfate or sulfuric acid electrolyte solutions. Journal of chemical and engineering data 35, 453–463.

Irish, D.E., Chen, H., 1970. Equilibriums and proton transfer in the bisulfate-sulfate system. The Journal of Physical Chemistry 74, 3796–3801.

Ismael, M.R.C., Carvalho, J.M.R., 2003. Iron recovery from sulphate leach liquors in zinc hydrometallurgy. Minerals Engineering 16, 31–39.

Izatt, R.M., Eatough, D., Christensen, J.J., Bartholomew, C.H., 1969. Calorimetrically determined logK, H, and S values for the interaction of sulphate ion with several bi-and ter-valent metal ions. J. Chem. Soc. A , 47–53.

Jarzecki, A., Anbar, A., Spiro, T., 2004. DFT analysis of $Fe(H_2O)_6^{3+}$ and $Fe(H_2O)_6^{2+}$ structure and vibrations; implications for isotope fractionation. The Journal of Physical Chemistry A 108, 2726–2732.

Jaumot, J., Gargallo, R., de Juan, A., Tauler, R., 2005. A graphical user-friendly interface for MCR-ALS: A new tool for multivariate curve resolution in MATLAB. Chemometrics and Intelligent Laboratory Systems 76, 101–110.

Jeffery, G., Bassett, J., Mendham, J., Denney, R., 1961. Vogel's yextbook of quantitative chemical analysis. Longman Scientific & Technical, Essex, England. 5th edition.

Johnson, D.B., Hallberg, K.B., 2005. Acid mine drainage remediation options: a review. Science of The Total Environment 338, 3–14.

Jones, M.W., Papangelakis, V.G., Steyl, J.D., 2009. Kieserite solubility in the aqueous $FeCl_3$ + $MgCl_2$ + HCl system between (338 and 378) k. Journal of Chemical Engineering Data 54, 1986–1990.

Kalman, E., Radnai, T., Palinkas, G., Hajdu, F., Vertes, A., 1988. Hydration of iron(II) ion in aqueous solutions. Electrochimica acta 33, 1223–1228.

Kanno, H., 1988. Hydrations of metal ions in aqueous electrolyte solutions: a raman study. The Journal of Physical Chemistry 92, 4232–4236.

Kao, C.F., 1979. Thermodynamic and kinetic studies of the iron-sulfite system by electrochemical methods. Ph.D. thesis. Columbia University.

Karraker, D.G., 1963. The kinetics of the reaction between sulfurous acid and ferric ion. Journal of Physical Chemistry 67, 871–874.

Kell, G.S., 1975. Density, thermal expansivity, and compressibility of liquid water from 0 to 150 °C: Correlations and tables for atmospheric pressure and saturation reviewed and expressed on 1968 temperature scale. Journal of Chemical & Engineering Data 20, 97–105.

Kestin, J., Sokolov, M., Wakeham, W.A., 1978. Viscosity of liquid water in the range -8°C to 150°C. Journal of Physical and Chemical Reference Data 7, 941–948.

Kinnunen, P.M., Heimala, S., Riekkola-Vanhanen, M.L., Puhakka, J., 2006. Chalcopyrite concentrate leaching with biologically produced ferric sulphate. Bioresource Technology 97, 1727–1734.

Klamt, A., 2005. COSMO-RS: From Quantum Chemistry to Fluid Phase Thermodynamics and Drug Design. Elsevier.

Knopf, D.A., Luo, B.P., Krieger, U.K., Koop, T., 2003. Thermodynamic dissociation constant of the bisulfate ion from raman and ion interaction modeling studies of aqueous sulfuric acid at low temperatures. The Journal of Physical Chemistry A 107, 4322–4332.

Kobylin, P., Kaskiala, T., Salminen, J., 2007. Modeling of H_2SO_4-$FeSO_4$-H_2O and H_2SO_4-$Fe_2(SO_4)_3$-H_2O systems for metallurgical applications. Industrial & Engineering Chemistry Research 46, 2601–2608.

Kohn, W., Sham, L.J., 1965. Self-consistent equations including exchange and correlation effects. Physical Review 140, A1133.

Kormanyos, B., Peintler, G., Nagy, A., Nagypal, I., 2008. Peculiar kinetics of the complex formation in the iron(III)-sulfate system. International Journal of Chemical Kinetics 40, 114–124.

Kraft, J., Van Eldik, R., 1989a. Kinetics and mechanism of the iron (III)-catalyzed autoxidation of sulfur(IV) oxides in aqueous solution. 2. Decomposition of transient iron(III)-sulfur(IV) complexes. Inorganic Chemistry 28, 2306–2312.

Kraft, J., Van Eldik, R., 1989b. Kinetics and mechanism of the iron(III)-catalyzed autoxidation of sulfur(IV) oxides in aqueous solution. 1. Formation of transient iron(III)-sulfur(IV) complexes. Inorganic Chemistry 28, 2297–2305.

Krissmann, J., Siddiqi, M.A., Lucas, K., 1997. Absorption of sulfur dioxide in dilute aqueous solutions of sulfuric and hydrochloric acid. Fluid Phase Equilibria 141, 221–233.

Krissmann, J., Siddiqi, M.A., Lucas, K., 2000. Improved thermochemical data for computation of phase and chemical equilibria in flue-gas/water systems. Fluid Phase Equilibria 169, 223–236.

Kuo, D., Kirk, D., Jia, C., 2006. The chemistry of aqueous S(IV)-Fe-O_2 system: state of the art. Journal of Sulfur Chemistry 27, 461–530.

Kuznetsov, D., 1941. Study of the equilibrium pressures of sulfur dioxide over water and aqueous solutions of sulfuric acid (transl.). Zh. Khim. Prom 18, 3–7.

Lagarias, J.C., Reeds, J.A., Wright, M.H., Wright, P.E., 1998. Convergence properties of the nelder-mead simplex method in low dimensions. SIAM Journal of Optimization 9, 112–147.

Laliberte, M., Cooper, W.E., 2004. Model for calculating the density of aqueous electrolyte solutions. Journal of Chemical & Engineering Data 49, 1141–1151.

Lebowitz, J.L., Percus, J.K., 1966. Mean spherical model for lattice gases with extended hard cores and continuum fluids. Physical Review 144, 251.

Lente, G., Fabian, I., 1998. The early phase of the iron (III)-sulfite ion reaction. Formation of a novel iron (III)-sulfito complex. Inorganic chemistry 37, 4204–4209.

Lente, G., Fabian, I., 2002. Kinetics and mechanism of the oxidation of sulfur(iv) by iron(iii) at metal ion excess. Journal of the Chemical Society, Dalton Transactions , 778.

Levenberg, K., 1944. A method for the solution of certain non-linear problems in least squares. The Quarterly of Applied Mathematics 2, 164–168.

Lewis, G.N., Randall, M., 1921. The activity coefficient of strong electrolytes. 1. Journal of the American Chemical Society 43, 1112–1154.

Lewis, I.R., Edwards, H., 2001. Handbook of Raman Spectroscopy: From the Research Laboratory to the Process Line. CRC Press.

Lindstrom, R.E., Wirth, H.E., 1969. Estimation of the bisulfate ion dissociation in solutions of sulfuric acid and sodium bisulfate. The Journal of Physical Chemistry 73, 218–223.

Linek, V., Vacek, V., 1981. Chemical engineering use of catalyzed sulfite oxidation kinetics for the determination of mass transfer characteristics of gas-liquid contactors. Chemical Engineering Science 36, 1747–1768.

Linke, W.F., Seidell, A., 1965. Solubilities: Inorganic and Metal-Organic Compounds; A Compilation of Solubility Data from the Periodical Literature. volume 2. American Chemical Society, Washington DC.

Liu, H., Papangelakis, V., Alam, M., Singh, G., 2003. Solubility of hematite in H_2SO_4 solutions at 230-270 °C. Canadian metallurgical quarterly 42, 199–207.

Liu, H., Papangelakis, V.G., 2005. Chemical modeling of high temperature aqueous processes. Hydrometallurgy 79, 48–61.

Lopes, L., de Laat, J., Legube, B., 2002. Charge transfer of iron(III) monomeric and oligomeric aqua hydroxo complexes: Semiempirical investigation into photoactivity. Inorganic Chemistry 41, 2505–2517.

Lund Myhre, C.E., Christensen, D.H., Nicolaisen, F.M., Nielsen, C.J., 2003. Spectroscopic study of aqueous H_2SO_4 at different temperatures and compositions: variations in dissociation and optical properties. The Journal of Physical Chemistry A 107, 1979–1991.

Magini, M., 1979. Solute structuring in aqueous iron(lIl) sulphate solutions. evidence for the formation of iron(III)-sulphate complexes. Journal of Chemical Physics 70, 317–324.

Magini, M., Caminiti, R., 1977. On the structure of highly concentrated iron(III) salt solutions. Journal of Inorganic and Nuclear Chemistry 39, 91–94.

Magini, M., Radnai, T., 1979. X-ray diffraction study of ferric chloride solutions and hydrated melt. analysis of the iron (III)-chloride complexes formation. The Journal of Chemical Physics 71, 4255.

Majzlan, J., Myneni, S.C.B., 2005. Speciation of iron and sulfat in acid waters. aqueous clusters to mineral precipitates. Environmental Science & Technology 39, 188–194.

Marcus, R.A., 1964. Chemical and electrochemical electron-transfer theory. Annual Review of Physical Chemistry 15, 155–196.

Marcus, Y., 1988. Ionic radii in aqueous solutions. Chemical Reviews 88, 1475–1498.

Marcus, Y., 2006. On the activity coefficients of charge-symmetrical ion pairs. Journal of Molecular Liquids 123, 8–13.

Martell, A.E., Smith, R.M., 1976. Critical stability constants: Inorganic complexes. Plenum Press.

MATLAB, 2014. Release 2014a. The MathWorks, Inc., Natick, Massachusetts, United States.

McCarthy, F., Brock, G., 2011. The direct nickel process - continued progress on the pathway to commercialisation, in: Proceedings of Nickel-Cobalt-Copper sessions at ALTA 2011, Perth, Australia.

McDonald, R., Whittington, B., 2008. Atmospheric acid leaching of nickel laterites review part i. sulphuric acid technologies. Hydrometallurgy 91, 35–55.

McMillan, W.G., Mayer, J.E., 1945. The statistical thermodynamics of multicomponent systems. Journal of Chemical Physics 13, 276.

McQuarrie, D.A., 2000. Statistical mechanics. University Science Books.

Meijer, E.J., Sprik, M., 1998. A density functional study of the addition of water to SO_3 in the gas phase and in aqueous solution. The Journal of Physical Chemistry A 102, 2893–2898.

Meissner, H.P., Kusik, C.L., 1973. Aqueous solutions of two or more strong electrolytes. vapor pressures and solubilities. Industrial & Engineering Chemistry Process Design and Development 12, 205–208.

Meyer, B., Ospina, M., Peter, L., 1980. Raman spectrometric determination of oxysulfur anions in aqueous systems. Analytica Chimica Acta 117, 301–311.

Mohr, P.J., Taylor, B.N., Newell, D.B., 2006. CODATA recommended values of the fundamental physical constants. National Institute of Standards and Technology .

Mudd, G.M., 2010. Global trends and environmental issues in nickel mining: Sulfides versus laterites. Ore Geology Reviews 38, 9–26.

Murata, K., Irish, D., Toogood, G., 1989. Vibrational spectral studies of solutions at elevated temperatures and pressures. 11. A Raman spectral study of aqueous iron(III) chloride solutions between 25 and 300 °C. Canadian Journal of Chemistry 67, 517–524.

Myers, J.A., Sandler, S.I., Wood, R.H., 2002. An equation of state for electrolyte solutions covering wide ranges of temperature, pressure, and composition. Industrial & engineering chemistry research 41, 3282–3297.

Nakamoto, K., 1997. Infrared and Raman Spectra of Inorganic and Coordination Compounds: Applications in coordination, organometallic, and bioinorganic chemistry. Wiley.

Ninkovic, R., Miladinovic, J., Todorovic, M., Gruji, S., Rard, J.A., 2007. Osmotic and activity coefficients of the $[x\mathrm{ZnCl_2}+(1-x)\mathrm{ZnSO_4}](\mathrm{aq})$ system at 298.15 K. Journal of Solution Chemistry 36, 405–435.

Norgate, T., Jahanshahi, S., 2010. Low grade ores - smelt, leach or concentrate? Minerals Engineering 23, 65–73.

Oykova, T., Balarew, C., 1974. Thermodynamic study of magnesium sulphate-ferrosulphate-water system at 25 °C. Comptes 'Rendus de l' Academmie Bulgare des Sciences 27, 1211–1214.

Pahlman, J.E., Khalafalla, S.E., 1988. Leaching of domestic manganese ores with dissolved SO_2. US Department of the Interior, Bureau of Mines.

Papangelakis, V., Blakey, B., Liao, H., 1994. Hematite solubility in sulphate process solutions, in: Hydrometallurgy. Springer, pp. 159–175.

Perdew, J.P., Burke, K., Wang, Y., 1996. Generalized gradient approximation for the exchange-correlation hole of a many-electron system. Physical Review B 54, 16533.

Perry, R.H., Green, D.W., Maloney, J.O., 1997. Perry's chemical engineers' handbook. McGraw-Hill.

Pitzer, K., 1991. Ion interaction approach: Theory and data correlation. Activity coefficients in electrolyte solutions., CRC Press, Boca Raton, FL, 2nd edition.

Pitzer, K.S., 1973. Thermodynamics of electrolytes. i. Theoretical basis and general equations. The Journal of Physical Chemistry 77, 268–277.

Pitzer, K.S., 1975. Thermodynamics of electrolytes. v. effects of higher-order electrostatic terms. Journal of Solution Chemistry 4, 249–265.

Pitzer, K.S., Mayorga, G., 1974a. Thermodynamics of electrolytes. III. activity and osmotic coefficients for 2-2 electrolytes. Journal of Solution Chemistry 3, 539–546.

Pitzer, K.S., Mayorga, G.B., 1974b. Thermodynamics of electrolytes. III. Activity and osmotic coefficients for 2-2 electrolytes. Journal of Solution Chemistry 3, 539–546.

Pitzer, K.S., Roy, R.N., Silvester, L.F., 1977. Thermodynamics of electrolytes. 7. sulfuric acid. Journal of the American Chemical Society 99, 4930–4936.

Pitzer, K.S., Wang, P., Rard, J.A., Clegg, S.L., 1999. Thermodynamics of electrolytes. 13. Ionic strength dependence of higher-order terms; equations for $CaCl_2$ and $MgCl_2$. Journal of Solution Chemistry 28, 265–282.

Pourbaix, M., Pourbaix, A., 1992. Potential-pH equilibrium diagrams for the system S-H_2O from 25 to 150°C: Influence of access of oxygen in sulphide solutions. Geochimica et Cosmochimica Acta 56, 3157–3178.

Prinsloo, F.F., Brandt, C., Lepentsiotis, V., Pienaar, J.J., van Eldik, R., 1997. Formation of transient iron(III)-sulfur(IV) complexes revisited. Application of rapid-scan techniques. Inorganic Chemistry 36, 119–121.

Pye, C.C., Rudolph, W.W., 2001. An ab initio and raman investigation of sulfate ion hydration. The Journal of Physical Chemistry A 105, 905–912.

Pye, C.C., Ziegler, T., 1999. An implementation of the conductor-like screening model of solvation within the Amsterdam Density Functional package. Theoretical Chemistry Accounts 101, 396–408.

Rard, J., Clegg, S., 1999. Isopiestic determination of the osmotic and activity coefficients of $z$$H_2SO_4$+$(1-z)$$MgSO_4$(aq) atT = 298.15 K. II. Results for z = (0.43040, 0.28758, and 0.14399) and analysis with Pitzer's model. The Journal of Chemical Thermodynamics 31, 399–429.

Reardon, E.J., Beckie, R.D., 1987. Modelling chemical equilibria of acid mine-drainage: The $FeSO_4$-H_2SO_4-H_2O system. Geochimica et Cosmochimica Acta 51, 2355–2368.

Robinson, R.A., Stokes, R.H., 1970. Electrolyte Solutions. Butterworths, London. 2nd edition.

Rodriguez-Sevilla, J., Alvarez, M., Liminana, G., Diaz, M.C., 2002. Dilute SO_2 absorption equilibria in aqueous HCl and NaCl solutions at 298.15 K. Journal of Chemical & Engineering Data 47, 1339–1345.

Roine, A., 2002. Outokumpu HSC chemistry for windows: chemical reaction and equilibrium software with extensive thermochemical database. Pori, Finland: Outokumpu Bibtex: roine1999outokumpu.

Rosenblatt, G., 1981. Estimation of activity coefficients in concentrated sulfite-sulfate solutions. AIChE Journal 27, 619–626.

Rudolph, W., 1996. Structure and dissociation of the hydrogen sulphate ion in aqueous solution over a broad temperature range: a Raman study. Zeitschrift fur Physikalische Chemie 194, 73–95.

Rudolph, W., Brooker, M.H., Tremaine, P.R., 1997. Raman spectroscopic investigation of aqueous $FeSO_4$ in neutral and acidic solutions from 25 °C to 303 °C: inner- and outer-sphere complexes. Journal of Solution Chemistry 26, 757–777.

Rudolph, W., Irmer, G., 1994. Raman and infrared spectroscopic investigation of contact ion pair formation in aqueous cadmium sulfate solutions. Journal of solution chemistry 23, 663–684.

Rudolph, W.W., 2010. Raman and infrared spectroscopic investigation of speciation in $BeSO_4$(aq). Journal of solution chemistry 39, 1039–1059.

Rudolph, W.W., Brooker, M.H., Tremaine, P.R., 1999. Raman spectroscopy of aqueous $ZnSO_4$ solutions under hydrothermal conditions: Solubility, hydrolysis, and sulfate ion pairing. Journal of solution chemistry 28, 621–630.

Rudolph, W.W., Irmer, G., Hefter, G.T., 2003. Raman spectroscopic investigation of speciation in $MgSO_4$(aq). Physical Chemistry Chemical Physics 5, 5253.

Rudolph, W.W., Mason, R., 2001. Study of aqueous $Al_2(SO_4)_3$ solution under hydrothermal conditions: sulfate ion pairing, hydrolysis, and formation of hydronium alunite. Journal of solution chemistry 30, 527–548.

Rudolph, W.W., Pye, C.C., 1999. Zinc (II) hydration in aqueous solution. a raman spectroscopic investigation and an ab-initio molecular orbital study. Physical Chemistry Chemical Physics 1, 4583–4593.

Rumpf, B., Maurer, G., 1993. Solubility of sulfur dioxide in aqueous solutions of sodium- and ammonium sulfate at temperatures from 313.15 K to 393.15 K and pressures up to 3.5 MPa. Fluid Phase Equilibria 91, 113–131.

Rumyantsev, A.V., Hagemann, S., Moog, H.C., 2004. Isopiestic investigation of the systems $Fe_2(SO_4)_3$-H_2SO_4-H_2O, $FeCl_3$-H_2O, and Fe(III)-(Na, K, Mg, Ca)Cl_n-H_2O at 298.15 K. Zeitschrift für Physikalische Chemie 218, 1089–1127.

Sako, T., Wu, A.H., Prausnitz, J.M., 1989. A cubic equation of state for high-pressure phase equilibria of mixtures containing polymers and volatile fluids. Journal of applied polymer science 38, 1839–1858.

Sapieszko, R.S., Patel, R.C., Matijevic, E., 1977. Ferric hydrous oxide sols. 2. Thermodynamics of aqueous hydroxo and sulfato ferric complexes. The Journal of Physical Chemistry 81, 1061–1068.

Schrodle, S., Rudolph, W.W., Hefter, G., Buchner, R., 2007. Ion association and hydration in 3:2 electrolyte solutions by dielectric spectroscopy: Aluminum sulfate. Geochimica et Cosmochimica Acta 71, 5287–5300.

Schrodle, S., Wachter, W., Buchner, R., Hefter, G., 2008. Scandium sulfate complexation in aqueous solution by dielectric relaxation spectroscopy. Inorganic Chemistry 47, 8619–8628.

Schulze-Messing, J., Alexander, D., Sole, K., Steyl, J., Nicol, M., Gaylard, P., 2007. An empirical rate equation for the partial removal of manganese from solution using a gas mixture of sulfur dioxide and oxygen. Hydrometallurgy 86, 37–43.

SCM, 2013. Theoretical chemistry. Vrije Universiteit, Amsterdam, The Netherlands, see http://www. scm. com .

Senanayake, G., Childs, J., Akerstrom, B., Pugaev, D., 2011. Reductive acid leaching of laterite and metal oxides - A review with new data for Fe(Ni,Co)OOH and a limonitic ore. Hydrometallurgy 110, 13–32.

Shannon, R.D., 1976. Revised effective ionic radii and systematic studies of interatomic distances in halides and chalcogenides. Acta Crystallographica Section A 32, 751–767.

Shock, E.L., Helgeson, H.C., 1988. Calculation of the thermodynamic and transport properties of aqueous species at high pressures and temperatures: Correlation algorithms for ionic species and equation of state predictions to 5 kb and 1000 °C. Geochimica et Cosmochimica Acta 52, 2009–2036.

Shock, E.L., Sassani, D.C., Willis, M., Sverjensky, D.A., 1997. Inorganic species in geologic fluids: Correlations among standard molal thermodynamic properties of aqueous ions and hydroxide complexes. Geochimica et Cosmochimica Acta 61, 907–950.

Smit, J., Steyl, J., 2006. Leaching process in the presence of hydrochloric acid for the recovery of a valuable metal from an ore. WIPO, WO/2006/043158, Anglo Operations Limited .

Smit, J.T., Steyl, J.D.T., Pelser, M., 2011. Process for the recovery of metals from an iron-containing ore. WIPO, WO/2006/043158, Anglo Operations Limited .

Smit, J.T., Steyl, J.D.T., Pelser, M., 2012. Process for the recovery of metals such as nickel from an iron-containing ore by leaching with acidic sulfate solution. EP2462249 A2, Anglo Operations Limited .

Sobron, P., Rull, F., Sobron, F., Sanz, A., Medina, J., Nielsen, C., 2007. Modeling the physico-chemistry of acid sulfate waters through raman spectroscopy of the system $FeSO_4$-H_2SO_4-H_2O. Journal of Raman Spectroscopy 38, 1127–1132.

Stefansson, A., 2007. Iron(III) hydrolysis and solubility at 25 °C. Environmental Science & Technology 41, 6117–6123.

Stefansson, A., Seward, T.M., 2008. A spectrophotometric study of iron(III) hydrolysis in aqueous solutions to 200 °C. Chemical Geology 249, 227–235.

Stenstrom, M.K., Gilbert, R., 1981. Effects of alpha, beta and theta factor upon the design, specification and operation of aeration systems. Water Research 15, 643–654.

Steyl, J., 2009. Kinetic modelling of chemical processes in acid solution at T< 200°C. (i) Thermodynamics and speciation in H_2SO_4-Metal(II)SO_4-H_2O systems., in: SAIMM Hydrometallurgy Conference 2009, pp. 401–443.

Steyl, J., 2012. Simulating the medium temperature chalcopyrite oxidation system in batch and continuous autoclaves. Ph.D. thesis. Stellenbosch University. Stellenbosch, South Africa.

Steyl, J.D.T., Smit, J.T., 2008. Producing a metal like zinc from sulphide ores by chloride leaching and electrowinning. WIPO, WO2008139412 A1, Anglo Operations Limited .

Stipp, S.L., 1990. Speciation in the iron(II)-iron(III)-sulfate-water system at 25 °C and low pH: Sensitivity of an equilibrium model to uncertainties. Environmental Science & Technology 24, 699–706.

Swart, M., Ehlers, A.W., Lammertsma, K., 2004a. Performance of the OPBE exchange-correlation functional. Molecular Physics 102, 2467–2474.

Swart, M., Groenhof, A.R., Ehlers, A.W., Lammertsma, K., 2004b. Validation of exchange-correlation functionals for spin states of iron complexes. The Journal of Physical Chemistry A 108, 5479–5483.

Sweeton, F.H., Baes Jr., C.F., 1970. The solubility of magnetite and hydrolysis of ferrous ion in aqueous solutions at elevated temperatures. The Journal of Chemical Thermodynamics 2, 479–500.

Systems, O.L.I., 2006. Aqueous modeling course and workshop, New Jersey. p. 112.

Thomsen, K., 2008. Electrolyte solutions: Thermodynamics, crystallisation, separation methods - course notes.

Tosca, N.J., Smirnov, A., McLennan, S.M., 2007. Application of the Pitzer ion interaction model to isopiestic data for the $Fe_2(SO_4)_3$-H_2SO_4-H_2O system at 298.15 and 323.15 K. Geochimica et Cosmochimica Acta 71, 2680–2698.

Turner, D.J., 1972. Raman spectral study of bisulphate ion hydration. Journal of the Chemical Society, Faraday Transactions 2: Molecular and Chemical Physics 68, 643–648.

Vchirawongkwin, V., Kritayakornupong, C., Rode, B.M., 2010. Structural and dynamical properties and vibrational spectra of bisulfate ion in water: A study by ab initio quantum mechanical charge field molecular dynamics. The Journal of Physical Chemistry. B 114, 11561–11569.

Vchirawongkwin, V., Rode, B.M., Persson, I., 2007. Structure and dynamics of sulfate ion in aqueous solution an ab initio QMCF MD simulation and large angle X-ray scattering study. The Journal of Physical Chemistry B 111, 4150–4155.

Velazquez-Rivera, M., Palmer, D., Kettler, R., 2006. Isopiestic measurement of the osmotic coefficients of aqueous $x H_2SO_4 + (1-x)Fe_2(SO_4)_3$ solutions at 298.15 and 323.15 K. Journal of Solution Chemistry 35, 1699–1730.

te Velde, G., Bickelhaupt, F.M., Baerends, E.J., Fonseca Guerra, C., van Gisbergen, S.J.A., Snijders, J.G., Ziegler, T., 2001. Chemistry with ADF. Journal of Computational Chemistry 22, 931–967.

Wagman, D.D., Evans, W.H., Parker, V.B., Schumm, R.H., Halow, I., 1982. The NBS tables of chemical thermodynamic properties. Selected values for inorganic and C1 and C2 organic substances in SI units. Technical Report. DTIC Document.

Wang, P., Anderko, A., Young, R.D., 2002. A speciation-based model for mixed-solvent electrolyte systems. Fluid Phase Equilibria 203, 141–176.

Wang, P., Springer, R., Anderko, A., Young, R., 2004. Modeling phase equilibria and speciation in mixed-solvent electrolyte systems. Fluid phase equilibria 222, 11–17.

Wang, S., 2005. Copper leaching from chalcopyrite concentrates. JOM 57, 48–51.

Weir, D., Kerfoot, D., Scheie, H., 1982. Removal of selenium (IV) and (VI) from acidic copper sulphate solutions. Google Patents. US Patent 4,330,508.

Welham, N.J., Malatt, K.A., Vukcevic, S., 2000. The stability of iron phases presently used for disposal from metallurgical systems - a review. Minerals Engineering 13, 911–931.

Whiteker, R.A., Davidson, N., 1953. Ion-exchange and spectrophotometric investigation of iron(III) sulfate complex ions. Journal of the American Chemical Society 75, 3081–3085.

Wildner, M., Giester, G., 1991. The crystal structures of kieserite-type compounds. I. Crystal structures of Me(II)$SO_4 \cdot H_2O$ (Me=Mn,Fe,Co,Ni,Zn). Neues Jahrbuch für Mineralogie Monatshefte , 296–306.

Wilson, G.M., 1964. Vapor-liquid equilibrium. XI. a new expression for the excess free energy of mixing. Journal of the American Chemical Society 86, 127–130.

Wright, M.R., 2007. An Introduction to Aqueous Electrolyte Solutions. Wiley and Sons Limited, Chichester.

Xia, J., Rumpf, B., Maurer, G., 1999. The solubility of sulfur dioxide in aqueous solutions of sodium chloride and ammonium chloride in the temperature range from 313 K to 393 K at pressures up to 3.7 MPa: experimental results and comparison with correlations. Fluid Phase Equilibria 165, 99–119.

Yue, G., Zhao, L., Olvera, O.G., Asselin, E., 2014. Speciation of the H_2SO_4-$Fe_2(SO_4)_3$-$FeSO_4$-H_2O system and development of an expression to predict the redox potential of the Fe^{3+}/Fe^{2+} couple up to 150 °C. Hydrometallurgy 147-148, 196–209.

Zemaitis, J.F., 1980. Predicting vapor-liquid-solid equilibria in multicomponent aqueous solutions of electrolytes. In: Newman, S.A., Barner, H.E., Klein, M., Sandler, S.I. (Eds.), Thermodynamics of Aqueous Systems with Industrial Applications, ACS Symposium Series, American Chemical Society, Washington DC, pp. 227–246.

Zhang, H., Zhang, Y.H., Wang, F., 2009. Theoretical understanding on the ν_1-SO_4^{2-} band perturbed by the formation of magnesium sulfate ion pairs. Journal of computational chemistry 30, 493–503.

Zhang, W., 2000. SO_2/O_2 as an oxidant in hydrometallurgy. PhD thesis. Murdoch University. Perth, Australia.

Zhang, W., Muir, D.M., Singh, P., 2000a. Iron(II) oxidation by SO_2/O_2 in acidic media: Part II. Effect of copper. Hydrometallurgy 58, 117–125.

Zhang, W., Singh, P., Muir, D., 2000b. Iron(II) oxidation by SO_2/O_2 in acidic media:: Part i. Kinetics and mechanism. Hydrometallurgy 55, 229–245.

Zhang, W., Singh, P., Muir, D.M., 2000c. SO_2/O_2 as an oxidant in hydrometallurgy. Minerals Engineering 13, 1319–1328.